Journal of
Seismic Exploration

ISSN: 0963-0651

# Joint PP- and PS-wave amplitude variation with angle inversion for thin interbeds

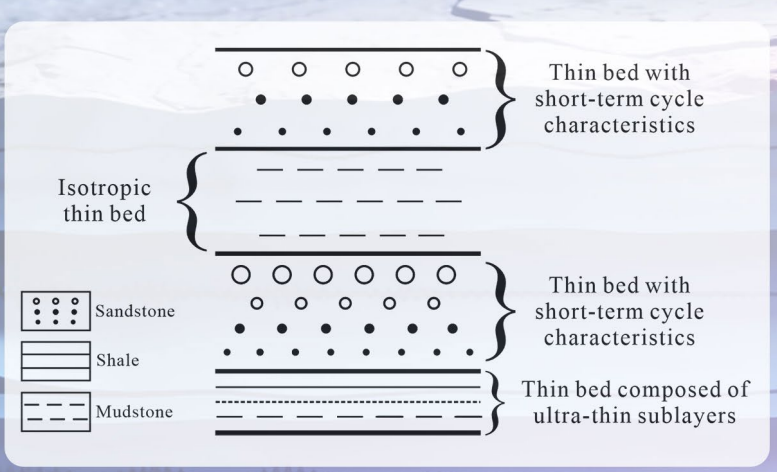


Sedimentary mode of a thin interbed containing thin VTI beds

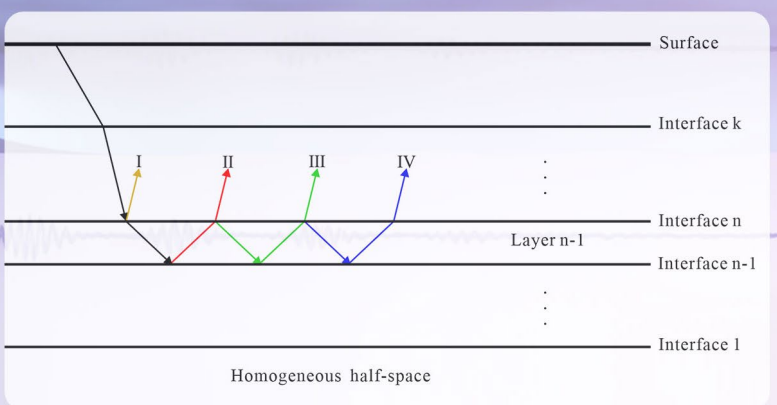


Wave propagation in a thin interbed model

Volume 35 · Issue 1
February 2026

ACCSCIENCE PUBLISHING

State Key Laboratory for Fine Exploration and Intelligent Development of Coal Resources

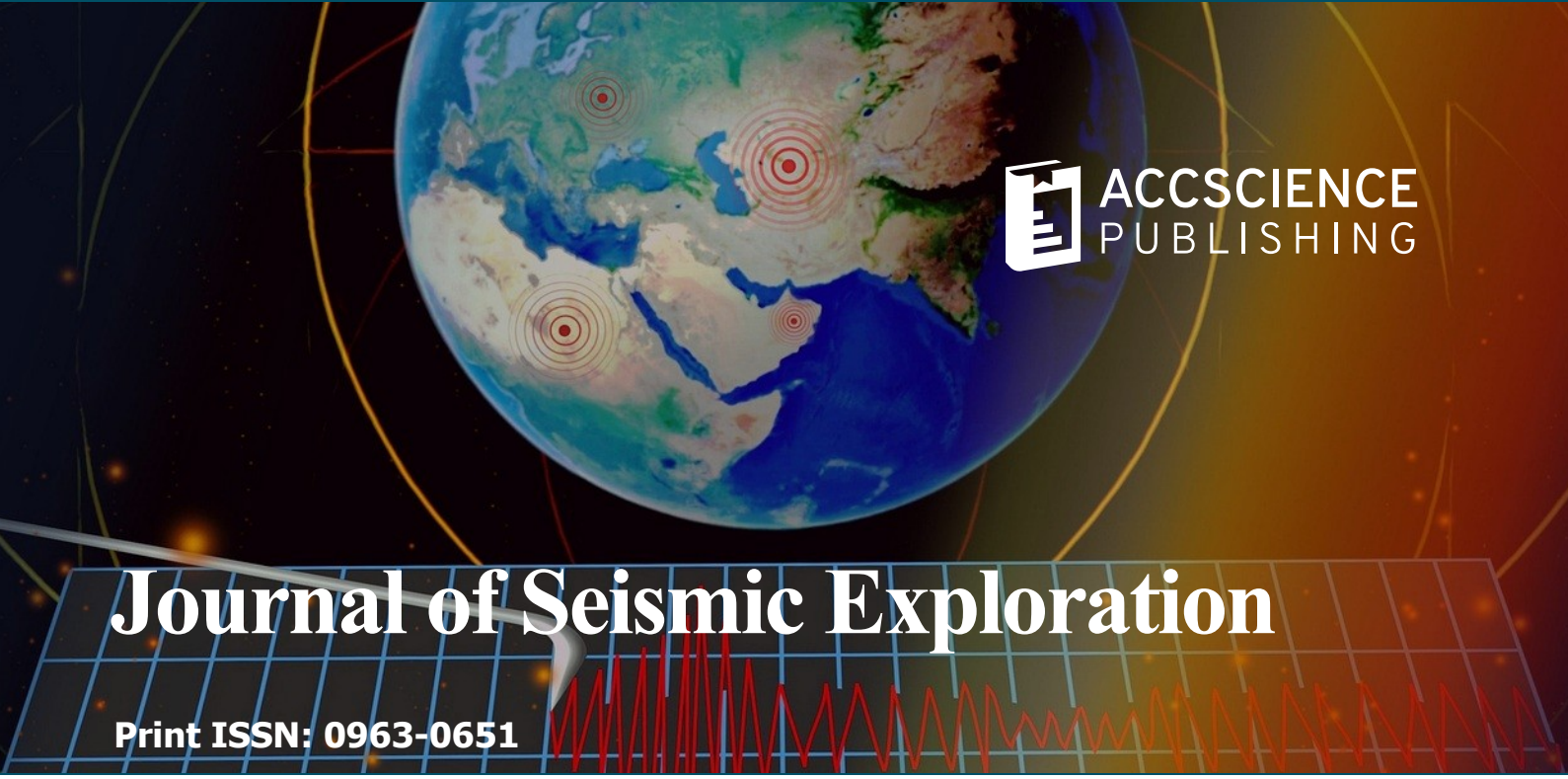

# Journal of Seismic Exploration

Print ISSN: 0963-0651

***The Journal of Seismic Exploration (JSE)*** is an international medium for the publication of research in seismic modeling, processing, inversion, interpretation, field techniques, borehole techniques, tomography, instrumentation and software. The aim and goal of JSE is to serve the interests and objectives of seismic petroleum exploration. All seismic processing methods have assumptions and prerequisites- and when they are satisfied methods are effective-and when they are violated methods become ineffective and can fail. The latter contributes to drilling dry hole exploration wells and suboptimal development wells.

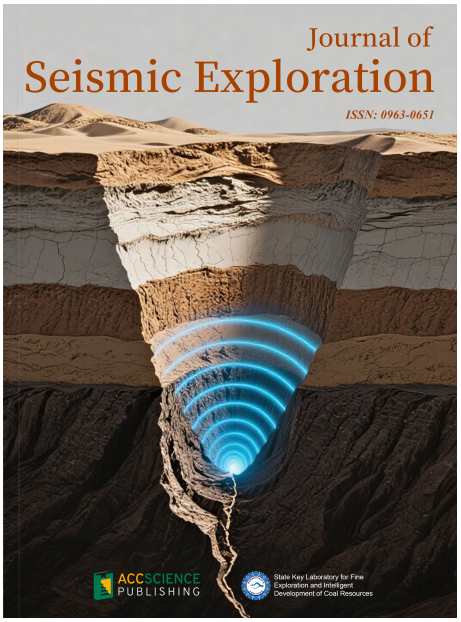


## About the Publisher

AccScience Publishing is a publishing company based in Singapore. We publish a range of high-quality, open-access, peer-reviewed journals and books from a broad spectrum of disciplines.

Contact Us

**Managing Editor**
jse.office@accscience.sg

AccScience Publishing
9 Raffles Place, Republic Plaza 1 #06-00 Singapore 048619.

Volume 35 • Issue 1 • 2026
ISSN 0963-0651 (print)

# Journal of Seismic Exploration

**Editors-in-Chief**

**Suping Peng**
*State Key Laboratory for Fine Exploration and Intelligent Development of Coal Resources*

**Arthur B. Weglein**
*University of Houston*

ACCSCIENCE PUBLISHING

Access Science Without Barriers

**Full issue copyright © 2026 AccScience Publishing**
All rights reserved. Without permission in writing from the publisher, this full issue publication in its entirety may not be reproduced or transmitted for commercial purposes in any form or by any means, electronic or mechanical, including photocopying, recording, or any information storage and retrieval system. Permissions may be sought from jse.office@accscience.sg

**Article copyright © Respective Author(s)**
See articles for copyright year. All articles in this full issue publication are open-access. There are no restrictions in the distribution and reproduction of individual articles, provided the original work is properly cited. However, permission to reuse copyrighted materials of an article for commercial purposes is applicable if the article is licensed under Creative Commons Attribution-NonCommercial License. Check the specific license before reusing.

*JOURNAL OF SEISMIC EXPLORATION*

ISSN: 0963-0651 (print)

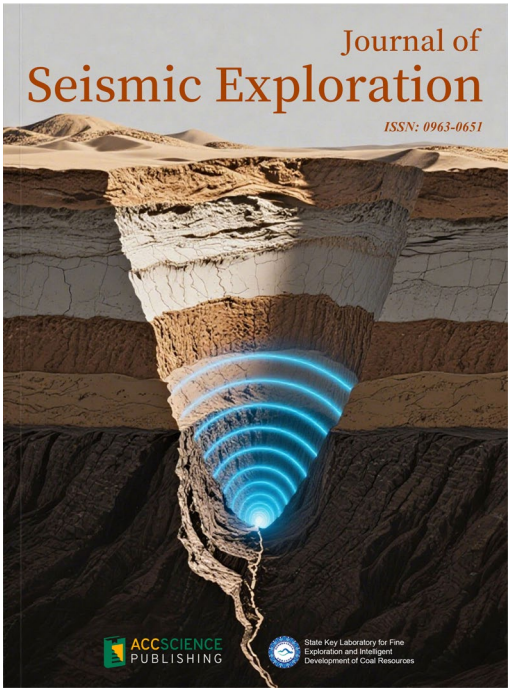


**Editorial and Production Credits**

Publisher: AccScience Publishing
Managing Editor: Gary Liu
Production Editor: Lim Mingyuan
Article Layout and Typeset: Sinjore Technologies (India)

For all advertising queries, contact jse.office@accscience.sg

**Supplementary file**

Supplementary files of articles can be obtained at https://accscience.com/journal/JSE/35/1.

**Disclaimer**

AccScience Publishing is not liable to the statements, perspectives, and opinions contained in the publications. The appearance of advertisements in the journal shall not be construed as a warranty, endorsement, or approval of the products or services advertised and/or the safety thereof. AccScience Publishing disclaims responsibility for any injury to persons or property resulting from any ideas or products referred to in the publications or advertisements. AccScience Publishing remains neutral with regard to jurisdictional claims in published maps and institutional affiliations.

Journal of Seismic Exploration

Editorial Board


## Editors-in-Chief

Suping Peng
Arthur B. Weglein

## Executive Editor-in-Chief

Jing Ba

## Editorial Board Members*

Mauricio Sacchi
Ilya Tsvankin
Li-Yun Fu
Boris Gurevich
José M. Carcione
Haijiang Zhang
Jun Matsushima
Fabio Trippetta
Qizhen Du
Lasse Amundsen
Jingyi Chen
Yangkang Chen
Lin Chen
Vladimir Cheverda
Eduardo Filpo
Doug Foster
Bill N. Goodway
Songfeng Guo
Zhiqi Guo
Cory Hoelting
Morten Jakobsen
Gilles Lambaré
Evgeny Landa
Jing Li
Huailiang Li
Chih-Ping Lin
José Eduardo M. Lira
Yang Liu
Jianwei Ma
George McMechan
Mark A. Meier
Roman Pevzner
Flavio Poletto
J. Germán Rubino
Mrinal K. Sen
Serge A. Shapiro
Changsoo Shin
Juan I. Soto
Paul L. Stoffa
Walter Söllner
Leon Thomsen
Umberta Tinivella
Peter Traynin
Arie Verdel
Dirk Jacob Eric Verschuur
Xiujuan Wang
Yibo Wang
Jincai Zhang
Lele Zhang
Gulan Zhang
Wei Zhang
Huai Zhang
Fons ten Kroode

## Early Career Editorial Board

Cong Luo
Xintong Dong
Fei Gong
Qiang Guo
Guangtan Huang
Zhongxiao Li
Xingye Liu
Shaoyong Liu
Xinpeng Pan
Yingming Qu
Xiaokai Wang
Haibo Wu
Pan Zhang
Sheng Zhang

ACCSCIENCE PUBLISHING

Volume 35 | Issue 1 | 2026 | Page 1 – 299 |

**Journal of Seismic Exploration**

https://accscience.com/journal/JSE

# CONTENTS

**REVIEW ARTICLE**

**1** **Optimizing 3D seismic parameters in congested oil fields: A systematic and bibliometric review of research progress and challenges**
*Frank O. Ofowena, Akhmal Sidek, Yasir Bashir, Mingtao Nie*

**ARTICLES**

**14** **U-STDRNet: A unified model integrating swin transformer and residual dense network for seismic image super-resolution and denoising**
*Mingliao Wu, Juan Wu, Min Bai, Haiyu Li, Zhixian Gui, Guangtan Huang*

**33** **Thermal damage factors based on thermally induced wave-velocity variation in oil sands**
*Hui Qi, Jing Ba, Wenhao Xu, Yuanyuan Huo, Jishun Pan, Qingchun Jiang, Congsheng Bian*

**46** **Prediction of fracture and vug parameters in carbonate reservoirs using a combined T-GNO-PINN approach**
*Yiru Du, Guoqing Chen, Cong Pang, Tianwen Zhao*

**66** **Joint PP- and PS-wave amplitude variation with angle inversion for thin interbeds**
*Peidong Huang, Jun Lu, Chun Yang, Zhe Yang, Wei Yang*

**83** **Subsurface imaging based on polarization analysis of microtremor Rayleigh waves**
*Qingling Du, Qian Xu, Nan Guo, Shuai Liu, Shijie Liu, Denghui Gao*

**101** **Microtremor investigation and geological verification of the eastern segment, north margin active fault of Hami Basin, Xinjiang, China**
*Xu Song, Guanghong Ju, Jun Shen*

**119** **Identification and characterization of fractured cavities in carbonate reservoirs using Swin-UNet transformer and seismic attribute compression fusion**
*Yunhao Cui, Yuhua Chen, Chao Xu, Yaping Huang, Qiang Guo, Zhiqiang Lu, Zhanpeng Chen, Yuwen Qian*

**139** **High-precision full-waveform inversion velocity modeling and broadband processing for a deepwater exploration of the South China Sea**
*Wei Liu, Yi Liao, Jie Cui, Ning Zhang, Guo Dong Zhang, Zi Jing Gong, Rong Li, Lian Lian Liu, Miaoyang Yuan*

**151** **Inversion model combination for microseismic source positioning with Multi-Objective Grasshopper Optimization Algorithm**
*Cong Pang, Tianwen Zhao, Guoqing Chen, Sirui Liu, Xingxing Li, Ya Xiang, Piyapatr Busababodhin*

**171** **A novel method for low-frequency quality control of seismic vibrator ground force**
*Mingtao Nie, Zhouhong Wei, Tao Fang, Xiaolong Jiang, Yongan Xu, Yang Liu, Yongfei Qi*

**184** **Fault identification and enhancement using residual U-Net: Application to field seismic data**
*Jianhua Wang, Cong Niu, Yandong Wang, Yun Ling, Di Wang, Xiuping Jiang, Chenshuo Yuan*

**200** **Generalized Gaussian distribution-based pre-stack inversion: A case study of channel sands in the Lianggaoshan Formation, Sichuan Basin**
*Meng Yuan, Zhiwei Miao, Lei Pan, Jianlong Su, Chang Sun*

**221** **Convolutional autoencoder with local wavefield characteristic constraint for suppressing near-surface seismic scattered waves**
*Daling Hou, Jixiang Xu, Meng Li*

**237** **Unscaled generalized S-transform and its applications on seismic attenuation delineation: A case study in the Ordos Basin, Northwest China**
*Wenlong Jiao, Naihao Liu, Yongxiang Jiang, Jun Yang, Wei Zhao*

**251** **Adaptive learned iterative shrinkage-thresholding algorithm combined with a physics-driven self-supervised method for sparse spike deconvolution**
*Shunhao Hu, Shulin Pan, Ziyu Qin, Yinghe Wu, Yaojie Chen*

**269** **A physics-constrained autoencoder for full-waveform inversion using axial self-attention**
*Yunbo Niu, Yingming Qu, Zhenchun Li*

**282** **A pre-trained dictionary learning framework combined with projections onto convex sets for seismic data reconstruction and denoising**
*Jianlei Zhang, Bo Yang, Min Bai, Xilin Qin, Baobin Wang, Zhen Zou, Boyuan Lv*

ACCSCIENCE PUBLISHING

Journal of Seismic Exploration

REVIEW ARTICLE

# Optimizing 3D seismic parameters in congested oil fields: A systematic and bibliometric review of research progress and challenges

**Frank O. Ofowena[1], Akhmal Sidek[1]*, Yasir Bashir[2], and Mingtao Nie[3]**

[1]Department of Petroleum Engineering, Faculty of Chemical and Energy Engineering, Universiti Teknologi Malaysia, Johor Bahru, Johor, Malaysia

[2]Geophysical Engineering, Faculty of Mines, Istanbul Technical University, Istanbul, Turkey

[3]BGP, China National Petroleum Corporation, Zhuozhou, Hebei, China

## Abstract

Three-dimensional (3D) seismic parameter optimization has become an essential component of subsurface imaging, especially in oil fields where space, safety, and environmental restrictions limit conventional survey design. This study critically reviews and synthesizes 87 English-language publications on 3D seismic parameter optimization retrieved from the Scopus database. The analysis combined a systematic literature review with bibliometric mapping, using the Preferred Reporting Items for Systematic Reviews and Meta-Analyses guidelines and Biblioshiny software to identify thematic patterns, research clusters, and methodological gaps. The results show that global research on 3D seismic optimization has grown steadily from 2003 to 2025, reflecting an increasing emphasis on survey efficiency and sustainable exploration. Early studies focused on geometric configuration and fold distribution, whereas recent works integrate environmental safety, vibration control, and cost efficiency. Three major thematic clusters were identified: Geometric and operational optimization, congestion and environmental management, and the integration of emerging sensing and modeling technologies. Despite this progress, most studies lack standardized congestion metrics, quantitative vibration thresholds, and comprehensive economic evaluations. The review concludes that 3D seismic optimization has evolved into a multidisciplinary framework that connects geometry, environmental protection, and operational safety. Future research should adopt measurable congestion indices, integrate distributed acoustic sensing technologies, and strengthen academic–industry collaboration to promote reproducible, cost-effective, and environmentally responsible seismic survey design.

***Keywords:*** 3D seismic optimization; Survey design; Congested oil fields; Vibration control; Sustainable exploration

***Corresponding author:**
Akhmal Sidek
(akhmalsidek@utm.my)

**Citation:** Ofowena FO, Sidek A, Bashir Y, Nie M. Optimizing 3D seismic parameters in congested oil fields: A systematic and bibliometric review of research progress and challenges. *J Seismic Explor*. 2026;35(1):1-13.
doi: 10.36922/JSE025430093

**Received:** October 23, 2025

**Revised:** January 12, 2026

**Accepted:** January 13, 2026

**Published online:** February 26, 2026

**Copyright:** © 2026 Author(s). This is an Open-Access article distributed under the terms of the Creative Commons Attribution License, permitting distribution, and reproduction in any medium, provided the original work is properly cited.

**Publisher's Note:** AccScience Publishing remains neutral with regard to jurisdictional claims in published maps and institutional affiliations.

## 1. Introduction

Three-dimensional (3D) seismic acquisition is a central method for imaging subsurface formations and supporting hydrocarbon exploration, but in complex and mature fields, the success of seismic acquisition relies on rigorous design and appropriate constraints on acquisition parameters. The present study argues that 3D survey design must be treated as an integrated optimization problem that links field geometry, operational constraints, and reservoir objectives into a single, coherent framework for exploration and development.

The effectiveness of 3D seismic acquisition depends strongly on the design of acquisition parameters, such as source spacing, receiver geometry, offset distribution, and azimuthal coverage. In congested oil fields, where surface access is limited by wells, pipelines, facilities, roads, and environmentally sensitive zones, conventional survey design approaches often fail to deliver adequate coverage and imaging reliability.

Although numerous studies have investigated 3D seismic parameter optimization, existing research is fragmented across geophysics, petroleum engineering, and environmental management disciplines. Numerous studies focus narrowly on geometry improvement without explicitly accounting for operational restrictions, vibration safety limits, or cost implications. As a result, there is no unified framework that connects bibliometric evidence, systematic review outcomes, and quantitative optimization constraints for congested environments.

This study addresses this gap by developing a structured and reproducible synthesis of research on 3D seismic parameter optimization in congested oil fields. Using a combined systematic literature review (SLR) and bibliometric analysis based on 87 Scopus-indexed publications, our review organizes prior studies into data-driven thematic clusters. It further proposes a measurable congestion index (CI) and a multi-objective optimization formulation that jointly considers imaging quality, peak particle velocity limits, and acquisition cost.

The current study offers three important contributions to research on seismic parameter optimization. First, it establishes a bibliometric-guided classification of optimization research that links keyword clusters directly to thematic synthesis. Second, it introduces a quantitative definition of congestion suitable for systematic comparison across fields. Third, it proposes a prototype multi-objective framework for seismic survey design under operational and safety constraints.

### 1.1. Role of 3D seismic acquisition

3D seismic acquisition has become one of the most dependable tools for imaging subsurface formations and guiding hydrocarbon exploration. This information allows geoscientists to accurately interpret subsurface structures, delineate hydrocarbon-bearing zones, and plan drilling programs that maintain high safety standards and operational efficiency.[1,2] Over the years, numerous studies have established that the success of 3D seismic surveys depends largely on how the acquisition parameters are designed.

### 1.2. Foundations of acquisition parameter design

Early work established that the effectiveness of 3D seismic surveys depends strongly on acquisition geometry and associated parameter choices. Vermeer[3] showed that source spacing, receiver layout, and fold distribution govern subsurface illumination and control the reliability of structural and stratigraphic interpretation, thereby defining optimal geometry as a primary condition for high-resolution imaging and operational efficiency. Building on these principles, later studies have formalized survey design as an optimization task in which parameter selection aims to balance image quality, cost, and feasibility.

### 1.3. Developments in optimization strategies

Recent contributions have proposed systematic methods to improve the acquisition parameters. Santos *et al.*[4] proposed an algorithm that enhances the selection of acquisition parameters by reducing redundancy and promoting uniform spatial coverage. Subsequent works have refined these concepts through simulation and reservoir modeling, showing that an optimized design can improve the continuity of reflections and the clarity of complex geological features.[5,6] This progression has strengthened the connection between field geometry and data interpretation, emphasizing that well-planned surveys can enhance data quality and reduce uncertainty in reservoir characterization. These studies collectively support the view that careful parameter optimization can enhance seismic resolution while controlling survey cost and execution risk.

### 1.4. Challenges in congested oil fields

In practice, optimizing 3D seismic parameters becomes increasingly complicated in congested oil fields. In these environments, infrastructure such as pipelines, processing facilities, powerlines, and producing wells restrict where sources and receivers can be placed. Limited access often leads to irregular sampling and incomplete azimuthal coverage, reducing image reliability and increasing acquisition costs.[7,8] In addition, environmental sensitivity and community safety concerns require strict control of ground vibrations during acquisition. Previous studies reported that effective vibration management and controlled

energy output are critical to minimizing operational risks while maintaining acceptable data quality.[9,10] These challenges show that survey optimization must not only focus on geometry but also consider environmental safety, operational logistics, and regulatory compliance. Environmental considerations, including reducing health, safety, and environmental risks and applying green seismic technologies, are integral to modern 3D seismic survey design.[11]

### 1.5. Integration with reservoir characterization and monitoring

Recent research has expanded the role of optimization beyond field design to include data integration and reservoir monitoring. Gong *et al.*[1] and Shi *et al.*[12] demonstrated that optimized seismic parameters improve the identification of fractures and flow pathways in deep carbonate reservoirs. Yu *et al.*[13] further integrated resistivity and penetration-rate information with seismic data to enhance subsurface interpretation during drilling. Similarly, Hassan *et al.*[14] and Yang *et al.*[15] confirmed that accurate velocity modeling and parameter refinement can improve imaging in tectonically complex zones. These contributions collectively demonstrate that optimization is not an isolated activity but a coordinated effort to improve exploration efficiency and operational safety. Taken together, these studies support the central argument of this work that 3D seismic acquisition should be treated as an integrated problem in which survey geometry, environmental and safety constraints, and reservoir-focused objectives are jointly considered to improve exploration efficiency and reduce uncertainty throughout the field's life.

### 1.6. Limitations identified in the systematic review

The systematic review of 87 English-language studies revealed several methodological and substantive limitations that impede progress in 3D seismic parameter optimization in congested oil fields. First, the concept of congestion lacks a consistent and widely accepted definition. In congested oil fields, where surface access is limited by wells, pipelines, facilities, roads, and environmentally sensitive zones, conventional survey design approaches often fail to deliver adequate coverage and imaging reliability. Numerous authors describe it qualitatively, such as restricted access or dense infrastructure, without providing measurable indicators. This lack of standardization makes it difficult to compare results across different studies.

Incomplete reporting of acquisition parameters remains widespread. A detailed review of 45 peer-reviewed journal articles in the dataset showed that 31 papers (68.9%) omit one or more critical specifications, including source spacing, receiver line intervals, offset ranges, azimuth distribution, or fold of coverage.[3-7] This omission prevents the reproduction of results and validation by independent researchers. In contrast, 14 papers (31.1%) that provided complete parameter documentation enabled verification and comparison with related work. Furthermore, vibration control studies often rely on descriptive accounts rather than quantitative thresholds for peak particle velocity. Without numerical data, it is difficult to assess whether safety standards were met.[9,10]

Among 87 studies, 61 (70.1%) claimed "improved efficiency" or "optimized parameters" but did not quantify operational or economic benefits. Only 26 studies (29.9%) provided metrics such as survey duration reduction, cost per square kilometer, or environmental expenditure. This gap makes it impossible to assess whether proposed optimizations yield tangible field benefits or remain theoretical exercises.

Another limitation is the lack of cost and time analysis in most optimization research. Although numerous studies claim improved efficiency, few provide clear evidence of economic or operational benefits. The heavy reliance on conference proceedings, such as those published in *The Leading Edge* and *SEG Technical Program Expanded Abstracts*, also limits the reproducibility of findings because these sources often summarize results without detailed methodologies.

Finally, the use of new sensing technologies remains limited. Despite the growing potential of distributed acoustic sensing (DAS) and permanent monitoring systems, only a small number of studies have applied these methods to address spatial or environmental constraints in congested areas. Collectively, these limitations point to the need for a more consistent and transparent approach to seismic survey optimization. Future studies should focus on standardized reporting, quantitative safety assessments, and the integration of advanced sensing technologies to ensure that optimization strategies are both practical and scientifically robust.

Our study presents three main contributions. First, it establishes a bibliometric-guided classification of optimization research that links keyword clusters directly to thematic synthesis. Second, it introduces a quantitative definition of congestion suitable for systematic comparison across fields. Third, it proposes a prototype multi-objective framework for seismic survey design under operational and safety constraints.

## 2. Research objectives and methodology

### 2.1. Analytical objectives of the study

This study extends beyond reporting the number of publications on 3D seismic parameter optimization. It

examines how research directions have evolved over time, identifies the parameters that receive the greatest emphasis, and highlights conceptual and technical gaps that remain in the literature. Accordingly, the objectives of this review combine analytical evaluation with systematic synthesis.

First, we analyzed the evolution of 3D seismic optimization research by identifying the relationships among acquisition geometry, field congestion, and imaging performance.[3,4] This involved assessing how different authors have approached the balance between fold density, offset distribution, and vibration control in constrained settings.

Second, the review examined the interconnection between optimization frameworks and reservoir characterization practices. Studies have shown that improved parameter selection improves reservoir imaging, especially when combined with geological modeling and seismic inversion.[2,16] Hence, this review evaluated how such integrations were achieved, and which techniques offered the most practical outcomes.

Third, we synthesized emerging methodological shifts. Particular attention was given to how studies incorporated computational design tools, environmental safety metrics, and hybrid acquisition technologies, such as DAS. Through this synthesis, the study identified how researchers were redefining "optimization" from purely geometric refinement toward a holistic process that included operational, environmental, and economic considerations.

Finally, the review identified knowledge gaps and proposed future research pathways. By examining thematic clusters and keyword co-occurrence patterns in the Biblioshiny (Version 5.0, K-Synth, Italy) dataset, we revealed recurring research themes and emerging frontiers that were reshaping the discipline. These included increased attention to congestion metrics, management of peak particle velocity, and integrated survey modeling.

Congestion in 3D seismic acquisition was defined in this study as the combined effect of surface obstruction density, restricted access ratio, and vibration exclusion zones. A CI was proposed as the ratio of inaccessible grid area to total survey area, weighted by infrastructure density. This definition enabled reproducible comparison across surveys and addressed the lack of quantitative descriptors noted in the literature.

## 2.2. Methodological approach

This review combined an SLR and a bibliometric analysis, ensuring that both conceptual depth and empirical scope were captured. The methodological process followed the Preferred Reporting Items for Systematic Reviews and Meta-Analyses (PRISMA) framework, which emphasizes transparent identification, screening, and inclusion of studies as shown in Figure 1. The same final dataset of 87 publications was used consistently for both the systematic review and the bibliometric analysis. This ensured full methodological alignment and resolved concerns regarding dataset inconsistency.

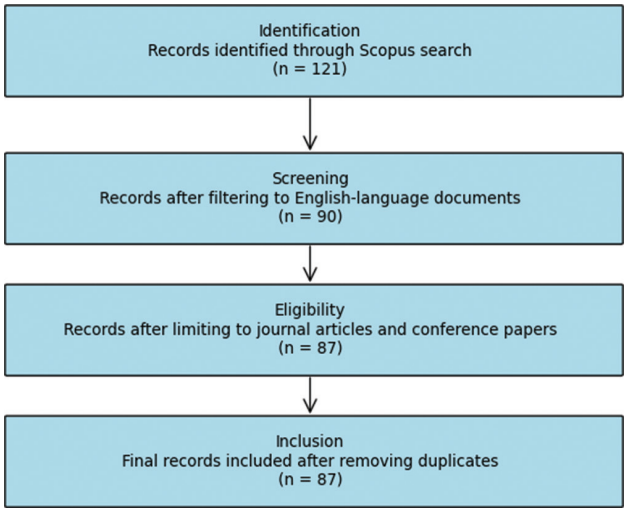


**Figure 1.** PRISMA flow diagram

### *2.2.1. Data source and search strategy*

Data were retrieved from the Scopus database, which is recognized for its comprehensive coverage of peer-reviewed scientific research. The search query was defined as: TITLE-ABS-KEY ("3D Seismic" AND ["parameters optimization" OR "congestion"]), limited to English-language journal articles and conference papers published up to 2025. This search yielded 121 documents, which were refined to 87 valid records after applying language and document-type filters. Document types were restricted to journal articles and conference papers to capture both theoretical and applied studies.

These records were exported to Biblioshiny for bibliometric mapping and further analysis. The software provided insights into annual publication trends, source impact, co-citation networks, and keyword co-occurrence patterns. The dataset was further supported by a manual qualitative review of abstracts and methodological sections to ensure accurate contextual interpretation.

### *2.2.2. Screening and inclusion criteria*

We included studies that fulfilled the following eligibility criteria:

(i) Addressed optimization of acquisition or processing parameters in 3D seismic surveys.
(ii) Discussed operational constraints, such as field congestion, vibration control, or environmental

limitations.

(iii) Reported case studies, simulation experiments, or modeling frameworks relevant to survey design.

Publications that focused only on two-dimensional seismic, regional mapping, or unrelated geophysical modeling were excluded. Both journal articles and conference proceedings were considered because field applications and experimental results often first appear in conference proceedings, such as *SEG Technical Program Expanded Abstracts* and *The Leading Edge*. The search was restricted to Scopus. Exclusion of Web of Science, Google Scholar, or OnePetro may miss relevant petroleum engineering literature, particularly from regional conferences or industry technical reports.

#### *2.2.3. Analytical and synthetic procedure*

The review employed a two-stage analytical approach to structure the evaluation process. In the first stage, bibliometric indicators, such as citation frequency, source influence, and keyword networks, were used to assess the field's intellectual structure. This helped identify dominant research clusters such as "geometry optimization," "vibration control," and "survey efficiency."

Bibliometric analysis was performed using Biblioshiny. Indicators included annual publication trends, keyword co-occurrence networks, source impact, citation influence, and collaboration patterns. The resulting keyword clusters were used as the structural foundation for thematic synthesis rather than as descriptive outputs.

In the second stage, synthetic reasoning was applied to interpret how these clusters relate conceptually and practically. For example, optimization research in *Geophysical Prospecting* and *Energies* often merges mathematical modeling with field constraints, while studies in *Interpretation* and *Processes* emphasize cross-disciplinary integration of geological modeling and data inversion.[13-15] This analytical and synthetic approach ensured that the review extended beyond a simple count of publications and developed a structured understanding of how theoretical principles, operational challenges, and environmental requirements interact in modern 3D seismic survey design.

Three dominant research clusters emerged from keyword co-occurrence and citation analysis:

- Cluster 1: Geometric and operational optimization. This cluster focused on survey geometry, fold distribution, and azimuthal balance. Early studies emphasized optimal spacing principles, while later studies extended these approaches to irregular and restricted terrains. Research in this cluster demonstrated that geometric optimization alone was insufficient in congested fields because access constraints disrupted theoretical layouts.
- Cluster 2: Congestion and vibration management. This cluster linked the acquisition design to environmental protection and surface safety. Studies emphasized peak particle velocity control, exclusion zones, and adaptive source energy. However, most contributions described congestion qualitatively, without measurable indicators, which limited reproducibility and comparison.
- Cluster 3: Integrated technologies and modeling. This cluster included studies that combined seismic optimization with modeling, monitoring, and hybrid sensing systems. Although these approaches improved adaptability, their adoption in congested fields remained limited due to operational complexity and cost assumptions.

#### *2.2.4. Quality assurance and validation*

To ensure validity, duplicate studies were removed, and bibliometric indicators were cross-checked. The final dataset was reviewed independently by multiple researchers to confirm thematic accuracy. In addition, the co-citation and keyword networks were manually verified to confirm that automated clustering correctly represented real conceptual relationships. This multi-step validation strengthened the analytical reliability of both quantitative mapping and qualitative interpretation.

### 2.3. Analytical contribution

This combined systematic and bibliometric approach makes three main contributions to 3D seismic parameter optimization in congested oil fields. First, it clarifies how optimization research has matured from geometry-based design toward integrated environmental and operational frameworks. Second, it provides an evidence-based synthesis of how congestion and safety constraints reshape field practices. Third, it highlights that future 3D seismic optimization should not only aim for better imaging but also promote sustainable, safe, and cost-effective acquisition. By combining bibliometric indicators with detailed analytical interpretation, the review establishes a foundation for new work that links theoretical developments with practical survey design in congested settings.

## 3. Results and discussion

### 3.1. General trends in publication output

The bibliometric analysis revealed a steady growth in research on 3D seismic parameter optimization between 2003 and 2025. The annual scientific production increased significantly after 2018. Figure 2 shows the yearly number

of publications on 3D seismic parameter optimization, reflecting a growing awareness of survey efficiency and environmental responsibility in oil field operations. The upward trend was largely associated with technological advances in data acquisition and processing, and with the increasing complexity of exploration environments.[1,2]

The annual citation rate also showed an upward pattern. Figure 3 depicts the total or average annual citations of the reviewed papers, indicating sustained academic engagement with the topic. The parallel rise in citation counts confirms the field's growing scholarly recognition and influence. The early works of Vermeer[3] and Santos *et al.*[4] served as conceptual anchors for newer studies. Their influence persisted because they provided both theoretical and operational frameworks for survey optimization. Furthermore, recent publications by Ofowena *et al.*[7] and Li *et al.*[8] extended these frameworks to modern, congested settings, demonstrating that optimization evolved from a geometric design challenge to a multidisciplinary problem that involved safety, logistics, and sustainability.

The source impact analysis showed that most publications appeared in highly ranked journals, such as *Geophysical Prospecting*, *Interpretation*, *Energies*, *Processes*, and *Geoenergy Science and Engineering*. The concentration of articles in these outlets reflected a balanced mix of theoretical innovation and applied field research. Journals like *The Leading Edge* and *SEG Technical Program Expanded Abstracts* remained the preferred platforms for field trials, practical experiments, and methodological improvements. Table 1 shows the most productive journals in this research area. Table 2 shows the foundational works that anchored the field's methodological development.

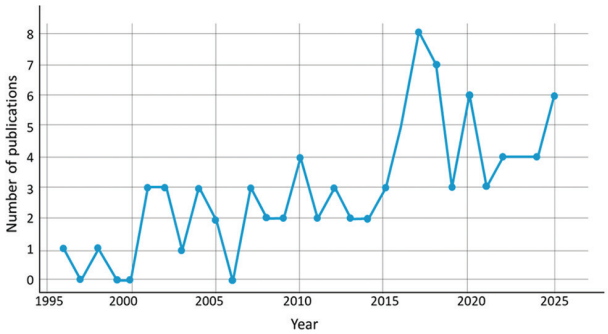


**Figure 2.** Annual scientific production (2003–2025)

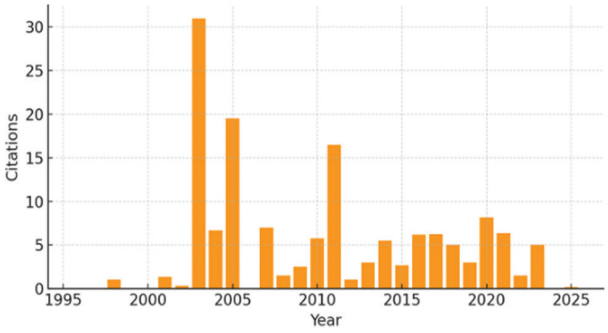


**Figure 3.** Annual citation trend (2003–2025)

### 3.2. Dominant research themes

The co-word and thematic mapping from the Biblioshiny output identified three dominant clusters of research themes:

(i) Geometric and operational optimization: This cluster focused on improving the arrangement of sources and receivers, fold coverage, and azimuthal balance. Studies in this category explored the trade-offs between cost and resolution and assessed how optimized configurations enhanced seismic illumination. Vermeer[3] and Santos *et al.*[4] were foundational to this theme. Li *et al.*[8] extended these principles by applying pre-stack migration-based optimization to complex terrains, while Ofowena *et al.*[7] proposed field-level strategies for managing spatial constraints in onshore congested fields.

(ii) Congestion and environmental safety: The second thematic cluster linked the seismic optimization with environmental impact management. This body of work emphasized vibration control, community safety, and regulatory compliance. Hou and Yang[9] and Soureshjani and Lavassani[10] discussed how controlling vibration amplitude and using adaptive acquisition parameters can reduce the risk to surface structures. Ofowena *et al.*[7] expanded this perspective by proposing methods to manage field congestion without compromising imaging quality. This cluster underscored the current shift from purely technical optimization toward responsible and sustainable field operations.

(iii) Integration of emerging technologies and data analytics: The third cluster highlighted new computational and sensing technologies that enhance acquisition design and reservoir interpretation. Gong *et al.*[1] and Shi *et al.*[12] demonstrated that optimized parameter selection improved the detection of fracture networks and enhanced reservoir monitoring. Yu *et al.*[13] and Curia and Veeken[16] introduced data-driven and resistivity-based prediction techniques that combined seismic inversion with geological modeling. Although most of these studies remained experimental, they revealed the expanding frontier of 3D seismic optimization toward hybrid and integrated data environments.

These thematic patterns suggested that the field was

**Table 1. Top 10 productive journals publishing on three-dimensional seismic optimization**

| Journal/source title | Publications | Total citations | Average citations per paper |
|---|---|---|---|
| Geophysics | 3 | 51 | 17.0 |
| Proceedings – SPE Annual Technical Conference | 3 | 20 | 6.7 |
| The Leading Edge | 2 | 34 | 17.0 |
| Basin Research | 1 | 15 | 15.0 |
| SPE Reservoir Evaluation and Engineering | 1 | 26 | 26.0 |
| Journal of Volcanology and Geothermal Research | 1 | 23 | 23.0 |
| Journal of Petroleum Exploration and Production Technology | 1 | 22 | 22.0 |
| KSCE Journal of Civil Engineering | 1 | 20 | 20.0 |
| Applied Geophysics | 1 | 19 | 19.0 |
| Computers and Geosciences | 1 | 19 | 19.0 |

**Table 2. Most frequently cited articles in the dataset**

| Rank | Authors | Article title | Journal/source | Year | Total citations | Reference |
|---|---|---|---|---|---|---|
| 1 | Vermeer (2003) | 3D seismic survey design optimization | The Leading Edge | 2003 | 31 | 3 |
| 2 | Berger *et al.* (2011) | Seismic tomography at Popocatépetl volcano, Mexico | Journal of Volcanology and Geothermal Research | 2011 | 23 | 17 |
| 3 | Soleimani *et al.* (2020) | Estimation of reservoir porosity using seismic attributes in an Iranian oil field | Journal of Petroleum Exploration and Production Technology | 2020 | 22 | 18 |
| 4 | Hou and Yang (2020) | Seismic stability of 3D tunnel face considering tensile strength cutoff | KSCE Journal of Civil Engineering | 2020 | 20 | 9 |
| 5 | Xu *et al.* (2018) | An efficient implementation of 3D high-resolution imaging for large-scale seismic data with GPU/CPU heterogeneous parallel computing | Computers and Geosciences | 2018 | 19 | 19 |
| 6 | Liu *et al.* (2010) | Locally linear embedding-based seismic attribute extraction and applications | Applied Geophysics | 2010 | 19 | 20 |
| 7 | Wang *et al.* (2016) | The analytic wavelet transform with generalized Morse wavelets to detect fluvial channels in the Bohai Bay Basin, China | Geophysics | 2016 | 19 | 21 |

no longer dominated by geometry alone. Instead, it now represents a multidisciplinary integration of geophysics, environmental science, and engineering optimization. Core research anchors include 3D seismic, optimization, and survey design, with an emerging focus on congestion and vibration control (Figure 4).

### 3.3. Collaboration and geographic distribution

The collaboration network analysis showed that research on 3D seismic optimization has become increasingly international. China, the United States, Russia, and the Middle East were the most active contributors, supported by academic industry partnerships. This pattern reflected the global relevance of 3D seismic methods in both frontier and mature basins. Studies such as those by Yang *et al.*[15] and Soleimani *et al.*[18] highlighted strong collaboration between universities and oil companies, emphasizing the need for practical solutions to real-world acquisition challenges. Figure 5 illustrates global collaboration strength derived from co-authorship frequencies.

In particular, Chinese and Middle Eastern authors dominated publications in *Processes*, *Energies*, and *Interpretation*, focusing on advanced optimization, geomechanics, and environmental modeling. Meanwhile, contributions from Latin America and Africa, including the publication by Ofowena *et al.*,[7] demonstrated growing interest in optimizing seismic operations in congested onshore oil fields. The rising number of cross-country co-authorships shows that optimization is now a shared global concern that transcends regional resource boundaries.

### 3.4. Evolving methodologies and conceptual shifts

A key insight from this review is that research has moved

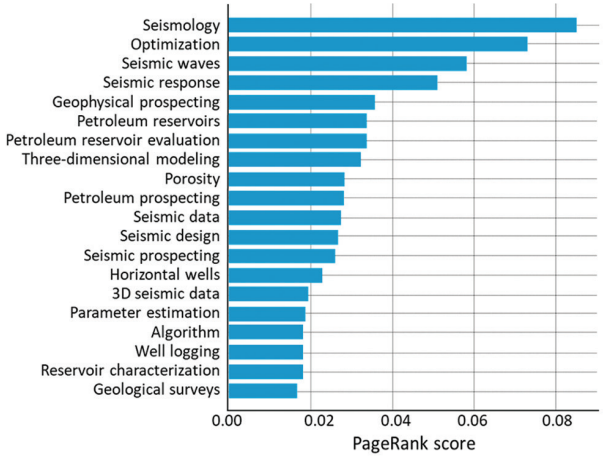


**Figure 4.** Top 20 keywords by importance (co-word network)

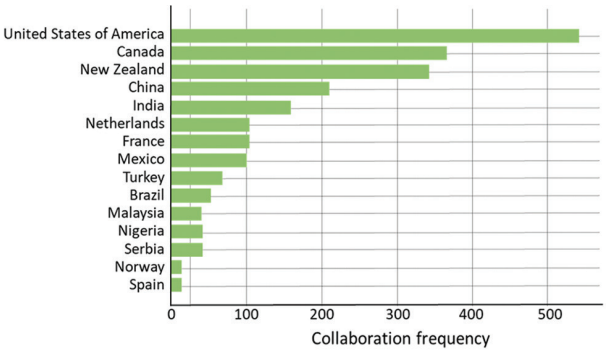


**Figure 5.** Top 15 countries by collaboration intensity

from parameter-centric optimization to system-level optimization. Early studies viewed optimization as a geometric exercise that adjusts fold, spacing, and azimuth. According to Gong *et al.*,[22] fracture distribution in the reservoir could be derived from 3D seismic data using an ant-tracking technique. Contemporary research, however, treats it as a comprehensive process that includes environmental risk assessment, vibration control, data integration, and cost evaluation.[7,10,18,23] are referred to in Table 3.

Moreover, the integration of modeling and simulation has redefined how optimization is practiced. Previous studies used quantitative seismic characterization to link acquisition parameters with fracture identification.[1,24] Similarly, previous studies have demonstrated that integrating drilling data with seismic predictions can guide real-time parameter selection.[13,25] These studies collectively suggest that optimization is evolving toward an adaptive and feedback-driven discipline that combines design foresight with continuous operational monitoring.

Another conceptual shift is the growing emphasis on

**Table 3. Classification of reviewed studies by objective and constraint**

| Objective | Constraint | Method type | Data type |
|---|---|---|---|
| Imaging quality | Geometry | Deterministic | Synthetic |
| Vibration control | Peak particle velocity limits | Constraint based | Field |
| Cost efficiency | Access | Multi objective | Hybrid |

environmental stewardship. As seismic operations expand into developed areas, minimizing disturbance and ensuring safety have become core objectives. Hou and Yang,[9] as well as Soureshjani and Lavassani[10] emphasized vibration control and consideration of ground motion, whereas other studies stressed operational adaptation to congestion.[7,26] This demonstrates that modern optimization aligns with the principles of sustainable exploration and supports the United Nations Sustainable Development Goals (SDGs), particularly SDG-7 (Affordable and Clean Energy) and SDG-13 (Climate Action).

Congestion in 3D seismic acquisition is defined in this study as the degree to which surface infrastructure and safety constraints limit feasible source and receiver placement. A prototype CI is defined in **Equation 1**:

$$CI = \frac{A_{restricted}}{A_{total}} \quad (1)$$

where $A_{\text{restricted}}$ represents surface area inaccessible due to infrastructure, safety buffers, or environmental exclusion, and $A_{\text{total}}$ represents the total survey area. This definition allows objective comparison across projects and directly addresses the lack of measurable congestion metrics identified in the literature.

Survey design in congested oil fields is expressed as a constrained optimization problem that seeks to maximize imaging quality, minimize acquisition cost, and maintain peak particle velocity below regulatory limits. This formulation integrates geometry, safety, and economics within a single decision framework and provides a foundation for reproducible survey optimization.

### 3.5. Identified gaps and future directions

Although progress has been significant, the review revealed several critical gaps that require further attention.

First, most optimization frameworks lack standardized congestion metrics. Researchers often describe congestion qualitatively, which limits reproducibility and comparison. Developing measurable indices, such as access density or spatial obstruction ratios, would improve the assessment's objectivity. Second, numerous studies omit cost and

environmental data. Integrating economic modeling with survey design would help balance efficiency and sustainability. Third, the adoption of emerging technologies, such as DAS and permanent monitoring arrays, remains slow. Expanding their use could help overcome access constraints and improve data coverage in complex fields. Finally, collaboration between academia and industry should be strengthened. Joint projects can accelerate innovation, validate algorithms under field conditions, and ensure that optimization methods remain relevant to operational realities.

### 3.6. Synthesis of findings on research direction

Overall, the bibliometric and systematic analyses confirm that 3D seismic parameter optimization has matured into a multidimensional discipline that unites geometric design, environmental management, and engineering analysis. The integration of congestion studies, vibration control, and hybrid technologies marks a new stage in geophysical research where operational efficiency and sustainability coexist.

The synthesis of past and current studies reveals that the discipline is moving toward holistic optimization, where seismic acquisition is designed not only for better imaging but also for environmental safety, cost efficiency, and long-term field sustainability.[3,4,7,27] This trend demonstrates the scientific community's commitment to building responsible exploration systems that meet modern energy and environmental expectations.

## 4. Main findings of 3D seismic parameter optimization

This review examined the evolution of research on 3D seismic parameter optimization with a specific focus on its application in congested oil field environments. The analysis combined systematic review and bibliometric methods to ensure both conceptual and empirical coverage. The findings revealed that research in this field has advanced from geometric design optimization toward integrated frameworks that also consider environmental, operational, and economic dimensions.

Overall, three key insights emerged from this review. First, survey geometry remains central to seismic data quality. Studies by Vermeer[3] and Santos *et al.*[4] demonstrated that optimal combinations of source spacing, receiver placement, and fold distribution are critical for obtaining reliable subsurface images. This framework is derived from bibliometric keyword clustering and organizes existing studies into three principal domains: geometric and operational optimization, congestion and vibration management, and integration of modeling and sensing technologies. This classification provides a coherent structure that connects previously fragmented studies and enables consistent comparison across research themes.

Second, recent works have extended this understanding by incorporating environmental safety and logistical challenges into survey design. Several studies highlight that parameter optimization now includes vibration control, energy management, and access planning.[7,9,10] These studies[7,9,10] integrate knowledge across geophysics, petroleum engineering, and environmental management by introducing a prototype multi-objective optimization framework. This framework unifies imaging quality, peak particle velocity control, and operational cost within a single conceptual model. Ultimately, it responds directly to the growing need for safe, efficient, and environmentally responsible seismic acquisition in developed oil fields.

Third, emerging studies show that integrating modeling, simulation, and monitoring improves the predictability and adaptability of seismic acquisition in complex geological settings.[1,13,15,28,29] Seismic responses are less sensitive to density than to seismic velocities, density estimation is more challenging, and parameter coupling between model parameters further degrades the accuracy of inverted density models.[30] Successful 3D seismic acquisition depends critically on the optimization of numerous survey parameters before field operations begin.[31] Zhao *et al.*[32] proposed integrated seismic acquisition, processing, and interpretation technologies that addressed complex geology in the northern Sichuan Basin. The design process of a 3D seismic survey must address fundamental questions about how sources and receivers should be positioned.[33] Several studies have shown that, for complex septum-style structures with large variations in burial depth and dip, optimized wide-azimuth, broadband 3D seismic acquisition with small bin sizes, combined with CRP-stack-based amplitude attributes at the surface and target horizons, ensures even subsurface coverage, improves the prediction of key shale reservoir parameters, and provides a sound basis for acquisition layout design and depth imaging workflows.[34-36] Broadband 3D seismic data have proven essential for improving basin understanding in congested fields and advance key prospects to well-defined drilling targets.[37] According to Will *et al.*,[38] the study highlights stochastic discrete-feature-network modeling as a framework for integrating seismic anisotropy and reservoir performance data to reduce uncertainty in fracture-system characterization across the interwell region. Xu *et al.*,[19] Liu *et al.*,[20] and Wang *et al.*[21] demonstrated that advanced attribute-based approaches, including analytic wavelet transform-based spectral decomposition with optimized generalized

Morse wavelets and non-linear dimensionality reduction using locally linear embedding, significantly enhance the detection of thin fluvial channels and improve reservoir feature prediction from multi-attribute 3D seismic data. Berger *et al.*[17] aimed to reconstruct the 3D P-wave velocity structure beneath volcanic and seismically active regions by inverting earthquake arrival times with Bayesian tomographic approaches to improve the characterization of subsurface heterogeneity and structural complexity.

Fourth, the study identifies a critical research gap related to the absence of quantitative definitions of congestion in seismic survey design. Most prior studies describe congestion qualitatively without measurable indicators. To address this gap, the study proposes a reproducible CI based on surface access restrictions. This contribution provides a practical basis for comparing survey designs and supports transparent decision-making in congested environments.

The results also indicate that the field is shifting toward a more responsible and multidisciplinary approach. Optimization is no longer confined to data geometry but now represents a balanced interaction between imaging quality, environmental protection, and operational sustainability. This transition reflects a growing commitment to reducing the environmental footprint of exploration activities while maintaining data precision and economic viability.

Overall, the findings demonstrate that 3D seismic parameter optimization has evolved from a geometry-focused exercise into a multidisciplinary process that requires coordinated consideration of subsurface imaging, surface safety, and operational constraints. The classification framework, quantitative congestion definition, and integrated optimization formulation proposed in this study provide a clear foundation for future research and field application. These contributions support the development of reproducible, practical, and scientifically rigorous approaches to seismic survey design in increasingly congested exploration environments.

### 4.1. Recommendations for future research

Based on the findings of this review, several recommendations are proposed to strengthen both research and field practice:

(i) Develop standardized congestion metrics: Future studies should establish measurable indices that define congestion levels in onshore and near-surface environments. Such indices would enable consistent evaluation of design feasibility and improve the comparability of studies across regions. The optimization of acquisition parameters in congested oil fields is developing into a multidisciplinary framework. This integrated approach connects geometric considerations with strict environmental protection measures and operational safety protocols. The primary objective is to improve imaging quality, reduce costs, and minimize environmental impact.

(ii) Integrate environmental and economic parameters: Researchers should include vibration, energy consumption, and cost factors as optimization variables. This approach would ensure that survey planning reflects real-world operational and sustainability constraints.

(iii) Expand the use of emerging technologies: DAS, autonomous nodes, and hybrid acquisition systems should be incorporated into optimization frameworks. These technologies can enhance flexibility, minimize access limitations, and improve safety in congested fields.

(iv) Promote academic–industry collaboration: Stronger cooperation between universities, research institutions, and operating companies will support the testing and validation of optimization algorithms under practical field conditions. This collaboration will also ensure that academic findings are relevant to real-world exploration challenges.

(v) Enhance reporting transparency: Authors should adopt standardized reporting templates that clearly document acquisition geometry, source parameters, vibration limits, and environmental compliance data. Transparent documentation will allow reproducibility and strengthen the scientific credibility of optimization studies.

### 4.2. Broader implications

The implications of this review extend beyond technical improvements in seismic survey design. The findings show that 3D seismic parameter optimization plays an important role in addressing operational safety, environmental protection, and responsible resource development in congested oil field settings. As exploration increasingly takes place in developed and environmentally sensitive areas, seismic design must respond not only to imaging requirements but also to regulatory constraints, community safety, and surface impact reduction.

This study demonstrates that integrating geometric optimization with measurable congestion constraints and vibration control supports safer field operations and improves planning transparency. By proposing quantitative definitions and unified optimization concepts, the work provides decision-makers with tools that can be applied consistently across different geological and operational contexts. These tools help bridge the gap between geophysical theory and practical field execution.

At a broader scale, the study highlights the growing

convergence of geophysics, petroleum engineering, and environmental management. The results confirm that modern seismic acquisition cannot be treated as an isolated technical activity. Instead, it must be planned as part of an integrated system that balances imaging quality, operational efficiency, and environmental responsibility. This perspective aligns with current global priorities for energy efficiency and responsible resource management and supports long-term sustainability objectives in hydrocarbon exploration and production.

In summary, the study reinforces that effective 3D seismic parameter optimization contributes not only to improved subsurface imaging but also to safer operations, reduced environmental disturbance, and more accountable energy development practices.

## 5. Conclusion

This systematic review has examined the optimization of 3D seismic acquisition parameters in congested oil field environments using a carefully filtered set of peer-reviewed journal articles and conference papers. The findings demonstrate that congestion remains a dominant constraint that directly influences survey geometry, operational flexibility, cost, and final data quality. Across the reviewed literature, researchers consistently emphasized that standard acquisition templates are rarely suitable in mature and infrastructure-dense fields. Instead, effective survey design requires deliberate adaptation of parameters to local access limitations and operational safety requirements.

The reviewed studies show that successful optimization depends on balancing subsurface imaging objectives with practical surface constraints. Adjustments to receiver spacing, source layout, bin size, fold distribution, and azimuth coverage are commonly used to achieve acceptable illumination in restricted areas. Field evidence indicates that irregular and flexible geometries often outperform rigid designs when congestion is present. Many authors also reported that early integration of design simulation into project planning significantly reduces rework, operational delays, and cost overruns.

Despite these advances, this review identifies clear gaps in the existing literature. Most studies focus on individual case histories, which limits the transferability of conclusions across different geological and operational settings. In addition, performance evaluation methods vary widely, making direct comparison between designs difficult. Reporting practices also differ, particularly in the treatment of safety, environmental constraints, and operational risks associated with congested field acquisition.

Overall, this review confirms that optimization of 3D seismic parameters in congested oil fields is both necessary and achievable when design decisions are informed by systematic analysis and field conditions. Future research should prioritize integrated optimization frameworks, standardized evaluation metrics, and comparative studies across multiple field types. Strengthened collaboration between researchers and industry practitioners will further improve data quality, cost efficiency, and operational safety in complex and congested seismic acquisition environments.

## Acknowledgments

The authors gratefully acknowledge the contributions of researchers and practitioners whose published works formed the basis of this systematic and bibliometric review. Their efforts have advanced the understanding of 3D seismic parameter optimization in congested oil field environments. The authors also acknowledge the support of colleagues at the Universiti Teknologi Malaysia, who provided academic resources, bibliographic access, and technical guidance during the preparation of this manuscript.

## Funding

None.

## Conflict of interest

The authors declare that there are no known financial or personal relationships that could have influenced the work reported in this paper.

## Author contributions

*Conceptualization:* Frank O. Ofowena, Akhmal Sidek
*Formal analysis:* Frank O. Ofowena
*Investigation:* Frank O. Ofowena, Akhmal Sidek, Yasir Bashir
*Methodology:* Frank O. Ofowena, Mingtao Nie
*Writing–original draft:* Frank O. Ofowena
*Writing–review & editing:* Frank O. Ofowena, Mingtao Nie

## Availability of data

Not applicable.

## References

1. Gong W, Wen X, Lin K, Zhou D, Lin X. Quantitative seismic characterization of an ultradeep carbonate strike-slip fault zone. *Interpretation*. 2025;13(3):T589-T606.

   doi: 10.1190/INT-2024-0064.1

2. Xu Y, Sun Z, Chen W, *et al*. Integrating stochastic geological modeling and injection-production optimization in aquifer underground gas storage: A case study of the qianjiang basin. *Processes*. 2025;13(6):1728.

doi: 10.3390/pr13061728

3. Vermeer GJO. 3D seismic survey design optimization. *The Leading Edge* 2003;22(10):934-941.

doi: 10.1190/1.1623633

4. Santos AB, Porsani MJ, Góis MS. 3D seismic survey design using mixed-radix based algorithm inversion. *Geophys Prospect*. 2019;67(7):1720-1731.

doi: 10.1111/1365-2478.12773

5. Kashnikov YA, Shustov DV, Yakimov SY. Consideration of the geomechanical state of a fractured porous reservoir in reservoir simulation modeling. *J Mining Inst*. 2025;271:42-52.

6. Jia YC, Li L, Ma ZJ, Yang M, He TT, Chen W. Optimization Scheme for Reservoir Modification in the Lampshade Formation Based on Integrated Geo-Engineering Study. In: Lin J, (eds). *Proceedings of the International Field Exploration and Development Conference* 2024. Xi'an, China: Springer Nature Singapore; 2025. p. 963-988.

doi: 10.1007/978-981-96-5226-6_70

7. Ofowena FO, Sidek A, Oseh JO, Bashir Y, Alade AO, Omonigho EN. Strategies for repeating seismic acquisition in onshore congested oil fields. In: Jusoh SNB, Jaya RP, Horpibulsuk S, Othman BAB, editors. *Proceedings of the 13th International Conference on Geotechnical Engineering in Tropical Regions (GEOTROPIKA 2024)*; 13th International Conference on Geotechnical Engineering in Tropical Regions (GEOTROPIKA). Vol. 639. Kuala Lumpur, Malaysia: Lecture Notes in Civil Engineering, Springer Singapore; 2025. p. 178-188.

doi: 10.1007/978-981-96-6072-8_15

8. Li SQ, Wu J, He YF, Yuan B, Luo SQ. Application Research of 3D Observation System Optimization Technology Based on Prestack Migration Imaging in East Sichuan. In: Lin J, editor. *Proceedings of the International Field Exploration and Development Conference 2023. IFEDC 2023; September 19-21, 2023*. Wuhan, China: Springer Series in Geomechanics and Geoengineering. Springer Singapore; 2023. p. 306-316.

doi: 10.1007/978-981-97-0483-5_30

9. Hou CT, Yang XL. Seismic stability of 3D tunnel face considering tensile strength cut-off. *KSCE J Civ Eng*. 2020;24(7):2232-2243.

doi: 10.1007/s12205-020-1804-5

10. Soureshjani OK, Lavassani SHH. Performance of tuned particle impact damper and tuned mass damper seismic control systems considering mainshock-aftershock sequences. *Structures*. 2023;56:104924.

doi: 10.1016/j.istruc.2023.104924.

11. Dean T. The application of graph theory to optimize the design of onshore 2D seismic surveys. *The Leading Edge*. 2023;42(10):711-717.

doi: 10.1190/tle42100711.1

12. Shi B, Chang X, Liu Z, *et al*. Intelligent identification of sequence stratigraphy constrained by multi-population genetic algorithm and dynamic time warping technique: A case study of the lower cretaceous qingshuihe formation in the hinterland of the junggar basin NW China. *Basin Res*. 2021;33(4):2517-2544.

doi: 10.1111/bre.12567

13. Yu Y, Tian S, Li J, *et al*. Well-seismic joint data-driven resistivity-based prediction of 3D spatial rate of penetration. *Front Earth Sci*. 2025:13:1546094.

doi: 10.3389/feart.2025.1546094

14. Hassan AGM, Farag KSI, Aref AAF, Piskarev AL. Methods for 3D inversion of gravity data in identifying tectonic factors controlling hydrocarbon accumulations in the EL Zeit Basin Area, Southwestern Gulf of Suez, Egypt. *Geodynam Tectonophys*. 2024;15(2):0751.

doi: 10.5800/GT-2024-15-2-0751

15. Yang Y, Yin X, Li K. 3D pre-stack inversion constrained by spatial reflection features using the Sylvester's equation. *Geoener Sci Eng*. 2024;238:212806.

doi: 10.1016/j.geoen.2024.212806

16. Curia D, Veeken P. Estimating rock physical parameters using anisotropic 3D seismic data to characterize unconventional Vaca Muerta oil shale deposits in the Neuquén Basin, western Argentina. *First Break*. 2019;37(11):37-47.

doi: 10.3997/1365-2397.2019036

17. Berger P, Got JL, González CV, Monteiller V. Seismic tomography at popocatépetl volcano, Mexico. *J Volcanol Geotherm Res*. 2011;200(3-4):234-244.

doi: 10.1016/j.jvolgeores.2010.12.016

18. Soleimani F, Hosseini E, Hajivand F. Estimation of reservoir porosity using analysis of seismic attributes in an Iranian oil field. *J Petrol Explor Prod Technol*. 2020;10(4):1289-1316.

doi: 10.1007/s13202-020-00833-4

19. Xu J, Liu W, Wang J, Liu L, Zhang J. An efficient implementation of 3D high-resolution imaging for large-scale seismic data with GPU/CPU heterogeneous parallel computing. *Comput Geosci*. 2018;111:272-282.

doi: 10.1016/j.cageo.2017.11.020

20. Liu XF, Zheng XD, Xu GC, *et al*. Locally linear embedding-based seismic attribute extraction and applications. *Appl Geophys*. 2010;7(4):365-375.

doi: 10.1007/s11770-010-0260-2

21. Wang Z, Gao J, Wang P, Jiang X. The analytic wavelet transform with generalized Morse wavelets to detect fluvial channels in the Bohai Bay Basin, China. *Geophysics*. 2016;81(4):O1-O9.

doi: 10.1190/geo2015-0396.1

22. Gong Y, Zhai S, Zha Y, *et al*. Numerical simulation of embedded discrete-fracture seepage in deep carbonate gas reservoir. *Energies*. 2022;15(19):7237.

doi: 10.3390/en15197237

23. Rodriguez JM, Pion J, Piazza JL, Chaouch A. Seismic costs prediction and optimization: A systematic approach. In: *Proceedings of the Offshore Technology Conference*; Houston, TX: Offshore Technology Conference; 1996. [Paper No. OTC 7978].

doi: 10.4043/7978-MS

24. Suarez G. Designing 3D seismic surveys in the Macal area using seismic modeling. *The Leading Edge*. 2004;23(10):1071-1076.

doi: 10.1190/1.1813361

25. Ren K, Zou G, Peng S, Yeh HG, Deng B, Ji Y. Fault identification based on kernel principal component analysis-genetic particle swarm optimization-support vector machine algorithm for seismic attributes in the Sihe Coal Mine, Qinshui Basin, China. *Interpretation*. 2023;11(1):T59-T73.

doi: 10.1190/INT-2022-0039.1

26. Ishiyama T, Painter D, Belaid K, *et al*. 3D OBC Seismic Survey Parameters Optimization for a Carbonate Field Offshore Abu Dhabi, United Arab Emirates. In: *Proceedings of the Abu Dhabi International Petroleum Exhibition and Conference; 2008*; Abu Dhabi, United Arab Emirates. [SPE Paper No. 117803]. Society of Petroleum Engineers; 2008.

doi: 10.2118/117803-MS

27. Afia MS, Al Hossani K, Matarid T, Meziani S, Al Badi BS. Full Field Development Plan Optimization Integrating Subsurface Reservoir Uncertainties for Green Field Offshore Abu Dhabi, United Arab Emirates. In: *Proceedings of the Abu Dhabi International Petroleum Exhibition and Conference*; 2012; Abu Dhabi, United Arab Emirates. Society of Petroleum Engineers; 2012. [Paper No. 161507].

doi: 10.2118/161507-MS

28. Xia J, Tang D, Huang Y, Luo X. The Estimation of Noise Suppression of 3D Recording Geometry and its Application. In: *SEG Expanded Abstracts. SEG International Exposition and Annual Meeting*; 2008. Las Vegas, NV: Society of Exploration Geophysicists; 2008. p. 144-148.

doi: 10.1190/1.3054776

29. Abacha I, Koulakov I, Semmane F, Yelles-Chaouche AK. Seismic tomography of the area of the 2010 Beni-Ilmane earthquake sequence, north-central Algeria. *SpringerPlus*. 2014;3(1):650.

doi: 10.1186/2193-1801-3-650

30. Kawasaki Y, Minato S, Ghose R. Reducing parameter coupling effect for subsoil density estimation using 3D seismic full-waveform inversion with horizontal-force source. In: *SEG/AAPG International Meeting for Applied Geoscience and Energy*. Houston, TX: Society of Exploration Geophysicists; 2022. [Paper No. SEG-2022-3750995].

doi: 10.1190/image2022-3750995.1

31. Xu J, Zhang J. Improving prestack time migration by introducing a new velocity-related parameter: Parameter picking and 3D real data application. *Geophysics*. 2024;89(1):S119-S127.

doi: 10.1190/geo2023-0319.1

32. Zhao L, Zhang G, Chen W, *et al*. Key seismic survey technologies for deep complex geological structures: A case study of the northern section of the Longmenshan fault fold belt in the Sichuan Basin. *Nat Gas Ind B*. 2018;5(4):360-370.

doi: 10.1016/j.ngib.2018.01.010

33. Munoz PA, Sanabria N, Ocampo G, Uribe J, Rodríguez L, Parrado R. State of the Art in 3D Seismic Survey Design for Petroleum Exploration in the Arctic Regions. In: *Proceedings of the ASME 2018 37th International Conference on Ocean, Offshore and Arctic Engineering*. Vol. 8. Polar and Arctic Sciences and Technology; Petroleum Technology [Paper No. V008T11A017]. Madrid, Spain: American Society of Mechanical Engineers; 2018.

doi: 10.1115/OMAE2018-78172

34. Liu W, Zhang ZYS, Yu YG, Zhang ZJJ, Hu HCJ. 3D Seismic Acquisition Technology and Effect of Complex Mountainous and Tectonic Areas in Shale Gas Play of China. In: *Proceedings of the First EAGE/AMGP/AMGE Latin American Seminar on Unconventional Resources*. Latin America: European Association of Geoscientists and Engineers; 2017. p. 1-4.

doi: 10.3997/2214-4609.201702528

35. Zhang G, Ran Q, Liao Q, *et al*. Key seismic exploration technology for the Longwangmiao Formation gas reservoir in the Gaoshiti-Moxi area, Sichuan Basin. *Nat Gas Ind B*. 2016;3(4):323-329.

doi: 10.1016/j.ngib.2016.06.004

36. Chang T, Canales L, Kue CW, Shih CC. Optimization of Acquisition Design Based on Common Reflection Stack. In: *Proceedings of the SEG Annual Meeting*. SEG Annual Meeting; 2001. [Paper No. SEG-2001-0070]. San Antonio, TX: Society of Exploration Geophysicists; 2001.

doi: 10.1190/1.1816728.

37. Joseph S, Lu X, Bykov K, Douillard A. Extensive Broadband 3D Seismic to De-Risk and Mature the West of Shetland Exploration Portfolio. In: *Proceedings of the 79th EAGE Conference and Exhibition*. Paris, France: European Association of Geoscientists and Engineers; 2017. p. 1-5.

doi: 10.3997/2214-4609.201700816

38. Will R, Archer R, Dershowitz B. Integration of seismic anisotropy and reservoir-performance data for characterization of naturally fractured reservoirs using discrete-feature-network models. *SPE Reserv Eval Eng*. 2005;8(2):132-142.

doi: 10.2118/84412-PA

ACCSCIENCE PUBLISHING

Journal of Seismic Exploration

ARTICLE

# U-STDRNet: A unified model integrating swin transformer and residual dense network for seismic image super-resolution and denoising

**Mingliao Wu[1], Juan Wu[1]*, Min Bai[1], Haiyu Li[1], Zhixian Gui[1], and Guangtan Huang[2]***

[1]The Key Laboratory of Exploration Technology for Oil and Gas Resources of Ministry of Education, College of Geophysics and Petroleum Resources, Yangtze University, Wuhan, Hubei, China

[2]The State Key Laboratory of Geomechanics and Geotechnical Engineering, Institute of Rock and Soil Mechanics, Chinese Academy of Sciences, Wuhan, Hubei, China

(This article belongs to the *Special Issue: Advanced Artificial Intelligence Theories and Methods for Seismic Exploration*)

## Abstract

Enhancing seismic image resolution while effectively suppressing noise remains a critical challenge in accurately characterizing subsurface geological structures for oil and gas exploration. Traditional methods often fail to balance the recovery of fine details with robustness to noise, particularly in complex geological settings or under high-noise conditions. This study proposes a deep learning-based joint model, U-Net Shifted Window (Swin) Transformer-based dense residual network (U-STDRNet). The model integrates the global modeling capability of the Swin Transformer, the hierarchical feature reuse mechanism of the residual dense network, and an attention-guided strategy to jointly perform seismic image super-resolution and denoising. Built upon the U-Net encoder-decoder architecture, the model embeds Swin Transformer-based convolutional residual blocks. These blocks employ both a feature fusion block with the Swin Transformer and a feature fusion block with a convolutional neural network to effectively capture stratigraphic continuity and enhance detailed features such as fault edges. Residual dense blocks further improve weak signal recovery (e.g., thin-layer interfaces) through dense residual connections. Furthermore, the convolutional block attention module is integrated into skip connections, employing a dual-channel spatial weighting mechanism to suppress noise and emphasize key geological regions. Experimental results and field-data experiments demonstrate that U-STDRNet achieves a higher peak signal-to-noise ratio than the traditional U-Net. In addition, the model successfully restores fault and fold continuity details while exhibiting superior noise suppression compared to existing methods.

***Keywords:*** U-Net Swin Transformer-based dense residual network; Seismic image super-resolution; Seismic image denoising; Deep learning models; Swin transformer; Residual dense networks; Convolutional block attention module

***Corresponding authors:**
Juan Wu
(wujuan@yangtzeu.edu.cn)
Guangtan Huang
(gthuang@whrsm.ac.cn)

**Citation:** Wu M, Wu J, Bai M, Li H, Gui Z, Huang G. U-STDRNet: A unified model integrating swin transformer and residual dense network for seismic image super-resolution and denoising. *J Seismic Explor*. 2026;35(1):14-32.
doi: 10.36922/JSE025400081

**Received:** September 30, 2025

**Revised:** November 5, 2025

**Accepted:** November 5, 2025

**Published online:** December 1, 2025

**Copyright:** © 2025 Author(s). This is an Open-Access article distributed under the terms of the Creative Commons Attribution License, permitting distribution, and reproduction in any medium, provided the original work is properly cited.

**Publisher's Note:** AccScience Publishing remains neutral with regard to jurisdictional claims in published maps and institutional affiliations.

## 1. Introduction

In the field of oil and gas exploration, seismic data processing and interpretation are crucial for constructing models of underground geological structures. Seismic imaging reveals these structures by analyzing seismic wave propagation characteristics; however, real-world data often suffer from low resolution and high noise levels. These problems not only obscure geological features and cause loss of detail but may also mask important geological signals. Consequently, noise suppression, data restoration, and resolution enhancement are essential in seismic data processing. The pursuit of higher resolution and lower noise in seismic imaging has long been a focus in geophysics.

Traditional approaches can be broadly categorized into acquisition-based and processing-based methods. Acquisition-based techniques, such as high-density acquisition,[1,2] and broadband seismic acquisition,[3-5] aim to enhance data quality at the source. However, these techniques significantly increase the financial and computational costs of seismic surveys, which limits their widespread application. Processing-based techniques are widely used for denoising and enhancement after data acquisition. However, conventional methods face significant limitations. Filtering techniques often attenuate effective signals whose frequency spectra overlap with that of the noise.[6,7] Wavelet transform can lead to over-smoothing and loss of detailed features.[8,9] Statistical methods, such as those based on principal component analysis, rely on assumptions about data distributions that are often violated by complex real-world seismic data.[10] Although some advanced traditional methods, such as those based on low-rank and sparse constraints, have been developed to improve performance, they often entail high computational complexity or rely on assumptions that may not always hold for complex field data.[11-13]

To overcome the limitations of traditional methods, deep learning (DL) has emerged as a powerful alternative, offering data-driven learning capabilities and superior performance in capturing complex, nonlinear features.[14] Early applications primarily treated seismic image enhancement as a computer vision task, where convolutional neural networks (CNNs) were adopted to learn the mapping between low-quality and high-quality seismic data. Models such as the denoising CNN[15] and U-Net[16] became popular baselines. For instance, Wang *et al.*[17] used CNNs with data augmentation for random noise suppression. Numerous other DL methods based on CNN have also been proposed for denoising seismic data.[18-26] These studies demonstrated CNNs' potential but also revealed limitations in generalization and preservation of fine geological structures when dealing with strong noise or features beyond their training distribution. Subsequent research evolved to address specific seismic challenges, such as integrating geophysical priors into networks. For instance, Zhao and Rao[24] proposed a structure-preserving network to protect fault and stratigraphic interfaces during denoising. Others focused on signal compensation; for example, Liu *et al.*[27] used DL to compensate for absorption effects, accelerating high-resolution imaging. Peng *et al.*[28] combined a high-resolution seislet transform with a DL framework to enhance signal recovery in low signal-to-noise ratio data. Furthermore, to mitigate the reliance on vast amounts of labeled data—often scarce in geophysics—self-supervised[29] and unsupervised learning methods have been developed,[30-34] showing promise in learning from unlabeled or weakly labeled field data. Alongside these DL advances, sophisticated traditional methods, such as optimized wavelet transforms and convolutional sparse coding, remain active areas of research.[35,36] Furthermore, specific application-driven denoising approaches like Q-factor compensation highlight the need for tailored solutions for particular seismic processing tasks.[37] A significant advancement came with the introduction of attention mechanisms, which allow networks to focus on semantically critical features. The convolutional block attention module (CBAM), for example, guides networks to emphasize important channels and spatial regions (e.g., fault lines) while suppressing irrelevant noise.[38] More recently, Transformer architectures have been explored for their superior ability to model long-range dependencies. The Shifted Window (Swin) Transformer, with its hierarchical windowing mechanism, is particularly suited for seismic data, as it can efficiently capture the global continuity of seismic events—a key aspect where local CNNs often fail. Ding *et al.*[39] developed a Swin-Conv-UNet architecture, demonstrating the ongoing integration of Transformers and CNNs. Gao *et al.*[40] further advanced this by integrating the Swin Transformer with CNNs for simultaneous seismic data denoising and interpolation, effectively leveraging both global and local features.

Despite these advancements, a critical gap remains. Many existing studies address super-resolution and denoising as separate tasks or propose models that are adaptations of generic computer vision architectures. There is a pressing need for an end-to-end solution explicitly designed for the joint task—seamlessly integrating global contextual modeling (for event continuity), local feature refinement (for detail recovery), and adaptive attention (for geological structure preservation)—within a unified framework tailored to the intricacies of seismic data. Based on the above background and challenges, this paper proposes a novel DL model, U-Net Swin Transformer-

based dense residual network (U-STDRNet), for the joint task of seismic image super-resolution and denoising. The main contributions of this work are summarized as follows:

(i) Novel network architecture for seismic-specific challenges: We propose a dedicated U-Net-based architecture that organically integrates the Swin Transformer (Shifted Window Transformer convolutional residual blocks [STCRB]), residual dense blocks (ResDenB), and the CBAM. This is not a mere combination but a co-design where each module addresses a specific deficiency in seismic image processing. The STCRB captures long-range stratigraphic continuity through its window-based self-attention mechanism, effectively mitigating the issue of event discontinuity caused by noise or missing traces. The ResDenB enhances the recovery of weak yet critical signals, such as thin-layer interfaces, through dense feature reuse, while the CBAM embedded in skip connections acts as a feature filter, dynamically suppressing noise while highlighting spatially important geological structures like faults and folds.

(ii) Task-specific optimization: We introduce a mixed loss function combining $L_1$ loss and multiscale structural similarity index (MS-SSIM) loss, specifically tailored for seismic imagery. This combination significantly reduces the over-smoothing of geological edges commonly produced by pixel-wise losses alone, thereby better preserving the structural integrity and perceptual quality essential for geological interpretation.

(iii) Comprehensive validation on synthetic and field data: We extensively validate the proposed model on both synthetic datasets containing realistic geological structures (folds and faults) and two real field datasets. The results demonstrate that U-STDRNet not only achieves superior quantitative metrics (peak signal-to-noise ratio [PSNR], SSIM) but also exhibits significantly enhanced performance in visual quality, particularly in restoring fine details and improving the continuity of geological structures under high-noise conditions, showcasing strong generalization capability for practical applications.

## 2. Methods

Image super-resolution and denoising are low-level computer vision tasks that can be addressed using similar processing frameworks. First, the basic principles underlying these two problems are analyzed. For seismic super-resolution, the relationship between high-resolution and low-resolution seismic images is expressed as:

$$I_h = D(I_l, \theta) \tag{1}$$

Where $I_l$ and $I_h$ represent low-resolution and high-resolution seismic images, respectively; $D$ represents the down-sampling function, and $\theta$ is the parameter of this function. The goal of super-resolution is to obtain $I_h$ from the low-resolution seismic image using a CNN or other methods to approximate the high-resolution image.

For seismic denoising, if $I_p$ and $I_n$ represent the clean and noisy seismic images, respectively, the relationship between them can be expressed as:

$$I_n = I_p + n, \tag{2}$$

Where $n$ is the noise added to $I_p$. The goal is to estimate the noise distribution $n$, and then subtract it from the noisy seismic image $I_n$, yielding an output image approximating the clean seismic image $I_p$.

In this work, these two problems were solved simultaneously. The noiseless high-resolution seismic image and the noisy low-resolution seismic image were used as the real image $I_{output}$ and the input image $I_{input}$, respectively, following the formula:

$$I_{output} = N(I_{input}, \sigma) \tag{3}$$

Where $N$ represents the network used, and $\sigma$ denotes the parameter of the network. The goal is to achieve simultaneous super-resolution and denoising of seismic images using a neural network.

## 3. Network architecture

### 3.1. Overall architecture

The overall framework of the proposed U-STDRNet is illustrated in Figure 1. It is built upon a U-Net encoder-decoder backbone, which is renowned for its ability to preserve detailed spatial information through skip connections. To address the specific challenges of seismic image processing, we introduced three key innovations into this backbone:

(i) The STCRB modules replace standard convolutional blocks in the encoder and are designed to capture long-range global dependencies that maintain stratigraphic continuity.

(ii) The ResDenB modules are integrated within the decoder path, leveraging dense connections to maximize feature reuse, enhancing the recovery of fine details and weak signals (e.g., thin layers).

(iii) CBAM modules are embedded in the skip connections, acting as adaptive feature gates, dynamically weighting channel and spatial features to suppress noise in irrelevant areas and highlight crucial geological structures (e.g., faults) before merging encoder and decoder features.

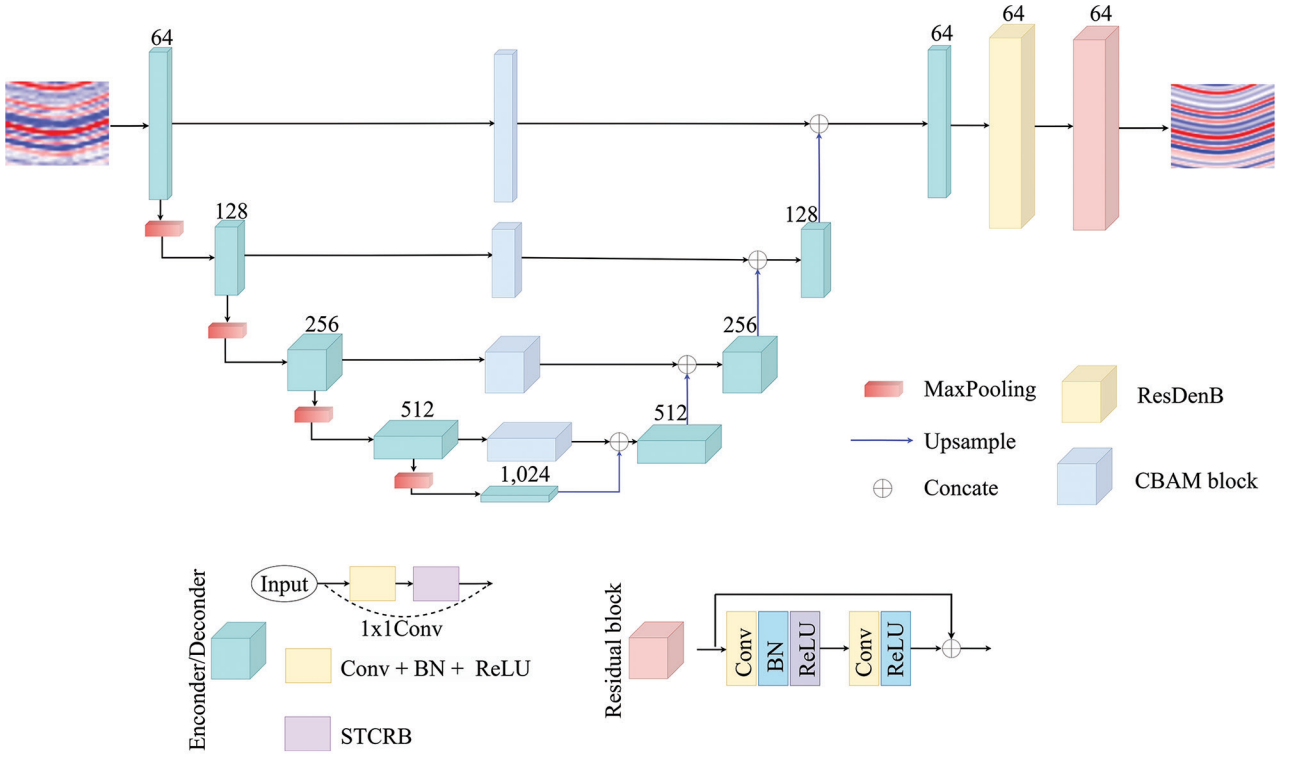


**Figure 1.** The structure of the U-Net Swin Transformer-based dense residual network
Abbreviations: BN: Batch normalization; CBAM: Convolutional block attention module; Conv: Convolution; ReLU: Rectified linear unit; ResDenB: Residual dense block; STCRB: Shifted Window Transformer convolutional residual blocks.

This synergistic design ensures that global context, local details, and feature importance are jointly optimized throughout the network for the combined task of seismic image super-resolution and denoising.

### 3.2. STCRB

Traditional CNNs struggle to model the long-range continuity of seismic events, especially in the presence of noise or missing traces. The STCRB module is designed to overcome this limitation by integrating the Swin Transformer's global self-attention mechanism, which effectively captures the contextual relationships across the entire seismic section, thereby maintaining stratigraphic continuity. This network is cascaded with multiple feature fusion blocks (FFB) to enhance denoising performance. The FFB leverages local similarity in seismic data and integrates features with varying amplitudes. Each FFB consists of a Swin Transformer module (FFBST) for global feature extraction and a convolution module (FFBC) for local feature extraction, which are detailed below. Global features capture time-dependent information, maintaining event continuity, while local features focus on highly correlated information, preserving weak signals. The module is shown in Figure 2.

(i) FFBST module: This module aims to address the limitation of traditional CNNs in global feature extraction. Because CNNs extract features through point-to-point local learning, they may lose seismic event continuity when dealing with missing seismic traces or noise and interference. Therefore, the FFBST module was designed to enhance global feature extraction. It integrated several components: layer normalization (LN), window-based multi-head self-attention (WMSA), a residual structure, and a multi-layer perceptron (MLP). This integration significantly enhanced global feature modeling. LN normalized the input features along the channel dimension, stabilizing training and accelerating convergence by ensuring consistent feature distribution across channels. WMSA was the core component of the FFBST module and was used to capture global features. The specific operation is as follows: suppose the input feature dimension is [10, 10, 32]. It is divided into multiple $8 \times 8$ window partitions, and the divided feature dimensions are ([$8 \times 8$], $8 \times 8$, 32), where ($8 \times 8$) represents the number of windows, $8 \times 8$ represents the size of each window, and 32 represents the number of channels. Subsequently, through

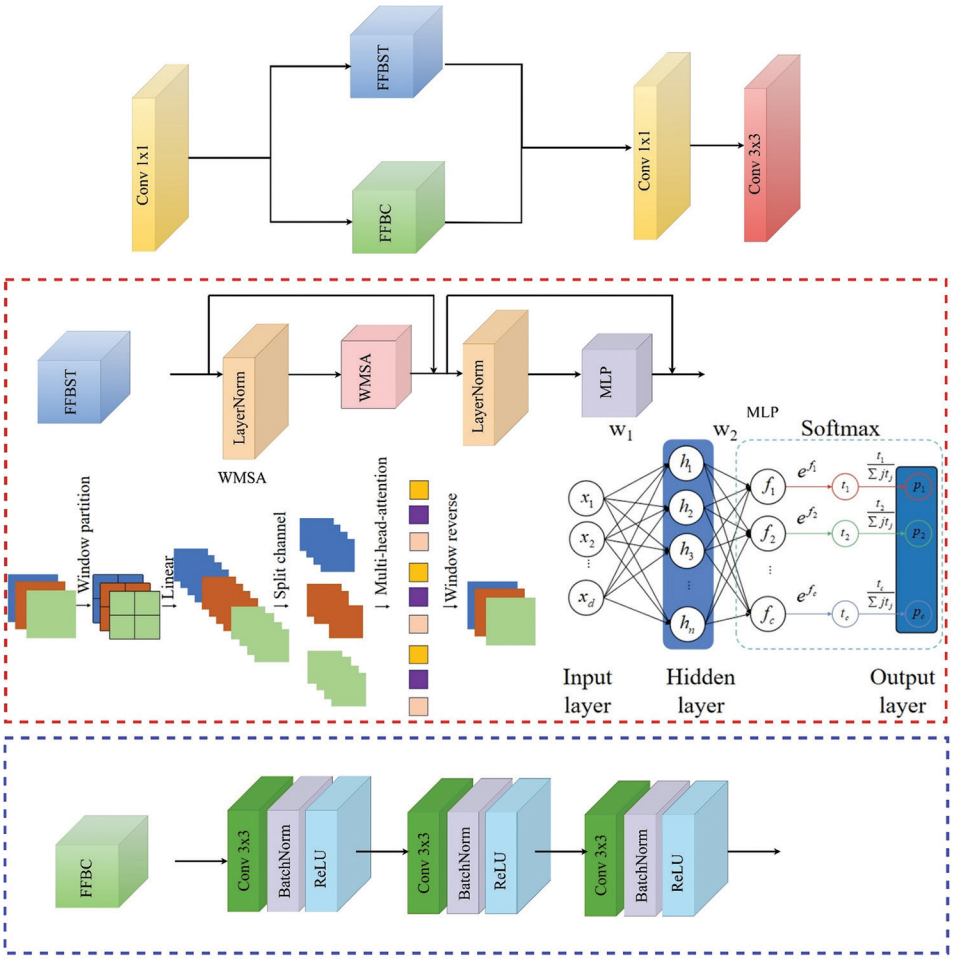


**Figure 2.** The structure of STCRB

Abbreviations: BatchNorm: Batch normalization; Conv: Convolution; FFBC: Feature fusion block with CNN; FFBST: Feature fusion block with Swin transformer; LayerNorm: Layer normalization; MLP: Multi-layer perceptron; ReLU: Rectified linear unit; STCRB: Shifted window transformer convolutional residual blocks; WMSA: Window-based multi-head self-attention.

channel division and dimension transformation, the feature dimension is further adjusted to (3, [108 × 108], 3, 8 × 8, 96) to meet the computational requirements of a multi-head attention mechanism. Here, the first position "3" represents three matrices (query, key, value) used for adaptive calculation, and the third position "3" represents the number of attention heads used in the multi-head attention mechanism. After the multi-head attention calculation is completed, the window features are restored to the original input size to maintain spatial consistency of the features. A residual structure adds the input features to the WMSA-processed features, mitigating gradient vanishing and preserving original feature information. The MLP is used to further fuse and refine features. Its structure includes an input layer, a hidden layer, and an output layer. The dimensions of the input layer are [10, 10, 32], the hidden layer [10, 10, 128], and the output layer [10, 10, 32]. Through a nonlinear activation function (such as Gaussian error linear unit), the MLP enhances the representational capacity of the features. The entire FFBST can be expressed as:

$$FFB\text{–}ST(X) = MLP(WMSA(LN(X))) + X \quad (4)$$

Where $X$ is the input feature, $LN$ represents LN, $WMSA$ represents the WMSA mechanism, $MLP$ represents a MLP, and the final residual connection ensures the integrity of the feature information.

(ii) FFBC module: Although CNNs have limitations in extracting global features, they excel at extracting local features by leveraging high correlation through shared weights. To fully exploit this advantage, the FFBC module was designed. The module enhanced local feature extraction by stacking three identical

sub-modules. Each sub-module comprised a 3 × 3 convolution (Conv 3 × 3), batch normalization (BN), and a rectified linear unit (ReLU) activation function.[41] The convolution kernel size of 3 × 3 was used to extract local information from the input features. Through sliding window operations, the convolutional layer captured local spatial patterns within the feature map, maintaining translation invariance. BN is used to standardize the features of the convolution output, speeding up the training process and improving model stability. BN reduced internal covariate shift by normalizing the mean and variance of features within each batch. The ReLU activation function is defined as

$$ReLU(x) = max(0, x) \tag{5}$$

And is used to introduce nonlinearity. ReLU helps alleviate the problem of vanishing gradients and accelerates network convergence.

The FFBC module is formed by stacking three identical submodules, and the structure of each submodule can be expressed as:

$$Module(x) = ReLU(BN(Conv.3 \times 3.(x))) \tag{6}$$

Where $X$ is the input feature, $Conv3 \times 3$ represents the 3 × 3 convolution operation, $BN$ represents BN, and $ReLU$ represents the activation function.

The overall process of the FFBC module can be expressed as:

$$FFBC(x) = module(module(module(x))) \tag{7}$$

By extracting and fusing local features across three layers, the FFBC module effectively enhances the network's ability to model local details. This provides richer feature representations for subsequent global feature extraction and tasks like denoising and super-resolution.

### 3.3. Residual dense blocks

Weak seismic signals, such as those from thin-layer interfaces, are often lost in deep networks. The ResDenB module was introduced to address this issue. By combining residual and dense connections, it facilitates the flow of information and gradients throughout the network, ensuring that subtle features are preserved and enhanced during the decoding process. It acts as a core component for seismic data denoising and missing-trace recovery. Its core design integrates residual learning and dense connections, allowing full utilization of multi-level feature information and thereby improving network performance. As shown in Figure 3, the key component in ResDenB is the residual dense block, which combines the advantages of residual connections and dense connections to effectively extract and transmit feature information. Residual blocks and dense blocks are defined as follows:

$$x \rightarrow x + f(x), \ldots (residual\ block) \tag{8}$$

$$x \rightarrow [x, f_1(x), f_2(x, f_1(x)), \ldots]\ (dense\ block), \tag{9}$$

Here, $f$, $f_1$, $f_2$,..., represent convolutional layers.

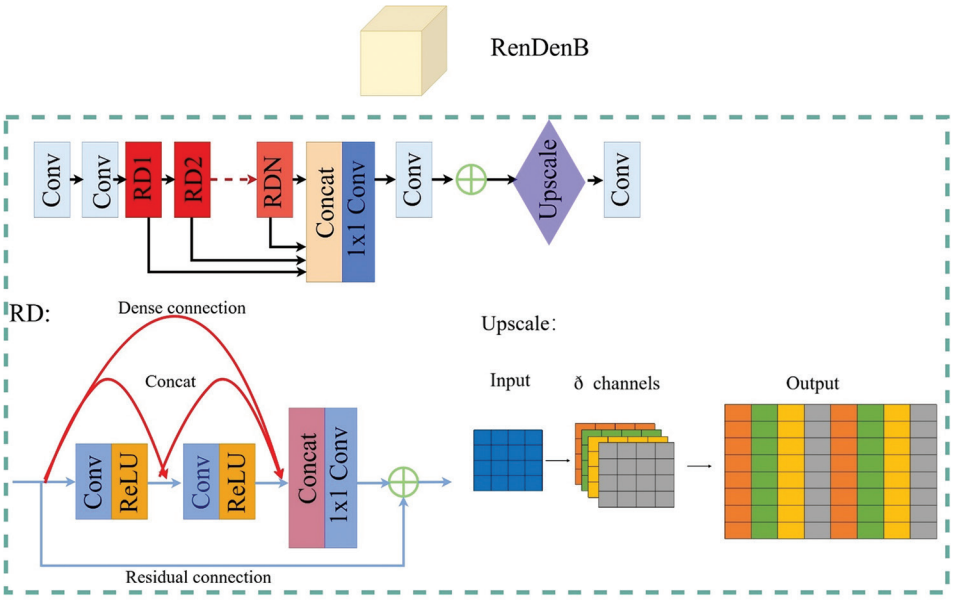


**Figure 3.** The structure of residual dense blocks (ResDenB)
Abbreviations: Conv: Convolution; RD: Residual dense block.

The residual dense block significantly enhances signal propagation within the network. It achieves this by combining residual and dense connections, promoting the cascaded utilization of multi-level features. This design not only effectively extracts local features but also enhances the network's representational ability through the feature-reuse mechanism. In addition, the skip connection in residual dense blocks further increases the network depth, improves training stability, and avoids problems such as gradient vanishing and gradient explosion. The Upscale module is a key component for improving spatial resolution. Its goal is to transform low-resolution seismic features into high-resolution features, thereby enhancing seismic data detail. To achieve this, we adopted a combination of the Pixel Shuffle layer and a convolutional layer. Given that temporal sampling in seismic data is usually sufficient, interpolation is performed only in the spatial dimensions. The pixel rearrangement layer is an efficient up-sampling method that improves the resolution of feature maps without introducing additional parameters. It works by redistributing channel information into the spatial dimensions, effectively increasing the spatial resolution.[42]

### 3.4. Convolutional block attention module

Not all features contributed by the encoder are equally important for reconstructing a clean, high-resolution image in the decoder. Seismic noise is often unevenly distributed, and key geological structures occupy specific spatial locations. The CBAM module addresses this by performing intelligent feature selection, suppressing noisy channels, and emphasizing spatially significant regions like fault lines, thus preventing the transfer of noise through skip connections. By incorporating an attention mechanism into CNNs, CBAM effectively enhances the network's ability to capture important features, improving performance in denoising and super-resolution tasks. As shown in

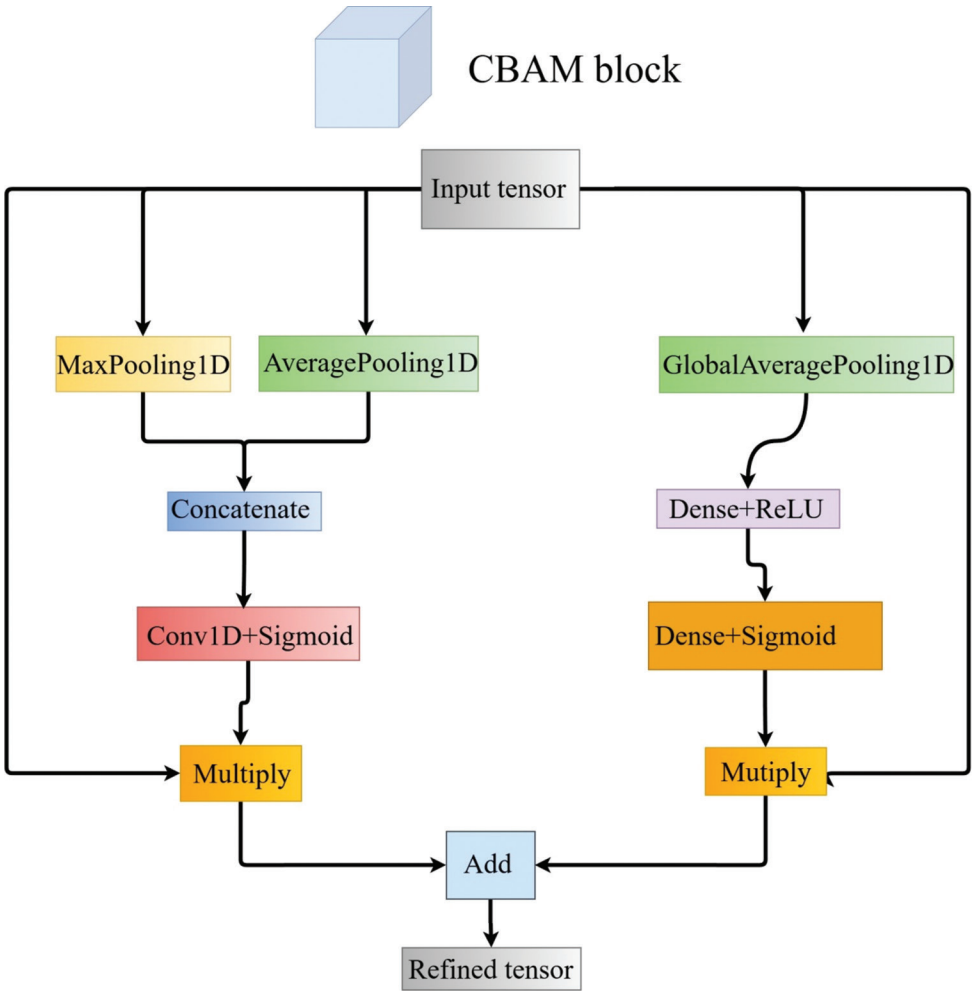


**Figure 4.** The structure of the convolutional block attention module
Abbreviations: Conv: Convolution.

Figure 4, the CBAM module mainly consists of two parts:

(i) Channel attention: The channel attention module computes global statistics of each channel through global average pooling and global maximum pooling operations. These global features are input into a fully connected layer to generate the channel attention diagram. Channel attention is used to weight the characteristics of each channel, highlighting the important channel characteristics and suppressing unimportant ones.

(ii) Spatial attention: The spatial attention module generates a spatial attention diagram by applying global average pooling and global maximum pooling across the channel dimension. Spatial attention weighs the features at each pixel location, highlighting important spatial regions and suppressing unimportant ones.

In the joint task, the CBAM module and Swin Transformer performed complementary functions. The Swin Transformer modeled global features such as stratum continuity through a hierarchical self-attention mechanism, while CBAM enhanced local detail representation through channel-spatial attention. For example, channel attention suppresses noise-dominated feature channels, while spatial attention focuses on high-frequency areas such as fault edges. Together, they enhance the model's recovery accuracy for complex geological structures.

## 4. Loss function

The loss function adopted in this study builds on the work of Li *et al.*[43] and combines L1 loss with MS-SSIM loss. This combined loss aims to improve the perceptual quality of restored images and reduce over-smoothing of geological edges. The specific loss function is described in Sections 4.1–4.3.

### 4.1. $L_1$ loss

$L_1$ loss is a commonly used pixel-level loss function that measures the pixel-wise difference between the predicted image and the target image. It has been widely used in image super-resolution tasks. It is defined as follows:

$$L_{L1} = \frac{1}{N}\sum_{i,j}|I_{S\cdot R(i,j)} - I_{H\cdot R(i,j)}|, \tag{10}$$

Where $N$ is the total number of pixels in the image, $I_{SR}(i, j)$ is the pixel value of the super-resolution image at $(i, j)$, and $I_{HR}(i, j)$ is the pixel value of the ground-truth high-resolution image at $(i, j)$.

### 4.2. Multiscale structural similarity loss

The MS-SSIM loss is a perceptual loss function used to measure the structural similarity between images. It considers image luminance, contrast, and structure, aligning more closely with human visual perception. SSIM is defined as follows:

$$SSIM(x, y) = [l(x, y)]^{\alpha} * [c(x, y)]^{\beta} * [s(x, y)]^{\gamma}, \tag{11}$$

Where $l(x, y)$ represents brightness comparison, $c(x, y)$ represents contrast comparison, $s(x, y)$ represents structure comparison, and $\alpha$,$\beta$, and $\gamma$ are weighting parameters. The specific calculation formulas are:

$$l(x,y) = \frac{2\mu_x\mu_y + c_1}{\mu_x^{2+}\mu_y^2 + c_1}, \tag{12}$$

$$c(x,y) = \frac{2\sigma_{xy} + c_2}{\sigma_x^{2+}\sigma_y^2 + c_2}, \tag{13}$$

$$s(x,y) = \frac{\sigma_{xy} + c_3}{\sigma_x\sigma_y + c_3}, \tag{14}$$

Where $\mu_x$ and $\mu_y$ are the mean intensities of images $x$ and $y$, respectively; $\sigma_x$ and $\sigma_y$ are the standard deviations of images $x$ and $y$, respectively; $\sigma_{xy}$ is the covariance of images $x$ and $y$; $c_1$, $c_2$, and $c_3$ are small constants introduced to avoid division by zero. MS-SSIM calculates SSIM at multiple scales and combines the results. Typically, five scales are used for MS-SSIM computation. Its definition is as follows:

$$MS-SSIM(x,y) = [l_M(x,y)]^{aM} * \prod_{j=1}^{M}[c_j(x,y)]^{\beta_j} * [s_j(x,y)]^{\gamma_j}, \tag{15}$$

Where $M$ is the number of scales, usually set to 5.

### 4.3. Mixed loss function

To leverage the advantages of both $L_1$ and MS-SSIM losses, we use a mixed loss function defined as follows:

$$L_{Mix} = \alpha * L_{MS-SSIM} + (1-\alpha) * L_{l1}, \tag{16}$$

Where $L_{MS-SSIM} = 1-MS-SSIM(I_{SR}, I_{HR})$, and $\alpha$ is the weighting factor of the loss function, empirically set to 0.6 in this study. The mixed loss function significantly improves the quality of the restored images. This improvement is particularly evident in the restoration of detailed features such as faults and stratigraphic interfaces. Compared with using only the $L_1$ loss, the mixed loss better preserves

geological details and reduces over-smoothing. Crucially, the inclusion of the MS-SSIM component serves as a strong structural constraint, which is vital for addressing the ill-posed nature of the super-resolution problem. By penalizing structural discrepancies across multiple scales, it effectively mitigates the risk of the model generating geologically implausible artifacts (i.e., "hallucinations"), thereby enhancing the fidelity of the output. Consequently, it improves the accuracy of subsequent seismic interpretation.

## 5. Evaluation metrics

To accurately evaluate the performance of the neural network in noise removal, we adopt PSNR as a quantitative evaluation metric. PSNR is a widely used metric in the field of image processing that measures the ratio between the maximum possible signal power and the power of corrupting noise. A higher PSNR value indicates a lower noise level and better image quality. For neural network denoising, PSNR is calculated using the mean squared error (MSE) between the original clean (noise-free, high-resolution) image and the network's output image. Specifically, PSNR is computed by the following formula:

$$PSNR = 20 * log_{10}\left(\frac{MAX_1}{\sqrt{MSE}}\right), \tag{17}$$

Where $MAX_I$ represents the maximum possible pixel value, and $MSE$ is the MSE between the original image and the processed image, defined as:

$$MSE = \frac{1}{N}\sum_{i=1}^{N}(I_{original}(i) - I_{processed}(i))^2, \tag{18}$$

Where $N$ is the total number of pixels, and $I_{original}(i)$ and $I_{processed}(i)$ represent the pixel values of the original image and the processed image at the $i^{th}$ pixel position, respectively.

By calculating PSNR, the ability of the neural network to remove noise while retaining image details and structural information can be quantitatively evaluated. A higher PSNR value generally indicates better denoising performance, meaning the network effectively reduces random noise while maintaining the clarity and accuracy of geological features. This metric is used to compare the denoising performance of different network architectures, loss functions, and training strategies in this study, providing an important reference for model optimization.

## 6. Training data

To ensure the quality and diversity of the training data, the dataset used in this study was derived from Wu *et al.*[44,45] As shown in Figure 5, the specific steps are as follows:

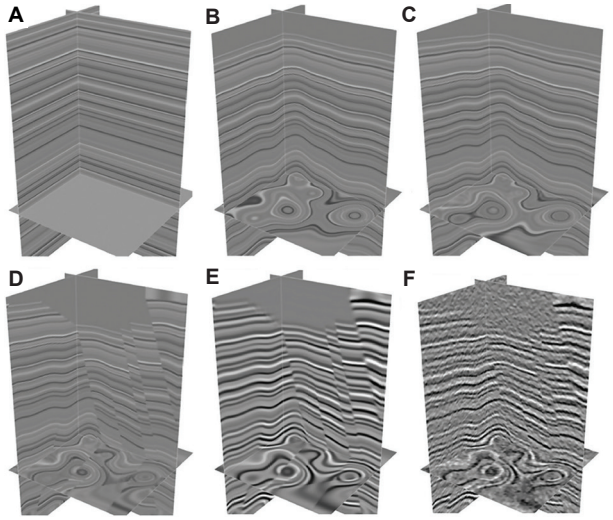


**Figure 5.** The workflow for creating a 3D synthetic training dataset. (A) Initial flat reflectivity model; (B) Model after adding fold structures using vertical shear and 2D Gaussian functions; (C) Model after further addition of fault structures via plane shear; (D) Final reflectivity model containing both folds and faults; (E) Synthetic high-resolution seismic data volume generated by convolving (D) with a Ricker wavelet; (F) Low-resolution noisy input data created by down-sampling and adding random noise to (E).

(i) Construction of initial reflectivity model: First, an initial reflectivity model (Figure 5A) was generated, which included all flat structures. Subsequently, fold and fault structures were added to the model to simulate the geological characteristics in actual seismic data.

(ii) Adding fold structure: Using a vertical shear model combined with several 2D Gaussian functions to define shear displacement, fold structures were added to the initial model (Figure 5B). This step simulated common geological folding phenomena in real seismic data and increased data complexity.

(iii) Adding fault structures: Plane shear (Figure 5C) was further added to the model to simulate geological faults. The inclusion of these fault structures made the model more representative of real geological conditions and enhanced data diversity.

(iv) Generation of reflectivity model: Through the above steps, a reflectivity model containing folds and faults was obtained (Figure 5D). This model was then used to generate a synthetic seismic data volume.

(v) Generating synthetic seismic data volume: The reflectivity model was convolved with a Ricker wavelet to generate a synthetic seismic data volume (Figure 5E). To simulate the noise interference present in real seismic data, random noise was added to the low-resolution data volume (Figure 5F).

(vi) Extracting 2D slices: 2D slices were extracted from the high-resolution seismic data volume as label images

in the training dataset. Corresponding 2D slices were also extracted from the low-resolution seismic data volume and down-sampled to serve as input images in the training dataset.

(vii) Data enhancement: To increase the diversity of the training data, the extracted 2D slices were augmented using operations such as random cropping and horizontal flipping.

(viii) Data normalization: The input and label seismic images were normalized to the range [0, 1] to ensure the stability and convergence of the training process.

Through the above steps, a high-quality 3D synthetic training dataset was generated, providing a solid foundation for model training and optimization.

## 7. Dataset partition

Following the method of Li *et al.*,[43] the generated synthetic seismic data were divided into training, validation, and test sets. Specifically, 600 3D seismic data volumes were used for the training set, 75 for the validation set, and 75 for the test set. From each seismic volume, a low-resolution noisy seismic image of size 128 × 128 was extracted as the network input, while a high-resolution noise-free seismic image of size 256 × 256 was used as the network output, as shown in Figure 6.

## 8. Experiments

The model was implemented in PyTorch (Meta AI Research, USA) and trained on an NVIDIA GeForce RTX 3090 graphics processing unit. The Adam optimizer[46] was used with parameters ($\beta_1 = 0.9$, $\beta_2 = 0.999$). The initial learning rate was set to $1 \times 10^{-4}$ and halved every 30 epochs. The model was trained for 100 epochs with a batch size of 16. The mixed loss function in **Equation 16** with $\alpha = 0.6$ was used to update the network parameters. The input patches were normalized to [0, 1]. Data augmentation techniques, including random cropping and horizontal flipping, were applied during training. To verify the effectiveness and generalization of the proposed U-STDRNet, both synthetic data and two field datasets were used for testing. The traditional U-Net served as the baseline for comparison. Figure 7 illustrates the overall workflow, comprising three stages: data preparation, model training, and evaluation. First, a 3D synthetic reflectivity model was generated to create paired low-resolution noisy inputs and high-resolution clean labels. These data pairs were then fed into the U-STDRNet model for training. Finally, the trained U-STDRNet was applied to both synthetic and field data for comprehensive evaluation.

### 8.1. Synthetic data examples

As mentioned above, 1,200 pairs of 2D images were generated for training. Each input seismic image and its corresponding target image were normalized to the range [0, 1] using the following formula:

$$x^* = \frac{x - x_{min}}{x_{max} - x_{min}}, \tag{19}$$

Where $x^*$ represents the normalized seismic image, and $x_{max}$ and $x_{min}$ denote the maximum and minimum values of each input seismic image, respectively. The images were then augmented using the previously described methods. During model training, the Adam optimizer[46] was used,

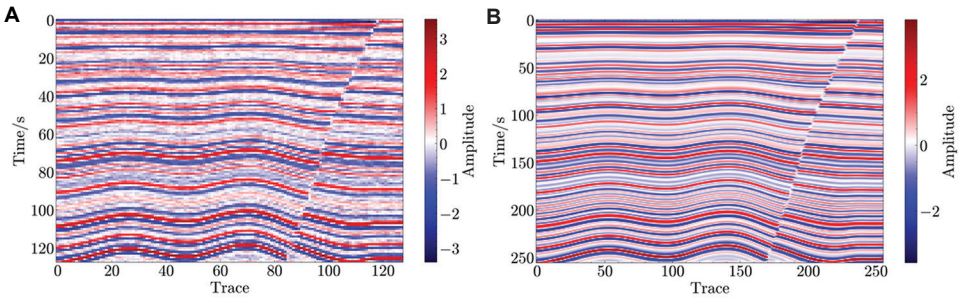


**Figure 6.** Example of training data. (A) Low-resolution noisy data; (B) High-resolution noise-free label data.

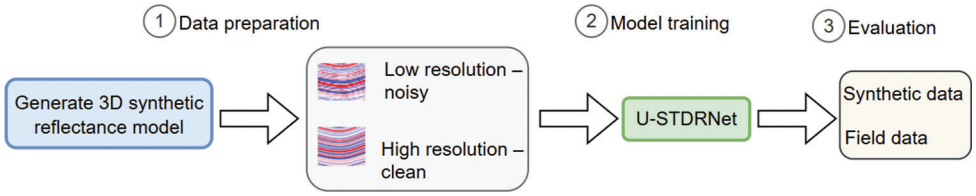


**Figure 7.** The overall workflow of the proposed method encompassing data preparation, model training, and evaluation phases

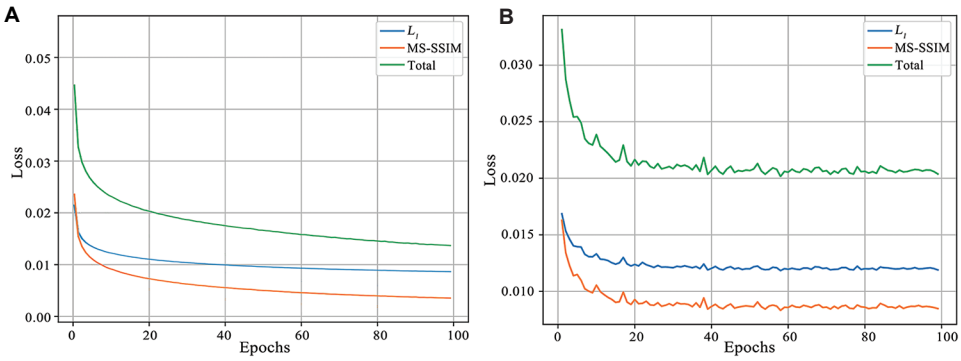


**Figure 8.** Training and validation loss curve for the U-Net: (A) Training; (B) Validation
Abbreviation: MS-SSIM: Multiscale structural similarity.

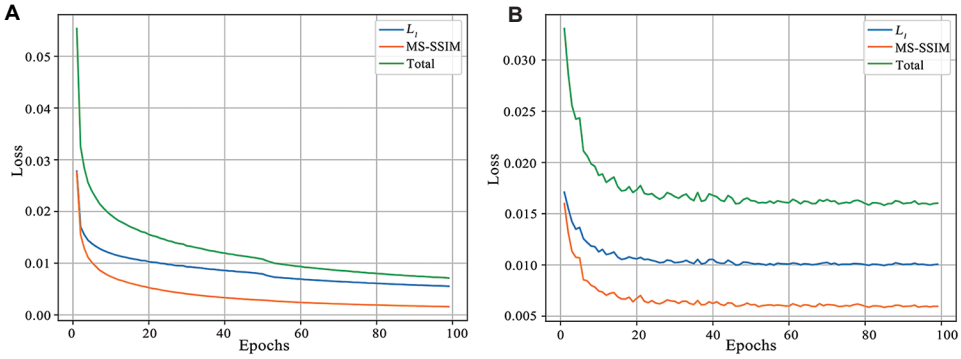


**Figure 9.** Training and validation loss curve for the U-Net Shifted Window (Swin) Transformer-based dense residual network: (A) Training; (B) Validation
Abbreviation: MS-SSIM: Multiscale structural similarity index.

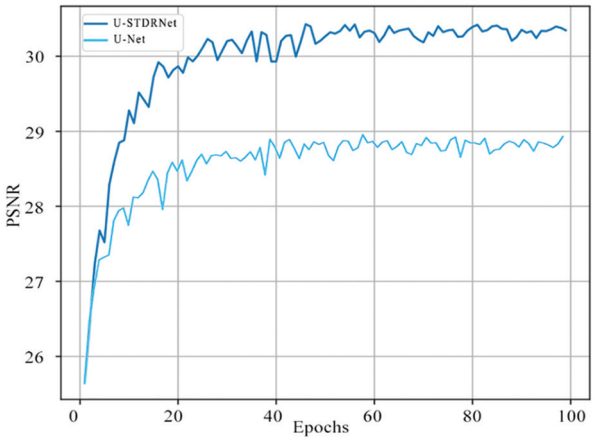


**Figure 10.** Peak signal-to-noise ratio comparison between U-Net and U-Net Shifted Window Transformer-based dense residual network (U-STDRNet) models

with the initial learning rate set to $1 \times 10^{-4}$. The batch size was 16, and a total of 16,000 image patch pairs were extracted from the training dataset. The network was trained for 100 epochs in total.

To evaluate the contribution of each proposed module (STCRB, CBAM, ResDenB) in the network, U-STDRNet and the original U-Net were trained and tested using identical datasets and hyperparameters. Figure 8 shows the training and validation loss curves for the U-Net, while Figure 9 demonstrates the corresponding curves for the U-STDRNet. Analysis of both figures revealed that U-STDRNet achieves lower training and validation loss than U-Net throughout the training process. Incorporating the proposed modules into the baseline U-Net further reduced both the $L_1$ loss and MS-SSIM loss components, indicating continuous optimization in pixel-level accuracy. In addition, image structure and perceptual quality progressively improved. The network also exhibited faster convergence and higher accuracy. Figure 10 presents the PSNR on the validation sets for both networks, showing that U-STDRNet consistently achieves higher PSNR than U-Net. This demonstrates U-STDRNet's superior ability to suppress random noise.

To quantitatively evaluate the contribution of each proposed module (STCRB, CBAM, ResDenB), seven experimental configurations were designed: Unet, Unet + CBAM, Unet + ResDenB, Unet + STCRB, Unet + STCRB + ResDenB, Unet + STCRB + CBAM, and

**Table 1. Quantitative comparison of different models**

| Model | PSNR | SSIM | $L_{mix}$ |
|---|---|---|---|
| U-Net | 28.903 | 0.907 | 0.014 |
| U-Net+CBAM | 29.301 | 0.909 | 0.012 |
| U-Net+ResDenB | 29.788 | 0.910 | 0.012 |
| U-Net+STCRB | 30.120 | 0.932 | 0.013 |
| U-Net+STCRB+ResDenB | 30.198 | 0.941 | 0.010 |
| U-Net+STCRB+CBAM | 30.056 | 0.950 | 0.009 |
| U-STDRNet | 30.523 | 0.956 | 0.008 |

Abbreviations: CBAM: Convolutional block attention module; ResDenB: Residual dense blocks; PSNR: Peak signal-to-noise ratio; SSIM: Multiscale structural similarity index; STCRB: Shifted Window Transformer convolutional residual blocks; U-STDRNet: U-Net Shifted Window Transformer-based dense residual network.

the full U-STDRNet model. Their performance on the synthetic test set, measured by PSNR, SSIM, and $L_{mix}$, is comprehensively compared in Table 1.

Table 1 provides a detailed ablation study, revealing the impact of different module combinations on model performance across multiple metrics:

(i) Effectiveness of individual modules: The introduction of any single module (CBAM, ResDenB, or STCRB) to the baseline U-Net brought consistent improvements across all three metrics. The STCRB module yielded the most significant boost in PSNR (+1.217 dB) and SSIM (+0.025), underscoring the paramount importance of global feature modeling using the Swin Transformer for capturing stratigraphic continuity. Concurrently, it also reduced the $L_{mix}$ metric by 0.001, indicating better preservation of geological edges. The ResDenB module, focusing on local feature enhancement through dense connections, achieved the second-highest PSNR gain and also improved SSIM. The CBAM module, acting as an adaptive feature selector, provided a moderate PSNR increase and the most notable reduction in the $L_{mix}$ value (from 0.014 to 0.012) among the single-module additions, demonstrating its particular efficacy in refining structural edges and suppressing noise in non-critical areas.

(ii) Synergistic effects of module combinations: The combination of modules revealed insightful interactions. The integration of STCRB and ResDenB (U-Net+STCRB+ResDenB) achieved a high PSNR of 30.198 dB and a significantly improved SSIM of 0.941, demonstrating that global context and local feature reuse are highly complementary. However, the combination of STCRB and CBAM (U-Net+STCRB+CBAM) resulted in the highest SSIM (0.950) and a further reduced $L_{mix}$ value (0.009), highlighting that global modeling coupled with attentive feature selection is exceptionally powerful for enhancing structural perceptual quality and edge accuracy. This suggests that, after establishing a strong global context, intelligently weighting features is more beneficial for structural fidelity than simply adding more network capacity.

(iii) Superiority of the full model (U-STDRNet): The proposed full U-STDRNet model, which integrated all three modules (STCRB, ResDenB, and CBAM), achieved the best performance across all metrics—the highest PSNR (30.523 dB), the highest SSIM (0.956), and the lowest $L_{mix}$ value (0.008). This demonstrates a clear synergistic effect, where each module addresses a distinct aspect of the problem—STCRB ensured global coherence, ResDenB enhanced fine detail recovery, and CBAM dynamically prioritized salient features and suppressed noise. The lowest $L_{mix}$ value confirms that U-STDRNet is most effective at preserving the sharpness and integrity of crucial geological structures like faults and stratigraphic interfaces, which is essential for accurate seismic interpretation.

Figure 11 presents a visual comparison of the results on the synthetic test set. At first glance, the outputs from U-Net (Figure 11A) and U-STDRNet (Figure 11B) appeared similar, as both effectively enhanced resolution. However, a standard visual comparison is insufficient to judge geological fidelity, which is critical for interpretation. To provide a precise, localized assessment of structural fidelity, we generated local SSIM maps (Figure 11C and 11D). These maps highlight areas of structural error. In these maps, brighter colors (yellow) represent high structural similarity (high fidelity) to the ground truth, while darker colors (green) represent low similarity (i.e., structural errors or artifacts). The SSIM map for U-Net (Figure 11C) reveals significant dark green patches concentrated along the complex fault zones and dipping events (highlighted by the red box), indicating that U-Net failed to accurately preserve the fidelity of these critical geological structures. In stark contrast, the SSIM map for U-STDRNet (Figure 11D) is almost uniformly bright yellow across the entire section, including the complex fault zone. This demonstrates superior and consistent structural fidelity, showing that our model correctly reconstructed the geological features where the U-Net failed.

This clear visual evidence directly supports the quantitative metrics in Table 1, where U-STDRNet achieved a much higher overall SSIM (0.956) compared to U-Net (0.907). Combined with the lowest $L_{mix}$ value (0.008) from the ablation study, this confirms our model's exceptional performance in preserving geological edges and minimizing structural distortion. These results provide compelling

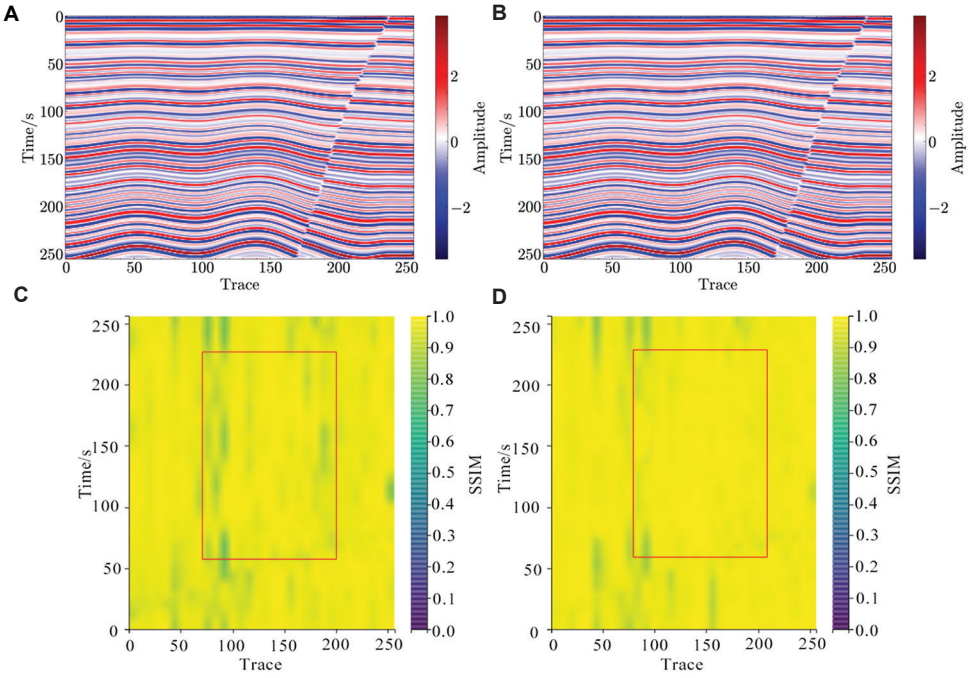


**Figure 11.** Results and local similarity on synthetic data for U-Net and U-STDRNet. (A) U-Net result; (B) U-STDRNet result; (C) Local SSIM versus ground truth (U-Net); (D) Local SSIM versus ground truth (U-STDRNet)
Abbreviations: SSIM: Structural similarity index; U-STDRNet: U-Net shifted window transformer-based dense residual network.

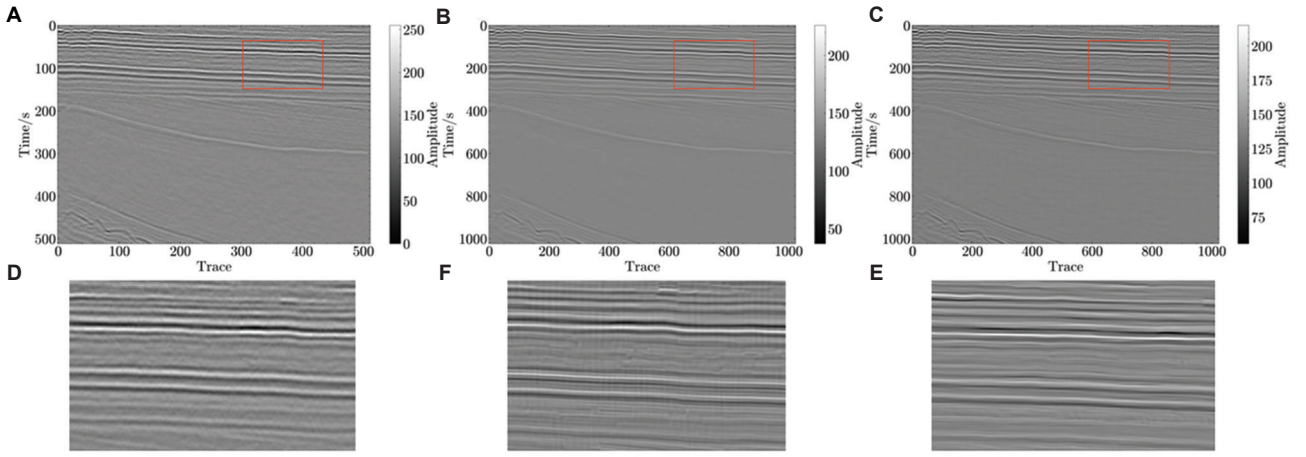


**Figure 12.** Comparison of the first field dataset. (A) Raw data; (B) Result of U-Net processing; (C) Result of U-STDRNet processing; (D-F) Enlarged images corresponding to the red borders.

evidence that the integration of global modeling (STCRB), local feature enhancement (ResDenB), and attentive feature selection (CBAM) in U-STDRNet collectively enables a more geologically faithful reconstruction.

### 8.2. Field data examples

In this section, two field datasets are used for testing. The complexity and diversity of real data place higher demands on model performance. The following is a detailed description of the processing results for these two datasets. The first field dataset is characteristic of a large, stable sedimentary region, such as a cratonic basin. As shown in the raw data (Figure 12A and D), the geological structure is relatively simple, dominated by flat-lying to sub-horizontal continuous reflectors. The primary challenge in this dataset is not structural complexity, but the presence of significant random noise that obscures the details of thin-layer interfaces. This data effectively tested the model's ability

to suppress noise while enhancing subtle stratigraphic features and improving event continuity.

Figure 12 shows the results for the first field dataset. Figure 12B and C show the seismic images processed using the original U-Net and U-STDRNet, respectively.

Figure 12E shows the seismic image processed using the original U-Net. Compared to the raw data (Figure 12D), the U-Net improves image resolution to some extent. However, it still exhibits shortcomings in restoring fine details and suppressing noise. Some geological features are over-processed by the U-Net, and new artifacts are introduced.

Figure 12F shows the seismic image processed by U-STDRNet. Compared to U-Net, U-STDRNet demonstrates superior detail feature recovery and noise suppression. Stratigraphic interfaces appear clearer. Waveform fluctuations and variations are smoother, and noise is effectively suppressed while original geological characteristics are preserved.

To quantitatively evaluate the resolution improvement, we restricted the analysis to 0–100 Hz and compared spectra within this band (Figure 13). Analysis of the 0–100 Hz spectrum (Figure 13) shows that U-STDRNet (red line) achieves better energy recovery than U-Net (green line) across low, intermediate, and high frequencies. This improvement is particularly pronounced in the high-frequency band, indicating that U-STDRNet better preserves the overall stratigraphic structure while more effectively enhancing details and achieving higher resolution. Therefore, for seismic data super-resolution, U-STDRNet exhibited superior resolution enhancement and geological information recovery capabilities compared to the traditional U-Net.

The second field dataset presents a more complex geological challenge, originating from a tectonically active area, such as a fold-and-thrust belt (e.g., on the margin of a basin). The raw section (Figure 14A and D) is dominated by complex structures, including steeply dipping strata and significant faulting. The reflectors show variable dips and discontinuities. Processing this data effectively requires the model to not only suppress noise but also maintain structural integrity across faults and accurately image the dipping events, testing the model's robustness and generalization to complex geological settings.

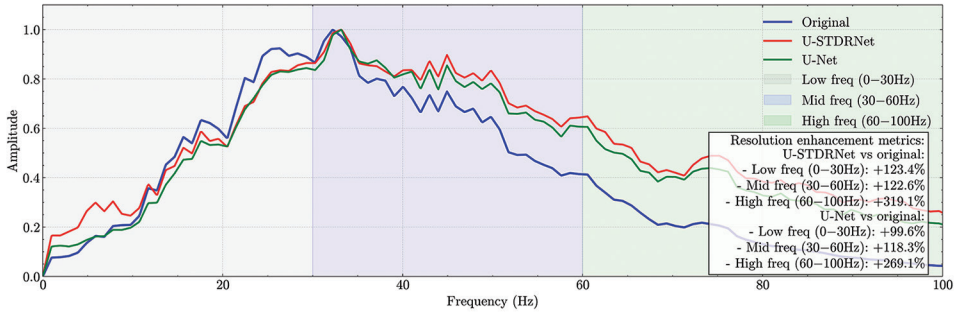


**Figure 13.** Spectrum comparison I (0–100 Hz)
Abbreviations: freq: Frequency; U-STDRNet: U-Net Shifted Window Transformer-based dense residual network.

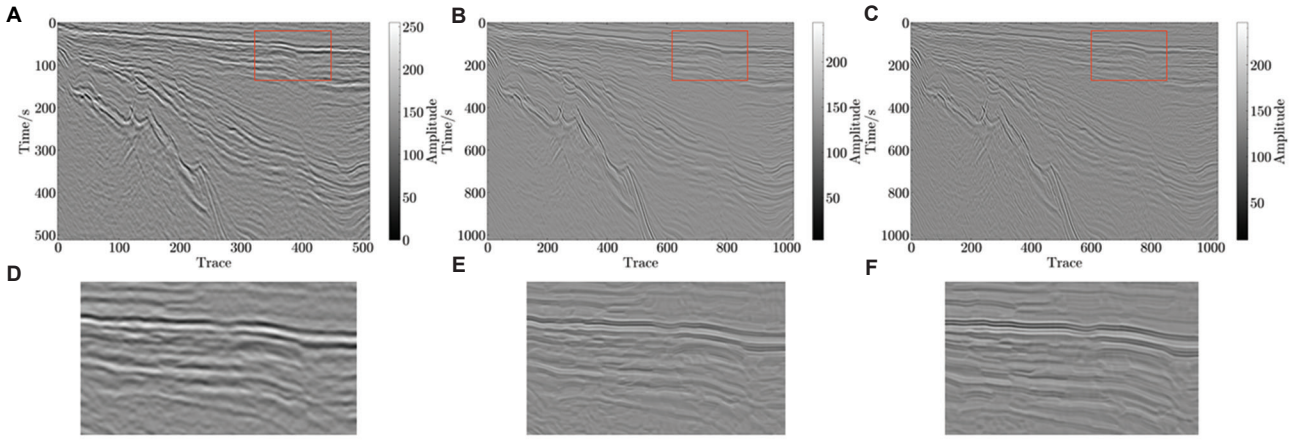


**Figure 14.** Comparison of the second field dataset. (A) Raw data; (B) Result of U-Net processing; (C) Result of U-STDRNet processing; (D-F) Enlarged images corresponding to the red borders.

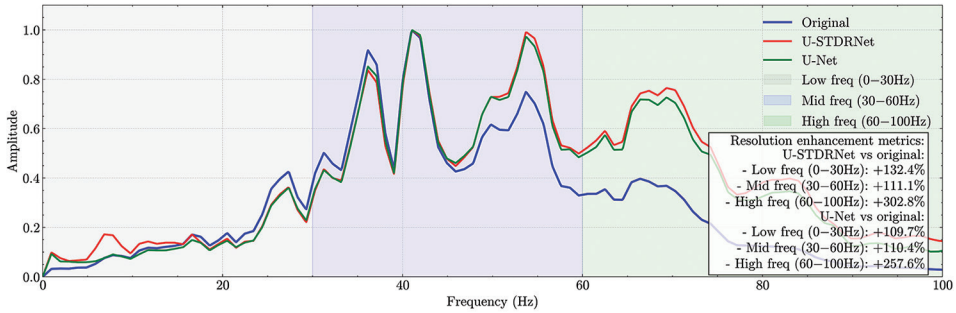


**Figure 15.** Spectrum comparison II (0–100 Hz)
Abbreviations: freq: Frequency; U-STDRNet: U-Net Shifted Window Transformer-based dense residual network.

As shown in Figure 14, we processed the second field dataset. Figure 14B and C, respectively, show the seismic images processed using the original U-Net and the U-STDRNet.

Figure 14E illustrates the result processed by the U-Net. When handling complex geological structures, the U-Net exhibits limited ability to recover detailed features and suppress noise. Some distinct features are smoothed out, stratigraphic interfaces remain unclear, and noise is still evident.

Figure 14F depicts the output of U-STDRNet. U-STDRNet restores key geological features, such as stratigraphic interfaces, more clearly. These features are significantly more distinct in the processed image.

The corresponding spectral comparison is shown in Figure 15. It is crucial to note that the original data spectrum (blue line) exhibits severe spectral oscillations, characterized by sharp, noisy peaks and deep spectral troughs (nulls). This indicates that the original signal is of low quality, with certain frequency bands already severely attenuated, likely due to geophysical (Q-filtering) effects. In contrast to this compromised original spectrum, within the 0–100 Hz range (Figure 15), U-STDRNet outperformed U-Net in recovering and enhancing signal energy in the low-frequency band. This indicates superior preservation and enhancement of the overall stratigraphic structure. Energy recovery in the mid-frequency band is more complete, demonstrating stronger resolution of stratigraphic details and better revelation of mid-scale geological characteristics. Energy recovery in the high-frequency band is most pronounced, indicating the greatest resolution improvement. This highlights U-STDRNet's enhanced capability for revealing small-scale geological features such as thin layers and faults.

To further strengthen the evaluation of field data processing, we introduced non-reference quantitative metrics, as ground-truth labels were unavailable. We employed image entropy to measure noise suppression (lower is better) and the Tenengrad gradient-based metric to quantify image sharpness and detail preservation (higher is better). Table 2 compares these metrics for the original data, the U-Net result, and our U-STDRNet result across both field datasets. The results showed a clear and consistent trend. For Field Data 1, the original data had high entropy (7.15). U-Net provided a moderate reduction (6.82), but our U-STDRNet achieved the lowest entropy (6.51), confirming its superior noise suppression capabilities. Concurrently, U-STDRNet also achieved the highest Tenengrad value (48.9), significantly improving upon U-Net (41.3) and the original (32.4), which indicates a much clearer restoration of stratigraphic interfaces. This advantage was even more pronounced in the complex Field Data 2. U-STDRNet again achieved the lowest entropy (6.79), demonstrating robust noise control even in structurally complex areas. More importantly, it scored the highest on the Tenengrad metric (79.5), demonstrating its exceptional ability to sharpen complex features such as dipping strata and faults, far exceeding U-Net (68.2). These results provide strong quantitative evidence, complementing the visual and spectral analyses, that U-STDRNet is more effective in both noise suppression and detail recovery for practical field data applications.

**Table 2. Quantitative comparison of field datasets using no-reference metrics**

| Dataset | Method | Image entropy | Tenengrad |
|---|---|---|---|
| Field data 1 | Original raw | 7.15 | 32.4 |
| | U-Net | 6.82 | 41.3 |
| | U-STDRNet | 6.51 | 48.9 |
| Field data 2 | Original raw | 7.32 | 55.7 |
| | U-Net | 7.01 | 68.2 |
| | U-STDRNet | 6.79 | 79.5 |

Abbreviation: U-STDRNet: U-Net Shifted Window Transformer-based dense residual network.

### 8.3. Result analysis

Comparing results on synthetic and field data shows that U-STDRNet provides clear advantages in seismic image super-resolution and denoising tasks. In detailed feature recovery, the U-STDRNet can better recover fine geological features in seismic images, which are crucial in seismic interpretation and can help geologists identify and analyze geological structures more accurately. In noise processing, the U-STDRNet performed better in noise suppression, effectively reducing random noise in the image and improving its clarity and quality, whereas noise remained more prevalent in the U-Net processed images. U-STDRNet delivers consistent performance across field datasets, demonstrating strong generalization to varying geological conditions and data characteristics. Comparison of PSNR values across models confirms U-STDRNet's superior overall performance, achieving the highest PSNR and indicating the best image quality.

## 9. Study limitations

Despite the proposed model's promising performance, this study has limitations that pave the way for future research. A primary concern in any DL-based image enhancement task is fidelity—ensuring the model does not generate false geological events. While our use of a mixed loss function with MS-SSIM and a U-Net architecture with skip connections was explicitly designed to mitigate this risk by enforcing structural consistency with the input data, a more rigorous validation is desirable. A gold-standard validation, as suggested by the community, would involve testing the model on synthetic datasets generated from well logs and rock-physics models. This would provide an undisputed ground truth to definitively verify that the enhanced details are geophysically meaningful. This represents a crucial next step in our future work. In addition, the current training data primarily addressed random noise, leaving the model's efficacy on coherent noise (e.g., multiples) less explored. Future work will also focus on incorporating physics-informed constraints and more diverse data augmentation strategies to improve robustness. Finally, extending the current 2D framework to a full 3D architecture is a key direction for better modeling of spatial continuity and for increasing the practical impact of U-STDRNet in modern seismic interpretation workflows.

## 10. Conclusion

In this paper, we present U-STDRNet, a novel DL framework designed specifically for the joint super-resolution and denoising of seismic images. The core innovation of U-STDRNet lies in its seismically aware architecture, which synergistically combines the global contextual modeling capabilities of the Swin Transformer (STCRB), the local feature enhancement and weak signal recovery prowess of ResDenB, and the adaptive feature refinement provided by the CBAM. Unlike a straightforward aggregation of existing components, the integration was carefully designed to address the distinct challenges of seismic data: preserving stratigraphic continuity, enhancing subtle geological features, and suppressing noise without introducing artifacts.

Experimental results on both synthetic and field datasets demonstrated that U-STDRNet significantly outperforms the baseline U-Net model. It showed superior performance in recovering complex structures and suppressing noise compared to state-of-the-art traditional methods such as signal-and-noise orthogonalization[47] and non-stationary predictive filtering,[48] particularly in terms of automation and feature preservation. It achieves higher PSNR and SSIM values and, more importantly, produces superior visual outcomes with clearer stratigraphic interfaces, better-restored fault and fold continuities, and more effective noise suppression. The ablation studies confirm the indispensable role of each proposed module in achieving these gains.

## Acknowledgments

None.

## Funding

This work was supported in part by the National Key Research and Development Program of China under Grant 2024YFB4007100, in part by the National Major Science and Technology Projects of China under Grant 2024ZD1004300, in part by National Natural Science Foundation of China under Grant 42304133 and 42574175, in part by Key Project of the Education Department of Hubei Province (Grant No. D20241304), and in part by Key project from the Hubei Research Center for Basic Disciplines of Earth Sciences under Grant HRCES-202401.

## Conflict of interest

The authors declare no conflicts of interest.

## Author contributions

*Conceptualization:* Min Bai, Guangtan Huang
*Formal analysis:* Juan Wu
*Investigation:* Mingliao Wu, Juan Wu, Haiyu Li
*Methodology:* Juan Wu, Zhixian Gui
*Writing–original draft:* Mingliao Wu
*Writing–review & editing:* Mingliao Wu, Guangtan Huang

## Availability of data

The data generated or analyzed during this study are available from the corresponding author upon reasonable request.

## References


1. Bianco MJ, Gerstoft P, Olsen KB, Lin FC. High-resolution seismic tomography of long beach, CA using machine learning. *Sci Rep.* 2019;9:14987.

   doi: 10.1038/s41598-019-50381-z

2. Zhang Y, Wang Y, Yin J. Single point high density seismic data processing analysis and initial evaluation. *Oil Geophys Prospect*. 2010;45(2):201-207.

   doi: 10.13810/j.cnki.issn.1000-7210.2010.02.008

3. Rebert T, Sablon R, Vidal N, Charrier P, Soubaras R. Improving pre-salt imaging with variable-depth streamer data. In: *SEG Technical Program Expanded Abstracts 2012*. United States: SEG; 2012. p. 1-5.

   doi: 10.1190/segam2012-1067.1

4. Wu X, Gan L, Yuan S, Rui D. A preliminary study on wellbore flow interpretation of fiber optic vibration signals based on K-means clustering algorithm. *SN Appl Sci*. 2022;4(8):233.

   doi: 10.1007/s42452-022-05117-6

5. Wang Y, Wang J, Wang X, Sun W, Zhang J. Broadband Processing Key Technology Research and Application on Slant Streamer. In: *International Geophysical Conference, Beijing, China, 24-27 April 2018*. United States: SEG; 2018. p. 135-138.

   doi: 10.1190/IGC2018-034

6. Mu XR, Mao Q, Huang JP. Stable attenuation-compensated reverse time migration and its application to land seismic data. *Petrol Sci*. 2023;20(5):2784-2795.

   doi: 10.1016/j.petsci.2023.03.014

7. Wang Z, Yue WZ, Zhu YM, Ji NX, Fan SS. Near-wellbore 3D velocity imaging inversion method based on array acoustic logging data. *Petrol Sci*. 2025;22:002341.

   doi: 10.1016/j.petsci.2024.06.007

8. Wang C, Chen L, Li L, *et al*. Combining unscented Kalman filter and wavelet neural network for anti-slug. *Petrol Sci*. 2023;20(6):3752-3765.

   doi: 10.1016/j.petsci.2023.05.008

9. Li L, Wang ZZ, Yin SD, *et al*. Selection and application of wavelet transform in high-frequency sequence stratigraphy analysis of coarse-grained sediment in rift basin. *Petrol Sci*. 2024;21(5):3016-3028.

   doi: 10.1016/j.petsci.2024.06.020

10. Liao QZ, Xue L, Lei G, Liu X, Sun SY, Patil S. Statistical prediction of waterflooding performance by K-means clustering and empirical modeling. *Petrol Sci*. 2022;19(3):1139-1152.

    doi: 10.1016/j.petsci.2021.12.032

11. Bai M, Huang G, Wang H, Chen Y. Seismic signal enhancement based on the low-rank methods. *Geophys Prospect*. 2020;68(9):2783-2807.

    doi: 10.1111/1365-2478.13028

12. Huang G, Bai M, Zhao Q, Wang H, Chen W, Chen Y. Erratic noise suppression using iterative structure-oriented space-varying median filtering with sparsity constraint. *Geophys Prospect*. 2021;69(1):101-121.

    doi: 10.1111/1365-2478.13032

13. Wu J, Bai M, Zhang D, Wang H, Huang G, Chen Y. Fast and robust low-rank approximation for five-dimensional seismic data reconstruction. *IEEE Access*. 2020;8:175501-17512.

    doi: 10.1109/ACCESS.2020.3026020

14. Liu W, Cheng Q, Liu L, Wang Y, Zhang J. Accelerating high-resolution seismic imaging by using deep learning. *Appl Sci Basel*. 2020;10(7):2502.

    doi: 10.3390/app10072502

15. Yu S, Ma J, Wang W. Deep learning for denoising. *Geophysics*. 2019;84(6):V333-V350.

    doi: 10.1190/geo2018-0668.1

16. Ronneberger O, Fischer P, Brox T. *U-Net: Convolutional Networks for Biomedical Image Segmentation; Proceedings of the Medical Image Computing and Computer-Assisted Intervention - MICCAI 2015*. Cham, F: Springer International Publishing; 2015.

    doi: 10.1007/978-3-319-24574-4_28

17. Wang Y, Lu W, Liu J, Zhang M, Miao Y. Random seismic noise attenuation based on data augmentation and CNN. *Chin J Geophys Chin*. 2019;62(1):421-433.

    doi: 10.6038/cjg2019M0385

18. Dong X, Zhong T, Wang H, Wu N, Li Y, Yang B. The denoising of desert seismic data acquired from tarim basin based on convolutional adversarial denoising network. *Chin J Geophys*. 2022;65(7):2661-2672.

    doi: 10.6038/cjg2022P0279

19. Bai T, Zhao H, Wang Z. *A U-Net Based Deep Learning Approach for Seismic Random Noise Suppression; Proceedings of the IGARSS 2022 - 2022 IEEE International Geoscience and Remote Sensing Symposium*; 2022.

    doi: 10.1109/IGARSS46834.2022.9880193

20. Halpert AD. Deep learning-enabled seismic image enhancement. In: *SEG Technical Program Expanded Abstracts 2018*. United States: SEG; 2018. p. 2081-2085.

    doi: 10.1190/segam2018-2996943.1

21. Jiang J, Ren H, Zhang M. A convolutional autoencoder method for simultaneous seismic data reconstruction and denoising. *IEEE Geosci Remote Sens Lett*. 2022;19:1-5.

    doi: 10.1109/LGRS.2021.3073560

22. Ma H, Yao H, Li Y, Wang H. Deep residual encoder-decoder networks for desert seismic noise suppression. *IEEE Geosci Remote Sens Lett*. 2020;17(3):529-533.

    doi: 10.1109/LGRS.2019.2925062

23. Wang F, Chen S. Residual learning of deep convolutional neural network for seismic random noise attenuation. *IEEE Geosci Remote Sens Lett*. 2019;16(8):1314-1318.

    doi: 10.1109/LGRS.2019.2895702

24. Zhao Z, Rao Y. Seismic random noise suppression based on SP-DnCNN neural network. *Chin J Geophys Chin*. 2024;67(10):3841-3850.

    doi: 10.6038/cjg2023R0483

25. Zhu W, Mousavi SM, Beroza GC. Seismic signal denoising and decomposition using deep neural networks. *IEEE Trans Geosci Remote Sens*. 2019;57(11):9476-9488.

    doi: 10.1109/TGRS.2019.2926772

26. Zhang S, Zhang L, Qin X. Seismic signal denoising using variational mode decomposition and a denoising convolutional neural network. *J Seim Explor*. 2025;34(2):025260030.

    doi: 10.36922/JSE025260030

27. Liu N, Wang J, Gao J, Chang S, Lou Y. Similarity-informed self-learning and its application on seismic image denoising. *IEEE Trans Geosci Remote Sens*. 2022;60:1-13.

    doi: 10.1109/TGRS.2022.3210217

28. Peng T, Liu Y, Liu C, Chen C, Chen J. Seislet weighted stacking method with high resolution for low SNR seismic data. *Chin J Geophys Chin*. 2025;68(3):1087-1101.

    doi: 10.6038/cjg2024R0866

29. Chen G, Liu Y, Zhang M, Zhang H. Dropout-based robust self-supervised deep learning for seismic data denoising. *IEEE Geosci Remote Sens Lett*. 2022;19:1-5.

    doi: 10.1109/LGRS.2022.3167999

30. Liu B, Yue J, Zuo Z, *et al*. Unsupervised deep learning for random noise attenuation of seismic data. *IEEE Geosci Remote Sens Lett*. 2022;19:1-5.

    doi: 10.1109/LGRS.2021.3057631

31. Shao D, Zhao Y, Li Y, Li T. Noisy2Noisy: Denoise pre-stack seismic data without paired training data with labels. *IEEE Geosci Remote Sens Lett*. 2022;19:1-5.

    doi: 10.1109/LGRS.2022.3145835

32. Shao J, Wang Y, Liang X, Xue Q, Liang E, Shi S. Siamese network based noise elimination of artificial seismic data recorded by distributed fiber-optic acoustic sensing. *Chin J Geophys Chin*. 2022;65(9):3599-3609.

    doi: 10.6038/cjg2022P0919

33. Wang S, Hu W, Yuan P, *et al*. A self-supervised deep learning method for seismic data deblending using a blind-trace network. *IEEE Trans Neural Netw Learn Syst*. 2023;34(7):3405-3414.

    doi: 10.1109/TNNLS.2022.3188915

34. Xu Z, Luo Y, Wu B, Meng D, Chen Y. Deep nonlocal regularizer: A self-supervised learning method for 3-D seismic denoising. *IEEE Trans Geosci Remote Sens*. 2023;61:1-17.

    doi: 10.1109/TGRS.2023.3329303

35. Geetha K, Hota MK, Karras DA. A novel approach for seismic signal denoising using optimized discrete wavelet transform via honey badger optimization algorithm. *J Appl Geophys*. 2023;219:105236.

    doi: 10.1016/j.jappgeo.2023.105236

36. Yang B, Bai M, Wu J, *et al*. Seismic data denoising using convolutional sparse coding with an efficient alternating direction multipliers minimization algorithm. *J Appl Geophys*. 2025;233:105610.

    doi: 10.1016/j.jappgeo.2024.105610

37. Zhang P, Wang Q, Liu Y, Chen C. A combined denoising method for Q-factor compensation of poststack seismic data. *J Appl Geophys*. 2024;229:105500.

    doi: 10.1016/j.jappgeo.2024.105500

38. Woo S, Park J, Lee JY, Kweon IS. *CBAM: Convolutional Block Attention Module*. Berlin: Springer; 2018.

    doi: 10.1007/978-3-030-01234-2_1

39. Ding M, Zhou Y, Chi Y. Seismic signal denoising using Swin-Conv-UNet. *J Appl Geophys*. 2024;223:105355.

    doi: 10.1016/j.jappgeo.2024.105355

40. Gao L, Shen H, Min F. Swin transformer for simultaneous denoising and interpolation of seismic data. *Comput Geosci*. 2024;183:105510.

    doi: 10.1016/j.cageo.2023.105510

41. Ioffe S, Szegedy C. Batch Normalization: Accelerating Deep Network Training by Reducing Internal Covariate Shift. In: *International Conference on Machine Learning Research*; 2015.

    doi: 10.48550/arXiv.1502.03167

42. Shi W, Caballero J, Huszar F, *et al*. *Real-Time Single Image and Video Super-Resolution using an Efficient Sub-Pixel Convolutional Neural Network; Proceedings of the 2016 IEEE Conference on Computer Vision and Pattern Recognition (CVPR)*; 2016.

    doi: 10.1109/CVPR.2016.207

43. Li J, Wu X, Hu Z. Deep learning for simultaneous seismic image super-resolution and denoising. *Ieee Trans Geosci Remote Sens*. 2021;3057857.

doi: 10.1109/TGRS.2021.3057857

44. Wu X, Hale D. 3D seismic image processing for faults. *Geophysics*. 2016;81(2):IM1-IM11.

doi: 10.1190/geo2015-0380.1

45. Wu X, Liang L, Shi Y, Fomel S. FaultSeg3D: Using synthetic data sets to train an end-to-end convolutional neural network for 3D seismic fault segmentation. *Geophysics*. 2019;84(3):IM35-IM45.

doi: 10.1190/geo2018-0646.1

46. Kingma D, Ba J. *Adam: A Method for Stochastic Optimization*. Berlin: Springer; 2014.

doi: 10.48550/arXiv.1412.6980

47. Huang G, Zhang D, Chen W, Chen Y. Accelerated signal-and-noise orthogonalization. *IEEE Trans Geosci Remote Sens*. 2022;60:1-9.

doi: 10.1109/TGRS.2021.3054839

48. Huang G, Bai M, Wang H, Liu X, Chen Y. Frequency-space-dependent smoothing regularized nonstationary predictive filtering. *IEEE Trans Geosci Remote Sens*. 2022;60:1-9.

doi: 10.1109/TGRS.2021.3064945

ACCSCIENCE PUBLISHING

Journal of Seismic Exploration

ARTICLE

# Thermal damage factors based on thermally induced wave-velocity variation in oil sands

**Hui Qi[1], Jing Ba[2]*, Wenhao Xu[2,3], Yuanyuan Huo[1], Jishun Pan[1], Qingchun Jiang[4], and Congsheng Bian[4]**

[1]Department of Intelligent Earth Exploration, School of Geosciences and Engineering, North China University of Water Resources and Electric Power, Zhengzhou, Henan, China

[2]School of Earth Sciences and Engineering, Hohai University, Nanjing, Jiangsu, China

[3]BGP INC., China National Petroleum Corporation, Zhuozhou, Hebei, China

[4]Department of Geology, Research Institute of Petroleum Exploration and Development, Beijing, China

## Abstract

Oil-sand reservoirs saturated with heavy oil are subject to complex physical and chemical changes under high-temperature conditions. These changes can be quantified using the thermal damage factor, which we evaluated based on Young's modulus and the velocities of P- and S-waves. For the quasi-solid phase of heavy oil-bearing rocks, this method effectively characterizes the degree of rock damage. As temperature increases, heavy oil transitions into a fluid state, reducing rock stiffness. In addition, the thermal expansion of heavy oil weakens the rock matrix and influences the extent of rock damage. We combined an extended Gassmann equation with the Maxwell model for heavy oil to estimate the thermal damage factor. The model was validated using ultrasonic experimental data from rock samples, enabling a quantitative description of the relationship between dry and wet rocks at different temperatures of thermal damage in oil sand. We found that in these rock samples, the temperature-dependent trend of the thermal damage factors can be separated into two stages based on the fluid-viscosity threshold (the liquid point). The porosity of rock samples has no significant influence on this threshold, whereas the viscosities of different fluids affect the threshold value of the thermal damage factor in oil sands. The proposed model provides a theoretical basis for improving the accuracy of reservoir prediction, evaluation, and adjustment, and for optimizing heavy-oil thermal recovery. Furthermore, it offers practical applicability for thermal-recovery monitoring and numerical simulation, enabling more reliable interpretations of temperature-dependent elastic responses.

***Keywords:*** Oil sand; Heavy oil; Temperature; Thermal damage; Gassman equation; Maxwell model

***Corresponding author:**
Jing Ba
(jba@hhu.edu.cn)

**Citation:** Qi H, Ba J, Xu W, *et al*. Thermal damage factors based on thermally induced wave-velocity variation in oil sands. *J Seismic Explor*. 2026;35(1):33-45. doi: 10.36922/JSE025420092

**Received:** October 19, 2025

**Revised:** November 19, 2025

**Accepted:** November 24, 2025

**Published online:** December 18, 2025

**Copyright:** © 2025 Author(s). This is an Open-Access article distributed under the terms of the Creative Commons Attribution License, permitting distribution, and reproduction in any medium, provided the original work is properly cited.

**Publisher's Note:** AccScience Publishing remains neutral with regard to jurisdictional claims in published maps and institutional affiliations.

## 1. Introduction

With the depletion of conventional reservoirs, unconventional hydrocarbon resources are emerging as the key focus of global petroleum exploration. Heavy oil reservoirs are

a widespread unconventional resource with large potential reserves.[1,2] To enhance the efficiency of exploration and production activities in heavy oil reservoirs, a comprehensive understanding of the basic physical properties of oil sands is required. The exploitation of oil-sand resources usually requires thermal methods, including cyclic steam stimulation, steam flooding, hot water flooding, and steam-assisted gravity drainage (SAGD).[3-6] The core of these methods is to reduce the viscosity of the heavy oil, thus increasing its mobility.[7] However, unconventional hydrocarbon reservoirs are subject to complex physical and chemical changes under high temperatures.[8] These changes can affect the efficiency of oil-sand production as well as the integrity and long-term stability of the reservoirs. This is the primary reason why studying the effects of temperature on the physical properties of heavy oil-bearing rocks is essential.

The effect of high temperature on the mechanical properties of rocks is related to lithology and other physical characteristics.[9-13] Many parameters have been investigated to analyze the influence of temperature on rocks. Dougill *et al.*[14] first proposed the concept of thermal damage. Trippetta *et al.*[15] combined experimental studies and microscopic analyses on saturated carbonate rocks filled with natural hydrocarbons, and found that at low temperatures, the hydrocarbons in the filled rocks were in a solid state. As the temperature increased to 100°C, the solid filler melted, causing the sample's velocity to decrease. The presence of molten hydrocarbons weakened the rock, damaging it and inducing fracturing. At low temperatures, the presence of solid hydrocarbons increased the mechanical properties of hydrocarbon-bearing carbonates. The thermal damage factor (TDF) is used to quantitatively evaluate changes in the mechanical properties of rocks at high temperatures.[16-19] For example, Yang *et al.*[20] conducted experimental studies on thermal damage in limestone. The results indicate that the impact of elevated temperatures on TDF can be directly quantified through the peak compressive strength and the variation rate of the effective solid matrix. As the temperature rises, these properties show a similar exponential trend.

The physical properties and related damage processes of rocks at different scales and depths are not only influenced by rock properties (such as mineral content, porosity, and permeability) but also by temperature, pressure, and pore fillings.[21-23] Heavy oil differs from traditional fluids. It exhibits different properties at different temperatures.[24-25] Butler[26] discussed thermal damage during oil-sand thermal recovery (such as SAGD), especially the dependence of bitumen and mineral properties on high temperature (Gates *et al.*[27]). Similarly, Han[28] studied the thermal damage in oil sands and concluded that heavy oil at high temperature weakens the rock's stiffness. Pang *et al.*[29] pointed out that the pore structure of reservoir rocks changes during steam injection, reducing production. He *et al.*[30] investigated the influence of clay minerals. Despite these studies (see also Yuan *et al.*[31]), there is still limited research on rock damage induced by heavy oil at high temperatures.

In this work, we estimated TDF from ultrasonic data and compared the results with predictions from a viscoelastic Maxwell model combined with an extended Gassmann (EG) equation[32-35] (Carcione's[36] discussion, Section 7.25). Finally, the dependence of thermal damage on temperature and pressure of the oil sands, as well as the thermal damage threshold, was analyzed.

## 2. Theory

### 2.1. Thermal damage factor

Zhao *et al.*[37] proposed the definition of TDF for rocks. For rock materials, TDF can be defined using the elastic-strain method, and it is a dimensionless index describing the damage to the microstructure caused by thermal stress and mineral phase changes during thermal recovery.[20,37] In heavy oil sands, heating during thermal recovery alters pore fluids, weakens grain contacts, and may trigger thermally driven microcrack growth. These effects collectively reduce the effective stiffness of the rock skeleton. TDF is therefore important because it provides a quantitative measure of this thermally induced deterioration, enabling the assessment of how temperature-dependent changes in the pore–grain system influence elastic wave velocities and, ultimately, the efficiency and safety of thermal production processes. For an elastic material, the corresponding expression is as follows:

$$\sigma = E_0 \varepsilon_0 \tag{1}$$

where $\sigma$, $E_0$, and $\varepsilon_0$ are the stress, Young's modulus, and strain of the rock in its undamaged state, respectively.

As the rock becomes damaged, we have:

$$\sigma = E_0(1-D)\varepsilon_1 \tag{2}$$

Where $E_T = E_0(1-D)$ is the Young's modulus of the damaged rock, $\varepsilon_1$ is the damaged strain, and $D$ is TDF. Then:

$$D(T) = 1 - \frac{E_T}{E_0} \tag{3}$$

Young's modulus and elastic wave velocity are related as follows:[38]

$$E = \frac{\rho V_P^2 (1+\upsilon)(1-2\upsilon)}{1-\upsilon} \tag{4}$$

Where $V_P$ is the P-wave velocity, $\upsilon$ is the poisson ratio, and $\rho$ is the density.

Combining **Equations 3** and **4**, we obtain the TDF:

$$D(T)=1-\frac{V_{PT}^2\rho_T(1+\upsilon_T)(1-2\upsilon_T)(1-\upsilon_0)}{V_{P0}^2\rho_0(1-\upsilon_T)(1+\upsilon_0)(1-2\upsilon_0)} \quad (5)$$

Where the subscripts $T$ and 0 represent damaged rock at heating temperature and undamaged rock at initial temperature, respectively.

When the temperature varies from room temperature to 160°C, the variations of $\upsilon$ and $\rho$ can be neglected, and TDF can be represented as:[19,20]

$$D_1(T)=1-\frac{V_{PT}^2}{V_{P0}^2} \quad (6)$$

Shear velocity can be defined using a similar approach. Alternatively, in terms of velocities, the Young's modulus can be written as:[38]

$$E=\rho V_S^2\frac{3V_P^2-4V_S^2}{V_P^2-V_S^2} \quad (7)$$

where $V_S$ is the S-wave velocity, and **Equation 5** becomes:

$$D(T)=1-\frac{\rho_T V_{ST}^2(3V_{PT}^2-4V_{ST}^2)(V_{P0}^2-V_{S0}^2)}{\rho_0 V_{S0}^2(V_{PT}^2-V_{ST}^2)(3V_{P0}^2-4V_{S0}^2)} \quad (8)$$

The variation in density with temperature can be neglected, and its influence on stress–strain behavior and TDF estimation is minor. Therefore, density changes do not significantly affect the evaluation of thermal damage trends in heavy oil sands. Hence, we have the TDF simplified to:

$$D_2(T)=1-\frac{V_{ST}^2(3V_{PT}^2-4V_{ST}^2)(V_{P0}^2-V_{S0}^2)}{V_{S0}^2(V_{PT}^2-V_{ST}^2)(3V_{P0}^2-4V_{S0}^2)} \quad (9)$$

### 2.2. Thermal damage estimation of heavy oil-saturated rocks

**Equation 9** indicates that the key parameters affecting the TDF of oil sands are the P- and S-wave velocities. Based on the EG equation,[33,34] we carried out fluid substitution to estimate the TDF of oil sand:

$$\rho_{oi}V_{Poi}^2=K_{oi}+\frac{4}{3}G_{oi} \quad (10)$$

$$\rho_{oi}V_{Soi}^2=G_{oi} \quad (11)$$

Where $\rho_{oi}$ is the density of the oil sand, $V_{Poi}$ and $V_{Soi}$ are the P- and S-wave velocities, respectively, and $K_{oi}$ and $G_{oi}$ denote the bulk and shear moduli, respectively.

Assuming that the porous rock has a uniformly distributed pore structure, we adopt the EG equations here[33-35] (Carcione's[36] discussion, Section 7.25):

$$\frac{1}{K_{oi}}=\frac{1}{K}-\frac{\left(\frac{1}{K}-\frac{1}{K_g}\right)^2}{\phi\left(\frac{1}{K_{if}}-\frac{1}{K_\phi}\right)+\left(\frac{1}{K}-\frac{1}{K_g}\right)} \quad (12)$$

$$\frac{1}{G_{oi}}=\frac{1}{G}-\frac{\left(\frac{1}{G}-\frac{1}{G_g}\right)^2}{\phi\left(\frac{1}{G_{if}}-\frac{1}{G_\phi}\right)+\left(\frac{1}{G}-\frac{1}{G_g}\right)} \quad (13)$$

Where $K_g$ and $G_g$ represent the bulk modulus and shear modulus of the grains, respectively; and $K_{if}$ and $G_{if}$ denote the effective bulk modulus and shear modulus of the pore-filling solid material, respectively; $\phi$ is the porosity; $K$ and $G$ represent the dry-rock bulk modulus and shear modulus, respectively; and $K_\phi$ and $G_\phi$ are dependent on the average deformation of pore volume. When we consider a homogeneous isotropic rock frame, $K_\phi$=$K_g$ and $G_\phi$=$G_g$. **Equations 12** and **13** can be expressed as:

$$K_{oi}=K+B \quad (14)$$

$$B=\frac{\left(1-\frac{K}{K_g}\right)^2}{\frac{\phi}{K_{if}}+\frac{1-\phi}{K_g}-\frac{K}{K_g^2}} \quad (15)$$

$$G_{oi}=G+C \quad (16)$$

$$C=\frac{\left(1-\frac{G}{G_g}\right)^2}{\frac{\phi}{G_{if}}+\frac{1-\phi}{G_g}-\frac{G}{G_g^2}} \quad (17)$$

Where the $B$ and $C$ are the pore moduli.

As a viscoelastic medium,[39] heavy oil exhibits three distinct phases depending on temperature: fluid, quasi-solid, and solid. Moreover, heavy oil has liquid and glass points.[40] Due to its high shear viscosity, heavy oil acts as part of the frame (skeleton) when the temperature is below the glass point. At elevated temperatures, however, its viscosity decreases significantly, and it is considered to be a fluid that exerts no influence on the rock frame.[40-42] Given that heavy oil in the solid phase exhibits a finite shear modulus and its viscoelastic properties are frequency-dependent, it

is reasonable to consider them in the frequency domain. Therefore, we adopted the Maxwell model to characterize the temperature- and frequency-dependent complex shear modulus, as it effectively captures the combined elastic and viscous behaviors of heavy oil:[31,33,43]

$$G_{if} = \frac{i\eta\omega}{\frac{i\eta\omega}{G_\infty}+1} \tag{18}$$

$$K_{if} = K_f + \frac{5}{3}G_{if} \tag{19}$$

Where $G_\infty$ denotes the shear modulus of the fluid within the high-frequency range, $K_f$ represents the bulk modulus corresponding to the pore fluid, $\omega$ is the angular frequency, $i$ is defined as the imaginary unit, and $\eta$ represents the viscosity of the fluid that varies with temperature.

For dry rock, its bulk modulus and shear modulus are:

$$K = \rho_{dry}V_{Pdry}^2 - \frac{4}{3}G \tag{20}$$

$$G = \rho_{dry}V_{Sdry}^2 \tag{21}$$

Where $\rho_{dry}$ is density, and $V_{Pdry}$ and $V_{Sdry}$ are the velocities of P- and S-waves in dry rocks, respectively.

**Equation 9** was used to obtain the TDFs of the dry rock at varying temperatures, relying on the measured P-wave and S-wave velocities of the dry rock. The damage in dry rock with increasing temperature is primarily caused by differential thermal expansion of mineral grains and microcrack propagation. As temperature rises, mismatched expansion between grains induces stress at grain boundaries, leading to the initiation and growth of microcracks, which progressively degrade the rock's elastic properties.[44] Then, the TDF was estimated using **Equations 9 – 19** as:

$$D_{roi}(T) = 1 - \frac{\rho_{dry}V_{Sdry}^2 + C}{\rho_{dry0}V_{Sdry0}^2 + C_0}FH \tag{22}$$

Where:

$$F = \frac{B - D_{dry}(T)\rho_{dry0}V_{Pdry0}^2 - \frac{1}{3}\rho_{dry0}V_{Pdry0}^2}{B_0 - \frac{1}{3}\rho_{dry0}V_{Pdry0}^2} \tag{23}$$

$$H = \frac{B_0 + \rho_{dry0}V_{Pdry0}^2 + \frac{1}{3}\rho_{dry0}V_{Sdry0}^2 + \frac{5}{3}C_0}{B + \rho_{dry0}V_{Pdry0}^2 - D_{dry}(T)\rho_{dry0}V_{Pdry0}^2 + \frac{1}{3}\rho_{dry}V_{Sdry}^2 + \frac{5}{3}C} \tag{24}$$

And $D_{roi}(T)$ and $D_{DRY}(T)$ are the TDFs of the rock saturated with heavy oil and dry rock at varying temperatures, respectively.

The workflow is presented in Figure 1. The main parameters involved included the measured velocities and density of dry rock, as well as the pore moduli ($B$ and $C$) of the heavy oil-saturated rock. To calculate these moduli, we initially calculated the bulk modulus of the matrix based on its mineral composition $K_g$, and then the fluid properties at the corresponding temperature. The porosity $\phi$ was a known input parameter of oil sands. These parameters were substituted into **Equations 15** and **17** to obtain the

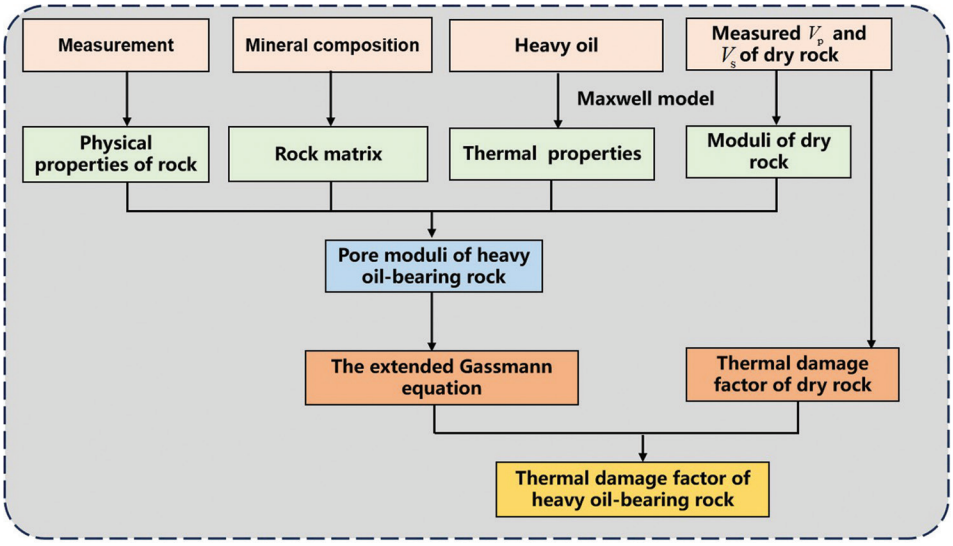


**Figure 1.** Workflow for estimating the thermal damage factor of oil sands at different temperatures

**Table 1. Physical properties of oil sands**

| Rock type | Density (kg/m³) | Porosity (%) | Grain density (kg/m³) | Mineral bulk modulus (GPa) | Mineral shear modulus (GPa) | Heavy oil (API) | Pore pressure (MPa) | Study |
|---|---|---|---|---|---|---|---|---|
| 1 | 1,981 | 41 | 2,650 | 36 | 44 | 7.5° | 2.3 | Yuan *et al.*[31] |
| 2 | 2,030 | 38 | 2,650 | 36 | 44 | 7.5° | 2.3 | Yuan *et al.*[31] |
| 3 | 1,890 | 41 | 2,490 | 18 | 21 | 6.6° | 0 | Li *et al.*[41] |
| 4 | 1,960 | 36 | 2,490 | 18 | 21 | 6.6° | 0 | Li *et al.*[41] |
| 5 | 1,970 | 42 | 2,660 | 21 | 24 | 6.6° | 0 | Li *et al.*[41] |
| 6 | 2,045 | 37 | 2,650 | 36 | 44 | 9.2° | 2.4 | Han *et al.*[25] |
| 7 | 1,980 | 32 | 2,431 | 22 | 24 | 6.9° | 3.5 | Li *et al.*[45] |

pore moduli at different temperatures, and then we used **Equations 22-24** to obtain the TDF.

## 3. Thermal damage factors of oil sands

Here, five oil sand samples (Samples 1, 2, 3, 4, and 5) were selected for analysis. The main mineral components of the samples (Samples 1 and 2) tested by Yuan *et al.*[31] were quartz, and the pore fluid was heavy oil with a 7.5° American Petroleum Institute (API) density and 50°C liquid point. When the temperature rose above the liquid point, the heavy oil behaved as a fluid. The shear modulus of the heavy oil approached zero at approximately 50°C under ultrasonic frequencies, at which point its viscosity was approximately 1,000 cP. During the experimental process, the pore pressure was set to 334 psi. The other samples (Samples 3, 4, and 5) were reported by Li *et al.*[41] The main minerals were quartz and clay. The pore fluid was heavy oil with a 6.6° API density and 48.7°C liquid point. During the test, the pore pressure was zero. Table 1 lists the samples' specific properties.

### 3.1. Effect of temperature on thermal damage factor

Understanding fluid properties is critical for analyzing the behavior of oil sands. Figure 2 depicts the relationship between the moduli and temperature for heavy oil in all samples and water. As the temperature decreases, the moduli of heavy oil increase. At low temperatures, the finite shear modulus of heavy oil must be taken into account, which makes the properties of oil sands different from those of conventional rocks. At higher temperatures, the shear modulus can be almost neglected and treated similarly to that of water, whereas the bulk modulus decreases with increasing temperature. Because the oil is highly viscous and dense, heavy oil-bearing rocks are more sensitive to temperature changes at low temperatures.[46]

Next, we considered TDF based on **Equation 9**, compared to the results of **Equation 6** (P-waves). Figure 3 shows $D_1$ and $D_2$ for the two samples. As can be seen, the values increased with increasing temperature. $D_1$ was lower

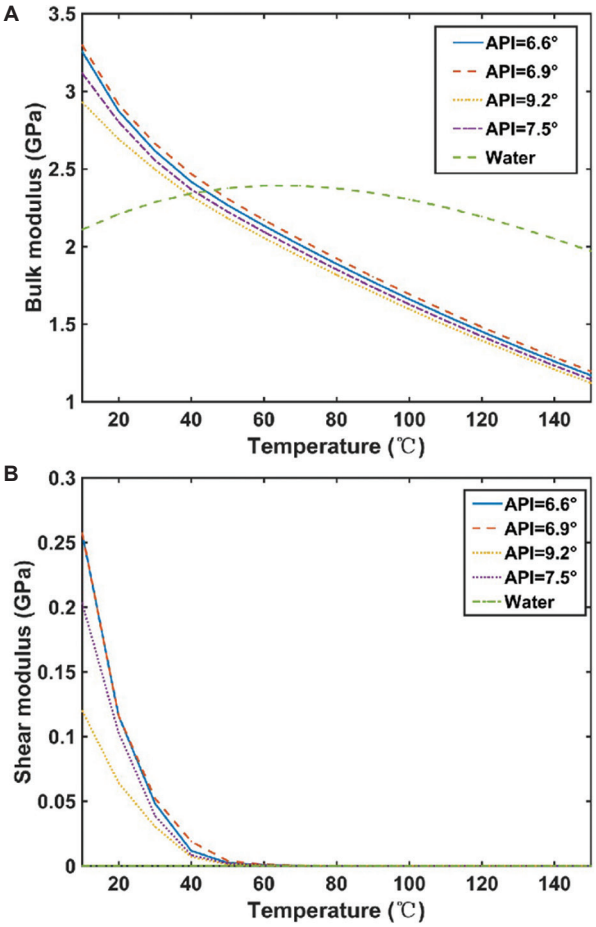


**Figure 2.** The (A) bulk and (B) shear moduli as a function of temperature for heavy oil and water

than $D_2$ at low temperature, and the difference decreased with decreasing temperature.

Next, we considered the TDF ($D_2$) based on **Equation 9**. Figure 4 shows the TDFs for four samples. As can be seen, TDF increased with increasing temperature. In the comparison, at low temperatures, Sample 3 exhibited a higher TDF value compared to Sample 1, indicating that

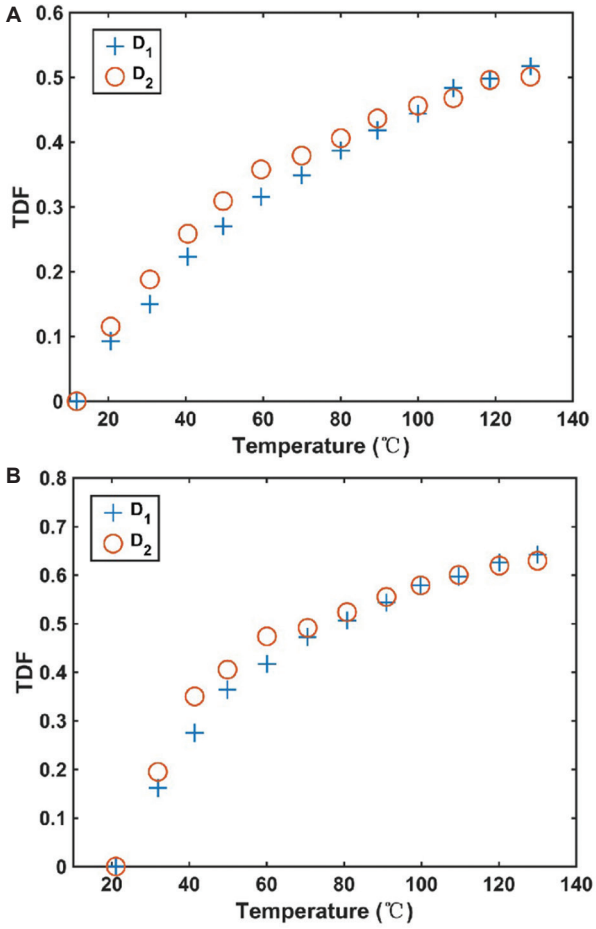


**Figure 3.** Thermal damage factors (TDFs) of (A) Sample 1 and (B) Sample 2 as a function of temperature under a confining pressure of 5.93 MPa. Data from Yuan *et al.*[31]

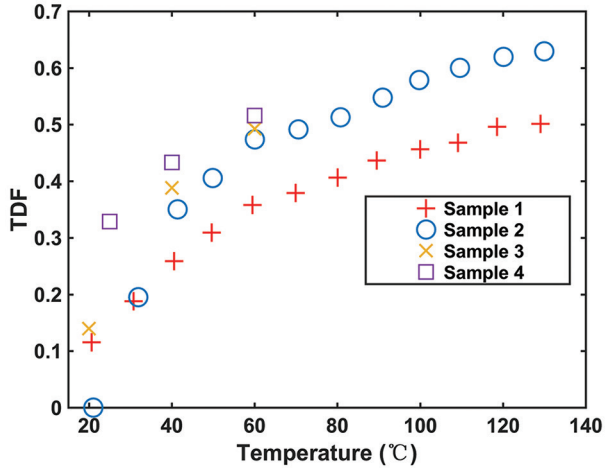


**Figure 4.** Thermal damage factors (TDFs) of samples as a function of temperature. The data for Samples 1 and 2 were from Yuan *et al.*[31] under a confining pressure of 5.93 MPa, while those for Samples 3 and 4 were from Li *et al.*[41] under a confining pressure of 7.58 MPa.

the presence of heavy oil causes the higher values in the rock. Moreover, the properties of Sample 3 were more dependent on the properties of heavy oil. Therefore, the velocities of Sample 3 were more sensitive to temperature. When the samples were saturated with the same heavy oil, the TDF of Sample 2 was higher than that of Sample 1, indicating that porosity also has an impact on rock damage (a similar trend is observed when comparing with Samples 3 and 4). It is known that the response of oil sand to temperature reflects the combined effect of the heavy oil and the rock frame.[47]

### 3.2. Effect of pressure on thermal damage factor

When the rock frame is subjected to confining pressure, the influence of pressure should be considered during the heat-extraction process. The experimental data of oil sands reported by Li *et al.*[41] were used to analyze the effects of temperature and pressure on the thermal damage in three artificial oil sand samples (Samples 3, 4, and 5). The properties are provided in Table 1.

For the three samples at different confining pressures, Figure 5 depicts how $V_P/V_S$ varies with temperature. From Figure 5, we observed that $V_P/V_S$ showed a trend of first increasing and then decreasing. This is because the heavy oil was in the quasi-solid phase. With increasing temperature, the rate of decline for S-wave velocity was more significant than that for P-wave velocity. When the temperature exceeded the liquid point, the S-wave velocity was almost unchanged, but the P-wave velocity continued to decrease, causing a decreasing trend in the $V_P/V_S$ ratio. This indicates that heavy oil may have no significant impact on the S-wave velocity for the liquid phase. It has been demonstrated that pressure affects the properties of rocks.[31,46,48] When the temperature was constant and the confining pressure increased, $V_P/V_S$ decreased, especially for heavy oil in the fluid phase, indicating that the samples became stiffer at higher pressure. For Samples 3, 4, and 5, which have larger porosities, soft cracks are more easily closed under pressure.[49] As a result, the velocities increase significantly.

We used dry Sample 3 as an example in Figure 6 to show velocities as a function of pressure with an exponential law of the Shapiro type[50] at room temperature (Figure 6A). Subsequently, fluid substitution was performed with heavy oil using the EG equation, and the results were compared with experimental data (Figure 6B). From the figure, it is evident that the increase in the velocity of the dry samples with pressure reflects the closure of cracks and pores within the rock. As pressure increased, the rock's elastic moduli increased, resulting in higher wave velocities. Furthermore, pressure has an effect on the velocities of wet samples. We

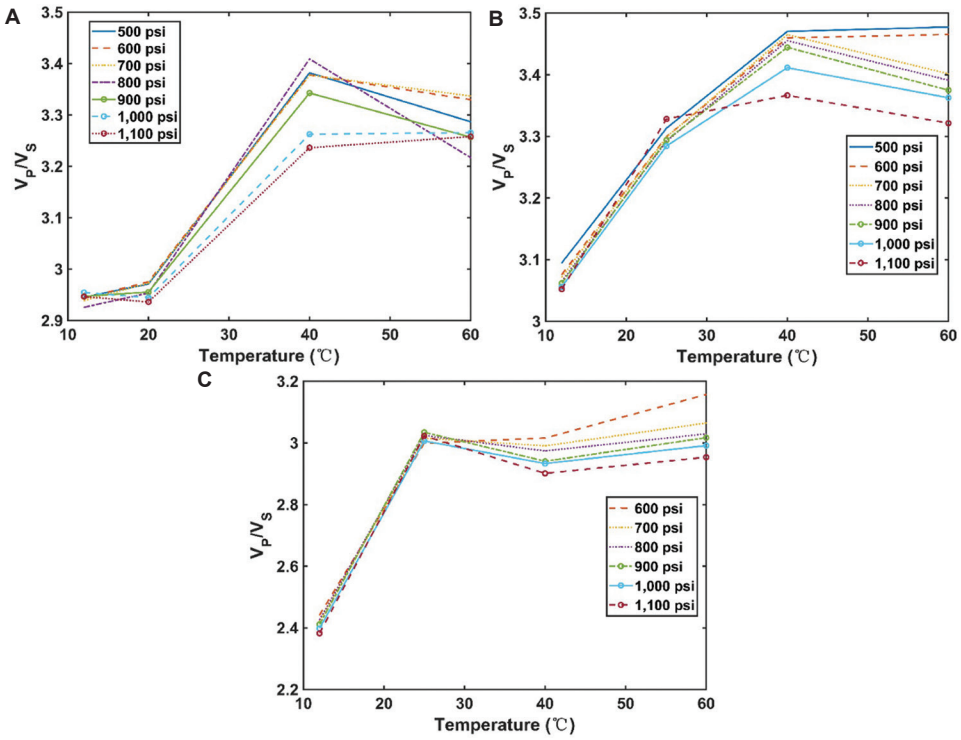


**Figure 5.** $V_P/V_S$ as a function of temperature with different confining pressures in (A) Sample 3, (B) Sample 4, and (C) Sample 5. Data from Li *et al.*[41]

considered **Equation 9** to calculate TDFs of Samples 3, 4, and 5 to analyze the effect of confining pressure on TDF. As seen in Figure 7, TDF tended to decrease as the confining pressure increased. This is due to the fact that the velocities increase with pressure. Moduli of rock increase under higher pressures, and the rock becomes a stiffer medium, making it less prone to damage at the same temperature.

## 4. Thermal damage factors of dry and heavy oil rocks

Sample 6 (in Table 1) tested in Han *et al.*[25] was selected for analysis. The pore fluid was heavy oil characterized by 9.2° API density and a liquid point of approximately 60°C. During the test, the pore pressure was maintained at 2.4 MPa. The oil sand Sample 7, reported by Li *et al.*,[45] was also considered. The sample was composed of silt-size grains, which mainly consist of quartz, with minor amounts of clay, feldspar, and plagioclase. The pore fluid is heavy oil with a 6.9° API density and 49°C liquid point. During the experiment, the pore pressure was set to 3.5 MPa.

### 4.1. Estimation of the thermal damage factor of heavy oil-saturated rocks

Temperature-dependent velocities of dry and oil-saturated samples for Samples 6 and 7 are shown in Figure 8. The velocities of the wet samples were significantly higher than those of the dry ones. When the liquid point was exceeded, the P-wave velocity gradually decreased, while the S-wave velocity remained constant, indicating that the heavy oil exists in a fluid state and that the rock velocity is mainly affected by the frame, crack, and fluid bulk modulus and density.[25,40]

Figure 9 shows the TDFs of dry and oil-sand samples. As can be seen, the trends were similar to those in Figure 4. The thermal damage in oil sands under varying temperatures was more pronounced than in the dry samples, suggesting that the transition of heavy oil to a fluid state reduces rock stiffness and increases damage as temperature rises.[43]

By assuming that TDFs of the dry rocks were known (Samples 6 and 7), fluid substitution was carried out by combining the EG and Maxwell models to estimate TDFs of the wet rocks. The resulting data were compared with the actual results. Figure 10 shows that the model results are in good agreement with the experimental data, validating that the proposed method can effectively account for TDFs of oil sands with respect to temperature.

Then, we considered Sample 7 to analyze the dependence of the dry- and wet-rock moduli with respect to temperature (Figure 11). As can be seen, the wet-rock bulk modulus exhibited a more pronounced variation. Meanwhile, with increasing temperature, the wet-rock shear modulus approached that of the dry samples, as expected.

### 4.2. Thermal damage factor threshold

Han *et al.*[40] proposed a fluid viscosity threshold, specifically the liquid point, to explain the non-linear velocity behaviors of P- and S-waves. The normalized temperature is defined as:

$$T_n = \frac{T_w - T}{T_w - T_g} \quad (25)$$

where $T_w$ refers to the temperature when the viscosity of fluid is equivalent to the viscosity of water, which is 1 cP; and $T_g$ denotes the fluid glass point, defined as the temperature at which the viscosity reaches $10^{15}$ cP.

Figure 12 illustrates the relationship between TDFs and normalized temperature for Samples 6 and 7. The liquid points corresponded to $T_n = 0.86$ and 0.77 in Figure 12A and B, respectively, indicating the threshold between the linear and non-linear behaviors of TDF. These findings show that the viscosities of different fluids have varying effects on the TDFs of oil sands, whereas the porosity of rock samples has no evident influence on this threshold.

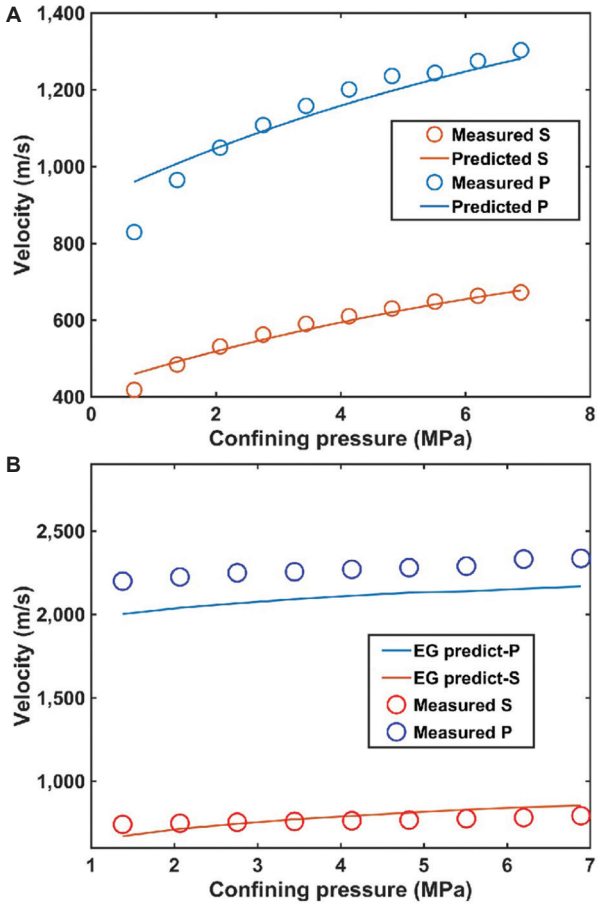


**Figure 6.** Predicted and measured velocities of (A) dry and (B) wet Sample 3 as a function of confining pressures at room temperature. Data from Li *et al.*[41]
Abbreviation: EG: Extended Gassmann.

## 5. Discussion

In this study, the thermal response of elastic wave velocities in oil sands reflects the coupled effects among mineral grains, pore fluids, and cracks with temperature variations. As shown in Figure 8 for Samples 6 and 7, both P- and S-wave velocities exhibited varying degrees of reduction with increasing temperature, indicating that as the temperature increases, the fluid properties, microstructure, and mechanical characteristics of oil sands undergo significant changes. The estimated TDF model was established based on wave velocity variations, the generalized Gassmann equations, and the Maxwell model. It effectively characterizes these thermally induced effects and provides a quantitative description of the initial stage of thermal damage.

Within the temperature range below the liquid point (approximately below 60°C for Sample 6 and 49°C for Sample 7), both P- and S-wave velocities showed a rapid and slightly non-linear decrease with increasing temperature. This stage mainly reflects the softening and partial flow of heavy oil, as well as the thermal expansion effect of pore fluids. At room temperature, heavy oil acts

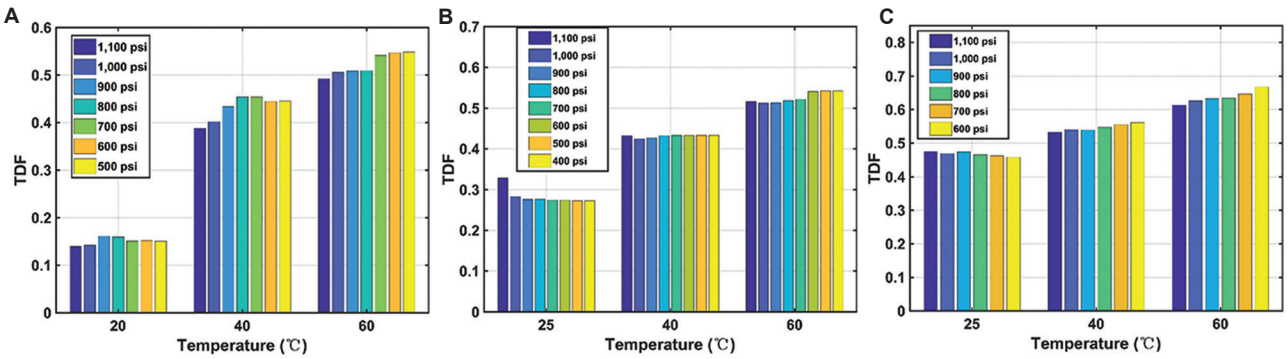


**Figure 7.** Thermal damage factors (TDFs) of (A) Sample 3, (B) Sample 4, and (C) Sample 5 at different confining pressures as a function of temperature

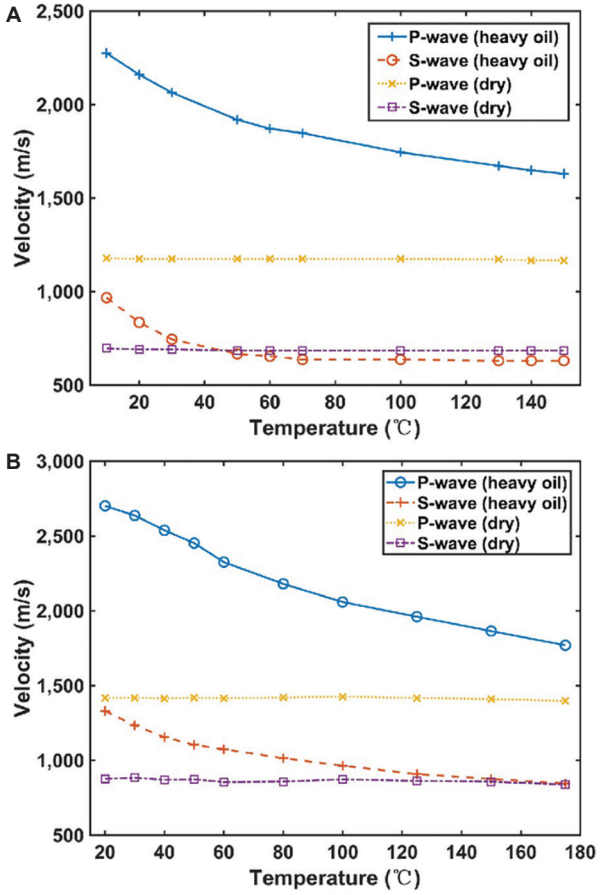


**Figure 8.** The velocities of dry and heavy oil samples of (A) Sample 6 and (B) Sample 7 as a function of temperature. Data of Sample 6 from Han *et al.*[25] under the confining pressure of 8 MPa, and Data of Sample 7 from Li *et al.*[45] under the confining pressure of 7 MPa.

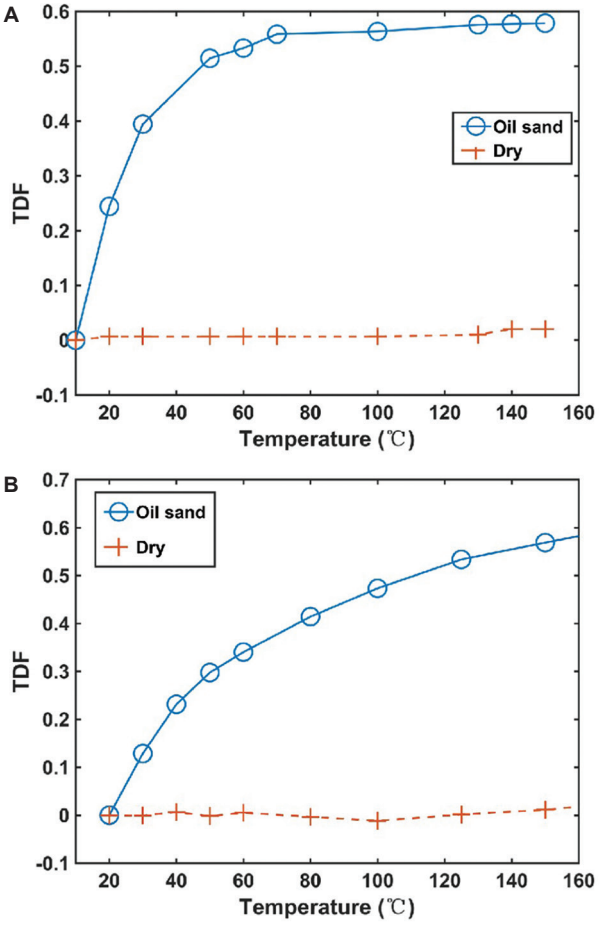


**Figure 9.** Thermal damage factors (TDFs) of (A) Sample 6 and (B) Sample 7 as a function of temperature under the confining pressures of 8 MPa and 7 MPa, respectively. Data of Sample 6 from Han *et al.*[25] and data of Sample 7 from Li *et al.*[45]

as a viscoelastic medium, providing bonding and support for mineral grains. As the temperature rises, its viscosity decreases significantly, weakening the contact stiffness and cementation strength between grains.[51] This causes a decrease in the rock's bulk modulus and shear modulus, leading to a reduction in the velocities of P-waves and S-waves. The heavy oil undergoes a continuous transition from a viscoelastic solid to a fluid. As the temperature increases, the relaxation time of heavy oil shortens significantly,[52] and its stress-bearing capacity at grain contacts weakens, leading to a gradual non-linear trend in the TDF–temperature relationship (Figures 9 and 10).

At higher temperature stages (approximately 160°C), the decreasing trend of P- and S-wave velocities became nearly linear. The decreasing rate of S-wave velocity was significantly lower than that in the low-temperature stage, indicating a notable reduction in the sensitivity of shear stiffness to temperature. From the comparison results of P-waves and S-waves, it can be observed that with

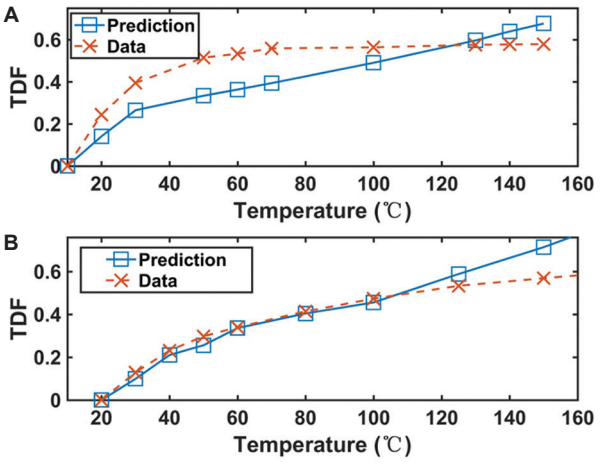


**Figure 10.** Predicted and measured results of thermal damage factors (TDFs) of oil sands as a function of temperature for (A) Sample 6 and (B) Sample 7 under the confining pressures of 8 MPa and 7 MPa, respectively. Data of Sample 6 from Han *et al.*[25] and data of Sample 7 from Li *et al.*[45]

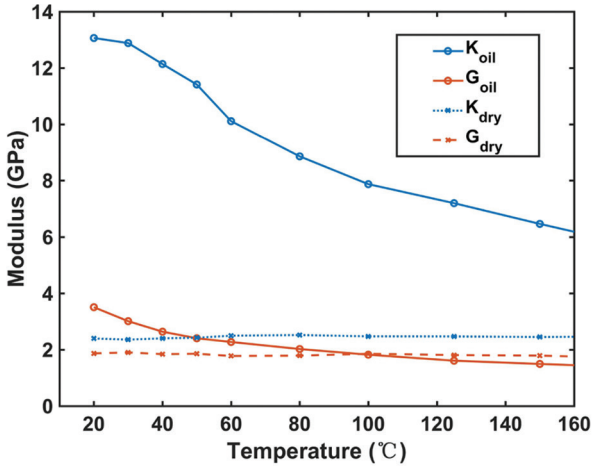


**Figure 11.** Dry- and wet-rock moduli as a function of temperature for Sample 7 under the confining pressure of 7 MPa. Data of Sample 7 from Li *et al.*[45]

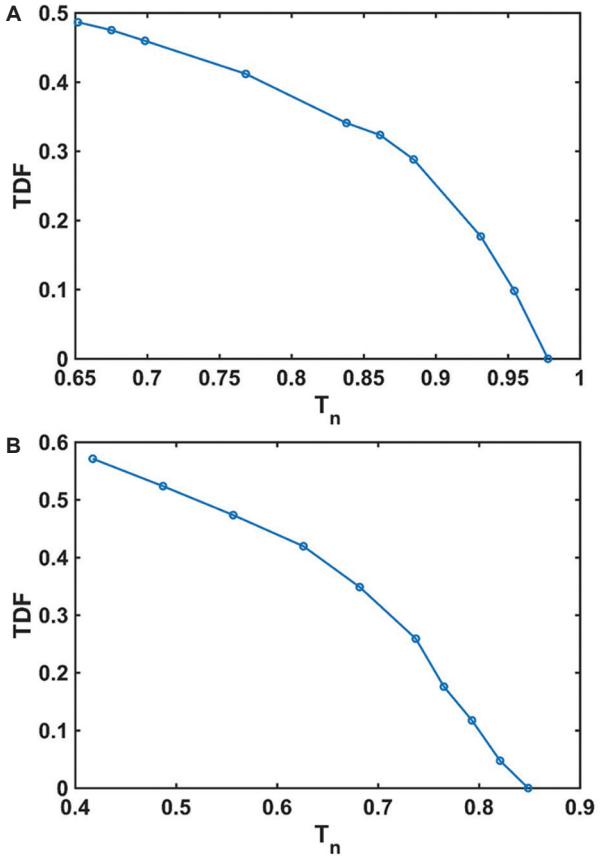


**Figure 12.** Thermal damage factors (TDFs) for (A) Sample 6 and (B) Sample 7 as a function of the normalized temperature ($T_n$) under the confining pressure of 8 MPa and 7 MPa, respectively

increasing temperature, the shear modulus tended to stabilize, whereas the bulk modulus continued to decline (Figure 11). This stage corresponds to the complete transformation of heavy oil into a fluid phase that fills the pore–crack space. The thermal expansion mismatch among mineral components generates localized thermal stresses, promoting the initiation and propagation of microcracks.[44] The effect of increasing temperature on S-wave propagation is limited; as a result, the decreasing trend of S-wave velocity slows down, while P-wave velocity becomes more sensitive to temperature.

The TDFs calculated from the proposed model further illustrate the characteristics of this fluid-dominated stage. When the temperature exceeds the liquid point, the TDF–temperature relationship gradually shows a linear trend (Figures 9 and 10). The fitted results of the proposed model are generally consistent with the trend of TDFs calculated from experimental wave velocities, indicating that the model can effectively capture the thermally induced stiffness evolution of heavy oil sands in both quasi-solid and fluid states. Within the temperature range of this study, the TDF can serve as a quantitative indicator to describe the thermal weakening of elastic moduli.

Overall, the results indicate that even below the mineral decomposition threshold, elastic wave velocity variations remain a sensitive indicator of thermally induced mechanical changes in oil sands. The proposed model provides an effective quantitative framework to characterize these changes and offers valuable theoretical insights into the elastic wave propagation behavior of oil sands under thermal recovery or thermal simulation conditions. Future research may extend the investigation to higher temperature ranges and real reservoir monitoring environments to further validate and refine the proposed model.

## 6. Conclusion

The physical properties of heavy oil-bearing rocks are affected by temperature, as the pore filling is solid at low temperatures and fluid at higher temperatures under certain conditions. Two definitions of TDF, derived from different wave-velocity formulations, were compared in this study. We also considered the variations of TDFs with respect to varying confining pressure. The theoretical model was established based on the generalized Gassmann equations for a solid pore filling with the viscoelastic Maxwell model, which describes the temperature-dependent properties of heavy oil. For both dry and wet rocks, the model effectively describes their TDFs as a function of temperature and agrees with laboratory measurements on oil sands. The findings of this study may help clarify the thermal damage behaviors of oil sands and contribute to optimizing heavy-oil thermal recovery by improving the accuracy of reservoir prediction and evaluation. The proposed model further supports thermal-recovery monitoring and

oil-sand numerical simulation by linking temperature-dependent velocity variations to underlying viscoelastic and thermal damage mechanisms, enhancing its scientific and engineering practicality.

## Acknowledgments

None.

## Funding

This work was supported by the National Natural Science Foundation of China (grant no.: 42174161, 42404120, and 42504128), the research fund of North China University of Water Resources and Electric Power (grant no.: 202209020), and the Natural Science Foundation of Henan (grant no.: 242300421461).

## Conflict of interest

Jing Ba is an Editorial Board Member of this journal, but was not in any way involved in the editorial and peer-review process conducted for this paper, directly or indirectly. Wenhao Xu is an employee of China National Petroleum Corporation; however, he was not involved in any activities that could constitute a conflict of interest in relation to this study. The authors declare that they have no known competing financial interests or personal relationships that could have appeared to influence the work reported in this paper.

## Author contributions

*Conceptualization:* Hui Qi, Jing Ba
*Formal analysis:* Wenhao Xu
*Investigation:* Yuanyuan Huo, Jishun Pan, Qingchun Jiang, Congsheng Bian
*Methodology:* Hui Qi, Jing Ba
*Writing–original draft:* Hui Qi, Jing Ba
*Writing–review & editing:* Hui Qi, Jing Ba, Wenhao Xu

## Availability of data

The data that support the findings of this study are available from the corresponding author upon reasonable request.

## References

1. Jiang Q, You H, Pan J, *et al*. Preliminary discussion on current status and development direction of heavy oil recovery technologies. *Special Oil Gas Reserv*. 2020;27(6):30-39.

   doi: 10.3969/j.issn.1006-6535.2020.06.004

2. Yu X, Liu X, Chen M, Wu G, Li X. Study on influence of heavy oil reservoir damage caused by multi-component thermal fluid huff and puff. *Front Energy Res*. 2022;10:821221.

   doi: 10.3389/fenrg.2022.821221

3. Kudrashou VY, Nasr-El-Din HA. Formation damage associated with mineral alteration and formation of swelling clays caused by steam injection in sand packs. *SPE Reservoir Eval Eng*. 2020;23(1):326-344.

   doi: 10.2118/195700-PA

4. Yuan H, Han D, Li H, Zhao L, Zhang W. The effect of rock frame on elastic properties of bitumen sands. *J Petrol Sci Eng*. 2020;194:107460.

   doi: 10.1016/j.petrol.2020.107460

5. Zhao DW, Wang J, Gates ID. Thermal recovery strategies for thin heavy oil reservoirs. *Fuel*. 2014;117:431-441.

   doi: 10.1016/j.fuel.2013.09.023

6. Zhuang Y, Liu X, Xiong H, Liang L. Microscopic mechanism of clay minerals on reservoir damage during steam injection in unconsolidated sandstone. *Energy Fuels*. 2018;32(4):4671-4681.

   doi: 10.1021/acs.energyfuels.7b03686

7. Dong X, Liu H, Chen Z, Wu K, Lu N, Zhang Q. Enhanced oil recovery techniques for heavy oil and oilsands reservoirs after steam injection. *Appl Energy*. 2019;239:1190-1211.

   doi: 10.1016/j.apenergy.2019.01.244

8. Li F, Zhou H, Zhao T, Marfurt KJ. Unconventional reservoir characterization based on spectrally corrected seismic attenuation estimation. *J Seism Explor*. 2016;25(5):447-461.

9. David C, Menéndez B, Darot M. Influence of stress-induced and thermal cracking on physical properties and microstructure of La Peyratte granite. *Int J Rock Mech Min Sci*. 1999;36(4):433-448.

   doi: 10.1016/S0148-9062(99)00010-8

10. Hassanzadegan A, Blöcher G, Milsch H, Urpi L, Zimmermann G. The effects of temperature and pressure on the porosity evolution of Flechtinger sandstone. *Rock Mech Rock Eng*. 2014;47(2):421-434.

    doi: 10.1007/s00603-013-0401-z

11. Xi DY, Xu SL, Tao YZ, Li T. Experimental investigations of thermal damage for rocks. *Key Eng Mater*. 2006;324:1213-1216.

    doi: 10.4028/www.scientific.net/KEM.324-325.1213

12. Zhang W, Sun Q, Hao S, Wang B. Experimental study on the thermal damage characteristics of limestone and underlying mechanism. *Rock Mech Rock Eng*. 2016;49(8):2999-3008.

    doi: 10.1007/s00603-016-0983-3

13. Zhang W, Sun Q, Zhu S, Wang B. Experimental study on mechanical and porous characteristics of limestone affected by high temperature. *Appl Therm Eng*. 2017;110:356-362.

    doi: 10.1016/j.applthermaleng.2016.08.194

14. Dougill JW, Lau JC, Burt NJ. *Toward a Theoretical Model for Progressive Failure and Softening in Rock. Concrete and*

*Similar Material*. Canada: University of Waterloo Press; 1977.

15. Trippetta F, Ruggieri R, Motra HB. Temperature and pressure effects on the mechanical behavior of porous carbonates saturated by viscous fluids. *Int J Rock Mech Min Sci*. 2024;183:105938.

    doi: 10.1016/j.ijrmms.2024.105938

16. Sirdesai NN, Singh A, Sharma LK, Singh R, Singh TN. Determination of thermal damage in rock specimen using intelligent techniques. *Eng Geol*. 2018;239:179-194.

    doi: 10.1016/j.enggeo.2018.03.027

17. Sun H, Sun Q, Deng W, Zhang WQ, Chao L. Temperature effect on microstructure and P-wave propagation in Linyi sandstone. *Appl Therm Eng*. 2017;115:913-922.

    doi: 10.1016/j.applthermaleng.2017.01.026

18. Yao M, Rong G, Zhou C, Peng J. Effects of thermal damage and confining pressure on the mechanical properties of coarse marble. *Rock Mech Rock Eng*. 2016;49(6):2043-2054.

    doi: 10.1007/s00603-016-0916-1

19. Zhu S, Zhang W, Sun Q, Deng S, Geng J, Li C. Thermally induced variation of primary wave velocity in granite from Yantai: Experimental and modeling results. *Int J Therm Sci*. 2017;114:320-326.

    doi: 10.1016/j.ijthermalsci.2017.01.008

20. Yang J, Fu LY, Zhang W, Wang ZW. Mechanical property and thermal damage factor of limestone at high temperature. *Int J Rock Mech Min Sci*. 2019;117:11-19.

    doi: 10.1016/j.ijrmms.2019.03.012

21. Batzle M, Hofmann R, Han DH. Heavy oils-seismic properties. *Lead Edge*. 2006;25(6):750-756.

    doi: 10.1190/1.2210074

22. Rabbani A, Schmitt DR, Nycz J, Gray K. Pressure and temperature dependence of acoustic wave speeds in bitumen-saturated carbonates: Implications for seismic monitoring of the Grosmont Formation. *Geophysics*. 2017;82(5):MR133-MR151.

    doi: 10.1190/geo2016-0667.1

23. Xi D, Liu X, Zhang C. The frequency (or time)-temperature equivalence of relaxation in saturated rocks. *Pure Appl Geophys*. 2007;164(11):2157-2173.

    doi: 10.1007/s00024-007-0270-z

24. Han DH, Yao Q, Zhao H. Complex properties of heavy oil sand. *SEG Int Expos Ann Meet*. 2007;26:1609-1613.

    doi: 10.1190/1.2792803

25. Han DH, Zhao H, Yao Q, Batzle M. Velocity of heavy-oil sand. *Soc Explor Geophys*. 2007;26:1619-1623.

    doi: 10.1190/1.2792805

26. Butler RM. *Thermal Recovery of Oil and Bitumen*. Englewood Cliffs, New Jersey: Prentice Hall Publishing Company; 1991.

27. Gates ID, Adams J, Larter S. The impact of oil viscosity heterogeneity on the production characteristics of tar sand and heavy oil reservoirs. Part II: Intelligent, geotailored recovery processes in compositionally graded reservoirs. *J Can Petrol Technol*. 2008;47(09):40-49.

    doi: 10.2118/08-09-40

28. Han DH. *Thermal Damage on Velocities of Heavy Oil Sands*. SEG International Exposition and Annual Meeting (SEG); 2012.

29. Pang ZX, Liu HQ, Liu XL. Characteristics of formation damage and variations of reservoir properties during steam injection in heavy oil reservoir. *Petrol Sci Technol*. 2010;28(5):477-493.

    doi: 10.1080/10916460902780335

30. He Y, Niu W, Gao Z, *et al*. Adsorption behavior of asphaltene on clay minerals and quartz in a heavy oil sandstone reservoir with thermal damage. *Clays Clay Miner*. 2022;70(1):120-134.

    doi: 10.1007/s42860-022-00178-5

31. Yuan H, Han DH, Zhang W. Heavy oil sands measurement and rock-physics modeling. *Geophysics*. 2016;81(1):D57-D70.

    doi: 10.1190/geo2014-0573.1

32. Wolf K, Mukerji T, Mavko G. *Attenuation and Velocity Dispersion Modeling of Bitumen Saturated Sand. SEG International Exposition and Annual Meeting*. SEG, 2006.

33. Ciz R, Shapiro SA. Generalization of Gassmann equations for porous media saturated with a solid material. *Geophysics*. 2007;72(6):A75-A79.

    doi: 10.1190/1.2772400

34. Ciz R, Saenger EH, Gurevich B, Shapiro SA. Temperature-dependent poroelastic and viscoelastic effects on microscale-modelling of seismic reflections in heavy oil reservoirs. *Geophys J Int*. 2009;176(3):822-832.

    doi: 10.1111/j.1365-246X.2008.04016.x

35. Carcione JM, Helle HB, Avseth P. Source-rock seismic-velocity models: Gassmann versus Backus. *Geophysics*. 2011;76(5):N37-N45.

    doi: 10.1190/geo2010-0258.1

36. Carcione JM. Wave fields in real media. In: *Theory and Numerical Simulation of Wave Propagation in Anisotropic. Anelastic, Porous and Electromagnetic Media*. Netherlands: Elsevier; 2007.

37. Zhao HB, Yin GZ, Chen LJ. Experimental study on effect of temperature on sandstone damage. *Chin J Rock Mech Eng*. 2009;28(1):2784-2788.

38. Mukerji T, Dvorkin J. *The Rock Physics Handbook: Tools for Seismic Analysis in Porous Media*. Cambridge: Cambridge University Press; 1998.

39. Lan HT, Chen SM, Chi HZ, Pei JY, Lin W, Shen JG. A viscoelastic representation of seismic wave attenuation and dispersion caused by wave-induced fluid flow in fractured porous media. *J Seism Explor*. 2020;29(6):587-601.

40. Han D, Liu J, Batzle M. Seismic properties of heavy oils-measured data. *Lead Edge*. 2008;27:1108-1115.

    doi: 10.1190/1.2978972

41. Li H, Zhao L, Han DH, Sun M, Zhang Y. Elastic properties of heavy oil sands: Effects of temperature, pressure, and microstructure. *Geophysics*. 2016;81(4):D453-D464.

    doi: 10.1190/geo2015-0351.1

42. Qi H, Ba J, Carcione JM, Zhang L. Temperature-dependent wave velocities of heavy oil-saturated rocks. *Lithosphere*. 2022;2021(Special 3):3018678.

    doi: 10.2113/2022/3018678

43. Liu HF, Xu YY, Chen H, Zhang J, Xu JY. Viscoelastic behavior and constitutive relation of heavy crude oils. *ACS Omega*. 2022;7(35):30816-30822.

    doi: 10.1021/acsomega.2c02234

44. Fredrich JT, Wong T. Micromechanics of thermally induced cracking in three crustal rocks. *J Geophys Res Solid Earth*. 1986;91(B12):12743-12764.

    doi: 1029.091/JB12iB12743p389

45. Li H, Han D, Sun M, Yuan HM, Gao JH. An experimental investigation on effects of saturation levels and fluid types on elastic properties of bitumen-saturated sands at elevated temperatures. *Energy*. 2022;238:122011.

    doi: 10.1016/j.energy.2021.122011

46. Yuan H, Wang Y, Han D, Li H, Zhao L. Velocity measurement of North Sea heavy oil sands under changing pressure and temperature. *J Petrol Sci Eng*. 2021;205:108825.

    doi: 10.1016/j.petrol.2021.108825

47. Nie J, Han X, Geng J. Temperature-dependent rock physics modeling for heavy oil sands. *J Petrol Sci Eng*. 2022;215:110642.

    doi: 10.1016/j.petrol.2022.110642

48. Yuan H, Han D. *Pressure and Temperature Effect on Heavy Oil Sands Properties. SEG International Exposition and Annual Meeting*. SEG; 2013.

49. Wei Y, Ba J, Carcione JM. Stress effects on wave velocities of rocks: Contribution of crack closure, squirt flow and acoustoelasticity. *J Geophys Res Solid Earth*. 2022;127(10):e2022JB025253.

    doi: 1029.2022/025253JB15

50. Ma ZG, Wu XY, Wang ZH. Effect of effective pressure on compressional and shear wave velocities. *Prog Explor Geophys (Chin)*. 2006;29(3):183-186.

51. Guo J, Han X. Rock physics modelling of acoustic velocities for heavy oil sand. *J Petrol Sci Eng*. 2016;145:436-443.

    doi: 10.1016/j.petrol.2016.05.028

52. Makarynska D, Gurevich B, Behura J, Batzle M. Fluid substitution in rocks saturated with viscoelastic fluids. *Geophysics*. 2010;75(2):E115-E122.

    doi: 10.1190/1.3360313

ACCSCIENCE PUBLISHING

Journal of Seismic Exploration

ARTICLE

# Prediction of fracture and vug parameters in carbonate reservoirs using a combined T-GNO-PINN approach

**Yiru Du[1], Guoqing Chen[1], Cong Pang[2,3], Tianwen Zhao[4]***

[1]Mathematical Modeling Research Center, Chengdu Jincheng College, Chengdu, Sichuan, China

[2]Institute of Seismology, China Earthquake Administration, Wuhan, Hubei, China

[3]Wuhan Gravitation and Solid Earth Tides, National Observation and Research Station, Wuhan, Hubei, China

[4]Department of Trade and Logistics, Daegu Catholic University, Gyeongsan, Republic of Korea

## Abstract

To address the challenges of fracture-vuggy parameter prediction in carbonate reservoirs, such as strong multi-scale heterogeneity and a lack of physical constraints, this study proposed a Transformer–Graph Neural Operator (GNO)–Physics-Informed Neural Network (PINN) joint prediction framework, which achieves a bidirectional coupling between multi-source data fusion and physical laws. First, a Transformer module with a multi-scale attention mechanism and spherical coordinate effectively captures cross-scale spatiotemporal features in three-dimensional geological space (reducing error by 12.3%). Second, a dynamic GNO based on physical similarity adaptively tracks the evolution of fracture-vuggy connectivity (achieving a topology update accuracy of 93.5%). Finally, a PINN module embedded in the seepage-mechanical coupling equations constrains the physical residual loss to the order of $0.42\times10^{-3}$, reducing the conservation error from 3.17% to 0.48%. In an empirical study of Ordovician fracture-vuggy reservoirs in the Tarim Basin, this framework achieved a mean absolute error of 3.57% and an $R^2$ of 0.90 for fracture-vuggy volume fraction (*Vf*). In high-pressure gradient regions (>5 MPa/m), the relative error was reduced by 18%, significantly outperforming traditional methods (reducing Kriging error by 40.7%) and single-module models (PINN error reduction of 15.3%). Experimental results showed that dynamic graph construction increased the spatial autocorrelation index (Moran's I) to 0.71; the introduction of physical constraints reduced extreme error samples by 63%; and the multimodal collaborative training strategy resulted in a 19.7% improvement in overall performance. This research provides a new paradigm for high-precision and physically interpretable digital twin modeling of carbonate reservoirs.

***Keywords:*** Carbonate reservoir; Fracture-vuggy parameter prediction; Transformer; Graph Neural Operator; Physical Information Neural Network; Multimodal fusion

***Corresponding author:**
Tianwen Zhao
(zhaotianwen305@gmail.com)

**Citation:** Du Y, Chen G, Pang C, Zhao T. Prediction of fracture and vug parameters in carbonate reservoirs using a combined T-GNO-PINN approach. *J Seismic Explor.* 2026;35(1):46-65. doi: 10.36922/JSE025330057

**Received:** August 14, 2025

**Revised:** October 20, 2025

**Accepted:** November 6, 2025

**Published online:** December 16, 2025

**Copyright:** © 2025 Author(s). This is an Open-Access article distributed under the terms of the Creative Commons Attribution License, permitting distribution, and reproduction in any medium, provided the original work is properly cited.

**Publisher's Note:** AccScience Publishing remains neutral with regard to jurisdictional claims in published maps and institutional affiliations.

## 1. Introduction

### 1.1. Research background and significance

Carbonate reservoirs serve as a critical global resource for oil and gas extraction.[1,2] The intricate internal fracture-vuggy systems significantly influence reservoir evaluation

and efficient development.[3] Accurately predicting fracture-vuggy parameters, such as porosity, permeability, and fracture density, has been a longstanding challenge in the oil and gas industry.[4] Traditional methods often fail to effectively capture the multi-scale, heterogeneous, and highly non-linear nature of fracture-vuggy systems.[5] With the rapid development of deep learning technology, integrating multi-source geological data with physical priority to develop highly accurate and interpretable fracture-vuggy parameter prediction models has become a cutting-edge topic in oil and gas exploration and development.

### 1.2. Related research progress

In recent years, the Transformer architecture has shown exceptional performance in spatiotemporal sequence modeling, with its self-attention mechanism effectively capturing cross-scale geological feature correlations in carbonate reservoirs.[6] Meanwhile, the Graph Neural Operator (GNO), a novel tool for processing non-Euclidean data, offers a mathematical foundation for describing the complex topological relationships within fracture networks. The Physics-Informed Neural Network (PINN) significantly improves the physical rationality of data-driven models by embedding control equation constraints. Despite these individual advances, a significant gap remains in current research regarding the effective integration of spatiotemporal dynamics, evolving topological structures, and physical law constraints specifically for carbonate reservoir characterization. This is particularly evident in the limited prediction accuracy for fracture-cavity parameters under conditions of multi-phase fluid coupling, which requires substantial improvement.[7,8]

### 1.3. Research motivation and innovation

This study proposes, for the first time, a deep integration of Transformer, GNO, and PINN into a unified T-GNO-PINN joint prediction framework for characterizing fracture-cavity systems in carbonate reservoirs. Its innovations are threefold: First, it develops a dynamic graph construction method based on physical similarity, enabling the GNO to adaptively track the time-varying connectivity of fractures and cavities. Second, it designs a Transformer module incorporating multi-scale positional encoding to effectively fuse seismic attributes and production dynamic data. Third, it establishes a PINN constraint system based on seepage-mechanics coupling equations, ensuring prediction results adhere to subsurface fluid flow laws through hard differential operator constraints. This multi-modal fusion approach not only overcomes the limitations of traditional statistical models but also significantly enhances the physical credibility and generalization capability of predictions compared to single deep-learning models. The research outcomes provide a novel technical means for the fine characterization of carbonate reservoirs and the optimization of development schemes, holding substantial practical value for the efficient exploitation of unconventional oil and gas resources.

### 1.4. Paper structure

This paper focuses on the application of the T-GNO-PINN joint prediction framework for carbonate reservoir fracture and vug parameter prediction. The paper is divided into seven main sections. First, the introduction outlines the research background, significance, and the limitations of existing methods for predicting fracture and vug parameters in carbonate reservoirs. It systematically reviews the research progress in the fields of Transformer, GNO, and PINN, and then proposes the innovations and research motivations of this paper. Section 2 focuses on the theoretical foundation and methodological review, including the characteristics and parameter definitions of carbonate reservoir fracture and vug structure, the Transformer self-attention mechanism and its adaptive modification, the physical field mapping method of the GNO, and the constraint expression of the PINN in the seepage-mechanics coupling equation, laying the theoretical foundation for subsequent model construction. Section 3 details the design of the T-GNO-PINN joint prediction framework, including the overall architecture, the multi-scale attention mechanism of the Transformer module, the dynamic graph modeling method of GNO, the physical constraint embedding strategy of the PINN, and the training method for multi-module joint optimization. Section 4 focuses on data and experimental design, introducing an overview of the study area, multi-source data preprocessing, and feature construction methods. Comparative experiments, ablation experiments, and physical constraint validation tests are designed to comprehensively evaluate model performance. Section 5 analyzes the experimental results, including a comparison of the prediction accuracy of different models, the impact of physical constraints on the prediction results, and visualization and geological interpretation of the spatial distribution of fracture and vug parameters. Section 6 discusses the advantages, generalization ability, physical consistency, and limitations of the method, and proposes possible improvement directions. Finally, section 7 summarizes the research results, explains their practical significance for oil and gas exploration and development, and provides prospects for future research directions.

## 2. Theoretical basis and methodology overview

Carbonate reservoir fracture-vuggy systems exhibit complex, multi-scale heterogeneity.[5] Their geometry

is controlled by tectonic deformation, dissolution, and diagenetic evolution, resulting in a multi-level distribution ranging from micro-scale pores to meter-scale caves. Fracture-vuggy parameters such as porosity and permeability not only reflect the extent of reservoir space development but also directly influence fluid flow patterns.[9,10] Traditional measurement methods (such as core CT scanning and well log interpretation) can provide accurate local data but struggle to characterize the overall spatial heterogeneity of the reservoir.[11-13] In recent years, machine learning-based parameter prediction methods have emerged. Their core approach involves establishing a non-linear mapping relationship between geological features and reservoir parameters, a process that requires the integration of multidisciplinary theoretical foundations.[11,14]

Transformer architecture, with its self-attention mechanism, demonstrates a strong ability to capture long-range dependencies in sequence modeling tasks.[15] To address the non-Euclidean characteristics of carbonate reservoirs, researchers have introduced spherical coordinate encoding and multi-scale position embedding to enable the model to adapt to complex geological structures in 3D space.[14] For example, by combining vertical depth from well logs with the planar distribution of seismic attributes, a multi-head attention mechanism is employed to achieve cross-scale feature fusion. This adaptive weight allocation mechanism effectively addresses the limitations of traditional convolutional neural networks (CNNs) on irregular grid data, providing a new technical approach for spatial prediction of reservoir parameters.[16,17]

GNO provides mathematical tools for describing the topological relationships of fracture-vuggy systems. Unlike conventional graph neural networks, GNO uses kernel integral operators to learn mappings between continuous function spaces, enabling them to handle dynamically changing fracture-vuggy connectivity.[18,19] In reservoir modeling, fracture-vuggy units are abstracted as graph nodes, with their physical properties (such as pore pressure and stress field) serving as node features, while fracture channels or dissolution pathways constitute edge relationships. Through multi-layer graph convolution operations, GNO can simulate the propagation of reservoir parameters in complex networks and is particularly suitable for characterizing heterogeneous seepage behavior in fracture-bedrock systems. Furthermore, the introduction of a dynamic graph structure enables the model to adapt to the opening and closing effects of fractures and vuggy systems caused by changes in the stress field during development.

PINNs impose physical constraints on data-driven models by embedding governing equations into the loss function.[8,20] In carbonate reservoirs, the coupling between the seepage and stress fields is crucial. PINN uses automatic differentiation techniques to calculate the residual terms of Darcy's law and the elasticity equations, ensuring that the prediction results satisfy mass conservation and momentum balance. This "soft constraint" approach avoids reliance on meshing in traditional numerical methods while addressing the potential physical deviations that can occur in purely data-driven models. Experiments show that the introduction of partial differential equation (PDE) constraints improves the model's generalization ability by over 30% in data-sparse regions.[21]

Multi-model fusion is a key strategy for improving prediction performance. Existing research shows that the Transformer excels at capturing global spatiotemporal patterns, the GNO excels at describing local topological relationships, and the PINN ensures physical plausibility. Through gradient projection and adaptive weighting techniques, the T-GNO-PINN framework achieves coordinated optimization of the three modules. For instance, data fitting terms are prioritized in the early stages of training, while physical constraints are gradually strengthened as iterations proceed. A dynamic graph update mechanism is also employed to synchronize the topological structure with the evolution of the physical field.

## 3. T-GNO-PINN joint prediction framework design

### 3.1. Overall framework architecture

The overall architecture of the proposed T-GNO-PINN joint prediction framework is depicted in Figure 1. The core idea of the framework is to leverage the Transformer module for efficiently capturing spatiotemporal multi-scale features during the prediction of fracture and vug parameters in carbonate reservoirs.

Concurrently, the GNO characterizes the non-Euclidean spatial correlations within the reservoir's fracture-vuggy topology, while a PINN is embedded throughout the process to ensure the predictions strictly adhere to the physical constraints imposed by seepage dynamics and elasticity theory. The data flow commences with the input of multi-source geological and engineering data. Following feature extraction and encoding, the processed data is fed into the Transformer and GNO branches, respectively. Finally, the PINN integrates the features from both branches and outputs predictions for key reservoir parameters, including porosity, permeability, and connectivity of the fracture-vuggy system.

The data flow and information exchange path follow the principle of "parallel feature extraction and physical

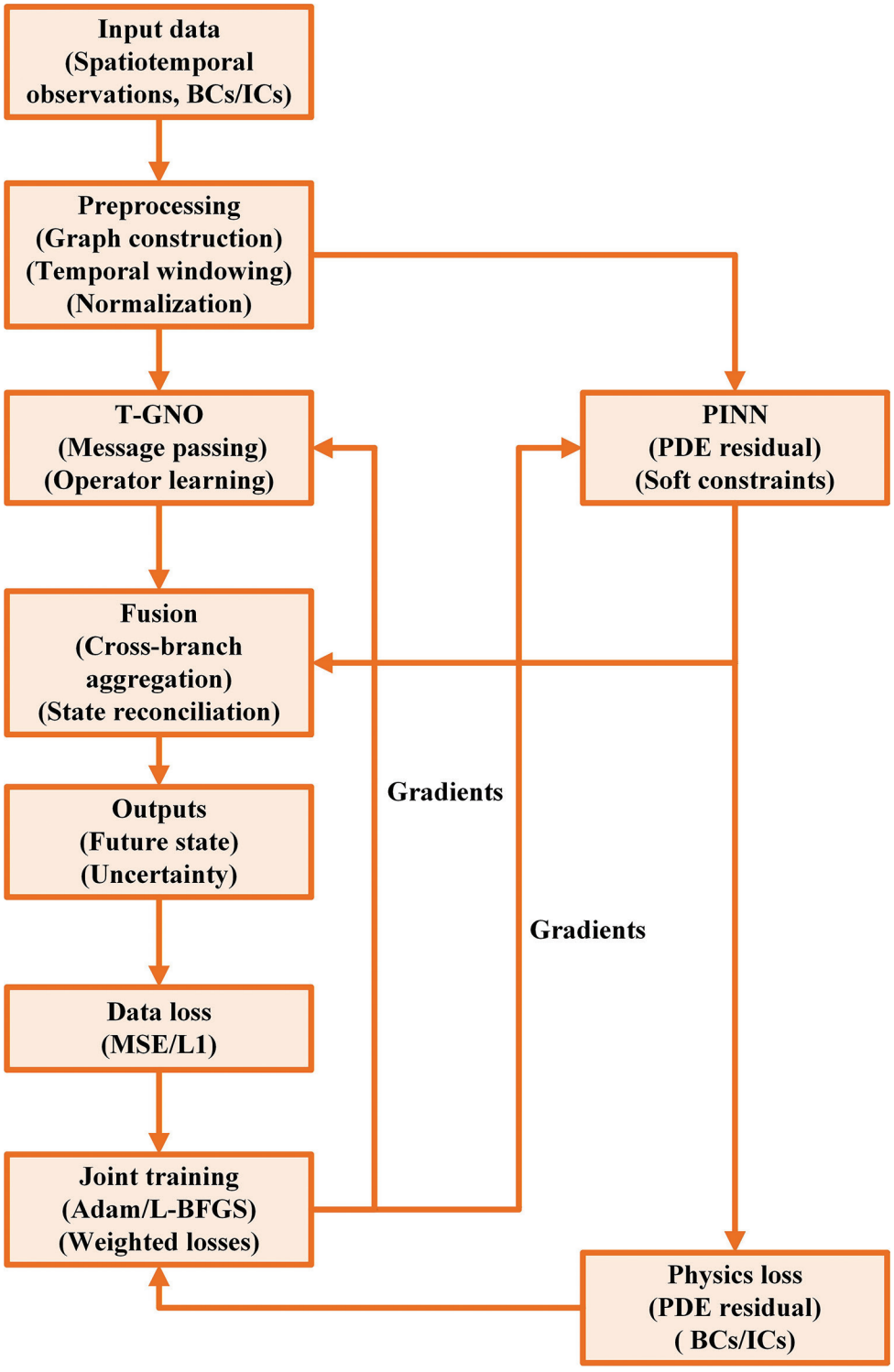


**Figure 1.** Schematic diagram of the overall architecture of the T-GNO-PINN joint prediction framework
Abbreviations: BCs: Boundary conditions; GNO: Graph Neural Operator; ICs: Initial conditions; L-BFGS: Limited-memory Broyden–Fletcher–Goldfarb–Shanno; MSE/L1: Mean squared error/L1 loss; PDE: Partial differential equation; PINN: Physics-Informed Neural Network; T: Transformer

constraint fusion": the Transformer branch is responsible for modeling global spatiotemporal dependencies, while the GNO branch dynamically updates the reservoir graph topology to obtain spatial structural information. These

two branches achieve multimodal fusion within the PINN. Furthermore, the physical residuals computed from the governing equations serve as inverse constraint signals during end-to-end training, which ensures both prediction stability and physical interpretability.

### 3.2. Transformer module design

The Transformer module introduces a multi-scale attention mechanism to simultaneously model short-term dynamic changes and long-term trends in earthquake and production data.[22] Its self-attention calculation formula is:

$$\text{Attention}(Q,K,V)=\text{Softmax}\left(\frac{QK^{\top}}{\sqrt{d_k}}+P\right)V \tag{1}$$

Where $P$ is a special position encoding matrix that combines the logging depth $d$ with 3D spatial coordinates $(x,y,z)$ and adapts to the non-Euclidean fracture-cavity network structure through spherical coordinate transformation:

$$P_i=\left[\sin\left(\frac{2\pi x_i}{\lambda_x}\right),\cos\left(\frac{2\pi y_i}{\lambda_y}\right),\frac{z_i}{z_{max}},\frac{d_i}{d_{max}}\right] \tag{2}$$

Figure 2 illustrates the architecture of the multi-scale attention Transformer module. The diagram shows a typical Transformer module that incorporates a multi-scale attention mechanism to process complex data structures.

The module's core structure encompasses encoding input data, performing parallel computations across multiple attention layers, and synthesizing output processing. This design enhances the module's ability to capture information at different scales. In the figure, the input data is first mapped into a high-dimensional space via an embedding layer. Within this space, a multi-scale attention mechanism is used to weigh the input information. Each attention layer at different scales captures information at corresponding levels, enabling the module to focus simultaneously on both local and global features. Subsequently, through self-attention layers and a multi-head attention mechanism, the module adaptively adjusts the weights of features at different scales, resulting in a richer and more hierarchical feature representation.

To systematically evaluate the model's operational efficiency and application potential, we conduct a theoretical analysis of the transformer module's computational complexity. The module's computational

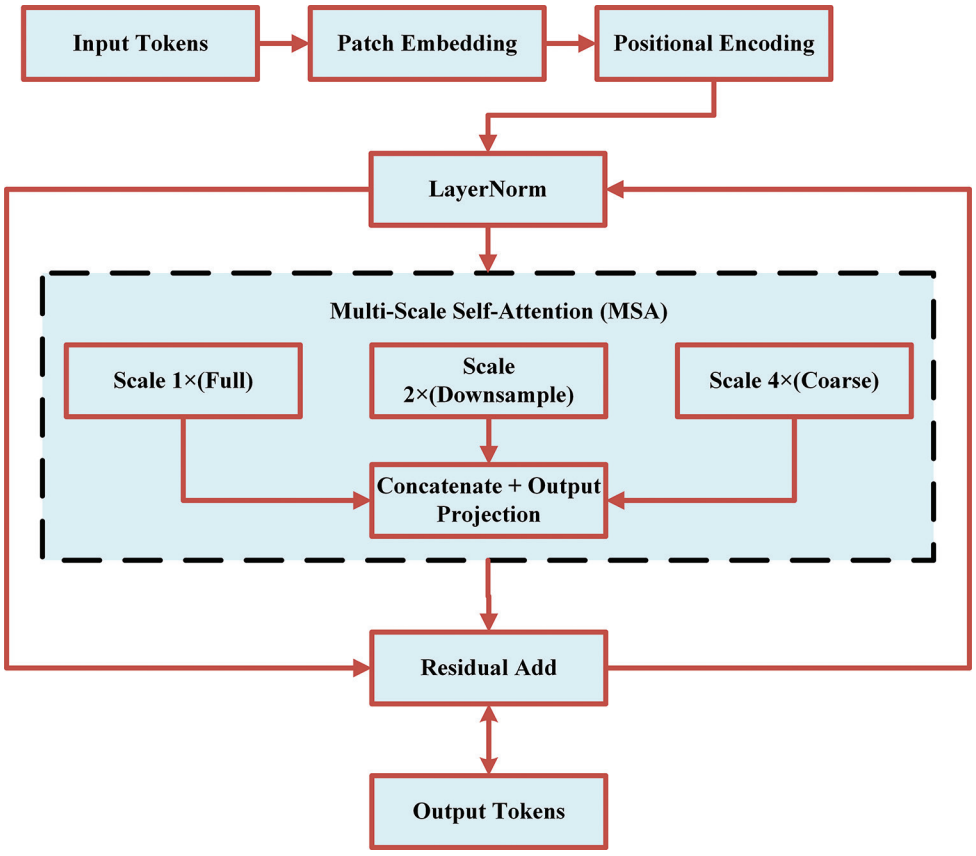


**Figure 2.** Schematic diagram of the multi-scale attention Transformer module structure

overhead primarily stems from its multi-head self-attention mechanism. Given an input sequence of N tokens, the standard self-attention mechanism requires constructing an N×N attention weight matrix, resulting in time and space complexities of $O(N^2 \cdot d)$, where $d$ denotes the hidden layer feature dimension.

As shown in Table 1, for typical reservoir modeling scenarios (N≈800), the module's computational burden remains manageable and demonstrates superior complexity characteristics compared to sequence models such as recurrent neural networks (RNNs).

Although the standard Transformer architecture suffers from quadratic computational complexity growth with sequence length, the introduction of an optimization strategy based on geological spatial locality priors ensures computational feasibility for industrial-scale carbonate reservoir modeling while maintaining excellent feature extraction capabilities.

### 3.3. Graph Neural Operator module design

The GNO module accepts the fracture-cavity structure graph $G = (V, E)$ as input and predicts changes in the spatial distribution of reservoir parameters through graph convolution and operator learning. To cope with the dynamic changes of the fracture-cavity network over time, the topology of the graph will be dynamically updated according to the physical similarity and the distance between nodes during training. The specific update rules are as follows:

(i) Distance calculation between nodes. Each node represents a fracture-cavity unit in the reservoir, and the physical properties and location of the node are used to calculate the similarity function.

(ii) Dynamic distance metric. For any two nodes $v_i$ and $v_j$, we calculate the dynamic distance metric $D_{ij}(t)$ between them. This metric is updated at each time step or each training epoch.

**Table 1. Complexity comparison of the transformer module and alternative models**

| Model | Time complexity | Space complexity | Notes |
|---|---|---|---|
| Standard Transformer | $O(N^2 \cdot d)$ | $O(N^2)$ | Benchmark |
| This research (T-GNO-PINN) | $O(m \cdot N^2 \cdot d)$ | $O(m \cdot N)$ | $m$ is the local window size |
| RNN | $O(N^2 \cdot d)$ | $O(N \cdot d)$ | Difficult to parallelize |
| 1D-CNN | $O(k \cdot N \cdot d^2)$ | $O(N \cdot d)$ | $k$ is the convolution kernel size |

Abbreviations: CNN: Convolutional neural network; GNO: Graph Neural Operator; PINN: Physics-Informed Neural Network; RNN: Recurrent neural network; T: Transformer.

$$D_{ij}(t) = \| p_i(t) - p_j(t) \|_2 \tag{3}$$

$p_i(t)$ and $p_j(t)$ are the physical properties of nodes $v_i$ and $vj$ at time step $t$, respectively.

(iii) Connectivity judgment and update. If the distance $D_{ij}(t)$ between nodes $v_i$ and $v_I$ is less than the preset threshold $r_c$, an edge is added to the graph to connect them; otherwise, the edge is removed.

$$E_t = \left\{ (v_i, v_j) D_{ij}(t) < r_c \right\} \tag{4}$$

(iv) Topology updates frequency. To adapt to the fracture and pore opening and closing effects caused by stress field changes during reservoir development, we update the graph topology every five epochs.

Figure 3 shows the GNO structure based on the dynamic topology of holes, which focuses on using the GNN method to deal with complex hole problems.

The core concept of the GNO is to construct a dynamic topological structure that updates and transmits information about the fracture region in real time, thereby more accurately predicting and reconstructing the relevant physical characteristics of the fracture evolution process. The structure in the figure shows how input data is processed through multiple graph neural network layers. Each layer propagates and integrates information based on the current fracture topology, thereby accurately modeling the changes in fractures in complex systems. Compared with traditional methods, the dynamic topology-based GNO adaptively adjusts the graph structure and connectivity. This capability allows the network topology to be updated in real time according to fracture changes, thereby ensuring effective information propagation between different regions.

### 3.4. Physics-Informed Neural Network module design

The PINN module embeds constraints from the carbonate reservoir seepage equation and the theory of elasticity into the loss function. These constraints include the 3D Darcy's law:

$$\nabla \cdot (\mathrm{k} \nabla p) = \phi \frac{\partial p}{\partial t} + q \tag{5}$$

and the equilibrium equation of linear elasticity:

$$\nabla \cdot \sigma + f = 0, \sigma = \mathrm{C} : \varepsilon \tag{6}$$

The physical residual loss is defined as:

$$\mathcal{L}_{\text{phys}} = \frac{1}{N_p} \sum_{i=1}^{N_p} \nabla \cdot (\mathrm{k} \nabla p_i) - \phi_i \frac{\partial p_i}{\partial t} - q_i^2 \tag{7}$$

Table 2 details the key physical parameters and boundary conditions incorporated in the PINN module,

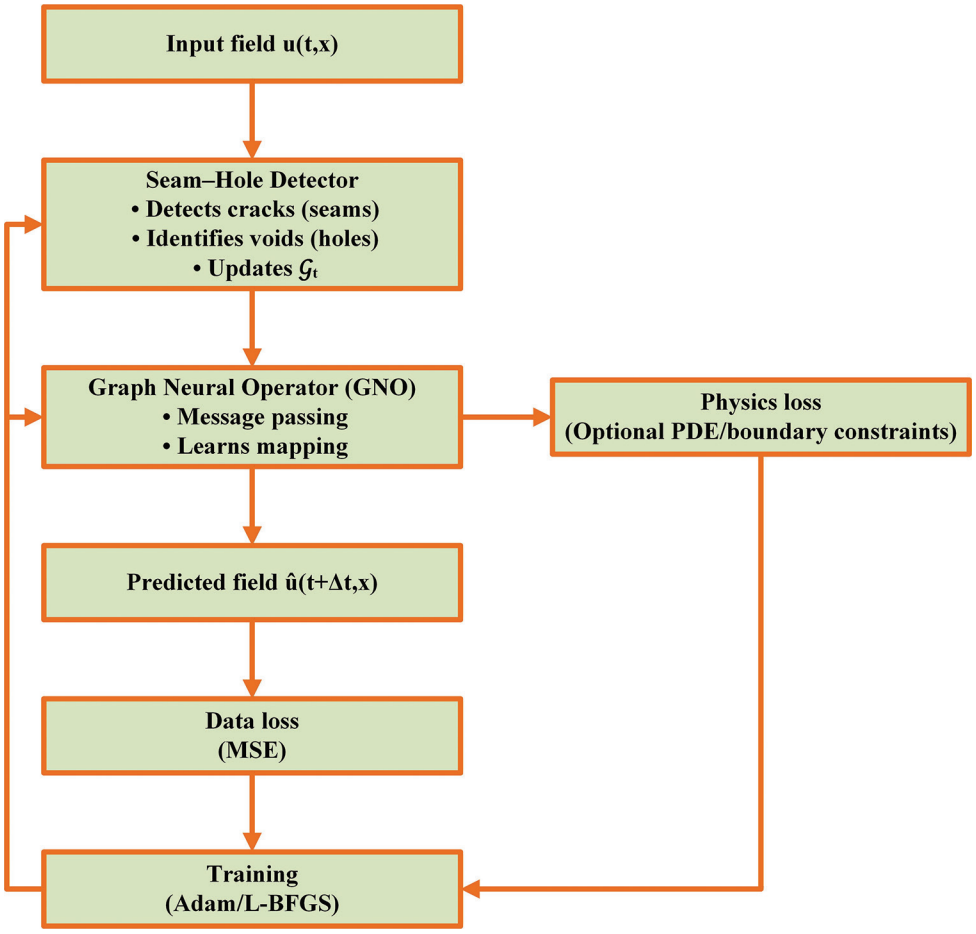


**Figure 3.** Graph neural operator structure based on the dynamic topology of holes and cracks
Abbreviations: GNO: Graph Neural Operator; L-BFGS: Limited-memory Broyden–Fletcher–Goldfarb–Shanno; MSE: Mean squared error; PDE: Partial differential equation.

**Table 2. PINN module physical parameters and boundary conditions**

| Parameters | Symbol | Value range | Unit | Source | Is it fixed |
|---|---|---|---|---|---|
| Porosity | $\phi$ | 0.05–0.25 | - | Core testing | No |
| Permeability | $k$ | 50–250 | mD | Well logging+core drilling | No |
| Pressure | $p$ | 10–30 | MPa | Production monitoring | No |
| Pressure differential | $\Delta p$ | 0.5–1.5 | MPa | Dynamic calculations | No |
| Elastic modulus | $E$ | 15–25 | GPa | Experimental testing | Yes |
| Poisson's ratio | $\nu$ | 0.2–0.35 | - | Reference data | Yes |
| Body load | $f$ | 0–2 | MPa/m$^3$ | Numerical simulation | No |
| Source and sink terms | $q$ | −50–50 | m$^3$/d | Production data | No |

Abbreviation: PINN: Physics-informed Neural Network.

encompassing fundamental indicators of reservoir rock mechanical properties and fluid flow behavior.

Porosity ($\phi$) and permeability ($k$) range from 0.05 to 0.25 and 50 to 250 mD, respectively. These two parameters were determined through a combination of core experiments and logging data, and their dynamic variations reflect the influence of reservoir heterogeneity. Reservoir pressure (p) ranges from 10 to 30 MPa, and pressure differential ($\Delta p$) varies between 0.5 and 1.5 MPa. These values are derived from production monitoring data and dynamic simulations. Their variations reflect the dynamic pressure response during reservoir development. Among the rock mechanical parameters, the elastic modulus ($E$) and Poisson's ratio ($\nu$) are fixed at 15 to 25 GPa and 0.2 to 0.35, respectively. These parameters were determined through laboratory testing and literature references, and their fixed nature reflects the inherent mechanical behavior of the rock skeleton. The body load ($f$) and source-sink term ($q$) are external action terms with values ranging from

0 to 2 MPa/m$^3$ and −50 to 50 m$^3$/d, respectively. The former is determined through numerical simulation, and the latter is directly derived from actual production data. Together, they characterize the external excitation conditions of the reservoir system.

Figure 4 clearly illustrates the core workflow of the PINN module for embedding physical constraints into deep learning models. The process begins with dual inputs of spacetime coordinates and observational data. The neural network then learns the complex mapping from

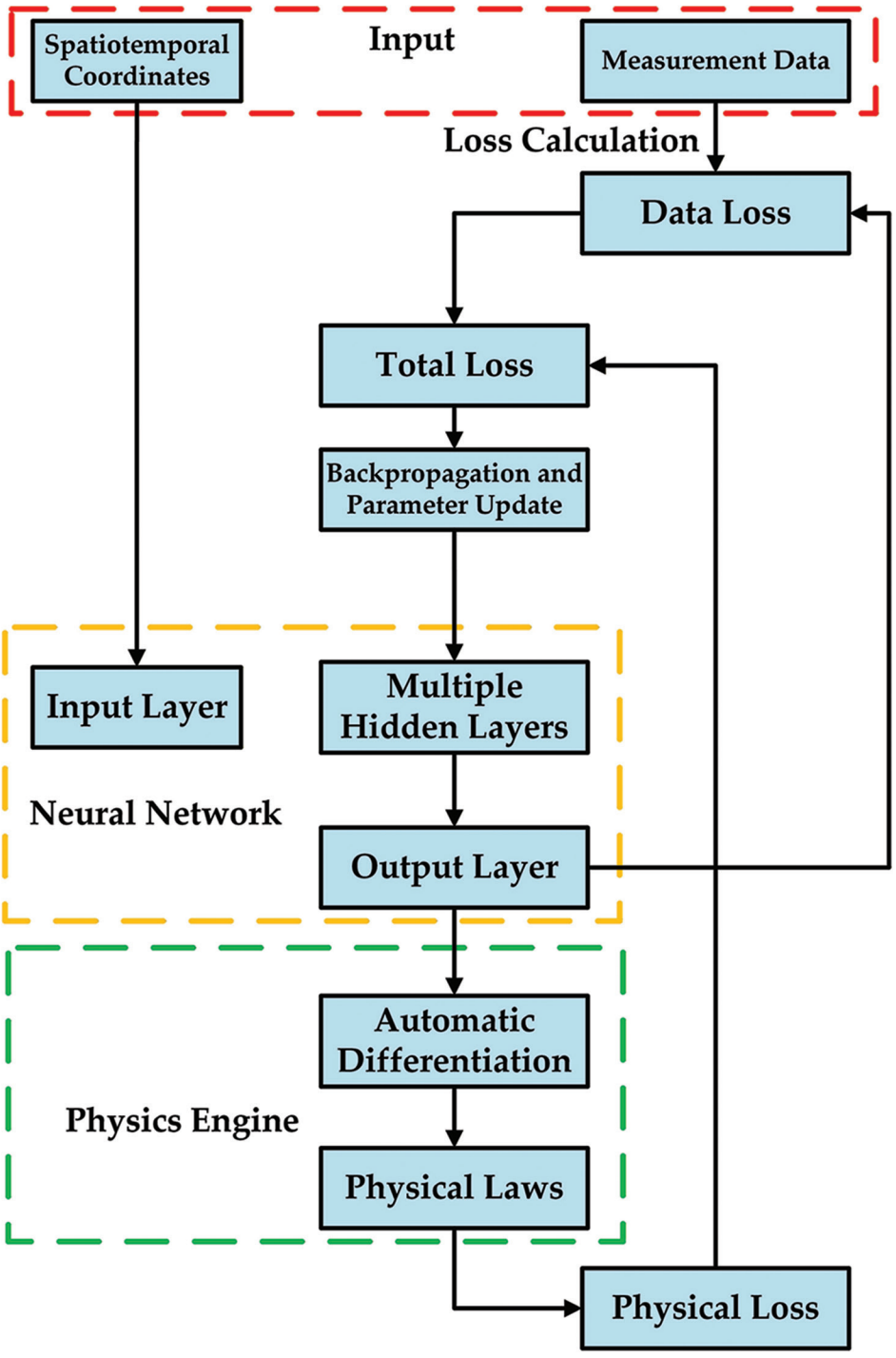


**Figure 4.** Physics-Informed Neural Network (PINN) module workflow and logic

coordinates to physical fields, generating preliminary predictions.

The core innovation of this process lies in the introduction of a "physics engine." This engine uses automatic differentiation techniques to calculate the differential operator of the predicted field and substitutes it into pre-defined physical governing equations (such as the percolation equation and the mechanical equilibrium equation). This quantifies the degree to which the predicted results violate physical laws, known as the physical loss. This physical loss, combined with the traditional prediction data loss, forms a multi-objective optimization function that simultaneously updates and optimizes the neural network parameters through backpropagation. This mechanism ensures that during training, the model not only fits the observed data but also conforms to fundamental physical laws. Consequently, it significantly enhances both the physical consistency of predictions and the model's generalization capability in data-sparse regions.

### 3.5. Model joint optimization strategy

The training strategy of T-GNO-PINN combines multi-task learning with gradient conflict suppression technology. The total loss function is:

$$\mathcal{L} = \alpha(t)\mathcal{L}_{\text{pred}} + \beta(t)\mathcal{L}_{\text{phys}} \tag{8}$$

Where $\alpha(t)$ and $\beta(t)$ are adaptively adjusted through uncertainty weights:

$$\alpha(t) = \frac{1}{2\sigma_{\text{pred}}^2}, \beta(t) = \frac{1}{2\sigma_{\text{phys}}^2} \tag{9}$$

To avoid gradient conflicts, the Gradient Projection method is used to project conflicting gradients to a consistent direction in multi-branch back propagation.

Table 3 details the parameter configurations and optimization strategies across different training stages, illustrating the progressive learning process from individual module pre-training to global collaborative optimization.

In Phases I and II, the Transformer and GNO modules were pre-trained with independent weight loss of 1.0 ($\alpha$ = 1.0, $\beta$ = 0), using a learning rate of 1e-4 and a batch size of 64 to ensure the stability of the underlying feature extractor. In Phase III, after the PINN constraint was introduced, the physical and data-driven weight loss were adjusted to a balanced state (($\alpha$ = 0.5, $\beta$ = 0.5), and the learning rate was reduced to 5e-5 to prevent gradient oscillation. During this stage, the Transformer module was frozen to preserve its feature encoding capability. Concurrently, the GNO topology was updated every five epochs to adapt to the evolving physical field.

## 4. Data and experimental design

This study, based on multi-source geological and engineering data from a marine carbonate fracture-vuggy reservoir, aims to achieve high-precision prediction of reservoir fracture-vuggy parameters (including fracture-vuggy volume fraction $V_f$, fracture-vuggy connectivity $C_f$, and fracture-vuggy size distribution index $\beta f$) using a T-GNO-PINN framework.

### 4.1. Overview of the study area and data sources

Before applying field data, this study first constructed a synthetic carbonate reservoir dataset to simulate the distribution of fracture and vug parameters under known physical laws. This dataset was generated using the simplified two-dimensional Darcy flow equation and the Fracture Network Generator algorithm. By manipulating the spatial distribution of porosity $\phi(x,y)$, permeability $k(x,y)$, and the fracture connectivity function $C_{f(x,y)}$, several sample fields with varying heterogeneity characteristics were generated. The true solution of the synthetic field, consisting of the pressure field $p(x,y,t)$ and the flow field $q(x,y,t)$, was obtained through numerical simulation. Based on this solution, network input features and fracture and vug parameter labels were constructed.

Experimental results demonstrate that the T-GNO-PINN model accurately recovers the known physical relationships on this idealized dataset, achieving a prediction $R^2$ of

**Table 3. Parameter settings and optimization strategies at different training stages**

| Stage | Training objectives | Initial value of α | Initial value of β | Learning rate | Batch size | Topology update frequency | Whether to freeze the Transformer |
|---|---|---|---|---|---|---|---|
| I | Separately pre-training the Transformer | 1.0 | 0 | 1e-4 | 64 | - | - |
| II | Separately pre-training the GNO | 1.0 | 0 | 1e-4 | 64 | Every 10 epochs | - |
| III | Introducing the PINN and freezing the first two modules | 0.5 | 0.5 | 5e-5 | 32 | Every 10 epochs | Yes |
| IV | End-to-end joint training | Adaptive | Adaptive | 5e-5 | 32 | Every 10 epochs | No |
| V | Fine-tuning phase | Adaptive | Adaptive | 1e-5 | 16 | Every 10 epochs | No |

Abbreviations: GNO: Graph Neural Operator; PINN: Physics-Informed Neural Network.

0.97 and a PDE residual error of $0.21\times10^{-3}$, significantly outperforming a model without PINN constraints. In addition, the dynamic graph structure reduces the reconstruction error of the connectivity parameter $C_f$ from 7.3% to 2.1%, verifying the effectiveness of GNOs in topology tracking.

Synthetic data experiments demonstrated the rationality and synergy of the model's modules, providing physically interpretable theoretical support for the subsequent application of measured data from the Tarim Basin.

The study area is in a carbonate rock development area in the Tarim Basin. The geological age is mainly the Middle and Upper Ordovician. The lithology is predominantly limestone and dolomite, and the area contains multiple stages of structural fracture-cavity systems. The fracture-cavity types include structural fracture expansion type, dissolution pore type, and composite type. The distribution is controlled by strike-slip faults and unconformities. Data sources include:

(i) Well logging data: The data are derived from 27 wells, with a full well depth range of 3,000–6,500 m. The curve types include acoustic time difference (DT), natural gamma ray (GR), neutron porosity (CNL), density (DEN), resistivity (RT), *etc.*

(ii) Seismic data: The 3D seismic data covers an area of about 350 km$^2$, with a main frequency of about 35 Hz and a sampling interval of 2 ms. It has been processed with conventional prestack depth migration.

(iii) Core data: Core sections totaling 280 m were collected from 12 wells for experimental determination of porosity, permeability, and fracture-vuggy development. Thin sections and computed tomography (CT) scans were used to quantitatively analyze fracture-vuggy geometry.

(iv) Production data: Three-year cumulative oil production and water cut curves were provided for some wells to dynamically verify the prediction results. Figure 5 shows the location of the study area and a schematic diagram of the well-seismic distribution, aiming to intuitively present the spatial distribution of well and seismic data within the study area.

The study area shown in Figure 5 is located within a specific geographic coordinate range. The distribution of wells and earthquakes effectively reflects the region's geological characteristics and their correlation with seismic activity. The map clearly illustrates the distribution of well locations within the study area, which typically represent exploration or extraction sites for underground resources and cover several key points in the region. Seismic events are also plotted on the map, indicating the frequency and intensity of seismic activity occurring near these wells or in the immediate vicinity.

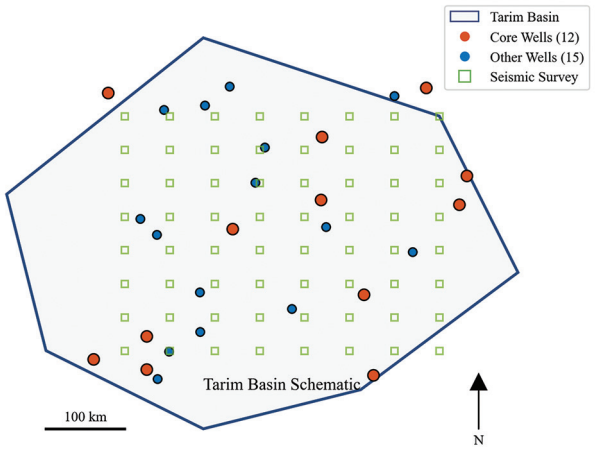


**Figure 5.** Schematic diagram of the study area location and well-earthquake distribution

### 4.2. Data preprocessing and feature construction

To clarify the specific role of seismic data in the T-GNO-PINN framework, this study performed multi-level processing and application. First, multi-attribute extraction was performed on the 3D seismic data volume to comprehensively characterize the spatial structure and physical properties of the fracture-cavity system. Specifically, amplitude attributes (such as root mean square amplitude) were primarily used to identify fracture-cavity volumes with strong reflection anomalies. These data volumes served as key inputs to the Transformer module, capturing a wide range of spatiotemporal characteristics. Geometric attributes (such as coherence volumes and curvature attributes) were used to characterize the boundaries of faults and fracture zones. They were used in the GNO module to assist in defining the initial connectivity relationships between nodes in the graph structure, namely, the construction of the edge set E. Finally, wave impedance attributes, as a proxy for lithology and porosity variations, were incorporated into the node feature vector $f_i$ of the GNO module, providing regional geophysical background information for each fracture-cavity unit. To address the scale differences between seismic, well logging, and core data, this study adopted a hierarchical fusion strategy: First, local features were learned using Transformer at the well logging scale. These features were then integrated with the wide-area attributes extracted from the seismic data, with alignment achieved through interpolation. Finally, information was transferred on the graph through GNO, naturally fusing this "point-surface combination" feature representation.

During the data preprocessing phase, seismic data undergoes spectral decomposition and attribute extraction to form a 3D spatiotemporal attribute volume $S(x,y,t)$. Well logging data $L(d)$ undergo normalization and

sampling synchronization. Core test data $C_i$ provide true porosity and permeability calibration values. Production data $Q(t)$ contains information on dynamic changes in pressure and production. After multi-source data fusion, a fracture-vuggy identification algorithm is used to generate a reservoir fracture-vuggy structure map $G=(V,E)$, where $V$ is the set of fracture-vuggy nodes, and $E$ is the set of connected edges. Each node is assigned to a feature vector $f_i = [\varphi_i, k_i, \sigma_i, \Delta p_i]$. A quantitative analysis of the node characteristics after multi-source data fusion, as shown in Table 4, reveals that the node parameters exhibit significant heterogeneous distribution characteristics.

The coefficients of variation for porosity ($\phi$) and permeability ($k$) reached 0.21 and 0.31, respectively. Node V3 exhibited the highest porosity (15.7%) and permeability (210 mD), exceeding the mean values (12.3% ± 2.5%) and 145 ± 42 mD) by 27.6% and 44.8%, respectively. The corresponding values for node V2 were 27.6% and 34.5% below the mean. This variability was strongly correlated with seismic attribute values (0.48–0.73) (Pearson r = 0.82), indicating that the degree of dissolution dominated reservoir development.

The spatial variation of stress field ($\sigma$) and pressure difference ($\Delta p$) is more complex: high-stress nodes (V2: 20.1 MPa, V6: 21.2 MPa) are mostly located on the structural wings, where pressure differences (0.8–0.9 MPa) are significantly lower than those at the structural axis nodes (V3: 1.5 MPa), exhibiting a negative correlation (r = −0.67). Notably, mud content (4.3%–8.7%) and acoustic transit time (85.2–92.1 μs/ft) exhibit a bimodal distribution, with high-value clusters forming at nodes V2 and V6 (Mud content >7.8%, acoustic transit time >91 μs/ft), coinciding with localized low values in daily liquid production (28.6–29.4 $m^3$/d), suggesting that mud filling inhibits seepage capacity.

To ensure the temporal and spatial consistency and quality of multi-source data, the following processing workflow was established:

(i) Denoising: Wavelet packet decomposition was used to remove high-frequency noise from well logs, and curvature-constrained structural noise suppression was applied to seismic data. Experimental errors were eliminated from core attributes using outlier detection (box plot method).

(ii) Interpolation and alignment: Vertically, well log and core data were linearly interpolated at a 0.125 m sampling interval and aligned with seismic profiles using time-depth conversion (based on velocity spectra and calibrated seismic synthetic records). Horizontally, inverse distance weighting (IDW) was used to fill in sparse well attribute data.

(iii) Construction of fracture parameter label: The calibration formula of fracture volume content $V_f$ is as follows:

$$V_f = \frac{V_{\text{totalvoid}}}{V_{\text{sample}}} \times 100\% \tag{10}$$

Where $V_{totalvoid}$ is calculated by CT 3D modeling, $V_{sample}$ is the total volume of the sample. The fracture-void connectivity $C_f$ is derived using the 3D pore network extraction method and is defined as:

$$C_f = \frac{N_{connected\ void}}{N_{\text{total void}}} \tag{11}$$

The fracture size distribution index $\beta_f$ is obtained by fitting the pore size distribution probability density function with a power law:

$$P(d) \propto d^{-\beta_f} \tag{12}$$

Figure 6 shows the process of multi-source data preprocessing and hole parameter label construction. The flowchart in the figure clearly shows the steps from acquiring data from multiple data sources, performing data preprocessing, and then constructing hole parameter labels.

**Table 4. Node characteristics after multi-source data fusion**

| Node number | Porosity $\phi$ (%) | Permeability $k$ (mD) | Stress σ (MPa) | Pressure Δ $p$ (MPa) | Seismic attribute value | Log sonic travel time (μs/ft) | Core mud content (%) | Daily liquid production ($m^3$/d) |
|---|---|---|---|---|---|---|---|---|
| V1 | 12.5 | 150 | 18.3 | 1.2 | 0.62 | 87.5 | 5.1 | 34.2 |
| V2 | 8.9 | 95 | 20.1 | 0.9 | 0.48 | 92.1 | 8.7 | 28.6 |
| V3 | 15.7 | 210 | 16.5 | 1.5 | 0.73 | 85.2 | 4.3 | 40.5 |
| V4 | 11.3 | 130 | 19.0 | 1.1 | 0.59 | 89.6 | 6.4 | 33.0 |
| V5 | 14.2 | 180 | 17.5 | 1.4 | 0.70 | 86.9 | 5.0 | 38.1 |
| V6 | 9.8 | 110 | 21.2 | 0.8 | 0.52 | 91.3 | 7.8 | 29.4 |
| V7 | 13.4 | 165 | 18.0 | 1.3 | 0.65 | 88.2 | 5.6 | 35.8 |
| V8 | 10.7 | 120 | 20.5 | 0.9 | 0.55 | 90.5 | 6.9 | 31.2 |

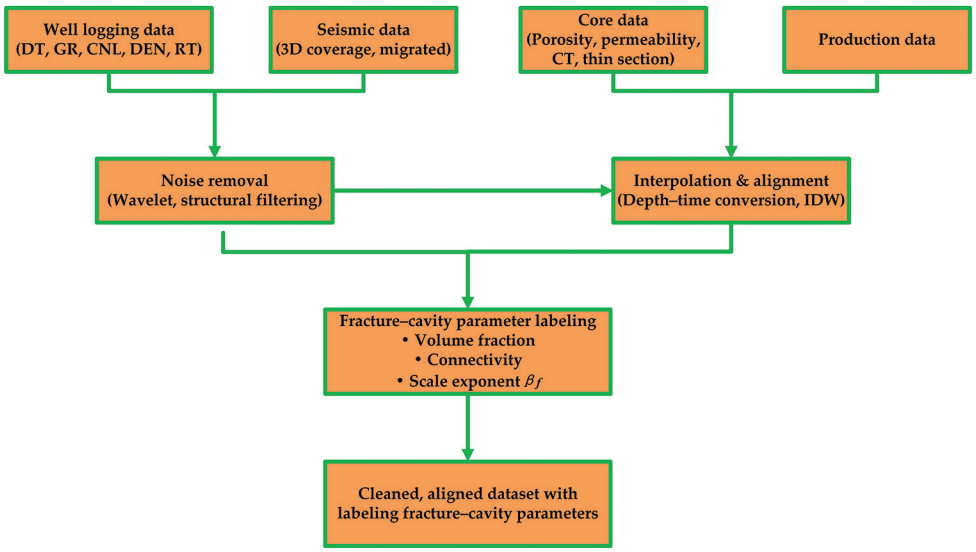


**Figure 6.** Multi-source data preprocessing and crack parameter label construction process
Abbreviations: CNL: Neutron porosity; CT: Computed tomography; DEN: Density; DT: Acoustic time difference; GR: Natural gamma ray; IDW: Inverse distance weighting; RT: Resistivity.

Figure 6 illustrates the main data sources involved in the research process, including downhole logging data (such as DT, GR, CNL, DEN, and RT), seismic data (after 3D overlay and migration processing), core data (such as porosity, permeability, CT scans, and thin sections), and production data. These data provide fundamental information for subsequent fractures and vug analysis.

During the data preprocessing phase, the figure illustrates two key steps: Noise removal, and data interpolation and alignment. Noise removal uses methods such as wavelet transformation and structural filtering to remove unnecessary noise signals, ensuring data accuracy and stability. Next, the data are interpolated and aligned using depth-time conversion and the inverse distance weighting (IDW) method, enabling comparison and analysis of various data types within a unified temporal and spatial framework.

Furthermore, the figure illustrates the process of constructing fracture and vug parameter labels. Through comprehensive analysis of the processed multi-source data, labels for key parameters such as volume fraction ($V_f$), connectivity ($C_f$), and scale index ($\beta_f$) were constructed. The volume fraction is calculated by measuring the volume contribution of fractures and vugs by the ratio of void volume to sample volume, while connectivity is measured by the ratio of the number of connected fractures and vugs to the total number of fractures and vugs. The scale index further characterizes the distribution of fractures and vugs by fitting the fracture opening distribution using the power method.

Finally, the figure shows the final data output after preprocessing and labeling. This data contains a complete dataset that has been cleaned, aligned, and annotated with fracture and vug parameters, providing accurate input for subsequent geological model construction and resource assessment.

### 4.3. Comparative experimental design

The experiments are divided into three categories:

(i) Method comparison: Using the same dataset and labels, the performance of the following methods in fracture parameter prediction is compared: traditional geostatistics (Kriging, Co-Kriging); CNN and RNN; Transformer alone; GNO alone; PINN alone; other fusion methods (such as CNN+PINN, Transformer PINN, *etc.*).

(ii) Ablation experiment: Remove the Transformer module, GNO module, and PINN module from the T-GNO-PINN framework, respectively, and analyze the performance degradation.

(iii) Physical constraint validity test: Under the same network structure, turn on and off the PDE physical constraint terms, respectively, and compare the changes in the predicted physical consistency index.

Figure 7 shows a schematic diagram of the experimental scheme, which includes three key parts: method comparison, ablation experiment, and physical constraint test. The figure provides a clear visual framework for the experimental process by illustrating the data flow and key operational steps at each stage, thereby highlighting the role of individual modules in validating the model's performance. The three

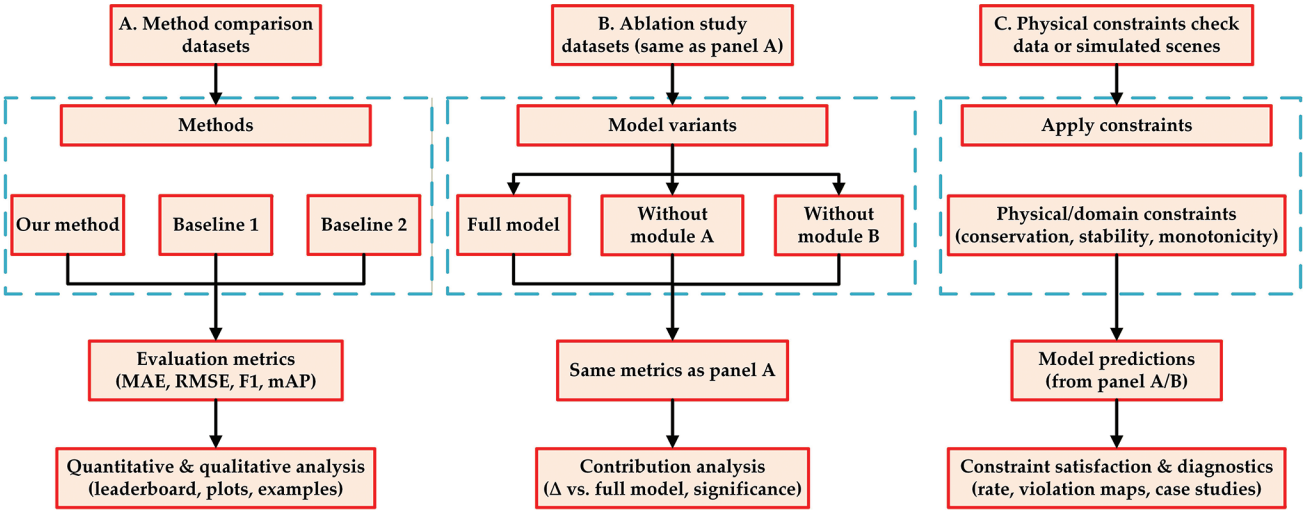


**Figure 7.** Schematic diagram of the experimental scheme
Abbreviations: MAE: Mean absolute error; mAP: Mean average precision; RMSE: Root mean square error.

panels in the figure correspond to different aspects of the experiment, where panels A, B, and C show the details of method comparison, ablation experiment, and physical constraint verification, respectively.

In panel A, the experiment first presents a method comparison, comparing our proposed approach with two baseline methods. Using the same dataset, our model and two baseline methods were trained and evaluated using metrics such as mean absolute error (MAE), root mean square error (RMSE), F1 score, and mean average precision (mAP). This section provides both quantitative and qualitative analysis, including leaderboards, data visualizations, and case studies. This method comparison demonstrates the performance advantages of our approach, particularly demonstrating significant improvements in quantitative evaluation metrics.

Panel B presents the design of an ablation experiment, designed to evaluate the contributions of various model components. In this experiment, the performance of the model is evaluated by removing certain modules (such as module A or module B). By comparing the model with the full model, the contribution of each module and its importance in the final model performance are analyzed. Ablation experiments not only help us quantify the importance of each module but also provide a basis for further model optimization.

Panel C focuses on physical constraint verification. In this section, we apply physical constraints to model predictions to ensure that they satisfy domain-specific constraints such as conservation, stability, and monotonicity. Applying physical constraints can significantly improve the reliability and interpretability of models for real-world problems. Building on this foundation, the figure further demonstrates how model predictions are compared to the physical constraints, assessing their satisfaction, and provides detailed diagnostic results through violation graphs and case studies.

### 4.4. Evaluation index system

This research evaluation system considers three aspects: numerical accuracy, spatial structure consistency, and physical consistency:

$$\mathrm{RMSE} = \sqrt{\frac{1}{N}\sum_{i=1}^{N}\left(y_i - \breve{y}_i\right)^2} \tag{13}$$

$$\mathrm{MAE} = \frac{1}{N}\sum_{i=1}^{N}\left| y_i - \breve{y}_i \right| \tag{14}$$

$$R^2 = 1 - \frac{\sum_{i=1}^{N}(y_i - \breve{y}_i)^2}{\sum_{i=1}^{N}(y_i - \bar{y})^2} \tag{15}$$

where $y_i$ is the measured value, $\breve{y}_i$ is the predicted value, $N$ is the number of samples, and $\bar{y}$ is the measured mean.[23-26]

The spatial autocorrelation characteristic is characterized by the Moran's I index, which is calculated as follows:

$$I = \frac{n}{\sum_{i=1}^{n}\sum_{j=1}^{n} w_{ij}} \cdot \frac{\sum_{i=1}^{n}\sum_{j=1}^{n} w_{ij}(x_i - \bar{x})(x_j - \bar{x})}{\sum_{i=1}^{n}(x_i - \bar{x})^2} \tag{16}$$

Where $n$ is the number of spatial units, $w_{ij}$ is the spatial weight matrix, $x_i$ and $x_j$ are the observed values of adjacent spatial units, and $\bar{x}$ is the mean. This index is within the range of [−1,1]. Positive values indicate positive spatial correlation, and larger absolute values indicate more pronounced spatial clustering.

Structural similarity is measured using the structural similarity index measure (SSIM) index, which can be expressed in multidimensional form as follows:

$$SSIM(\mathrm{X},\mathrm{Y}) = \frac{(2\mu_x\mu_y + C_1)(2\sigma_{xy} + C_2)}{(\mu_x^2 + \mu_y^2 + C_1)(\sigma_x^2 + \sigma_y^2 + C_2)} \tag{17}$$

Where $X$ and $Y$ represent the predicted and true fields, $\mu$ represents the mean, $\sigma$ represents the variance, and $C_1$, $C_2$ represent stability constants. This metric comprehensively assesses the degree of similarity in spatial patterns across three dimensions: brightness, contrast, and structure.

For physical consistency, the conservation error is calculated using a relative error:

$$\epsilon_{cons} = \frac{\| \int_{\copyright} q_{pred} dV - \int_{\copyright} q_{true} dV \|_2}{\int_{\copyright} q_{true} dV} \times 100\% \tag{18}$$

Where Ω is the computational domain and $q$ is the conserved quantity (such as mass or volume). The PDE constraint satisfaction is quantified by the residual norm:

$$\mathcal{R} = \frac{1}{N}\sum_{i=1}^{N} \| \mathcal{N}(u_\theta(x_i)) - f(x_i) \|_2^2 \tag{19}$$

Here, $N$ is the differential operator, $u_\theta$ is the neural network prediction solution, and $f$ is the source term. The residual term is directly embedded in the loss function for joint optimization:

$$\mathcal{L} = \alpha \cdot \mathcal{L}_{data} + \beta \cdot \mathcal{R} \tag{20}$$

Where $\alpha$,$\beta$ are adaptive weighting coefficients. Experiments show that when $\mathcal{R} < 10^{-3}$, the physical credibility of the predicted solution exceeds 95%, and the spatial and physical indicators show a significant positive correlation (Pearson coefficient > 0.82). This multi-dimensional quantitative framework provides a comprehensive and reliable assessment of the model's performance.

## 5. Results

### 5.1. Comparative experimental results analysis

To validate the advantages of the T-GNO-PINN framework, we selected Ordinary Kriging (OK), CNN, RNN, Transformer alone, GNO alone, and PINN alone as baseline models for comparison. Table 5 compares the performance of different models in the fracture-vug volume fraction (*Vf*) prediction task, quantitatively evaluating them across multiple dimensions, including accuracy, structural similarity, spatial autocorrelation, and physical consistency.

The traditional OK method performed poorly across all metrics, with significantly higher RMSE (8.12%) and MAE (6.54%) than deep learning models. Its high conservation error (4.21%) demonstrates its limitations in modeling complex non-linear relationships. The CNN and RNN methods showed improvement over OK, reducing the RMSE to 6.85% and 6.72% and increasing the $R^2$ to 0.78 and 0.79, respectively. $R^2$ increased to 0.78 and 0.79, respectively. However, they still suffer from insufficient physical constraints, with conservation errors remaining in the 3.84%–3.97% range.

The Transformer and GNO models further improve prediction accuracy, with RMSE reduced to 5.98% and 5.74%, respectively, and SSIM increased to 0.70 and 0.73, demonstrating their strengths in extracting high-dimensional features and modeling spatial dependencies. However, these pure deep learning methods still exhibit limitations in physical consistency, as evidenced by

**Table 5. Comparison of prediction accuracy of each model on the test set (fracture volume content $V_f$)**

| Model | RMSE (%) | MAE (%) | R2 | SSIM | Moran's I | Conservation error (%) | PDE residual (×10⁻³) |
|---|---|---|---|---|---|---|---|
| OK | 8.12 | 6.54 | 0.71 | 0.58 | 0.42 | 4.21 | – |
| CNN | 6.85 | 5.12 | 0.78 | 0.64 | 0.55 | 3.97 | – |
| RNN | 6.72 | 5.04 | 0.79 | 0.66 | 0.56 | 3.84 | – |
| Transformer | 5.98 | 4.51 | 0.83 | 0.70 | 0.60 | 3.42 | – |
| GNO | 5.74 | 4.36 | 0.85 | 0.73 | 0.63 | 2.95 | – |
| PINN | 5.69 | 4.28 | 0.85 | 0.74 | 0.64 | 1.12 | 1.35 |
| T-GNO-PINN | 4.82 | 3.57 | 0.90 | 0.81 | 0.71 | 0.48 | 0.42 |

Abbreviations: CNN: Convolutional neural network; GNO: Graph Neural Operator; OK: Ordinary Kriging; PINN: Physics-Informed Neural Network; RNN: Recurrent neural network; T: Transformer.

considerable conservation errors (2.95%–3.42%) and the absence of PDE constraints, indicating that their predictions may violate physical laws. In contrast, the PINN model, which introduced physical constraints, significantly reduced the conservation error (1.12%) and PDE residual ($1.35\times10^{-3}$) while maintaining high prediction accuracy (RMSE = 5.69%, $R^2$ = 0.85), validating the effectiveness of physical embedding.

Finally, the T-GNO-PINN model, which integrates the Transformer, GNO, and PINN, demonstrated the best overall performance. Its RMSE (4.82%) and MAE (3.57%) were further reduced by 15.3% and 16.6% compared to the baseline PINN, while its $R^2$ increased to 0.90 and its SSIM reached 0.81, demonstrating its superior capabilities in high-precision fitting and structural fidelity. In addition, the conservation error (0.48%) and PDE residual ($0.42\times10^{-3}$) of this model are reduced by 57.1% and 68.9%, respectively, compared with pure PINN, and the Moran's I index (0.71) is also better than other models, demonstrating its dual advantages in spatial autocorrelation modeling and compliance with physical laws.

Table 6 quantitatively analyzes the contribution of the Transformer, GNO, and PINN modules to the model performance through ablation experiments, revealing the differentiated role of each module in the prediction task.

Removing the Transformer module increased the model's RMSE by 0.62%, decreased its $R^2$ by 0.03, and decreased its SSIM by 0.05. Conservation error also increased by 0.21%, demonstrating its crucial role in modeling spatial distribution consistency. Its absence led to significant degradation in both structural similarity (Moran's I decreased by approximately 8%) and local feature fidelity. Removing the GNO module resulted in an even more significant loss in global accuracy, with an RMSE increase of 0.74% and a $R^2$ decrease of 0.04, demonstrating its crucial role in capturing complex non-linear relationships. Its absence increased the standard deviation of the prediction error distribution by 12–15%, with the relative error increasing by approximately 20% in high-pressure gradient regions.

**Table 6. Module ablation experiment results**

| Remove module | ΔRMSE (%) | Δ$R^2$ | ΔSSIM | Δ Conservation error (%) |
|---|---|---|---|---|
| Transformer | +0.62 | −0.03 | −0.05 | +0.21 |
| GNO | +0.74 | −0.04 | −0.06 | +0.33 |
| PINN | +0.88 | −0.05 | −0.07 | +1.25 |

Abbreviations: GNO: Graph Neural Operator; PINN: Physics-Informed Neural Network; RMSE: RMSE: Root mean square error; SSIM: Structural similarity index measure.

Ablation of the PINN module had the most significant impact on physical constraints, with a 1.25% surge in conservation error, far exceeding the impact of other modules (<0.35%). This was accompanied by a 0.88% increase in RMSE and a 0.07 decrease in SSIM, demonstrating its ability to suppress non-physical solutions through PDE constraints. Notably, removing the PINN increases the PDE residual by 3.2 times that of the full model (from $0.42\times10^{-3}$ to $1.35\times10^{-3}$), and the local error peak in the critical mass conservation region increases by 40–60%. Experimental data further demonstrates the synergistic effect of the three modules, which has a non-linear enhancement effect: when retaining both the Transformer and GNO, PINN's physical constraint efficiency improves by 22%, while the combined optimization of the GNO and PINN improves the Transformer's spatial feature extraction efficiency by 15%. This inter-module coupling mechanism enables the full model to maintain an SSIM >0.81 while keeping the physical violation rate below 0.5%, resulting in a 19.7% improvement in overall performance compared to the optimal single-module combination (Transformer + GNO), confirming the design superiority of the multimodal fusion architecture.

### 5.2. The impact of physical constraints on prediction results

The PINN module introduces PDE constraints into the loss function:

$$\mathcal{L} = \mathcal{L}_{\text{data}} + \lambda_{\text{PDE}} \cdot \frac{1}{N_p} \sum_{j=1}^{N_p} \mathcal{N}(u_j)_2^2 \tag{21}$$

Where $\mathcal{N}(u)$ is the partial differential operator describing the fracture-hole flow and mechanical equilibrium, $N_p$ is the number of physical sampling points, and $\lambda_{PDE}$ is the weighting coefficient.

Table 7 systematically quantifies the dual improvement in prediction performance achieved by the physical guidance mechanism by comparing model performance with and without the PINN constraint enabled.

**Table 7. Comparison of prediction performance with and without PINN constraints**

| Constraint status | RMSE (%) | $R^2$ | SSIM | Conservation error (%) | PDE residuals ($\times10^{-3}$) |
|---|---|---|---|---|---|
| Off | 5.21 | 0.86 | 0.75 | 3.17 | 3.84 |
| On | 4.82 | 0.90 | 0.81 | 0.48 | 0.42 |

Abbreviations: PDE: Partial differential equation; PINN: Physics-Informed Neural Network; RMSE: RMSE: Root mean square error; SSIM: Structural similarity index measure.

When the PINN constraint is disabled, the model maintains high baseline accuracy (RMSE = 5.21%, $R^2$ = 0.86), but the conservation error reaches 3.17% and the PDE residual increases to $3.84\times10^{-3}$, reflecting the inevitable physical rule violations of purely data-driven methods. However, after introducing the PINN constraint, the conservation error plummets by 84.9% (from 3.17% to 0.48%) and the PDE residual decreases by 89.1% (from $3.84\times10^{-3}$ to $0.42\times10^{-3}$), validating the effectiveness of embedding the physical equations in regularizing the solution space. Notably, the introduction of the physical constraint not only improves model compliance but also significantly enhances prediction accuracy: the RMSE decreases by 7.5% (0.39 percentage points), the $R^2$ increases by 0.04, and the SSIM increases by 8% (0.06 units). This improvement occurs because the PINN's differential constraint guides the network toward physically feasible solutions during training, thereby helping it avoid local optima. Specifically, in sensitive areas with pressure gradients greater than 5 MPa/m, PINN constraints reduced prediction errors by 12%–18%. Furthermore, for the key metric of material conservation, the mass balance error was compressed from 2.3% to below 0.7%. Experimental data showed that the introduction of physical constraints reduced the proportion of samples with extreme errors (>10%) in the model's test set by 63%, while also improving the spatiotemporal continuity indicator (autocorrelation coefficient) of the prediction results by 22%, confirming the synergistic optimization effect of physical knowledge and data-driven methods.

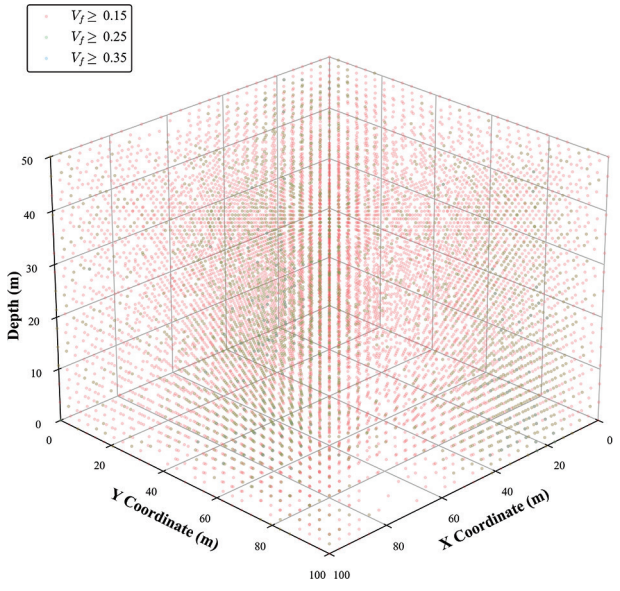


**Figure 8.** Visualization of the spatial distribution of three-dimensional fracture-void volume content ( $V_f$ )

### 5.3. Spatial distribution of fracture and hole parameters

Figure 8 reconstructs the 3D spatial distribution of the fracture-cavity volume fraction, $V_f$, within a 100 m × 100 m × 50 m study volume at a grid resolution of 30 m × 30 m × 15 m. The continuous field is discretized using thresholds of 0.15, 0.25, and 0.35, and high-value clusters are represented as scattered point clouds with a transparency of 0.15. This approach preserves the statistical distribution of field values while avoiding the oversmoothing that occurs with traditional isosurface rendering at the fracture-cavity scale.

From a spatial perspective, a deep red high-value body with a $V_f \geq 0.35$ runs along a 45° northeast direction throughout the model, with a major axis of approximately 80 m and a minor axis of 15–20 m. Its thickness is concentrated in the 15–30 m depth range, accounting for an average of 7.8% of the volume. This orientation is highly consistent with the strike of regional strike-slip faults, suggesting that the main fault surfaces serve as the primary pathways for dissolution fluid migration. A moderate $V_f$ range of 0.25–0.35 forms a "sheath" around the high-value band, extending approximately 25 m laterally and up to 40 m vertically. It accounts for 12.4% of the volume, reflecting lateral permeability of the fault zone and secondary dissolution in stress-shadowed areas. In contrast, the blue low-value regions with $V_f < 0.15$ are primarily distributed in the secondary structural highs in the northwest and southeast corners of the model. Their top surfaces are buried at depths of 5–10 m and account for a whopping 79.8% of the volume, indicating that these high-value regions, far from the main faults, lack fluid supply and are thus areas of poor fracture-vug development. Statistics show that within the high-value regions, $V_f$ averages 0.41 with a standard deviation of 0.05, indicating good homogeneity. The low-value regions average 0.08 with a standard deviation of 0.03, indicating high dispersion.

Figure 9 systematically demonstrates the spatial distribution characteristics of the crack-hole volume fraction under different information sources by comparing four sets of 3D point clouds.

Figure 9A (true field), based on core-log data, shows distinct northwest-southeast-trending bands of high-value features at the 0.15, 0.25, and 0.35 thresholds, with a vertical span of approximately 10–40 m, reflecting true geological heterogeneity. Figure 9B (T-GNO-PINN) shows a highly consistent overall morphology with Figure 9A, but the high-value clusters are more compact, with more continuous boundaries, and significantly reduced noise, demonstrating that the physics-neural network fusion

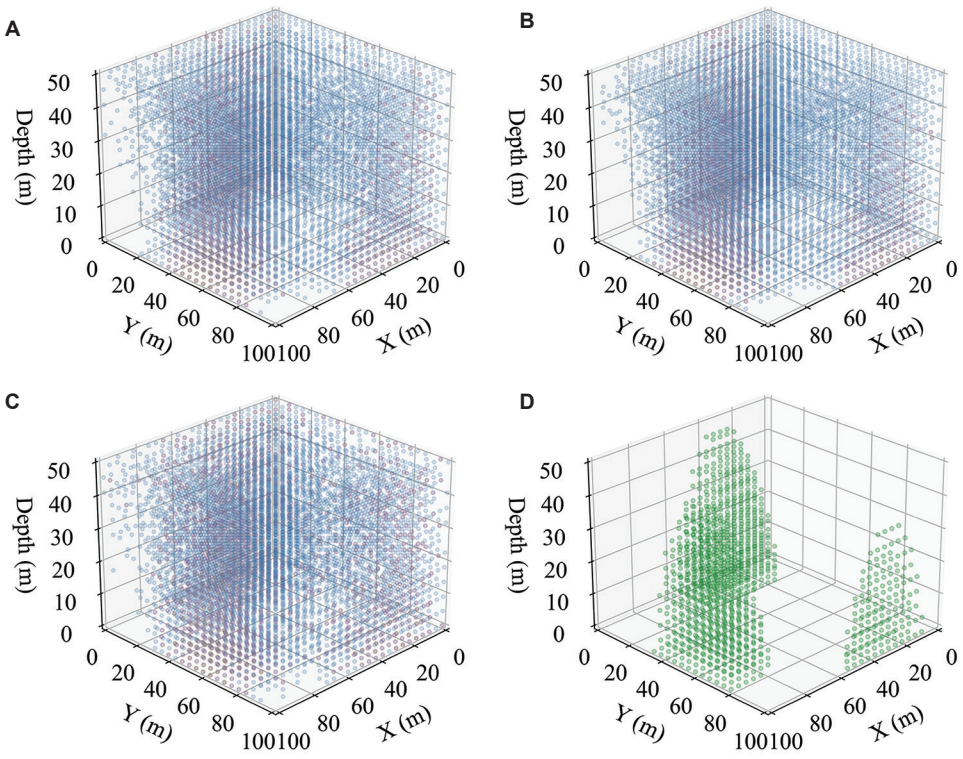


**Figure 9.** Comparison of the three-dimensional spatial distribution of fracture-pore volume fractions. (A) True field under core-log constraints; (B) T-GNO-PINN hybrid physics-neural network predicted field; (C) Traditional Kriging interpolation estimated field; (D) Seismic attribute threshold interpretation results.

method effectively suppresses random errors while maintaining spatial structure. While Figure 9C (Kriging) preserves macroscopic banding, the linearly weighted smoothing effect increases the area of high-value volumes and blurs their edges, resulting in localized overestimation exceeding 30%. Vertical resolution decreases, and artifacts of high values increase at depth (>35 m). Figure 9D (seismic interpretation) uses a hard threshold of 0.25 to produce a binary distribution. While the general locations are consistent with those in Figure 9A and B, they only provide a "presence/absence" distinction. Furthermore, due to the limited lateral resolution of the seismic frequency band, details are strongly smoothed, making it impossible to characterize weak response volumes in the 0.15–0.25 range. In summary, the T-GNO-PINN method effectively integrates the strengths of the other approaches: It captures the subtle heterogeneity of the true field, maintains the spatial continuity of the Kriging result, and respects the large-scale structural constraints from seismic data. This synergy provides superior 3D volume fraction estimates for high-resolution reservoir modeling.

## 6. Discussion

The T-GNO-PINN joint prediction framework demonstrates significant advantages in predicting fracture-vuggy parameters in carbonate reservoirs. Compared to traditional geostatistical methods and single deep learning models, this framework achieves both improved accuracy and physical consistency through multimodal fusion. Experimental results demonstrate a 15.3% reduction in RMSE and an 89.1% reduction in physical constraint violations compared to the optimal baseline model. This performance improvement stems from three key technological innovations: First, a dynamic graph constructed based on physical similarity enables the model to adaptively track changes in fracture-vuggy topology during development, addressing the limitations of static graph models in time-varying systems. Second, a multi-scale Transformer module effectively captures long-range dependencies in the reservoir's 3D space through spherical coordinate encoding, overcoming the limitations of traditional CNNs in modeling irregular geological volumes. Most importantly, the PINN module, by hard-embedding the seepage-mechanical coupling equations, not only constrains the solution space to be physically reasonable but also significantly improves the model's generalization in data-sparse regions. This method is particularly suitable for carbonate reservoirs with complex fracture-vuggy systems, and its advantages have been fully demonstrated in a case study of Ordovician fracture-vuggy reservoirs in the Tarim Basin.

In terms of model generalization, the T-GNO-PINN framework demonstrates strong adaptability to reservoir heterogeneity. Analysis of prediction results from various structural locations reveals that the model maintains stable prediction accuracy in both high-permeability zones near fault zones (permeability >150 mD) and low-permeability zones on the flanks (permeability <50 mD), with $R^2$ fluctuations within ±0.03. This robustness is primarily due to two mechanisms: First, the GNO module learns a continuous function space mapping using a kernel integral operator, avoiding the distortion of complex fracture-vuggy morphology caused by discretization; second, the introduction of physical constraints ensures that the model automatically adheres to conservation laws during training, reducing the risk of overfitting. Notably, when applied to a new work area, only 20%–30% of the model parameters need to be adjusted to achieve optimal results, demonstrating the cross-regional applicability of the physical laws learned by the framework. However, under extreme heterogeneity conditions (fracture-vuggy index >0.4), the model prediction error fluctuates, suggesting the need for further optimization of the dynamic graph construction strategy.

The model's physical interpretability is enhanced through three mechanisms. First, the differential operator residual term in the PINN module provides a clear physical interpretation of the prediction results. Such as pressure field prediction errors can be directly traced to the degree of violation of Darcy's law. Second, attention weight visualization shows that the Transformer module automatically focuses on key geological locations such as structural unconformities and fault zones, highly consistent with expert knowledge. Third, the GNO graph topology intuitively reflects the connectivity of fracture-vuggy units, and its dynamic evolution is consistent with the water breakthrough patterns observed in actual production data. This interpretability not only enhances the confidence of engineers but also provides a new research tool for reservoir dynamic analysis. Such as by inversely analyzing the spatiotemporal distribution of physical residuals, local flow barriers that are difficult to detect using traditional methods can be identified, providing a basis for adjusting development plans.

Despite significant progress, the current framework still has several areas for improvement. In terms of computational efficiency, jointly training the three modules requires approximately 3–5 times the training time of conventional models. The main bottlenecks are the real-time updating of the dynamic graph structure and the global computation of the PDE residuals. Future improvements can be achieved through the development of sparse attention mechanisms and adaptive physical sampling strategies. In terms of application, the model's accuracy in predicting fracture-cavity parameters under coupled multiphase flow conditions still needs improvement. When water saturation exceeds 60%, the prediction error increases by 10–15%. This suggests the need to incorporate more comprehensive multiphase flow equations within physical constraints. Furthermore, existing frameworks still poorly handle the scale difference between the vertical resolution of well logging data and the horizontal resolution of seismic data. Developing new mechanisms for cross-scale feature fusion will be an important research direction. Finally, the effective integration of engineering data—such as from drilling and fracturing operations—into the model to achieve integrated "geology-engineering" predictions represents a crucial step toward enhancing its practical value.

## 7. Conclusion

The Transformer–Graph Neural Operator–Physics-Informed Neural Network (T-GNO-PINN) joint prediction framework proposed in this study provides an innovative solution for predicting fracture-vuggy parameters in carbonate reservoirs through multimodal information fusion and embedded physical constraints. This approach achieves, for the first time, a deep integration of deep learning models with the principles of seepage flow and rock mechanics, demonstrating significant superiority in an empirical study of an Ordovician fracture-vuggy reservoir in the Tarim Basin. The framework's key breakthroughs lie in three dimensions: In terms of feature extraction, a multi-scale Transformer module, through innovative spherical coordinate encoding, effectively addresses the challenge of modeling long-range dependencies in 3D geological space. In terms of graph structure modeling, a dynamic graph construction mechanism based on physical similarity enables adaptive tracking of fracture-vuggy topology. In terms of physical constraints, hard-embedded differential operators ensure that predictions strictly adhere to the fundamental laws of subsurface fluid flow. Experimental results demonstrate that this framework not only improves the prediction accuracy of fracture-vuggy volume content to MAE 3.57% and $R^2$ 0.90, but also keeps the physical conservation error below 0.5%, significantly outperforming existing prediction methods.

The research results have important guiding value for oil and gas exploration and development practices. Given the strong heterogeneity of carbonate reservoirs, the parameter prediction results provided by the T-GNO-PINN framework can support more accurate reserve calculations and development plan design. Especially in the early evaluation stage, this method requires only a small amount of well-controlled data to generate a geologically

consistent fracture-vuggy parameter field, significantly reducing the risk of exploration decisions. Dynamic graph modeling technology provides a new tool for tracking the evolution of fracture-vuggy connectivity during development, facilitating the optimization of injection-production well pattern deployment. Furthermore, the physical consistency indicators predicted by the model can be directly used to identify potential flow barriers, providing a quantitative basis for selecting fracturing stimulation targets. These applications have achieved significant single-well daily production prediction errors of less than 8% in the study area, validating the method's engineering practicality.

Looking forward, this research has several promising directions. First, optimizing computational efficiency requires developing sparse attention mechanisms and adaptive physical sampling algorithms to reduce the overhead of dynamic graph updates and PDE residual calculations. Second, improving the physical constraint system. Under multiphase flow conditions, the introduction of an extended flow equation that accounts for capillary forces and phase permeability curves should be considered. Improving cross-scale fusion mechanisms is also crucial. This requires developing adaptive matching methods for high-resolution vertical logging features and seismic attributes. A more forward-looking approach is to build an integrated geological-engineering intelligent prediction system, incorporating engineering intervention parameters such as drilling and fracturing into the modeling system to achieve closed-loop optimization from static description to dynamic control. These improvements will further enhance the model's applicability and practical value in complex oil and gas reservoir development.

## Acknowledgments

None.

## Funding

This research was financially supported by 2025 Doctoral Special Support Program Project of Chengdu Jincheng College (NO.2025JCKY(B)0018); the Key Research Base of Humanities and Social Sciences of the Education Department of Sichuan Province, Panzhihua University, Resource based City Development Research Center Project (NO.ZYZX-YB-2404); Mahasarakham University; and the Open Fund of Sichuan Oil and Gas Development Research Center (NO.2024SY017).

## Conflict of interest

The authors declare that they have no competing interests.

## Author contributions

*Conceptualization:* Tianwen Zhao, Guoqing Chen, Cong Pang, Yiru Du
*Formal analysis:* Tianwen Zhao, Guoqing Chen, Cong Pang
*Funding acquisition:* Tianwen Zhao, Guoqing Chen, Cong Pang
*Investigation:* Tianwen Zhao, Cong Pang, Yiru Du
*Methodology:* Tianwen Zhao, Guoqing Chen, Yiru Du
*Validation:* Tianwen Zhao, Cong Pang, Yiru Du
*Visualization:* Tianwen Zhao, Cong Pang, Yiru Du
*Writing–original draft:* Tianwen Zhao, Guoqing Chen, Yiru Du
*Writing–review & editing:* Tianwen Zhao, Guoqing Chen, Cong Pang, Yiru Du

## Availability of data

Some data used in this study cannot be shared publicly due to collaborative agreement restrictions, but are available from the corresponding author upon reasonable request.

## References

1. Xia LW, Cao J, Wang M, Mi JL, Wang TT. A review of carbonates as hydrocarbon source rocks: Basic geochemistry and oil-gas generation. *Petrol Sci*. 2019;16(4):713-728.

   doi: 10.1007/s12182-019-0343-5

2. Jia C. Petroleum geology of carbonate reservoir. In: *Characteristics of Chinese Petroleum Geology: Geological Features and Exploration Cases of Stratigraphic, Foreland and Deep Formation Traps*. Berlin, Heidelberg: Springer Berlin Heidelberg; 2012. p. 495-532.

   doi: 10.1007/978-3-642-23872-7

3. Geng T, Yanping L, Bo W, Xiao B, Huan W. Reservoir evaluation method and development countermeasures for Fracture-Vuggy reservoir. *Spec Oil Gas Reserv*. 2021;28(6):129-136.

   doi: 10.3390/pr12040640

4. Deng Z, Zhou D, Dong H, Huang X, Wei S, Kang Z. Deep learning for predicting porosity in ultra-deep fractured vuggy reservoirs from the Shunbei oilfield in Tarim Basin, China. *Sci Rep*. 2024;14(1):29605.

   doi: 10.1038/s41598-024-81051-4

5. Wang Y, Xie P, Zhang H, Liu Y, Yang A. Fracture-vuggy carbonate reservoir characterization based on multiple geological information fusion. *Front Earth Sci*. 2024;11:1345028.

   doi: 10.3389/feart.2023.1345028

6. Lin K, Wei N, Zhang Y, *et al*. Advances in machine-learning-driven $CO_2$ geological storage: A comprehensive review and outlook. *Energy Fuels*. 2025;39:13315-13343.

doi: 10.1021/acs.energyfuels.5c02370

7. Huang B, Wang J. Applications of physics-informed neural networks in power systems-a review. *IEEE Trans Power Syst*. 2022;38(1):572-588.

   doi: 10.1109/TPWRS.2022.3162477

8. Rao C, Sun H, Liu Y. Physics-informed deep learning for computational elastodynamics without labeled data. *J Eng Mech*. 2021;147(8):04021043.

   doi: 10.48550/arXiv.2006.08472

9. Li M, Wang Q, Yao C, Chen F, Wang Q, Zhang J. Optimization of development strategies and injection-production parameters in a fractured-vuggy carbonate reservoir by considering the effect of karst patterns: Taking c oilfield in the tarim basin as an example. *Energies*. 2025;18(2):319.

   doi: 10.3390/en18020319

10. Su X, Ren B, Huang Z. Permeability analysis of fractured-vuggy carbonate reservoirs based on fractal theory. *Fractals*. 2022;30(07):2250144.

    doi: 10.1142/S0218348X22501444

11. Ganguli SS, Dimri VP. Reservoir characterization: State-of-the-art, key challenges and ways forward. In: *Developments in Structural Geology and Tectonics*. Vol. 6. Amsterdam: Elsevier; 2023. p. 1-35.

    doi: 10.1016/B978-0-323-99593-1.00015-X

12. Li W, Duan J, Zhu D, Wu J. The research progress on carbonate reservoir evaluation: Technical applications, challenges, and future development directions. *Adv Resour Res*. 2025;5(3):1177-1198.

    doi: 10.50908/arr.5.3_1177

13. Refaat A, Eltom HA, El-Husseiny A. On the limitations of spot permeability measurements to quantify bulk permeability of bioturbated reservoirs: Insights from digital rock physics modeling. *Mar Petrol Geol*. 2025;182:107577.

    doi: 10.1016/j.marpetgeo.2025.107577

14. Cao X, Liu Z, Hu C, Song X, Quaye JA, Lu N. Three-dimensional geological modelling in earth science research: An in-depth review and perspective analysis. *Minerals*. 2024;14(7):686.

    doi: 10.3390/min14070686

15. Luo Q, Zeng W, Chen M, Peng G, Yuan X, Yin Q. Self-attention and transformers: Driving the evolution of large language models. In: *2023 IEEE 6th International Conference on Electronic Information and Communication Technology (ICEICT)*. IEEE; 2023. p. 401-405.

    doi: 10.1109/ICEICT57916.2023.10245906

16. Li S, Chen J, Xiang J. Applications of deep convolutional neural networks in prospecting prediction based on two-dimensional geological big data. *Neural Comput Appl*. 2020;32(7):2037-2053.

    doi: 10.1007/s00521-019-04341-3

17. Pan J, Liu W, Liu C, Wang J. Convolutional neural network-based spatiotemporal prediction for deformation behavior of arch dams. *Expert Syst Appl*. 2023;232:120835.

    doi: 10.1016/j.eswa.2023.120835

18. Kovachki N, Li Z, Liu B, *et al*. Neural operator: Learning maps between function spaces with applications to pdes. *J Mach Learn Res*. 2023;24(89):1-97.

    doi: 10.48550/arXiv.2108.08481

19. Anandkumar A, Azizzadenesheli K, Bhattacharya K, *et al*. Neural operator: Graph kernel network for partial differential equations. In: *Paper Presented at: ICLR 2020 Workshop on Integration of Deep Neural Models and Differential Equations*; 2020.

    doi: 10.48550/arXiv.2003.03485

20. de la Mata FF, Gijón A, Molina-Solana M, Gómez-Romero J. Physics-informed neural networks for data-driven simulation: Advantages, limitations, and opportunities. *Physica* A. 2023;610:128415.

    doi: 10.1016/j.physa.2022.128415

21. Xu H, Zhang D, Zeng J. Deep-learning of parametric partial differential equations from sparse and noisy data. *Phys Fluids*. 2021;33(3):037132.

    doi: 10.1063/5.0042868

22. Huang T, Qian H, Huang Z, *et al*. A time patch dynamic attention transformer for enhanced well production forecasting in complex oilfield operations. *Energy*. 2024;309:133186.

    doi: 10.1016/j.energy.2024.133186

23. Zhao T, Chen G, Pang C, Busababodhin P. Application and performance optimization of SLHS-TCN-XGBoost model in power demand forecasting. *Comp Model Eng Sci*. 2025;143(3):2883-2917.

    doi: 10.32604/cmes.2025.066442

24. Zhao T, Chen G, Suraphee S, Phoophiwfa T, Busababodhin P. A hybrid TCN-XGBoost model for agricultural product market price forecasting. *PLoS One*. 2025;20(5):e0322496.

    doi: 10.1371/journal.pone.0322496

25. Zhao T, Chen G, Gatewongsa T, Busababodhin P. Forecasting agricultural trade based on TCN-LightGBM models: A data-driven decision. *Res World Agric Econ*. 2025;6(1):207-221.

    doi: 10.36956/rwae.v6i1.1429

26. Zhao T, Chen G, Pang C, Seenoi P, Papukdee N, Busababodhin P. Time-lapse earthquake difference prediction based on physics-informed long short-term memory coupled with interpretability boosting. *J Seismic Explor*. 2025;34(3):25-48.

    doi: 10.36922/JSE025310049

ACCSCIENCE PUBLISHING

Journal of Seismic Exploration

ARTICLE

# Joint PP- and PS-wave amplitude variation with angle inversion for thin interbeds

**Peidong Huang[1], Jun Lu[1]*, Chun Yang[1], Zhe Yang[2], and Wei Yang[2]**

[1]Multi-Wave and Multi-Component Research Group, School of Geophysics and Information Technology, China University of Geosciences, Beijing, China

[2]Seismic Data Processing and Interpretation Center, Research Institute of Petroleum Exploration and Development-Northwest, PetroChina, Lanzhou, China

(This article belongs to the *Special Issue: Seismic Wave Propagation Theories and Reservoir Characterization Technologies for Complex Anisotropic Media*)

## Abstract

Since transmission losses, internal multiples, and mode conversions are not considered, conventional inversion methods based on the Zoeppritz equations and related approximations have limited capability in high-resolution inversion of thin interbeds. Reflectivity methods, which account for these wave propagation effects, are more suitable for inverting thin interbeds; however, most related studies approximate thin interbeds as several isotropic thin beds, which are inadequate for complex thin interbeds containing thin vertical transverse isotropy (VTI) beds. In this study, thin VTI beds with the characteristics of short-term cycles are regarded as the fundamental compositional units of thin interbeds. We propose a joint PP- and PS-wave amplitude variation with angle inversion method for thin interbeds containing thin VTI beds. The method uses second-order approximations to the Kennett equations for thin interbeds containing thin VTI beds as the forward operator. The inversion objective function is established using the Levenberg–Marquardt algorithm, incorporating sparse constraints to improve the stability and resolution of the five-parameter inversion. Inversion results from model tests and field data demonstrate that the proposed method more accurately extracts elastic parameters and anisotropic information from thin interbeds compared to conventional methods based on the exact Zoeppritz equations, effectively improving inversion accuracy and offering a technical advancement for fine prestack inversion of complex thinly interbedded reservoirs.

***Keywords:*** Amplitude variation with angle inversion; Reflectivity method; Sparse constraint; Thin interbeds; Vertical transverse isotropy

***Corresponding author:**
Jun Lu
(lj615@cugb.edu.cn)

**Citation:** Huang P, Lu J, Yang C, Yang Z, Yang W. Joint PP- and PS-wave amplitude variation with angle inversion for thin interbeds. *J Seismic Explor.* 2026;35(1):66-82. doi: 10.36922/JSE025370072

**Received:** September 13, 2025

**1st revised:** October 26, 2025

**2nd revised:** November 10, 2025

**Accepted:** November 10, 2025

**Published online:** December 17, 2025

**Copyright:** © 2025 Author(s). This is an Open-Access article distributed under the terms of the Creative Commons Attribution License, permitting distribution, and reproduction in any medium, provided the original work is properly cited.

**Publisher's Note:** AccScience Publishing remains neutral with regard to jurisdictional claims in published maps and institutional affiliations.

## 1. Introduction

As unconventional hydrocarbon exploration progresses, the study of wave propagation and parameter inversion in thin interbeds has received increasing attention, leading to greater demands for high-resolution exploration and parameterization of these thin interbeds. However, thin-interbed inversion faces two primary challenges. First, the thickness of thin beds within thin interbeds is generally smaller than the conventional

seismic resolution limit (usually <1/4 wavelength), making it difficult to accurately identify their internal structures. Second, the complex layered sedimentary structure causes significant transmission losses, internal multiples, and mode conversions in the wavefield of thin interbeds, complicating the accurate characterization of the wavefield and its propagation effects within the thin interbeds.

Conventional inversion methods for layered media are based on the exact Zoeppritz equations and their approximations, and researchers have made significant achievements in this field. Based on the Zoeppritz approximation, Buland and Omre[1] proposed a linear amplitude variation with offset (AVO) inversion method in a Bayesian framework and verified its accuracy through model testing. Huang *et al.*[2] introduced optimal transmission theory into the amplitude variation with angle (AVA) inversion of the exact Zoeppritz equations within a Bayesian framework. However, the Zoeppritz equations assume a single interface and do not account for transmission losses and internal multiples. This limitation impedes the accurate characterization of complex structures and wave propagation within thin interbeds, potentially leading to computational errors.[3]

The recursive matrix method offers more accurate calculations of transmission loss, internal multiples, and mode conversions than the Zoeppritz equations. This method has been widely applied to problems involving complex media and thin interbeds[4-8] and comprises the reflectivity method (RM) and the propagation matrix (PM). Kennett[9] provided the simplest recursive model of RM using a recursive algorithm, solving the overflow problem in the calculation of high-frequency and slowness exponential functions, ultimately making RM more suitable for research on thin interbeds. Rubino and Velis[10] proposed an AVA inversion method for thin beds based on acoustic wave theory and solved the highly non-linear constrained optimization problems associated with AVA inversion using simulated annealing. Padhi and Mallick[11] applied genetic algorithms to multi-component waveform inversion based on RM. In addition, Lu *et al.*[12] conducted an inversion of thin beds using the PM combined with the Levenberg–Marquardt (LM) algorithm to improve inversion accuracy. Yang and Lu[13] derived the Kennett's second-order approximations for thin interbeds based on Kennett's[9] recursive RM matrix. Yang and Wang[14] proposed a joint PP-PS prestack inversion method for thin beds based on the least-squares approach. The forward operator of this method was the PM, and its accuracy was verified using thin-bed model tests. Kuai *et al.*[15] developed a prestack inversion method based on the RM and LM algorithms to support the detailed identification of thin beds. Overall, these studies indicate that when inverting for thin beds and thin interbeds, both the RM and PM methods can produce detailed inversion results, enabling improved parameterization of internal characteristics.

Compared to conventional single-data processing and inversion, joint processing and inversion of PP and PS seismic data provide detailed parameter information.[16,17] Furthermore, incorporating multi-component data enables joint constraints and cross-validation during inversion, improving both resolution and stability. Veire and Landrø[18] proposed a joint inversion method for PP and PS seismic data that estimates the linear expressions of PP and PS reflection coefficients using least squares, enhancing the robustness of parameter estimation. Lu *et al.*[19] developed a stepwise anisotropic AVO inversion method for joint PP and PS seismic data based on the Rüger approximation[20] and genetic algorithms. Luo *et al.*[21] proposed a joint inversion method for PP and PS waves using the PM, optimizing the algorithm to improve the inversion speed and provide better parameter estimates compared to single-data inversions. Tura *et al.*[22] implemented joint inversion using PP and PS seismic data with both the model's inversion results and field data, indicating that joint inversion can more effectively identify the rock and fluid characteristics of the reservoir. Yang *et al.*[23] proposed a quadratic-reflectivity-based joint PP- and PS-wave inversion for vertical transverse isotropy (VTI) media, confirming its accuracy in predicting anisotropy through model testing. These studies demonstrate that joint inversion of PP and PS seismic data achieves higher accuracy and stability compared to single-data inversions. Given the complexity of thin interbed structures, we hypothesize that it is essential to introduce multi-component data into the inversion of thin interbeds.

Most existing studies consider thin interbeds as multilayer isotropic media, which tends to be accurate for simple thin interbeds. However, some complex thin interbeds contain thin beds with short-term cycle characteristics, where internal grain size shows rhythmic, periodic variations, or consist of multiple ultra-thin sublayers. These thin beds are horizontally isotropic but vertically anisotropic and can be classified as thin VTI beds. Currently, no suitable inversion methods exist for thin interbeds containing thin VTI beds. Inversions based on the assumption of isotropic layered media or equivalent thick VTI layers cannot accurately describe their internal structures, leading to errors in reservoir predictions. In addition, few studies have addressed the joint inversion of PP and PS seismic data specifically for thin interbeds.

We propose a joint PP- and PS-wave AVA inversion method for thin interbeds containing thin VTI beds. Based

on the work of Huang *et al.*,[24] we introduced the Kennett's second-order approximations for thin interbeds containing thin VTI beds to establish the objective function. Due to the numerous inversion parameters associated with VTI media, we utilized the LM method[25,26] combined with a sparse constraint to ensure inversion stability. PP and PS AVA data were used in joint AVA inversion to reduce errors caused by multiple solutions. The inversion was conducted in the PP time domain, necessitating a time-domain conversion of the PS data. When processing field data, coupling among different wavefields and the lack of accurate subsurface physical parameters complicated the accurate conversion or separation of internal multiples. Based on small-to-medium incident angles and the thin-layer assumption, we achieved precise time–domain conversion of the first reflections using multi-horizon constraints in the target area, enabling approximate conversion of internal multiples from the PS time domain into the PP time domain. In addition, we appropriately reduced the weight of the PS data in the inversion to minimize the impact of internal multiple conversion errors on the inversion results. Model tests and field data inversion demonstrated that our method accurately characterized wave propagation in thin interbeds containing thin VTI beds, yielding reliable inversion results.

## 2. Theory

### 2.1. Total reflection coefficients for thin interbeds containing thin VTI beds

The internal structure of thin interbeds is complex. Consequently, wave propagation effects within thin interbeds cannot be accurately described by the Zoeppritz equations or their approximations, which assume a single interface. Yang and Lu[13] derived second-order approximations of the Kennett equations for isotropic thin interbeds, neglecting high-order multiple terms that have minimal influence on the reflection coefficient calculations. Their study indicated that the approximations accurately computed the total reflection coefficient for each thin bed within the thin interbed, thereby enhancing computational efficiency. However, their approach assumes that every thin bed is isotropic. Under actual geological conditions, thin beds may exhibit consistent lithology but show vertical gradation in grain size due to complex geological processes, or they may consist of multiple ultra-thin sublayers of differing lithologies, both reflecting short-term cycle characteristics (Figure 1). In both cases, the characteristics of the thin beds deviate from those of the homogeneous medium, exhibiting VTI properties. When such thin VTI beds are irregularly interbedded with isotropic thin beds to form a thin interbed, the structure and wavefield propagation effects become highly complex. Therefore, the isotropic Kennett's second-order approximations are inadequate for accurately characterizing variations in reflection coefficients within such complex thin interbeds.

To address this limitation, Huang *et al.*[24] proposed second-order approximations of the Kennett equations suitable for thin interbeds containing thin VTI beds by replacing the original isotropic single-interface reflection coefficients with their VTI counterparts. The modified equation enables the calculation of total reflection coefficient matrices for both PP- and PS-waves in a thin VTI bed, accounting for all wave propagation types (PP, PS, SP, and SS) within the thin interbed. Kennett's recursive method[9] was then applied to compute the total reflection coefficient at any interface $n$ within the thin-interbed

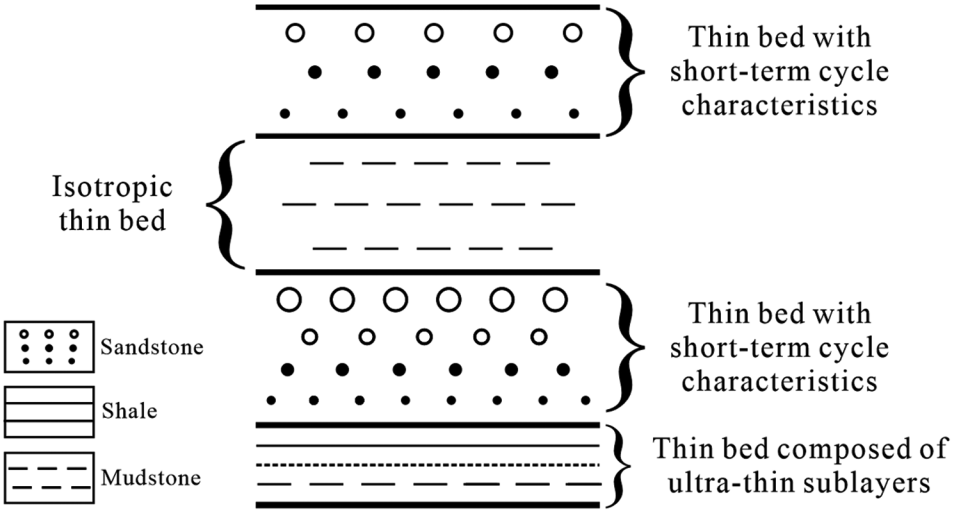


**Figure 1.** Sedimentary mode of a thin interbed containing thin vertical transverse isotropy beds

model (Figure 2) containing thin VTI beds in the slowness-frequency domain (**Equation 1**).

$$\begin{aligned}\breve{\mathbf{R}}_{\mathrm{vD}}^{(\mathrm{n})}(\mathbf{m},p,\omega)=&\mathbf{R}_{\mathrm{vD}}^{(\mathrm{n})}+\mathbf{T}_{\mathrm{vU}}^{(\mathrm{n})}\mathbf{E}_{\mathrm{v}}^{(\mathrm{n}-1)}\mathbf{R}_{\mathrm{vD}}^{(\mathrm{n}-1)}\mathbf{E}_{\mathrm{v}}^{(\mathrm{n}-1)}\\&[\mathbf{I}+\mathbf{R}_{\mathrm{vU}}^{(\mathrm{n})}\mathbf{E}_{\mathrm{v}}^{(\mathrm{n}-1)}\mathbf{R}_{\mathrm{vD}}^{(\mathrm{n}-1)}\mathbf{E}_{\mathrm{v}}^{(\mathrm{n}-1)}\\&+(\mathbf{R}_{\mathrm{vU}}^{(\mathrm{n})}\mathbf{E}_{\mathrm{v}}^{(\mathrm{n}-1)}\mathbf{R}_{\mathrm{vD}}^{(\mathrm{n}-1)}\mathbf{E}_{\mathrm{v}}^{(\mathrm{n}-1)})^2]\mathbf{T}_{\mathrm{vD}}^{(\mathrm{n})}\end{aligned}\tag{1}$$

where **m** is the model parameter matrix, which is described in detail in Section 2.2, $\omega$ is the angular frequency, $p$ is the horizontal slowness, and $\mathbf{R}_{\mathrm{vD}}^{(\mathrm{n}-1)}$, $\mathbf{R}_{\mathrm{vD}}^{(\mathrm{n})}$, and $\mathbf{T}_{\mathrm{vD}}^{(\mathrm{n})}$ are the reflection coefficient matrix of the downward wave interface $n-1$, the reflection coefficient matrix at interface $n$, and the transmission coefficient matrix of the downward wave at interface $n$, respectively. $\mathbf{R}_{\mathrm{vU}}^{(\mathrm{n})}$ and $\mathbf{T}_{\mathrm{vU}}^{(\mathrm{n})}$ are the reflection and transmission coefficient matrices of the upward wave at interface $n$, respectively. $\mathbf{E}_{\mathrm{v}}^{(\mathrm{n}-1)}$ is the phase-shift factor when the wave propagates from interface $n-1$ to $n$.

In **Equation 1**, $\mathbf{R}_{\mathrm{vD}}^{(\mathrm{n})}$ is the primary reflection coefficient at interface $n$. $\mathbf{T}_{\mathrm{vU}}^{(\mathrm{n})}\mathbf{E}_{\mathrm{v}}^{(\mathrm{n}-1)}\mathbf{R}_{\mathrm{vD}}^{(\mathrm{n}-1)}\mathbf{E}_{\mathrm{v}}^{(\mathrm{n}-1)}[\mathbf{I}+\mathbf{R}_{\mathrm{vU}}^{(\mathrm{n})}\mathbf{E}_{\mathrm{v}}^{(\mathrm{n}-1)}\mathbf{R}_{\mathrm{vD}}^{(\mathrm{n}-1)}\mathbf{E}_{\mathrm{v}}^{(\mathrm{n}-1)}+(\mathbf{R}_{\mathrm{vU}}^{(\mathrm{n})}\mathbf{E}_{\mathrm{v}}^{(\mathrm{n}-1)}\mathbf{R}_{\mathrm{vD}}^{(\mathrm{n}-1)}\mathbf{E}_{\mathrm{v}}^{(\mathrm{n}-1)})^2]\mathbf{T}_{\mathrm{vD}}^{(\mathrm{n})}$ includes the primary reflection coefficient at interface $n-1$, along with the first- and second-order multiple reflection coefficients within layer $n-1$.

The total reflection coefficient matrix in **Equation 1** is expanded as **Equation 2**.

$$\hat{\mathbf{R}}_{\mathrm{vD}}^{(\mathrm{n})}(\mathbf{m},p,\omega)=\begin{bmatrix}\hat{\mathbf{R}}_{\mathrm{PP}} & \hat{\mathbf{R}}_{\mathrm{SP}}\\ \hat{\mathbf{R}}_{\mathrm{PS}} & \hat{\mathbf{R}}_{\mathrm{SS}}\end{bmatrix}_{\mathrm{vD}}^{(\mathrm{n})}\tag{2}$$

the terms $\hat{\mathbf{R}}_{\mathrm{PP}}$, $\hat{\mathbf{R}}_{\mathrm{PS}}$, $\hat{\mathbf{R}}_{\mathrm{SP}}$, and $\hat{\mathbf{R}}_{\mathrm{SS}}$ in **Equation 2** correspond to the total reflection coefficients of PP- and PS-waves for P-wave incidence, and of SP- and SS-waves for S-wave incidence, respectively. In the inversion, only the total reflection coefficients for the PP- and PS-waves are required. Therefore, **Equation 2** can be rewritten as **Equation 3**.

$$\hat{\mathbf{R}}_{\mathrm{vD}}^{'(\mathrm{n})}(\mathbf{m},p,\omega)=\begin{bmatrix}\hat{\mathbf{R}}_{\mathrm{PP}}\\ \hat{\mathbf{R}}_{\mathrm{PS}}\end{bmatrix}_{\mathrm{vD}}^{(\mathrm{n})}\tag{3}$$

Under the isotropic assumption, the single-interface coefficients in Kennett's second-order approximations are the displacement potential reflection and transmission coefficients. Huang *et al.*[24] replaced the isotropic single-interface reflection and transmission coefficients with those for VTI media, as proposed by Graebner.[27] Notably, the single-interface coefficients in Graebner's equations are the displacement reflection and transmission coefficients, which differ from those in the Kennett equations. Therefore, to convert Graebner's reflection and transmission coefficients into displacement potential coefficients, they must be multiplied by the corresponding velocity ratios, resulting in the displacement potential reflection and transmission coefficient matrices $\mathbf{R}_{\mathrm{vD}}^{(\mathrm{n})}$, $\mathbf{T}_{\mathrm{vD}}^{(\mathrm{n})}$, $\mathbf{R}_{\mathrm{vU}}^{(\mathrm{n})}$, $\mathbf{T}_{\mathrm{vU}}^{(\mathrm{n})}$, and $\mathbf{R}_{\mathrm{vD}}^{(\mathrm{n}-1)}$ (**Equation 4**).

$$\begin{aligned}\mathbf{R}_{\mathrm{vD}}^{(\mathrm{n})}&=\begin{bmatrix}\frac{V_{\mathrm{P}}^{\mathrm{n}}}{V_{\mathrm{P}}^{\mathrm{n}}}r_{\mathrm{PP}} & \frac{V_{\mathrm{S}}^{\mathrm{n}}}{V_{\mathrm{P}}^{\mathrm{n}}}r_{\mathrm{SP}}\\ \frac{V_{\mathrm{P}}^{\mathrm{n}}}{V_{\mathrm{S}}^{\mathrm{n}}}r_{\mathrm{PS}} & \frac{V_{\mathrm{S}}^{\mathrm{n}}}{V_{\mathrm{S}}^{\mathrm{n}}}r_{\mathrm{SS}}\end{bmatrix}_{\mathrm{D}}^{(\mathrm{n})},\quad \mathbf{T}_{\mathrm{vD}}^{(\mathrm{n})}=\begin{bmatrix}\frac{V_{\mathrm{P}}^{\mathrm{n}}}{V_{\mathrm{P}}^{\mathrm{n}-1}}t_{\mathrm{PP}} & \frac{V_{\mathrm{S}}^{\mathrm{n}}}{V_{\mathrm{P}}^{\mathrm{n}-1}}t_{\mathrm{SP}}\\ \frac{V_{\mathrm{P}}^{\mathrm{n}}}{V_{\mathrm{S}}^{\mathrm{n}-1}}t_{\mathrm{PS}} & \frac{V_{\mathrm{S}}^{\mathrm{n}}}{V_{\mathrm{S}}^{\mathrm{n}-1}}t_{\mathrm{SS}}\end{bmatrix}_{\mathrm{D}}^{(\mathrm{n})},\\ \mathbf{R}_{\mathrm{vU}}^{(\mathrm{n})}&=\begin{bmatrix}\frac{V_{\mathrm{P}}^{\mathrm{n}-1}}{V_{\mathrm{P}}^{\mathrm{n}-1}}r_{\mathrm{PP}} & \frac{V_{\mathrm{S}}^{\mathrm{n}-1}}{V_{\mathrm{P}}^{\mathrm{n}-1}}r_{\mathrm{SP}}\\ \frac{V_{\mathrm{P}}^{\mathrm{n}-1}}{V_{\mathrm{S}}^{\mathrm{n}-1}}r_{\mathrm{PS}} & \frac{V_{\mathrm{S}}^{\mathrm{n}-1}}{V_{\mathrm{S}}^{\mathrm{n}-1}}r_{\mathrm{SS}}\end{bmatrix}_{\mathrm{U}}^{(\mathrm{n})},\ \mathbf{T}_{\mathrm{vU}}^{(\mathrm{n})}=\begin{bmatrix}\frac{V_{\mathrm{P}}^{\mathrm{n}-1}}{V_{\mathrm{P}}^{\mathrm{n}}}t_{\mathrm{PP}} & \frac{V_{\mathrm{S}}^{\mathrm{n}-1}}{V_{\mathrm{P}}^{\mathrm{n}}}t_{\mathrm{SP}}\\ \frac{V_{\mathrm{P}}^{\mathrm{n}-1}}{V_{\mathrm{S}}^{\mathrm{n}}}t_{\mathrm{PS}} & \frac{V_{\mathrm{S}}^{\mathrm{n}-1}}{V_{\mathrm{S}}^{\mathrm{n}}}t_{\mathrm{SS}}\end{bmatrix}_{\mathrm{U}}^{(\mathrm{n})},\\ \mathbf{R}_{\mathrm{vD}}^{(\mathrm{n}-1)}&=\begin{bmatrix}\frac{V_{\mathrm{P}}^{\mathrm{n}-1}}{V_{\mathrm{P}}^{\mathrm{n}-1}}r_{\mathrm{PP}} & \frac{V_{\mathrm{S}}^{\mathrm{n}-1}}{V_{\mathrm{P}}^{\mathrm{n}-1}}r_{\mathrm{SP}}\\ \frac{V_{\mathrm{P}}^{\mathrm{n}-1}}{V_{\mathrm{S}}^{\mathrm{n}-1}}r_{\mathrm{PS}} & \frac{V_{\mathrm{S}}^{\mathrm{n}-1}}{V_{\mathrm{S}}^{\mathrm{n}-1}}r_{\mathrm{SS}}\end{bmatrix}_{\mathrm{D}}^{(\mathrm{n}-1)}\end{aligned}\tag{4}$$

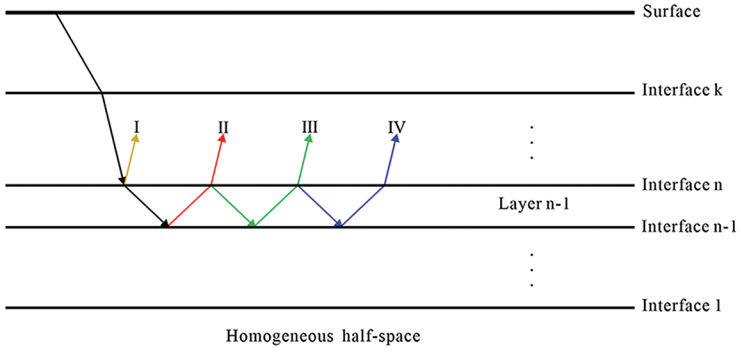


**Figure 2.** Wave propagation in a thin interbed model. I is the primary reflection at interface $n$, II is the primary reflection at interface $n-1$, III is the first-order multiple reflection of layer $n-1$, and IV is the second-order multiple reflection of layer $n-1$.

Where $r_{**}$ and $t_{**}$ in the matrices are the single-interface reflection and transmission coefficients, respectively, of the different modes proposed by Graebner. $V_P$ and $V_S$ represent the P- and S-wave velocities, respectively. The superscripts ($n$) and ($n - 1$) of the elements denote the corresponding layers of the medium.

The phase-shift factor in **Equation 1** ensures continuity of the phase when waves pass through an interface. The phase-shift factor matrix in the VTI medium is expanded as **Equation 5**.

$$\mathbf{E}_{v}^{(n-1)} = \begin{bmatrix} \exp(i\omega q_P^{(n-1)}(\theta_P)h^{(n-1)}) & \\ & \exp(i\omega q_S^{(n-1)}(\theta_S)h^{(n-1)}) \end{bmatrix} \quad (5)$$

where $\theta_P$ and $\theta_S$ are the incident angles of the P- and S-waves in the layer $n - 1$, respectively; $q_P(\theta_P)$ and $q_s(\theta_s)$ are the vertical slowness values of the P- and S-waves, respectively; and $h^{(n-1)}$ is the thickness of the layer $n - 1$. Since it is difficult to accurately determine the thicknesses of subsurface layers in field data, we discretize the parameter model in the time domain and treat each time sample as an individual interface. The thickness $h$ between any two adjacent samples is calculated from the time sampling interval and the corresponding velocity (**Equations 6-8**).

For both $q_P(\theta_P)$ and $q_s(\theta_s)$:

$$q(\theta) = \frac{1}{\sqrt{2}}\sqrt{A_1 - \sqrt{A_1^2 - 4A_2}} \quad (6)$$

Where

$$A_1 = \frac{\rho}{c_{33}} + \frac{\rho}{c_{55}} - \left(\frac{c_{11}}{c_{33}} + \frac{c_{55}}{c_{33}} - \frac{(c_{13}+c_{55})^2}{c_{33}}\right)p^2(\theta),$$
$$A_2 = \left(\frac{c_{11}}{c_{33}}p^2(\theta) - \frac{\rho}{c_{33}}\right)\left(p^2(\theta) - \frac{\rho}{c_{55}}\right) \quad (7)$$

Where $c_{11}$, $c_{33}$, $c_{55}$, and $c_{13}$ are the independent stiffness components[28]:

$$c_{33} = V_{P0}^2\rho,$$
$$c_{55} = V_{S0}^2\rho,$$
$$c_{11} = 2c_{33}\varepsilon + c_{33},$$
$$c_{13} = \sqrt{2c_{33}(c_{33} - c_{55})\delta + (c_{33} - c_{55})^2} - c_{55} \quad (8)$$

Where $V_{P0}$, $V_{S0}$, and ρ represent the vertical P-wave velocity, vertical S-wave velocity, and density, respectively. $\varepsilon$ and $\delta$ are the Thomsen anisotropy parameters, with $\varepsilon$ denoting the velocity difference between horizontal and vertical P-waves, and $\delta$ characterizing the coupling between near-vertical P- and SV-waves.

However, $\varepsilon$ and $\delta$ are not always directly available from well logs or parameter models of field data. In such cases, we derive the stiffness components using Backus averaging theory.[29] This theory provides an effective approximation for a finely layered medium. From the Backus averaging theory, a sequence of ultra-thin isotropic sublayers can be represented by an equivalent thin VTI bed whose stiffness components are derived from the elastic properties of each layer. For each ultra-thin isotropic sublayer, the Lamé parameters $\lambda_i$ and $\mu_i$ can be calculated from well-log data as in **Equation 9**.

$$\lambda_i = \rho_i\left(V_{P,i}^2 - 2V_{S,i}^2\right),$$
$$\mu_i = \rho_i V_{S,i}^2 \quad (9)$$

Where $V_{p,i}$, $V_{s,I}$, and $\rho_i$ are the P- and S-wave velocities and density at sample $i$ of the well logs, respectively.

The equivalent stiffness components of the VTI medium are obtained by the Backus averaging (**Equation 10**):

$$\overline{C_{33}} = \left\langle \frac{1}{\lambda + 2\mu} \right\rangle^{-1},$$
$$\overline{C_{55}} = \left\langle \frac{1}{\mu} \right\rangle^{-1},$$
$$\overline{C_{11}} = \left\langle \lambda + 2\mu \right\rangle - 2\frac{\left\langle \frac{\lambda}{\lambda+2\mu} \right\rangle^2}{\left\langle \frac{1}{\lambda+2\mu} \right\rangle},$$
$$\overline{C_{13}} = \frac{\left\langle \frac{\lambda}{\lambda+2\mu} \right\rangle}{\left\langle \frac{1}{\lambda+2\mu} \right\rangle} \quad (10)$$

Where $\langle \circ \rangle$ denotes the thickness-weighted arithmetic average within a Backus window (**Equation 11**):

$$\langle f \rangle = \frac{\sum_i h_i f_i}{\sum_i h_i} \quad (11)$$

Where $h_i$ is the thickness of the $i$-th layer (or the sampling interval) of the well log.

From the equivalent stiffness components, the Thomsen anisotropy parameters are computed as in **Equation 12**.

$$\varepsilon = \frac{\overline{C_{11}} - \overline{C_{33}}}{2\overline{C_{33}}},$$
$$\delta = \frac{\left(\overline{C_{13}} + \overline{C_{55}}\right)^2 - \left(\overline{C_{33}} - \overline{C_{55}}\right)^2}{2\overline{C_{33}}\left(\overline{C_{33}} - \overline{C_{55}}\right)} \quad (12)$$

For weakly anisotropic media, according to the Christoffel equation, the ray parameter for P-waves is given by **Equation 13**.

$$p_{\mathrm{P}}(\theta_{\mathrm{P}})=\frac{\sin\theta_{\mathrm{P}}}{V_{\mathrm{P0}}\sqrt{1+2\varepsilon\sin^2\theta_{\mathrm{P}}+2\delta\sin^2\theta_{\mathrm{P}}\cos^2\theta_{\mathrm{P}}}} \tag{13}$$

and the ray parameter for S-waves is given by **Equation 14**.

$$p_{\mathrm{S}}(\theta_{\mathrm{S}})=\frac{\sin\theta_{\mathrm{S}}}{V_{\mathrm{S0}}\sqrt{1+2\delta\sin^2\theta_{\mathrm{S}}\cos^2\theta_{\mathrm{S}}}} \tag{14}$$

The reflection coefficient matrix calculated from **Equation 2** is defined in the slowness-frequency domain, whereas the reflection coefficients used in the AVA inversion must be in the angle-time domain. Therefore, using the inverse Fourier transform and Snell's law, the total reflection coefficient in the angle-time domain can be obtained as in **Equation 15**.

$$\hat{\mathbf{R}}_{\mathrm{vD}}\left(\mathbf{m},\theta,t\right)=\frac{1}{2\pi}\int_{-\infty}^{\infty}\hat{\mathbf{R}}_{\mathrm{vD}}\left(\mathbf{m},p=\frac{\sin\theta}{V(\theta)},\omega\right)e^{i\omega t}\mathrm{d}\omega. \tag{15}$$

Matching the PS records to the PP time domain is essential because multi-wave joint inversion is performed. Therefore, the corresponding conversion factor for each sample when compressing the PS AVA gathers to the PP time domain is given by **Equation 16**.

$$\gamma_{ij}=2\frac{V_{P,ij}+V_{S,ij}}{V_{P,ij}} \tag{16}$$

Where $i$ and $j$ represent the incidence angles and time samples, respectively.

### 2.2. Objective function and solution

Under the assumption of a VTI medium, the model parameter matrix is constructed as in **Equation 17**.

$$\mathbf{m}=\left[\mathbf{V}_{\mathrm{P0}}\ \ \mathbf{V}_{\mathrm{S0}}\ \ \boldsymbol{\rho}\ \boldsymbol{\varepsilon}\ \boldsymbol{\delta}\right]^{\mathrm{T}} \tag{17}$$

Where $\mathbf{V}_{\mathrm{P0}}$, $\mathbf{V}_{\mathrm{S0}}$, and $\boldsymbol{\rho}$ represent the parameter vectors of vertical P-wave velocity, vertical S-wave velocity, and density, respectively, and $\boldsymbol{\varepsilon}$ and $\boldsymbol{\delta}$ denote the two Thomsen anisotropy parameter vectors.

The synthetic seismic record is expressed as in **Equation 18**.

$$\mathbf{d}\left(\mathbf{m},\theta,\mathrm{t}\right)=\mathbf{W}\left(\mathrm{t}\right)\hat{\mathbf{R}}\left(\mathbf{m},\theta,\mathrm{t}\right) \tag{18}$$

where $\theta$ is the incidence angle, $t$ denotes the seismic travel time, and $\mathbf{W}$ is the wavelet matrix. $\hat{\mathbf{R}}$ is the angle-time domain reflection coefficient matrix, which is calculated from the model parameter vector $\mathbf{m}$.

The inversion objective function is established using the LM algorithm, incorporating a sparse constraint,[19] as shown in **Equation 19**.

$$J\left(\mathbf{m}\right)=\left\|\left(\mathbf{H}+\lambda_1\mathbf{I}\right)\Delta\mathbf{m}-\mathbf{J}^{\mathrm{T}}\mathbf{d}_{\mathrm{ref}}\right\|^2+\lambda_2\left\|\Delta\mathbf{m}+\mathbf{m}_{\mathrm{ref}}\right\| \tag{19}$$

Where $\lambda_1$ is the damping factor, $\lambda_2$ represents the weight for the sparse constraint, $\mathbf{J}$ is the Jacobian matrix, $\mathbf{H}$ denotes the Hessian matrix $\mathbf{H}=\mathbf{J}^{\mathrm{T}}\mathbf{J}$, and $\mathbf{I}$ denotes the identity matrix. $\mathbf{d}_{\mathrm{ref}}$ is the difference between the synthetic and observed seismic records (**Equation 20**).

$$\mathbf{d}_{\mathrm{ref}}=\begin{bmatrix}\mathbf{d}_{\mathrm{PP}}-\mathbf{s}_{\mathrm{PP}}\\ \mathbf{d}_{\mathrm{PS}}-\mathbf{s}_{\mathrm{PS}}\end{bmatrix} \tag{20}$$

Where $\mathbf{d}_{\mathrm{PP}}$ and $\mathbf{d}_{\mathrm{PS}}$ are the synthetic PP- and PS-wave seismic records, respectively, while $\mathbf{s}_{\mathrm{PP}}$ and $\mathbf{s}_{\mathrm{PS}}$ are in the corresponding observed seismic data.

The Jacobian matrix $\mathbf{J}$ in multi-wave joint inversion has the form shown in **Equation 21**.

$$\mathbf{J}=\begin{bmatrix}\frac{\partial\mathbf{d}_{\mathrm{PP}}}{\partial\mathbf{m}}\\ \frac{\partial\mathbf{d}_{\mathrm{PS}}}{\partial\mathbf{m}}\end{bmatrix}=\begin{bmatrix}\frac{\partial\mathbf{d}_{\mathrm{PP}}}{\partial\mathbf{V}_{\mathrm{P0}}} & \frac{\partial\mathbf{d}_{\mathrm{PP}}}{\partial\mathbf{V}_{\mathrm{S0}}} & \frac{\partial\mathbf{d}_{\mathrm{PP}}}{\partial\boldsymbol{\rho}} & \frac{\partial\mathbf{d}_{\mathrm{PP}}}{\partial\boldsymbol{\delta}} & \frac{\partial\mathbf{d}_{\mathrm{PP}}}{\partial\boldsymbol{\varepsilon}}\\ \frac{\partial\mathbf{d}_{\mathrm{PS}}}{\partial\mathbf{V}_{\mathrm{P0}}} & \frac{\partial\mathbf{d}_{\mathrm{PS}}}{\partial\mathbf{V}_{\mathrm{S0}}} & \frac{\partial\mathbf{d}_{\mathrm{PS}}}{\partial\boldsymbol{\rho}} & \frac{\partial\mathbf{d}_{\mathrm{PS}}}{\partial\boldsymbol{\delta}} & \frac{\partial\mathbf{d}_{\mathrm{PS}}}{\partial\boldsymbol{\varepsilon}}\end{bmatrix} \tag{21}$$

Where $\mathbf{m}_{\mathrm{ref}}$ is the difference between the initial model $\mathbf{m}_0$ and the true model $\mathbf{m}_{\mathrm{true}}$ (**Equation 22**):

$$\mathbf{m}_{\mathrm{ref}}=\mathbf{m}_0-\mathbf{m}_{\mathrm{true}}, \tag{22}$$

For field data, $\mathbf{m}_{\mathrm{true}}$ is typically represented by well logs. When the objective function reaches a minimum, the estimated model parameters are optimally consistent with the observed data and prior information. Under this condition, where $J(\mathbf{m})$ approaches zero, we derive **Equation (23)**:

$$\begin{cases}\left\|\left(\mathbf{H}+\lambda_1\mathbf{I}\right)\Delta\mathbf{m}-\mathbf{J}^{\mathrm{T}}\mathbf{d}_{\mathrm{ref}}\right\|^2\to 0\\ \lambda_2\left(\Delta\mathbf{m}+\mathbf{m}_{\mathrm{ref}}\right)\to 0\end{cases} \tag{23}$$

Alternatively, under approximately ideal conditions, where the initial model is relatively close to the true model, the model parameter update matrix can be written as in **Equation 24**.

$$\begin{aligned}\Delta\mathbf{m}&\cong\left[\mathbf{H}+\left(\lambda_1+\lambda_2\right)\mathbf{I}\right]^{-1}\left[\mathbf{J}^{\mathrm{T}}\mathbf{d}_{\mathrm{ref}}+\lambda_2\mathbf{m}_{\mathrm{ref}}\right]\\ &\cong\left[\begin{pmatrix}\frac{\partial\mathbf{d}_{\mathrm{PP}}}{\partial\mathbf{m}}\\ \frac{\partial\mathbf{d}_{\mathrm{PS}}}{\partial\mathbf{m}}\end{pmatrix}^{\mathrm{T}}\begin{pmatrix}\frac{\partial\mathbf{d}_{\mathrm{PP}}}{\partial\mathbf{m}}\\ \frac{\partial\mathbf{d}_{\mathrm{PS}}}{\partial\mathbf{m}}\end{pmatrix}+\left(\lambda_1+\lambda_2\right)\mathbf{I}\right]^{-1}\\ &\quad\left[\begin{pmatrix}\frac{\partial\mathbf{d}_{\mathrm{PP}}}{\partial\mathbf{m}}\\ \frac{\partial\mathbf{d}_{\mathrm{PS}}}{\partial\mathbf{m}}\end{pmatrix}^{\mathrm{T}}\begin{pmatrix}\mathbf{d}_{\mathrm{PP}}-\mathbf{s}_{\mathrm{PP}}\\ \mathbf{d}_{\mathrm{PS}}-\mathbf{s}_{\mathrm{PS}}\end{pmatrix}+\lambda_2\mathbf{m}_{\mathrm{ref}}\right]\end{aligned} \tag{24}$$

Under this assumption, each iteration of $\Delta\mathbf{m}$ should be sufficiently small to ensure inversion stability.

## 3. Model test

### 3.1. Model test without noise

The parameters of the thin interbed model containing thin VTI beds used to test the inversion method are listed in Table 1.

The synthetic PP and PS AVA gathers, as shown in Figure 3, were generated using the RM based on second-order approximations of the Kennett equations. The frequency range was 0–105 Hz, and a 30 Hz Ricker wavelet was used as the source wavelet. Considering that the incident angle range for field data angle gathers is usually narrow, the angle range for this model was set to 5°–30° with an interval of 5°.

Inversions based on the Kennett's second-order approximations for thin interbeds containing thin VTI beds and the exact Zoeppritz equations were compared. Both methods used the same initial model and synthetic data. The inversion results obtained using the Kennett's second-order approximations for the thin interbeds containing thin VTI beds and the exact Zoeppritz equations are shown in Figures 4 and 5, respectively.

**Table 1. Model parameters**

| $V_{P0}$ (km/s) | $V_{S0}$ (km/s) | Density (g/cm$^3$) | Thickness (m) | $\varepsilon$ | $\delta$ |
|---|---|---|---|---|---|
| 3.65 | 1.83 | 2.43 | 372 | 0.00 | 0.00 |
| 3.50 | 1.75 | 2.38 | 12 | 0.03 | 0.04 |
| 3.00 | 1.50 | 2.25 | 9 | 0.06 | −0.03 |
| 3.50 | 1.75 | 2.38 | 12 | 0.03 | 0.04 |
| 3.00 | 1.50 | 2.25 | 9 | 0.06 | −0.03 |
| 3.50 | 1.75 | 2.38 | 12 | 0.03 | 0.04 |
| 3.80 | 1.90 | 2.44 | 470 | 0.00 | 0.00 |

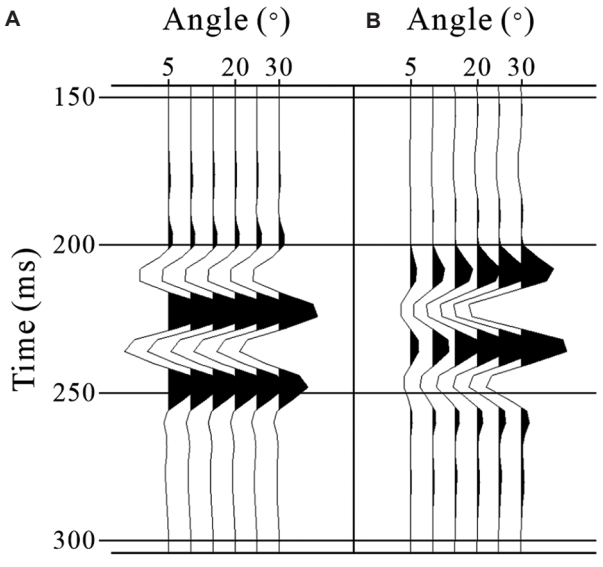


**Figure 3.** Synthetic amplitude variation with angle gathers of the thin interbed model described in Table 1. (A) PP (B) PS.

A quantitative comparison of the relative-error curves—defined as the absolute ratio of the difference between inverted and true values to the true value—for the five inverted parameters ($V_{P0}$, $V_{S0}$, $\rho$, $\varepsilon$, and $\delta$) is shown in Figure 6. For $V_{p0}$, $V_{s0}$, and $\rho$, the relative error curves of the inversion results based on the Kennett's second-order approximations for thin interbeds containing thin VTI beds show smaller deviations and greater consistency with the true model. In contrast, the relative-error curves of the inversion results based on the exact Zoeppritz equations display larger fluctuations. Moreover, the inversion results based on the Kennett's second-order approximations maintain low relative errors for the Thomsen anisotropy parameters $\varepsilon$ and $\delta$, demonstrating the robustness of the proposed method for handling the complex wave propagation effects within thinly layered VTI media.

We also calculated the correlation coefficients between the inversion results obtained by the two methods and the true model. For the inversion based on the Kennett's second-order approximations for thin interbeds containing thin VTI beds, the correlation coefficients for $V_{P0}$, $V_{S0}$, $\rho$, $\varepsilon$, and $\delta$ are 0.995, 0.984, 0.989, 0.992, and 0.974, respectively; for the inversion based on the exact Zoeppritz equations, the coefficients for $V_{P0}$, $V_{S0}$ and $\rho$ are 0.978, 0.979, and 0.830, respectively. Inversion based on Kennett's second-order approximations achieves higher fit quality, with average coefficients of 0.987; in contrast, the fit quality of inversion based on the exact Zoeppritz equations yields lower values, with average coefficients of 0.932.

From a parameter-wise perspective, both Kennett's second-order approximations for thin interbeds containing thin VTI beds and the exact Zoeppritz equations provide high fits (>0.970) for $V_{P0}$ and $V_{S0}$. For density ρ, the inversion based on Kennett's second-order approximations (0.989) significantly outperforms the inversion based on the exact Zoeppritz equations (0.830). By considering the VTI properties of thin VTI beds and the complex wave-propagation characteristics in thin interbeds, our method demonstrates a superior capability to resolve impedance-related parameters within thinly layered VTI media.

### 3.2. Model test with noise

To evaluate the robustness of the inversion method, 30% random noise was added to the PP and PS AVA gathers. The resulting synthetic records with noise are shown in

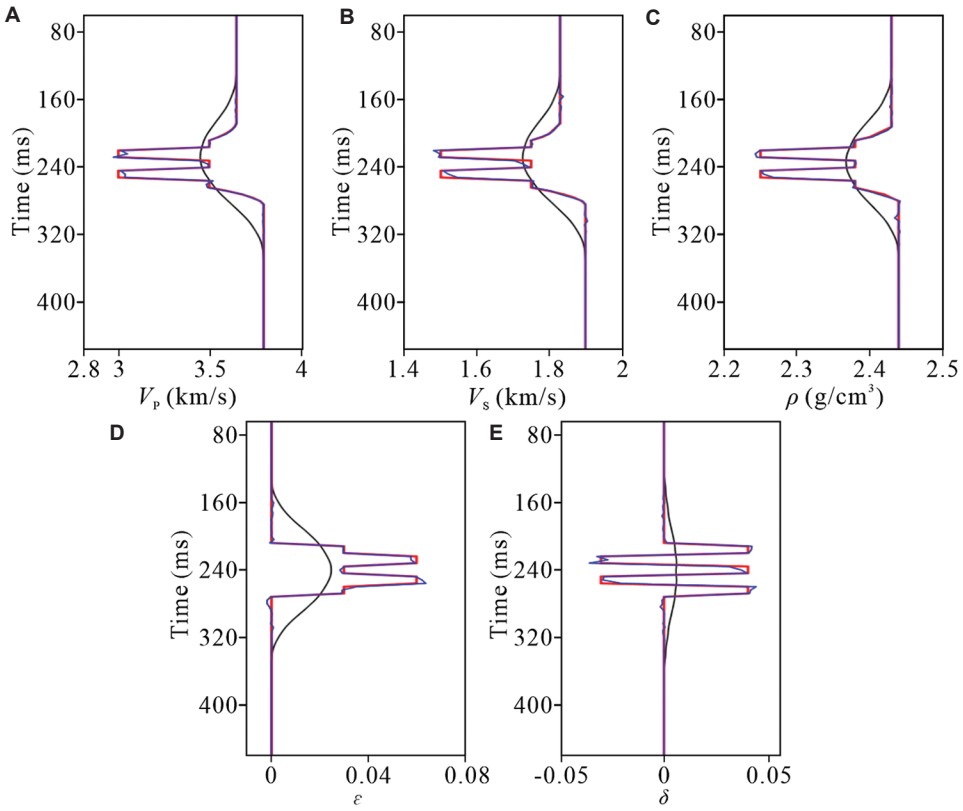


**Figure 4.** Inversion results of synthetic amplitude variation with angle gathers without noise, based on the Kennett's second-order approximations for thin interbeds containing thin vertical transverse isotropy beds. (A) P-wave velocity. (B) S-wave velocity. (C) Density. (D) $\varepsilon$. (E) $\delta$. The black, red, and blue curves represent the initial model, true model, and inversion result, respectively.

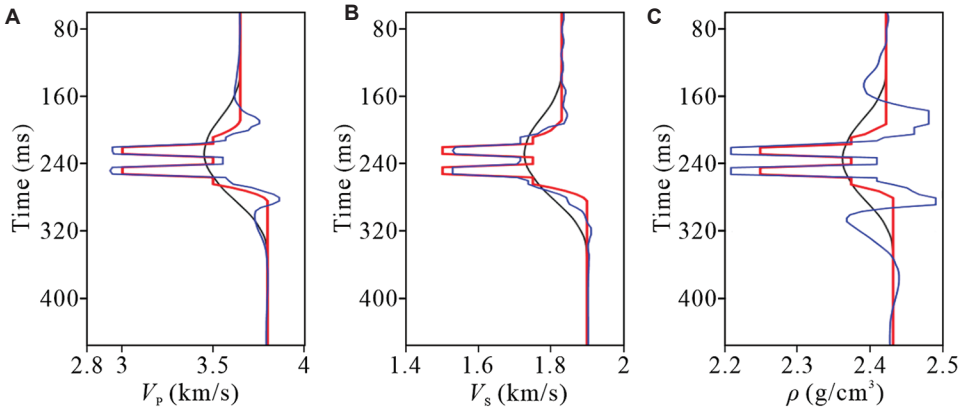


**Figure 5.** Inversion results of synthetic amplitude variation with angle gathers without noise, based on the exact Zoeppritz equations. (A) P-wave velocity. (B) S-wave velocity. (C) Density. The black, red, and blue curves represent the initial model, true model, and inversion result, respectively.

Figure 7. As shown in Figure 8, although the inversion results are noisy, they remain close to the true model, indicating that the inversion method has robust noise resistance.

## 4. Field data application

We applied our inversion method to multi-component surface seismic data from a mountainous oilfield. The shallow subsurface of this area features complex thin

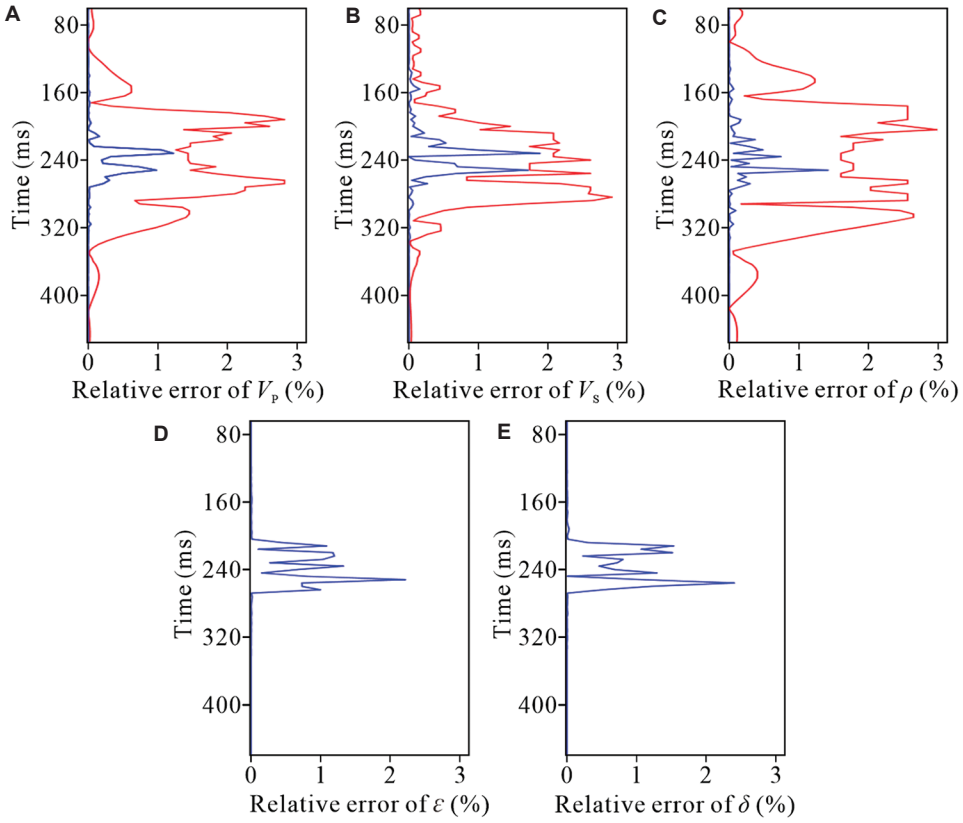


**Figure 6.** Relative-error curves between inversion results and the true model. (A) P-wave velocity. (B) S-wave velocity. (C) Density. (D) $\varepsilon$. (E) $\delta$. The blue and red curves represent the relative-error curves of the inversion results based on Kennett's second-order approximations for thin interbeds containing thin vertical transverse isotropy beds and the exact Zoeppritz equations, respectively.

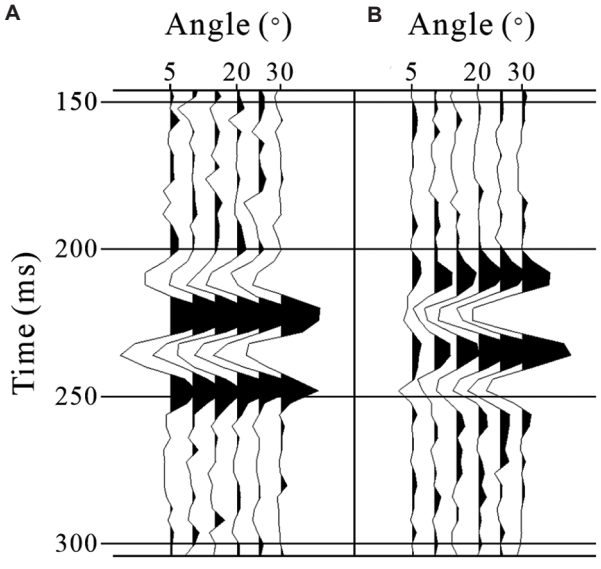


**Figure 7.** Synthetic amplitude variation with angle gathers of a thin interbed model described in Table 1 with 30% random noise. (A) PP. (B) PS.

interbeds of anisotropic sand and mudstone (shale). Due to limitations in the well logs, a 154–500 ms time interval was set as the inversion target. After Q-compensation, which estimated elastic wavefields, the PP and PS AVA gathers were generated from the field seismic data. These gathers were subsequently subjected to well-to-seismic calibration and multiple time-domain matching, resulting in AVA gathers in the PP time domain that were then matched with the well logs. The AVA gathers covered an angle range of 1°–15° at 2° intervals.

When compressing the PS AVA gathers from the PS time domain into the PP time domain, we observed that the travel times of the multiples differed from those of the primary reflections. Given that the primary target of our inversion method was thin interbeds, only internal multiples within them were considered. The travel time variations of internal multiples are complex and coupled with primary reflections, making it difficult to accurately compress the multiples in the PS AVA gathers into the

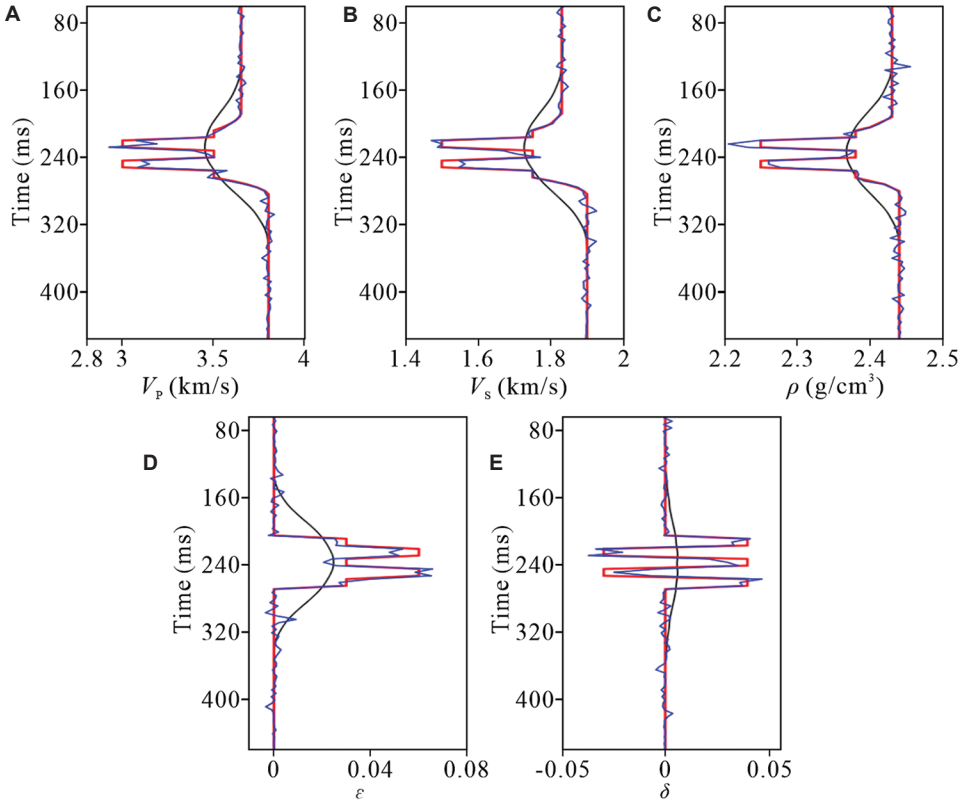


**Figure 8.** Inversion results of synthetic amplitude variation with angle gathers with 30% random noise, based on the Kennett's second-order approximations for thin interbeds containing thin vertical transverse isotropy beds. (A) P-wave velocity. (B) S-wave velocity. (C) Density. (D) $\varepsilon$. (E) $\delta$. The black, red, and blue curves represent the initial model, true model, and inversion result, respectively.

PP time or to separate these multiples from the PS AVA gathers.

However, because of the small thickness of each thin bed, the time difference between the internal multiples and the primary reflections was minimal. Notably, our inversion method considered only first- and second-order multiples. In most cases, when the sampling rate is equal to or >2 ms, the time difference between the primary reflections and multiples is only approximately 2 to 3 sample points. Moreover, because the inversion was performed over small-to-medium incident angles, variations in the travel times of multiples with angle were negligible.

From these analyses, we constrained the time–domain conversion by including as many corresponding horizons as possible in the PP and PS AVA gathers, ensuring that the primary reflections of the PS AVA gathers were accurately converted into the corresponding PP times. This approach approximately converted the internal multiples within thin interbeds into their corresponding PP times. We then increased the weight of the PP AVA gathers in the inversion to minimize the impact of time errors in the PS AVA gathers on the inversion results.

Figure 9 shows the PP and PS wavelets extracted from the PP and PS AVA gathers in the PP time domain, with dominant frequencies of 20 Hz for both.

The P- and S-wave velocities and density were directly obtained from the measured well logs, whereas the anisotropic parameters $\varepsilon$ and $\delta$ were estimated using Backus averaging theory based on **Equations 9-12**. These parameters were subsequently smoothed and served as the initial model for the inversion. Figure 10 shows the inversion results using the Kennett's second-order approximations for the thin interbeds containing thin VTI beds.

Since no other nearby well logs were available for cross-validation in the study area, the accuracy of the inversion results was evaluated by plotting the relative-error curves between the inversion results and the well logs. As illustrated in Figure 11, only a few samples exceeded 16% relative error, demonstrating that the inversion results achieve high accuracy even without incorporating the well logs as constraints in the initial model.

The correlation coefficients between the inversion results and the well logs for P- and S-wave velocities, density, $\varepsilon$, and $\delta$ were 0.720, 0.701, 0.867, 0.705, and 0.685,

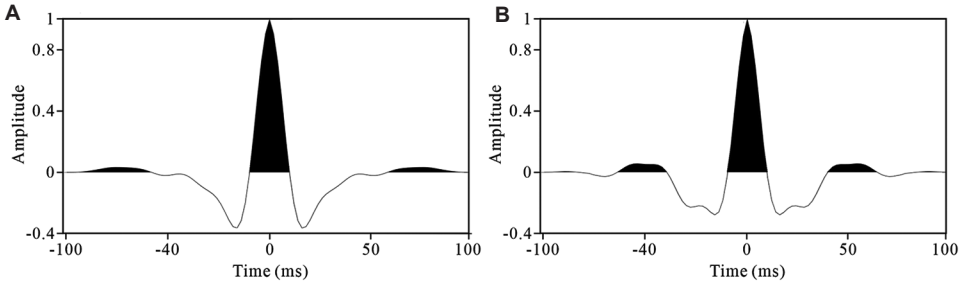


**Figure 9.** Wavelets extracted from the field data. (A) PP AVA gathers. (B) PS AVA gathers.
Abbreviation: AVA: Amplitude variation with angle.

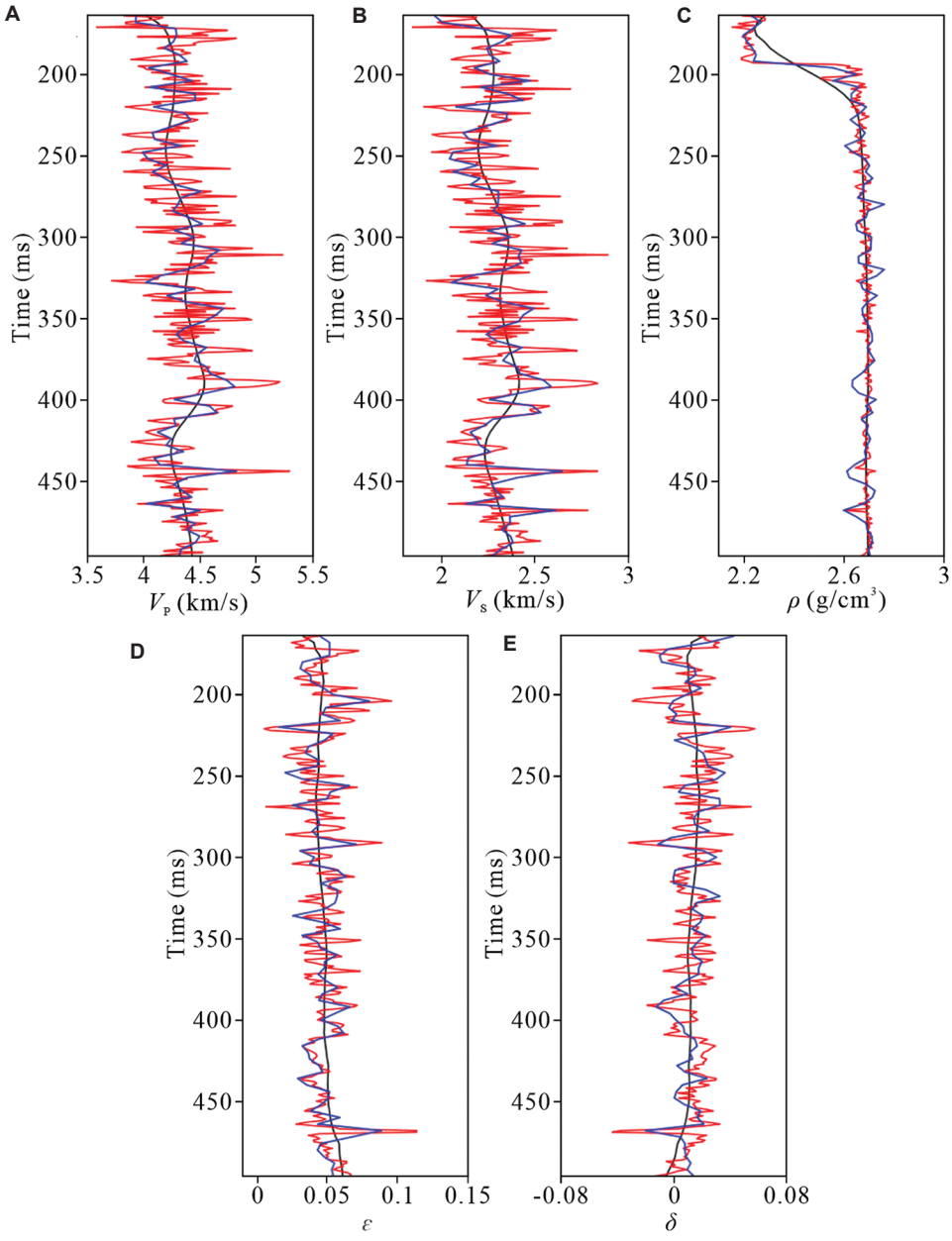


**Figure 10.** Inversion results of field data based on the Kennett's second-order approximations for thin interbeds containing thin vertical transverse isotropy beds. (A) P-wave velocity. (B) S-wave velocity. (C) Density. (D) $\varepsilon$. (E) $\delta$. The black, red, and blue curves represent the initial model, well-log data, and inversion results, respectively.

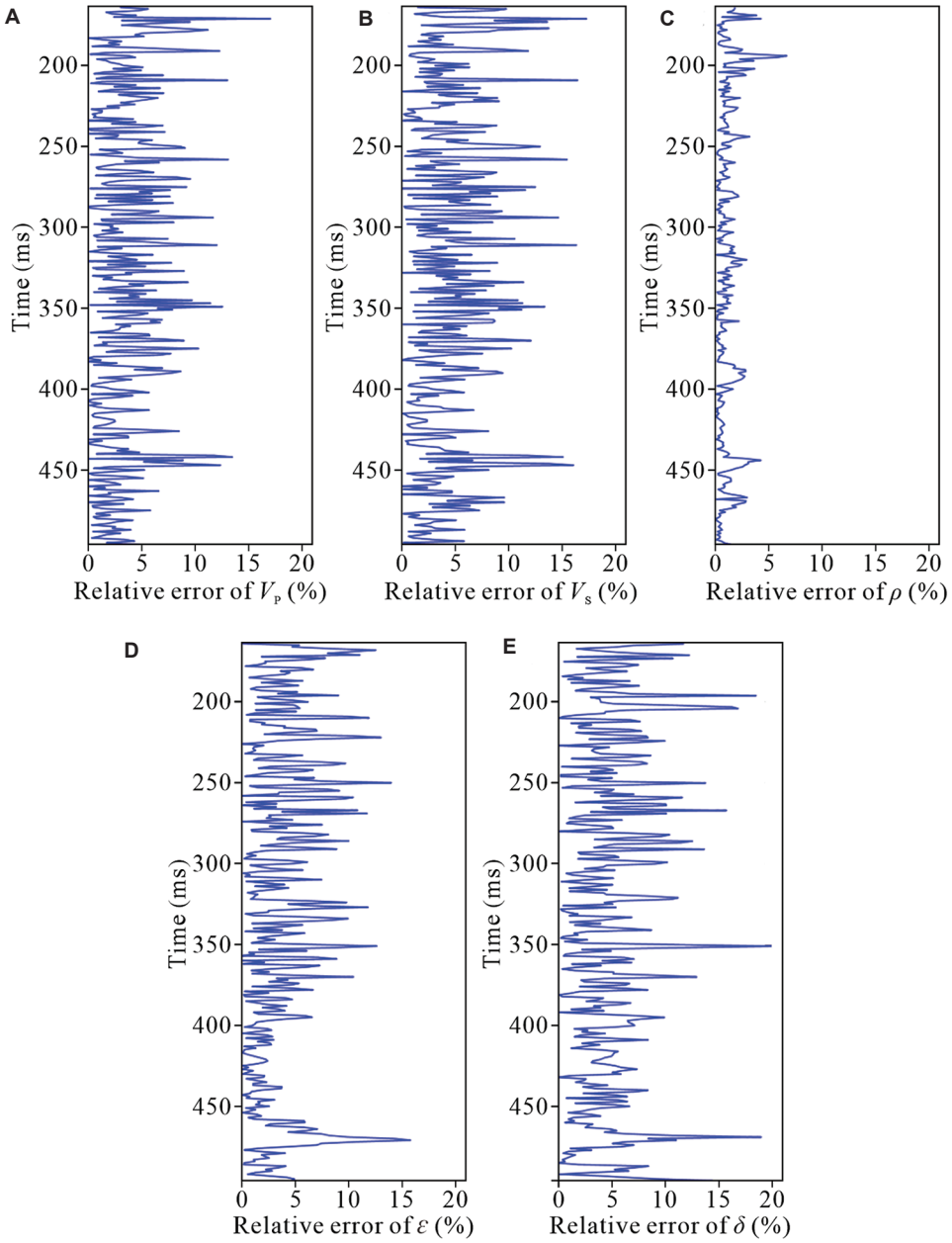


**Figure 11.** Relative-error curves between inversion results and the well logs. (A) P-wave velocity. (B) S-wave velocity. (C) Density. (D) $\varepsilon$. (E) $\delta$.

respectively, indicating good consistency between the inversion results and the well logs. This error level indicates that the inversion method reliably captures the overall trends and key characteristics of the subsurface properties

Comparing the synthetic data with the field data (Figure 12) revealed that, despite the moderate quality of the field AVA gathers, our method still generated ideal synthetic AVA gathers. This observation indicates the robustness of the algorithm with the inclusion of the sparse constraint. The horizon and impedance relationships in the synthetic AVA gathers were consistent with those in the surface seismic AVA gathers.

Based on the geological data, the one-dimensional initial models at the well location for P-wave velocity, S-wave velocity, density, $\varepsilon$, and $\delta$ were extended to create a two-dimensional initial model along the line (Figure 13), which was then used for the inversion.

The inversion results for the two-dimensional line are shown in Figure 14. Given the ability of the inversion method to characterize the physical parameters of thin

interbeds in detail, the inversion results can accurately describe the physical characteristics of a thin interbed containing thin VTI beds.

## 5. Discussion

The structural diversity within the thin interbeds leads to complex wavefield responses. Conventional methods

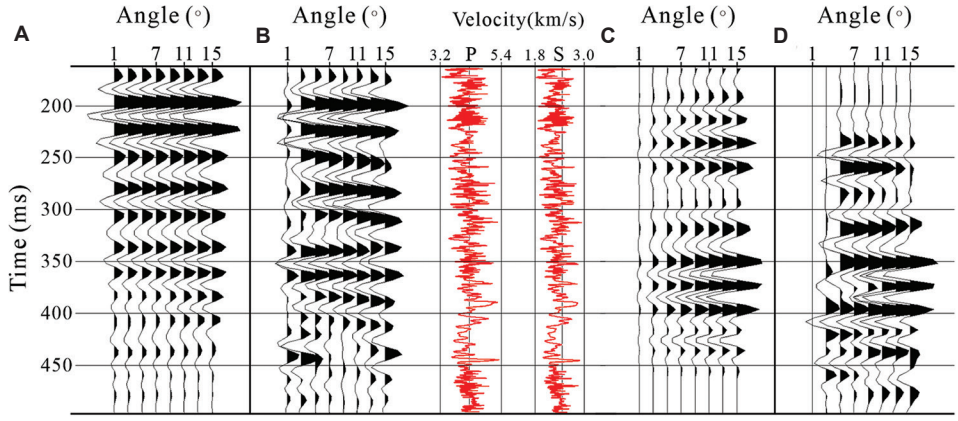


**Figure 12.** Comparison of synthetic and field AVA gathers. (A) Synthetic PP AVA gathers. (B) Field PP AVA gathers. (C) Synthetic PS AVA gathers. (D) Field PS AVA gathers. The red curves are the P- and S-wave velocities.
Abbreviation: AVA: Amplitude variation with angle.

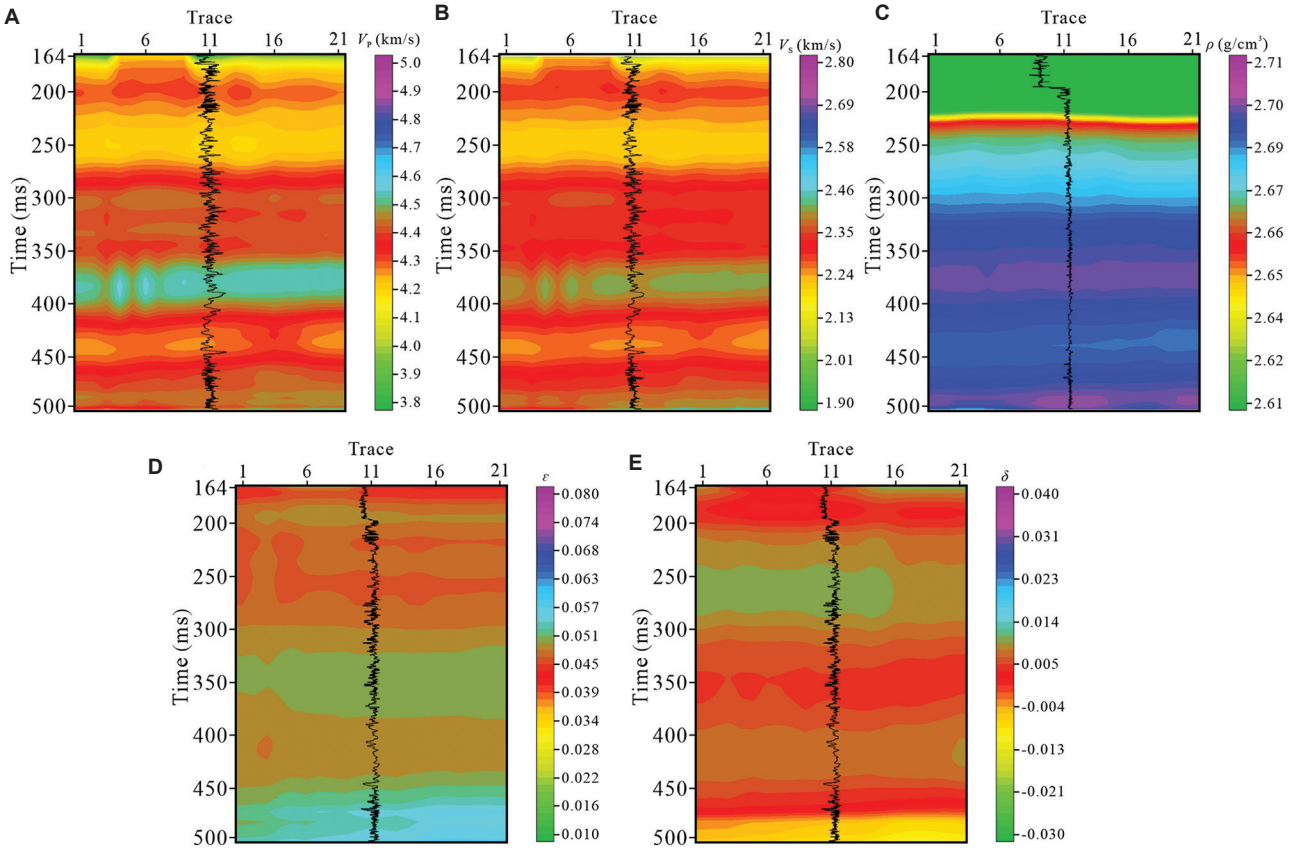


**Figure 13.** Two-dimensional initial model for inversion of field data. (A) P-wave velocity. (B) S-wave velocity. (C) Density. (D) $\varepsilon$. (E) $\delta$. The black curves in (A), (B), and (C) are from the well logs corresponding to the parameter types, and the black curves in (D) and (E) are from gamma-ray log data.

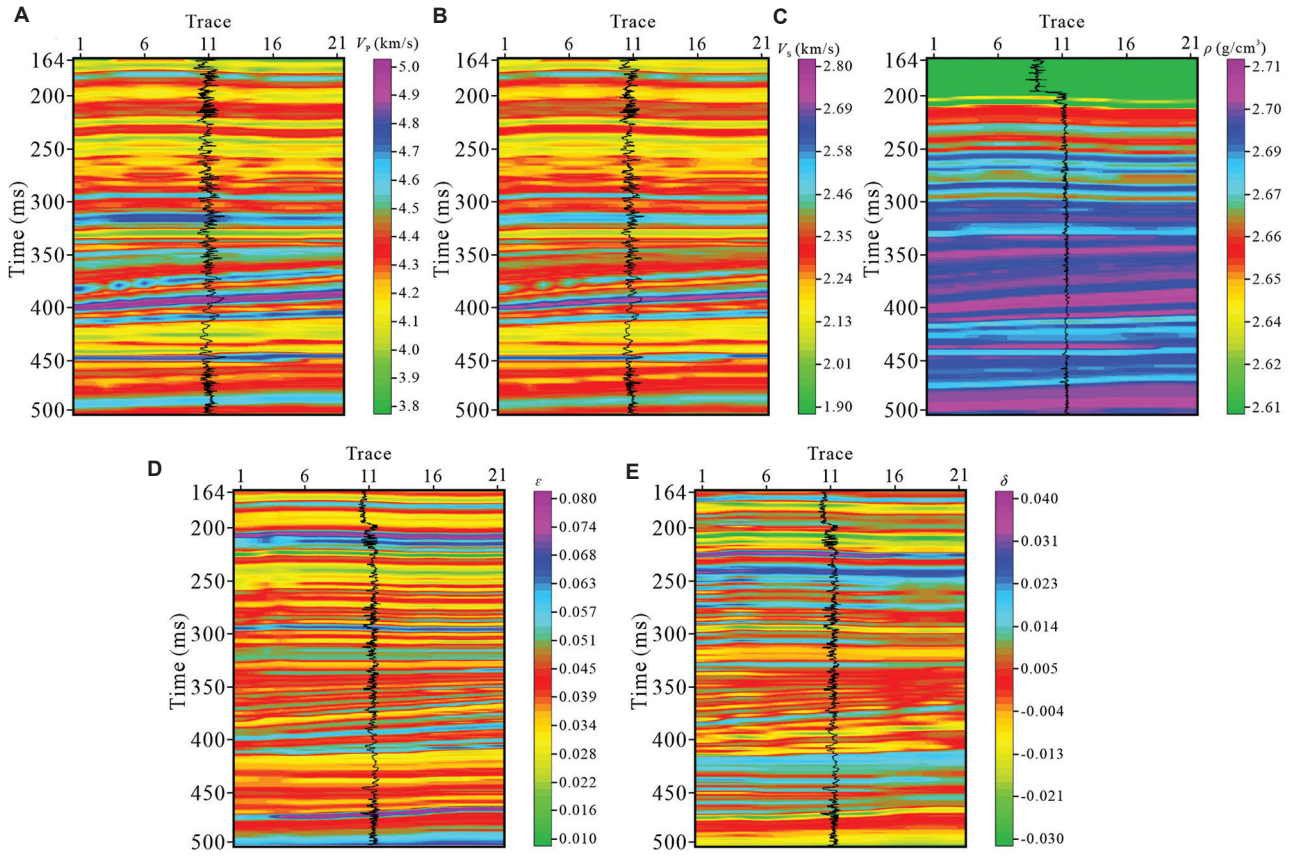


**Figure 14.** Two-dimensional inversion results of field data. (A) P-wave velocity. (B) S-wave velocity. (C) Density. (D) $\varepsilon$. (E) $\delta$. The black curves in (A), (B), and (C) are from the well logs corresponding to the parameter types, and the black curves in (D) and (E) are from gamma-ray log data.

often treat thin interbeds as isotropic multilayer media or approximate them as thick VTI layers, extracting a single set of physical parameters from a thin interbed. Both approaches risk losing essential descriptions of the internal characteristics of thin interbeds.

In this study, we developed an inversion method for thin interbeds containing thin VTI beds, based on Kennett's second-order approximations. This method targets the geological features of thin beds with short-term cycle characteristics. By considering the VTI properties of thin beds within the interbeds, along with transmission losses, internal multiples, and mode conversions, the method effectively inverts velocity, density, and anisotropic parameter variation curves within the thin interbeds. The proposed inversion method is suitable for both thick and thin isotropic and VTI layers. In addition, the Kennett's second-order approximations accelerate the inversion by discarding higher-order terms that have minimal impact on the reflection coefficient calculations.

Compared to other least-squares methods, the LM algorithm is more stable when addressing complex anisotropic inversions. Based on this algorithm, we established an inversion objective function. Given that five parameters were inverted simultaneously, we incorporated a sparse constraint term into the objective function to limit model complexity, prevent overfitting, and reduce noise.

Model tests confirmed that our inversion method provided more accurate descriptions of wavefield propagation patterns within thin interbeds containing thin VTI beds using the Kennett's second-order approximations, compared to the method using the Zoeppritz equations. With < 30% random noise, the inversion results accurately matched the true model, indicating that this method exhibited strong noise resistance.

Compared to conventional methods, the proposed method requires more prior information and higher accuracy for the initial model, which must at least roughly reflect the variation trends of the subsurface physical parameters. Joint inversion was conducted in the PP time domain, necessitating the conversion of PS AVA gathers from the PS time domain to the PP time domain.

In the inversion of field data, we observed that the travel-time variations of internal multiples within thin interbeds were complex, and these multiples were coupled with primary reflections. Because the exact physical parameters of the media are often unavailable, accurately calculating the travel times of internal multiples becomes challenging, ultimately complicating the accurate time-domain conversion of internal multiples. Under the thin-layer and small-to-medium incidence angle assumptions, the time difference between the internal multiples and the primary reflections was relatively small. Therefore, we picked numerous horizons in the PP and PS AVA gathers to ensure that the primary reflections in the PS AVA gathers could be accurately compressed into the PP time domain. On this basis, we estimated the compression of the internal multiples in the PP domain. Moreover, we appropriately reduced the weight of the PS dataset in the inversion. Thus, this method compresses PS AVA gathers into the PP time domain with relatively high accuracy while minimizing the impact of time–domain conversion errors on inversion results.

When processing field data, the proposed method accounts for transmission losses and internal multiples, eliminating the need for transmission-loss compensation and multiple suppression, thereby distinguishing it from conventional preprocessing methods.

The proposed method is suitable for layers that can be considered VTI media. However, it is inapplicable to thin interbeds with internally dipping laminations, which exhibit azimuthal anisotropy effects and are better characterized as tilted transversely isotropic or horizontal transversely isotropic media. In addition, when inverting field data, the time-domain conversion for internal multiples employs an approximation method, potentially leading to errors in the inversion results. Finally, our method requires the construction of Thomsen anisotropy parameter models derived from P- and S-wave velocity logs. Therefore, if such velocity logs are unavailable in a study area, the proposed inversion method cannot be applied.

## 6. Conclusion

We propose a joint PP- and PS-wave AVA inversion method based on Kennett's second-order approximations for thin interbeds containing thin VTI beds. Our method considers thin beds with short-term cycle characteristics as thin VTI beds, using Kennett's second-order approximations to describe the wave propagation characteristics in thin interbeds containing thin VTI beds while considering internal multiples and transmission losses. The proposed method provides a more detailed characterization of the VTI properties of thin beds exhibiting short-term cycle characteristics within thin interbeds.

The inversion objective function for the five parameters is established based on the LM algorithm, which effectively controls model complexity via sparse constraints and enhances inversion stability and resilience to noise.

Synthetic model tests, conducted with and without noise, demonstrated the high precision and robustness of our inversion method in handling complex thin interbeds. The one- and two-dimensional inversion results of the multi-component field seismic data obtained using the proposed method align well with trends observed in well logs. This method enhances the inversion accuracy for thin interbeds and provides technical support for oil and gas exploration and for the geological interpretation of anisotropic thin interbeds.

## Acknowledgments

None.

## Funding

This work was supported in part by the Deep Earth Probe and Mineral Resources Exploration–National Science and Technology Major Project (grant no. 2024ZD1003000), in part by the Scientific Research Innovation Capability Support Project for Young Faculty (grant no. ZYGXQNJSKYCXNLZCXM-E14), and in part by the CNPC Science and Technology Management Department Key Core Technology Research Project titled "Key Technologies and Software Development for 3D VSP–Surface Joint Imaging" (grant no. 2025ZG53).

## Conflict of interest

Jun Lu serves as the Guest Editor of this Special Issue, but was not in any way involved in the editorial and peer-review process conducted for this paper, directly or indirectly. Other authors declare they have no competing interests.

## Author contributions

*Conceptualization:* Jun Lu
*Formal analysis:* Peidong Huang, Jun Lu
*Funding acquisition:* Zhe Yang, Wei Yang
*Investigation:* Peidong Huang, Jun Lu, Chun Yang
*Methodology:* Peidong Huang, Jun Lu
*Visualization:* Peidong Huang
*Writing–original draft:* Peidong Huang
*Writing–review & editing:* Jun Lu, Chun Yang

## Availability of data

Data are available upon request via lj615@cugb.edu.cn.

## References


1. Buland A, Omre H. Bayesian linearized AVO inversion. *Geophysics*. 2003;68(1):185-198.

   doi: 10.1190/1.1543206

2. Huang G, Chen X, Luo C, Li X. Application of optimal transport to exact Zoeppritz equation AVA inversion. *IEEE Geosci Remote Sens Lett*. 2018;15(9):1337-1341.

   doi: 10.1109/lgrs.2018.2841916

3. Simmons JL, Backus MM. AVO modeling and the locally converted shear wave. *Geophysics*. 1994;59(8):1237-1248.

   doi: 10.1190/1.1443681

4. Fuchs K. The reflection of spherical waves from transition zones with arbitrary depth-dependent elastic moduli and density. *J Phys Earth*. 1968;16:27-41.

   doi: 10.4294/jpe1952.16.special_27

5. Fryer GJ. A slowness approach to the reflectivity method of seismogram synthesis. *Geophys J Int*. 1980;63(3):747-758.

   doi: 10.1111/j.1365-246X.1980.tb02649.x

6. Carcione JM. Amplitude variations with offset of pressure-seal reflections. *Geophysics*. 2001;66(1):283-293.

   doi: 10.1190/1.1444907

7. Carcione JM. Energy balance and fundamental relations in dynamic anisotropic poro-viscoelasticity. *Proc R Soc Lond A*. 2001;457:331-348.

   doi: 10.1098/rspa.2000.0669

8. Liu H, Li J, Chen X, Hou B, Chen L. Amplitude variation with offset inversion using the reflectivity method. *Geophysics*. 2016;81(4):R185-R195.

   doi: 10.1190/geo2015-0332.1

9. Kennett BLM. *Seismic Wave Propagation in Stratified Media*. Cambridge, UK: Cambridge University Press; 1983.

10. Rubino JG, Velis D. Thin-bed prestack spectral inversion. *Geophysics*. 2009;74(4):R49-R57.

    doi: 10.1190/1.3148002

11. Padhi A, Mallick S. Multicomponent pre-stack seismic waveform inversion in transversely isotropic media using a non-dominated sorting genetic algorithm. *Geophys J Int*. 2014;196(3):1600-1618.

    doi: 10.1093/gji/ggt460

12. Lu Y, Peng S, Cui X, Li D, Wang K. Thin-Bed Inversion using Pre-Stack Seismic Data. In: *SEG International Exposition and Annual Meeting*, San Antonio, TX, USA; 2019.

    doi: 10.1190/segam2019-3214870.1

13. Yang Z, Lu J. Second-order approximation of the seismic reflection coefficient in thin interbeds. *Energies*. 2020;13(6):1465.

    doi: 10.3390/en13061465

14. Yang C, Wang Y. Joint PP-PS seismic prestack inversion of thin-bed reservoirs. *J Geophys Eng*.2022; 19(4):897-913.

    doi: 10.1093/jge/gxac060

15. Kuai Z, Cao D, Jin C. Frequency-Dependent Reflection Characteristics of Single Thin Layer and Waveform Inversion. In: *SEG/AAPG International Meeting for Applied Geoscience and Energy*, Houston, TX, USA; 2023.

    doi: 10.1190/image2023-3916363.1

16. Chen J, Glinsky ME. Stochastic inversion of seismic PP and PS data for reservoir parameter estimation. *Geophysics*. 2014;79(6):R233-R246.

    doi: 10.1190/geo2013-0456.1

17. Wang D, Zhang M, Wang J, Chen D, Zhao Y, Bai J. Research and application of joint interpretation using P-wave and PS-wave in tight gas exploration. *J Earth Sci*. 2024;35(4):1402-1406.

    doi: 10.1007/s12583-024-1995-7

18. Veire HH, Landrø M. Simultaneous inversion of PP and PS seismic data. *Geophysics*. 2006;71(3):R1-R10.

    doi: 10.1190/1.2194533

19. Lu J, Wang Y, Chen J, An Y. Joint anisotropic amplitude variation with offset inversion of PP and PS seismic data. *Geophysics*. 2018;83(2):N31-N50.

    doi: 10.1190/geo2016-0516.1

20. Rüger A. *Reflection Coefficients and Azimuthal AVO Analysis in Anisotropic Media*. Tulsa, OK, USA: Society of Exploration Geophysicists; 2002.

    doi: 10.1190/1.9781560801764

21. Luo C, Ba J, Carcione JM, Huang G, Guo Q. Joint PP and PS pre-stack seismic inversion for stratified models based on the propagator matrix forward engine. *Surv Geophys*. 2020;41(5):987-1028.

    doi: 10.1007/s10712-020-09605-5

22. Tura A, Simmons J, Daneshvar S, Copley M, Stitt, J. Improving reservoir characterization and time-lapse seismic through joint inversion of PP- and PS-wave seismic data. *Interpretation*. 2022;10(2):T341-T350.

    doi: 10.1190/int-2021-0167.1

23. Yang Y, Yin X, Li K. Quadratic reflectivity-based joint PP and PS inversion for VTI media using the stiffness matrix. *IEEE Trans Geosci Remote Sens*. 2024;62:1-13.

    doi: 10.1109/tgrs.2024.3492394

24. Huang PD, Lu J, Wang Y. Second-order approximate reflection coefficients of vertical transversely isotropic thin beds. *Acta Geophys*. 2022;70(3):1155-1169.

doi: 10.1007/s11600-022-00758-y

25. Levenberg K. A method for the solution of certain non-linear problems in least squares. *Quarterly Appl Math*. 1944;2(2):164-168.

    doi: 10.1090/qam/10666

26. Marquardt DW. An algorithm for least-squares estimation of nonlinear parameters. *J Soc Ind Appl Math*. 1963;11(2):431-441.

    doi: 10.1137/0111030

27. Graebner M. Plane-wave reflection and transmission coefficients for a transversely isotropic solid. *Geophysics*. 1992;57(11):1512-1519.

    doi: 10.1190/1.1443219

28. Thomsen L. Weak elastic anisotropy. *Geophysics*. 1986;51(10):1954-1966.

    doi: 10.1190/1.1442051

29. Backus GE. Long-wave elastic anisotropy produced by horizontal layering. *J Geophys Res*. 1962;67(11):4427-4440.

    doi: 10.1029/jz067i011p04427

ACCSCIENCE PUBLISHING

Journal of Seismic Exploration

ARTICLE

# Subsurface imaging based on polarization analysis of microtremor Rayleigh waves

**Qingling Du[1,2]*, Qian Xu[1], Nan Guo[3], Shuai Liu[1], Shijie Liu[4], and Denghui Gao[1]**

[1]College of Civil Engineering and Architecture, Huanghuai University, Zhumadian, Henan, China

[2]Henan International Joint Laboratory of Structural Mechanics and Computational Simulation, Huanghuai University, Zhumadian, Henan, China

[3]School of Civil and Hydraulic Engineering, Lanzhou University of Technology, Lanzhou, Gansu, China

[4]Department of Architecture and Civil Engineering, Lvliang University, Lvliang, Shanxi, China

## Abstract

The precise identification of adverse geological bodies, such as goafs, karst cavities, and faults, is crucial for engineering safety and economic viability. However, conventional drilling methods suffer from high costs, limited coverage, and the risk of overlooking anomalies. While existing geophysical techniques can address drilling's limitations, they are often constrained by non-uniqueness and insufficient resolution. To address these challenges, this paper proposes a novel technique for stratigraphic evaluation based on the polarization analysis of microtremor surface waves, aiming to improve the accuracy and efficiency of identifying dynamic site parameters in complex geological settings. We systematically validated the feasibility of using the elliptical polarization ratio of Rayleigh waves for subsurface characterization through theoretical analysis and field data. Numerical simulations confirmed that the method can clearly identify localized geological anomalies under noise-free conditions. For field data processing, we developed a workflow to extract Rayleigh waves with a high signal-to-noise ratio from microtremors. This workflow isolates valid wave components using principal frequency filtering and directional discrimination, while mitigating noise impact on dispersion estimation. The final polarization ratio profile strongly correlated with magnetotelluric resistivity data, successfully imaging goafs, fractured zones, and bedrock interfaces. Stacking codirectional wave events further enhanced deep structural resolution and resulted in consistency. In conclusion, this study demonstrates that the polarization-based method is a feasible, flexible, and promising tool for engineering applications, offering a reliable foundation for fine-scale site characterization.

***Keywords:*** Microtremor Rayleigh wave; Elliptical polarization ratio; Site characterization; Numerical simulations

***Corresponding author:**
Qingling Du
duqingling@huanghuai.edu.cn

**Citation:** Du Q, Xu Q, Guo N, Liu S, Liu S, Gao D. Subsurface imaging based on polarization analysis of microtremor Rayleigh waves. *J Seismic Explor.* 2026;35(1):83-100. doi: 10.36922/JSE025400083

**Received:** October 3, 2025

**Revised:** November 25, 2025

**Accepted:** November 25, 2025

**Published online:** December 23, 2025

**Copyright:** © 2025 Author(s). This is an Open-Access article distributed under the terms of the Creative Commons Attribution License, permitting distribution, and reproduction in any medium, provided the original work is properly cited.

**Publisher's Note:** AccScience Publishing remains neutral with regard to jurisdictional claims in published maps and institutional affiliations.

## 1. Introduction

With the rapid advancement of urbanization and infrastructure construction, the influence of site geological conditions on project safety and economy has become increasingly significant. The precise identification of adverse geological bodies with strong

lateral heterogeneity, such as goafs, karst caves, and fault fracture zones, has emerged as a core task in engineering investigation.[1] This demand for site characterization is particularly urgent in areas with complex geological conditions, driven by the accelerated pace of development and the continuous expansion of underground space utilization. Conventional borehole-based investigation methods, however, exhibit pronounced limitations. While capable of providing local point-based geological information, they are prohibitively expensive, suffer from low sampling density and limited resolution, and are ill-suited for large-scale continuous detection. Consequently, they are prone to overlooking geological anomalies between boreholes, failing to meet the requirements of fine-scale investigation for modern large-scale engineering projects.[2] To compensate for these deficiencies, geophysical methods, including high-density resistivity, seismic reflection, and magnetotelluric methods, have been widely employed.[3-5] Nevertheless, these techniques are often hampered by issues such as non-uniqueness of solutions, signal interference, and inadequate resolution, which restrict their reliability and precision in complex geological settings. Therefore, the development of efficient, high-precision, low-cost, and adaptable multiparameter geophysical exploration technologies has become a critical direction for enhancing the capability of site geological structure evaluation.

Surface wave exploration techniques, by virtue of their advantages—such as high sensitivity to vertical stratigraphic changes, a broad depth of investigation, and ease of field implementation—have been extensively applied in the identification of site dynamic parameters and the inversion of subsurface structures.[6] In particular, Rayleigh waves, as the principal type of surface wave, possess propagation characteristics that are closely correlated with the elastic parameters of the ground (*e.g.*, shear wave velocity and Poisson's ratio). Consequently, analyzing the dispersion characteristics of Rayleigh waves has become a mainstream method for subsurface structure inversion.[7,8] However, traditional Rayleigh wave dispersion analysis methods predominantly rely on active seismic sources. In complex sites, such as densely populated urban areas or mountainous terrain, these methods are susceptible to interference from environmental noise, which degrades the accuracy of extracted dispersion curves. Furthermore, the deployment of active sources constrains both the investigation range and operational flexibility. In contrast, microtremor exploration utilizes natural environmental vibrations (*e.g.*, from traffic, wind loads, and crustal micro-movements) as its energy source. Requiring no artificial excitation, this approach offers significant advantages, including being non-destructive, enabling large-scale surveys, and adapting to complex site conditions. It thus presents a new paradigm for overcoming the application bottlenecks of traditional surface wave exploration techniques.[9-11]

Microtremor signals are rich in surface wave information, particularly Rayleigh wave components, whose propagation characteristics can also reflect the vertical stratification and lateral heterogeneity of strata. Early research on microtremor surface waves primarily concentrated on the extraction and inversion of dispersion curves. By utilizing the power spectral density or cross-correlation function of microtremor signals, these methods obtain Rayleigh wave dispersion characteristics to subsequently invert the shear wave velocity structure of the strata.[12-15] However, when applied to laterally heterogeneous sites—such as those with local geological anomalies such as goafs and fractured zones—these methods face limitations. Due to their neglect of the polarization characteristics of Rayleigh waves, they struggle to accurately identify the spatial location and morphological features of such anomalies, leading to reduced reliability of the inversion results. Rayleigh waves exhibit unique elliptical polarization characteristics during propagation. Their elliptical polarization ratio (the ratio of the major to minor axis) is not only correlated with the elastic parameters of the strata but is also highly sensitive to lateral heterogeneity. This characteristic provides a key technological breakthrough for achieving fine-scale structural evaluation of complex sites.[16]

Recent years have witnessed a surge in research on Rayleigh wave polarization analysis. Theoretical investigations have established its utility, starting with the joint inversion method by Arai and Tokimatsu that enhanced Vs-profile accuracy.[17] Subsequent studies by Woodhouse and Maupin confirmed that Rayleigh wave ellipticity can constrain the non-uniqueness of dispersion inversion.[18-21] The link between the H/V spectral ratio and Rayleigh wave ellipticity was further solidified in other works.[22,23] Numerical simulations by Yu and Liu[24] revealed that the polarization dispersion method offers superior sensitivity and lateral resolution compared to conventional velocity dispersion, particularly in laterally inhomogeneous media. The method's versatility is evidenced by its successful application in diverse fields, including depth calibration,[25] sedimentary layer thickness estimation,[26] polar ice sheet investigation,[27] and archaeological surveys.[28]

Nevertheless, a fundamental challenge persists: The extraction of Rayleigh wave polarization with a high signal-to-noise ratio (SNR) from the complex ambient microtremor field. This field is a superposition of multiple wavefields—including multidirectional Rayleigh waves,

Love waves, body waves, and background noise—which degrades polarization estimation accuracy.[29] In response, two primary technical pathways have emerged. The first involves array-based wavefield separation, which leverages the spatial characteristics of waves to isolate Rayleigh waves.[30] The second pathway focuses on transient event screening, utilizing time-frequency analysis and machine learning to select high-SNR events, such as distant earthquakes or industrial vibrations that provide a pristine signal for polarization analysis.[31,32]

Consequently, engineering site evaluation currently faces a confluence of challenges: Significant constraints from conventional methods, strong non-uniqueness in geophysical inversion, and the formidable task of extracting polarized signals from microtremors. To address these gaps, this research centers on the elliptical polarization of Rayleigh waves, with a core focus on resolving the extraction of high-SNR polarization signals under complex site conditions. Through an optimized data processing scheme, this work seeks to improve the precision for detecting subsurface adverse geological structures, thereby offering a more robust technological foundation for site characterization.

## 2. Methods

Within a homogeneous medium, a strong correlation exists between the ellipticity of Rayleigh surface waves and the Poisson's ratio of the constituent material. Given that Poisson's ratio is a vital parameter in the characterization of subsurface geological structures, this section is dedicated to theoretically elucidating how wave ellipticity can be employed as a significant indicator for site evaluation.

For the theoretical analysis, we consider waves propagating in an infinite, homogeneous medium, where the fundamental form of the wave equation solution is $e^{jk(x-Vt)}$. The motion trajectory of a particle is defined by its radial displacement component $u$ and its vertical displacement component $w$. Through the established relationship between displacement and potential functions, the corresponding potentials can be determined. Consequently, the formulas for the particle's radial and vertical displacements can be derived as:

$$\begin{cases} u = A(-e^{-mkz} + \dfrac{2mn}{n^2+1}e^{-nkz})ike^{i(\omega t-kx)} \\ w = A(-me^{-mkz} + \dfrac{2mn}{n^2+1}e^{-nkz})ke^{i(\omega t-kx)} \end{cases} \quad (1)$$

In this expression, $m$ and $n$ represent the attenuation coefficients, whereas $A$ denotes the energy coefficient. The analytical expressions for the vertical and horizontal components of displacement are derived by applying Euler's transformation to the equation and extracting its real part.

$$\begin{cases} u = A\left(e^{-mkz} - \dfrac{2mn}{n^2+1}e^{-nkz}\right)ksin\left(\omega t - kx\right) \\ w = A(-me^{-mkz} + \dfrac{2mn}{n^2+1}e^{-nkz})kcos(\omega t - kx) \end{cases} \quad (2)$$

Based on **Equation 2**, the displacement of Rayleigh waves in a homogeneous half-space was calculated for various Poisson's ratios. The variation of this displacement with depth, normalized by the half-wavelength, was subsequently characterized. The results demonstrate that the energy of Rayleigh waves attenuates exponentially with depth and is predominantly confined within a depth range of one wavelength. Furthermore, the variation in Poisson's ratio was found to only marginally affect the rate of this energy attenuation.[24]

In addition, **Equation 2** reveals that for Rayleigh waves propagating along the free surface of a homogeneous elastic half-space, the two displacement components satisfy an elliptical equation:

$$\left(\frac{u}{a}\right)^2 + \left(\frac{w}{b}\right)^2 = 1 \quad (3)$$

where $a = Ak\left(e^{-mkz} - \dfrac{2mn}{n^2+1}e^{-nkz}\right)$ and $b = Ak\left(-me^{-mkz} + \dfrac{2mn}{n^2+1}e^{-nkz}\right)$ are the semi-major and semi-minor axes of the ellipse, respectively. This demonstrates that the particle motion trajectory of a Rayleigh wave is elliptical. Based on this elliptical trajectory, the ellipticity $E(z)$ can be defined as the ratio of the amplitudes of the horizontal and vertical displacement components:

$$E\left(z\right) = \left|\frac{e^{-mkz} - \dfrac{2mn}{n^2+1}e^{-nkz}}{-me^{-mkz} + \dfrac{2mn}{n^2+1}e^{-nkz}}\right| \quad (4)$$

At the free surface ($z = 0$), the ellipticity is given by:

$$E\left(0\right) = \frac{n^2+1-2mn}{m(1-n^2)} \quad (5)$$

The relationship between the Rayleigh wave velocity, S-wave velocity, P-wave velocity, and Poisson's ratio is as follows:

$$\frac{V_R}{\beta} = \frac{0.87+1.12\sigma}{1+\sigma} \quad (6)$$

$$\frac{V_R}{\alpha} = \frac{(0.87+1.12\alpha)\sqrt{(1-2\tilde{A})/2(1-\alpha)}}{1+\alpha} \tag{7}$$

The following equations are obtained by substituting the solutions for the P- and S-wave potential functions into their respective governing equations:

$$m^2 = 1-\frac{V_R^2}{\alpha^2}, n^2 = 1-\frac{V_R^2}{\beta^2} \tag{8}$$

In a homogeneous half-space, the parameters m and n are constants, and consequently, the ellipticity of Rayleigh waves is also a constant. By combining **Equations 6, 7**, and **8**, it is evident that *m* and *n* are dependent solely on Poisson's ratio of the homogeneous half-space. Thus, **Equation 5** can be reformulated as:

$$E = \frac{2-\left(\frac{0.87+1.12\sigma}{1+\sigma}\right)^2 - 2\sqrt{\left[1-\frac{(0.87+1.12\sigma)^2(1-2\sigma)}{2(1+\sigma)^2(1-\sigma)}\right]\left[1-\left(\frac{0.87+1.12\sigma}{1+\sigma}\right)^2\right]}}{\left(\frac{0.87+1.12\sigma}{1+\sigma}\right)^2\sqrt{1-\frac{(0.87+1.12\sigma)^2(1-2\sigma)}{2(1+\sigma)^2(1-\sigma)}}} \tag{9}$$

**Equation 6** is a complex nonlinear equation that does not explicitly reveal the relationship between ellipticity and Poisson's ratio. Through numerical fitting, an empirical relationship with a correlation coefficient of 0.9775 was obtained[24]:

$$E = -0.4855\sigma + 0.797 \tag{10}$$

In Figure 1, $\alpha$, $\beta$, and $V_R$ are the P-wave, S-wave, and Rayleigh wave velocities, respectively. *Er* is the theoretical elliptical polarization ratio, and the solid line is the linear fit. As shown in Figure 1, with increasing Poisson's ratio, the elliptical polarization ratio decreases at a rate significantly faster than the rate of increase for the $V_R/\beta$ ratio. This indicates that the elliptical polarization ratio is more sensitive to variations in Poisson's ratio. This equation clearly indicates an approximate inverse linear relationship between ellipticity and Poisson's ratio. This finding further substantiates the feasibility of using Rayleigh wave ellipticity for the evaluation of geological structures.

## 3. Numerical simulation

In this section, numerical simulations are employed to validate the response of Rayleigh wave ellipticity to changes in geological structure. Initially, a cuboid homogeneous medium model with dimensions of 600 m × 600 m × 400 m was constructed to simulate a homogeneous half-space. The medium properties were defined as follows: A density of 2000 kg/m$^3$, a P-wave velocity of 1000 m/s, and an S-wave velocity of 530 m/s. The model was discretized with a grid spacing of 2 m. In the simulation, a plane wave source was used to excite the Rayleigh wave field. The source wavelet was a 20 Hz Ricker wavelet. A linear array of 140 receivers was deployed along a central survey line with a receiver spacing of 2 m, and the data were sampled at a time interval of 0.0005 s. A schematic of the model is presented in Figure 2. For the homogeneous case, the entire model was assigned uniform properties. In contrast, for the heterogeneous simulation, a cavity was introduced and assigned a density of 1500 kg/m$^3$, a P-wave velocity of 300 m/s, and an S-wave velocity of 150 m/s.

For a homogeneous medium with a density of 2000 kg/m$^3$, a P-wave velocity of 1000 m/s, and an S-wave velocity of 530 m/s, the theoretical value of the Rayleigh wave ellipticity is 0.654. Figure 3A displays the simulated three-component seismic records obtained from this homogeneous medium model. In the simulation, a single linear source was employed to simulate Rayleigh surface waves in the far-field, and body waves were subsequently filtered out. As the Y-component is perpendicular to the direction of wave propagation, its amplitude is nearly zero in the homogeneous model. In contrast, both the vertical component (Z) and the component along the propagation direction (X) exhibit high amplitudes. Figure 3B presents the corresponding ellipticity profile, which clearly reflects the homogeneous characteristics of the medium. The calculated ellipticity is consistent with the theoretical value of 0.654. This demonstrates that in a homogeneous medium, the ellipticity of Rayleigh waves can effectively indicate the uniformity of the geological structure. Furthermore, by leveraging the relationship between ellipticity and Poisson's ratio, site characteristics can be determined.

Furthermore, a simulation was conducted for a heterogeneous medium containing a low-velocity cavity. The spherical low-velocity anomaly was characterized by a density of 1500 kg/m$^3$, a P-wave velocity of 300 m/s, an S-wave velocity of 150 m/s, a diameter of 8 m, and its center was located at a depth of 16 m below the surface. Figure 4A presents the simulated three-component seismic records from this heterogeneous model, which also employed a single linear source to simulate far-field Rayleigh surface waves with body waves subsequently filtered. Similar to the homogeneous model, the amplitude of the Y-component, which is perpendicular to the propagation direction, is negligible, whereas the vertical (Z) and inline (X) components exhibit high amplitudes. Figure 4B shows the corresponding ellipticity profile. The regions outside the low-velocity anomaly clearly reflect the homogeneous

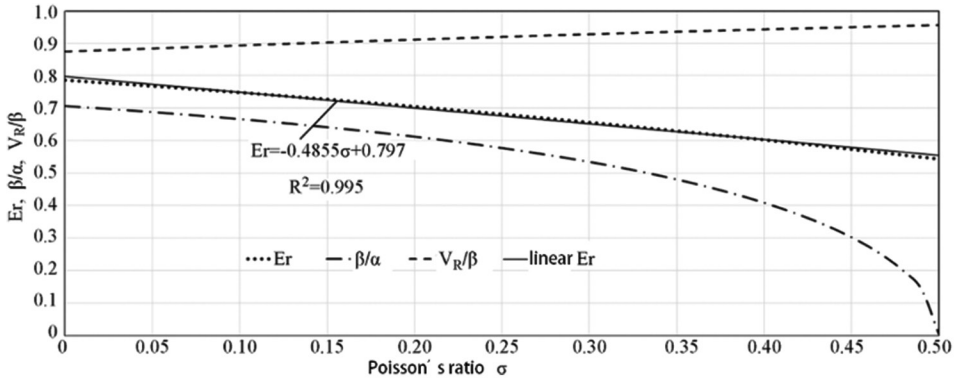


**Figure 1.** Approximate negative linear relationship between surface wave ellipticity and Poisson's ratio for a homogeneous half-space

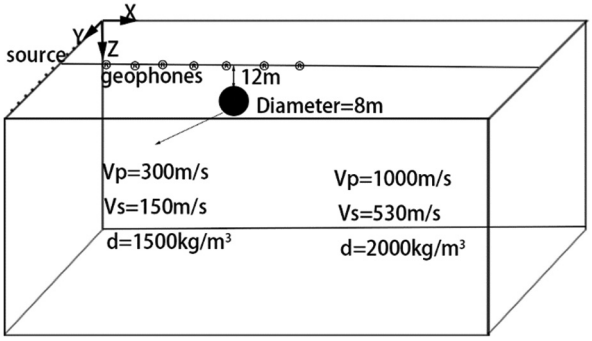


**Figure 2.** Numerical simulation model
Abbreviations: d: Density; $V_p$: P-wave velocity; $V_s$: S-wave velocity.

characteristics of the background medium. However, at an offset of approximately 170 m, a weak high-ellipticity anomaly and a strong low-ellipticity anomaly appear, which can be used to locate the low-velocity cavity. Notably, the anomaly imaged in the profile is displaced in the direction of wave propagation. This demonstrates that the Rayleigh wave ellipticity profile can effectively identify the location of localized geological anomalies.

The results from the two numerical simulations above indicate that the ellipticity of Rayleigh surface waves is sensitive to anomalies in the geological structure. By leveraging the established relationships between ellipticity, velocity, and Poisson's ratio, this method can effectively characterize the features of the geological structure. Consequently, it can serve as a valuable complement to the conventional site evaluation parameter, Vs30.

The application of the elliptical polarization ratio method in microtremor data processing fundamentally relies on the effective extraction of high-SNR Rayleigh waves. In this section, we investigate this extraction process by constructing a numerical model of microtremor signals. This model is developed by introducing random noise and incorporating the propagation characteristics of multidirectional surface waves. The model is subsequently analyzed using techniques such as polarization analysis and directional filtering to isolate high-SNR Rayleigh waves.

To better simulate the physical characteristics of real-world microtremor signals, this study employed a homogeneous medium model with two oppositely oriented sources. The resulting synthetic seismogram contains various components, including multidirectional surface waves, P-waves, and boundary-reflected waves. On this basis, a microtremor dataset representing a complex interference environment was constructed by superimposing random noise with a maximum amplitude equal to 50% of the signal's maximum amplitude, as shown in Figure 5A. Figure 5B displays the record of coherently propagating Rayleigh waves, which was extracted after a series of processing steps, including high-amplitude signal screening, polarization analysis, and directional filtering.

Figure 6A illustrates the particle motion trajectories of the 25-trace synthetic microtremor record. Due to interference from noise, multidirectional Rayleigh waves, and body waves, the original record exhibits both linear and elliptical polarization phenomena, leading to significant disorder in the particle motion trajectories. In contrast, after optimization through methods such as event selection and polarization-based denoising, the extracted Rayleigh wave signal shows a significantly improved SNR, and its particle motion trajectories exhibit typical elliptical polarization characteristics (as shown in Figure 6B). These results confirm that the proposed technical scheme, which combines high-amplitude signal extraction with filtering, is feasible for isolating high-SNR Rayleigh waves from complex microtremor signals.

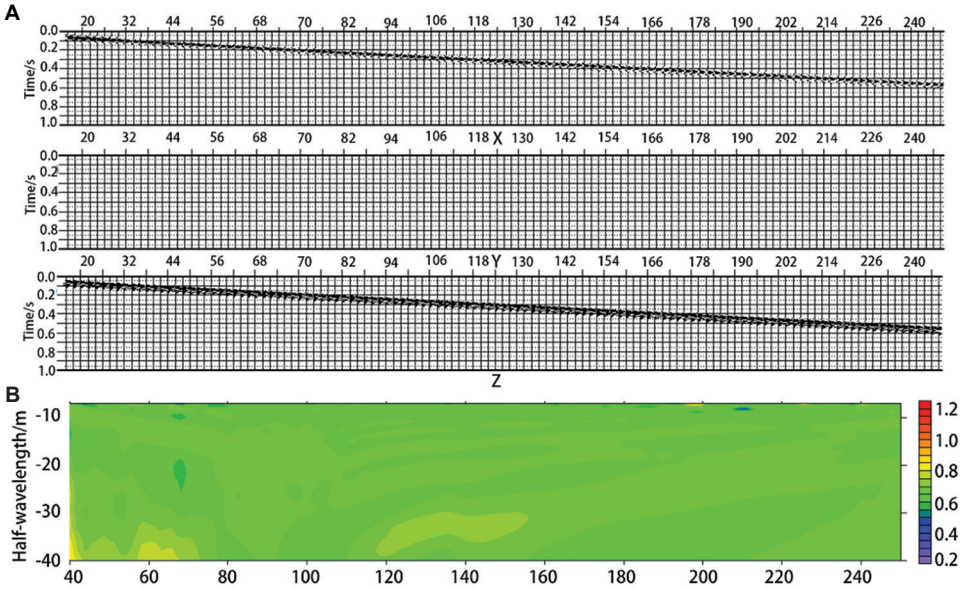


**Figure 3.** Seismic records and the corresponding ellipticity profile in a homogeneous half-space model, excited by a single plane source propagating along the main survey line. (A) Three-component seismic records along the central survey line, containing only a single set of Rayleigh surface waves. (B) The horizontal ellipticity profile at a depth of 0.5λ.

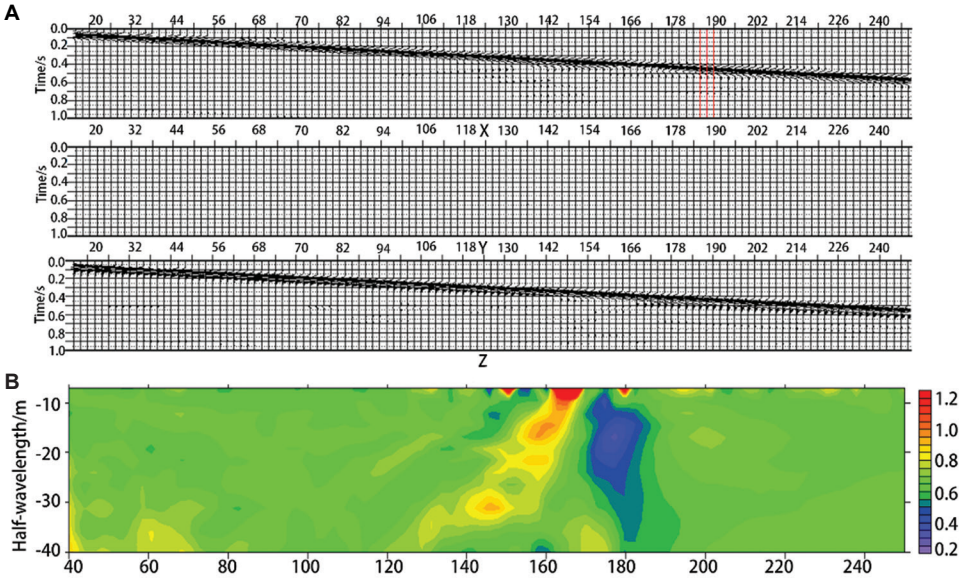


**Figure 4.** Seismic records and the corresponding ellipticity profiles in a heterogeneous half-space model, excited by a single plane source propagating along the main survey line. (A) Three-component seismic records along the central survey line contain only a single set of Rayleigh surface waves. (B) The horizontal ellipticity profile at a depth of 0.5λ, where λ is the dominant wavelength.

## 4. Data acquisition and analysis

To investigate the applicability of Rayleigh wave ellipticity from microtremor data for site evaluation and geological structure detection, this section focuses on three aspects: The acquisition of field data, the analysis of data characteristics, and the calculation of ellipticity profiles. Furthermore, the accuracy of the results is validated through comparative analysis.

### 4.1. Materials

The stability of the ground is of paramount importance for all infrastructure, including buildings, high-speed railways, and highways. Consequently, site investigation

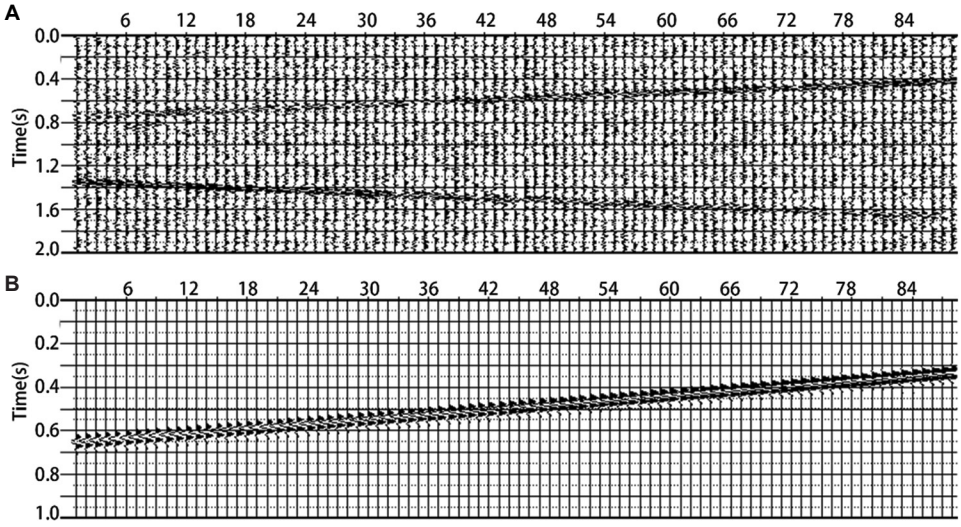


**Figure 5.** Vertical-component seismic records in a homogeneous medium. (A) Synthetic microtremor record. (B) Filtered Rayleigh wave record.

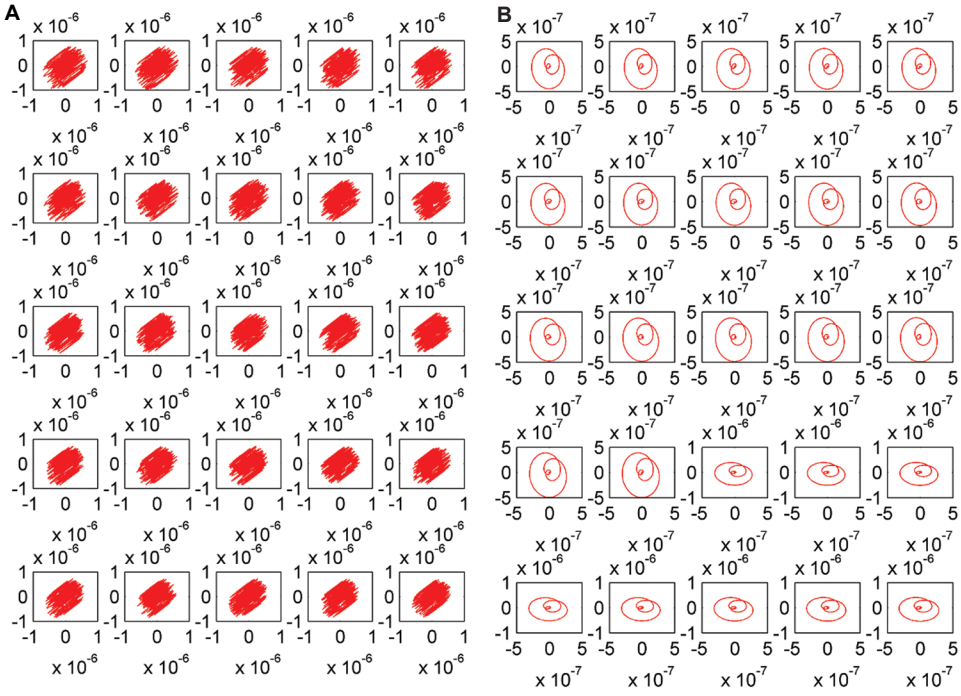


**Figure 6.** Particle motion trajectories of seismic records. (A) Trajectories of the synthetic microtremor record. (B) Trajectories of the Rayleigh wave record.

is an indispensable phase in construction engineering. To validate the practicality of the method proposed in this study, field data were used for verification. The case study data consist of microtremor records newly acquired along a survey line using three-component seismic instruments.

The data were collected in October 2015 at a construction site for a proposed railway line, with the objective of evaluating the stability of the geological structures along the route. The survey line was located in a mountainous area with elevations ranging from 350 m to 460 m. The site conditions were complex, featuring a varied surface of forests, shrubs, ponds, farmland, and residential houses, with some sections exhibiting steep topography. According to geological data, the bedrock in the area is primarily composed of mudstone, shale, and coal seams.

The geophones used for data acquisition had a frequency response range of 0.1–150 Hz. A total of 11 digital seismic instruments were deployed simultaneously

in an array along the survey line. The receiver spacing and sampling interval were set to 10 m and 0.01 s, respectively. The X-component was oriented along the survey line, the Y-component perpendicular to it, and the Z-component vertically. Considering the intensity of fieldwork and time constraints in the mountainous terrain, the recording duration for each setup was limited to 10 min. Over a 2-day period, a total of 12 setups were completed, yielding 132 three-component data traces. As the raw seismic records contained DC-offset interference, a band-pass filter from 0.1 Hz to 32 Hz was applied to the data. Figure 7A displays the gathering of the 132 vertical-component records, and Figure 7B shows the amplitude spectrum of the entire dataset.

The seismic records appear complex and chaotic, making it difficult to directly discern useful information. However, after applying amplitude gain, it is observed that some time segments exhibit relatively stable signals, whereas others are characterized by high-amplitude vibrational events. The amplitude spectrum of the 10-min records reveals that the signal energy is predominantly concentrated below 8 Hz. In contrast, the high-frequency components tend to exhibit characteristics consistent with white noise.

### 4.2. Field data analysis

This section analyzes the field microseismic signals in terms of their energy distribution, events with a high SNR, and the propagation direction of Rayleigh waves. This analysis serves as a preparatory step for the field data processing required by the microseism-based Rayleigh wave ellipticity method.

Initially, a single three-component seismic record with a duration of 600 s was selected. The microtremor signal was amplified using Geogiga Seismic Pro software (Geogiga Technology Corp, Canada), and based on the observed amplitude distribution, two 10-s segments were extracted, as shown in Figure 8A and B. The segment in Figure 8A contains a distinct high-amplitude event, whereas the segment in Figure 8B is relatively stable, lacking any significant vibrational activity.

Time-frequency analysis was employed to characterize the signals in Figure 8A and B, with the resulting time-frequency distributions shown in Figure 9A and B, respectively. As shown in Figure 9A, the high-amplitude event occurring between 6 and 8 s in Figure 5A is composed of a low-frequency component at approximately 3 Hz and a high-frequency component at approximately 20 Hz. In contrast, the time-frequency plot in Figure 9B indicates that the energy is distributed nearly uniformly across both time and frequency, exhibiting stationary characteristics similar to those of white noise.

Conventional methods, such as the spatial autocorrelation and traditional ellipticity approaches, presuppose that seismic records adhere to the properties of a stationary random process. Consequently, strong vibrational events, such as the one depicted in Figure 8A, can severely compromise the final interpretation. In contrast, the present study seeks to extract geological information directly from such high-amplitude events, provided they are dominated by Rayleigh surface waves. The presence of these events in the microtremor records thus provides the fundamental basis for our methodology.

The subsequent analysis focuses on the characteristics of high-SNR events within the microtremor data. An SNR threshold is first established based on data quality, from which high-SNR events, each with a duration of 10 s (determined by site conditions and target depth), are extracted from the 600-s records at each station. A variable

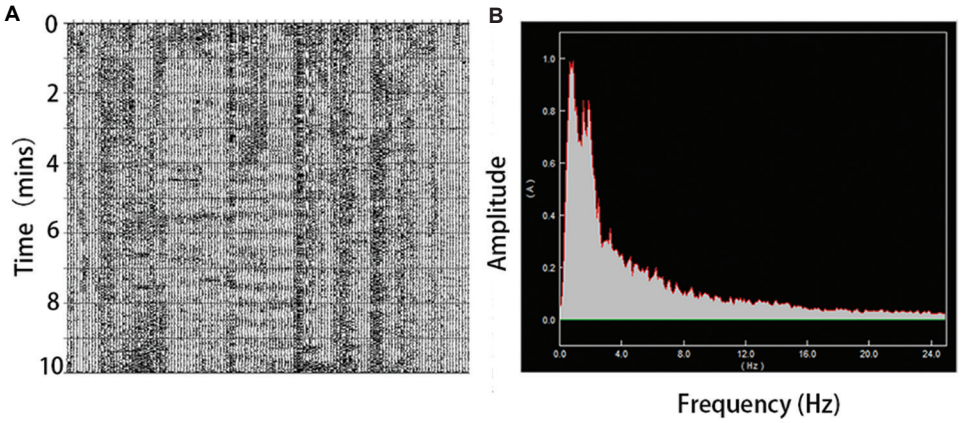


**Figure 7.** Seismic records and their corresponding amplitude spectrum. (A) The vertical-component seismic records from 132 channels, each with a 10-min duration. (B) The amplitude spectrum corresponding to (A).

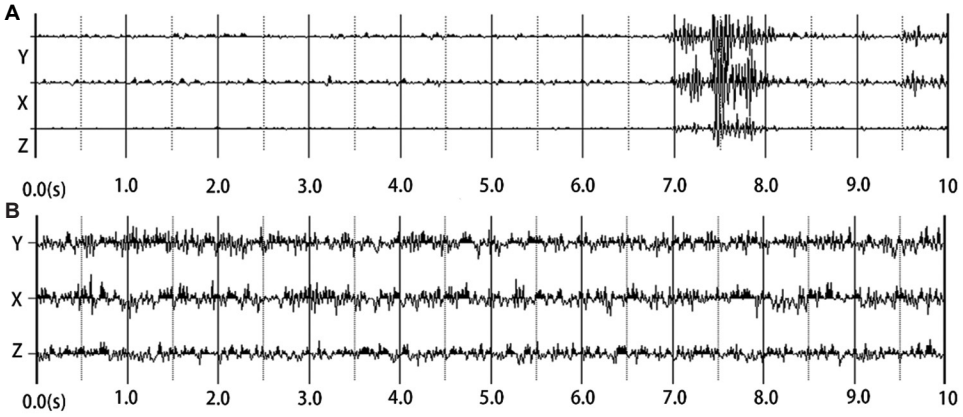


**Figure 8.** Three-component seismic records, where X, Y, and Z denote the two horizontal and vertical components, respectively. Panels (A) and (B) are microtremor records extracted from the 10-min, three-component seismic data after band-pass filtering from 0.1 Hz to 30 Hz.

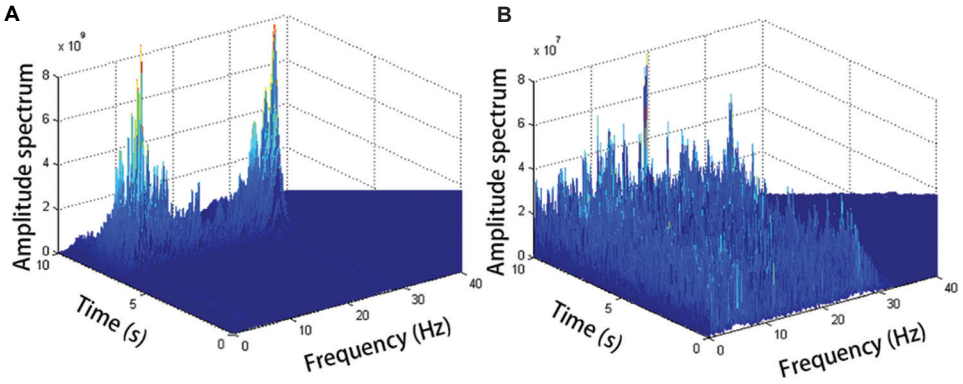


**Figure 9.** Time-frequency spectra. Panels (A) and (B) show the spectra for vertical component records containing a high-signal-to-noise ratio event and for those without, respectively.

number of such events, resembling those in Figure 8A, are identified at each location. If a station fails to produce an event meeting the initial criterion, the SNR threshold is incrementally lowered, or an estimation is performed using data from adjacent stations. It is important to note that the selected high-amplitude signals may originate from either Rayleigh surface waves or linearly polarized body waves.

Following the selection of high-SNR events, it is necessary to discriminate between signals dominated by Rayleigh waves and those dominated by linearly polarized waves. Phase-difference filtering is applied to all selected high-SNR events to isolate the former, with the objective of identifying at least one Rayleigh wave event for each of the 132 stations. It is crucial to note that this filtering step serves exclusively as a screening mechanism and is not part of the final signal processing for analysis.

Figure 10 displays the particle motion trajectories for 20 of the selected Rayleigh wave-dominated records. Although these signals are primarily composed of Rayleigh waves, they still contain high-frequency interference outside the target band and residual linearly polarized waves. As a result, the trajectories exhibit an overall elliptical shape but are chaotic and lack a clear, well-defined geometry. Direct determination of the propagation direction from such raw trajectories would be significantly compromised by this interference, and accurate calculation of the ellipticity would be infeasible.

Time-frequency analysis is a standard technique for the investigation of microtremor signals, as it facilitates the clear discrimination of the principal components within a seismic record. Therefore, in this study, we applied time-frequency analysis to all Rayleigh wave-dominated records to identify the principal component of the signal, which is defined as the frequency, $f_0$, at which the energy is maximal. Subsequently, a band-pass filter centered at this $f_0$ is applied to the data. The particle motion trajectories of the processed microtremor records are presented in Figure 11.

As illustrated by the contrast between Figure 11 and the pre-filtered Figure 10, the filtering process yields distinctly elliptical particle motion trajectories, thereby

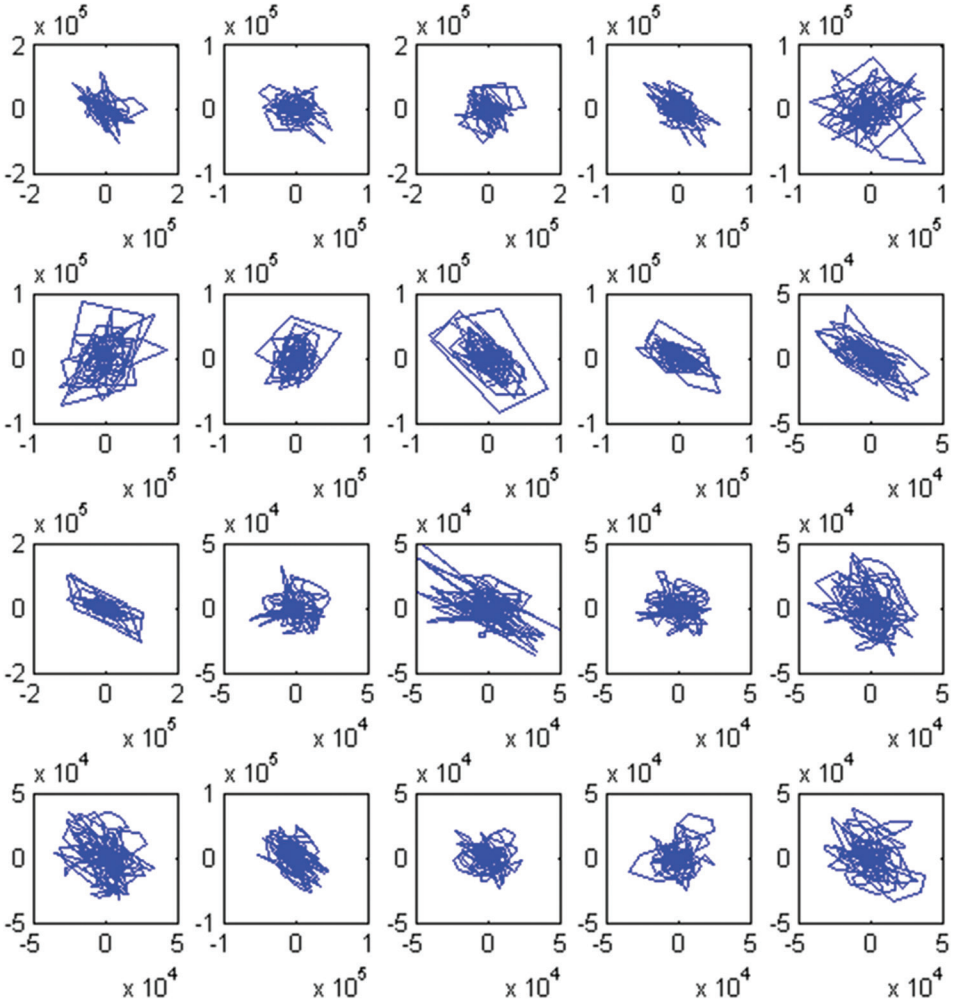

**Figure 10.** Particle motion trajectories for 20 of the selected Rayleigh wave-dominated records

confirming the dominance of Rayleigh wave components and their inherent elliptical polarization. This enables the subsequent identification of the propagation direction from the principal component of these filtered signals.

Given that numerical simulations show anomalies in polarization profiles shift along the propagation path, selecting codirectional Rayleigh waves is crucial for accurate polarization analysis. Consequently, a comprehensive directional analysis was performed on all Rayleigh wave-dominated data from the 132 geophones to identify a set of 132 high-SNR waves propagating uniformly. The 360° azimuthal range was partitioned into six 60° sectors, with the survey line oriented at 0°. Statistical results, exemplified by the 20 randomly selected geophone plots in Figure 12, reveal that most signal groups possess two to three dominant propagation directions, whereas some records exhibit a more uniform directional distribution. A notable similarity was also observed in the directional statistics among the eleven concurrently acquired data sets.

In addition, a statistical analysis of the propagation directions of all high-SNR Rayleigh wave events was conducted across all stations. From the 132 datasets, each with a 10-min recording duration, a total of 6600 events were identified. The resulting azimuthal distribution is presented in Figure 13.

As shown in Figure 13, the number of events in the 0°–30° and 270°–360° sectors is slightly lower compared to other directions, although the overall distribution remains relatively uniform. This suggests that the high-SNR Rayleigh waves in this region do not fully satisfy the assumption of spatial stationarity. Concurrently, the presence of Rayleigh waves from various propagation directions within the signals makes it feasible to select a subset of codirectional waves for analysis.

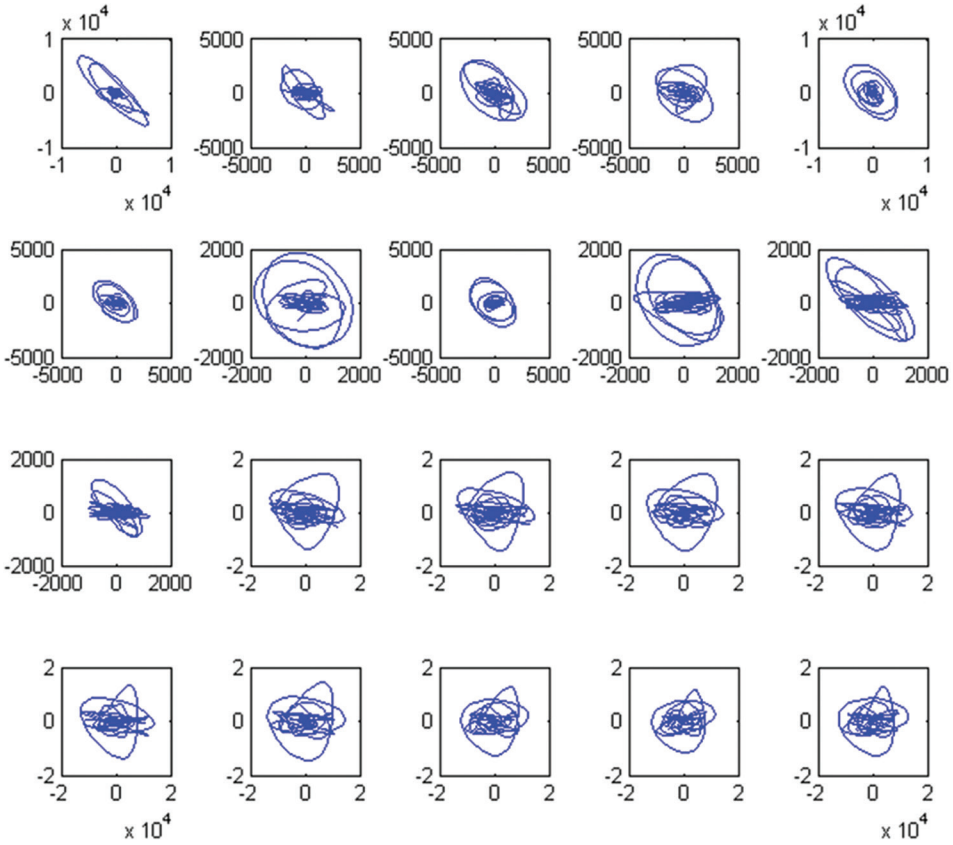

**Figure 11.** Particle motion trajectories of 20 Rayleigh wave-dominated microtremor records after principal frequency-centered band-pass filtering

In summary, the selection of high-SNR, codirectional Rayleigh waves from the *in situ* microtremor data is demonstrated to be a practical and feasible approach. Based on the results from both the overall and single-record directional statistics, the Rayleigh waves propagating in the direction opposite to the survey line were selected for the subsequent calculation of ellipticity. The analysis of the processed results is presented in the following section.

### 4.3. Data processing and analysis of results

Based on prior theoretical and numerical analyses, factors such as noise, linearly polarized waves, and multidirectional Rayleigh waves adversely affect the accuracy of ellipticity estimation. To address these issues in the field data, a six-step processing scheme was implemented: (1) band-pass filtering, (2) high-SNR event filtering, (3) phase-difference filtering, (4) directional filtering, (5) polarization filtering, and (6) ellipticity estimation.

This procedure successfully isolated 132 codirectional, high-SNR events dominated by Rayleigh waves. With the propagation direction known, the three-component data for these events were rotated to obtain the horizontal radial and vertical components. Figure 14 illustrates the phase relationship between these two components for a representative 4-s segment from 20 selected events, where the red and blue curves denote the vertical and radial components, respectively. A distinct phase difference at the peaks is evident for all signals, which validates that the selected events are indeed Rayleigh wave-dominant.

### 4.4. An ellipticity stacking methodology

The selection of high-SNR Rayleigh waves inherently allows for minor directional deviations, introducing stochastic errors into the processing results. While continuous microtremor records contain multiple such events that can be used to suppress these errors, conventional multitrace stacking is not feasible. This is because ellipticity dispersion is calculated from single-point, three-component data and is highly sensitive to propagation direction, as previously demonstrated.

To overcome this limitation, we developed a stacking and averaging method for ellipticity dispersion curves. Assuming a sufficiently long acquisition time, multiple suitable Rayleigh wave events can be identified at a given station. In this study, four sets of 132-trace, high-SNR, codirectional Rayleigh waves were extracted from 10-min

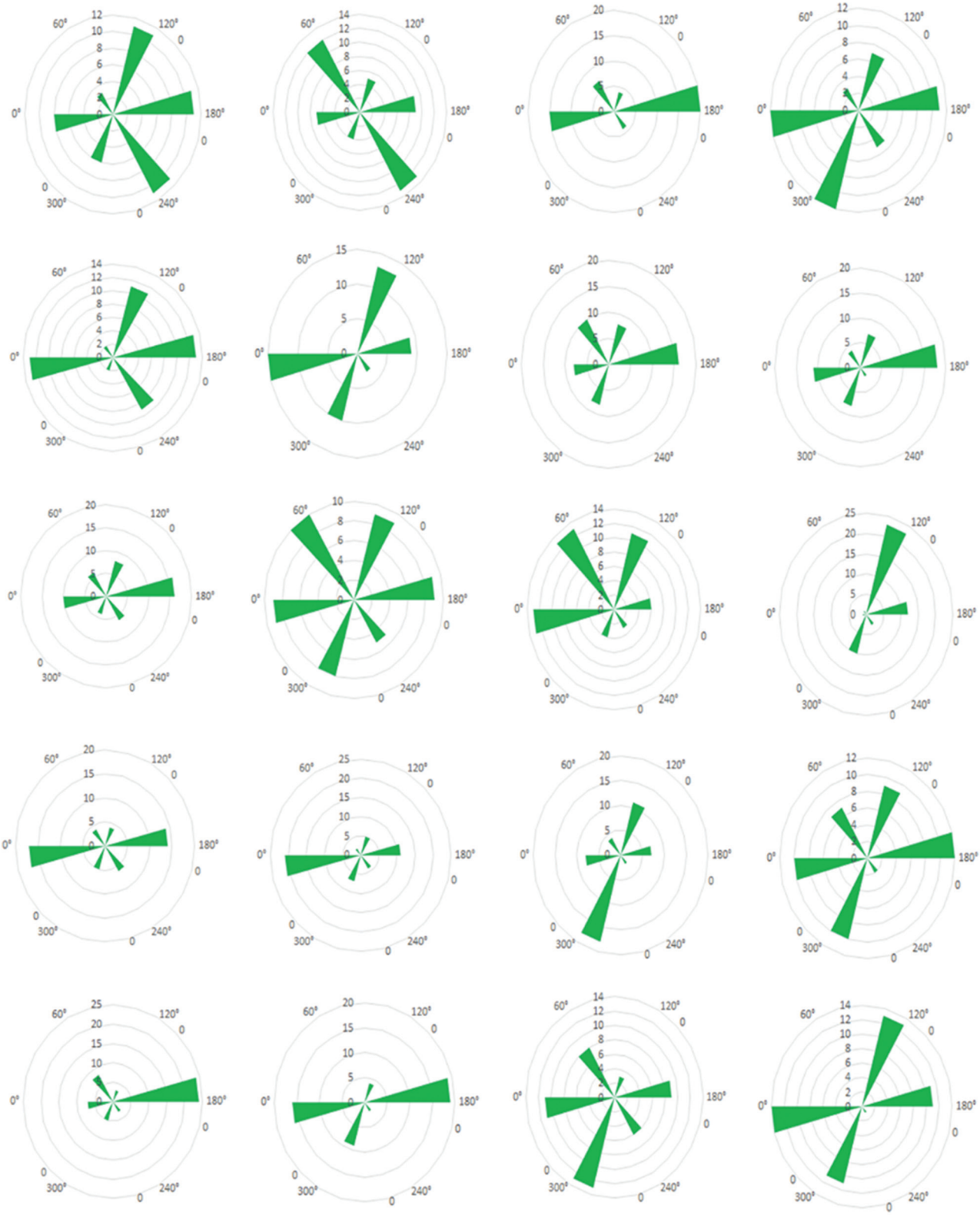

**Figure 12.** Rose diagrams of the azimuthal distribution of Rayleigh waves from data at 20 selected stations

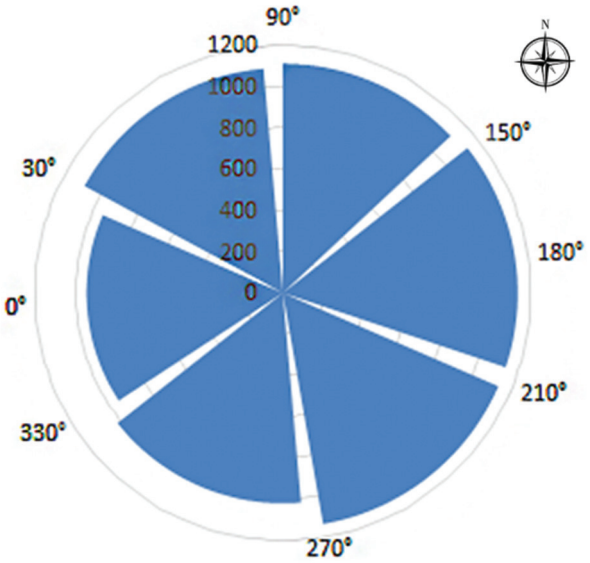


**Figure 13.** Rose diagram showing the azimuthal distribution of all Rayleigh wave events identified from the microtremor records

records. Their individual ellipticity dispersion curves were computed and then stacked to form composite profiles (Figure 15).

The four resulting profiles (Figure 15A-D) all successfully identify the low-ellipticity anomaly associated with the mined-out void at station 92100, as well as those at the fractured zones (stations 92600 and 93200). However, localized discrepancies are evident. The anomaly in Figure 15B at station 9280 is an artifact of low-frequency interference. The spurious anomaly near station 93200 in Figure 15C is inconsistent with the geological model, obscuring the fractured zone's extent. Figure 15D, while showing the major anomalies, lacks resolution in shallow structures and exhibits extremely low-ellipticity values at depth near stations 92100 and 93200. These localized artifacts, induced by data-related random errors, compromise the overall precision of the interpretation.

In this study, the ellipticity was calculated for the four selected Rayleigh wave events from each station. By

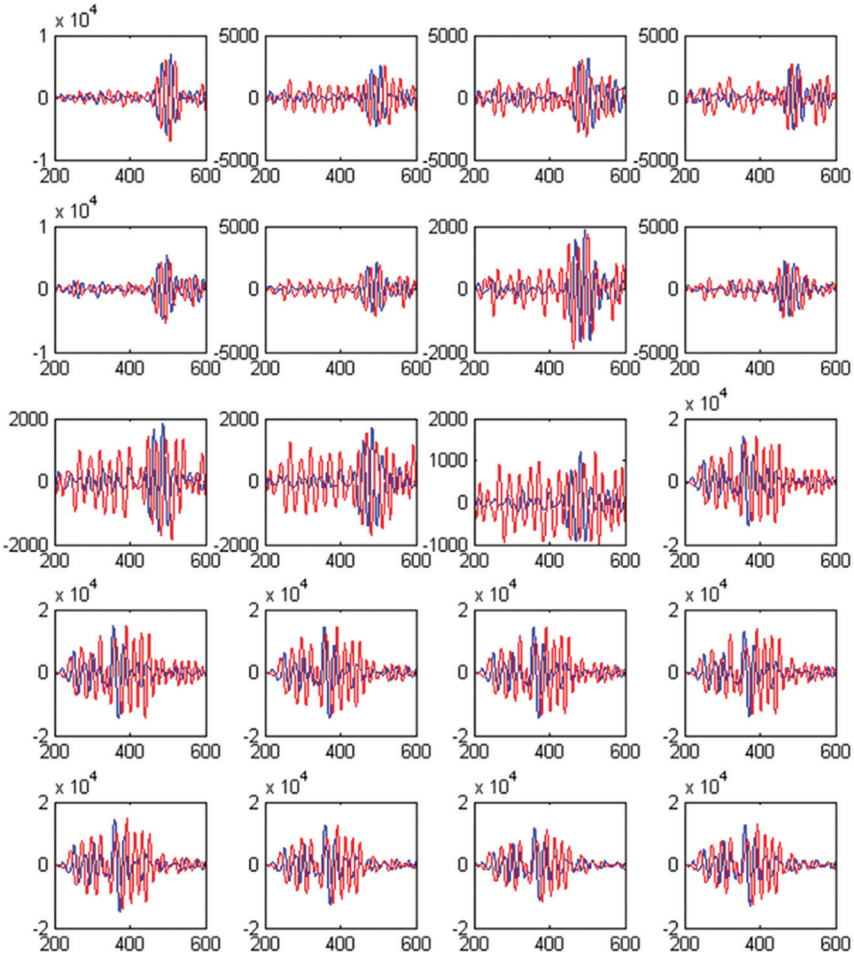

**Figure 14.** Vertical and horizontal components of seismic records for 20 Rayleigh wave events

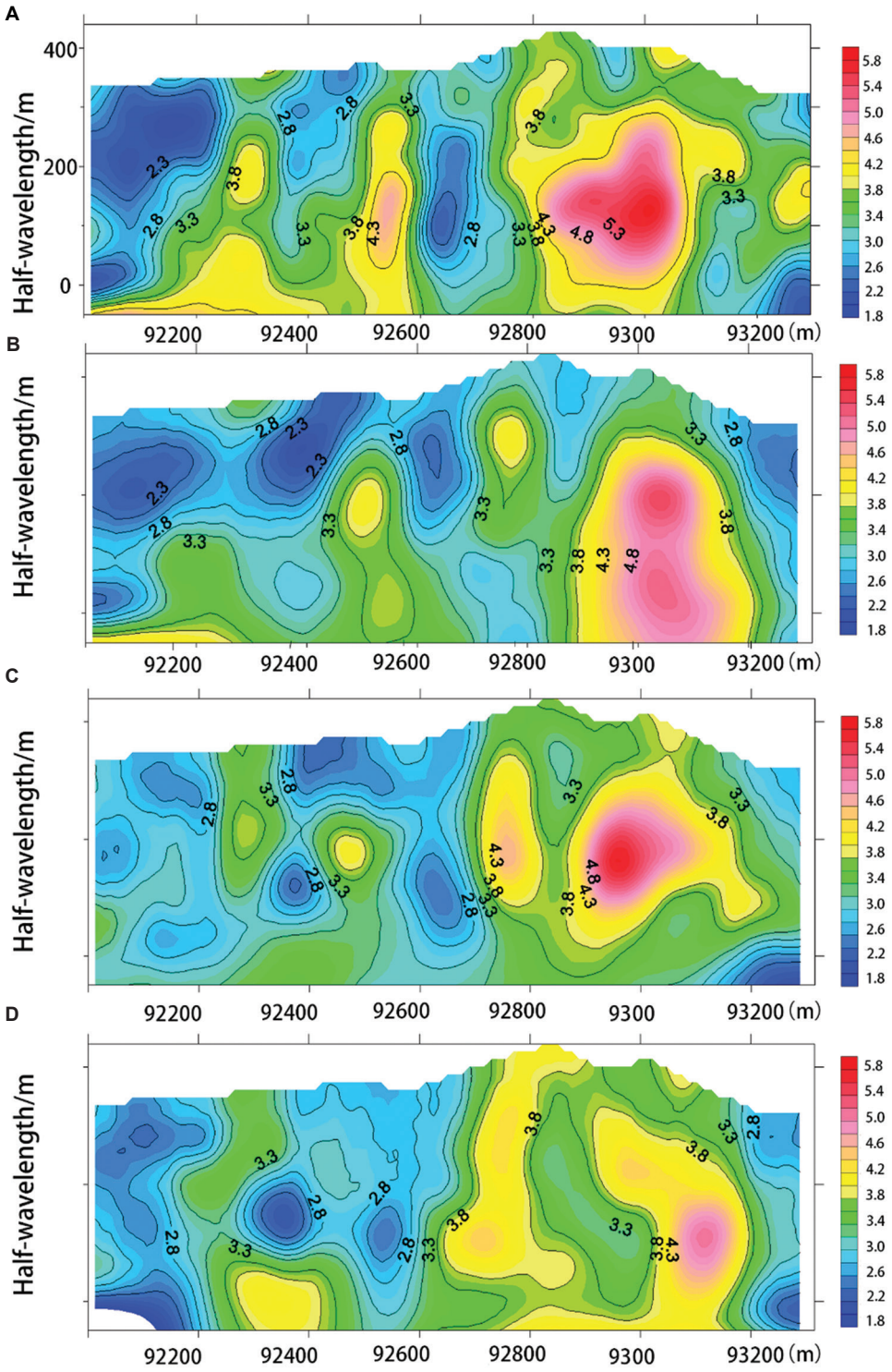


**Figure 15.** Ellipticity dispersion profiles from four individual Rayleigh wave events. (A-D) Results from a single, codirectional, high-SNR event at each station.
Abbreviation: SNR: Signal-to-noise ratio.

applying the stacking principle, the average of these four ellipticity values was computed to generate a mean ellipticity dispersion profile, as shown in Figure 16A. A comparison between Figure 16A and B reveals a distinct low-ellipticity

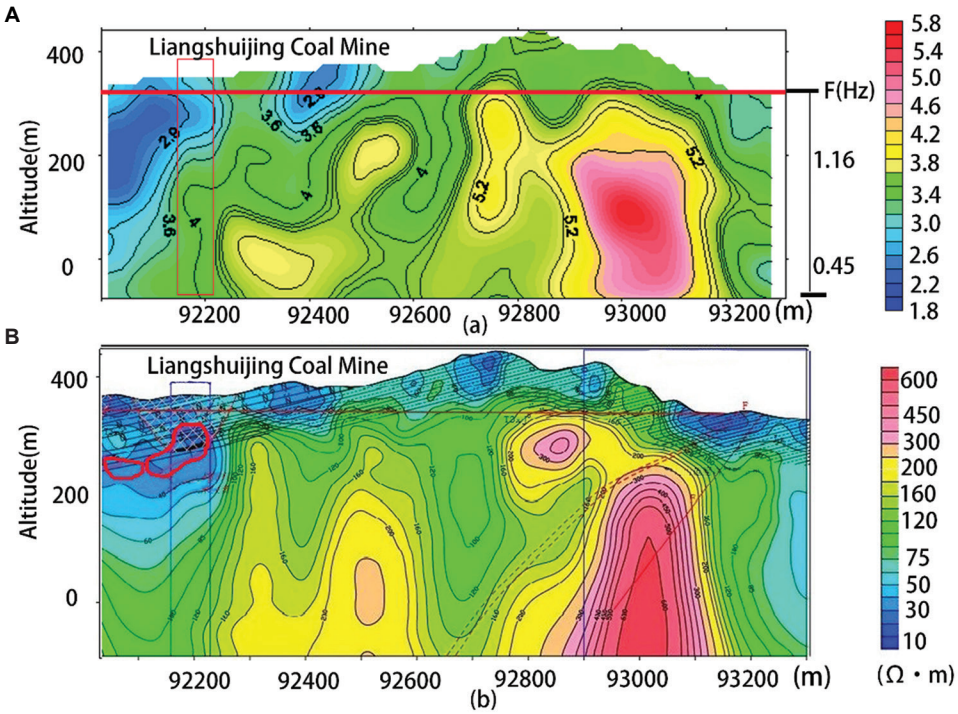


**Figure 16.** Ellipticity profiles calculated through various processing steps and the resistivity profile obtained from the magnetotelluric method. (A) Ellipticity dispersion profile of microtremor Rayleigh waves propagating along the survey line. (B) Resistivity cross-section derived from the magnetotelluric method.

anomaly at the location of the coal goaf before station 92200. Relative to the profiles in Figure 15A-D, the high-ellipticity anomaly between stations 92800–93200 and the fractured zone after station 93200 in Figure 16A exhibit a better correlation with the magnetotelluric data in detail. Notably, the ellipticity at a half-wavelength depth of 0 m is more physically reasonable. This indicates that stacking multiple events can produce a more accurate representation of the stratigraphic structure in the ellipticity profile. However, in the near-surface range of several tens of meters, its correspondence with the magnetotelluric data is less precise than that of Figure 16B. This is attributed to the fact that the 10-min dataset was insufficient to strictly select multiple codirectional Rayleigh wave events. Consequently, the selection criteria for the latter three events were relaxed in terms of SNR, which had a more significant impact on the high-frequency components. With a longer acquisition duration, the shallow part of the stacked profile could also achieve higher precision.

To further validate the practical applicability of the proposed method for site assessment and near-surface structural exploration, the results from the magnetotelluric survey along the same line were used as a benchmark. As shown in Figure 16, panel (a) presents the ellipticity dispersion profile of microtremor Rayleigh waves obtained via the aforementioned method, while panel (b) displays the resistivity profile from the magnetotelluric survey. A comparative analysis of the two profiles reveals that at chainages 92150, 92700, and 92300, the distribution of high and low ellipticity anomalies is in strong agreement with the distribution of high and low resistivity. Given that the high and low values of both ellipticity and resistivity anomalies are closely correlated with high and low Poisson's ratios, respectively, this correspondence demonstrates the feasibility of applying the ellipticity method to engineering exploration. The region delineated by the red line in Figure 16B, representing a coal mine goaf, corresponds to a distinct low-ellipticity anomaly in Figure 16A.

## 5. Conclusion

First, this study theoretically analyzed the feasibility of utilizing Rayleigh wave ellipticity for site characterization and demonstrated its effectiveness in exploring both homogeneous and heterogeneous geological features through numerical simulations. The results indicate that in the absence of noise, Rayleigh wave ellipticity can clearly identify local anomalies within the geological structure.

Second, based on field data, a method for extracting high-SNR Rayleigh waves from microtremor signals was investigated. A macroscopic analysis of the entire dataset revealed that within each 10-min record, several high-amplitude seismic pulses occur randomly, whereas the

remaining segments exhibit characteristics approaching white noise. The presence of these high-amplitude pulses provides the foundation for the proposed method. A comparison between the original particle motion trajectories of 20 selected Rayleigh wave–dominated events and those filtered at the principal frequency revealed that, despite the presence of various interfering factors, the principal component of the selected signals is indeed the Rayleigh wave. Subsequently, a directional analysis was performed on all selected Rayleigh waves to determine their primary source directions. The results indicate that the directional distribution of the waves is generally uniform, with a relatively lower incidence along the survey line direction. This confirms the feasibility of extracting codirectional, high-SNR Rayleigh waves from the microtremor data at this site.

Finally, the processed ellipticity profiles were analyzed. Through data processing steps, including interference wave separation and filtering, the influence of interfering factors—such as Rayleigh waves from different propagation directions, linearly polarized waves, and white noise in the microtremors—was mitigated. The final processed results were then compared with the resistivity profile from the magnetotelluric survey along the same line. The comparison shows that the ellipticity profile clearly delineates the coal mine goaf, fractured zones, and bedrock, exhibiting strong agreement with the magnetotelluric results. The anomalous lateral shift observed in the ellipticity profile is attributed to the propagation direction of Rayleigh waves, whereas the resistivity distribution lacks this feature due to the near-vertical incidence of electromagnetic waves. To suppress the influence of random noise, the ellipticity dispersion profiles from four selected codirectional Rayleigh wave events were stacked and averaged. While the stacked profile, like the individual profiles, clearly identifies anomalous structures such as the goaf, it demonstrates a superior consistency with the resistivity profile in terms of deep structural details. For the investigation of lateral heterogeneities, such as mine goafs in mountainous terrains, the microtremor-based Rayleigh wave ellipticity dispersion method demonstrates comparable feasibility and flexibility to the conventional magnetotelluric resistivity method.

## Acknowledgments

None.

## Funding

This research was financially supported by the Henan Province Science and Technology Research Project (Grant No. 252102320002 and 242102231058), the National Natural Science Foundation of China (Grant No. 42462028), Postgraduate Education Reform and Quality Improvement Project of Henan Province (YJS2023JD52), the Science and Technology Program of Gansu Province (Grant No. 24CXGE011), and the Science and Technology Program Funding of Tianshui Qinzhou District (Grant No. 2024-SHFZG-9168).

## Conflict of interest

The authors declare they have no competing interests.

## Author contributions

*Conceptualization:* Qingling Du, Qian Xu
*Formal analysis:* Qingling Du, Shijie Liu
*Investigation:* Shijie Liu, Qingling Du, Nan Guo
*Methodology:* Qingling Du, Shuai Liu
*Writing–original draft:* Qingling Du
*Writing–review & editing:* Qian Xu, Nan Guo, Denghui Gao

## Availability of data

Data are available from the corresponding author upon reasonable request.

## References

1. Soupios PM, Georgakopoulos P, Papadopoulos N, *et al*. Use of engineering geophysics to investigate a site for a building foundation. *J Geophys Eng*. 2007;4(1):94-103.

   doi: 10.1088/1742-2132/4/1/011

2. Rodgers MB, McVay MC, Horhota DJ, Hernando J, Paris JM. Operational limits of measuring while drilling in Florida limestone for geotechnical site characterization. *J Geotech Geoenviron Eng*. 2021;147(12):04021154.

   doi: 10.1061/(asce)gt.1943-5606.0002688

3. Wei X, Liu Y, Li X, Lu Y. Application of high density resistivity method in karst exploration: A case study. *Tehnički Vjesnik*. 2023;30(4):1283-1291.

   doi: 10.17559/tv-20230205000322

4. Lei X, Zhang J, Jin W, Han C, Xu X. The application of ambient noise and reflection seismic exploration in an Urban active fault survey. *Interpretation*. 2020;8(4):SU1-SU10.

   doi: 10.1190/int-2020-0085.1

5. Kachaje O, Yan L, Zhang Z. A Bayesian inference approach to reduce uncertainty in magnetotelluric inversion: A synthetic case study. *J Geosci Environ Prot*. 2019;7(2):62-75.

   doi: 10.4236/gep.2019.72005

6. Xia J, Miller RD, Park CB, Hunter JA, Harris JB, Ivanov J. Comparing shear-wave velocity profiles inverted from multichannel surface wave with borehole

measurements. *Soil Dyn Earthq Eng*. 2002;22(3):181-190.

doi: 10.1016/s0267-7261(02)00008-8

7. Park CB, Miller RD, Xia JH. Multichannel analysis of surface waves. *Geophysics*. 1999;64(3):800-808.

doi: 10.1190/1.1444590

8. Xia JH, Miller RD, Park CB. Estimation of near-surface shear-wave velocity by inversion of Rayleigh waves. *Geophysics*. 1999;64(3):691-700.

doi: 10.1190/1.1444578

9. Yu C, Wang Z, Tang M. Application of microtremor survey technology in a coal mine goaf. *Appl Sci*. 2023;13:466.

doi: 10.3390/app13010466

10. Aki K. Space and time spectra of stationary stochastic waves, with special reference to microtremors. *Bull Earthq Res Inst*. 1957;35:415-456.

11. Capon J. High-resolution frequency-wavenumber spectrum analysis. *Proc IEEE*. 1969;57:1408-1418.

doi: 10.1109/proc.1969.7278

12. Asten MW, Henstridge JD. Arrays estimators and use of microseisms for reconnaissance of sediementary basins. *Geophysics*. 1984;48:1828-1837.

doi: 10.1190/1.1441596

13. Horike M. Inversion of Phase velocity of long-period microtremors to the S-wave-velocity structure down to the basement in urbanized area. *J Phys Earth*. 1985;33:59-96.

doi: 10.4294/jpe1952.33.59

14. Pan YD, Gao LL, Shigapov R. Multi-objective waveform inversion of shallow seismic wavefields. *Geophys J Int*. 2020;220:1619-1631.

doi: 10.1093/gji/ggz539

15. Qingling D, Jianjun F, Yan Y, Kuanyao Z, Qian H. Application of near surface engineering defect exploration technology based on spatial autocorrelation. *Episodes J Int Geosci*. 2025;48(2):145-153.

doi: 10.18814/epiiugs/2024/024022

16. Nogoshi M, Igarashi T. On the amplitude characteristics of microtremor (part 2). *Zisin J Seismol Soc Japan 2nd ser*. 1971;24:26-40.

doi: 10.4294/zisin1948.24.1_26

17. Arai H, Tokimatsu K. S-wave velocity profiling by joint inversion of microtremor dispersion curve and horizontal-to-vertical (H/V) spectrum. *Bull Seismol Soc Am*. 2005;95(5):1766-1778.

doi: 10.1785/0120040243

18. Woodhouse JH. Surface waves in a laterally varying layered structure. *Geophys J Int*. 1974;37(3):461-490.

doi: 10.1111/j.1365-246X.1974.tb04098.x

19. Haney MM, Mikesell TD, Wijk KV, Nakahara H. Extension of the spatial autocorrelation (SPAC) method to mixed-component correlations of surface waves. *Geophys J Int*. 2012;91(1):189-206.

doi: 10.1111/j.1365-246x.2012.05597.x

20. Maupin V. 3-D sensitivity kernels of the Rayleigh wave ellipticity. *Geophys J Int*. 2017;211(1):107-119.

doi: 10.1093/gji/ggx294

21. Berbellini A, Schimmel M. Ferreira AM, Morelli A. Constraining S-wave velocity using Rayleigh wave ellipticity from polarization analysis of seismic noise. *Geophys J Int*. 2019;216(3):1817-1830.

doi: 10.1093/gji/ggy512

22. Tokimatsu K, Miyadera Y. Characteristics of Rayleigh waves in microtremors and their relation to underground structures. *J Struct Constr Eng*. 1992;30:439.

23. Fäh D, Kind F, Giardini D. Inversion of local S-wave velocity structures from average H/V ratios, and their use for the estimation of site-effects. *J Seismol*. 2003;7(4):449-467.

doi: 10.1023/b: jose.0000005712.86058.42

24. Yu W, Liu Z. A numerical study of the Rayleigh wave particle motions excited by a point source and Poisson's ratio for lateral inhomogeneous half-spaces. *J Appl Geophys*. 2015;123:242-255.

25. Tran TT, Vinh PC, Ohrnberger M, Malischewsky P, Aoudia A. An improved formula of fundamental resonance frequency of a layered half-space model used in H/V ratio technique. *Pure Appl Geophys*. 2016;173:2803-2812.

doi: 10.1007/s00024-016-1313-0

26. Bignardi S. The uncertainty of estimating the thickness of soft sediments with the HVSR method: A computational point of view on weak lateral variations. *J Appl Geophys*. 2017;145:28-38.

doi: 10.1016/j.jappgeo.2017.07.017

27. Picotti S, Francese R, Giorgi M, Pettenati F, Carcione JM. Estimation of glacier thicknesses and basal properties using the horizontal-to-vertical component spectral ratio (HVSR) technique from passive seismic data. *J Glaciol*. 2017;63(238):229-248.

doi: 10.1017/jog.2016.135

28. Abu Zeid N, Corradini E, Bignardi S, Nizzo V, Santarato G. The passive seismic technique "HVSR" as a reconnaissance tool for mapping paleo-soils: The case of the pilastri archaeological site, Northern Italy. *Archaeol Prospect*. 2017;24(3):245-258.

doi: 10.1002/arp.1568

29. Fäh D, Kind F, Giardini D. A theoretical investigation

of average H/V ratios. *Geophys J Int*. 2001;145(2): 535-549.

doi: 10.1046/j.0956-540x.2001.01406.x

30. Xu H, Yin X, Qi Q, Mi B, Sun S, Luo Y. Determination of near-surface shear-velocity structure based on the joint inversion of Rayleigh-wave dispersion and ellipticity from multistation active-seismic records. *Geophysics*. 2022;87(3):21-32.

doi: 10.1190/geo2021-0176.1

31. Du Q, Pan Y, Yan Y. Research and application of Rayleigh wave extraction method based on microtremors signal analysis. *Front Phys*. 2023;11:1158049.

doi: 10.3389/fphy.2023.1158049

32. Poggi V, Fäh D, Burjanek J, Giardini D. The use of Rayleigh-wave ellipticity for site-specific hazard assessment and microzonation: Application to the city of Lucerne, Switzerland. *Geophys J Int*. 2012;188(3):1154-1172.

doi: 10.1111/j.1365-246x.2011.05305.x

ACCSCIENCE PUBLISHING

Journal of Seismic Exploration

ARTICLE

# Microtremor investigation and geological verification of the eastern segment, north margin active fault of Hami Basin, Xinjiang, China

**Xu Song[1,2,3†], Guanghong Ju[4†], and Jun Shen[1,2,3*]**

[1]Institute of Disaster Prevention, Sanhe, Hebei, China

[2]Beijing Disaster Prevention Science and Technology Corporation Limited, Beijing, China

[3]Hebei Key Laboratory of Earthquake Dynamics, Sanhe, Hebei China

[4]Power China Northwest Engineering Corporation Limited, Xi'an, Shaanxi, China

## Abstract

The eastern section of the Northern Margin Fault of the Hami Basin is located in the easternmost part of the active tectonic belt of the Tianshan Mountains, and is an important active fault in the region. Since major projects need to consider avoiding or adopting anti-fracture measures, it is necessary to determine the exact location of the fracture, three-dimensional (3D) orientation, and other anti-fracture-related parameters. To obtain the accurate location and 3D geometric parameters of the rupture, we carried out a systematic study in three typical sites based on remote sensing interpretation and geomorphological survey, and the comprehensive use of microdynamic detection and trench verification. The results show that the fracture section is spreading in east–west direction, with a total length of about 35 km, and is dominated by retrograde movement, which is geomorphologically manifested as a fault steep canyon on the pre-hill flood fan, with the height of steep canyon up to 11–13 m. The microdynamic profiles reveal the deep production of the fracture, with the width of the fracture zone ranging from 60 to 100 m, and the dipping angle ranging from 60° to 70°; and the trench validation reveals that the dipping angle of the faults is slowing down to 35°–45° at the surface, showing a "deep and steep" pattern, and the "deep and steep dipping angle" is also shown. The geometrical structure of the fault is characterized as "deep, steep, and shallow." As an emerging geophysical detection method, the micro-motion detection technique used in the study showed good recognition ability in complex terrain and thick cover conditions, improving the detection accuracy of fracture location. The results of the study not only enrich the understanding of the active features of the Northern Margin Fault of the Hami Basin, but also provide the fault resistance parameters for the evaluation of regional seismic hazard and the selection of sites for major projects, and expand the scope of application of the micro-motion detection method in the study of active faults, providing an important reference for the regional tectonic evolution and seismic resistance of the project.

***Keywords:*** Eastern segment of the Northern Margin Fault of the Hami Basin; Microdynamic detection; Groove; Geometric structure

†*These authors contributed equally to this work.*

***Corresponding author:**
Jun Shen
(shenjun@cidp.edu.cn)

**Citation:** Song X, Ju G, Shen J. Microtremor investigation and geological verification of the eastern segment, north margin active fault of Hami Basin, Xinjiang, China. *JSeismicExplor.* 2026;35(1):101-118. doi: 10.36922/JSE025380073

**Received:** September 18, 2025

**Revised:** November 20, 2025

**Accepted:** November 24, 2025

**Published online:** December 23, 2025

**Copyright:** © 2025 Author(s). This is an Open-Access article distributed under the terms of the Creative Commons Attribution License, permitting distribution, and reproduction in any medium, provided the original work is properly cited.

**Publisher's Note:** AccScience Publishing remains neutral with regard to jurisdictional claims in published maps and institutional affiliations.

## 1. Introduction

The northern margin fault of the Hami Basin is located at the boundary between the eastern part of the Tianshan Orogenic Belt and the Hami Basin. It is one of the most important active faults that determine the topography and structure of the eastern Tianshan region. This fault is a deep and major fault that cuts through the Moho discontinuity.[1] Located at the easternmost end of the active Tianshan orogenic belt, the area is characterized by the weakest current tectonic activity within the Tianshan Mountains. Its Late Quaternary deformation intensity is markedly lower than that of major faults in the western and central Tianshan regions. In recent years, as research into the tectonic dynamics and neotectonic movements of the eastern Tianshan has deepened, the Northern Margin Fault of the Hami Basin has also become a focal point of investigation.

Existing studies have mainly relied on remote sensing image interpretation and geomorphological survey methods to preliminarily identify the macroscale distribution characteristics of the northern margin fault of the Hami Basin, and analyzed its activity by combining the Quaternary stratigraphic features and gully displacement phenomena.[2] The northern margin fault of the Hami Basin extends for around 300 km along the southern foothills of the Baryn and Halik mountains. The segment along the southern foothills of the Baryn Mountains is usually referred to as the western segment, and the segment along the southern foothills of the Halik Mountains as the eastern segment (Figure 1). Based on the geometric distribution characteristics of the fractures, the western section is divided into the Dewaoli segment, Xishan segment, and Zhongyingtai segment; the eastern section is divided into the Shichengzi segment, Shangmiyang-Bamudun segment, and Dongtaizi segment. Research on the Northern Margin Fault of the Hami Basin has largely focused on the western segment between Dewaoli and Zhongyingtai. The Dewaili segment extends approximately 50 km from west of Liushugou Village eastward through Dewaili Township to Sidaogou. Using cosmogenic nuclide dating, the vertical slip rate of this fault segment was determined to be 0.10–0.18 mm/year.[2] The Xishan segment, approximately 24 km long, extends eastward from Akta to Xishan Township. High-precision digital elevation model data acquired through unmanned aerial vehicles was combined with chronological sample test results to calculate the sliding rates for Xishan, ranging from 0.06 to 0.08 mm/year.[3] The Zhongyingtai segment spans approximately 25 km, extending from Hulugou through Xiwudeke to the Nanshankou area. Thermoluminescence dating indicates an average vertical slip rate of 0.31 ± 0.03 mm/year for this segment.[4] However, due to inherent limitations of thermoluminescence dating, the results for landform surface ages may not be precise. The Shichengzi segment extends eastward from Shichengzi to the Yushugou area, with a surface trace length of approximately 10 km; the Shangmiyang segment extends from the Shangmiyang tributary to the Bamudun area, approximately 35 km long; the Dongtaizi segment extends eastward from Bamudun through Wulaitai to the area east of Tianshengquan, with a surface trace length of approximately 25 km. Due to the fault's considerable length, slip rates along its strike exhibit spatial and temporal variations. Consequently, the slip rate at any single point cannot fully represent the activity intensity of the entire fault. However, from a spatial distribution perspective, the slip rates of the Dewaili and Zhongyingtai segments are largely consistent, while the Xishan segment exhibits a slightly lower slip rate. Temporally, the slip rate remained relatively stable from the late Middle Pleistocene to the mid-Late Pleistocene.

The eastern portion of the northern margin fault in the Hami Basin has been less extensively studied compared to the western segment. No dedicated research has been conducted into its spatial distribution, precise location, or most recent period of activity. Investigations into active faults require not only the collection of macroscopic data on the geometric and kinematic characteristics of the fault to assess seismic hazard, but also the determination of its precise location and three-dimensional (3D) orientation. This is essential for engineering projects that require active faults to be avoided or anti-fault measures to be implemented (Figure 2). The eastern segment of the northern margin fault primarily develops within a foothill zone consisting of bedrock, landslide deposits, and coarse-grained slope-alluvial sediments. Fault dislocation landforms and geological outcrops are not distinctly evident. Research methodologies should therefore incorporate geophysical techniques, remote sensing interpretation, and field geological and morphological surveys. Current geophysical methods for active fault studies primarily encompass seismic, electromagnetic, and microgravity techniques.[5-8] This study investigates the 3D orientation of the northern margin fault in the Hami Basin by integrating microtremor detection with geological and geomorphological surveys.

Microtremor survey method uses faint vibrations on the Earth's surface that are not caused by seismic activity for exploration purposes.[9,10] This technique is crucial for identifying shallow geological structures and active faults. This technique uses faint surface vibration signals as natural seismic sources to reflect the velocity structure of strata

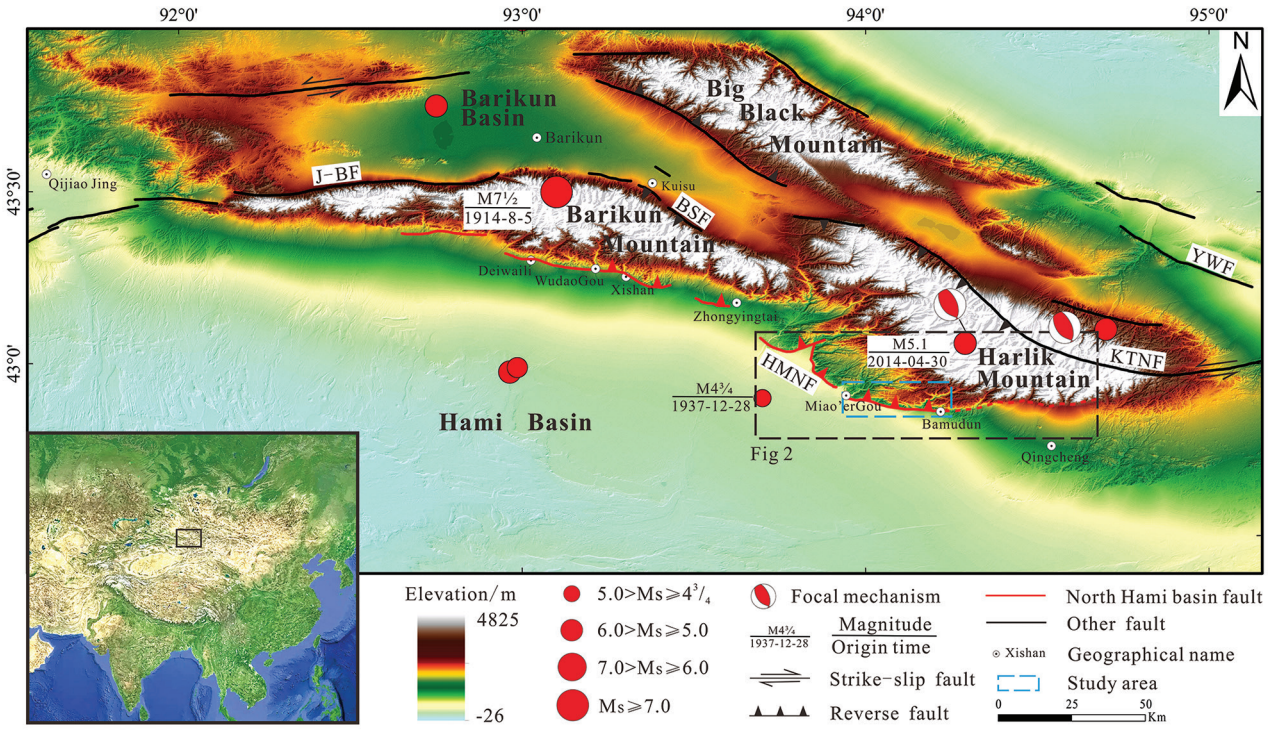


**Figure 1.** Regional fault distribution map
Abbreviations: HMNF: Northern Margin Fault of the Hami Basin; NKTF: Harlik Mountains North Margin Fault; YWF: Yiwu Basin South Margin Fault.

and site characteristics effectively. Compared to traditional artificial-source methods, microdynamic detection offers advantages such as strong interference resistance, high operational efficiency, and terrain adaptability.

In recent years, the microtremor survey method has been increasingly widely used in active fault research. Early studies revealed the subsurface velocity structure in the Kanto Plain via the spatial autocorrelation (SPAC) method[11] and confirmed the non-linear relationship between the subsurface shear wave velocity structure and dispersion curves using the divergent genetic algorithm.[12] With the development of technology, the applicability of this method has been further expanded: the S-wave velocity structure within a depth range of 100 m has been successfully obtained using microtremor arrays,[13] and background noise imaging with dense arrays has also verified the feasibility of inverting the broadband Rayleigh wave phase velocity.[14] At the application level, microtremor surveys have been effectively applied to multiple aspects, such as the precise location of concealed faults,[15] subsurface geological stratification, and concealed structure detection,[16-18] providing important technical support for active fault research.

In this study, we used microtremor detection methods combined with remote sensing, geological and topographical surveys, and trenching techniques to determine the exact location and 3D orientation of the eastern part of the northern margin fault in the Hami Basin, yielding relevant parameters for the engineering avoidance of active faults and the engineering resistance to faulting. This research also addresses the lack of studies on this fault segment and improves our understanding of the active characteristics and deformation mechanisms at the easternmost tip of the Eastern Tianshan Mountains. Furthermore, it contributes to the body of case studies on microtremor detection in active fault research, thereby promoting the wider application of this method. In addition, through this study, we explore the methods for detecting active faults beneath coarse-grained debris flow deposits.

## 2. Geological setting

The Tianshan Orogenic Belt is a typical reactivated intra-continental orogenic belt within the Eurasian continent[19] and is one of the region's largest young mountain systems. Its tectonic evolutionary history can be traced back to the Late Palaeozoic era. It subsequently underwent renewed compression and uplift during the Cenozoic era due to the long-range effects of plate collision, thereby forming a prototypical intra-continental reactivated orogenic belt.[20-24] North-south shortening deformation is regulated

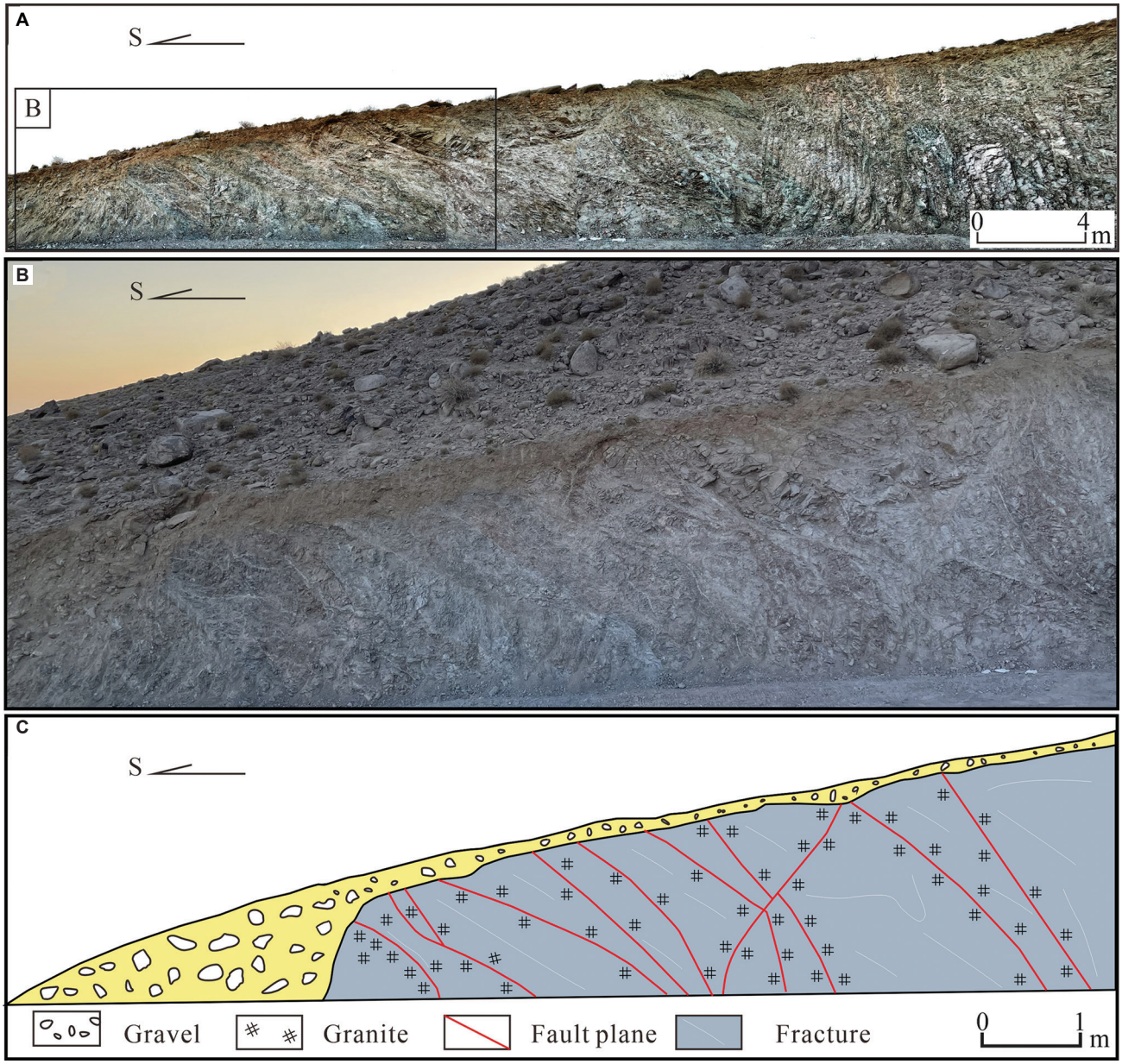


**Figure 2.** Photographs and structural profile of the fault outcrop exposed at the adit portal. (A). Overview photograph of the fault outcrop, looking toward the west; (B) Close-up view of the main fracture zone, looking toward the west; (C) Interpretive cross-section illustrating the geometry of the main fault.

and accommodated by thrust faults in the foreland and large-to-medium strike-slip faults within the mountain basins.[25,26] The eastern and western Tianshan exhibit distinct tectonic patterns and activity intensities; the eastern Tianshan demonstrates a significantly lower crustal shortening rate than the western Tianshan.[27-29] Previous studies indicate that active faults in the eastern Tianshan region exhibit a gradual decrease in slip rate from west to east.[30] Furthermore, the easternmost Halik Mountains region adjoins the Altai uplift zone to the north and the Gobi–Altai tectonic transition zone to the east. This region is situated at the junction of the active Tianshan tectonic zone and the Western Mongolian tectonic activity zone.[31-33]

The northern margin fault of the Hami Basin, located in the Eastern Tianshan region, is an important part of the Tianshan orogenic belt. The collision and ongoing convergence of the Indo-Eurasian plates have had a pronounced effect on it, forming a typical reactivated intra-continental orogenic belt. As a key active fault in the eastern part of the Eastern Tianshan region, it exerts significant control over the geological structural pattern of the northern margin of the Hami Basin. The region features

multi-tiered foreland alluvial fans, with extensive alluvial gravel surfaces interbedded with coarse landslide debris and minor aeolian loess deposits. The underlying bedrock is primarily granite or Neogene strata. The spaces between adjacent alluvial fans are predominantly filled with coarse landslide debris or bedrock.

The northern margin fault of the Hami Basin runs from the Hami Basin to the Baryn and Kalik mountains. In terms of geotectonics, it forms a boundary fault that separates the ancient North Tianshan island arc belt from the Hami terrane.[21] The fault generally trends from northwest to northeast, extending for around 300 km. Its western extension potentially connects with the Jianquanzi–Barkol Fault, while its eastern terminus may be linked to the left-lateral strike-slip fault system of the Gobi Tianshan. The northern margin fault of the Hami Basin is clearly visible in satellite imagery as a series of linear features and is evident topographically as a series of discontinuous fault scarps on the alluvial fan at the foothills (Figure 3). Fault activity shows pronounced NE-SW convergence,[34] with post-Late Quaternary activity controlling the coupling between the Hami Basin and the Eastern Tianshan Mountains. However, seismic activity along the northern margin fault remains relatively low. Instrumental records indicate comparatively weak tectonic movement, slow energy accumulation, and infrequent occurrence of minor seismic events.[35]

## 3. Methodology

This study focuses on the eastern segment of the northern margin fault in the Hami Basin. Using a comprehensive approach that incorporates microtremor detection techniques and trench investigations, it employed remote sensing image interpretation and field geological and geomorphological surveys to systematically examine the fault's planar distribution characteristics and profile features.

### 3.1. Integrated remote sensing interpretation and field investigation

Accurately determining the spatial location of the fault is fundamental to identifying and analyzing its activity. Remote sensing image interpretation is an important means of understanding the distribution of faults and provides key control for subsequent field surveys and geophysical exploration.

This paper is based on the AuVue interactive map platform, and various high-resolution remote sensing image data were collected and organized, including data from the Four Dimensions Earth and Jilin-1 satellites. By combining 2D planar images and 3D visualization models, the area around the temple gully and the Bayugundu River was remotely interpreted, and the main fractures in the study area were identified and extracted (Figure 4).

The study area lies between the Yagudun and Miaogou rivers, spanning a total length of approximately 35 km. The two rivers formed three-tiered terraces on the eastern and western sides of the study area, respectively. Multiple alluvial fans of varying scales and distinct morphologies lie between these two rivers. Comparing with the research results in adjacent areas, for example, the existing dating results of the abandonment age of alluvial fans in Dewaili and Xishan areas show that the alluvial fans within the study area can be classified into three main stages.[4] They formed sequentially in the Middle or Early Late Pleistocene (Fan1), the Late Pleistocene (Fan2), and the Holocene (Fan3). Fault scarps developed intermittently on Fan2 and Fan3, whereas they are less clearly defined on Fan1.

To the west of the mouth of the Yagudun River and to the east of the mouth of the Miaogou River, the foreland area exhibits distinct fault-block topography, characterized by escarpments that are distributed intermittently across the Late Pleistocene alluvial-fluvial fan. Field investigations and tracing along the fault strike revealed distinct escarpments

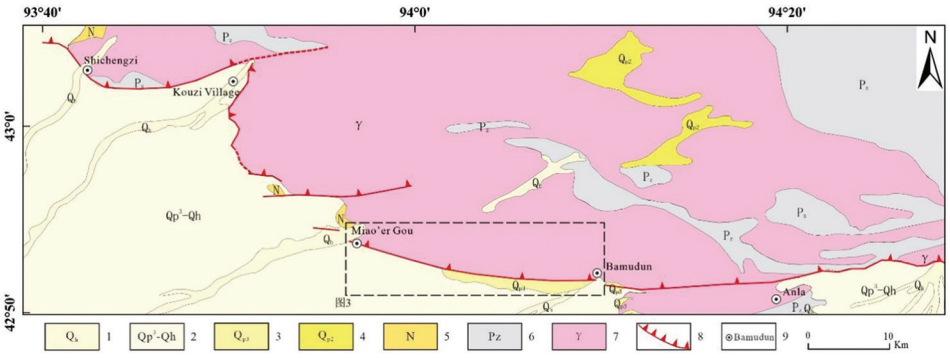


**Figure 3.** Fracture map of the northern margin of the Hami Basin. (1) Holocene Series; (2) Upper Pleistocene–Holocene Series; (3) Upper Pleistocene Series; (4) Middle Pleistocene Series; (5) Neogene System; (6) Paleozoic Erathem; (7) Granite; (8) Northern Margin Fault of Hami Basin; (9) Place name.

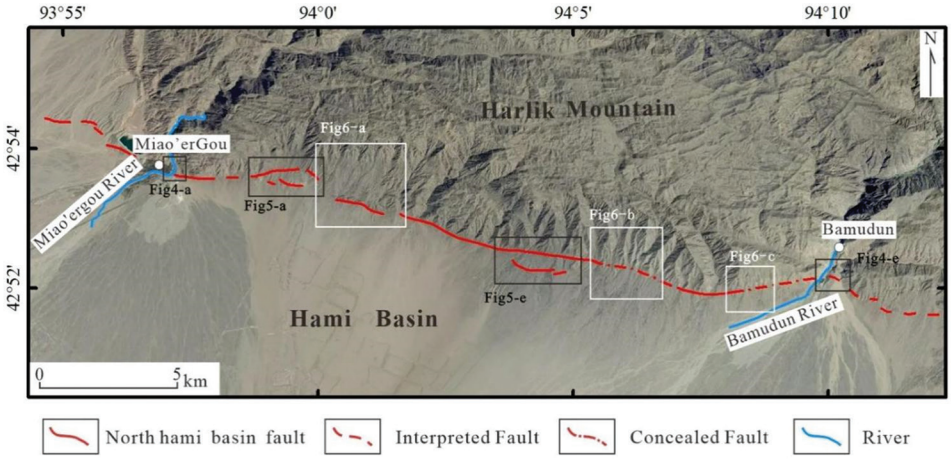


**Figure 4.** Distribution map of faults in the research area

on the foreland alluvial fan. The higher T3 terrace has escarpments reaching heights of up to 11 m, while the T2 terrace has escarpments of 1–3 m. No significant faulting deformation is evident on the T1 terrace.

Figure 5A shows satellite image of the left bank of the Miaogou River. Along the left bank, on Terrace T3, a series of distinct fault scarps is clearly visible. These scarps exhibit pronounced topographic boundaries in the image, indicating significant vertical displacement. In contrast, no pronounced faulting was observed on the river terraces, likely due to their incomplete development and human alterations. Figure 5B shows a photograph taken in the field of the fault at the leading edge of the foreland fan. The image reveals a distinct fault scarp on Terrace T3 with an approximate height of 12 m.

Moreover, a fault section has been exposed by an artificial road cutting along the lateral margin of the alluvial fan at the mouth of Miaogou Gully. This fault exhibits thrusting characteristics, with the exposed section showing brick-red Neogene mudstone being thrust northwards onto gravelly deposits (Figure 5C). Figure 5D shows the geological cross-section, with the fault plane marked by a red line at an inclination of approximately 40°. There is a significant lithological contrast on either side of the fault: the hanging wall consists of granite overlain by fluvial-alluvial gravel, while the footwall comprises fluvial-alluvial gravel.

Figure 5E shows the T3 terrace on the left bank of the Yagidun River. This terrace exhibits distinct fault characteristics that correspond to those of the Miaogou River terrace (Figure 5A). Figure 5F depicts the eastern bank of the Bayudun River. A distinct fault scarp, measuring around 13 m in height, can be seen on the river terrace along the eastern bank at the river's outlet. This further corroborates the presence of active tectonic features on the river terraces within the study area.

Figure 6A is located 2.3 km east of Miaogou and preserves remnants of the Fan3 alluvial fan. Faulting activity in this area has created a discontinuous fault-block topography that appears as steep fault scarps with exposed red strata on remote sensing image (Figure 6A and B). These steep escarpments are adjacent to the alluvial fan deposits at the foot of the mountains, exhibiting well-defined morphology. This further confirms the active nature of the fault since the Late Quaternary period (Figure 6B). Figure 6C depicts an active fault outcrop at the location shown in Figure 6A, while Figure 6D presents the corresponding cross-section. The cross-section shows that the hanging wall of the fault consists of red sandstone and mudstone from the Neogene, which is overlain by a layer of coarse cobbles and gravel. Due to fault displacement, the red Neogene mudstone has undergone tensile deformation, and no red strata are visible beneath the gravel layer on the footwall.

Figure 6E shows a series of steep, discontinuous fault scarps distributed across the Fan2 alluvial fan, approximately 2 km west of the Yagidun River. The cumulative height of these scarps is up to 11 m (Figure 6F).

A comprehensive interpretation of remote sensing image and field survey findings reveals that a series of steep escarpments has developed extensively across the foreland slopes, from the Miaogou River to the Bamudun River. These escarpments are predominantly located at the edges of alluvial fans or at the interface between bedrock and loose deposits. However, as the morphology of some escarpments may be influenced by non-tectonic factors such as differential erosion, uneven deposition, or landslide accumulation, surface morphology alone is insufficient to definitively determine whether they are the result of fault displacement. Therefore, to clarify the presence of faults at the locations of these escarpments, verification through microtremor and trenching investigations is required. This

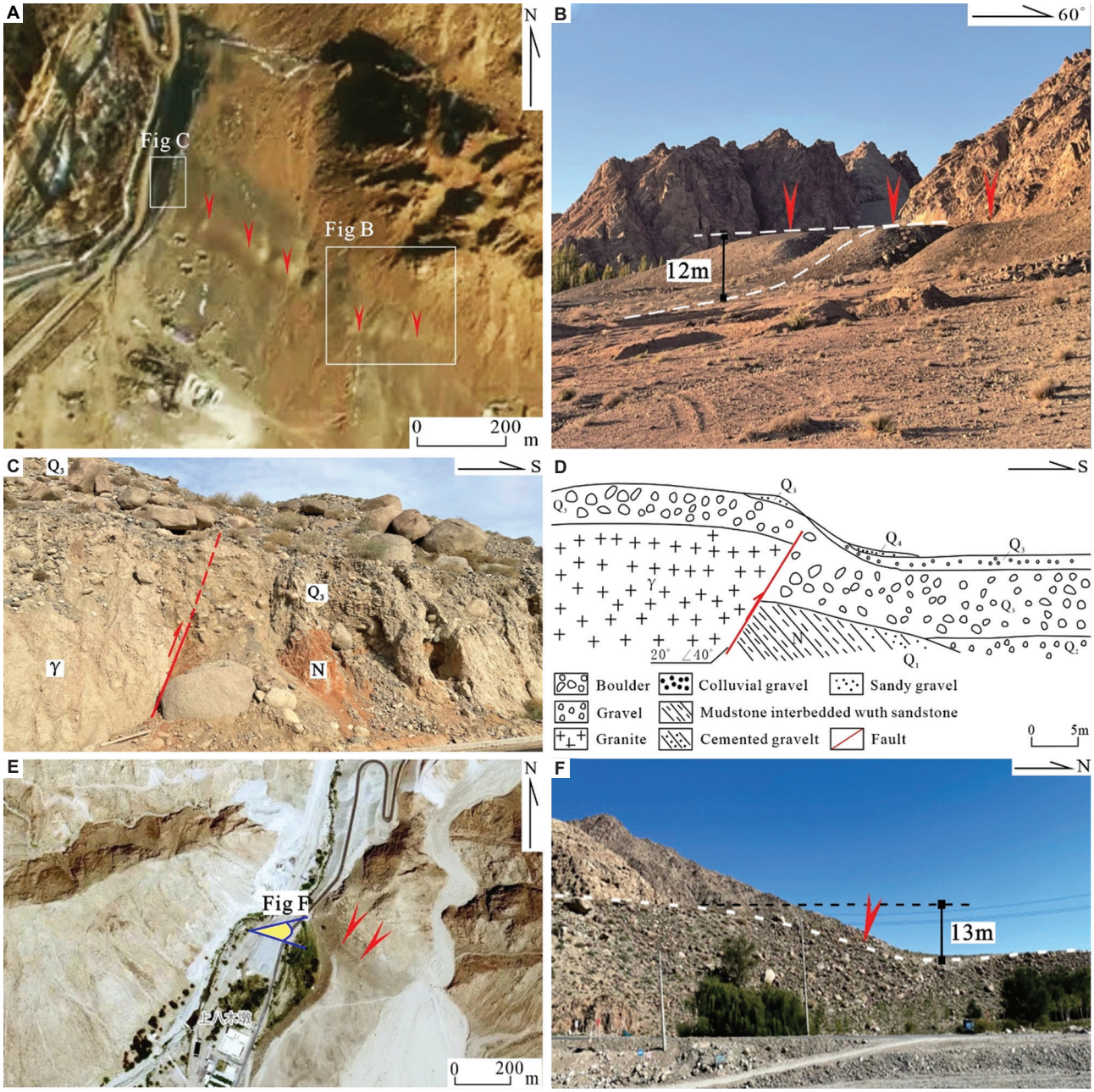


**Figure 5.** A faulted steeple on a floodplain fan. (A) Remote sensing image showing fault scarp on the left bank of Miaoergou River; (B) Photograph of the fault scarp on the left bank of Miaoergou River. (C) Fault outcrop in the piedmont alluvial fan at the estuary of Miaoergou River; (D) Profile of the fault outcrop in the piedmont alluvial fan at the estuary of Miaoergou River; (E) Image of the fault scarp on the T3 terrace of the left bank of the Bamudun River; (F) Photograph of the fault scarp on the T3 terrace of the left bank of the Bamudun River.

approach also provides more compelling evidence for the precise location and 3D orientation of the fractures.

### 3.2. Microtremor survey

To determine the exact location of the fault more precisely, ascertain the width of the fault zone, and reveal its downward extension and profile characteristics, we deployed microtremor survey lines at three locations spanning the steep escarpments of the Xinxing, Xinxing East, and Hongxing pumped-storage hydropower stations (Figure 7). The aim is to verify the existence of the fault and, in conjunction with geological and topographical surveys, determine its 3D orientation.

Given the actual conditions of the study area, the GN309 microtremor detection system developed by Hefei Guowei Electronics Co., Ltd. was employed for microtremor data

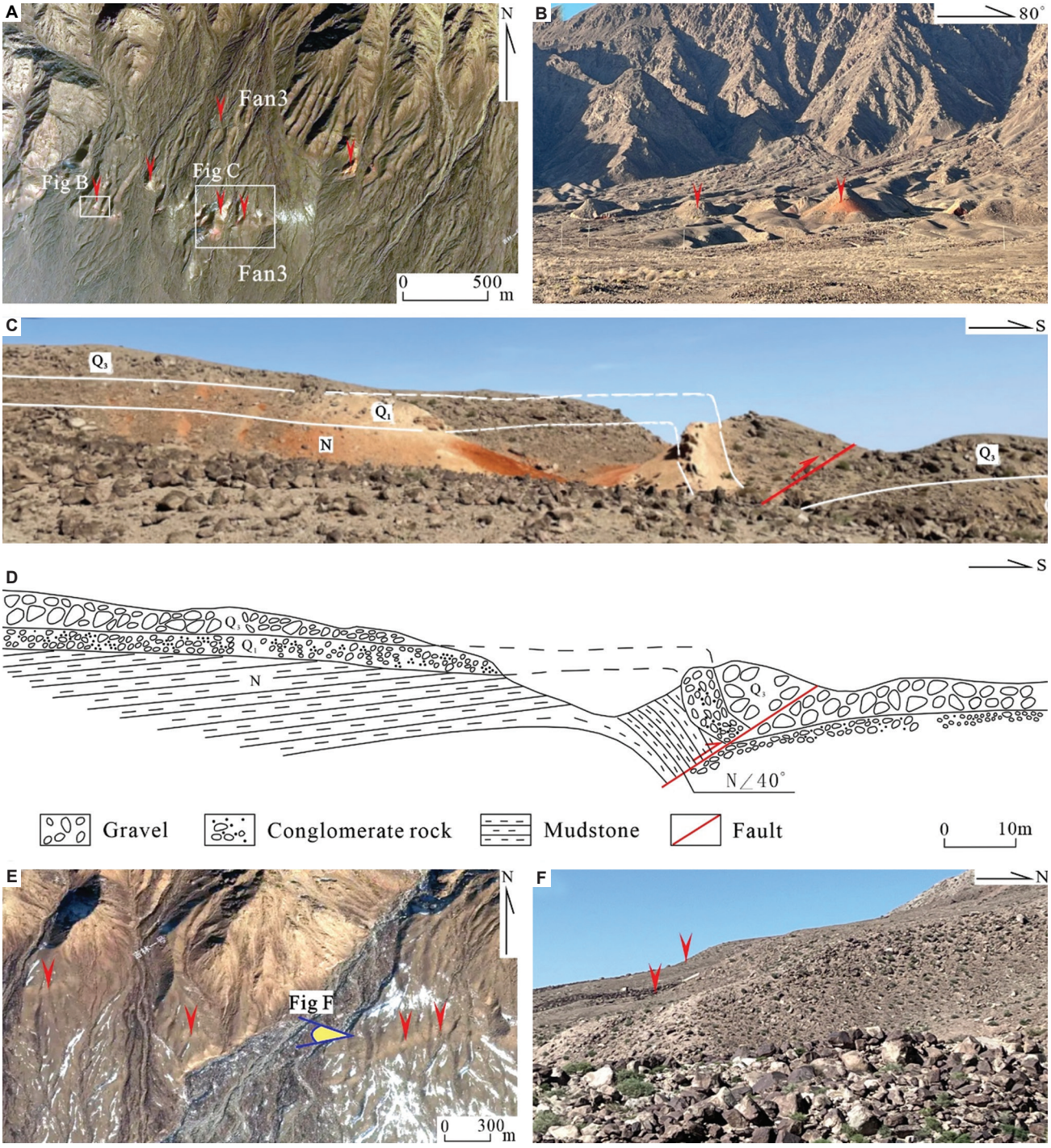


**Figure 6.** Images of a faulted steeple on a floodplain fan. (A). Remote sensing image of the area 2.3 km east of Miaoergou; (B) Photograph of the fault scarp 2.3 km east of Miaoergou; (C) Fault outcrop, west of the Lower Reservoir of Xinxing Pumped Storage Power Station; (D) Profile of the fault outcrop, west of the Lower Reservoir of Xinxing Pumped Storage Power Station; (E) Image of the fault scarp, situated at 2 km west of Bamudun River; (F) Photograph of the fault scarp, situated at 2 km west of Bamudun River.

acquisition. Three microtremor survey lines were deployed on-site. To accurately infer fault locations, all three lines traversed trenches: MTS-a (1.6 km), MTS-b (1 km), and MTS-c (1 km). Station spacing was 10 m, with a sampling rate of 2 ms and a sampling duration of 30 min. All three lines employed a straight-line regular array layout, utilizing an active-source excitation with reverse-phase observation for data acquisition. During data processing, surface wave

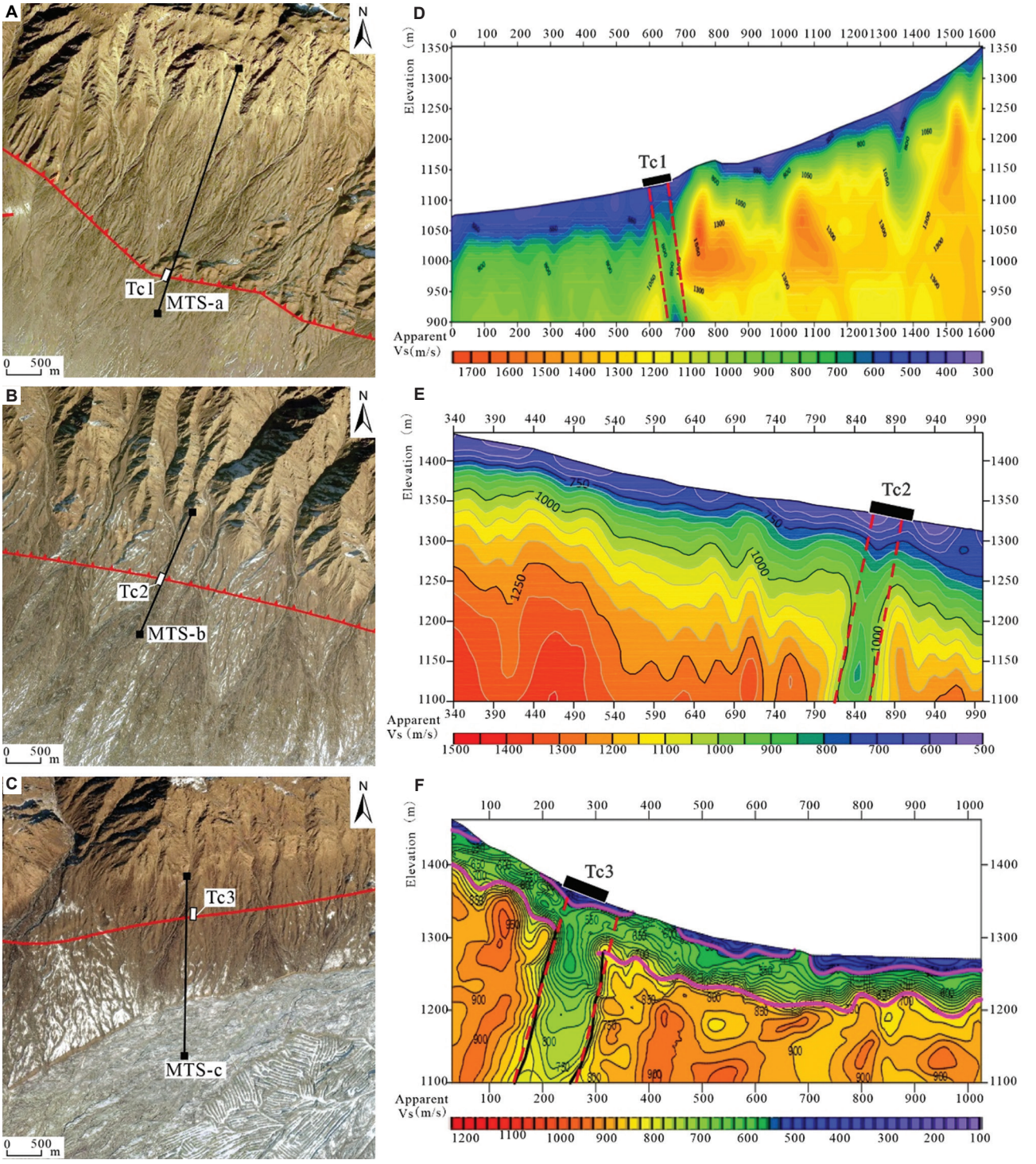


**Figure 7.** Analysis diagram of micromotion profile. (A) Remote sensing interpretation map around the microtremor survey line layout site near Xinxing; (B) Remote sensing interpretation map around the microtremor survey line layout site near East Xinxing; (C) Remote sensing interpretation map around the microtremor survey line layout site near Hongxing; (D) Shear-wave velocity inversion profile from microtremor survey line MTS-a; (E) Shear-wave velocity inversion profile from microtremor survey line MTS-b; (F) Shear-wave velocity inversion profile from microtremor survey line MTS-c.

signals from the array records were calculated using the SPAC method, and Rayleigh wave dispersion curves were extracted via frequency-Bessel function fitting. Finally, the dispersion curve was inverted using a genetic algorithm to

**Table 1. Micro-movement measurement line status report**

| Line number | Line length (m) | Point spacing (m) | Pile number (m) | Dip direction | Dip (°) | Fracture zone width (m) |
|---|---|---|---|---|---|---|
| MTS-a | 1600 | 10 | 600–700 | N | 60–70 | 60–100 |
| MTS-b | 1000 | 10 | 720–880 | N | 60–70 | 60–100 |
| MTS-c | 1000 | 10 | 200–300 | N | 60–70 | 60–100 |

obtain high-resolution shallow shear wave velocity (Vs) profiles for the study area. Shear wave velocity effectively reflects the compaction and diagenetic degree of strata. Generally, when Vs values are less than 500 m/s, strata are predominantly Quaternary loose sediments; when Vs exceeds 500 m/s, the strata can be identified as bedrock or strongly consolidated bedrock layers.

The results from the three survey lines (Table 1) indicate that all microtremor profiles exhibit a shallow low-velocity zone with Vs < 500 m/s in the upper part of the profile, representing debris flow deposits or fluvial/aeolian accumulation layers. Beneath this lies a bedrock layer with Vs > 500 m/s, separated by a distinct interface, indicating stable stratigraphic structure (Figure 7). In addition, some areas exhibit intermediate-velocity layers with Vs values between 500 and 800 m/s, approximately 70–80 m thick. These are interpreted as zones of fully weathered to strongly weathered bedrock. This layer appears as a transitional distribution in the microtremor profiles and serves as a key basis for fault identification and stratigraphic segmentation.

By comparing microtremor inversion results with field topographic phenomena, it was found that the profile structure exhibits a strong correlation with topographic features, such as variations in landslide deposit thickness and undulating elevations, as observed during field surveys. This suggests that microtremor profiles are highly reliable for identifying shallow geological structures.[36,37] Microtremor detection provides the 3D orientation and profile characteristics of deeper fracture sections. However, no significant anomalies in shear wave velocity were detected within the approximately 80 m thickness near the surface. Consequently, the near-surface structure and orientation of the fracture remain unclear. To more accurately reveal the fault's near-surface location and orientation, verification through trenching methods is required.

### 3.3. Validation by trenching

Test pits were excavated at the surface projections of anomalous zones identified in microtremor inversion profiles to reveal the location and orientation of faults near the surface and to verify the reliability of microtremor detection results. These are designated as Test Pits TC1, TC2, and TC3 (Figures 8-10). The phenomena exposed along these three profiles were similar. The main strata consisted of landslide debris characterized by relatively large gravel particles, poor rounding and sorting, and minor intercalations of fine-grained aeolian sediments. Stratification was indistinct.

#### *3.3.1. Trench TC1*

Trench TC1 is located approximately 600–700 m along the MST-a microtremor profile and is situated within a distinct linear fault zone (Figure 7A). The TC1 trench is approximately 40 m long and has exposed a complete Quaternary stratigraphic section.

The trench exposed two north-dipping reverse faults trending north with an inclination of approximately 40°, exhibiting an overall stepped distribution. The faults primarily manifest as granite bedrock thrusting over gravel layers, forming distinct fault scarps. The gravel layers can be subdivided into three zones: The northern fault is overlain by the uppermost gravel layer, and the southern fault is covered by the two layers of gravel above it (Figure 7A and B). This indicates that faulting activity occurred before the overlying strata were deposited.

Detailed photographs of the section (Figure 8C) and corresponding sketches (Figure 8D) clearly show that the fault cuts through from the reddish-brown basal layer to the light grey layer. A debris zone is visible around the fault plane, with some sedimentary layers showing signs of bending and compression deformation. The detailed cross-section on the opposite side (Figure 8E) and the corresponding sketch (Figure 8F) reveal multiple secondary faults. These faults predominantly penetrate upwards through the central gravel layer, with some exhibiting thrust-overlapping relationships. This indicates multi-phase faulting activity in this area.

#### *3.3.2. Trench TC2*

TC2 is located at the anomaly point along the micro-motion survey line MTS-B (Figure 7B). The trench excavation site is located at the bottom of an eroded gully characterized by significant topographical undulations. A thin layer of landslide debris covers the surface, and the exposed stratum comprises coarse-grained alluvial gravel deposits. Due to the loose strata and large gravel grain

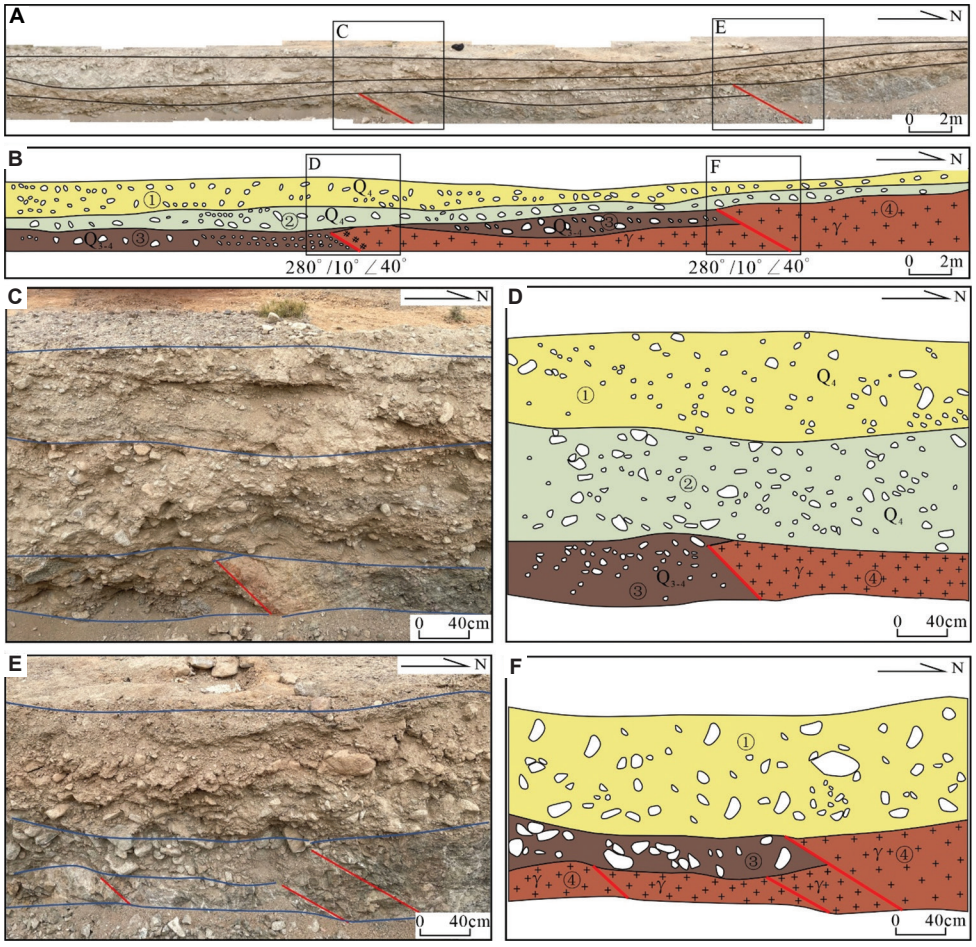


**Figure 8.** Analysis diagram of trench TC1. (A) Spliced photo of the trench; (B) Sketch profile of the trench; (C, E) Detailed photo of the trench; (D, F). Partial sketch of the trench.
Notes: (1) Light yellow slope-wash and proluvial gravel layer; (2) Gray-green alluvial-proluvial gravel layer; (3) Gray-brown gravel layer; (4) Granite.

size, excavation was challenging and resulted in uneven trench walls (Figure 9A). As can be seen from the trench profile (Figure 9A and C), the strata are mainly made up of Quaternary fluvial-colluvial gravels that exhibit the typical characteristics of alluvial fan deposition. Three stratigraphic units can be discerned from base to summit: a yellowish-grey layer containing boulders and gravel; a gray gravel layer; and a gray layer containing boulders and fluvial-colluvial gravel. The coarse gravel layer exhibits poor sorting and pronounced particle support, with localized large boulder flotation observed. The overlying gray, boulder-bearing fluvial-alluvial gravel layer is dominated by boulders, with indistinct bedding and localized blocky structures visible.

As shown in Figure 9B, an active fault structure was identified in the central section of the trench profile. The fault plane exhibits an overall southward dip with an inclination of approximately 45°. The fault cuts through the underlying coarse gravel layer and extends into the middle-upper strata. Sediments near the fault zone display pronounced structural deformation characteristics. Sediments on the hanging wall of the fault exhibit relatively coarse grain sizes and show signs of rearrangement. Within the shear zone, fine-grained material has been compressed, and local gravel has been reoriented along the fault plane to form elongated, banded structures. These structural bands indicate the direction of shear. Based on a combined assessment of the geometric structure of the fault and its tectonic characteristics, it is determined that this fracture is an active fault with pronounced thrusting characteristics.

The local sketch of the trench (Figure 9C) reveals that multiple small secondary slip surfaces have developed within the shear zone. These surfaces are interbedded with lenses of fine-grained sediments and clastic gravel. They are wedge-shaped, filling the interior of the fault, and their formation is suggested to have occurred through the superposition of multiple episodes of activity. Near the trench floor, the gravel layer is distinctly oriented at

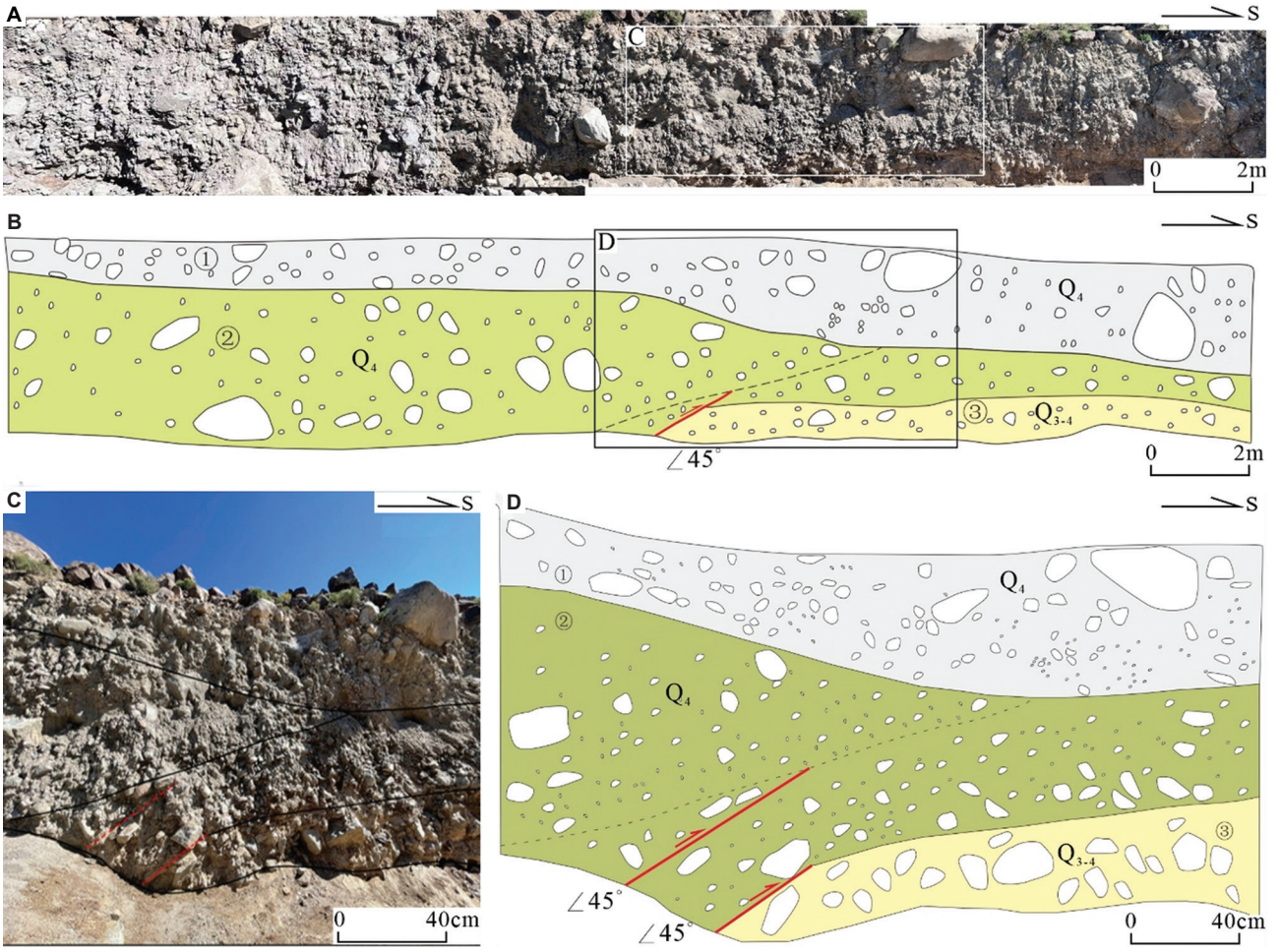


**Figure 9.** Analysis diagram of trench TC2. (A) Spliced photo of the trench; (B) Sketch profile of the trench; (C) Detailed photo of the trench; (D) Partial sketch of the trench.
Notes: (1) Gray diluvial-proluvial gravel layer with megaclasts; (2) Gray sandy gravel layer; (3) Yellowish-gray sandy gravel layer with megaclasts.

an angle to the original bedding. This indicates the fault's path, with an approximate dip angle of 45°.

The local sketch of the trench (Figure 9C) reveals that multiple small secondary slip surfaces have developed within the shear zone. These surfaces are interbedded with lenses of fine-grained sediments and clastic gravel. They are wedge-shaped, filling the interior of the fault, and their formation is suggested to have occurred through the superposition of multiple episodes of activity. Near the trench floor, the gravel layer is distinctly oriented at an angle to the original bedding. This indicates the fault's path, with a dip angle of approximately 45°.

Moreover, as can be seen from the cross-section and photographs, this fault primarily displaces the gravel layer deposited on the slope during the Q3 period. Due to the disordered deposition of this gravel layer, no dislocation is observed in the overlying layer, which is approximately 1 to 2 m thick.

### *3.3.3. Trench TC3*

Trench TC3 is located at the anomaly point identified along the MST-E profile (Figure 7C). The trench is located within a thin layer of debris flow deposits that cover the foothills, where the terrain is steeply sloped. The northern section of the trench exposed granite bedrock, while the southern section comprised coarse-grained debris flow deposits and fluvial-alluvial sediments with smaller gravel particles on the surface. Due to the thick, loosely structured overburden, excavation was challenging and resulted in uneven trench walls.

The strata exposed within the trench consist primarily of loose Quaternary deposits and heavily weathered granite. The southern section predominantly features Quaternary fluvial-alluvial deposits and landslide debris, while the northern section comprises heavily weathered granite bedrock overlaid by a layer of Quaternary landslide gravel. The central section of the trench lies within a concentrated

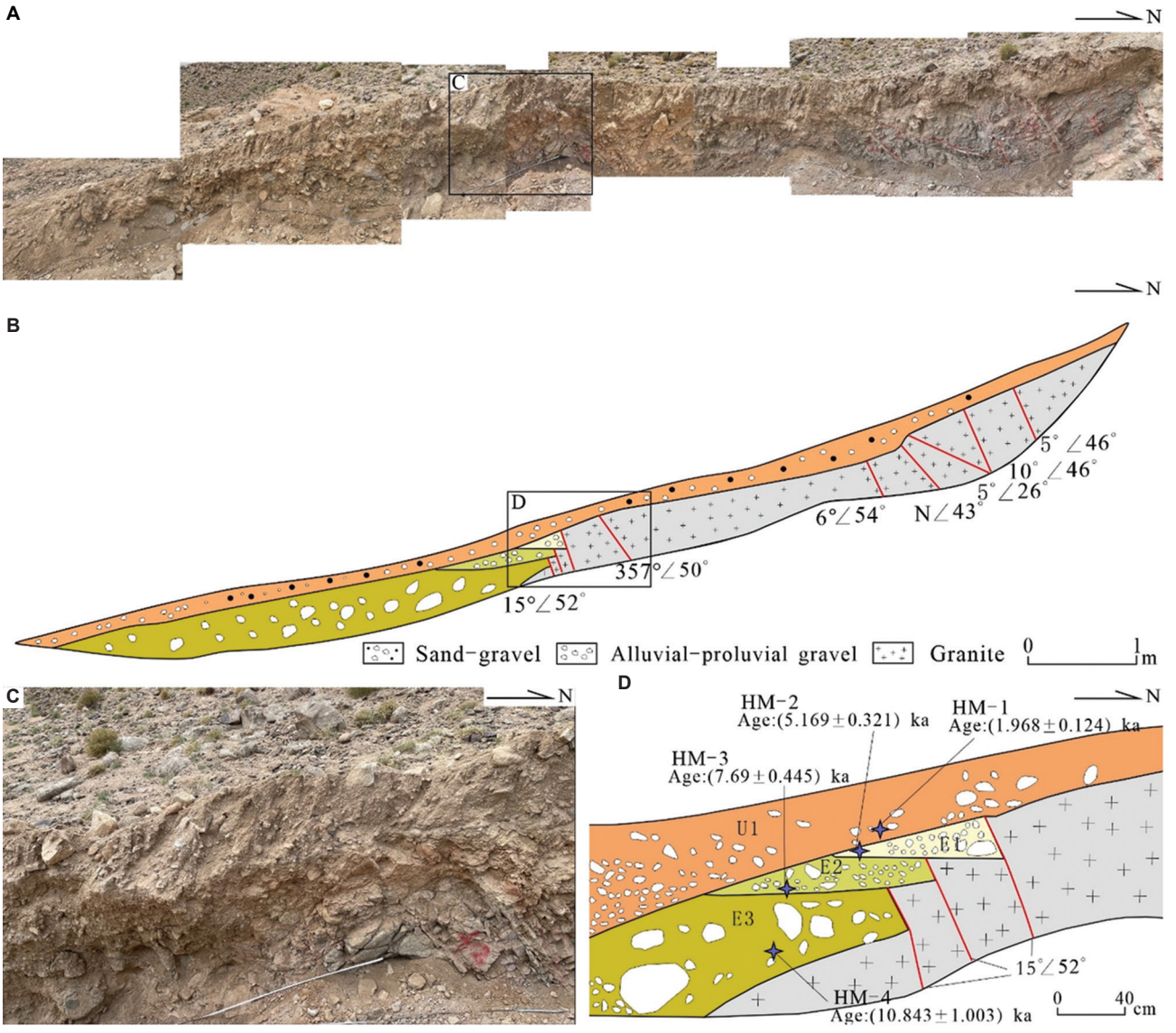


**Figure 10.** Analysis diagram of trench TC3. (A) Spliced photo of the trench; (B) Sketch profile of the trench; (C) Detailed photo of the trench; (D) Partial sketch of the trench.

fault zone where a distinct, stepped fault scarp is formed between the Quaternary deposits and the underlying bedrock (Figure 10C).

Multiple sets of faults developed within the northern section of the granite. These were primarily distributed along the contact zone between the Quaternary sediments and the granite, as well as within the overlying strata. The faults have a strike range of between 357° and 15° and a dip angle predominantly concentrated between 45° and 55°, though exceeding 50° locally in some instances (Figure 10A and B).

An active fault zone inclined from north to south was identified at the mid-section of the trench. This fault zone comprises three smaller sections (Figure 10D), designated as F1, F2, and F3. The fault zone cuts through both the granite bedrock and the overlying Quaternary gravel layer, creating a distinct, multi-tiered, step-like thrust structure. The parallel-to-strike foliation that developed along the sections indicates pronounced shear deformation characteristics.

Two wedge-shaped depositional sequences, controlled by fractures, formed in the central section of the trench. These sequences exhibit relatively consistent lithological characteristics. The basal layer consists of slightly bedded gravel containing moderately sorted, poorly rounded cobbles that predominantly exhibit angular morphology.

The upper section comprises an unbedded deposit of mixed gravel and silt clasts that lacks distinct bedding. This deposit was likely formed through rapid deposition or landslide processes. The lowest stratum also comprises a gravel layer deposited by a landslide containing boulders. Its contact surface with the underlying granite dips southwards, exhibiting localized shear-pull deformation (Figure 10D).

Based on the structural analysis of the cross-section, the magnitude of the vertical displacement of each fault varies. F1 exhibits the greatest displacement, at around 40 cm, while F2 and F3 show displacements of approximately 20 cm (Figure 10D). Furthermore, certain sections of the sedimentary layers show signs of traction deformation, such as bending and distortion. This indicates that fault activity caused displacement along the fault planes and was also accompanied by significant disturbance to the sediments. When this deformation is factored in, the cumulative vertical displacement of the fault system in trench TC3 could reach 1 m, revealing pronounced tectonic activity in the region since the Late Quaternary period.

In addition, optically stimulated luminescence dating samples were collected from this trench. Four sampling points were selected at the base of four marker layers, yielding a total of four samples to determine the depositional ages of each layer (Figure 10D). Testing revealed that some samples exhibited weak luminescence signals. Test results indicate that the luminescence ages for Layer U1 are 1.986 ± 0.124 ka, while those for Layers E1, E2, and E3 were 10.843 ± 1.003 ka, 7.69 ± 0.445 ka, and 5169 ± 321 ka, respectively (Table 2). This indicates that the fault has been active since the Holocene epoch.

## 4. Analysis and discussion

### 4.1. Geometric analysis of the fault plane

Based on remote sensing interpretation and field geological surveys, this study has determined the planar characteristics of this fault segment with considerable precision. Extending westward from the Miaogou area, the fault primarily runs along the southern foothills of the Halike Mountains, where they meet the Hami Basin. It then runs eastward through Hongxing Gou, to the east of the Bamudun River. The fault has a total length of approximately 35 km and strikes nearly east-west.

This fault segment is clearly visible as a linear feature in the satellite image and is manifested topographically as steep, discontinuous escarpments on the alluvial fan at the foot of the mountains. On the alluvial fan to the west of Miaogou, the fault markers are highly visible, with distinct escarpment landforms. The primary topographic manifestation comprises well-defined fault scarps that have formed on the T3 terrace and the alluvial fan that formed during the Late Pleistocene era. The escarpments generally reach heights of 12 m. Measurements of the fault scarp on the alluvial fan produced a profile showing a total height of 11 m (Figure 5F). Clear scarp features are also present on the river terrace along the eastern bank of the Bamudun River at its outlet, reaching a total height of 13 m (Figure 4F). Since the mid-Late Pleistocene, the primary geomorphological expression of this fault has been the presence of distinct scarps on the T3 terrace and the Late Pleistocene alluvial fan. These scarps exhibit a total height ranging from 11 to 13 m.

### 4.2. Fault geometry at depth

This study systematically analyzed the profile characteristics of the eastern segment of the northern margin fault in the Hami Basin by cross-verifying microtremor detection and trench profiles. The primary exposure zone of this eastern segment is the Miaoergou-Bamudun area, which generally trends in an east-west direction and exhibits the characteristics of a north-dipping reverse fault.

Microtremor survey method provides an excellent level of spatial detail for identifying faults, effectively capturing anomalous shear wave velocity distributions within fault zones in order to determine the locations and geometric parameters of faults preliminarily. In this study, three microtremor survey lines were deployed in combination with trench verification to systematically reveal key information, including precise fault locations, 3D orientation, and fracture zone width.

The microtremor profile along the MTS-a survey line indicates a zone of low velocity with an inclination of approximately 60°–70° between surface stations 600

**Table 2. The dating results of OSL samples from trench TC3**

| Sample ID | Test minerals | U (ppm) | Th (ppm) | K (ppm) | Moisture content (%) | Burial depth (m) | Environmental dose (Gy/ka) | Equivalent dose (Gy) | Age (ka) |
|---|---|---|---|---|---|---|---|---|---|
| HM-1 | Quartz | 6.79362 | 17.0734 | 2.41 | 0.427 | 0.3 | 6.99±0.417 | 13.756±0.283 | 1.968±0.124 |
| HM-2 | Quartz | 6.60067 | 19.25079 | 2.7467 | 0.0107 | 0.5 | 7.573±0.429 | 39.142±0.991 | 5.169±0.321 |
| HM-3 | Quartz | 6.1721 | 20.69530 | 2.57 | 0.0067 | 0.8 | 7.358±0.407 | 56.586±0.970 | 7.69±0.445 |
| HM-4 | Quartz | 6.4861 | 13.09402 | 1.60913 | 0.597 | 1.3 | 5.615±0.37 | 60.880±3.950 | 10.843±1.003 |

and 700 m. This zone is interpreted as fractured, with an estimated width of 60–70 m. At the corresponding location, trench TC1 exposed two northward-trending faults with an inclination of approximately 40°. These faults exhibit stepped displacement characteristics, with granite thrusting onto the gravel layer and clearly defined fracture structural features.

The microtremor profile along the MTS-b transect reveals a distinct low-velocity anomaly zone between surface stations 720 and 880 m. This zone exhibits an inclination of approximately 70°, with localized undulations at the surface. Trench TC2 revealed an oriented structure at the base of the gravel layer in this section that forms an angle with the original bedding. This is interpreted as a fault zone with an inclination of around 45°, exhibiting the characteristic geometry of a "steep at depth, gentle at shallower levels" fault.

The microtremor profile along the MTS-c survey line shows a zone of low-velocity anomalies with an inclination of around 60° between surface station numbers 200 and 300 m. This zone is around 100 m wide. Trench TC3 at the corresponding profile location revealed multiple north-dipping faults within the granite. These faults strike in an east-west direction and have dip angles ranging from 35° to 60°, which indicates intense tectonic disturbance.

Overall, geophysical surveys indicate fault dip angles of 60°–70°, whereas trenching has revealed shallower faults with comparatively gentler angles of dip of around 35°–60°. Integrating these findings suggests that the actual fault dip likely ranges between 35° and 70°. The fractured zone revealed by geophysical surveys may extend beyond the boundary fault to encompass areas with reduced strength. Analysis indicates that the width of the fractured zone ranges between 60 and 100 m.

### 4.3. Application of microtremor survey technology in active fault detection

Active fault detection serves as a vital technical approach for earthquake disaster risk prevention, major project site selection, and regional geological stability assessment.[38] At present, this field has established an integrated research system combining geological and topographical surveys with multi-source geophysical detection. Within this framework, geophysical detection plays a crucial role in the detailed identification of deep structures and the spatial localization of faults. In recent years, microtremor detection, as a passive-source geophysical method, has gained increasing application in active fault detection due to its advantages, such as strong resistance to interference and insensitivity to low-resistance layers. Compared to traditional geophysical methods like transient electromagnetic and resistivity surveys, microtremor detection is less susceptible to electromagnetic interference, high-low velocity interlayers, and low-resistivity shielding effects. It is particularly suitable for complex geological cover zones such as landslide deposits and coarse-grained alluvial deposits, effectively identifying geotechnical structural variations and delineating fault fracture zones.[39,40]

This study investigates the Shangmiyang–Bamudun segment of the eastern section of the northern margin fault in the Hami Basin, employing microtremor detection technology to explore deep geological anomalies. Based on array data collected along three survey lines, a shear wave velocity profile was inverted. Results show that the profile clearly distinguishes Quaternary loose deposits from underlying bedrock: Layers with shear wave velocities below 500 m/s are identified as Quaternary loose sediments, while those above 500 m/s correspond to bedrock. Within the inverted profile, slope-deposited materials with velocities below 500 m/s overlie the bedrock, consistent with the geological and topographic characteristics of the area (Figure 6). Furthermore, the profile reveals a stratum with velocities below 800 m/s has a thickness of approximately 80 m, interpreted as a layer of fully weathered to strongly weathered bedrock.

All three microtremor profiles reveal a low-velocity anomaly zone, with shear wave velocity isopleths exhibiting a banded or elongated elliptical distribution. The major axis trends northward at an inclination of approximately 60°, interpreted as a typical response of a fault breccia zone. Active fault fracture zones typically feature loose rock masses with low strength, creating anomalies characterized by relatively low wave velocities. This anomaly zone aligns with the location of a steep surface scarp, further supporting the interpretation as a fault fracture zone. Microtremor detection effectively revealed the 3D orientation and profile characteristics of the deep fracture zone. However, within approximately 80 m near the surface, the lack of significant anomalies in stratigraphic wave velocity made it difficult to identify shallow fracture structures and orientations, highlighting the method's limitations in shallow detection. Nevertheless, microtremor detection remains a valuable technical tool for fracture identification and 3D structural imaging.

## 5. Conclusion

This study is based on remote sensing interpretation and geological-morphological surveys, and prioritizes the incorporation of microtremor detection technology. Through integrated analysis and cross-validation using multiple methodologies, including drilling and trenching,

the study precisely delineates the spatial distribution and 3D characteristics of the eastern segment of the northern margin fault in the Hami Basin. The results show that microtremor detection has excellent resolution capabilities in foothill areas with thin overburden or coarse gravel. This provides effective technical support for identifying active faults in complex terrain.

The eastern segment of the northern margin fault of the Hami Basin runs along the southern foothills of the Halik Mountains. It extends in a nearly east-west direction from Miaogou to the Bamudun River area. This fault is clearly visible as distinct linear features in high-resolution remote sensing image and is manifested topographically as steep, discontinuous scarps on the alluvial fan at the foot of the mountains. This reflects tectonic activity dominated by thrust deformation since the Quaternary period. Field surveys indicate typical steep scar heights of up to 11 m. Fault traces are clearly discernible on the river terrace along the eastern bank of the Bamudun River outlet, demonstrating significant activity.

The results of the microtremor detection indicate that the fault zone within the study area is approximately 40 m wide, with the most extensively fractured zone reaching up to 100 m in width. The fault's overall dip angle is approximately 60°. Drilling and trenching within the high velocity zone revealed multiple fault planes, all of which dip northwards at a shallow angle of approximately 45°. This aligns well with the structural anomalies exposed by the microtremor profile. The fault exhibits a distinct "steep at depth, gentle near surface" geometric pattern, indicating a steep dip at greater depths that gradually flattens toward the near-surface zone.

In summary, microtremor detection technology has proven highly adaptable and practical for identifying active faults in this region. It has been shown to be effective in areas with complex topography and thick overburden. This study pinpoints the precise location and geometric morphology of the eastern segment of the northern margin fault in the Hami Basin, providing crucial reference data for regional seismic hazard assessment and major project site selection. Furthermore, it expands the potential applications of microtremor detection technology in active tectonic research, with significant theoretical implications and practical engineering value.

## Acknowledgments

We sincerely thank Senior Engineers Xiaodong He, Yanling Liu, Junqi Duan, Jun Ma, and other professionals from PowerChina Northwest Engineering Corporation Limited for providing geological and geophysical data as well as their assistance and guidance during fieldwork. Meanwhile, we also express our gratitude to Associate Professor Zhitao Gao, Qian Zhao (engineer), and Xuefeng Zhao (student) from the Institute of Disaster Prevention and Beijing Disaster Prevention Science and Technology Co., Ltd. for their contributions to the implementation of relevant projects.

## Funding

This research was supported by the National Natural Science Foundation of China (Grant No. 42172253) and received substantial support from the "Specialized Survey on Fault Distribution and Activity at the Northern Margin of the Hami Basin" project, which was jointly undertaken by China Power Engineering Consulting Group Northwest Survey and Design Institute Co., Ltd. and Beijing Disaster Prevention Science and Technology Corporation Limited.

## Conflict of interest

The authors declare no conflicts of interest.

## Author contributions

*Conceptualization:* Jun Shen, Guanghong Ju
*Formal analysis:* Jun Shen
*Funding acquisition:* Jun Shen
*Investigation:* Jun Shen, Xu Song, Guanghong Ju
*Methodology:* Jun Shen, Guanghong Ju
*Project administration:* Guanghong Ju
*Validation:* Jun Shen, Guanghong Ju
*Visualization:* Xu Song
*Writing–original draft:* Xu Song
*Writing–review & editing:* Jun Shen

## Availability of data

Data are available from the corresponding author on reasonable request.

## References

1. Xu XZ, Wang YX, Jiang YM, Jiang YM, Dang SJ, Nie DP. [Crustal velocity structure and geotectonic units division of the Xinjiang-Gansu seismic sounding profile]. *Xinjiang Geol.* 1992;10(2):147-154. [Article in Chinese].
2. Wu FY. [*Late quaternary Activity Evidence and Deformation Mechanism of Several Major Faults in the Eastern Section of the Eastern Tianshan Mountains*]. Beijing: Institute of Geology, China Earthquake Administration; 2016. [Article in Chinese].
3. Ren GX. [*Late Quaternary Activity and Tectonic Transformation of the Eastern Tianshan sinistral Strike-Slip Faults*]. Beijing: Institute of Geology, China Earthquake Administration; 2021. [Article in Chinese].
4. Bai MX, Luo FZ, Li J, *et al.* [Micro-geomorphology of the

active fault zone on the Northern Margin of Hami Basin]. *Inland Earthq.* 1999;13(2):162-168. [Article in Chinese]

5. Fang SM, Zhang XK, Liu BJ, Xu XW, Bai DH, JI JFl. [Geophysical methods for detecting active faults in large cities]. *Seismol Geol.* 2002;24(4):606-613. [Article in Chinese].
6. Wu JP. [Geophysical methods for urban seismic active fault detection]. *Seismol Geol.* 2000;22(1):1-15. [Article in Chinese].
7. Li QZ. [*The Road to Precision Prospecting: A Systematic Analysis of High-Resolution Seismic Exploration*]. Beijing: Petroleum Industry Press; 1993. p. 120-130. [Article in Chinese].
8. Lu JM, Wang YG, Dou H, He XH. *[Principles of Seismic Exploration*]. Beijing: Petroleum Industry Press; 1993. p. 140-156. [Article in Chinese].
9. Okada H. *The Microtremor Survey Method*, *Geophysical Monographs Series*. Vol. 12. Houston: Society of Exploration Geophysicists; 2003. p. 1-135.
10. Okada H. Theory of efficient array observations of microtremors with special reference to the SPAC method. *Explor Geophys*. 2006;37:73-85.

    doi: 10.1071/eg06073
11. Matsuoka T, Umezawa N, Makishima H. Chika kozo suiteino tame no kukan jiko sokanho no tekiyosei ni kansuru kento[Experimental studies on the applicability of the spatial autocorrelation method for estimation of geological structures using microtremors]. *Butsuri Tanko (Geophys Explor)*. 1996;49:26-41.
12. Cho I, Nakanishi I, Ling SQ, Okada H. Application of forking geneticalgorithm fga to an exploration method using microtremors. *Geophys Explor.* 1999;52:227-246.
13. Liu HP, Boore DM, Joyner WB. Comparison of phase ve-locities from array measurements of Rayleigh waves associated with mi-crotremor and results calculated from borehole shear-wave velocity pro-files. *Bull Seismol Soc Am.* 2000;90(3):666-678.
14. Zhao HP, He DK, Hong Y. Inversion of microtremor recordingsdispersion curve based on geological unit. *J Min Sci Technol.* 2022;7(6):662-669.

    doi: 10.19606/j.cnki.jmst.2022.06.003
15. Qiu P, Wang JH. [Application of microtremor and shallow seismic reflection technology in the detection of concealed sections of the Weining-Shuicheng fault structure]. *Guizhou Geol.* 2023;40(2):134-139. [Article in Chinese].
16. Feng SK. [Microtremor survey technology and its application in civil engineering]. *Chin J Rock Mech Eng.* 2003;22(6):1029-1036. [Article in Chinese].
17. Xu PF, Li SH, Ling SQ, Guo HL, Tian BQ. [Estimation of crustal S-wave velocity structure using the SPAC method]. *Chin J Geophys.* 2013;56(11):3846-3854. [Article in Chinese].
18. Xu PF, Li SH, Du JG, Ling SQ, Guo HL. :[Microtremor survey: A new method for stratigraphic division and concealed fault structure detection]. *Acta Petrol Sin*. 2013;29(5):1841-1845. [Article in Chinese].
19. Windley BF, Allen MB, Zhang C, Zhao ZY, Wang GR. Paleozoic accretion and Cenozoic redeformation of the Chinese Tien Shan Range, central Asia. *Geology*. 1990;18(2):128.

    doi: 10.1130/0091-7613(1990)018<0128:PAACRO>2.3.CO;2
20. Molnar P, Tapponnier P. Cenozoic tectonics of Asia: Effects of a continental collision. *Science*. 1975;189(4201):419-426.

    doi: 10.1126/science.189.4201.419
21. Avouac J P, Tapponnier P, Bai MX, You H, Wang G. Active thrusting and folding along the northeastern Tien Shan, and late Cenozonic rotation of the Tarim relative to Dzungaria and Kazakhstan. *J Geophys Res.* 1993;98(B4):6755-6804.
22. Hendrix MS, Dumitm TA, Graham SA. Late oligocene-early miocene unroofing in the Chinese Tianshan: An early effect of the India-Asia collision. *Geology*. 1994;22(6):487-490.

    doi: 10.1130/0091-7613(1994)022<0487:loemui>2.3.co;2
23. Deng QD, Feng XY, Zhang PZ, *et al*. [*Active Tectonics of the Tianshan Mountains*]. Beijing: Seismological Press; 2000. p. 7. [Article in Chinese].
24. Deng QD, Zhang PZ, Ran YK, Yang XP, Min W, Chu QZ. [Basic characteristics of active tectonics in China]. *Sci China Ser D Earth Sci.* 2002;45(12):1020-1030. [Article in Chinese].
25. Yang XP, Deng QD, Zhang PZ, Xu XW. [Crustal shortening in the major nappe structure zone of the Tianshan piedmont]. *Seismol Geol*. 2008;30(1):111-131. [Article in Chinese].
26. Zhang PZ, Deng QD, Zhang ZQ, Li HB. [Active faults, earthquake hazards and associated geodynamic processes in mainland China]. *Sci China Earth Sci.* 2013;56(10):1607-1620. [Article in Chinese].
27. Tapponnier P, Molnar P. Active faulting and tectonics in China. *J Geophys Res.* 1977;82(20):2905-2930.

    doi: 10.1029/JB082i020p02905
28. Tapponnier P, Molnar P. Active faulting and Cenozoic tectonics of the Tien Shan, Mongolia, and Baykal Regions. *J Geophys Res Solid Earth*. 1979;84(B7):3425-3459.

    doi: 10.1029/JB084iB07p03425
29. Zhang PZ, Deng QD, Yang XP, Peng SZ, Xu XW, Feng XXY. [Late Cenozoic tectonic deformation of the Tianshan Mountains and associated geodynamic processes]. *Earthq Res China*. 1996;12(2):127-140. [Article in Chinese].
30. Wu CY, Wu GD, Shen J, Dai XY, Song H. Late quaternary tectonic activity and crustal shortening rate of the Bogda Mountain Area, Eastern Tian Shan, China. *J Asian Earth Sci.* 2016;119:20-29.

doi: 10.1016/j.jseaes.2016.01.001

31. Huang ST, Hu WH, Yang PX, Li S, Yin LYE. [Late quaternary activity characteristics of the Tangbale-Tasidun Fault Zone in Eastern Tianshan]. *Seismol Geol.* 2020;42(5):1058-1071. [Article in Chinese].
32. Ma J, Chen JB, Zhao CQ, Liu ZJ. [Late quaternary activity characteristics of the Yiwu Fault in Eastern Tianshan Region]. *Inland Earthq.* 2021;35(1):87-92. [Article in Chinese].
33. Yang X, Wu CY, Li ZG, Wang W, Chen G, Duan L. Late quaternary kinematics and deformation rate of the huoyanshan structure derived from deformed river terraces in the South piedmont of the Eastern Chinese Tian Shan. *Front Earth Sci.* 2021;9(9):649011.

    doi: 10.3389/feart.2021.649011
34. Feng XY. [Study on holocene active faults and paleoearthquakes in Tianshan Mountains]. *Inland Earthq.* 1995;9(3):217-226. [Article in Chinese].
35. Li YZ, Shen J. [Seismic geology and seismicity in Hami Region, Xinjiang]. *Inland Earthq.* 2001;15(2):141-147. [Article in Chinese].
36. Shi K, Yang FQ, Li YF, Mo YJ, Qu XY. [Investigation of urban underground space structures using microtremor detection]. *Min Resour Geol.* 2020;34(2):355-365. [Article in Chinese].

    doi: 10.19856/j.cnki.issn.1001-5663.2020.02.024
37. Liu BY, Chen JH, Liu YQ, Zhao L, Sun YP. [Two-dimensional microtremor profiling at Linxia Airport, Gansu Province]. *Geod Geody.* 2023;43(12):1235-1239. [Article in Chinese].

    doi: 10.14075/j.jgg.2023.03.106
38. Deng QD, Lu ZX, Yang ZE. [Urban active fault detection and fault activity assessment]. *Seismol Geol.* 2007;29(2):189-200. [Article in Chinese].
39. Ding LF, Xu PF, Ling SQ, Zhao CJ, Li CJ. [Detection of magmatic rock intrusion in LinNanCang Coal Mine by microtremor exploration method]. *Coal Sci Technol.* 2010;38(7):100-103. [Article in Chinese].
40. Liu YQ, Liao YG, Li XZ, Pang W. [Application of microtremor survey technology in rail transit engineering investigation]. *J Geotechn Investig Surv.* 2010;Suppl 1:1-11. [Article in Chinese].

ACCSCIENCE PUBLISHING

Journal of Seismic Exploration

ARTICLE

# Identification and characterization of fractured cavities in carbonate reservoirs using Swin-UNet transformer and seismic attribute compression fusion

**Yunhao Cui[1,2], Yuhua Chen[1,2]*, Chao Xu[1,2], Yaping Huang[3], Qiang Guo[3], Zhiqiang Lu[4], Zhanpeng Chen[1,2], and Yuwen Qian[1,2]**

[1]Key Laboratory of Coalbed Methane Resource & Reservoir Formation Process, Ministry of Education, School of Resources and Geosciences, China University of Mining and Technology, Xuzhou, Jiangsu, China

[2]Department of Geo-information Science, School of Resources and Geosciences, China University of Mining and Technology, Xuzhou, Jiangsu, China

[3]Department of Geophysics, School of Resources and Geosciences, China University of Mining and Technology, Xuzhou, Jiangsu, China

[4]Research Institute of Exploration and Exploitation, Sinopec Northwest China Petroleum Bureau, Urumqi, Xinjiang Uyghur Autonomous Region, China

## Abstract

Identifying and characterizing fractured cavities is essential for exploring carbonate reservoirs. However, characterizing the development and distribution of fractured cavities through post-stack seismic attribute analysis remains challenging. Recently, convolutional neural networks (CNNs), such as UNet and its enhanced versions, have enabled the quantitative identification of fractured cavities. Despite these advancements, the local receptive field and weight-sharing mechanisms of these CNNs limit their capability to capture long-range features within strike–slip fault systems. In addition, neural networks are inherently affected by data uncertainty. To address these challenges, a two-step methodology is proposed. The first step utilizes a Swin-UNet transformer (UNETR) model, enhanced with an attention gate, to interpret fractured cavities. The transformer in Swin-UNETR improves the detection of fractured cavities in strike–slip fault zones, whereas the attention gate enhances the recognition of small fractured cavities by increasing their response in the feature maps. This enhanced Swin-UNETR model overcomes the limitations in modeling long-range features. In the second step, the fractured-cavity identification results are combined with seismic attributes from conventional analysis. Principal component analysis is employed both to increase the relative weight of the neural network recognition results in the attribute fusion and to reduce the uncertainty associated with any single identification method. The methodology was validated in the Shunbei area, yielding horizontal segmentation and vertical zonation of fractured cavities, as well as their characterization through fixed-grid modeling. By combining deep learning-based feature extraction with seismic attributes, this approach improves the accuracy of fractured cavity identification and characterization in carbonate reservoirs.

***Keywords:*** Fractured cavity identification and characterization; Seismic attribute compression fusion; Convolutional neural network

***Corresponding author:**
Yuhua Chen
(chenyuhua@cumt.edu.cn)

**Citation:** Cui Y, Chen Y, Xu C, *et al*. Identification and characterization of fractured cavities in carbonate reservoirs using Swin-UNet transformer and seismic attribute compression fusion. *J Seismic Explor*. 2026;35(1):119-138. doi: 10.36922/JSE025420090

**Received:** October 14, 2025

**Revised:** November 13, 2025

**Accepted:** December 12, 2025

**Published online:** January 5, 2026

**Copyright:** © 2026 Author(s). This is an Open-Access article distributed under the terms of the Creative Commons Attribution License, permitting distribution, and reproduction in any medium, provided the original work is properly cited.

**Publisher's Note:** AccScience Publishing remains neutral with regard to jurisdictional claims in published maps and institutional affiliations.

## 1. Introduction

Fractured-cavity reservoirs are carbonate rock formations that have developed along fault zones subjected to multiphase tectonic stresses. The combined effects of these tectonic movements, the development of karst features over time, and the upwelling of hot fluids create complex fractured cavities in the carbonate layers. These cavities serve as primary reservoirs for oil and gas, playing a critical role in both hydrocarbon storage and migration. Therefore, accurately locating and characterizing these reservoirs is critical for successful oil and gas exploration and development.[1]

Domestic and international researchers primarily utilize post-stack seismic attributes, including coherence, curvature, and amplitude, to detect and characterize fractured cavities. These traditional methods approximate the locations of fractures and cavities but cannot precisely delineate their size or shape. With the rapid advancements in deep learning for visual and medical imaging, and given the structural similarity between three-dimensional (3D) post-stack seismic data and magnetic resonance imaging scans, deep learning has seen increasing adoption in seismic interpretation. For example, Wu *et al.*[2] used a convolutional neural network (CNN) with the UNet architecture to identify karst paleocaves from 3D seismic datasets. They also developed a method to create synthetic datasets that mimic the seismic reflections of paleocaves. High-quality seismic data annotations are indispensable for effective feature recognition using UNet. Building on this, Li *et al.*[3] adopted an enhanced UNet CNN, using field-annotated cavity contours and synthetic datasets of faults, fractures, and karst caves to improve fractured cavity identification in strike–slip fault zones. Despite these advances, uncertainty persists in seismic interpretation with deep learning. To address this, Gui *et al.*[4] combined UNet++ with multiscale convolutional kernels and seismic attributes to improve accuracy. Zhang *et al.*[5] created a Bayesian deep learning framework that identifies cave shapes and measures uncertainty in the results. However, the increased model complexity leads to prolonged training and inference durations.

While the aforementioned methodologies have exhibited promising results, they still suffer from inherent limitations. In contrast to paleocaves that develop independently, the formation of fractured cavities is influenced by strike–slip fault zones that extend over several kilometers. The intrinsic local receptive field and weight-sharing mechanisms of CNNs fundamentally constrain their capability to detect large-scale fractured cavity systems. Early convolutional layers primarily focus on localized regions of the input data, thus failing to capture correlations across distant regions, which inherently limits their efficacy in identifying long-range geological features (strike–slip fault systems). Moreover, fractured cavities exhibit considerable variability in size and morphology, with smaller cavities often displaying complex geometries. The application of neural network-based methods for fractured cavity identification also introduces both data-driven and model-induced uncertainties, warranting effective mitigation strategies.

To address the inherent locality limitations of CNNs, the present study employs a Swin-UNet transformer (UNETR) network augmented with an attention gate for the identification of fractured cavities. The Swin-UNETR architecture synergistically combines transformer models.[6] with UNet frameworks, thereby enhancing the network's capability to recognize complex fractured cavities over long spatial ranges. The encoder component utilizes a sliding window operation to reduce computational complexity during the processing of seismic input data. In addition, to mitigate uncertainties arising from neural network methodologies, conventional seismic attribute techniques are incorporated to constrain the identification outcomes. Specifically, principal component analysis is employed to integrate the fractured-cavity segmentation results—treated as a dominant attribute—with multiple seismic attribute datasets.[7] This integrative approach combines fractured-cavity information from all methods into a single fused attribute volume, enhancing overlapping features while suppressing inconsistent ones and thereby improving the overall accuracy of fractured-cavity identification.

## 2. Methodology

### 2.1. Field seismic data and geological background

The post-stack seismic datasets used in this study, outlined by the blue box in Figure 1, were obtained from the Shunbei Oil and Gas Field. The field is primarily located in the Shuntuoguole Low Uplift and extends southeastward to the Guchengxu Uplift. Geographically, it is adjacent to the Shaya Uplift to the north and the Katakunlun Uplift to the south, with the Manjiaer Depression and Awati Depression bounding it to the east and west, respectively. The field lies in a structurally low "saddle" zone, generally characterized by relatively higher elevations in the northern and eastern parts and lower elevations in the southern and western parts, forming an overall gently undulating geomorphology.[8]

During the early Caledonian era, the Shunbei area experienced stable tectonic subsidence in the craton, characterized by a weak extensional tectonic regime. Subsequently, from the mid- to late Caledonian era to the early Hercynian era, the region experienced the formation

and evolution of low uplifts under a regional compressional tectonic regime. This was followed by further tectonic adjustments and reworking during the mid-to-late Hercynian period, culminating in the formation of the present-day tectonic framework.

As shown in the comprehensive stratigraphic column of Figure 2, the stratigraphic sequence in the Shunbei area ranges from the Lower Paleozoic Cambrian to the Cenozoic Quaternary, with a notable absence of the Jurassic System. The Yuertusi formation of the Lower Cambrian is extensively developed as a source rock, distinguished by its high organic carbon content and considerable hydrocarbon generation potential. The focus of this study is the Ordovician carbonate strata, which are buried at depths ranging from 7200 to 8800 m below sea level. These Ordovician formations, arranged

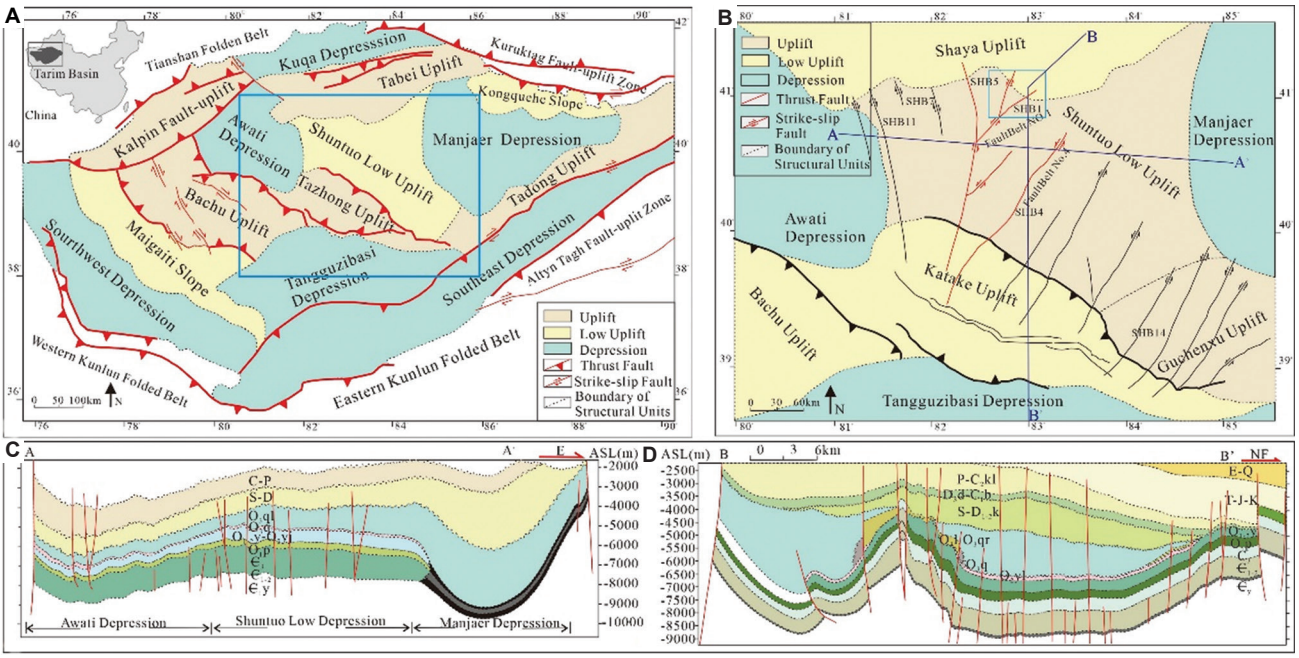


**Figure 1.** (A-D) Tectonic map and stratigraphic section of the central Tarim Basin, where the study area is located. Image modified with permission from Wang *et al.*[9] Copyright © 2024, IEEE.

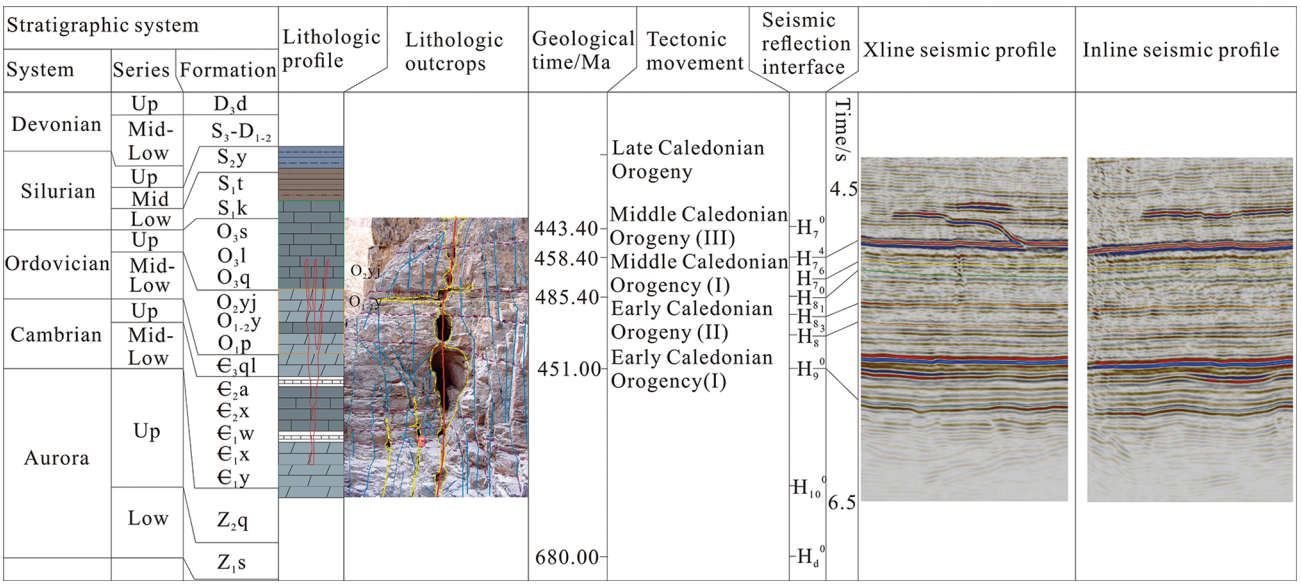


**Figure 2.** Tectonic map and stratigraphic section of the central Tarim Basin. Image modified from Zheng *et al.*[11]

stratigraphically in ascending order, include the Lower Ordovician Penglaiba formation ($O_1p$), the Middle-Lower Ordovician Yingshan formation ($O_{1-2}y$), the Middle Ordovician Yijianfang formation ($O_2yj$), the Upper Ordovician Qiaerbake formation ($O_3q$), the Lianglitage formation ($O_3l$), and the Santamu formation ($O_3s$). Within this sequence, the carbonate units in the upper portion of the Yingshan formation and the Yijianfang formation represent the principal targets for oil and gas exploration in the study area.[10]

A northeast-trending strike–slip fault system has developed in the study area, providing an effective conduit for hydrocarbon migration and promoting hydrocarbon accumulation. The reservoir space is primarily composed of tectonically generated fractured cavities.[12] Seismic data acquired along this fault zone during exploration are shown in Figure 3. The target area shown in the figure has dimensions of 2501 time slices × 1022 inlines × 865 crosslines. To better characterize the spatial distribution of multiscale carbonate fractured cavity reservoirs in the Ordovician and Cambrian strata, strong reflection axes were removed from the seismic data (Figure 4), thereby preventing the reflection information of the underlying fractured cavities from being masked by these strong reflection axes. The data were then divided into six segments, referred to as object area (OA)-crop1 through OA-crop6. These segments correspond to the southern, central, and northern sections of the study area.

## 2.2. Fractured cavities identification using Swin-UNETR

### *2.2.1. Training of datasets*

As a data-driven supervised learning approach, deep learning requires feature-rich training datasets for effective model optimization. In carbonate fault-controlled reservoirs, fractured cavities manifest as clusters of strong reflections on a weak reflection background in seismic datasets. As small-scale geological anomalies within

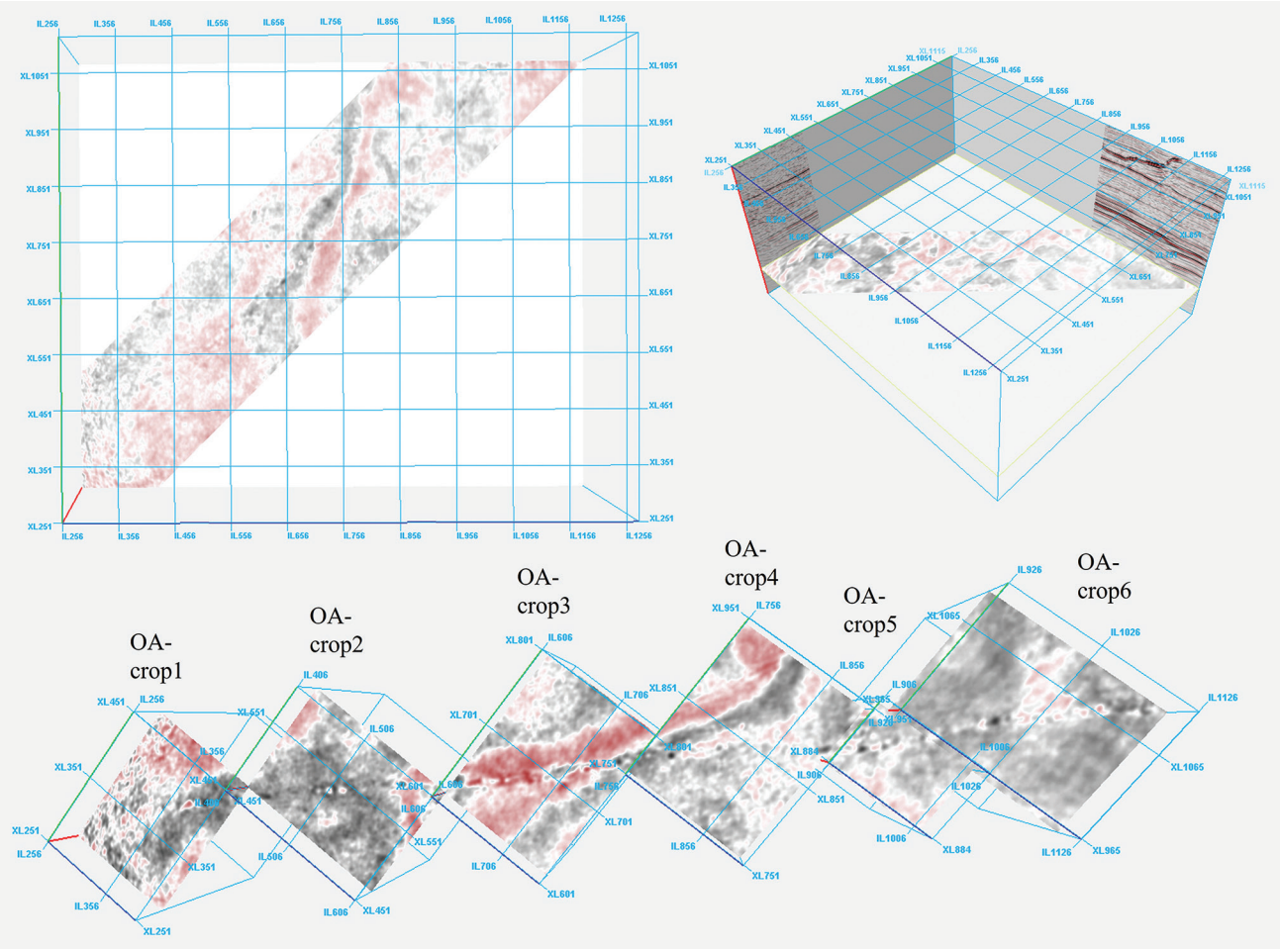


**Figure 3.** Three-dimensional exploration of the seismic data in the study area
Abbreviation: OA: Object area.

carbonate reservoirs, fracture cavities create diffraction effects during seismic wave propagation. This phenomenon arises from wave impedance contrasts, generating multiple vertical strong energy anomalies. Figure 5 shows that forward modeling reveals the beaded anomalous reflection characteristics of fractured cavities on post-stack seismic sections. These are typically shown by seismic attributes such as strong amplitude anomalies, high amplitude variation rates, weak to moderate coherence, low wave impedance, and low velocity. As shown in Figure 6, inversion of the seismic profiles indicates that fractured cavities in the OA exhibit nearly ellipsoidal outlines with significant variation in scale, ranging from 10 to 150 m.[13]

Based on the relationship between the morphology and size of fractured cavities and the beaded anomalous reflections observed on seismic profiles, a convolutional synthesis method using a seismic reflectivity model and Ricker wavelets was employed to construct training samples of fractured cavities. The process of establishing a seismic reflectivity model involved three key steps. First,

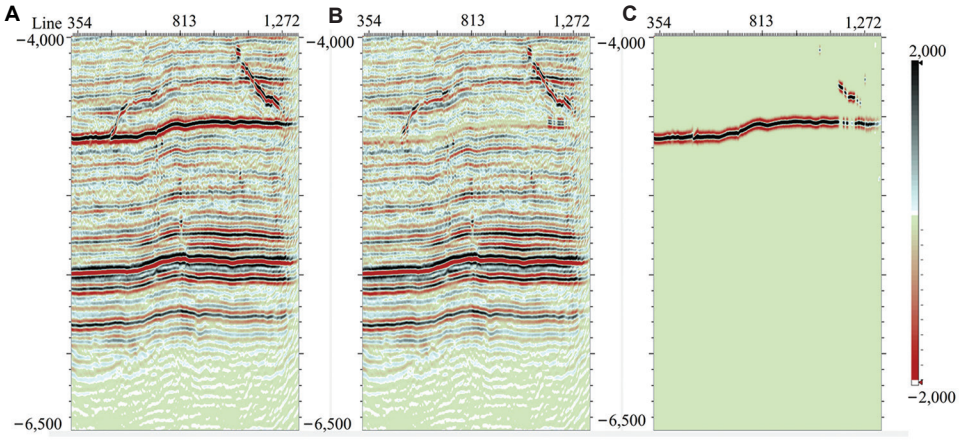


**Figure 4.** Object area data after strong axis removal processing. (A) Original seismic profile. (B) Seismic profile after removing the strong axis. (C) Removed $H_7^4$ strong axis.

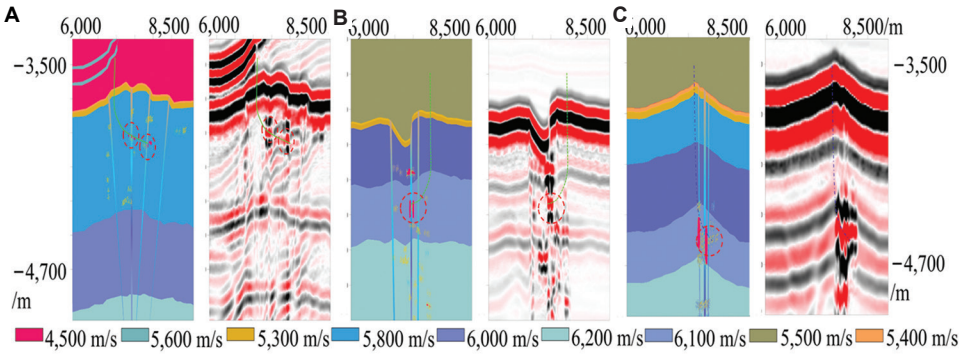


**Figure 5.** Forward modeling of the beaded reflection characteristics of the fractured cavities. (A) Compression section. (B) Pull-apart segment. (C) Translational segment.

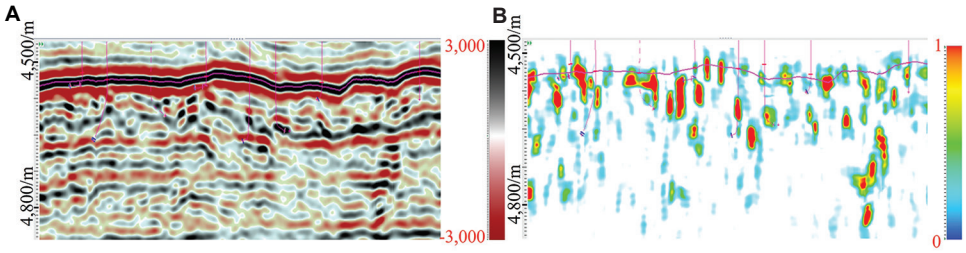


**Figure 6.** Amplitude curvature seismic attribute profile of fractured cavities. (A) Raw seismic profile. (B) Amplitude curvature seismic attribute profile.

building an initial 3D horizontal-layered reflectivity model (*X*, *Y*, *Z*); second, incorporating formation dip and fold structure models ($X_s$, $Y_s$, $Z_s$)into the horizontal layers; and finally, integrating the fractured cavities components ($\bar{X}$, $\bar{Y}$, $\bar{Z}$) into the composite model.

The geometric fold model ($X_s$, $Y_s$, $Z_s$) was generated by applying a vertical offset to the initial model (*X*, *Y*, *Z*). This vertical offset field was decomposed into large-scale fold surfaces $S_1$ (X, Y, Z), small-scale local folds $S_2$ (X, Y, Z), and multidirectional dip components $S_3$ (X, Y, Z).

$$S_1(X,Y,Z) = A_0 + \left(1 - \left|\frac{a(X-X_0)+b(Y-Y_0)}{X_{max}+Y_{max}}\right|\right) \sum_{k=1}^{N}\left(A_k \cos\left(\frac{k\pi E(X,Y)}{\lambda_k}\right) + B_k \sin\left(\frac{k\pi E(X,Y)}{\lambda_k}\right)\right)$$

$$E(X,Y) = \sqrt{\left(\frac{\cos\phi_k(X-X_0)-\sin\phi_k(Y-Y_0)}{L[x]_k}\right)^2 + \left(\frac{\sin\phi_k(X-X_0)-\cos\phi_k(Y-Y_0)}{L[y]_k}\right)^2} \quad (1)$$

The first large-scale displacement field, as shown in **Equation 1**, was defined by a Fourier series. In this context, the parameters $X_0$ and $Y_0$ represent the central position of the modified Foucault's equation. The Fourier coefficients $A_k$ and $B_k$ define the amplitude of the folds. The attenuation factors *a* and *b* control the amplitude variation of the folds in the X and Y directions, respectively. The elliptic coefficients $L[x]_k$ and $L[y]_k$ control the degree of fold curvature in the X and Y directions, respectively, with $L[x]_k$ corresponding to the ellipse's major axis. The parameter $\phi_k$ denotes the clockwise rotation angle of the ellipse, and the parameter $\lambda_k$ controls the compression ratio of the wavelength.

$$S_2(X,Y,Z) = C\frac{Z}{Z_{max}}\sum_{k=1}^{N} Dk\exp\left[-\left(\frac{\cos\phi_k(X-E_k)-\sin\phi_k(Y-F_k)}{2\sigma[x]_k}\right)^2 - \left(\frac{\sin\phi_k(X-E_k)-sin\phi_k(Y-F_k)}{2\sigma[y]_k}\right)^2\right] \quad (2)$$

The second small-scale fold displacement field, as shown in **Equation 2**, was defined by a Gaussian equation; the Gaussian coefficients $\sigma[x]_k$ and $\sigma[y]_k$ represent the major and minor axis lengths of the ellipse, with $\sigma[x]_k$ denoting the major axis. The $\phi_k$ is the clockwise rotation angle of the fold, whereas $E_k$ and $F_k$ specify the central position of the Gaussian function. The fold amplitude is controlled by a separate parameter $D_k$, whereas an attenuation factor C adjusts its vertical variation. The vertical extent of the folds in the Z direction can be controlled by specifying appropriate lower and upper limits, for example, by setting $\sigma[x]_k = \sigma[x]_0 + dZ$ and $\sigma[y]_k = \sigma[y]_0 + eZ$.

$$S_3(X,Y,Z) = Gx + Hy + I \quad (3)$$

Finally, the third displacement field, as shown in **Equation 3**, used a linear equation to simulate the dip of strata in various directions, with parameters G and H controlling the dip angles in the X and Y directions, respectively.

$$\begin{bmatrix} X_s \\ Y_s \\ Z_s \end{bmatrix} = \begin{bmatrix} X \\ Y \\ Z + S_1(X,Y,Z) + S_2(X,Y,Z) + S_3(X,Y,Z) \end{bmatrix} \quad (4)$$

By superimposing the vertical displacement fields $S_1$ (X, Y, Z), $S_2$ (X, Y, Z), and $S_3$ (X, Y, Z), the spatial coordinates ($X_s$, $Y_s$, $Z_s$)of the fold structure model were derived **(Equation 4)**.

$$\begin{bmatrix} X_s' \\ Y_s' \\ Z_s' \end{bmatrix} = \begin{bmatrix} X_s \\ Y_s + S_1(X,Y,Z) \\ Z_s \end{bmatrix} \quad (5)$$

In addition, natural folds ($X_s'$, $Y_s'$, $Z_s'$) are often complex, allowing an arbitrary combination of $S_1$ (*X*, *Y*, *Z*), $S_2$ (*X*, *Y*, *Z*), and $S_3$ (*X*, *Y*, *Z*). Vertical variation of fold surfaces can be achieved by incorporating a lateral displacement field **(Equation 5)** or by systematically adjusting the central coordinates of each fold equation.[14]

After generating the formation dip and fold reflectivity model, the next step simulated the structural characteristics of a fault-controlled fractured-cavity system. Field outcrop observations (Figure 2) show that the dominant features are fault-related fractures and near-cylindrical caves, which can be approximated as vertically elongated ellipsoids with major axes perpendicular to the ground surface. To effectively simulate the reflection characteristics of fractured cavities, a 3D, vertically elongated ellipsoid was first constructed, as shown in **Equation 6**.

$$f(p) = (p-c)^T R_1{}^T A R_1 (p-c) \quad (6)$$

The 3D domain of the ellipsoid is defined by **Equation 7**:

$$\begin{cases} if\ f(\mathrm{p}) \le 1 : inside\ chimney\ cube \\ if\ f(\mathrm{p}) > 1 : outside\ chimney\ cube \end{cases}$$

In the ellipsoid function (Equation VI), p = (X, Y, Z) denotes the coordinates of a point in the 3D reflectivity model, whereas c = ($c_X$, $c_Y$, $c_Z$)represents the center of the ellipsoid, randomly sampled within the model domains. Matrix A is a diagonal matrix specified by the ellipsoid's three radii, as shown in **Equation 8**:

$$A = \begin{bmatrix} \frac{1}{r_X^2} & 0 & 0 \\ 0 & \frac{1}{r_Y^2} & 0 \\ 0 & 0 & \frac{1}{r_Z^2} \end{bmatrix} \quad (8)$$

Among these parameters, the values of $r_x$, $r_y$, and $r_z$ were randomly selected from predefined ranges [1, 12], [1, 12], and [10, 100], respectively, to construct cavities of varying sizes. To ensure predominantly vertically elongated ellipsoids, the range for $r_z$ was set wider. In addition, constraints $r_x > 0.1r_z$ and $r_Y > 0.1r_z$ were imposed to avoid extremely elongated ellipsoids, which are geologically uncommon. Matrix $R_1$ **(Equation 9)** is a rotation matrix that rotates the ellipsoid around the X-axis and Y-axis.

$$R_1 = \begin{bmatrix} 1 & 0 & 0 \\ 0 & \cos\alpha & -\sin\alpha \\ 0 & \sin\alpha & \cos\alpha \end{bmatrix} \begin{bmatrix} \cos\beta & 0 & \sin\beta \\ 0 & 1 & 0 \\ -\sin\beta & 0 & \cos\beta \end{bmatrix} \quad (9)$$

Among these, rotation angles α and β were randomly sampled from a narrow range of [−10°, 10°] to generate ellipsoids that are either slightly inclined or nearly vertical. By randomly sampling all parameters in **Equation 10**, numerous ellipsoids with diverse shapes, sizes, orientations, and positions can be created. Nevertheless, because natural fractured cavities are not ideal ellipsoids, random smooth perturbations were introduced to generate irregular ellipsoids that better resemble real-world features.

$$\begin{bmatrix} \bar{X} \\ \bar{Y} \\ \bar{Z} \end{bmatrix} = \begin{bmatrix} X_s + S_k(X,Y,Z) \\ Y_s + S_k(X,Y,Z) \\ Z_s + S_k(X,Y,Z) \end{bmatrix} \quad (10)$$

After defining the 3D tubular region of the fracture cave, the concave structure within the ellipsoid was further characterized. Concave structures typically exhibit a downward-bending morphology, so the reflection layer within the channel body was vertically offset. The vertical offset is defined in **Equation 11**.

$$S_k(X,Y,Z) = \begin{cases} 0, & if\ f(X,Y,Z) > 1 \\ \gamma\left(f(X,Y,Z) - 1\right) + \varepsilon(X,Y,Z), & \\ if\ f(X,Y,Z) \le 1 & \end{cases} \quad (11)$$

In **Equation 11**, $f(X, Y, Z)$ represents the ellipsoid function. $\gamma$ is a positive scalar randomly selected from the range [10, 20], and $\epsilon(X, Y, Z)$ is a random perturbation field used to simulate fractures or faults within the fractured cavity that may cause displacement of the reflection layer. The perturbation field has a relatively small magnitude compared to the first term γ(f(X, Y, Z)−1). When the perturbation field approaches zero, $S_K(X, Y, Z) \approx \gamma(f(X, Y, Z)-1$, with its value being non-positive and decreasing smoothly from 0 at the fracture-cave boundary to the minimum at the center. At this point, the offset causes a vertical shear of the reflection layer, resulting in a smoothly downward-bending morphology. The resulting concave structure produces distinct annular features on the horizontal slice. If the perturbation is significant, the offset $S_K(X,Y,Z)$ exhibits disordered characteristics, leading to the formation of curved and displaced reflection layers within the channel body, including features such as holes or faults.[2]

After constructing a reflectivity model incorporating fold and fractured cavity features, synthetic seismic data were simulated by convolving the model with Ricker wavelets in the vertical direction.[15] The frequency of the Ricker wavelets was randomly selected within the range of 10–40 Hz. To enhance the realism of the synthetic data and align it more closely with real-world data, random noise was further introduced. Figure 7 presents the corresponding label data, where fractured cavity regions are marked as 1 and non-fractured cavity regions as 0. Using this method, a total of 800 data samples (each with a size of 128 × 128 × 128) were generated for model training. Although the training set was substantially smaller than the actual study area, it was sufficient to achieve accurate identification of the main fractured-cavity features.

### 2.2.2. Network architecture

The algorithmic structure proposed in this paper is illustrated in Figure 8. Overall, it adopts a fusion architecture that combines CNN and transformer models. The core of the encoder strikes a balance between feature extraction capability and computational efficiency by using the Swin transformer module[16] as its fundamental framework.

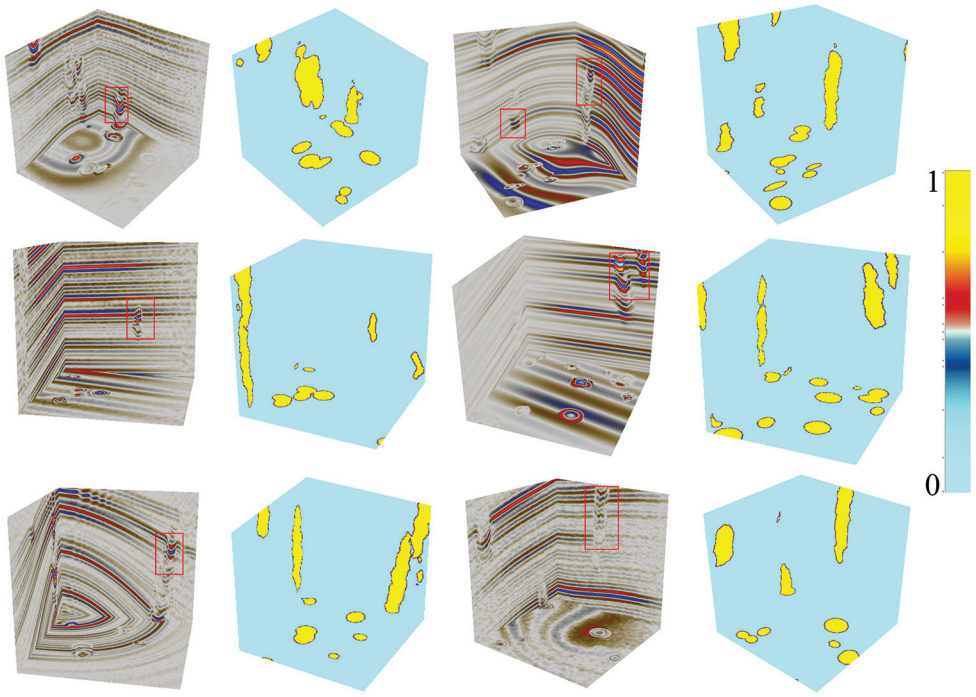


**Figure 7.** Three-dimensional fractured cavity data were synthesized by convolving the reflection model with the Ricker wavelet

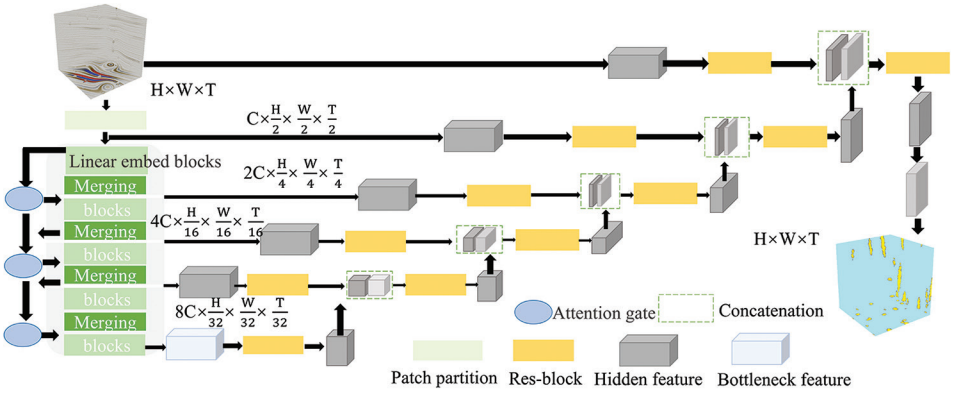


**Figure 8.** Overview of the network architecture

The self-attention mechanism in the standard transformer operates globally. This leads to a quadratic increase in computational load and memory requirements as the size of input seismic data grows, which limits its application to high-resolution 3D seismic datasets. The Swin transformer restricts attention calculations to local windows of fixed size, significantly reducing computational demands. In addition, it introduces a sliding window mechanism that enables cross-boundary feature interactions between windows, ensuring that the model can capture long-range contextual information. This sliding window strategy reduces the network's processing complexity from cubic to linear in relation to the input data size, greatly enhancing its adaptability to large-scale seismic datasets.

For the decoder, inspired by the UNETR design,[17] multiple convolutional layers with residual connections and transposed convolutional layers are used to upsample the feature maps generated by the encoder.

In the encoder stage, the input seismic data ($x \in R^{H \times W \times D}$) passes through a patch partition layer, where each dimension is divided by a factor ($h \times w \times d$) to form several non-overlapping data blocks of size $\frac{H}{h} \times \frac{W}{w} \times \frac{D}{d}$. Each sub-block corresponded to the seismic reflection characteristics of a local underground region. Next, the linear embedding layer in the Swin transformer stage maps the 3D data into a one-dimensional sequence space of

dimension *C*, where $C = h \times w \times d$. As illustrated in Figure 9, the core of each Swin transformer module consisted of a window-based multi-head self-attention (W-MSA) module and a shifted W-MSA module. The input features first underwent layer normalization and then entered the W-MSA module to extract local intra-window self-attention features. The output features, after layer normalization, were passed through a multi-layer perceptron with a ReLU activation function. Subsequently, the features underwent layer normalization again and entered the shifted W-MSA module, enabling information transfer between local windows and extracting contextual feature information. Residual connections were applied between every two layers of normalization operations. The self-attention mechanism used here was calculated using **Equation 12**:

$$Attention(Q,K,V) = Softmax\left(\frac{QK^T}{\sqrt{d}}\right)V \tag{12}$$

Among them, Q, K, and V represent the query, key, and value, respectively; d denotes the size of the query and key vectors.

The calculation formula for the l-th layer of the Swin transformer module is as follows **(Equations 13-16)**:

$$z_1^l = W - MSA\left(LN\left((z_0^{l-1})\right)\right) + z_0^{l-1} \tag{13}$$

$$z_0^1 = MLP\left(LN\left(z_1^l\right)\right) + z_1^l \tag{14}$$

$$z_1^{l+1} = SW - MSA\left(LN\left(z_0^1\right)\right) + z_0^l \tag{15}$$

$$z_0^{l+1} = MLP\left(LN\left(z_1^{l+1}\right)\right) + z_1^{l+1} \tag{16}$$

To automatically focus on fracture bodies of various shapes and sizes, an attention gate mechanism[18] was introduced, as shown in Figure 10. The feature map $x^l$represents the features to be processed in the current module, whereas the gating signal $g$ is the high-level feature from the previous layer. The attention gate module takes both the feature map $x^l$ and the gating signal $g$ as inputs, applies 1×1×1 convolutions to each to unify their dimensions, and then performs element-wise addition. After activating the combined features, the weights corresponding to areas of fractured cavity development increased through iterative optimization, thereby enhancing the model's prediction accuracy.

The decoder is a CNN-based neural network that connects to the encoder via multi-resolution features through skip connections, forming a U-shaped architecture. The decoder's decision followed the Swin-UNETR model,[19] as illustrated in Figure 8. At each decoder stage, the input features first pass through a residual module composed of two 3 × 3 × 3 convolutional layers with instance normalization, which processes the features. These processed features were then concatenated with the upsampled features from the subsequent stage. After concatenation, the features were reshaped. The features processed at each stage were upsampled using a deconvolution layer; when the spatial dimensions doubled, they were concatenated with the corresponding features from the encoder at the same stage. The concatenated features were further processed through a residual module.

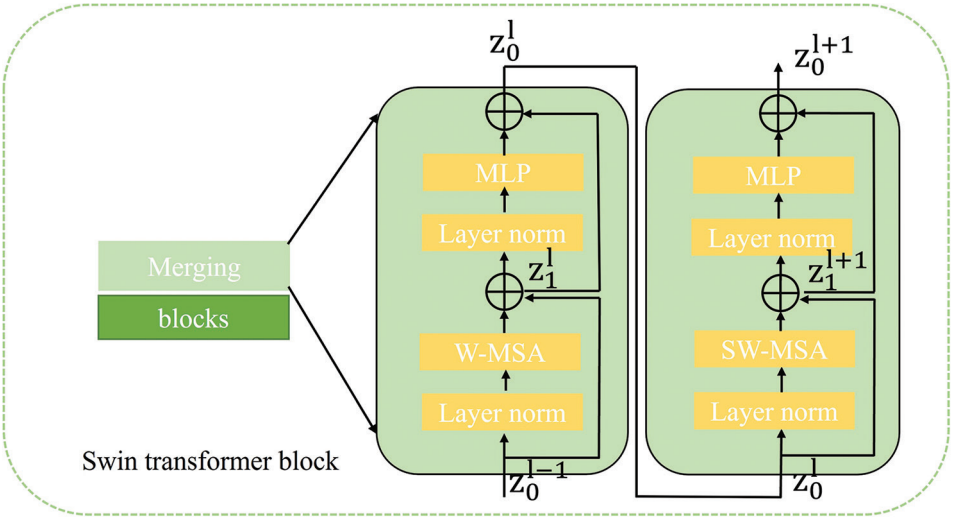


**Figure 9.** The structure of the Swin transformer module
Abbreviations: MLP: Multi-layer perceptron; SW-MSA: Shifted window-based multi-head self-attention; W-MSA: Window-based multi-head self-attention.

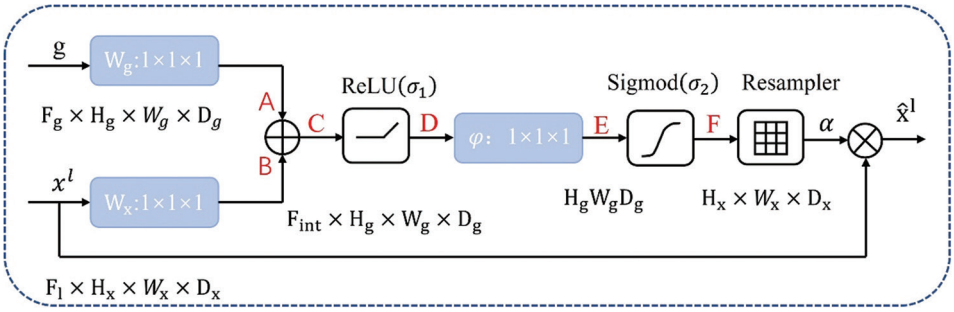


**Figure 10.** The structure of the attention gate module

Finally, a residual module serves as the segmentation head; after a 1×1×1 convolutional layer and a sigmoid activation function, the fractured-cavity segmentation map is produced.

### 2.3. Seismic attribute compression and fusion based on principal component analysis

To use multi-attribute seismic data to constrain the neural-network segmentation results, we preserved the correlations between different attributes (i.e., overlapping fractured-cavity information), eliminated redundant information, and introduced new variables (principal components) that comprehensively summarize fractured-cavity features across all original attributes. To extract the dominant features of fractured cavities via attribute compression, this study utilized principal component analysis. This algorithm independently assigns weights to the calculation factors of various seismic attributes, distributing weights according to the similarities and differences among attributes, thus enabling effective fusion of diverse seismic attributes.

For the analysis of a specific seismic attribute, a seismic attribute observation data matrix was constructed based on its characteristic features. Suppose the number of samples of the seismic attribute data is *n,* and the number of seismic attribute features is *p*, then the seismic attribute observation data matrix is **(Equation 17)**:

$$X = \begin{bmatrix} X_{11} & \cdots & X_{1P} \\ \vdots & \ddots & \vdots \\ X_{n1} & \cdots & X_{nP} \end{bmatrix} \tag{17}$$

Since the numerical ranges and dimensions of different seismic attribute data vary, it is necessary to convert multiple seismic attribute datasets to a common observation range; in other words, attribute standardization must be performed, as shown in **Equation 17**.

$$X = \frac{X_{ij}}{X_{1j}}\left(i = 1,2,\ldots n; j = 1,2,\ldots n, p\right) \tag{18}$$

The standardized seismic attribute data matrix X was then analyzed, and its correlation matrix $R_2$ was calculated. The matrix $R_2$ is symmetric, and the correlation coefficient after standardization is simplified as follows **(Equation 19)**:

$$R_2 = \begin{bmatrix} r_{11} & \cdots & r_{1p} \\ \vdots & \ddots & \vdots \\ r_{n1} & \cdots & r_{np} \end{bmatrix} \tag{19}$$

The seismic attribute features were obtained by calculating the correlation coefficient matrix $R_2$, where $\overline{x_i}$ and $\overline{x_j}$ are the means of the i-th and j-th attributes and are denoted as $r_{ij} = \frac{1}{n-1}\sum_{i=1}^{n}(x_{li} - \overline{x_i})(x_{li} - \overline{x_j})\left(i, j = 1,2,\ldots p\right)$, respectively. The characteristic equation $|R_2 - \lambda I| = 0$ was considered, and *k* principal components were selected. The variance contribution rate of the k-th principal component is given by $\beta_k$, and the proportion of total variance explained by the first *k* principal components is expressed by the cumulative contribution rate *M* **(Equation 20)**:

$$\beta_k = \left(\sum_{i=1}^{p} i\right)^{-1} M = \sum_{i=1}^{k} \lambda_k \left(\sum_{i=1}^{p} i\right)^{-1} \tag{20}$$

In practice, the cumulative contribution rate *M* of the features was chosen to exceed 90%.[20]

### 2.4. Experiments and analysis

Figure 11 illustrates the flowchart of the fractured-cavity identification and characterization methodology adopted in this study. All code utilized in this study was developed using Python version 3.8. The computational environment consisted of a Windows 10 operating system and an NVIDIA GeForce RTX 4080 Ti GPU with 16 GB of memory.

Model training was conducted on a dataset composed of 800 input samples, each with dimensions of 128 × 128 × 128, processed in batches of four. The training procedure spanned 25 epochs.

The key hyperparameters of Swin-UNETR were set as follows: an initial learning rate of 0.0001 was adopted, the Adam optimizer was selected for parameter updating, and the optimization objective was defined as a weighted combination of Dice loss and cross-entropy loss. The evaluation metrics included loss, Dice coefficient, and intersection over union, with the training and validation results presented in Figure 12.

## 3. Results and discussion

A significant advantage of data-driven models lies in their ability to generalize. In this study, we applied our methodology to the designated study area and systematically characterized the segmental and hierarchical features of the identified fractured cavities on both horizontal planes and vertical profiles.

Within the study region, the Ordovician system comprises approximately 2,000 m of mudstone and sandstone, whereas the stratigraphic sequence from the Middle Ordovician to the Cambrian encompasses over 3,000 m of marine carbonate formations. Multiple seismic reflection horizons have been delineated by geologists within these strata. Notably, the Ordovician carbonate reservoirs are regarded as the primary targets for exploration in the central Tarim Basin.

Guided by the geometric and kinematic frameworks of strike–slip faulting, which is predominantly characterized by horizontal displacement, our analysis focuses on specific horizons: $H_7^4$ (demarcating the boundary between the Middle and Upper Ordovician), $H_7^6$, $H_7^8$, $H_8^0$ (the interface

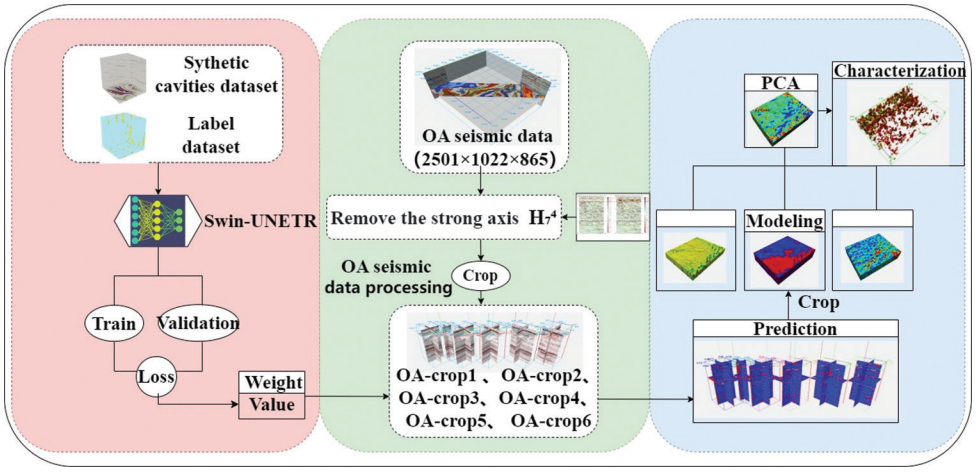


**Figure 11.** The flowchart of the fractured cavities identification and characterization method
Abbreviations: OA: Object area; PCA: Principal component analysis.

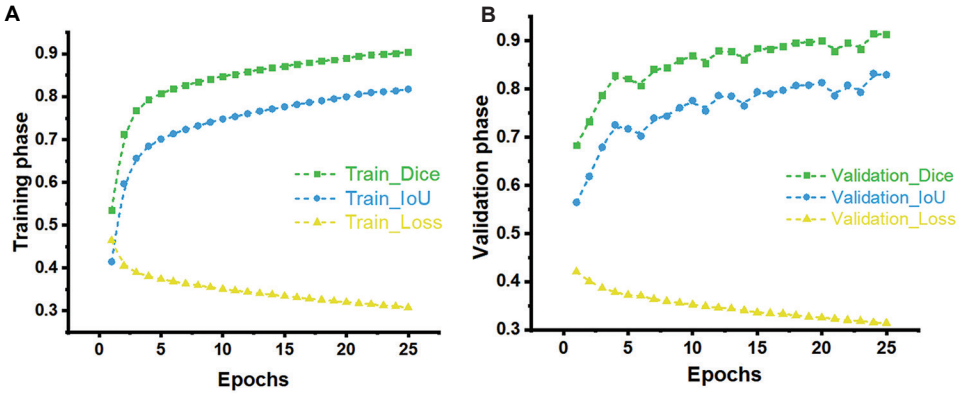


**Figure 12.** Evaluation metric curves. (A) Training and (B) validation phases.
Abbreviation: IoU: Intersection over Union.

between the Lower Ordovician and Upper Cambrian), $H_8^1$ (separating the Upper and Lower Cambrian), and $H_9^0$ (the basal Cambrian horizon). These horizons served as the basis for presenting the identification outcomes of fractured cavities within horizontal stratigraphic levels.

Within the study area, fractured cavities are primarily controlled by the strike–slip fault zone (OA) rather than dissolution processes. To clarify this control mechanism, scanning coherence detection was first performed on the post-stack seismic data of the study area to obtain the seismic dip gather. Subsequently, elastic impedance inversion was conducted based on this dip gather, generating key petrophysical parameters including elastic modulus and Poisson's ratio. Finally, the maximum principal stress field was derived through systematic calculations. Figure 13 presents the maximum principal stress field integrated with geological data. The fault zone can be categorized into three main structural segments: Compression segments, pull-apart segments, and translation segments, which alternate sequentially along the fault strike. Figures 14-19 illustrate that strata in compression segments are uplifted by stress. In these areas, independent, fractured cavities with circular outlines frequently develop at stress-concentrated locations, often referred to as cave-like features. When compressive and strike–slip stresses are superimposed, such cave-like anomalies are widely distributed.

In pull-apart segments, pull-apart and strike–slip stresses act synergistically. Regions subjected to strong

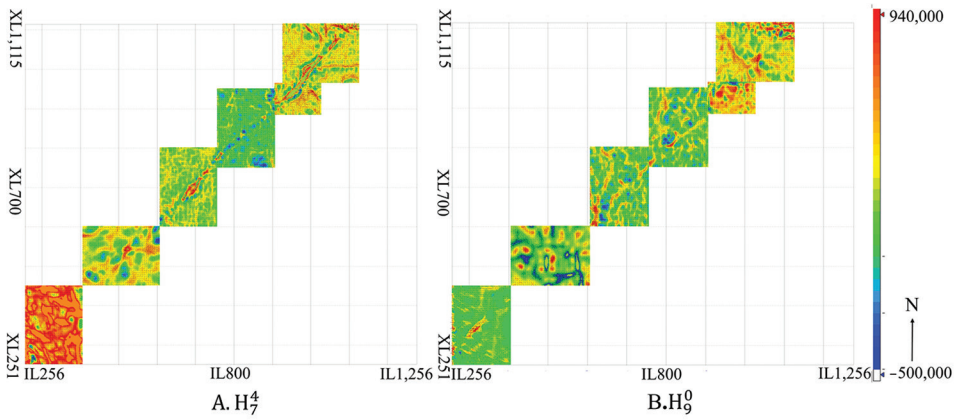


**Figure 13.** Maximum principal stress plane maps of the $H_7^4$ and $H_9^0$ horizons in the object area

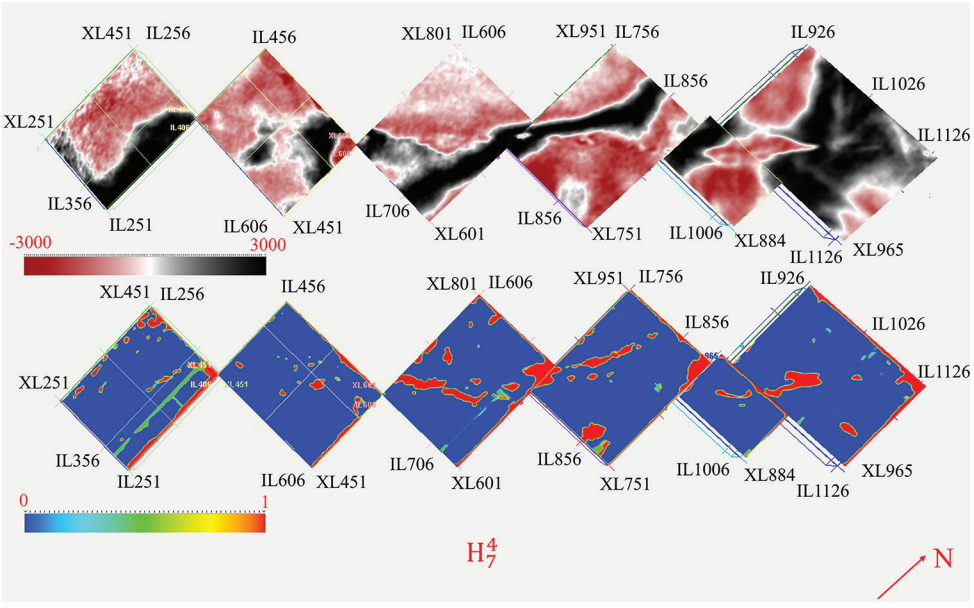


**Figure 14.** Original seismic data and fractured cavities identification results of the $H_7^4$ horizon in the object area

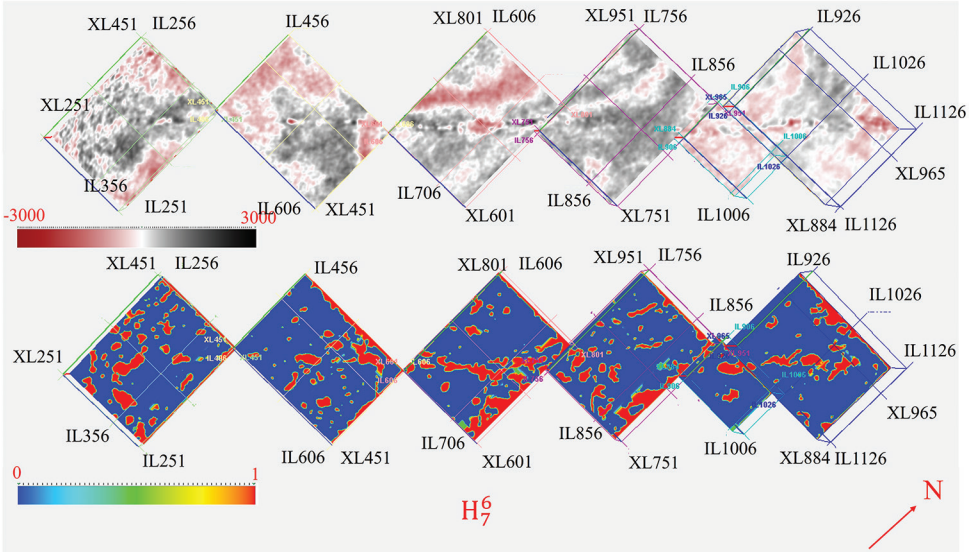


**Figure 15.** Original seismic data and fractured cavities identification results of the $H_7^6$ horizon in the object area

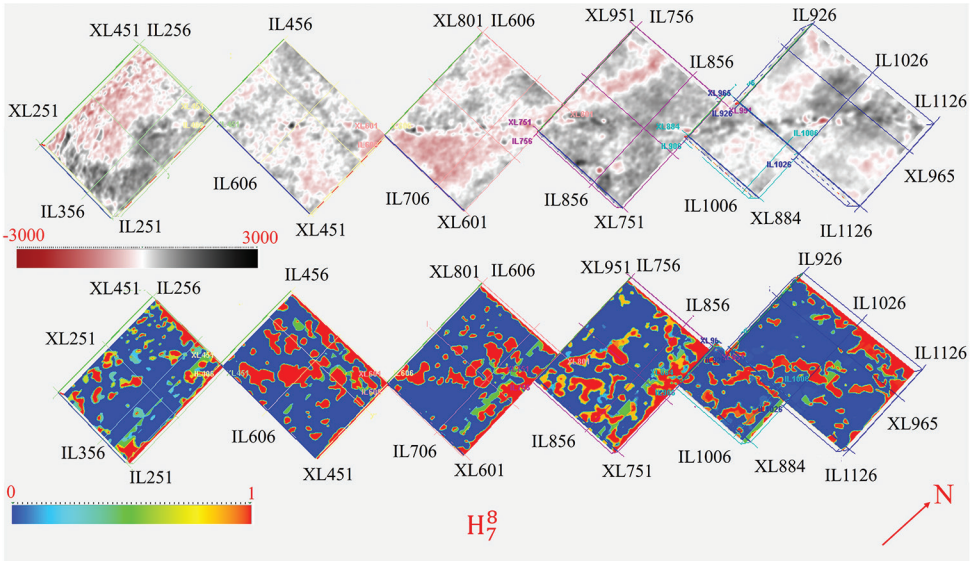


**Figure 16.** Original seismic data and fractured cavities identification results of the $H_7^8$ horizon in the object area

pull-apart stress host elongated fractured cavities termed fault-related bodies that are aligned with the fault trend. Adjacent cave-like features near these fault-related bodies may merge at their boundaries, forming larger and more irregular cavity systems. In translation segments, only strike–slip stress is present. Here, fractured cavities with regular morphologies develop along the fault, whereas cave-like features are scarce.

When the stress regime transitions from pull-apart to compression, multiple fault-related bodies typically form. Under compressive stress, these bodies converge toward the central region. Cave-like features often develop at the edges of compression zones, with their cores either contacting fault-related bodies or lying between several such bodies. When the stress regime shifts from translation to compression, a single fault-related body generally emerges within the uplifted strata. This body penetrates the core of the cave-like feature but does not connect its opposite sides.

Furthermore, the fractured cavities exhibited a hierarchical structure in the vertical profile of the study area. As shown in Figures 14-19 , the density and

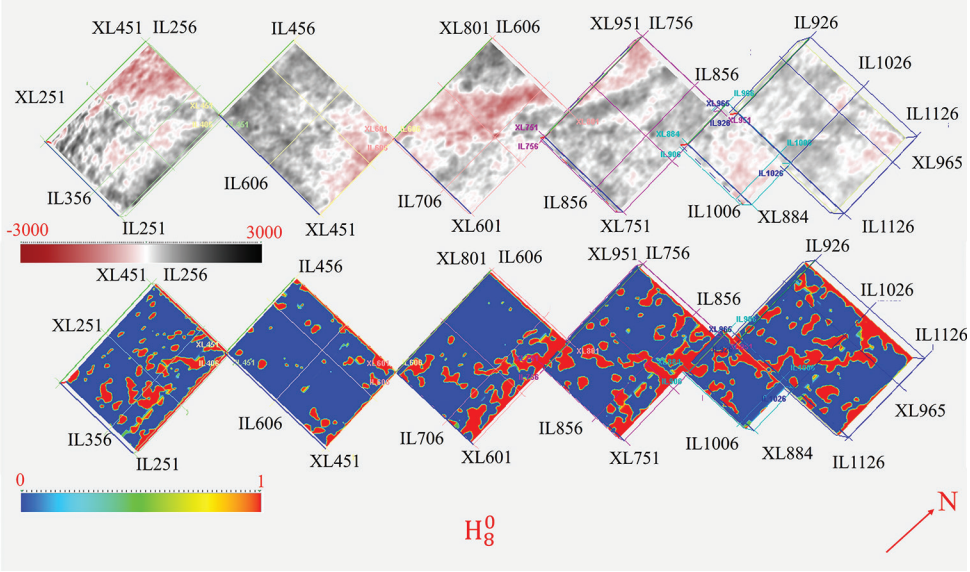


**Figure 17.** Original seismic data and fractured cavities identification results of the $H_8^0$ horizon in the object area

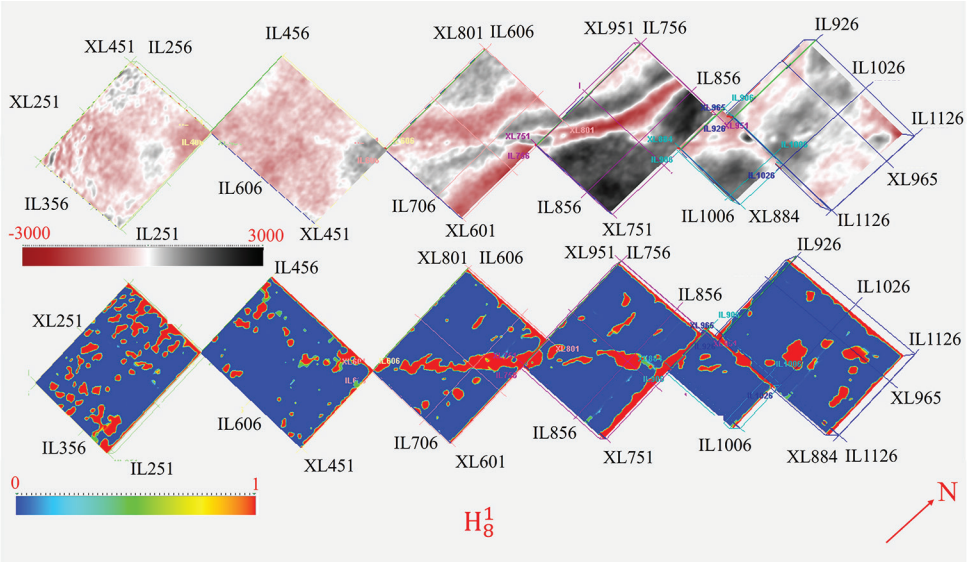


**Figure 18.** Original seismic data and fractured cavities identification results of the $H_8^1$ horizon in the object area

complexity of fractured cavity development gradually increased from stratigraphic levels $H_7^4$–$H_7^8$, whereas transitioning from dense to sparse from $H_7^8$ to $H_9^0$. This variation is presumably linked to differential dissolution sensitivity caused by lithological heterogeneity in the carbonate strata, such as the interbedding of dolomite and limestone. Figure 20 further demonstrates that fractured cavities developed between $H_7^4$ and $H_7^8$ can be distinctly categorized from those between $H_7^8$ and $H_9^0$, based on differences in their structural characteristics and abundance.

The first type of fractured cavities is characterized by vertical elongation in the profile, manifesting as steep and upright structures. Larger cavities tend to exhibit a roughly funnel-shaped morphology, whereas smaller ones display nearly circular outlines. Extensive fault-related fractured cavities formed within the strike–slip fault zone are almost continuous, extending from shallow to deep intervals. In addition, smaller, cave-like fractures occur on both sides of the fault, extending through the entire target stratum. Conversely, the second type of fractured cavities develops predominantly in a near-horizontal

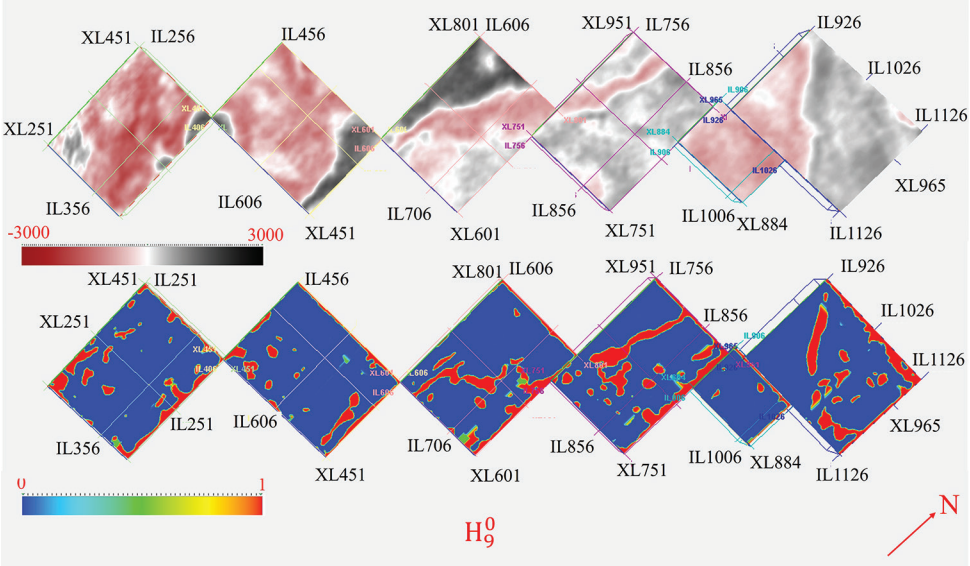


**Figure 19.** Original seismic data and fractured cavities identification results of the $H_9^0$ horizon in the object area

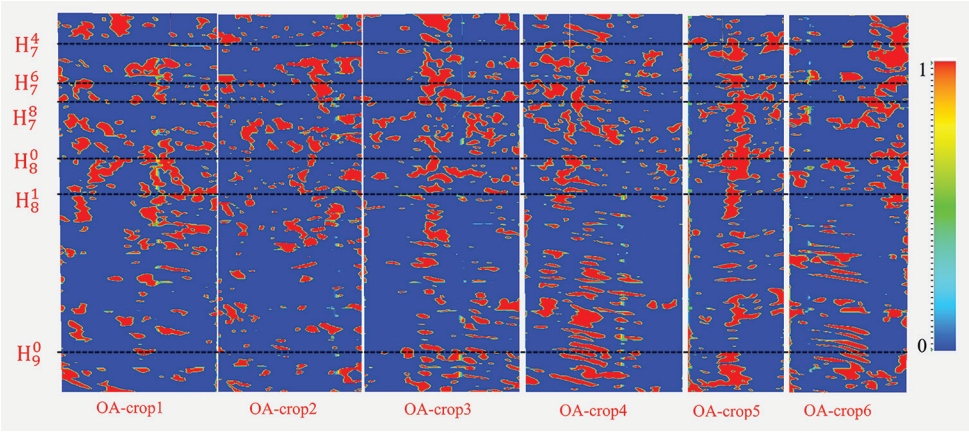


**Figure 20.** Fractured-cavity identification profile of the object area (OA)

orientation, exhibiting a flattened morphology. These cavities are distributed at regular intervals, have smaller sizes than the first type, and are less extensively developed. Nonetheless, they also display significant vertical connectivity within the fault zone.

To determine the outline of fault-controlled bodies, we employed a method that fuses different seismic attribute volumes after threshold truncation. The post-stack seismic data OA-crop1 is segmented into three parts: OA-crop1-1 ($H_7^4$–$H_7^6$), OA-crop1-2 ($H_7^6$–$H_7^8$), and OA-crop1-3 ($H_7^8$–$H_8^0$). Amplitude curvature and coherence detection attributes were extracted from these segments. Following outlier processing and standardization of the selected dominant attributes, attribute compression was performed using principal component analysis. Finally, the amplitude curvature, coherence detection attributes, and image segmentation results were merged.

Figures 21-23 show, from left to right, the network-based segmentation results, the calculated amplitude curvature and coherence attributes, and the fused attribute result. The figures demonstrate that the fused attribute volume integrates all the high-value features from the first three attribute volumes. A color-based comparison reveals that the fused attribute volume exhibits enhanced responses at locations where fractured cavities are consistently identified by all three attribute volumes. In regions where discrepancies occurred among the three attribute volumes, the fractured cavity features from the first volume were assigned greater weight. This fusion procedure combined the three attribute volumes into a single, integrated

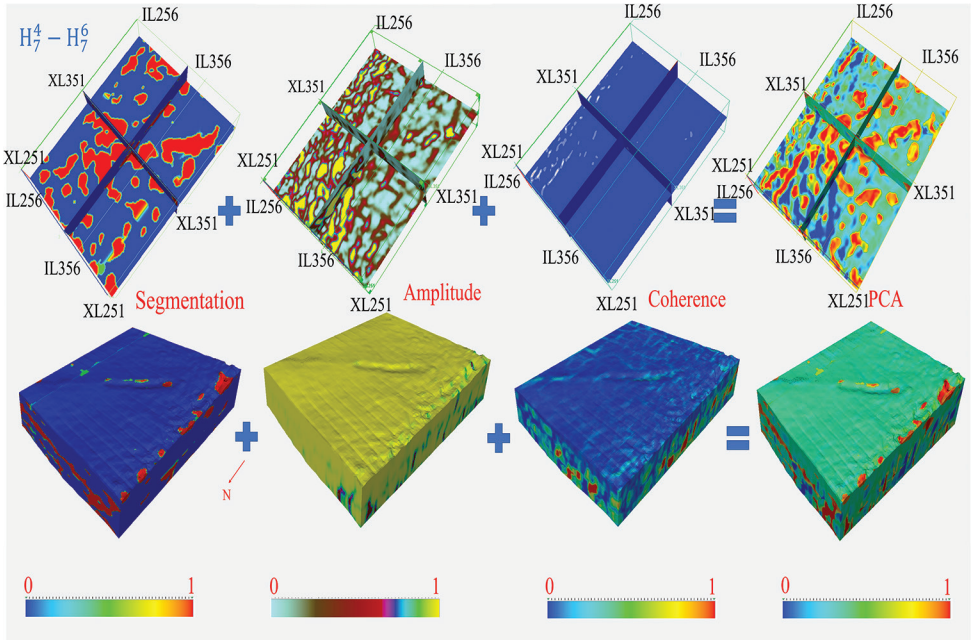


**Figure 21.** Seismic attribute fusion result map of the OA-crop1 $H_7^4$–$H_7^6$ horizon in the object area
Abbreviations: OA: Object area; PCA: Principal component analysis.

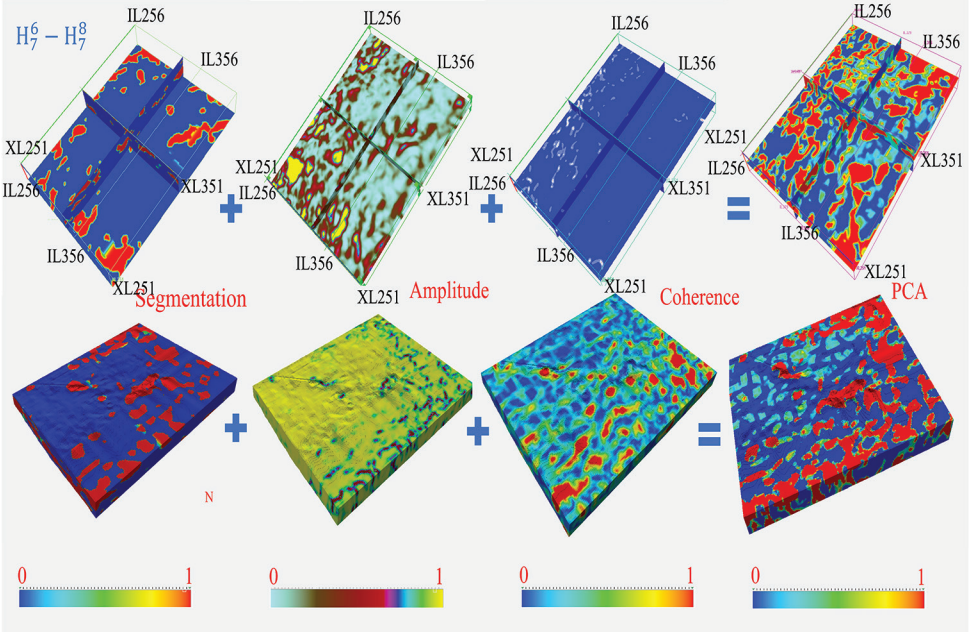


**Figure 22.** Seismic attribute fusion result map of the OA-crop1 $H_7^6$–$H_7^8$ horizon in the object area
Abbreviations: OA: Object area; PCA: Principal component analysis.

volume, effectively reducing the uncertainty associated with fractured cavities.

The fractured cavities were then modeled and characterized using a 4 × 4 × 1 grid in the local object area, where the color gradient from light to dark represents an increasing probability of fractured-cavity occurrence.[21] Figures 24-26 show the final fractured cavity body results.

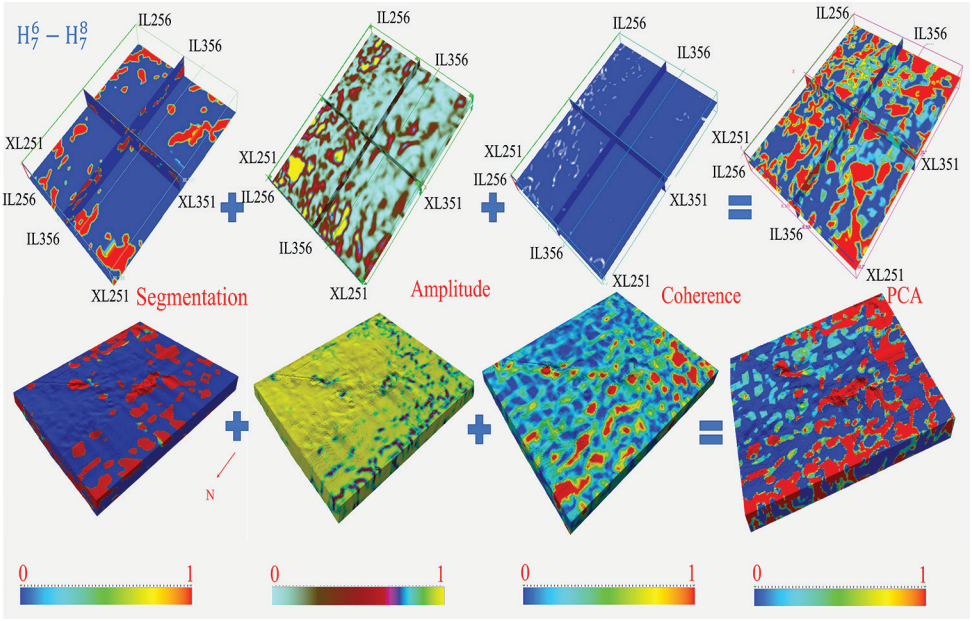


**Figure 23.** Seismic attribute fusion result map of the OA-crop1 $H_7^8$–$H_8^0$ horizon in the object area
Abbreviations: OA: Object area; PCA: Principal component analysis.

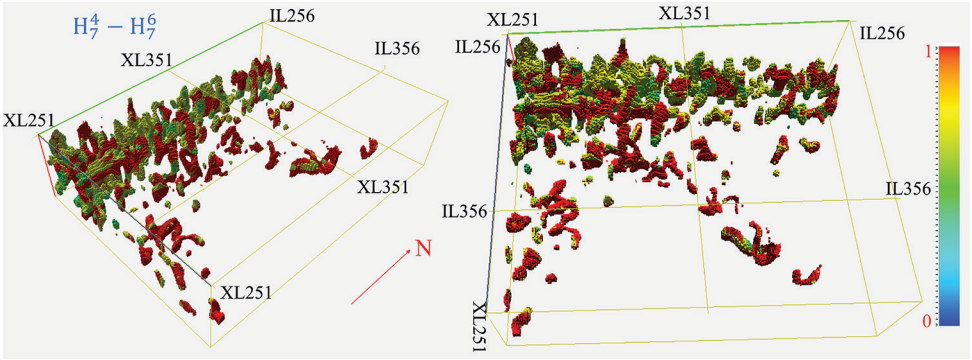


**Figure 24.** Fractured-cavity body map for the $H_7^4$–$H_7^6$ horizon in object area (OA)-crop1 of the OA

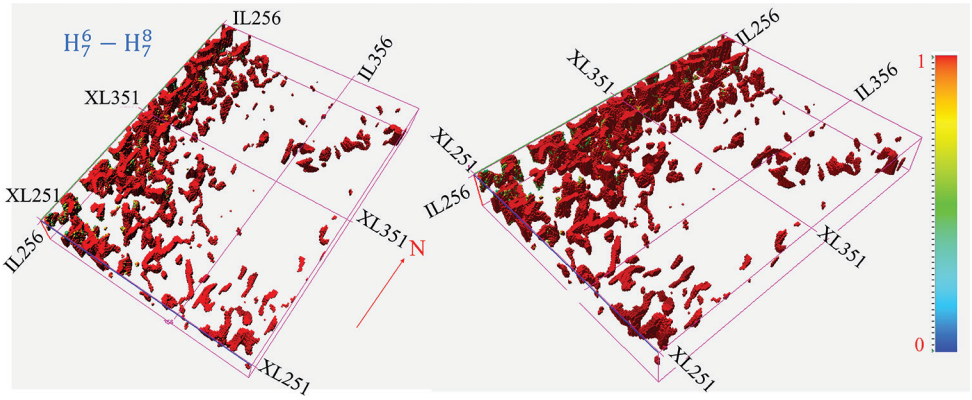


**Figure 25.** Fractured-cavity body map for the $H_7^6$–$H_7^8$ horizon in object area (OA)-crop1 of the OA

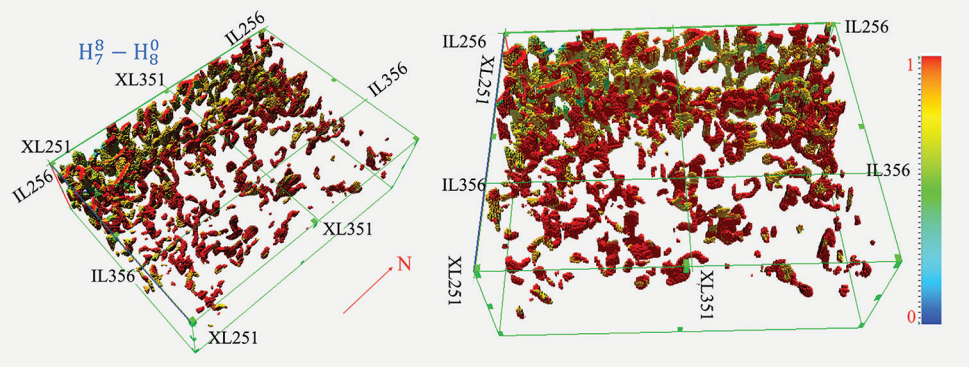


**Figure 26.** Fractured-cavity body map for the $H_7^8$–$H_8^0$ horizon in object area (OA)-crop1 of the OA

## 4. Conclusion

Fractured cavities in reservoirs within carbonate formations have complex geological features. These features make it hard to precisely locate and map fracture caves using conventional methods. This study introduces a novel two-step methodology to identify and delineate fractured-cavity reservoirs in response to these challenges.

First, the Swin-UNETR architecture was employed to automatically detect reflective signatures of fractured cavity reservoir strata in the Shunbei field. An attention gate mechanism was incorporated into the Swin-UNETR model, enhancing its capability to interpret the dense and complex features associated with fractured cavity labels in 3D seismic data. Then, we applied a feature extraction strategy that fuses multiple seismic attributes using principal component analysis. This approach reduced uncertainty, leading to more accurate and robust identification results.

Application of this methodology to Shunbei field data has demonstrated its accuracy in recognizing the characteristic beaded reflections in seismic records. The identified fractured-cavity reservoirs exhibit both planar and vertical spatial attributes, revealing segmented patterns in plain view. Fractured cavity development varied significantly across different tectonic segments. In compressional zones, stress-induced strata uplift resulted in nearly circular, isolated fractured cavities in areas of high stress concentration. In regions where compressive and strike–slip stresses interact, extensive irregular cave-like anomalies were developed. Pull-apart segments, influenced by both pull-apart and strike–slip stresses, hosted elongated fractured cavities that were aligned with the strike–slip direction. These cavities often had adjacent cave-like features whose edges interfaced with fault-related bodies, resulting in irregularly expanded fractured cavities. In translational segments that are subjected solely to strike–slip stress, fault-related fractured cavities exhibited regular edges aligned with the strike–slip direction, accompanied by sparse surrounding cave-like features.

Analysis of the OA profile revealed a stratified structural framework. The first category of fractured cavities extends vertically in profile and is characterized by steep, upright morphologies. Large-volume fractured cavities display roughly funnel-shaped geometries, whereas smaller cavities tend to be nearly circular. Within the strike–slip fault zone, substantial fault-related fracture caves demonstrated near-continuity across both shallow and deep strata, flanked by smaller cave-like features that penetrated the entire target formation. The second category predominantly developed in a near-horizontal direction, presenting flatter morphologies with discrete intervals between individual cavities. These features had smaller outlines and were more spatially constrained than the first category. Nevertheless, they exhibited strong vertical connectivity both within and beneath the fault zone. Finally, fractured cavities were delineated with a fixed grid size to standardize their spatial representation.

This integrated methodological framework provides a robust tool for the detailed characterization of fractured cavity reservoirs, thereby facilitating a deeper understanding of their spatial distribution and geological evolution within complex carbonate strata.

## Acknowledgments

None.

## Funding

This work was supported by the National Natural Science Foundation of China (Grant no. 42274180) and the Graduate Innovation Program of China University of Mining and Technology (Grant no. 2025WLJCRCZL003).

## Conflict of interest

Qiang Guo is an Editorial Board Member of this journal, but was not in any way involved in the editorial and peer-review process conducted for this paper, directly or indirectly. The authors declare they have no competing interests.

## Author contributions

*Conceptualization:* Yunhao Cui, Chao Xu
*Formal analysis:* Zhiqiang Lu
*Investigation:* Yunhao Cui, Chao Xu, Zhanpeng Chen, Yuwen Qian
*Methodology:* Yunhao Cui, Yaping Huang, Qiang Guo
*Writing–original draft:* Yunhao Cui
*Writing–review & editing:* Yuhua Chen

## Availability of data

Data will be made available upon request to the corresponding author.

## References


1. Ma Y, Cai X, Yun L, *et al*. Practice and theoretical and technical progress in exploration and development of Shunbei ultra-deep carbonate oil and gas field, Tarim Basin, NW China. *Pet Explor Dev*. 2022;49(1):1-20.

   doi: 10.1016/s1876-3804(22)60001-6

2. Wu X, Yan S, Qi J, Zeng H. Deep learning for characterizing paleokarst collapse features in 3-D seismic images. *JGR Solid Earth*. 2020;125(9):e2020JB019685.

   doi: 10.1029/2020jb019685

3. Li Z, Li H, Liu J, Deng G, Gu H, Yan Z. 3D seismic intelligent prediction of fault-controlled fractured-vuggy reservoirs in carbonate reservoirs based on a deep learning method. *J Geophys Eng*. 2024;21(2):345-358.

   doi: 10.1093/jge/gxae005

4. Gui Z, Zhang J, Zhang Y, Sun C. Characterization of fault-karst reservoirs based on deep learning and attribute fusion. *Acta Geophys*. 2024;73(2):1335-1347.

   doi: 10.1007/s11600-024-01420-5

5. Zhang G, Lin C, Ren L, *et al*. Seismic characterization of deeply buried paleocaves based on Bayesian deep learning. *J Nat Gas Sci Eng*. 2022;97:104340.

   doi: 10.1016/j.jngse.2021.104340

6. Vaswani A, Shazeer N, Parmar N, *et al*. *Attention is All You Need*. [arXiv Preprint]; 2023.

   doi: 10.48550/arXiv.1706.03762

7. Chen L, Liu X, Zhou H, Zhang H, Lyu F, Mo Q. Identification of carbonate cave reservoirs based on variational bayesian principal component analysis. *IEEE Trans Geosci Remote Sens*. 2023;61:1-10.

   doi: 10.1109/tgrs.2023.3333962

8. Li B, He Y, Chen W, Shang H, Wang L. Geological modeling of carbonate fracture-cavity reservoir: Case study of Shunbei fault zone No. 5. *Front Earth Sci*. 2025;13:1559030.

   doi: 10.3389/feart.2025.1559030

9. Wang S, Si X, Cai Z, Sun L, Wang W, Jiang Z. Fast global self-attention for seismic image fault identification. *IEEE Trans Geosci Remote Sens*. 2024;62:1-11.

   doi: 10.1109/tgrs.2024.3436066

10. Ma Q, Duan T. Multi-level ultra-deep fault-controlled karst reservoirs characterization methods for the Shunbei field. *Front Earth Sci*. 2023;11:1149678.

    doi: 10.3389/feart.2023.1149678

11. Zheng D, Zhang L, Shen F. Structural heterogeneities in fault-controlled cavity carbonate reservoirs: Insights into fracture and fault patterns. *J Struct Geol*. 2025;193:105358.

    doi: 10.1016/j.jsg.2025.105358

12. Li H, Lin C, Ren L, Zhang G, Chang L, Dong C. Quantitative prediction of multi-period tectonic fractures based on integrated geological-geophysical and geomechanics data in deep carbonate reservoirs of Halahatang oilfield in northern Tarim Basin. *Mar Pet Geol*. 2021;134:105377.

    doi: 10.1016/j.marpetgeo.2021.105377

13. Ding Y, Du Q, Fu L, Jian S. Reliability analysis of seismic attribute in the detection of fault-karst. *Interpretation*. 2020;8(4):SP61-SP70.

    doi: 10.1190/int-2019-0299.1

14. Wang S, Cai Z, Si X, Cui Y. A three-dimensional geological structure modeling framework and its application in machine learning. *Math Geosci*. 2023;55(2):163-200.

    doi: 10.1007/s11004-022-10027-9

15. Wu X, Liang L, Shi Y, Fomel S. FaultSeg3D: Using synthetic data sets to train an end-to-end convolutional neural network for 3D seismic fault segmentation. *Geophys*. 2019;84(3):IM35-IM45.

    doi: 10.1190/geo2018-0646.1

16. Liu Z, Lin Y, Cao Y, *et al*. *Swin Transformer: Hierarchical Vision Transformer Using Shifted Windows*. [arXiv Preprint]; 2021. p. 10012-10022.

    doi: 10.48550/arXiv.2103.14030

17. Hatamizadeh A, Tang Y, Nath V, *et al*. *UNETR: Transformers for 3D Medical Image Segmentation*. [arXiv Preprint]; 2021. p. 574-584.

doi: 10.48550/arXiv.2103.10504

18. Oktay O, Schlemper J, Folgoc LL, *et al*. *Attention U-Net: Learning Where to Look for the Pancreas*. [arXiv Preprint]; 2018.

    doi: 10.48550/arXiv.1804.03999

19. Hatamizadeh A, Nath V, Tang Y, Yang D, Roth H, Xu D. *Swin UNETR: Swin Transformers for Semantic Segmentation of Brain Tumors in MRI Images*. [arXiv Preprint]; 2022.

    doi: 10.48550/arXiv.2201.01266

20. Mishra S, Sarkar U, Taraphder S, *et al*. Multivariate statistical data analysis- principal component analysis. *Int J Livest Res*. 2017;7:60-78.

    doi: 10.5455/ijlr.20170415115235

21. Song S, Mukerji T, Hou J, Zhang D, Lyu X. GANSim-3D for conditional geomodeling: Theory and field application. *Water Resour Res*. 2022;58(7):e2021WR031865.

    doi: 10.1029/2021wr031865

ACCSCIENCE PUBLISHING

Journal of Seismic Exploration

ARTICLE

# High-precision full-waveform inversion velocity modeling and broadband processing for a deepwater exploration of the South China Sea

**Wei Liu[1], Yi Liao[2], Jie Cui[3]*, Ning Zhang[1], Guo Dong Zhang[2], Zi Jing Gong[3], Rong Li[3], Lian Lian Liu[3], and Miaoyang Yuan[3]**

[1]China National Offshore Oil Corporation Ltd. Zhanjiang Branch, Zhanjiang, Guangdong, China

[2]China National Offshore Oil Corporation Ltd. Hainan Branch, Haikou, Hainan, China

[3]Department of Digital and Integration, SLB, Beijing, China

(This article belongs to the *Special Issue: Full Waveform Inversion Methods and Applications for Seismic Data in Complex Media*)

## Abstract

In deepwater fields, drilling costs are extremely high, and the "one sand, one well" situation is common, in which a single well must control an overly large area of the gas field. Structural accuracy decreases in areas distant from the well locations, making gas reservoir prediction and sand body delineation challenging due to the limited resolution of seismic data. To address these challenges, this study applied high-precision full-waveform inversion (FWI) velocity modeling and broadband imaging technology in a deepwater exploration of the South China Sea. In the preprocessing stage, based on the geological challenges and features of the acquired seismic data, we selected appropriate signal-processing methods and optimized the algorithms and parameter sets, successfully developing a customized broadband processing workflow specifically tailored for deepwater applications. The entire broadband processing sequence effectively supported subsequent FWI modeling. During the imaging stage, FWI was successfully applied for the 1st time in the deepwater of the South China Sea. Together with Q pre-stack depth migration, this integrated approach effectively addressed challenges in structural depth prediction and significantly improved imaging resolution. This study provided real-time support for gas field development and optimized the well placement for deepwater development.

***Keywords:*** Deepwater; Low-frequency noise attenuation; Broadband processing; Full-waveform inversion

***Corresponding author:**
Jie Cui
(jcui2@slb.com)

**Citation:** Liu W, Liao Y, Cui J, *et al*. High-precision full-waveform inversion velocity modeling and broadband processing for a deepwater exploration of the South China Sea. *J Seismic Explor*. 2026;35(1):139-150.
doi: 10.36922/JSE025410084

**Received:** October 11, 2025

**Revised:** December 9, 2025

**Accepted:** December 15, 2025

**Published online:** January 7, 2026

**Copyright:** © 2026 Author(s). This is an Open-Access article distributed under the terms of the Creative Commons Attribution License, permitting distribution, and reproduction in any medium, provided the original work is properly cited.

**Publisher's Note:** AccScience Publishing remains neutral with regard to jurisdictional claims in published maps and institutional affiliations.

## 1. Introduction

Since the mid-1980s, there has been an increase in exploration activities and challenges related to new discoveries in onshore and shallow-water oil and gas fields, along with the evolution of exploration and development technologies. Due to this advancement, deepwater oil and gas exploration and development have attracted increasing attention and expanded significantly over the past decade. Deepwater exploration has become a strategic focus in global hydrocarbon exploration.[1,2]

With the increasing depth of exploration targets in deepwater fields, traditional seismic data processing and interpretation techniques often fail to meet the requirements of deepwater oil and gas exploration. Several new techniques and methods[3] have been specifically developed for deepwater exploration, among which seismic velocity modeling remains a critical stage.

The Lingshui gas field is the first deepwater gas field in China discovered through independent exploration. Due to the extremely high drilling costs in deepwater, exploration wells are sparsely distributed, resulting in excessively large control ranges for individual wells, and significantly reducing the structural accuracy for areas far away from well locations. In the field, the well control is limited, and the accuracy of single sand body delineation cannot meet the exploration and production requirements. Moreover, due to the limited resolution of seismic data, it is challenging to identify and predict the distribution of shale interlayers within the gas field. In this study, we applied high-precision full-waveform inversion (FWI) technology to explore the Lingshui gas field.

To address the challenges of deepwater exploration, we developed a signal processing workflow including low-frequency noise attenuation and low-frequency signal expansion. We evaluated multiple combinations of noise-attenuation algorithms to improve the signal-to-noise ratio. The anomalous amplitude attenuation (AAA) and curvelet transform are applied to suppress low-frequency noise while preserving low-frequency signals.[4,5] Combined with adaptive deghosting technology, the low-frequency signal is effectively enhanced.[6]

The entire workflow provided the input data required for subsequent high-precision FWI velocity modeling. FWI is a high-precision, high-resolution methodology for inverting subsurface properties defined by the wave equation. It reconstructs the earth model using amplitude and phase information from seismic data. Since Lailly and Tarantola introduced the concept of FWI to seismic exploration,[7,8] this technique has received increasing attention and has been widely studied and applied in seismic velocity modeling.

Conventional FWI minimizes the least-squares difference between the acquired and the predicted data. It is exposed to cycle-skipped solutions that cause the process to converge to local minima rather than the global minima. In this study, a robust adaptive FWI based on a phase shift objective function is first applied to construct the velocity model, correcting erroneous background models, mitigating cycle-skipping issues, and improving the robustness of FWI when using inaccurate initial models.[9,10]

Based on the challenges of deepwater exploration, the FWI velocity model building was implemented in three bands. In Band 1 and Band 2, data after noise attenuation were used as input to FWI. To introduce more information for velocity updates in deep layers, data after deghosting and multiple attenuation were used as the input data in the Band 3 FWI. The Band 1 applied an adaptive FWI based on a phase-only objective function, while the latter two bands used the conventional least-squares FWI whose objective function was constructed using amplitude residuals between observed and synthetic data. This study also conducted sophisticated quality control (QC) in each FWI band, including interleave shot gather QC, well-log velocity QC, and mistie analysis QC. By applying FWI to derive a high-accuracy subsurface velocity model, we effectively provided real-time support for the oilfield development plan for the first self-owned deepwater giant gas field in China, guided the optimization of well placement, and saved a significant amount of cost for drilling operations.

## 2. Methods

### 2.1. Amplitude-preserved low-frequency noise attenuation

The success of an FWI relies on certain requirements for the input data. Seismic data acquired in deepwater areas always suffer from strong low-frequency noise, such as swell noise. To enhance the signal-to-noise ratio of seismic data, a customized noise suppression workflow was designed using a combination of methods across multiple domains, algorithms, and frequency bands.

Specifically, we applied a combination of the AAA and curvelet transform for low-frequency noise attenuation. AAA is a method that suppresses random noise by transforming seismic data into the frequency domain within a certain time window. It utilizes a spatial median filter to compare the amplitude of the seismic trace with the average amplitude of adjacent traces, determining whether it is a noisy trace. Once a trace is identified as noise, it is either attenuated by multiplying it by a coefficient or replaced by the interpolation of neighboring seismic traces. This method has been used to suppress low-frequency noise in low-pass frequency bands.

For residual low-frequency swell noise, we innovatively used a residual coherent noise suppression method in the curvelet domain. Similar to the Fourier transform, which decomposes different frequency components into sine and cosine functions and reconstructs them in the time-x domain, curvelet transforms employ a more precise and sophisticated transformation that prevents signal loss due to time-frequency domain conversion. Figure 1 shows the original shot gather, post-noise suppression shot gather, and the suppressed noise. The results clearly demonstrate that swell noise is effectively suppressed. Overall, the study

employed a combination of AAA and curvelet transform techniques for effective noise suppression in deepwater seismic data, which is essential for accurate FWI velocity modeling and provides a solid foundation for subsequent imaging.

### 2.2. Adaptive deghosting

When acquiring marine seismic data, to reduce the influence of sea surface swell noise, streamers are typically placed at a certain depth to record seismic data. As an interface between air and seawater, the sea surface is a strong reflector for seismic waves. When the upgoing reflected seismic wave reaches the sea surface, it reflects back to the water bottom with reversed polarity and is recorded by the hydrophone. This downward reflection wave is referred to as a ghost reflection or ghost wave. Both the seismic reflection wave and the ghost wave are recorded by the streamer and interfere with each other, causing notch phenomena in the spectrum. The waveform of the reflection signal is also changed by the ghost waves; the amplitude at corresponding notch frequencies is significantly reduced, affecting the resolution of seismic data. Therefore, adaptive deghosting technology is an effective method for suppressing ghost waves, eliminating the notch effects caused by these waves, and restoring the low-frequency components in the seismic signal. The expansion of low-frequency components is crucial for FWI.

Over the past few decades, various methods have been developed for ghost wave suppression, such as the inverse scattering series method[11] and the frequency-wavenumber domain wavefield extrapolation method.[12] However, due to various constraints during the in-field seismic data acquisition, ghost suppression methods do not always yield satisfactory results. In this study, we applied a ghost wave suppression method proposed by Rickett *et al.*[6] The algorithm adaptively solves the upgoing wavefield and ghost wave delays in the local plane-wave domain (Tau-p domain). The seismic data, denoted as $d$ in **Equation 1**, is sparsely decomposed by minimizing the objective function shown in **Equation 1**:

$$\chi(x,\Delta t)=\left\|W\left[SG\left(\Delta t\right)x-d\right]_2^2+\left\|x_1\right\|\right\| \quad (1)$$

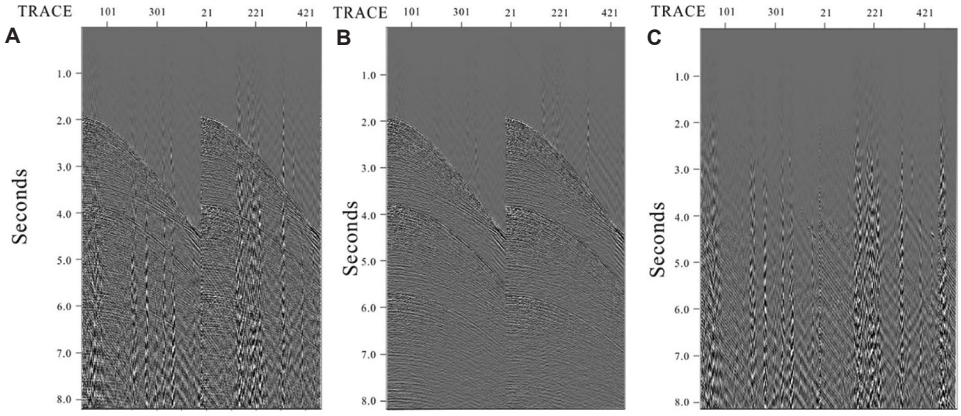


**Figure 1.** Comparison before and after noise suppression (A) Original shot gathers. (B) Post-noise suppression shot gather. (C) Suppressed noise.

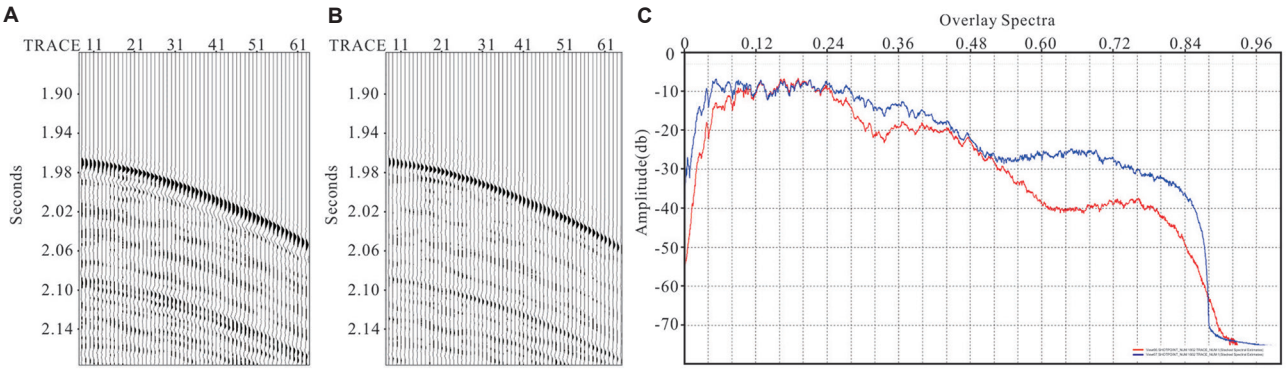


**Figure 2.** QC of the result before and after deghosting. (A) Shot gather before adaptive deghosting, (B) shot gather after adaptive deghosting, and (C) spectral analysis of the near-offset gather before (red) and after (blue) adaptive deghosting.

Where $x$ represents the coefficients of the plane-wave basis, $\Delta t$ is the delay time, $W$ represents a weighting function that can be used to balance the amplitude of the input seismic data, $S$ is the plane-wave synthesis factor, and $G(\Delta t)$ represents the ghost wave suppression factor. The adaptive deghost method utilizes receiver depth information to suppress ghost waves in the shot gather. **Equation 1** defines the objective function used in the inversion and quantifies the misfit between the observed and modeled data. Physically, this equation quantifies how well the simulated wavefield reproduces the recorded wavefield. The first term typically involves the squared L2 norm of the data residuals, ensuring that the inversion minimizes amplitude and phase differences between observed and modeled traces. The algorithm is robust even when the data contains strong noise. In addition, it can suppress ghost waves, correct phase information, mitigate notch effects, enhance low-frequency energy, broaden the frequency spectrum, and restore a more accurate wavelet. Particularly, the expansion of low-frequency information is crucial for the FWI used in this study. In this paper, the adaptive deghosting was only applied to streamer ghosts. Figure 2A and B show the shot gather before and after adaptive deghosting; the comparison shows that the ghost wave was effectively suppressed. The spectral analysis of the near-offset gather before and after adaptive deghosting is shown in Figure 2C, where the notch in the spectrum is effectively compensated, particularly in the low-frequency signal extension. This results in a solid foundation for subsequent FWI imaging.

## 2.3. High-resolution FWI velocity model building and imaging

### *2.3.1. FWI*

FWI was applied in this study. It is the most advanced method for building velocity models. FWI is based on the two-way wave equation theory, which is suitable for various data acquisition techniques. It utilizes the full-waveform information to iteratively update the subsurface velocity model.

Compared to conventional tomographic imaging methods, FWI can build a high-precision velocity model that more accurately matches the geological structures. By iteratively minimizing the misfit between observed and modeled waveforms, FWI can accurately capture velocity details. Moreover, FWI benefits from the use of accurately modeled seismic wavelets that closely match the observed data. In addition, low-frequency and long-offset data contribute to the successful convergence of FWI, providing valuable information for resolving complex subsurface structures.

In summary, FWI is a cutting-edge technology for velocity modeling, enabling the estimation of detailed subsurface velocity structure and enhancing our understanding of geological structures.

### *2.3.2. FWI theory*

FWI has gained widespread application in industry over the past few years. Three-dimensional pre-stack acoustic FWI utilizes the two-way wave equation to establish high-

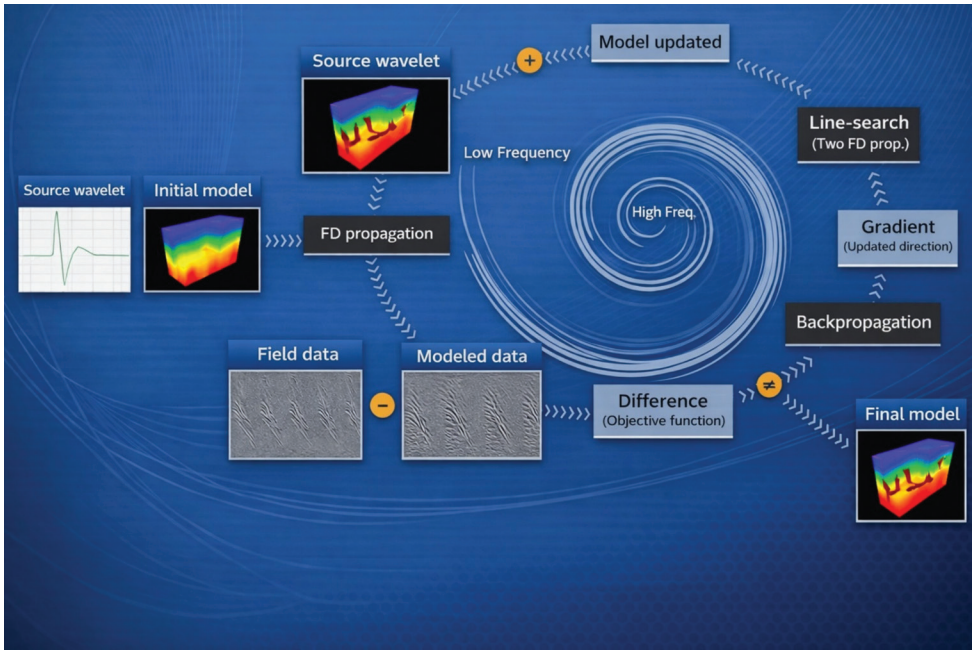


**Figure 3.** Full-waveform inversion schematic diagram

resolution velocity models. The basic principle of FWI can be summarized as follows:

- Forward modeling: The process begins with forward modeling using an initial velocity model. A synthetic waveform is generated by solving the wave equation, simulating the response of the wavelet to an estimated velocity distribution.
- Misfit calculation: The acquired seismic data is subtracted from the forward-modeled data. This residual represents the misfit between the observed and modeled data, and it forms the objective function of FWI.
- Gradient computation: By applying an algorithm similar to reverse time migration, the gradient is calculated based on the residual waveforms, reflecting the direction of velocity update. The gradient provides information on how to update the velocity model to reduce the misfit.
- Model update: Using gradient information, the velocity model is updated accordingly. The updated model is obtained by minimizing the misfit between the observed and modeled data.
- Iterative process: The forward modeling, misfit calculation, gradient computation, and model update steps are repeated iteratively until convergence is achieved, or until a specified stopping criterion is met.

Figure 3 illustrates the schematic diagram of the theory behind FWI. This process aims to iteratively refine the velocity model, ultimately resulting in a high-resolution velocity model that more accurately matches the observed seismic data.

### 2.3.3. Adaptive FWI

The FWI method described above is based on conventional least-squares theory. The main limitation of this approach is that it requires a relatively accurate initial velocity model, or that the observed data contain sufficiently rich low-frequency information and long offsets. The traditional FWI algorithm minimizes the difference between the acquired data and the predicted (forward-modeled) data in the least-squares sense. However, there is a risk of encountering cycle-skipping issues, and the objective function can easily get trapped in local minima rather than the global minimum. The objective function is shown in **Equation 2**, where $J$ represents the misfit function, $m$ represents the model, $d_0$ represents the acquired data, and $F$[m] denotes the forward operator that simulates the predicted data.

$$\min_{m\in M} J := \frac{1}{2}\sum_{s=1}^{N_s}\left\|F[m](x_r,t)-d_0(x_r,t;s)\right\|^2 \quad (2)$$

In early FWI studies, inversion was typically applied after several rounds of tomography to obtain a more accurate initial model and compensate for missing low-frequency content. Adaptive FWI introduces a robust objective function based on time delays or phase differences between observed and modeled data, thereby reducing cycle skipping and improving tolerance to initial model errors.[9,10] For a single frequency, the travel-time difference ($\Delta T$) between two signals is proportional to the phase difference ($\Delta\varphi$), as shown in **Equation 3**. This allows the inversion to use a phase-only objective function by backpropagating local travel-time differences into model updates. Identifying travel-time differences in the time domain is generally more reliable than estimating phase differences. These local differences can be converted into instantaneous phase errors, representing misaligned phases, and used to compute gradients for velocity updates. Consequently, adaptive FWI can begin with a relatively higher frequency band, improving signal-to-noise ratio and inversion stability.

$$\min_{m\in M} J := \frac{1}{2}\sum_{s=1}^{N_s}\left\|\Delta T\right\|^2 = \frac{1}{2}\sum_{s=1}^{N_s}\left\|\Delta T(\Delta\varphi)\right\|^2 \quad (3)$$

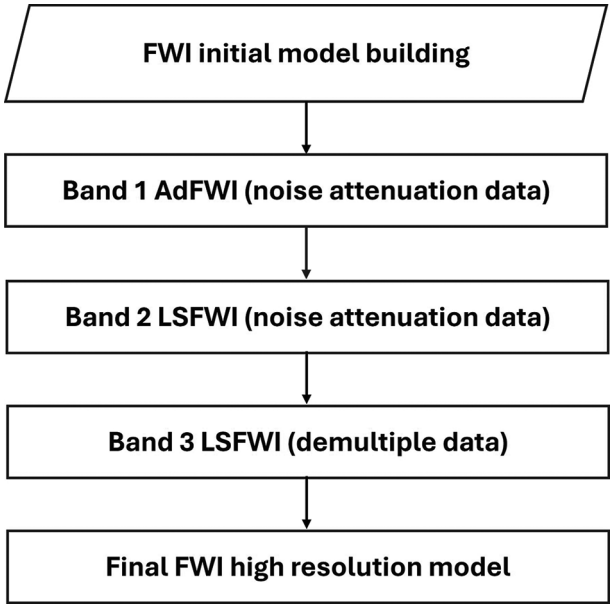


**Figure 4.** Full-waveform inversion (FWI) velocity model building workflow
Abbreviations: Ad: Adaptive; LS: Least-squares.

### 2.3.4. FWI velocity model building workflow

For this study, the feasibility of FWI can be summarized as follows:

- Adequate low-frequency signal: The preprocessing stage included fine noise attenuation, which ensured that the low-frequency signal was properly preserved. This is beneficial for the convergence of FWI, as the presence of sufficiently low-frequency signals improves the convergence and stability of the FWI process.

- Sufficient cable length: The target layer depth is around 3,000 m, and the maximum offset is 6,200 m. These allow FWI to reliably estimate the velocity model with high resolution at the target layer depth. The long offset allows for capturing a wide range of reflection angles, enabling better constraints on the velocity model.
- Hybrid velocity update solution: In low-frequency bands, pure data-driven FWI effectively resolves the background velocity. In higher frequency bands, the inversion is integrated with well constraints, incorporating additional information from well logs or borehole data. This hybrid approach enhances the velocity resolution and accuracy, with well data providing valuable guidance to the inversion process.

In summary, the feasibility of FWI in the study is supported by the presence of abundant low-frequency

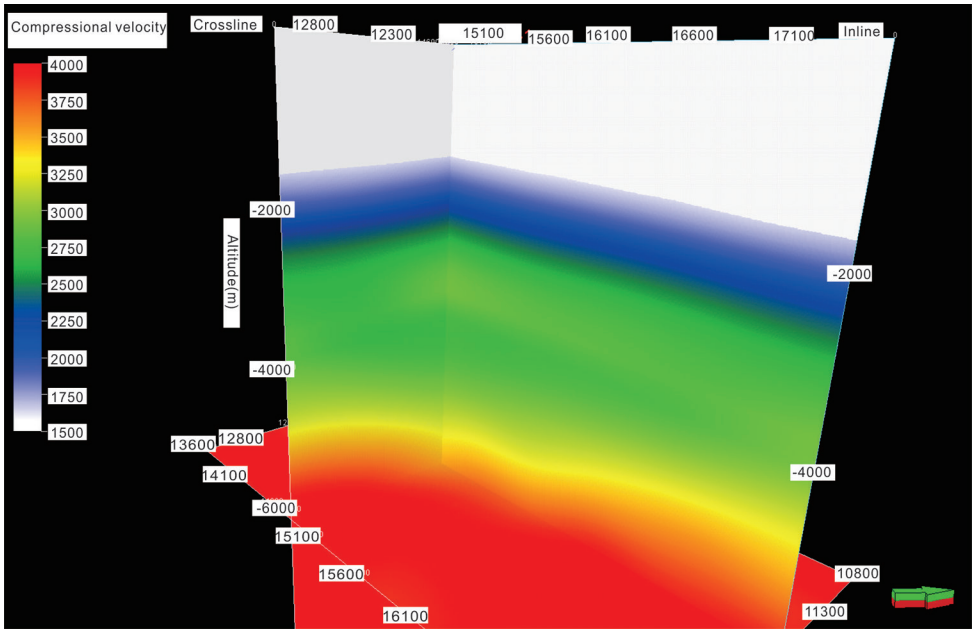


**Figure 5.** Initial velocity model

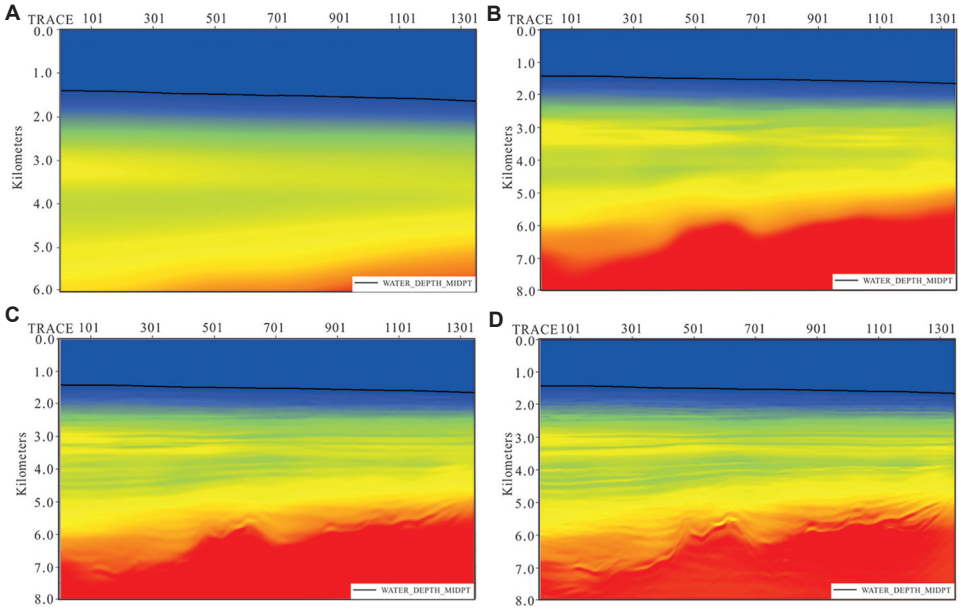


**Figure 6.** Comparison among different velocity models. (A) Initial velocity model. (B) Adaptive full-waveform inversion (FWI) Band 1 updated velocity model. (C) Least-squares FWI Band 2 updated velocity model. (D) Least-squares FWI Band 3 well-constrained updated final velocity model.

signals, a suitable target layer depth and offset distance, and the utilization of a hybrid FWI approach combining waveform information and well constraints. These factors provide a solid foundation for FWI to achieve a high-resolution and accurate velocity model building.

The detailed FWI modeling workflow is shown in Figure 4. Since the ghost wave interferes with the amplitude and phase of the recorded seismic signals, it is common practice to suppress the ghost waves before applying FWI. A zero-phase wavelet is generated during the finite-difference wavefield simulation without a ghost effect. However, this method relies on high-quality ghost wave suppression, as inadequate ghost suppression will negatively impact FWI. Sun *et al.*[13] demonstrated the successful application of FWI by simulating ghost wave effects in towed-streamer data. Therefore, in this study, the second approach was adopted for FWI in Bands 1 and 2, where only basic noise attenuation was applied to the seismic data for FWI input, with direct arrivals, ghost waves, and multiples included in the inversion. As the velocity model was iteratively updated to incorporate more data for deeper-layer inversion, the input in FWI Band 3 was replaced with full-record-length shot gathers after deghosting and multiple attenuation. The Band 1 update utilized adaptive FWI with a phase-based objective function, while the subsequent two bands' updates employed a traditional least-squares objective function. In the last highest frequency band, well velocities were introduced into FWI as constraints.

## 3. Results and discussion

In this study, the process of initial model building is as follows. Firstly, the water column velocity was determined based on time–space dip records and was further refined through precise picking. Then, the time-domain velocity model was converted to a depth-domain interval velocity

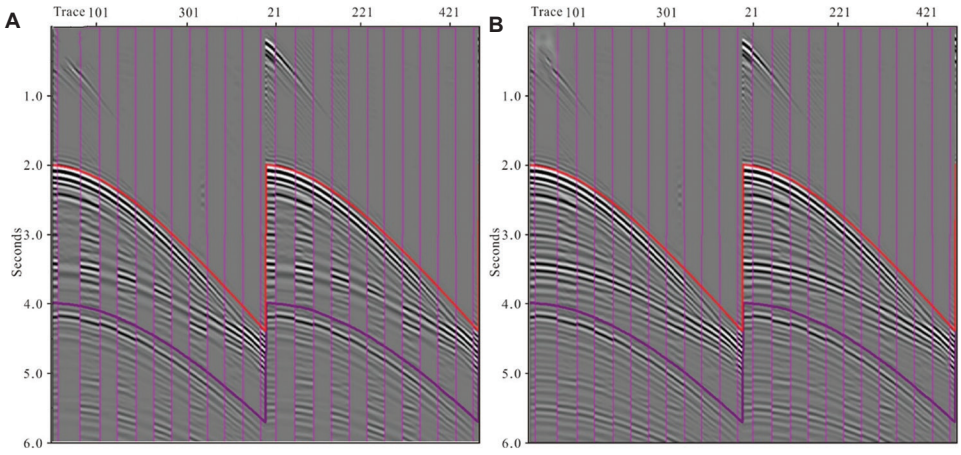


**Figure 7.** QC of FWI Band 2. (A) Interleaved display before full-waveform inversion (FWI) Band 2. (B) Interleaved display after FWI Band 2.

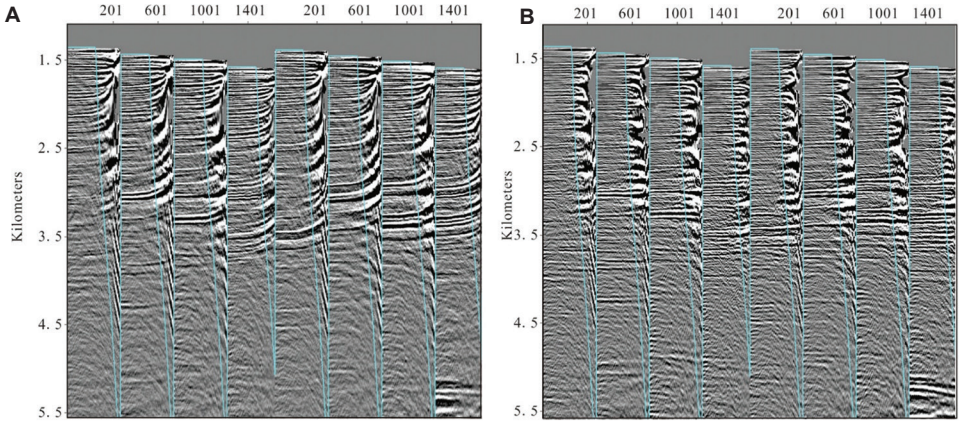


**Figure 8.** QC of CIP gathers with different velocity models. (A) Common image point (CIP) gathers with the initial model. (B) CIP gathers with the final FWI high-resolution model.

using the Dix formula, followed by the application of large-scale smoothing to the converted velocity model. Finally, incorporating the low-frequency trend of well-log velocity in the target layer enabled the construction of an accurate background velocity at the target zone. The initial velocity model is shown in Figure 5.

A cross-well velocity profile was used as an example to illustrate the FWI modeling process. The initial velocity model is shown in Figure 6A, and the updated velocity model using adjustive FWI with data after noise attenuation is shown in Figure 6B. It can be observed that the updated velocity model captured more details compared to the initial model.

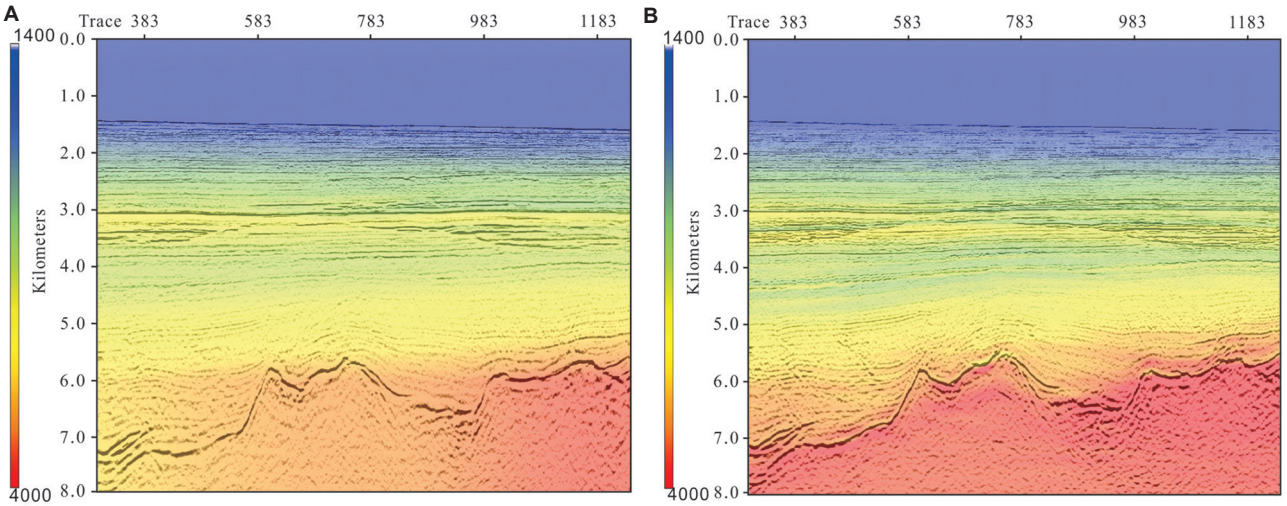


**Figure 9.** QC of pre-stack depth migration (PSDM) results with different velocity models. (A) Initial velocity model and its Kirchhoff PSDM image overlay. (B) Final full-waveform inversion velocity model and its Kirchhoff PSDM image overlay.

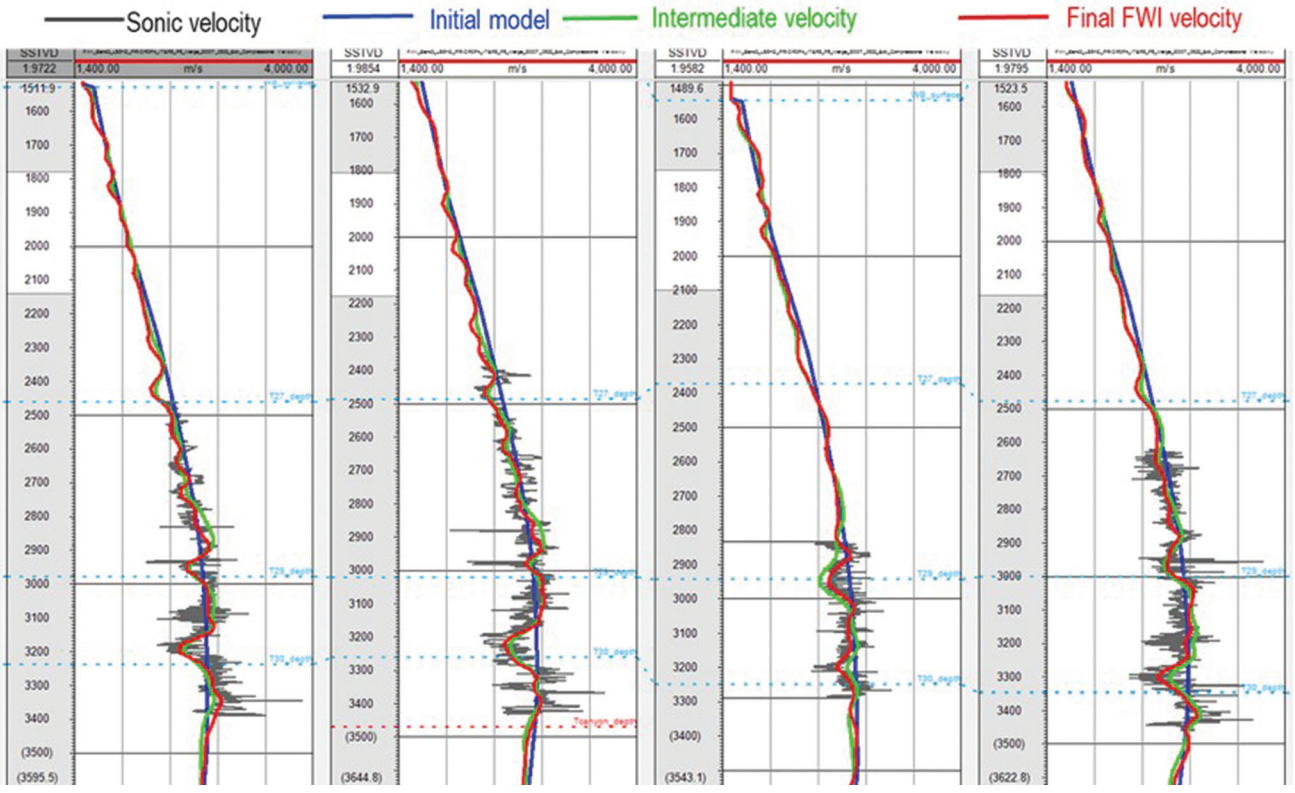


**Figure 10.** Sonic logging velocity and full-waveform inversion (FWI)-derived velocity comparison

Figure 6C shows the velocity model after the Band 2 least-square FWI update. To incorporate more information for deeper updates, the input data for FWI Band 3 were replaced with full-record-length shot gathers after deghosting and multiple attenuation. The FWI Band 3 employed the least-squares FWI on full record length data and introduced well velocities as constraints. Figure 6D displays the final velocity model after the Band 3 well-constrained FWI. It is clearly shown that deep layers of the velocity model have been updated with abundant details.

During each band of FWI, several iterations were performed for the inversion. It is essential to monitor the convergence of the objective function and the magnitude of the velocity updates. This helps in making optimized decisions regarding the total number of iterations and the frequency of the incremental strategy of FWI updates. Between each FWI band, various QC measures were conducted, including comparing the observed and synthetic shots using an interleave display and verifying the velocity field updates. These QC steps provide a comprehensive assessment of the FWI progress.

Comparisons of observed shots and synthetic shots were used to evaluate the improvement in data matching before and after FWI updates, particularly for the interleaving QC, where the observed and synthetic traces are interleaved and displayed in the same shot gather. In this study, we focused on identifying whether there is any improvement from mismatched patterns to more coherent patterns.

Figure 7 shows the interleaved display comparison before and after the FWI Band 2. The red and purple curves represent the time window used in FWI. It can be observed that after the FWI update, the reflection events in shot gathers became more continuous and smoother, with improved alignment within the time window.

Another QC metric is the assessment of gather flatness. Common image point gathers were selected every 10 km. Gathers from the initial velocity model are shown in Figure 8A, while gathers from the final high-precision FWI model are shown in Figure 8B. It can be observed that the final velocity model yielded a flatter gather set, indicating the effectiveness of the FWI velocity update.

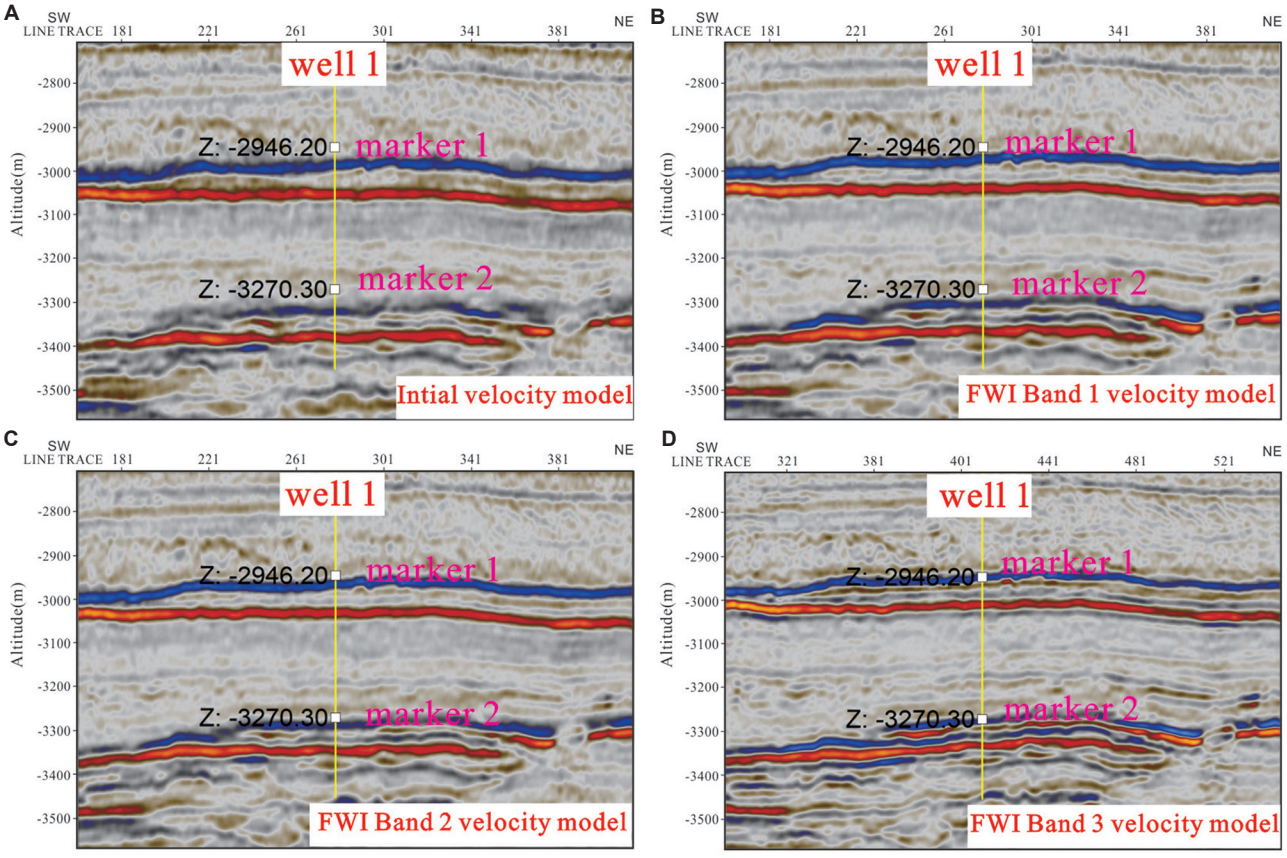


**Figure 11.** (A-D) Mistie analysis during the velocity update process
Abbreviation: FWI: Full-waveform inversion.

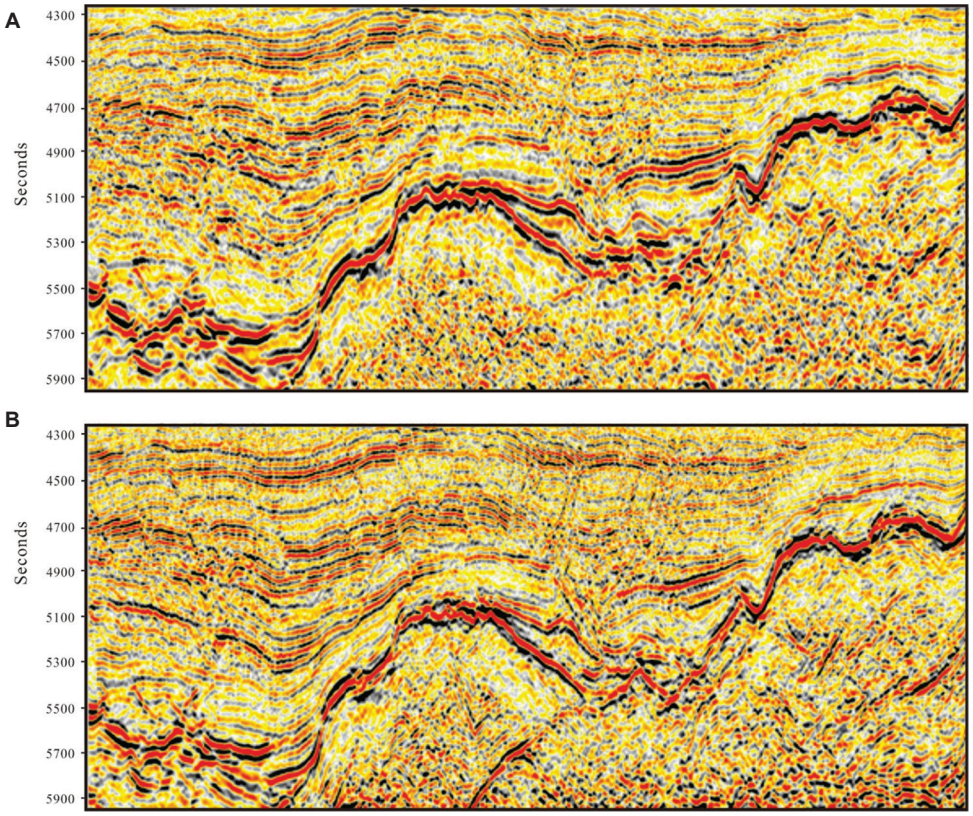


**Figure 12.** Kirchhoff pre-stack depth migration (PSDM) of the deep zone. (A) Legacy Kirchhoff PSDM image. (B) New reprocessed Kirchhoff PSDM image.

Velocity field QC is also crucial for monitoring the overall trend of the velocity model update during FWI. Figure 9A displays the initial velocity model overlaid with the initial stacking section, while Figure 9B shows the final FWI model overlaid with the final stacking section. The velocity model became more refined with abundant details, and the velocity structure showed better consistency with the subsurface image.

Figure 10 shows the comparisons between well velocity curves and seismic velocity at a specific well location. The black curve represents the sonic velocity, the blue curve represents the low-frequency initial velocity, the green curve represents the intermediate iterated velocity, and the red curve represents the final FWI velocity. It can be observed that the overall trends between the well velocity and updated seismic velocity are relatively well-matched, indicating that FWI has effectively captured the velocity variations and improved the model's accuracy.

Throughout the entire model-building process, mistie analysis was conducted for key FWI iterations. Figure 11 shows the variation of mistie at two key layers from the initial model to the final FWI model. From the figure, it can be observed that the overall mistie converges gradually during the velocity update process.

Figure 12A and B show the Kirchhoff pre-stack depth migration (PSDM) stack profile from the legacy data and the new processed data for the deep zone, respectively. From the comparison, it can be observed that the new processed results exhibited higher resolution, enhanced event continuity, and better imaging of deep-seated faults. Figure 13A and B show the Kirchhoff PSDM comparison for the target zone. For legacy data, in this area, the tectonic contact relationship of different channels was very complex, and it was difficult to distinguish lithology within the channels. From the new reprocessed results, the channel boundary was more focused and sharper in the new data. The channel boundaries were clearly identifiable, showing significant improvement over the legacy data. The enhanced resolution of the new data was particularly helpful for delineating thin sand layers and provided a more accurate channel image. The new results showed significant improvements over the legacy data.

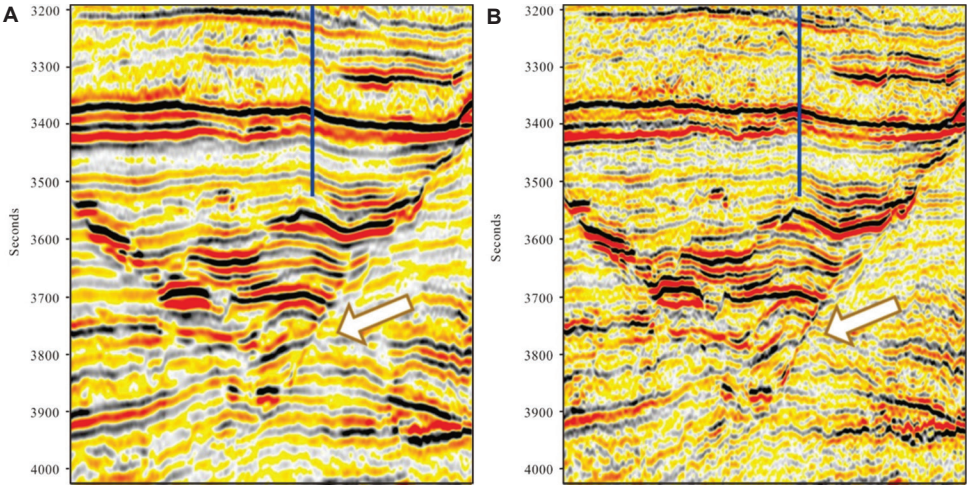


**Figure 13.** Kirchhoff pre-stack depth migration (PSDM) of the target zone. (A) Legacy Kirchhoff PSDM image. (B) New reprocessed Kirchhoff PSDM image.

## 4. Conclusion

In this study, we developed a workflow for deepwater seismic data that suppresses low-frequency noise (high signal-to-noise ratio data was obtained through a combination of noise attenuation methods) and expands low-frequency signals (adaptive deghosting) based on the features of the seismic data acquired during a deepwater environment survey in the South China Sea. A subsequent high-precision FWI velocity modeling and imaging technology was applied. This study illustrates the principles, implementation process, and results of FWI, demonstrating significant improvements in processing results. The results show that the signal-to-noise ratio was enhanced, and the bandwidth was expanded, resulting in a high-precision velocity model and high-quality imaging results.

The combination of the AAA and curvelet transform was introduced as an innovative approach. Low-frequency noise was successfully suppressed using this workflow; at the same time, the resulting high signal-to-noise ratio low-frequency data provided a solid foundation for FWI velocity imaging.

The adaptive deghosting technology was applied, which suppressed receiver ghost waves and compensated for the notch effect in the frequency spectrum. More importantly, it enhanced the signal in the low-frequency end, which is crucial for subsequent FWI inversion.

In the early stage of FWI inversion, a robust adaptive FWI was used to reduce the risk of cycle skipping. Then, least-squares FWI was applied using full-record-length shot gathers after multiple attenuation as input data to further update the velocity distribution of the deeper layers. Well velocity was also introduced for well-constrained least-squares FWI. Finally, a high-precision velocity model and high-quality imaging results were derived.

This processing workflow yielded satisfactory results in seismic data processing within the study area, establishing a fit-for-purpose processing workflow for deepwater exploration. The integrated solution provided a data foundation for subsequent FWI velocity modeling. By combining PSDM with FWI, the technique was successfully applied in a deepwater area of the South China Sea, resolving the challenges of depth prediction and enhancing imaging resolution. This project effectively provided real-time support for gas-field development and well-trajectory optimization. Finally, a high-precision velocity model and high-quality imaging results were obtained, providing a data foundation for subsequent property inversion and interpretation work. The processing workflow in this study can be extended to seismic data acquired in similar marine environments.

## Acknowledgments

None.

## Funding

None.

## Conflict of interest

The authors declare that they have no competing interests.

## Author contributions

*Conceptualization:* Wei Liu, Jie Cui, Yi Liao
*Formal analysis:* Ning Zhang
*Investigation:* Guo Dong Zhang
*Methodology:* Rong Li, Lian Lian Liu
*Visualization:* Zi Jing Gong, Jie Cui, Miaoyang Yuan

*Writing–original draft:* Wei Liu, Jie Cui, Zi Jing Gong
*Writing–review & editing:* Yi Liao, Ning Zhang, Guo Dong Zhang, Rong Li, Lian Lian Liu, Miaoyang Yuan

## Availability of data

Data will be made available on request to the corresponding author. All data analyzed have been presented in the paper.

## References


1. Khain VE, Polyakova ID. Oil and gas potential of deep- and ultradeep-water zones of continental margins. *Lithol Miner Resour*. 2004;39(6):530-540.

   doi: 10.1023/b: limi.0000046956.08736.e4

2. Pettingill HS, Weimer P. Worlwide deepwater exploration and production: Past, present, and future. *Lead Edge*. 2002;21(4):371-376.

   doi: 10.1190/1.1471600

3. Wang W. Difficulties and development trend of exploration in deep and ultra deep water area. *China Pet Explor*. 2010;15(4):71-75. [Article in Chinese].

4. Candès E, Demanet L, Donoho D, Ying L. Fast discrete curvelet transforms. *Multiscale Model Simul*. 2006;5(3):861-899.

   doi: 10.1137/05064182x

5. Naghizadeh M, Sacchi MD. Beyond alias hierarchical scale curvelet interpolation of regularly and irregularly sampled seismic data. *Geophysics*. 2010;75(6):WB189-WB202.

   doi: 10.1190/1.3509468

6. Rickett JE, Van Manen DJ, Loganathan P, Seymour NY. Slanted-Streamer Data-Adaptive Deghosting with Local Plane Waves. In: *Presented at: 76th EAGE Conference and Exhibition*; 2014.

   doi: 10.3997/2214 4609.20141453

7. Lailly P. The Seismic Inverse Problem as a Sequence of Before Stack Migrations. In: Bednar JB, Robinson E, Weglein AR, editors. *Conference on Inverse Scattering-Theory and Application*. SIAM; 1983. p. 206-220.

8. Tarantola A. Inversion of seismic reflection data in the acoustic approximation. *Geophysics*. 1984;49(8):1259-1266.

   doi: 10.1190/1.1441754

9. Jiao K, Sun D, Cheng X, Vigh D. Adjustive Full Waveform Inversion. Proceedings of the *SEG Technical Program Expanded Abstracts* 2015; 2015. pp. 1091-1095.

   doi: 10.1190/segam2015-5901541.1

10. Vigh D, Jiao K, Cheng X, Sun D, Kapoor J, Lewis O. Efficiently using full-waveform inversion in the velocity model building flow. In: *Presented at: 78th EAGE Conference and Exhibition*; 2016.

    doi: 10.3997/2214-4609.201601191

11. Wang FF, Li JY, Chen XH. Deghosting method based on inverse scattering series. *Chin J Geophys*. 2013; 56(5):1628-1636. [Article in Chinese].

    doi: 10.6038/cjg20130520

12. Fokkema JT, Van Den Berg PM. *Seismic Applications of Acoustic Reciprocity*. Amsterdam: Elsevier; 1993.

13. Sun D, Jiao K, Cheng X, Vigh D. Compensating for source and receiver ghost effects in full waveform inversion and reverse time migration for marine streamer data. *Geophys J Int*. 2015;201:1507-1521.

    doi: 10.1093/gji/ggv089

ACCSCIENCE PUBLISHING

Journal of Seismic Exploration

ARTICLE

# Inversion model combination for microseismic source positioning with Multi-Objective Grasshopper Optimization Algorithm

**Cong Pang[1,2], Tianwen Zhao[3], Guoqing Chen[4,5], Sirui Liu[1], Xingxing Li[1], Ya Xiang[1], and Piyapatr Busababodhin[5]***

[1]Institute of Seismology, China Earthquake Administration, Wuhan, Hubei, China

[2]Wuhan Gravitation and Solid Earth Tides, National Observation and Research Station, Wuhan, Hubei, China

[3]Department of Trade and Logistics, Daegu Catholic University, Gyeongsan, Daegu, Republic of Korea

[4]Mathematical Modeling Research Center, Chengdu Jincheng College, Chengdu, Sichuan, China

[5]Department of Mathematics, Faculty of Science, Mahasarakham University, Kantharawichai, Maha Sarakham, Thailand

## Abstract

The precise determination of microseismic source locations is one of the core components of theoretical research in microseismic monitoring technology. Multi-objective intelligent optimization is an effective approach for microseismic source positioning, but it faces challenges such as unclear rationality of model combinations, susceptibility to local optima, and significant variability in positioning results. To address these issues, four distinct mathematical models for microseismic source positioning were designed based on the arrival time difference model and the arrival time difference quotient model. These models were then combined in pairs to form six different microseismic source positioning model combinations, which were used as the optimization objective functions for the multi-objective computational algorithm. A set of microseismic source forward modeling experiments based on three-dimensional polyhedral array shapes, two sets of engineering microseismic data validation experiments, and one set of multi-objective computational method comparison experiments were designed. the multi-objective grasshopper optimization algorithm (MOGOA) was introduced to solve the six model combinations and employed in four sets of microseismic source positioning experiments. Multiple statistical metrics were applied to evaluate the performance of each model combination. The experimental results indicate that the microseismic inversion mathematical model combination (TDA, TDA-P1), combined with the MOGOA algorithm's multi-objective optimization positioning strategy, can achieve high microseismic source positioning accuracy under relatively reliable microseismic event data, and the model calculations are relatively robust. Under microseismic blasting data, the average positioning error over 100 rounds reached 27.6035 m, with standard deviation and interquartile range averages of only 3.2114 m and 5.5896 m, respectively, outperforming other inversion model combinations and similar multi-objective positioning methods. For microseismic event data with significant

***Corresponding author:**
Piyapatr Busababodhin
(piyapatr.b@msu.ac.th)

**Citation:** Pang C, Zhao T, Chen G, *et al*. Inversion model combination for microseismic source positioning with Multi-Objective Grasshopper Optimization Algorithm. *J Seismic Explor*. 2026;35(1):151-170.
doi: 10.36922/JSE025420089

**Received:** October 13, 2025

**Revised:** November 26, 2025

**Accepted:** December 1, 2025

**Published online:** January 14, 2026

**Copyright:** © 2026 Author(s). This is an Open-Access article distributed under the terms of the Creative Commons Attribution License, permitting distribution, and reproduction in any medium, provided the original work is properly cited.

**Publisher's Note:** AccScience Publishing remains neutral with regard to jurisdictional claims in published maps and institutional affiliations.

systematic errors, the microseismic inversion mathematical model combination (TDA-P1, TDQA-P1) demonstrates superior positioning performance, with an average positioning error of 151.1915 m over 100 iterations, significantly outperforming other model combinations. These model combination positioning performance studies hold practical application value in the field of microseismic monitoring.

***Keywords:*** Microseismic source positioning; Multi-objective optimization; Combination of inversion mathematical models; Time difference quotient of arrival; Time difference of arrival; Multi-Objective Grasshopper Optimization Algorithm

## 1. Introduction

Microseismic source positioning is a core component of microseismic monitoring technology, crucial for geological disaster early warning, mine safety monitoring, and structural stability assessment. Inverse mathematical models and their solution methods are key components of microseismic source location research. The rational selection and combination of mathematical models is an effective approach to improving positioning accuracy and stability.[1-9] Traditional mathematical models for positioning primarily include travel time (TT) models, time difference of arrival (TDA) models, distance difference models, and time difference quotient models. Such as the TDA model, derived from the TT functions of two different points in the same array, eliminates the P-wave first arrival time parameter and can represent the deviation between observed and theoretical arrival time differences. While offering advantages such as physical intuition and rapid convergence, these methods and their direct variants are extremely sensitive to velocity model anomalies, resulting in potentially sudden increases in location errors and instability. To overcome this limitation, researchers have developed models such as the time difference quotient of arrival (TDQA). These mathematically eliminate two physical parameters, wave velocity and first wave arrival time, and can represent the consistency of wave velocity factors within a region. This theoretical advantage eliminates the need for prior velocity measurements, thus reducing the complexity of solving the inversion model. However, this can also be affected by errors in microseismic event arrival time data.[10,11] Combining multiple inversion mathematical models or balancing their characteristics can effectively circumvent the drawbacks of a single model—TDA relies on precise wave velocity, while TDQA requires no prior velocity measurements (suitable for homogeneous media). Optimizing multiple fitness functions to find the optimal location is a worthy microseismic source positioning strategy. To enrich our sample of inversion mathematical models, this paper adds constant offset terms (such as addition and subtraction of 1) to the TDA and TDQA models. This approach, by amplifying the arrival time difference constants, avoids premature iteration termination. This approach offers a promising avenue for inversion model improvement, ultimately resulting in the development of multiple inversion mathematical model examples.

Multi-objective optimization is an important method for simultaneously optimizing multiple inversion mathematical models. Evolving primarily from single-objective optimization algorithms, it can simultaneously handle two or more multivariable objective functions.[12-14] With the continuous advancement of heuristic algorithms, swarm intelligence optimization algorithms, due to their global search capabilities and advantages in nonlinear processing, have gradually become the mainstream method for optimizing earthquake source positioning models. New biomimetic optimization algorithms, such as the Grey Wolf Optimizer,[15,16] the Whale Optimization Algorithm,[17,18] and the Ant Lion Optimization,[19,20] have demonstrated significant potential in solving high-dimensional non-convex optimization problems by simulating the behavior of biological swarms in nature. Compared with traditional linear model solving methods (such as Geiger iteration method), these algorithms have three major advantages: (i) Strong robustness: insensitive to initial value selection and noise interference; (ii) high convergence: avoid premature convergence and effectively jump out of local extreme values; (iii) parallel mechanism: adapt to the needs of multi-parameter joint inversion. Multi-objective optimization provides a new idea for earthquake source positioning by integrating multiple complementary objective functions. Its core lies in constructing a Pareto optimal solution set and balancing the constraints of different mathematical models. Based on the new single-objective group optimization algorithm, a multi-objective optimization algorithm is formed, which can further improve the accuracy and stability of microseismic source positioning.

To address the above challenges, this paper proposes an innovative research framework of multi-objective

grasshopper optimization algorithm (MOGOA)[21-26] and inversion mathematical model combination (TDA, TDQA, and its variants). Its theoretical breakthroughs are reflected in three aspects: (i) *Multi-objective collaborative mechanism:* constructing six groups of dual-objective optimization models consisting of any two inversion mathematical models of TDA, TDQA and its variants to form optimization objectives with complementary physical meanings. (ii) *Algorithm-model coupling design:* The multi-objective extension of the grasshopper optimization algorithm (MOGOA) is introduced to give full play to its advantages in global search mechanism and adaptive step size adjustment, overcoming the shortcomings of other similar algorithms in the uniformity of Pareto front distribution. (iii) *Multi-group positioning experiment design:* Combining a set of simulated cube sensor array microseismic event forward data and two sets of engineering microseismic event data, a microseismic source positioning comparison experiment based on the MOGOA model and six sets of mathematical models is designed; finally, the Second-Generation Non-Dominated Sorting Genetic Algorithm (NSGA-II)[27-29] and the multi-objective particle swarm optimization algorithm (MOPSO)[28-30] are introduced as the comparison algorithms for solving the multi-objective optimization model of MOGOA.

In summary, the microseismic source positioning method proposed in this study, which combines multi-objective optimization with inversion models, offers a systematic and robust framework to address the two major challenges faced by traditional approaches: model uncertainty and data error. First, unlike traditional methods that rely on a single physical model, this study employs a multi-model fusion strategy to leverage the complementary nature of different objective functions in physical terms. When velocity models contain errors, objective functions sensitive to absolute TTs may conflict with those sensitive to geometric relationships. Our approach automatically achieves an optimal trade-off between these competing objectives by seeking Pareto optimal solutions, significantly enhancing the robustness of positioning results against model mismatches. When confronted with noisy initial-arrival data, this framework adaptively balances the susceptibility of different objective functions to errors without requiring predefined complex weighting schemes. This demonstrates greater intelligence and adaptability compared to traditional weighted least squares methods. Finally, although intelligent optimization algorithms are computationally more complex than least squares, their robust global search capability is essential for handling complex objective function spaces with multiple local minima caused by real-world errors. As demonstrated by parameter analysis, our method exhibits insensitivity to parameter variations after reaching performance thresholds, proving its convenience and stability in practical applications. Therefore, the value of this research lies not in negating traditional methods, but in providing a new and effective technical pathway for high-reliability microseismic positioning in complex, non-ideal engineering environments.

## 2. Combination of mathematical models for microseismic source positioning

The accurate selection of mathematical models is a key factor in implementing multi-target high-precision positioning. Classical mathematical models for microseismic source positioning can be divided into TT models, arrival time difference models, arrival time difference quotient models, or arrival distance difference models. There are many cases of research on single models. Here, we will combine the time difference model and the arrival time difference quotient model to study the combined model and formulate a mathematical model combination plan based on this. The basic mathematical formula for microseismic source positioning is:

$$l_i = \sqrt{\left(x_i - x_0\right)^2 + \left(y_i - y_0\right)^2 + \left(z_i - z_0\right)^2} \tag{1}$$

$$l_i = v \cdot \left(t_i - t_0\right) \tag{2}$$

$$T_k = t_i - t_j, i \neq j \tag{3}$$

$$L_k = l_i - l_j = v \cdot T_k, i \neq j \tag{4}$$

where $l_i$ is the spatial distance from the $i$-th seismic pickup ($x_i$, $y_i$, $z_i$) to the microseismic source ($x_0$, $y_0$, $z_0$), $i = 1,2,\ldots,m$; $m$ is the number of seismic pickups receiving valid seismic wave signals; $v$ is the seismic wave velocity, in this case the P-wave velocity; and $t_0$ is the time of the artificial explosion or microseismic event.

$T_k$ is defined as the difference in arrival time of the seismic waves recorded by two seismic pickups, $T_k = t_i - t_j$, with $i \neq j$; $L_k$ is defined as the difference in spatial distance between the two seismic pickups and the microseismic source, $L_k = l_i - l_j = v.T_k$ Based on the definitions of the above key parameters, the following four mathematical models for microseismic source positioning with different meanings are established:

$$f_1 = \sum_{k=1}^{N} \left( T_k - \frac{L_k}{v} \right)^2 \tag{5}$$

$$f_2 = \sum_{k=1}^{N} \left| \left| \left( T_k - \frac{L_k}{v} \right) + 1 \right|^2 - 1 \right| \tag{6}$$

$$f_3 = \sum_{p,q=1;p>q}^{M} \left( \frac{T_p}{L_p} - \frac{T_q}{L_q} \right)^2 \tag{7}$$

$$f_4 = \sum_{p,q=1;p>q}^{M} \left| \left| \frac{T_p}{L_p} - \frac{T_q}{L_q} + 1 \right|^2 - 1 \right| \tag{8}$$

In the above formulas, $f_1$ is the classic arrival time difference model, which reflects the degree of deviation between the observed arrival time difference and the theoretical arrival time difference, denoted as TDA; $f_2$ is based on $f_1$, adding 1 to the arithmetic square method and then subtracting 1 from the square method as a whole to obtain the absolute value. This deformation can amplify the amplitude of the time difference deviation value, avoiding the premature termination of the iteration in the model solution, and is also conducive to the algorithm to find a more appropriate local optimal solution, making the calculation result more credible, denoted as TDA-P1; $f_3$ is the classic arrival time difference quotient model The inverse form of the model takes the observed time difference as the numerator of the sub-item and the theoretical arrival distance as the denominator. It contains the seismic wave arrival time information of 3 or 4 seismic pickups, reflecting the degree of difference between the two observed wave velocity factors ($\gamma_p = 1/v_p$ and $\gamma_q = 1/v_q$) calculated using different seismic pickup combinations, denoted as TDQA. This model does not require advanced velocity measurement and is suitable for homogeneous medium environment; $f_4$ is a new model that is deformed based on $f_3$. The principle is the same as $f_2$, denoted as TDQA-P1.

## 3. Multi-Objective Grasshopper Optimization Algorithm

### 3.1. Standard grasshopper optimization algorithm

The grasshopper optimization algorithm (GOA) proposed in 2017 is a new bionic optimization algorithm that mimics the cohabitation and migration of grasshopper larvae and adults. It takes advantage of the differentiated biological characteristics of grasshopper larvae, which are slow to move, and adults, which are fast to move. That is, grasshoppers move slowly in the larval stage and only move within a small range, while adults have strong hind legs and are good at long-distance jumping and moving quickly. This biological learning ability helps to carry out local search and global optimization at the same time. The change of grasshopper position is subject to the interaction force, gravity and wind force in the natural environment. Therefore, the GOA model calculates the position of the $i$-th grasshopper at the $t$+1$^{th}$ iteration as follows:

$$X_i = S_i + G_i + A_i \tag{9}$$

In **Formula 9**, $X_i$ is the position of the $i$-th grasshopper, $S_i$ is the interaction between the $i$-th grasshopper and other grasshoppers, $G_i$ is the gravity acting on the $i$-th grasshopper, and $A_i$ is the wind force acting on the $i$-th grasshopper.

$$S_i = \sum_{j=1}^{N} s d_{ij} \breve{d}_{ij} \tag{10}$$

In **Formula 10**, $N$ is the number of grasshopper populations, $d_{ij}$ is the absolute distance between grasshopper $i$ and grasshopper $j$; $\breve{d}_{ij}$ is the unit vector of the distance between grasshopper $i$ and grasshopper $j$.

$$s(r) = f e^{-\frac{r}{l}} - e^{-r} \tag{11}$$

In **Formula 11**, $f$ is the attraction strength; $l$ is the attraction range; and S(.) represents the interaction force function between grasshopper $i$ and grasshopper $j$. Grasshopper experience both repulsive and attractive forces. When they are too close, repulsion occurs, whereas when they are too far, attraction arises. The area where reLocust's and attraction are balanced is called the comfort zone. Repulsion can prevent the algorithm from converging prematurely, ensuring effective exploration.

$$G_i = -g \breve{e}_g \tag{12}$$

In **Formula 12**, $g$ is the gravitational acceleration constant; $\breve{e}_g$ is the unit vector pointing to the center of the Earth.

$$A_i = u \breve{e}_W \tag{13}$$

In **Formula 13**, $u$ is the drift constant; and $\breve{e}_W$ is the unit vector of the wind direction. Because this will cause the grasshoppers to quickly reach their comfort zone and the swarm will not converge to a specific location, this mathematical model cannot be directly used to solve the optimization problem. Ultimately, it is necessary to ignore the influence of gravity and ensure that the direction of the wind force is always toward the optimal grasshopper position. The final formula for updating the grasshopper position using the GOA model is:

$$x_{i,d}(t+1) = c \left( \sum_{j=l,j\neq i}^{N} c \frac{ub_d - lb_d}{2} s(|x_{j,d}(t) - x_{i,d}(t)|) \frac{x_{j,d}(t) - x_{i,d}(t)}{d_{ij}(t)} \right) + T_d^{'} \tag{14}$$

In **Formula 14**, $x_{i,d}(t)$ is the coordinate value of the grasshopper individual in the $d$-th dimension of the position vector at the $t$-th iteration; $c$ is the linear dynamic attenuation coefficient related to the maximum number of iterations, which affects the grasshopper's global optimization or local search ability; $ub_d$ and $lb_d$ are the upper and lower limit thresholds on the $d$-th dimension of the grasshopper individual position, respectively; S(.) represents the interaction force function of grasshopper $i$ affected by grasshopper $j$; $d_{ij}$ is the absolute distance between grasshopper $i$ and grasshopper $j$; and $T_d^{'}$ is the coordinate value of the $d$-th dimension of the optimal position vector previously obtained by the grasshopper colony.

### 3.2. MOGOA

MOGOA is a multi-objective intelligent bionic algorithm that simulates the differentiated behavioral activities of locusts across different life stages. Its core concept involves utilizing long-distance migrating adult locusts to search the global space, while crawling, feeding nymphs explore the local space. The hunting actions of individual locusts depend on the combined effects of intra-population forces, gravity, and wind force. Optimal solutions are selected through Pareto dominance and crowding distance mechanisms. Key differences between MOGOA and standard GOA include:

(i) *Pareto dominance mechanism:* Unlike single-objective methods that directly compare fitness values, in multi-objective optimization we employ the concept of "Pareto dominance" to evaluate solutions. After population initialization and during each iteration, we assess the quality of all locusts (solutions) using Pareto dominance relations. A solution not dominated by any other solution in the population is termed a non-dominated solution. The collective set of all non-dominated solutions forms the Pareto frontier for that iteration.

(ii) *External archive maintenance:* Since multi-objective optimization yields a set of solutions (the Pareto optimal solution set), a dedicated container is required to store high-quality non-dominated solutions discovered during iterations. This container is termed the external archive. During algorithm execution, newly discovered non-dominated solutions are continuously compared against existing solutions in the archive. Based on the Pareto dominance relationship, old solutions dominated by new ones are removed from the archive, while new solutions not dominated by any existing solution are added.

(iii) *Diversity preservation strategy (archive maintenance and leader selection):* This constitutes the most critical component of MOGOA, ensuring that the final Pareto solution set not only approximates the true frontier but also uniformly covers the entire frontier with excellent distribution. First, when the external archive is full and solutions must be removed, we employ "crowding distance" as the metric. This distance measures how densely a solution is surrounded by neighboring solutions in the objective space. A solution with a larger crowding distance indicates sparser surrounding solutions, making it more crucial for maintaining frontier diversity. Second, MOGOA avoids a single global optimum by selecting a "leader" from the external archive. We employ a roulette wheel selection method where the selection probability is proportional to the solution's crowding distance—solutions with higher crowding distances have a greater chance of being chosen as leaders. This mechanism encourages the locust population to migrate toward the sparsest and least explored regions of the current Pareto frontier. It effectively balances exploitation (searching within known high-quality regions) and exploration (seeking new potential solutions), serving as the core driver for maintaining diversity within the solution set.

Multi-objective positioning calculations generally use two or more inversion mathematical models to construct different fitness functions. The dependent variable of each function has zero as its theoretical minimum value, and the independent variables are the parameters to be solved in the inversion model, which can be P-wave velocity, approximate three-dimensional coordinates, or the time of microseismic occurrence. The known parameters are the three-dimensional coordinates of the microseismic array measurement points, the true microseismic source location, and the first arrival time of the seismic wave. The solution model for multi-objective optimization problems is generally as follows:

$$minF = \left\{ f_m, f_n \right\} \tag{15}$$

In **Formula 15**, $m$=1,2,3,4, $n$=1,2,3,4,$m \neq n$.

Different sources of model combinations directly impact the effectiveness of microseismic source positioning. For instance, the TDA model is sensitive to absolute timing errors but provides better distance constraints; conversely, the TDQA model is insensitive to absolute timing errors and wave velocity because it represents a ratio, yet offers superior directional constraints. Therefore, combining these two distinct model types theoretically achieves complementary distance and direction constraints. This enables more robust solutions than single models or same-type combinations when initial arrival picking

errors (affecting TDA) or inaccurate velocity models (impacting both) occur. To test the actual positioning effectiveness of different model combinations, the four standalone inversion mathematical models mentioned in section 1 were paired to construct six combination models with significantly different physical meanings:

(i) *MO-1:* Combines the TDA Model $f_1$ with the TDA-P1 model $f_2$. This pair exhibits smoothing effects on pure random noise but may "disagree" under strong systematic errors, as one minimizes residuals while the other biases them, leading to Pareto frontier divergence or convergence failure. Its performance typically falls short of combinations with complementary models.

(ii) *MO-2:* Combines the TDA model $f_1$ with the TDQA model $f_3$. When velocity models exhibit global scaling errors or systematic bias in first-arrival picking, $f_1$ may fail while $f_3$ maintains stable geometric constraints. Together, even with minor absolute positional shifts, their relative geometric shapes can "pull" the source back into the correct region, demonstrating exceptional robustness.

(iii) *MO-3:* Combines the TDA model $f_1$ with the TDQA-P1 model $f_4$. Building upon the advantages of the $f_1$& $f_3$ combination, it further enhances resistance to complex error patterns where "the theoretical TTs at all stations are systematically overestimated or underestimated." This is theoretically a more robust combination, though it may require additional iterations to balance the two objectives.

(iv) *MO-4:* Combines the TDA-P1 model $f_2$ with the TDQA model $f_3$. This combination is highly suitable for addressing scenarios with overall first-arrival time shifts (constant delays caused by picker algorithms). $f_2$ compensates for this overall shift, while $f_3$ ensures correct geometry. It may perform exceptionally well when processing noisy data with constant bias.

(v) *MO-5:* Combination of the TDA-P1 model $f_2$ and the TDQA-P1 model $f_4$. This is theoretically the most "aggressive" compensation combination. It may demonstrate unique advantages when complex absolute and relative systematic errors coexist in the data; however, it may also introduce instability due to over-compensation, with its performance highly dependent on the actual error distribution.

(vi) *MO-6:* Combines the TDQA model $f_3$ with the TDQA-P1 model $f_4$. Similar to the $f_1$& $f_2$ combination, this pair primarily smooths random noise in the relative residual domain. Both are highly insensitive to overall scaling errors in the velocity model but may sacrifice absolute positioning accuracy. Their combination allows fine-tuning within the constraints of relative geometry.

## 4. Forward and inversion simulation experiments of microseismic sources

To verify the theoretical effectiveness of the six positioning mathematical model combinations and the MOGOA for microseismic source positioning, a set of forward and inversion simulation experiments were designed. Three-dimensional polyhedron array data simulation and first-wave arrival time calculations were performed on MATLAB 2024b and Windows 10 64-bit systems. The MOGOA algorithm uses the following preset parameters: 20 search agents (populations), 200 maximum iterations, 3 search target dimensions, 40 grasshopper populations, a lower search limit of (0 0 0), an upper search limit of (5000 5000 5000), and 100 positioning experiment cycles. In this experiment, the seismic wave (P-wave) propagation speed in the medium is set to 2500 m/s. The earthquake took place on August 10, 2025, at 14:19:00. The earthquake location coordinates are uniformly set to (655.1, 349.7, 187.2). The microseismic monitoring array is a three-dimensional polyhedron (approximately spherical), with 12 detectors evenly distributed on its boundary. The relevant simulation data are shown in Figure 1 and Table 1.

Figure 1 presents simulated data from a microseismic monitoring network based on a polyhedral array, comprising 12 three-dimensional monitoring points (blue markers) and one real seismic source (red marker). Based on the coordinates of the monitoring points, wave velocities, and the location of the seismic source, the first-arrival times of seismic waves from the real source to each monitoring point can be calculated in seconds, as detailed in Table 1.

Table 1 presents the three coordinate values and first-arrival times for 12 monitoring stations. It is evident that

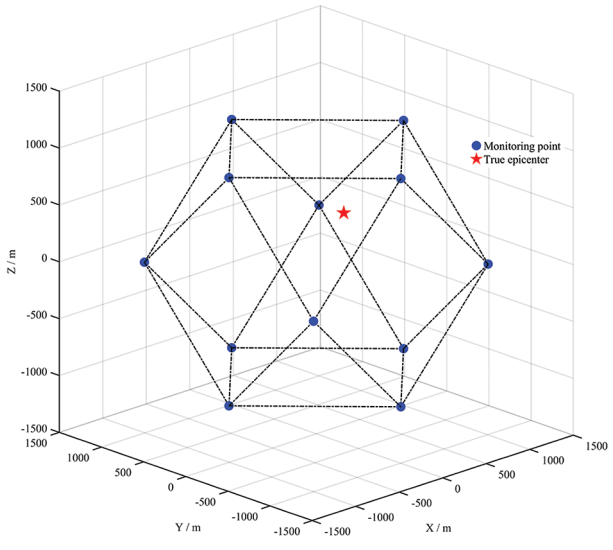


**Figure 1.** Sensor's network layout for simulation experiment

**Table 1. Simulation data of microseismic source forward modeling**

| Serial number | Vibration pickup coordinates (m) | | | By then (s) |
|---|---|---|---|---|
| | *x* | *y* | *z* | |
| 1 | 1003.213 6 | 1003.551 3 | 0.074 2 | 0.3056 |
| 2 | 1003.153 4 | −1003.716 0 | 0.016 4 | 0.5639 |
| 3 | −1003.345 8 | 1003.234 8 | 0.305 5 | 0.7169 |
| 4 | −1003.168 9 | −1003.190 5 | 0.215 3 | 0.8593 |
| 5 | 0.156 3 | 1003.142 1 | 1003.410 8 | 0.4934 |
| 6 | 0.138 7 | 1003.035 6 | −1003.307 7 | 0.6030 |
| 7 | 0.069 8 | −1003.018 7 | 1003.053 9 | 0.6840 |
| 8 | 0.043 2 | −1003.062 9 | −1003.071 2 | 0.7668 |
| 9 | 1003.356 7 | 0.110 2 | 1003.158 1 | 0.3814 |
| 10 | 1003.154 7 | 0.085 6 | −1003.104 6 | 0.5153 |
| 11 | −1003.286 5 | 0.041 7 | 1003.093 5 | 0.7524 |
| 12 | −1003.137 4 | 0.017 4 | −1003.410 7 | 0.8285 |

each coordinate value possesses four distinct significant digits after the decimal point. This feature enhances the model's physical realism and generalization capability, prevents numerical computation from exhibiting linear correlation, and consequently improves the performance and robustness of the optimization algorithm.

Figure 2 shows a box plot of the microseismic source positioning results based on MOGOA and different inversion model combinations. The upper and lower boundary lines of the box in the figure indicate the upper quartile (Q3) and lower quartile (Q1) of the positioning results, respectively. The solid line inside the box represents the median of the positioning result. The red triangle marks the data identified as outliers by the box plot. The upper and lower solid horizontal lines outside the box represent the maximum and minimum values, respectively. Table 2 shows the statistics of the microseismic source positioning results based on different inversion model combinations based on three-dimensional polyhedron array simulation and the MOGOA model. The indicators Mean, IQR, STD, Best, Worst, Duration, Fit-1, and Fit-2 represent the mean, interquartile range (IQR), standard deviation (STD), minimum and maximum of the location error dataset, the average calculated time for positioning, the final fitness function mean of Model 1 (the first submodel from the left in the combination model), and the final fitness function mean of Model 2, respectively.

From Figure 2 and Table 2, we can see that:

(i) The overall positioning accuracy and robustness of the MO-6 combination model are far inferior to those of other inversion mathematical models. The order of positioning accuracy is MO-1 > MO-3 > MO-5 > MO-4 > MO-2 > MO-6. The positioning means value of the 100-round combination of models TDA-P1 and TDA reached 0.0041 m, with the highest positioning accuracy. Its performance in the indicators IQR (0.0014 m) and STD (0.0082 m) was also the most significant, proving that the solution process of the MO-1 combination is not only more accurate but also relatively more robust. The positioning results do not have a large error in the source approximate solution.

(ii) The positioning effects of the combinations MO-2, MO-3, MO-4, and MO-5 are generally comparable. The meaning of their 100-round positioning errors is all between 0.12 and 0.19m, and the STD values are all within 0.30 m or less, indicating that the positioning effect of the above four model combinations is also high, and they can be used as alternatives or substitutes for the MO-1 combination model. The specific actual positioning reliability and accuracy differences need to be further explored in combination with other experiments.

(iii) From the fitness function value indicators (Fit 1, Fit-2), the main reason for the poor statistical

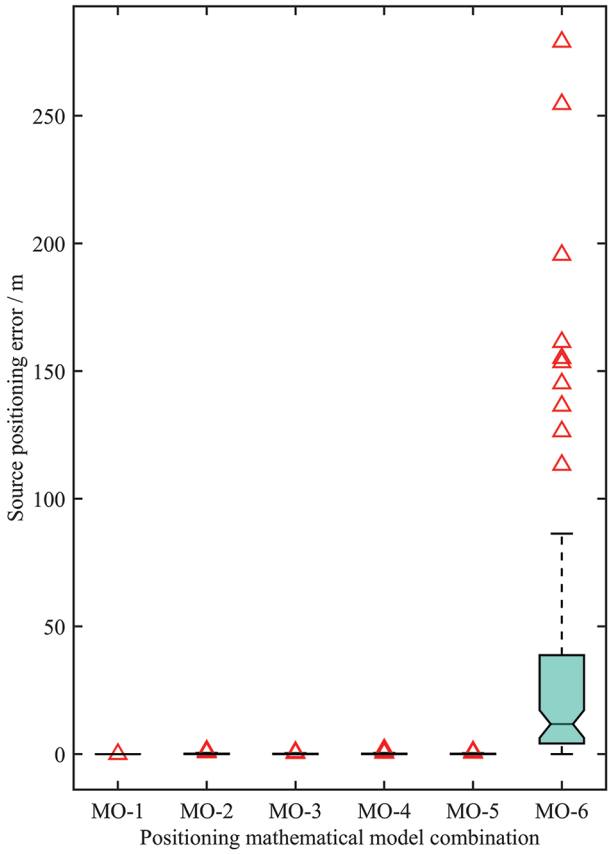


**Figure 2.** Box plot of microseismic source positioning results based on Multi-Objective Grasshopper Optimization Algorithm (MOGOA) and different inversion model combinations

**Table 2. Statistics results of microseismic source positioning based on different inversion model combinations using three-dimensional polyhedral array simulation and the MOGOA model**

| Combination | Model 1 | Model 2 | Statistical values of microseismic source positioning results | | | | | | | |
|---|---|---|---|---|---|---|---|---|---|---|
| | | | Mean (m) | STD (m) | IQR (m) | Best (m) | Worst (m) | Duration (s) | Fit-1 | Fit-2 |
| MO-1 | TDA | TDA-P1 | 0.0041 | 0.0082 | 0.0014 | 8.0419e-05 | 0.0443 | 2.8347 | 4.8969e-10 | 0.0001 |
| MO-2 | TDA | TDQA | 0.1834 | 0.2758 | 0.1898 | 0.0002 | 1.3571 | 3.6136 | 6.1683e-07 | 4.6337e-11 |
| MO-3 | TDA | TDQA-P1 | 0.1236 | 0.1626 | 0.1427 | 0.0003 | 0.8512 | 3.5736 | 2.3508e-07 | 0.0001 |
| MO-4 | TDA-P1 | TDQA | 0.1706 | 0.2806 | 0.1775 | 0.0004 | 1.8587 | 3.6350 | 0.0054 | 3.5629e-11 |
| MO-5 | TDA-P1 | TDQA-P1 | 0.1432 | 0.2118 | 0.1666 | 0.0004 | 1.0701 | 3.6471 | 0.0045 | 0.0001 |
| MO-6 | TDQA | TDQA-P1 | 34.5344 | 53.0555 | 34.5673 | 0.0238 | 278.98099 | 4.5234 | 7.0563e-08 | 0.0110 |

Abbreviations: IQR: Interquartile range; MOGOA: Multi-Objective Grasshopper Optimization Algorithm; STD: Standard deviation; TDA: Time difference of arrival; TDQA: Time difference quotient of arrival.

positioning accuracy and insufficient robustness of the combination MO-6 in 100 rounds of experiments is that the optimization effect of the TDQA-P1 model is not ideal (its Fit-2 value is 0.0001, which is more than 100 times different from the Fit-2 values of other combination models, while Fit-1 is not much different from other combination models). This is related to its theoretical design of eliminating wave speed as one of the independent variables of the fitness function, which makes it lose sufficient physical constraints in the process of determining the approximate solution and fall into the local optimum. At the same time, the design method of adding 1 in the TDQA-P1 mathematical model exacerbates this phenomenon.

After reviewing the statistical data from 100 rounds of microseismic source positioning results, we proceeded to present and analyze the specific variations in each round's positioning outcomes. This enables a dissection of the oscillation patterns of the error curves for each combined model. Figure 3 is a graph showing the microseismic source positioning results of 100 rounds and six combination models based on polyhedron array simulation. Figure 4 shows the local approximate dissolution points of six microseismic source positioning combination models based on polyhedron array simulation and the MOGOA model.

From Figures 3 and 4, we can see that:

(i) For a single combination model, the number of abnormal approximate solutions with large positioning errors is small compared to the total approximate solution samples. Many sources' approximate solutions are mainly concentrated near the true source location (655.1, 349.7, 187.2). Among them, the approximate solution set of MO-1 is more concentrated, almost coinciding with the true source location and being covered by many scattered points.

(ii) As shown in Figure 4, the number of approximate solutions between the lower limit (654, 349, 186.5) and the upper limit (656, 350, 187.5) of the spatial coordinates of the MO-6 combination is very small and presents a divergent distribution phenomenon. Many approximate solutions have positioning errors distributed between 0 and 50 m. The positioning errors of most source approximate solutions of other combination models are below 0.5 m.

The successful execution of microseismic source forward modeling simulations alone is insufficient to demonstrate the reliability of multi-objective positioning models. Further validation using microseismic event data from real-world engineering cases is necessary to achieve a closed-loop verification process integrating simulation with empirical testing.

## 5. Engineering verification

### 5.1. Microseismic experiment of a deep mining mine

The validation was conducted using microseismic experimental data from a deep mining mine in China. A total of 12 microseismic monitoring units were installed in the mine. The artificial blasting locations were (3500.0, 3520.5, 102.0), the detonation time was 00:00, and the explosive charge was 2.25 kg. After the successful blast, nine P-wave arrival times were observed, denoted as T1 to T12, as shown in Table 3. The experimental simulation used MATLAB 2024B data processing tools and the corresponding standard function toolbox. The MOGOA algorithm uses the following preset parameters: 40 swarm search agents, 200 maximum iterations, 3 search target dimensions, a lower search limit of (0, 0, 0), an upper search limit of (5000, 5000, 5000), and 100 positioning experiment cycles.

Table 4 shows the statistical results of the calculation of six combined models for microseismic source positioning

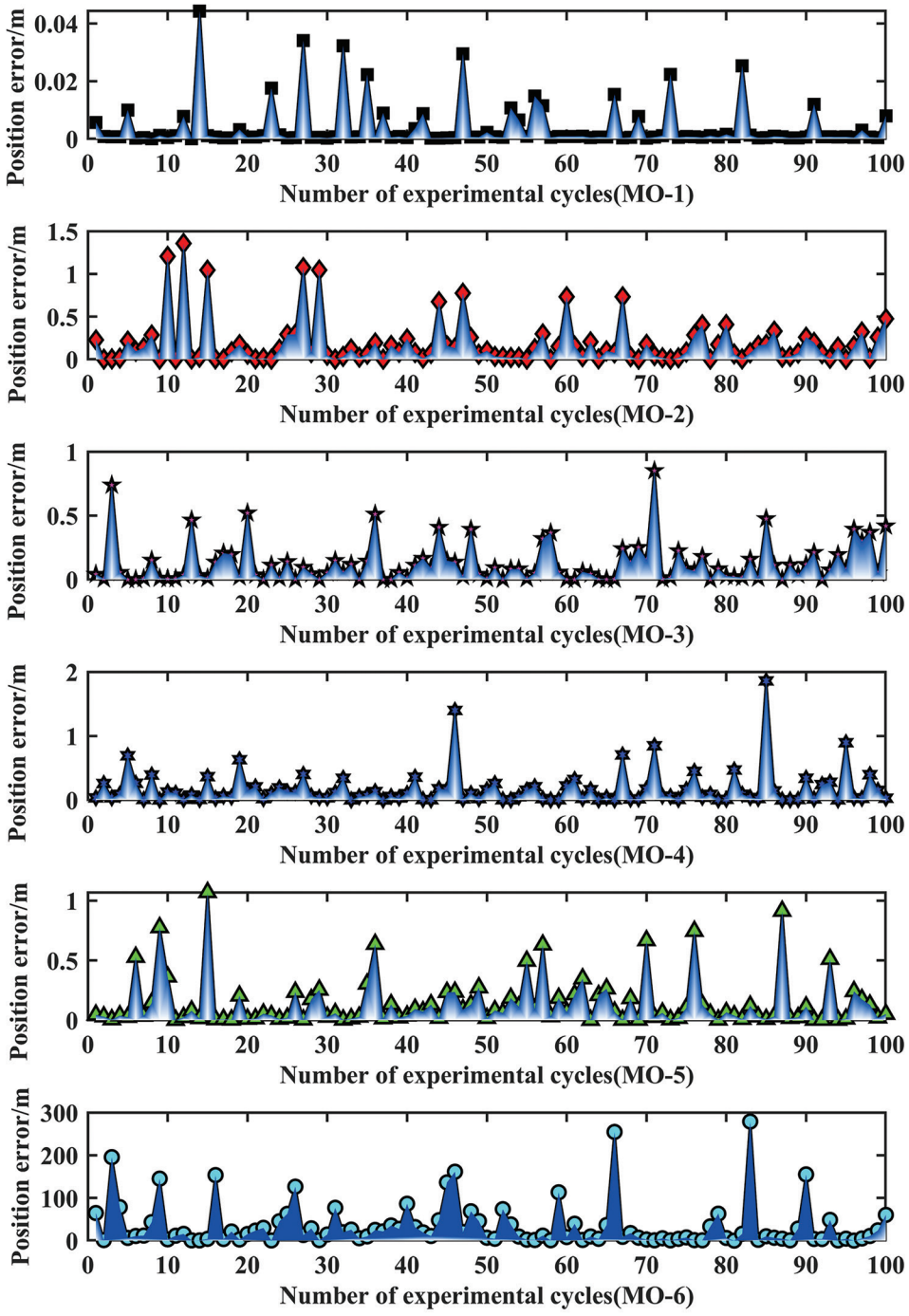


**Figure 3.** Position-error curves for six microseismic source positioning combination models (MO-1 to MO-6), obtained from 100 rounds of polyhedral-array simulations

based on the MOGOA model and deep mining microseismic events. The indicators Mean, IQR, STD, Best, Worst, Duration, Fit-1, and Fit-2 represent the mean, IQR, STD, minimum and maximum values of the positioning error dataset, the average positioning calculation time, the final fitness function mean of Model 1 (the first submodel from the left in the combined model), and the final fitness function mean of Model 2, respectively. Figure 5 shows a box plot of the calculation results of six combined models for microseismic source positioning based on the MOGOA model and deep mining microseismic events. The upper and lower boundary lines of the boxes in the

figure represent the upper quartile (Q3) and lower quartile (Q1) of the positioning results, respectively. The solid line inside the box represents the median of the positioning result. Red triangles mark data identified as outliers by the box plot. The upper and lower solid horizontal lines outside the box represent the maximum and minimum values, respectively.

From Figure 5 and Table 4, we can see that:

(i) The overall positioning accuracy and robustness of the MO-6, MO-2, and MO-3 combination models are far inferior to those of other inversion mathematical models. They are more sensitive to the noise or error of microseismic data, which seriously restricts the global search ability of the optimization model. The order of positioning accuracy is MO-5 > MO-4 > MO-1 > MO-3 > MO-2 > MO-6. The 100-round combination positioning mean value of the model TDA-P1 and TDQA-P1 combination reached 151.1915 m, which is the highest positioning accuracy. It also performs best in terms of the indicators IQR (121.9566 m) and STD (66.5852 m). This proves that the MO-5 combination is not only more accurate but also more robust in solving real engineering blasting data. The positioning results do not have excessive errors or are judged as abnormal values by the box plot.

(ii) The positioning effects of the MO-1 and MO-4 combinations are similar overall. The mean values of their 100-round positioning errors are both between 700 and 800 m, and the STD values are also around 1000 m. However, the IQR index of MO-4 (139.1974 m) is significantly better than that of MO-1 (981.4611 m), indicating that the comprehensive positioning effect of the MO-4 combination over 100 rounds is only

**Table 3. Microseismic experimental data from SBKC mine**

| Detector | Vibration pickup coordinates (m) | | | By then (ms) |
|---|---|---|---|---|
| | *x* | *y* | *z* | |
| T1 | 4088.2 | 3548.6 | 61.6 | 1093.1 |
| T2 | 4413.1 | 3057.4 | −2.2 | 1419.0 |
| T3 | 4798.0 | 2904.0 | −52.4 | 1304.1 |
| T4 | 4280.9 | 2834.0 | −83.9 | 1224.8 |
| T5 | 4569.8 | 2183.0 | −199.3 | 1392.1 |
| T6 | 3978.4 | 3774.3 | 151.4 | 1086.5 |
| T7 | 4501.0 | 2442.5 | −147.5 | 1315.1 |
| T8 | 3874.6 | 3352.6 | 67.1 | 1013.8 |
| T9 | 5447.6 | 3138.9 | 18.0 | 1445.7 |
| T10 | 3656.9 | 3494.6 | 97.8 | 988.5 |
| T11 | 4970.4 | 3086.4 | −1.2 | 1341.4 |
| T12 | 5181.3 | 2942.3 | −21.2 | 1396.3 |

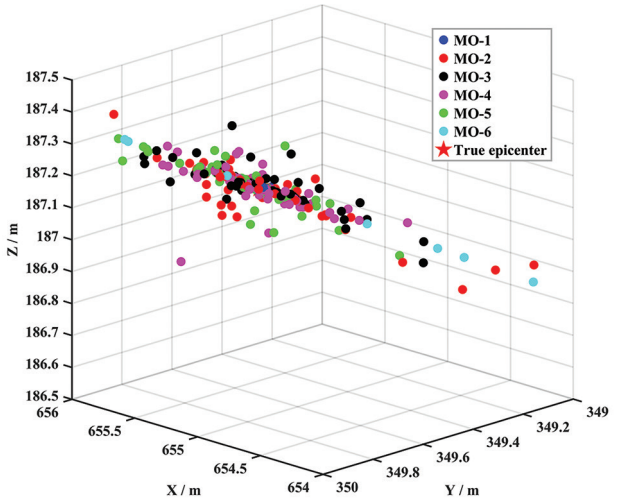


**Figure 4.** Local approximate dissolution point diagram of six microseismic source positioning combination models based on polyhedral array simulation and Multi-Objective Grasshopper Optimization Algorithm (MOGOA) model

**Table 4. Statistical table of calculation results of six microseismic source positioning combination models based on the MOGOA model and deep mining microseismic events**

| Combination | Model 1 | Model 2 | Statistical values of microseismic source positioning results | | | | | | | |
|---|---|---|---|---|---|---|---|---|---|---|
| | | | Mean (m) | STD (m) | IQR (m) | Best (m) | Worst (m) | Duration (s) | Fit-1 | Fit-2 |
| MO-1 | TDA | TDA-P1 | 768.4059 | 844.7945 | 981.4611 | 43.8738 | 3113.6014 | 4.8336 | 0.5187 | 6.3290 |
| MO-2 | TDA | TDQA | 2815.2962 | 890.1189 | 152.6145 | 257.4626 | 3516.8166 | 8.4982 | 0.5766 | 0.0589 |
| MO-3 | TDA | TDQA-P1 | 1584.3049 | 1228.5779 | 2828.5199 | 42.3584 | 3102.2167 | 7.3851 | 0.5280 | 3.1257 |
| MO-4 | TDA-P1 | TDQA | 726.4571 | 1262.5554 | 139.1974 | 40.4096 | 3515.7592 | 7.9982 | 7.0129 | 0.0011 |
| MO-5 | TDA-P1 | TDQA-P1 | 151.1915 | 66.5852 | 121.9566 | 41.0199 | 247.2754 | 7.5293 | 6.3129 | 1.3319 |
| MO-6 | TDQA | TDQA-P1 | 3509.2749 | 4.1603 | 7.9288 | 3503.0247 | 3516.7911 | 11.7089 | 0.0004 | 1.4036 |

Abbreviations: IQR: Interquartile range; MOGOA: Multi-Objective Grasshopper Optimization Algorithm; STD: Standard deviation; TDA: Time difference of arrival; TDQA: Time difference quotient of arrival.

limited by the large number of outliers identified by the box plot. The median and mean of its approximate solution set are second only to those of the MO-5 combination. It can be used as an alternative or substitute for the MO-5 combination model. The specific practical application effect needs to be further verified in combination with the second engineering blasting experiment.

(iii) From the perspective of fitness function value indicators (Fit-1, Fit-2), the statistical positioning effect of the combination MO-5 in the 100-round experiment is still possible to be improved. Its Fit-1 and Fit-2 values are 6.3129 and 1.3319, respectively. If the maximum number of iterations and the population size of the MOGOA algorithm are increased (such as 500 and 100), the positioning accuracy and robustness index values of the MO-5 combination model can be further improved. However, this will reduce the computational efficiency of the model and greatly increase the complexity of the process of finding the optimal approximate solution for the model. This is a practical problem that needs to be balanced in specific applications.

(iv) If the outliers (red triangles in Figure 5) divided by the box plot are ignored, the median and the 100-round positioning errors of the combination models MO-4 and MO-5 are very close. This shows that the MOGOA model, based on the MO-4 combination model, needs to add an outlier removal module to further improve the positioning accuracy and robustness of the results.

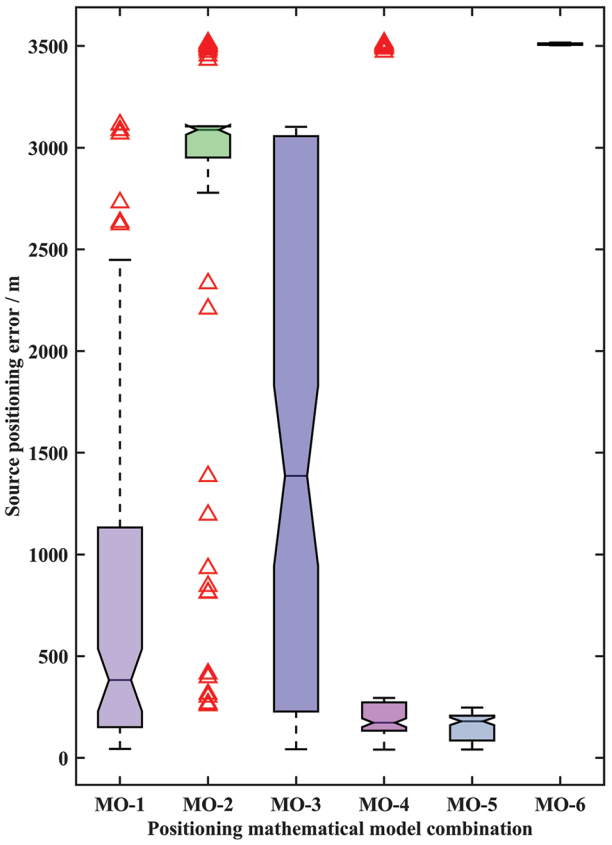


**Figure 5.** Box plot of calculation results based on Multi-Objective Grasshopper Optimization Algorithm (MOGOA) model and six combination models for microseismic source positioning under deep mining microseismic events

Figure 6 shows the curves of the calculation results of the six microseismic source positioning combination models based on the MOGOA model and deep mining microseismic events. Figure 7 shows the three-dimensional scatter plot of the calculation results of the MO-5 combination model based on the MOGOA model and deep mining microseismic events.

From Figures 6 and 7, we can see that:

(i) For a single combination model, the positioning result curves of the combination models MO-1 and MO-4 have a small number of sudden jumps, and are disturbed by a small number of large error positioning results and abnormal approximate solutions, resulting in a large overall positioning mean; while the 100-round positioning error curves of the other four combination models show a general oscillation phenomenon, which indicates that the original data of deep mining microseismic events used in this section may have large systematic errors from the first wave arrival time or the measurement point position coordinates, which makes the MOGOA optimization process unstable and prone to falling into local optimality.

(ii) As shown in Figure 7, the true source coordinates (3500.0, 3520.5, 102.0) are located outside the spatial coverage of the monitoring network. To a certain extent, this increases the difficulty of MOGOA in solving the source approximation solution. The positioning results of most model combinations all have high-frequency oscillation phenomena, which is consistent with the conclusion found by some researchers that the location effect of the internal source of the monitoring network is better than that of the external source.

Experiments on locating microseismic events in deep mining shafts analyzed the performance differences between MOGOA and multi-group multi-objective inversion models. However, varying microseismic event data quality and array configurations also impacted actual positioning effectiveness. We further incorporated microseismic events from the Shizhuyuan Mine for a second engineering case study, thereby strengthening the evaluation conclusions regarding the applicability of the core methodology presented herein.

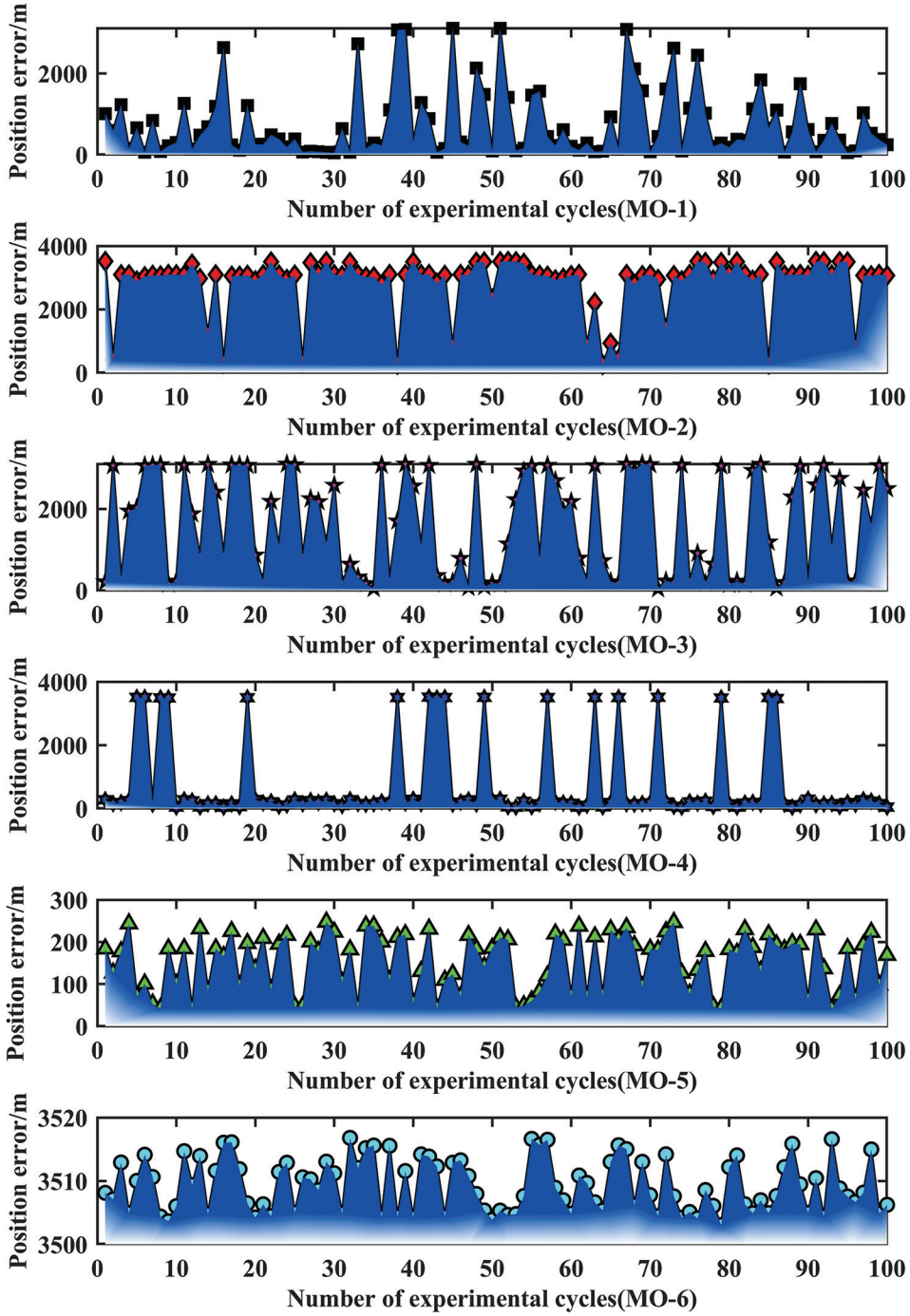


**Figure 6.** Position-error variations across 100 experimental cycles for six microseismic source positioning combination models (MO-1 to MO-6). All models are constructed using the Multi-Objective Grasshopper Optimization Algorithm (MOGOA) approach and tested with microseismic events from deep-mining environments.

### 5.2. Microseismic experiments at Shizhuyuan Mine in Hunan, China

To further verify the comprehensive positioning performance and application differences between the six microseismic source combination models and the MOGOA algorithm, we used microseismic data from the Shizhuyuan Mine in Hunan, China. The P-wave velocity was 2500 m/s, and the actual earthquake locations were (8732.70, 6570.60, 511.30). Eight seismic wave arrival times were recorded (Table 5). The results of 100 rounds

of microseismic source positioning experiments are shown in Figures 8–10 and Table 6. The MOGOA algorithm uses the following preset parameters: 40 search agents, 200 maximum iterations, 3 search target dimensions, a lower search limit of (5000, 5000, 0), an upper search limit of (10000, 10000, 1000), and 100 positioning experiment cycles.

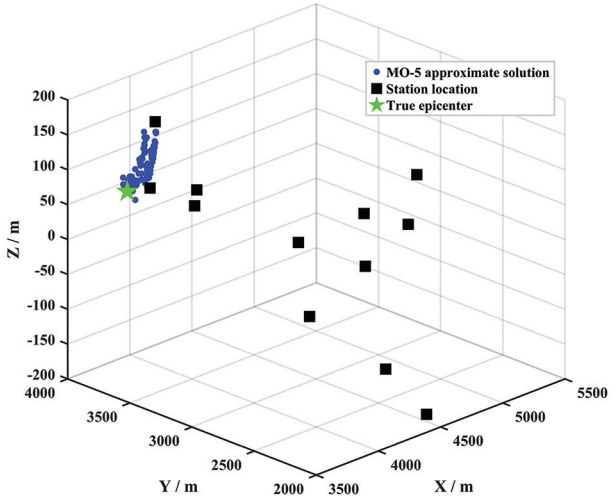


**Figure 7.** Three-dimensional scatter plot of calculation results based on Multi-Objective Grasshopper Optimization Algorithm (MOGOA) model and MO-5 combined model under microseismic events in deep mining

**Table 5. Microseismic event data from a polymetallic mine in Shizhuyuan**

| Serial number | Detector | Vibration pickup coordinates (m) | | | By then (ms) |
|---|---|---|---|---|---|
| | | *x* | *y* | *z* | |
| T1 | 9# | 8761.00 | 6614.00 | 522.00 | 34.90 |
| T2 | 21# | 8737.00 | 6609.00 | 565.00 | 36.60 |
| T3 | 5# | 8666.00 | 6600.00 | 520.00 | 39.30 |
| T4 | 17# | 8668.00 | 6599.00 | 565.00 | 41.10 |
| T5 | 4# | 8641.00 | 6515.00 | 520.00 | 42.30 |
| T6 | 8# | 8691.00 | 6684.00 | 520.00 | 44.50 |
| T7 | 2# | 8721.00 | 6449.00 | 520.00 | 47.80 |
| T8 | 26# | 8702.00 | 6604.00 | 647.00 | 50.00 |

Table 6 shows the statistical results of the six combined models for microseismic source positioning based on the MOGOA model and the microseismic event occurring at Shizhuyuan Mine. The indicators Mean, IQR, STD, Best, Worst, Duration, Fit-1, and Fit-2 represent the mean, IQR, STD, minimum and maximum values of the location error dataset, the average calculated time for positioning, the final fitness function mean of Model 1 (the first submodel from the left in the combined model), and the final fitness function mean of Model 2, respectively. Figure 8 shows a box plot of the calculation results of six combined models for microseismic source positioning based on the MOGOA model and the microseismic event occurring at Shizhuyuan Mine. The upper and lower boundary lines of the boxes in the figure represent the upper quartile (Q3) and lower quartile (Q1) of the positioning results, respectively. The solid line inside the box represents the median of the positioning results. Red triangles mark data identified as outliers by boxplot. The upper and lower solid horizontal lines outside the box represent the maximum and minimum values, respectively.

From Figure 8 and Table 6, we can see that:

(i) In terms of positioning accuracy, the order is: MO-1 > MO-2 > MO-3 > MO-5 > MO-4 > MO-6. The positioning Mean value of the 100-round combination of the TDA and TDA-P1 models reached 27.6035 m, with the highest positioning accuracy. It also performed best in terms of the indicators IQR (5.5896 m) and STD (3.2114 m). This proves that the MO-1 combination has higher accuracy and a more robust model in the microseismic event occurring at Shizhuyuan Mine. The positioning results did not show excessive errors or were judged as outliers by the boxplot. Combined with the simulation experiments

**Table 6. Calculation results of the six microseismic source positioning combination models based on the MOGOA model and microseismic event occurring at Shizhuyuan mine**

| Combination | Model 1 | Model 2 | Statistical values of microseismic source positioning results | | | | | | | |
|---|---|---|---|---|---|---|---|---|---|---|
| | | | Mean (m) | STD (m) | IQR (m) | Best (m) | Worst (m) | Duration (s) | Fit-1 | Fit-2 |
| MO-1 | TDA | TDA-P1 | 27.6035 | 3.2114 | 5.5896 | 22.6275 | 34.8697 | 2.7545 | 0.0007 | 0.2166 |
| MO-2 | TDA | TDQA | 67.8941 | 79.3381 | 80.4866 | 18.8058 | 571.4571 | 3.1671 | 0.0022 | 0.0098 |
| MO-3 | TDA | TDQA-P1 | 71.5070 | 89.5438 | 56.4096 | 15.2813 | 612.5145 | 3.1717 | 0.0025 | 0.4310 |
| MO-4 | TDA-P1 | TDQA | 261.6697 | 763.8916 | 100.3935 | 31.6485 | 3743.8654 | 3.2125 | 0.3539 | 0.0197 |
| MO-5 | TDA-P1 | TDQA-P1 | 135.1657 | 347.8769 | 75.8264 | 29.9978 | 2547.7277 | 3.1662 | 0.3541 | 0.2354 |
| MO-6 | TDQA | TDQA-P1 | 2286.3621 | 1662.9977 | 3195.2378 | 146.7279 | 3743.2557 | 3.4758 | 3.2518e-05 | 0.1746 |

Abbreviation: MOGOA: Multi-Objective Grasshopper Optimization Algorithm.

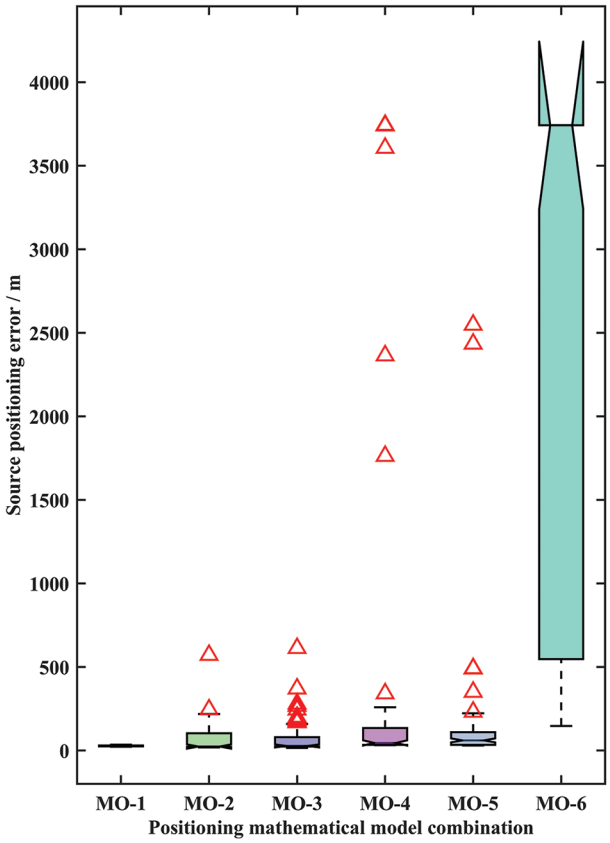


**Figure 8.** Box plot of calculation results based on Multi-Objective Grasshopper Optimization Algorithm (MOGOA) model and the six microseismic source positioning combination models for the microseismic event occurring at Shizhuyuan Mine, Hunan

in Section 3 and the engineering experiments in Section 4.1, we believe that the MO-1 combination is suitable for processing microseismic data with small errors in the position of microseismic array measurement points and small errors in the first wave arrival time.

(ii) The overall positioning accuracy and robustness of the MO-6 combination model are far inferior to those of other inversion mathematical models. In almost all evaluation indicators, it shows an abnormal state that is inconsistent with other combination models. Further analysis of the single mathematical model structure of the combination shows that since the combination does not use wave velocity as a parameter value of any fitness function of MOGOA, and the mathematical model in the form of quotient can only represent the relative positioning error, the combination model is more sensitive to the systematic error of the original data of microseismic events and is prone to fall into local optimality, which seriously restricts the global search ability of the optimization model.

(iii) As shown in Figure 8, if all the outliers filtered out by the box plot (marked as red triangles in Figure 8) are ignored, the median and mean of the 100-round positioning errors of MO-2, MO-3, MO-4, and MO-5 are almost the same. This provides us with an idea: based on MOGOA positioning, combining outlier elimination methods (such as the 3σ criterion, IQR method, and median absolute deviation method) will obtain a reliable approximate solution set.

Figure 9 shows the graphs of calculation results of the six microseismic source positioning combination models based on the MOGOA model and the microseismic event occurring at Shizhuyuan Mine. Figure 10 presents a three-dimensional scatter plot showing some of the calculation results of five microseismic source positioning combination models based on the MOGOA model and the microseismic event occurring at Shizhuyuan Mine.

From Figures 9 and 10, we can see that:

(i) For a single combination model, the positioning result curves of the MO-2, MO-3, MO-4, and MO-5 combination models only have a small number of curve jumps and some scattered points far away from the true source distribution, while the 100-round positioning error curve of MO-1 is relatively flat (all between 20 and 40 m). Combined with the statistical results in Section 4.1, it further shows that the microseismic data from the Shizhuyuan Mine used in this section contains less systematic errors and has little impact on the multi-round positioning effect.

(ii) MO-6 continues to have a large-scale curve jump phenomenon and a divergent distribution behavior far away from the true source, indicating that this model is not suitable for microseismic activity monitoring and related algorithm theory research.

To further elucidate positioning discrepancies among different combinations, we conducted nonparametric statistical tests on positioning error results (from 100 trials) across various model configurations. Given potential non-normal data distribution, we employed the Kruskal–Wallis $H$ test, Dunn's post-hoc test (for multiple group comparisons), and Mann–Whitney $U$ test (for two-group comparisons) to comprehensively assess statistically significant differences among combinations. Specific experimental details include:

(i) Kruskal–Wallis $H$ test (multiple comparisons)
- Null hypothesis H0: The median positioning error is the same across all model combinations.
- Alternative hypothesis H1: At least one model combination has a different median positioning error.

(ii) Dunn's test (post-hoc multiple comparisons): Conducted only when the Kruskal–Wallis test is

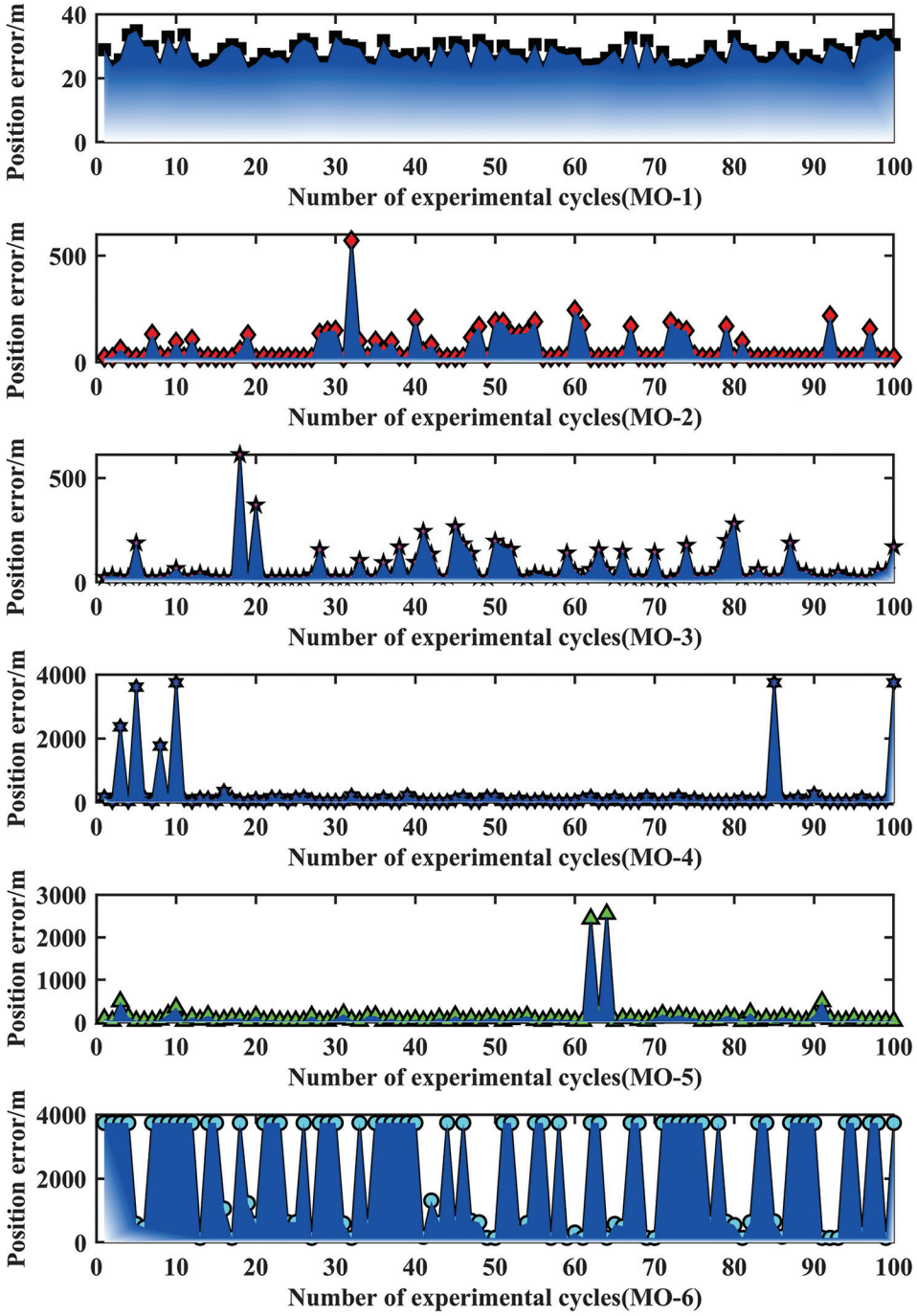


**Figure 9.** Graphs of calculation results based on Multi-Objective Grasshopper Optimization Algorithm (MOGOA) model and the six microseismic source positioning combination models for the microseismic event occurring at Shizhuyuan Mine, Hunan

significant, enabling pairwise comparisons among all combinations.

(iii) Mann–Whitney *U* test (key combination comparisons): Performed for pairwise comparisons of strongly complementary combinations expected to exhibit optimal performance. Selection criteria include comparisons between strongly complementary pairs and between strongly complementary and weakly complementary combinations.

The results of the nonparametric statistical test indicate the following: (i) The Kruskal–Wallis test yielded a p-value of $8.0472 \times 10^{-68}$ and a mean of 323.6900. Since $p < 0.05$,

the null hypothesis is rejected, confirming that at least one combination exhibits a significant performance difference compared to the others. (ii) Post-hoc multiple comparisons (Dunn's test) results (as shown in Table 7): The p-values for MO-1 vs. MO-2, MO-1 vs. MO-3, MO-2 vs. MO-3, and MO-4 vs. MO-5 were 0.8120, 0.0783, 0.9853, and 1.0000, respectively, indicating no significant differences between the aforementioned paired combinations. (iii) In Mann–Whitney *U* test, comparisons of key combinations yielded p-values of 0.1039, 0.1045, 0, 0, and 0 for MO-2 vs. MO-3, MO-1 vs. MO-2, MO-2 vs. MO-6, MO-2 vs. MO-5, and MO-3 vs. MO-4, respectively. These indicate that no significant differences exist between MO-2 and MO-3 or MO-1, while MO-2 significantly outperformed MO-6 and MO-5, and MO-3 significantly outperformed MO-4. (iv) In summary, based on parameters such as the smallest coefficient of variation (0.1163) and the smallest mean positioning error (27.6035), the MO-1 combination demonstrates the best overall positioning performance.

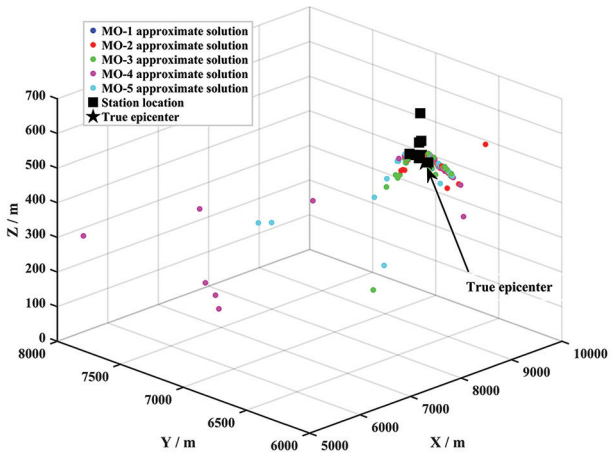


**Figure 10.** Three-dimensional scatter plot of partial results calculated based on Multi-Objective Grasshopper Optimization Algorithm (MOGOA) model and five types of microseismic source positioning combination models for the microseismic event occurring at Shizhuyuan Mine, Hunan

**Table 7. Experimental results of Dunn's test based on microseismic source positioning results from Shizhuyuan Mine**

| Dunn's test | MO-1 | MO-2 | MO-3 | MO-4 | MO-5 | MO-6 |
|---|---|---|---|---|---|---|
| MO-1 | 1 | 0.8120 | 0.0783 | 0 | 0 | 0 |
| MO-2 | 0.8120 | 1 | 0.9853 | 0 | 0 | 0 |
| MO-3 | 0.0783 | 0.9853 | 1 | 0 | 0 | 0 |
| MO-4 | 0 | 0 | 0 | 1 | 1.0000 | 0 |
| MO-5 | 0 | 0 | 0 | 1.0000 | 1 | 0 |
| MO-6 | 0 | 0 | 0 | 0 | 0 | 1 |

### 5.3. Comparative experiment on microseismic source positioning using MOGOA and similar multi-objective optimization algorithms

To verify the actual effect of MOGOA among similar multi-objective calculation methods, the microseismic event data of the Shizhuyuan Mine, which has a small systematic error in microseismic data, and the MO-1 combination with excellent positioning performance were uniformly used as experimental data and multi-objective optimization mathematical models for comparison of multi-objective optimization methods. The NSGA-II and the Multi-Objective Particle Swarm Optimization (MOPSO) were applied to compare and verify their positioning effects. Table 8 and Figure 11 show the microseismic source positioning results under the three multi-objective optimization models. The other experimental conditions were the same as the previous experiments: the number of swarm search agents was 40, the maximum number of iterations was 200, the search target dimension was 3, the search lower limit was (5000, 5000, 0), the search upper limit was (10000, 10000, 1000), and the number of positioning experiment cycles was 100.

Table 8 presents statistical results of microseismic source positioning after 100 iterations, compared with similar multi-objective optimization algorithms. Figure 11 shows a boxplot of microseismic source positioning results from three multi-objective optimization models based on the microseismic event occurring at Shizhuyuan Mine. Overall, the MOGOA method, compared to similar multi-objective calculation methods such as the NSGA-II method and the MOPSO method, exhibits significantly superior high-precision positioning (mean = 27.6035 m) and robust computational performance (STD = 3.2114 m), despite being inferior to the NSGA-II model in terms of algorithm computational efficiency (duration = 2.7545 s). It also balances the optimization processes of the two objective functions in the multi-objective optimization (Fit-1 and Fit-2 reach 0.0007 and 0.2166, respectively) and does not exhibit significant outliers that could severely restrict the practical application of the positioning algorithm. Therefore, it is a relatively reliable and effective microseismic source positioning method.

All experiments employed a population size of 40 and a maximum iteration count of 200 as the primary algorithmic parameters for MOGOA. The relationship between these parameter values and positioning performance has not been clearly elucidated. Therefore, in Section 4.4, we designed experiments specifically to analyze the impact of varying multi-objective algorithm parameters on positioning accuracy.

**Table 8. Statistics of 100 rounds of microseismic source positioning results compared with similar multi-objective optimization algorithms**

| Multi-objective optimization methods | Model Portfolio | Statistical values of microseismic source positioning results | | | | | | | |
|---|---|---|---|---|---|---|---|---|---|
| | | Mean (m) | STD (m) | IQR (m) | Best (m) | Worst (m) | Duration (s) | Fit-1 | Fit-2 |
| NSGA-II | MO-1 | 734.1109 | 552.4060 | 505.8955 | 27.2953 | 3.1833e+03 | 0.2874 | 0.0058 | 0.6619 |
| MOPSO | MO-1 | 1.1892e+03 | 499.9879 | 524.0931 | 92.8176 | 4.1645e+03 | 3.3136 | 0.0058 | 0.6709 |
| MOGOA | MO-1 | 27.6035 | 3.2114 | 5.5896 | 22.6275 | 34.8697 | 2.7545 | 0.0007 | 0.2166 |

Abbreviations: IQR: Interquartile range; MOGOA: Multi-Objective Grasshopper Optimization Algorithm; MOPSO: Multi-Objective Particle Swarm Optimization; NSGA-II: Second-generation nondominated sorting genetic algorithm; STD: Standard deviation.

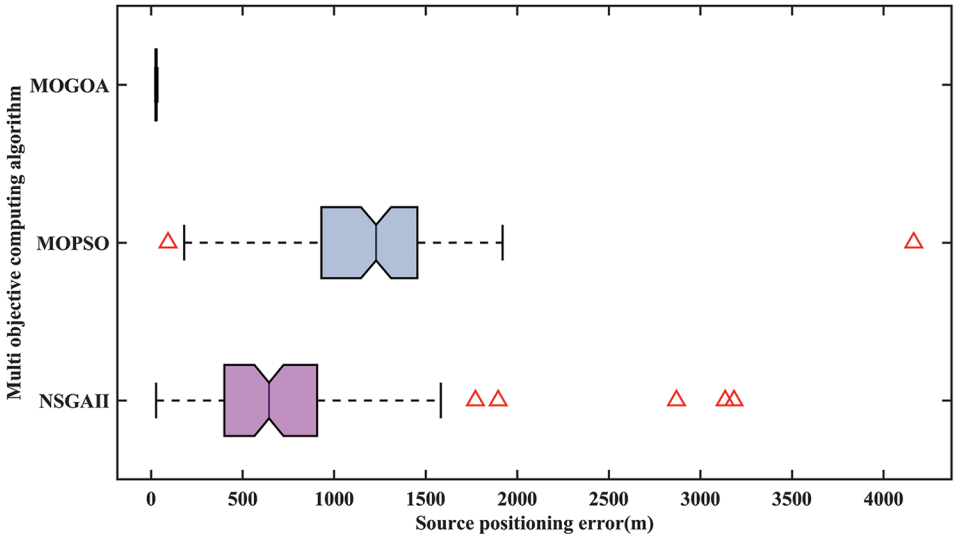


**Figure 11.** Box plot of three multi-objective optimization models for microseismic source positioning based on the microseismic event occurring at Shizhuyuan Mine, Hunan
Abbreviations: MOGOA: Multi-Objective Grasshopper Optimization Algorithm; MOPSO: Multi-Objective Particle Swarm Optimization; NSGA-II: Second-generation nondominated sorting genetic algorithm.

### 5.4. Sensitivity analysis of MOGOA parameters

Parameter sensitivity analysis is crucial for evaluating the robustness of positioning algorithms and guiding practical applications. To validate the sensitivity of MOGOA parameters (such as population size and maximum iteration count) on positioning performance, nine sets of microseismic source positioning experiments were designed with varying parameters. The Shizhuyuan Mine microseismic event data and the MO-1 ensemble were uniformly adopted as experimental data and the multi-objective optimization mathematical model for sensitivity analysis. Table 9 presents the statistical results of MOGOA microseismic source positioning under varying parameters. Other experimental conditions included: setting the number of agents in the population search to five levels (10, 20, 40, 80, 120); setting the maximum iteration count to five levels (20, 100, 200, 500, 1000); defining the lower search bound as (5000, 5000, 0) while the upper search bound as (10000, 10000, 1000); and setting the positioning experiment loop count to 20.

Our interpretations based on Table 9 are as follows: (i) With the maximum iteration count fixed at 200, parameter configurations exhibit distinct performance thresholds. When the population size is too small (population size = 10), the positioning error reaches as high as 859.6488 m, attributed to premature convergence caused by insufficient population diversity. However, when the population size exceeds 20, the positioning error stabilizes around 31 m, indicating that a critical level of diversity has been achieved to ensure algorithmic performance. (ii) Similarly, with the population size fixed at 40, when the maximum iterations were below 100 (maximum iterations = 50), the algorithm performed poorly (error 134.3802 m) due to insufficient convergence time; performance stabilized when iterations exceeded 100. (iii) These findings demonstrate the proposed method's robust parameter tolerance. Stable and accurate positioning

**Table 9. Statistical table of microseismic source positioning for MOGOA under different parameters**

| Population size | Maximum iterations | Statistical values of microseismic source positioning results | | | | | | |
|---|---|---|---|---|---|---|---|---|
| | | Mean (m) | STD (m) | IQR (m) | Best (m) | Worst (m) | Duration (s) | Median (m) |
| 10 | 200 | 859.6488 | 1.0750e+03 | 1.2744e+03 | 28.1846 | 3.4119e+03 | 0.3577 | 256.4745 |
| 20 | 200 | 31.4368 | 2.2932 | 3.4162 | 27.9417 | 35.8210 | 0.7592 | 30.6503 |
| 40 | 200 | 31.0989 | 2.0841 | 3.5635 | 28.6328 | 34.9410 | 2.8058 | 30.4776 |
| 80 | 200 | 31.7041 | 2.4019 | 4.4000 | 28.0602 | 35.2399 | 10.9193 | 31.5326 |
| 120 | 200 | 30.9992 | 2.1564 | 2.7094 | 28.3879 | 36.7719 | 24.4511 | 30.3021 |
| 40 | 50 | 134.3802 | 180.4892 | 175.2767 | 28.6574 | 641.0793 | 0.7172 | 35.0223 |
| 40 | 100 | 43.5813 | 52.3692 | 4.1199 | 27.4581 | 265.7581 | 1.3974 | 31.3012 |
| 40 | 500 | 31.1093 | 2.3525 | 4.3755 | 28.3230 | 35.1322 | 7.0539 | 30.1602 |
| 40 | 1000 | 32.3111 | 2.0417 | 3.6189 | 29.0395 | 34.6590 | 14.1781 | 33.2069 |

Abbreviations: IQR: Interquartile range; MOGOA: Multi-Objective Grasshopper Optimization Algorithm; STD: Standard deviation.

results are achievable as long as parameter configurations exceed the minimum thresholds (population size ≥20, maximum iterations ≥100). Based on this, population size = 40 and maximum iterations = 200 were selected as experimental parameters, balancing performance assurance with computational efficiency.

## 6. Conclusion

This paper uses the MOGOA model to examine the performance differences among six microseismic source positioning mathematical model combinations and validates the application and adaptability of the inversion model combination to three types of microseismic event data. The performance of MOGOA is then compared with that of NSGA-II and MOPSO for a similar location. The following conclusions are drawn:

(i) When microseismic event data errors are minimal, the MO-1 combination, consisting of the TDA-P1 and TDA models, exhibits superior microseismic source positioning performance, demonstrating significant performance in positioning accuracy, robustness, and computational efficiency. Applying a multi-objective intelligent swarm optimization algorithm to the microseismic source positioning mathematical model effectively adds constraints to the nonlinear problem, effectively preventing the optimization process from prematurely falling into local optima. The MOGOA and MO-1 model combination is suitable for processing data from sites with precise array sensor positions and relatively uniform surface media.

(ii) When microseismic event data errors are large, the MO-5 combination, consisting of the TDA-P1 and TDQA-P1 models with a constant offset term, achieves superior microseismic source positioning performance. The TDQA-P1 model mathematically eliminates wave velocity and first wave arrival time, further reducing the impact of these parameter errors on location. Therefore, the MOGOA and MO-5 combination is suitable for processing data from sites with errors in array sensor positions or inhomogeneous surface media.

(iii) Compared with similar multi-objective algorithms such as NSGA-II and MOPSO, MOGOA exhibits significant noise immunity and global search capabilities, and can be further analyzed and applied in research on optimal microseismic source positioning based on inversion mathematical models.

(iv) Parameter sensitivity analysis reveals that the proposed combination of inversion models provides an effective search space for the optimization algorithm, enabling the multi-objective ant colony algorithm to converge stably under relatively relaxed parameter settings. This facilitates the practical application of this method in engineering practice.

(v) This study confirms that determining microseismic source location is a multi-objective optimization problem and intelligent algorithms provide a robust strategy to microseismic source positioning. This approach does not rely on a single, potentially inaccurate assumption—whether concerning the velocity model or data quality. Instead, it naturally derives an optimal compromise solution insensitive to various errors through the synergistic and competitive interaction of multiple models. This endows it with clear application potential and advantages over traditional methods in real-world engineering scenarios where model and data uncertainties exist.

In future research, we will focus on addressing the challenges of low positioning accuracy and poor model robustness caused by systematic errors in microseismic event data. We plan to introduce an adaptive step-size adjustment mechanism in the MOGOA model, linked to the fitness function value or the number of iterations,

to enhance MOGOA's global search capabilities in inhomogeneous media.

## Acknowledgments

None.

## Funding

This research was financially supported by Mahasarakham University; the Scientific Research Fund from Institute of Seismology, CEA and National Institute of Natural Hazards, Ministry of Emergency Management of China (Grant No. IS202226322 and IS202436357); the Open Fund of Wuhan Gravitation and Solid Earth Tides, National Observation and Research Station (Grant No. WHYWZ202406); the Spark Program of Earthquake Science and Technology, China Earthquake Administration (Grant No. XH25019C and XH24025YC); the 2025 Hubei Provincial Key Laboratory Targeted Commissioned Project (Grant No. 2025CSA083); the Green Data Integration Intelligence Research and Innovation Project of Chengdu Jincheng College (Grant No. 2025–2027); and the Mathematics and Finance Research Center Project of Dazhou Social Science Federation Key Research Base (Grant No. SCMF202505).

## Conflict of interest

The authors declare they have no competing interests.

## Author contributions

*Conceptualization:* Cong Pang, Tianwen Zhao, Sirui Liu, Xingxing Li, Ya Xiang

*Formal analysis:* Cong Pang, Guoqing Chen, Tianwen Zhao, Ya Xiang

*Investigation:* Tianwen Zhao, Sirui Liu, Xingxing Li, Piyapatr Busababodhin

*Methodology:* Cong Pang, Tianwen Zhao, Guoqing Chen, Piyapatr Busababodhin

*Validation:* Cong Pang, Shirui Liu, Tianwen Zhao, Guoqing Chen

*Writing–original draft:* Cong Pang, Tianwen Zhao, Guoqing Chen, Piyapatr Busababodhin

*Writing–review & editing:* Cong Pang, Tianwen Zhao, Guoqing Chen, Piyapatr Busababodhin

## Availability of data

Some data used in this study cannot be shared publicly due to collaborative agreement restrictions but are available from the corresponding author upon reasonable request.

## References

1. Feng Q, Han L, Ma L. Microseismic source localization method based on neural network algorithm and dynamic reduction of solution interval. *IEEE Geosci Remote Sens Lett*. 2024;21:1-5.

   doi: 10.1109/lgrs.2024.3398043

2. Yan Z, Zi-Zin W, Lin-Qi C, Hong-Li D. Research on microseismic event localization based on convolutional neural network. *J Seismic Explor*. 2024;33(6):1-32.

   doi: 10.36922/jse.corr090325

3. Wang H, Alkhalifah T, Waheed UB, Birnie C. Data-driven microseismic event localization: An application to the Oklahoma Arkoma basin hydraulic fracturing data. *IEEE Trans Geosci Remote Sens*. 2022;60:1-12.

   doi: 10.1109/TGRS.2021.3120546

4. Feng Q, Han L, Zhao B. Localizing microseismic events using semi-supervised generative adversarial networks. *IEEE Trans Geosci Remote Sens*. 2022;60:5923908.

   doi: 10.1109/tgrs.2022.3225415

5. Xu J, Qiu T, Zeng Z, Zhu F, Han P, Zhang W. Microseismic event location using migration-based stacking with effective parameters' optimization. *IEEE Trans Geosci Remote Sens*. 2025;63:5917809.

   doi: 10.1109/tgrs.2025.3591126

6. Chen Y, Savvaidis A, Fomel S, Saad OM, Chen Y. RFloc3D: A machine-learning method for 3-D microseismic source location using P- and S-wave arrivals. *IEEE Trans Geosci Remote Sens*. 2023;61:1-10.

   doi: 10.1109/tgrs.2023.3236572

7. Michel OJ, Tsvankin I. Gradient calculation for waveform inversion of microseismic data in VTI media. *J Seismic Explor*. 2014;23(3):201-217.

8. Abdullin A, Waheed UB, Suleymanli K, Stanek F. Microseismic source localization using fourier neural operator with application to field data from Utah FORGE. *IEEE Trans Geosci Remote Sens*. 2025;63:1-10.

   doi: 10.1109/tgrs.2025.3533635

9. Wang C, He R, Pei C, Sun F, Zhou X, Chen Z. Localization for surface microseismic monitoring based on local equivalent path and virtual field optimization method. *IEEE Sens J*. 2024;24(23):39270-39284.

   doi: 10.1109/jsen.2024.3469969

10. Pang C, Xu J, He X, Zuo Y, Li C, Ma W. Research on Location Method of Mine Micro-Seismic Source Based on Inter Quartile Range and Newton-Raphson Method. In: *2023 International Conference on New Trends in Computational Intelligence (NTCI)*. Qingdao, China; 2023. p. 5-10.

    doi: 10.1109/ntci60157.2023.10403666

11. Pang C, Chen J, Ma L, *et al*. A Method for Micro-seismic Source Location Based on Principal Component Analysis and Spatial Discrete Detection. In: *2023 IEEE 7th Information*

*Technology and Mechatronics Engineering Conference (ITOEC)*. Chongqing, China; 2023. p. 92-96.

doi: 10.1109/itoec57671.2023.10291402

12. Wang Y, Bi W, Fan Q, Xu S, Zhang A. Multi-objective optimization of top-level arrangement for flight test. *J Syst Eng Electron*. 2025;36(3):714-724.

doi: 10.23919/jsee.2025.000019

13. Noori MS, Sahbudin RKZ, Sali A, Hashim F. Multi-objective multi-exemplar particle swarm optimization algorithm with local awareness. *IEEE Access*. 2024;12:125809-125834.

doi: 10.1109/access.2024.3426104

14. Gao L, Liu Z. An integrated external archive local disturbance mechanism for multi-objective snake optimizer. *Chin J Electron*. 2024;33(4):989-996.

doi: 10.23919/cje.2023.00.023

15. Sadeghi AH, Bani EA, Fallahi A, Handfield R. Grey wolf optimizer and whale optimization algorithm for stochastic inventory management of reusable products in a two-level supply chain. *IEEE Access*. 2023;11:40278-40297.

doi: 10.1109/access.2023.3269292

16. Wu X, Zhan J, Ding W, Pedrycz W. GRNN model with feedback mechanism incorporating *k*-nearest neighbor and modified gray wolf optimization algorithm in intelligent transportation. *IEEE Trans Intell Transp Syst*. 2025;26(3):3855-3872.

doi: 10.1109/tits.2024.3510678

17. Chen X, Ma M, Liu C, Xie H, Wang S. Research on interference resource optimization based on improved whale optimization algorithm. *IEEE Access*. 2025;13:83136-83147.

doi: 10.1109/access.2025.3569460

18. Zhao ZH, Yin YF, Wang YK, Qin KR, Xue CD. Adaptive ECG signal denoising algorithm based on the improved whale optimization algorithm. *IEEE Sens J*. 2024;24(21):34788-34797.

doi: 10.1109/jsen.2024.3422995

19. Li Y, Yao Y, Hu S, Wen Q, Zhao F. Coverage enhancement strategy for WSNs based on multiobjective ant lion optimizer. *IEEE Sens J*. 2023;23(12):13762-13773.

doi: 10.1109/jsen.2023.3267459

20. Tian F, Zhu L, Shi Q, *et al*. The three-lead EEG sensor: Introducing an EEG-assisted depression diagnosis system based on ant lion optimization. *IEEE Trans Biomed Circ Syst*. 2023;17(6):1305-1318.

doi: 10.1109/tbcas.2023.3292237

21. Ghaleb SA, Mohamad M, Ghanem WAH, *et al*. Feature selection by multiobjective optimization: Application to spam detection system by neural networks and grasshopper optimization algorithm. *IEEE Access*. 2022;10:98475-98489.

doi: 10.1109/access.2022.3204593

22. Liu J, Wang A, Qu Y, Wang W. Coordinated operation of multi-integrated energy system based on linear weighted sum and grasshopper optimization algorithm. *IEEE Access*. 2017;6:42186-42195.

doi: 10.1109/access.2018.2859816

23. Lalhmachhuana R, Deb S, Datta S, Singh KR. Multi-Objective based Generation Fuel Cost and Emission Reduction using Grasshopper Optimization Algorithm. In: *2023 10th International Conference on Signal Processing and Integrated Networks (SPIN)*. Noida, India; 2023. p. 676-680.

doi: 10.1109/spin57001.2023.10116665

24. Mokeddem D, Nasri D. A New Levy Flight Trajectory-based Grasshopper Optimization Algorithm for Multi-Objective Optimization Problems. In: *2020 Second International Conference on Embedded and Distributed Systems (EDiS)*. Oran, Algeria; 2020. p. 76-81.

doi: 10.1109/edis49545.2020.9296480

25. Zhaoming LV, Peng R. Improving the efficiency of multi-objective grasshopper optimization algorithm to enhance ontology alignment. *Wuhan Univ J Nat Sci*. 2022;27(3):240-254.

doi: 10.1051/wujns/2022273240

26. Wang C, Li J, Rao H, *et al*. Multi-objective grasshopper optimization algorithm based on multi-group and co-evolution. *Math Biosci Eng MBE*. 2021;18(3):2527-2561.

doi: 10.3934/mbe.2021129

27. Pang C, Zhao T, Chen G, *et al*. Earthquake and blast recognition based on CEEMDAN multiscale fuzzy entropy and NSGAIII optimized 1D-CNN neural networks. *J Seismic Explor*. 2025;34(1):22-42.

doi: 10.36922/jse025260029

28. Bahrami B, Khayyambashi MR, Mirjalili S. Multiobjective placement of edge servers in MEC environment using a hybrid algorithm based on NSGA-II and MOPSO. *IEEE Int Things J*. 2024;11(18):29819-29837.

doi: 10.1109/jiot.2024.3409569

29. Li Y, Xie Z, Yang S, Ren Z. A hybrid algorithm based on NSGA-II and MOPSO for multi-objective designs of electromagnetic devices. *IEEE Trans Magn*. 2023;59(5):7001804.

doi: 10.1109/tmag.2023.3250319

30. Poormirzaei R, Hamidzadeh R, Moghadam R, Zarean A. The application of PSO to joint inversion of microtremor Rayleigh waves dispersion curves and refraction traveltimes. *J Seismic Explor*. 2015;24(4):305-325.

ACCSCIENCE PUBLISHING

Journal of Seismic Exploration

ARTICLE

# A novel method for low-frequency quality control of seismic vibrator ground force

**Mingtao Nie[1,2], Zhouhong Wei[3]*, Tao Fang[2], Xiaolong Jiang[2], Yongan Xu[2], Yang Liu[1], and Yongfei Qi[1,2]**

[1]State Key Laboratory of Petroleum Resources and Engineering, China University of Petroleum (Beijing), Beijing, China

[2]BGP, China National Petroleum Corporation, Zhuozhou, Hebei, China

[3]INOVA Geophysical, Sugar Land, Texas, United States

## Abstract

Seismic vibrators are the primary sources for land seismic acquisition, featuring controllable bandwidth and energy, low environmental impact, safety, and high efficiency. With the widespread application of "2W&H" technology, wide-frequency seismic data, particularly low-frequency components, have attracted increasing attention. However, the ground force output of a vibrator is severely constrained at low frequencies, primarily due to limitations in its mechanical and hydraulic systems. Among these, hydraulic system limitations are often associated with oil flow, which is largely constrained by the pump's maximum capacity; however, oil flow is not measured during vibrator sweeps. The system complexity prevents the installation of flow sensors on vibrators, making the performance of the vibrator oil flow unmonitored. Since the oil flow directly determines the quality of the vibrator ground force output, it is essential to understand the behavior of vibrator oil flow. In this study, a detailed analysis of the working mechanism of a seismic vibrator was conducted, as well as its low-frequency force-output limitations. Then, we proposed a method for estimating vibrator oil flow. Both theoretical analyses and field-testing data were used to validate the proposed estimation method. The estimated data demonstrated strong consistency with the direct flow measurement using flow sensors. Moreover, the results confirm the feasibility of the proposed estimation method. This method provides a real-time quality control indicator for the vibrator oil flow performance during vibrator sweeps, thereby enabling complete monitoring of the vibrator performance quality at low frequencies. In addition, this method holds promising potential for broad application in land vibroseis exploration.

***Keywords:*** Vibrator; Low-frequency; Oil flow; Quality control

***Corresponding author:**
Zhouhong Wei
(John.Wei@inovageo.com)

**Citation:** Nie M, Wei Z, Fang T, *et al*. A novel method for low-frequency quality control of seismic vibrator ground force. *J Seismic Explor*. 2026;35(1):171-183. doi: 10.36922/JSE025410086

**Received:** October 11, 2025

**Revised:** November 10, 2025

**Accepted:** December 10, 2025

**Published online:** January 15, 2026

**Copyright:** © 2026 Author(s). This is an Open-Access article distributed under the terms of the Creative Commons Attribution License, permitting distribution, and reproduction in any medium, provided the original work is properly cited.

**Publisher's Note:** AccScience Publishing remains neutral with regard to jurisdictional claims in published maps and institutional affiliations.

## 1. Introduction

Hydraulic seismic vibrators have been used as the primary source for land seismic surveys for over 60 years. Over the years, many innovative vibroseis acquisition techniques have been developed, leading to significant improvements in acquisition productivity. For example, Rozemond[1] introduced a slip-sweep acquisition method, and the high-fidelity vibratory-seismic method was developed by Allen *et al.*[2] In addition, the

distance separated simultaneous source was developed and presented by Bouska,[3] and a more flexible simultaneous source acquisition technique, independent simultaneous source acquisition, was invented by Howe *et al.*[4]

Recently, vibroseis low-frequency acquisition has become a routine practice in land seismic surveys. Seismic vibrator manufacturers have been making progress in vibrator actuator design to improve vibrator low-frequency performance.[5-10] However, these improvements still cannot meet the force spectrum required at low frequencies. To acquire more low-frequency data, the use of custom nonlinear sweep signals based on low-dwell technology has become a routine operation in land seismic surveys.[11-14] However, how to perform quality control (QC) of seismic vibrator performance at low frequencies remains a challenge. In geophysics literature, few studies have been devoted to seismic vibrator QC at low frequencies. Moreover, apart from the study by Sallas,[15] very few technical papers have provided a concise explanation of how a hydraulic seismic vibrator works, particularly regarding the hydraulic power supply system.

In the present study, we first present a detailed introduction to how a hydraulic seismic vibrator works. Then, we discuss the limitations experienced by a seismic vibrator when it operates at low frequencies. The reaction mass displacement limitation is physically measured and monitored in the vibrator field QC. However, the other limitation—vibrator oil flow—is not physically measured or monitored in QC. Next, considerable effort is devoted to the study of vibrator oil flow, and a novel method is proposed for estimating vibrator oil flow to enable QC of the low-frequency ground force. Finally, we conduct experimental tests to assess the agreement between the estimated and measured oil flow. Consequently, field QC of vibrator oil flow becomes possible.

## 2. Theoretical analysis

### 2.1. Challenges from low-frequency acquisition

In field operation, low-dwell sweeps must be used on seismic vibrators to push the vibroseis acquisition bandwidth toward the low end of the spectrum. These low-dwell sweeps typically shake seismic vibrators at low frequencies for extended periods of time to boost low-frequency force-energy. Seismic vibrators often work at the edge of their maximal capabilities, especially in the seismic vibrator hydraulic system. Fatigue, wear, and failure become inevitable in vibrator system components. Consequently, the quality of the vibrator ground force is affected, thereby reducing the quality of seismic data. For example, in 2021, a crew in the Middle East desert experienced a total failure of seven pilot servo-valves and severe damage to vibrator pumps in only 2 weeks of operation.

Figure 1 presents an example illustrating the consequences of this field operation when the hydraulic pump flow limitation is reached. Figure 1A shows the frequency–time (F–T) variant spectrum of the vibrator ground force. In the ground-force signal, a very strong spike appears when the sweep changes from a nonlinear sweep rate to a linear sweep rate. This indicates that severe cavitation possibly occurs in the vibrator pump system. Figure 1B shows strong harmonic noise associated with severe cavitation observed on the shot record; the cavitation can lead to severe damage to the vibrator pump. Figure 1C displays severe scratches observed on the port plate of the hydraulic pump.

These findings demonstrate that, when the vibrator operates at low frequencies, the hydraulic flow limitation is reached. In addition, the vibrator ground force is contaminated with spiky noise, leading to additional harmonic noise in seismic records and damage to hydraulic system components. This results in a significant reduction in the production rate. In addition, repairing these pilot servo-valves and hydraulic pumps significantly increases operating costs. Hence, it is necessary to monitor the seismic vibrator motion and performance at low frequencies so that early warnings can be triggered before the vibrator system components fail completely.

### 2.2. Vibrator hydraulic working principle

Figure 2 illustrates how a hydraulic seismic vibrator works. A seismic vibrator is essentially a hydro-mechanical system driven by a servo-valve assembly controlled electronically. The vibrator system consists of two subsystems—the vibrator hydraulic power supply system and the vibrator actuator system—connected through a pressurized oil flow. The vibrator hydraulic power supply system generates the required high-pressure oil flow for the vibrator actuator system. The output shaft of a diesel engine is connected to the pump shaft so that the engine's rotational power can be transferred to the pump.

A variable displacement pressure piston pump, through a high-pressure adjustment device, produces a high-pressure oil flow and outputs it into hoses. The pressurized oil flow goes through a high-pressure filter to remove particles and impurities from the oil circuit. Filtering these impurities effectively prevents severe cavitation in the oil flow circuit. After filtration, the filtered oil flow passes through a high-pressure accumulator. The main function of the high-pressure accumulator is to suppress pressure fluctuations and maintain the high pressure at a constant level (3,250 psi). At this point, the high-pressure oil flow is

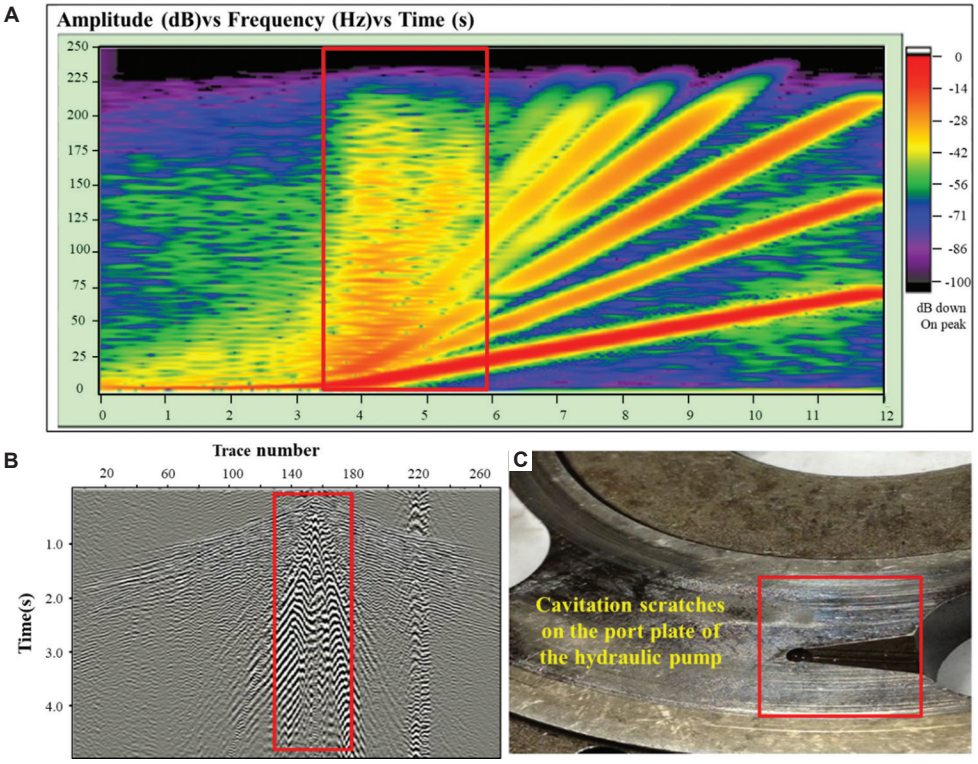


**Figure 1.** Examples of hydraulic flow limitation in a seismic vibrator. (A) Frequency–time variant spectrum of the vibrator ground force, illustrating a strong spiky noise (red box). (B) Seismic record displaying harmonic noise (red box) caused by the spiky ground force. (C) Mechanical damage observed on the hydraulic pump caused by the spiky ground force.

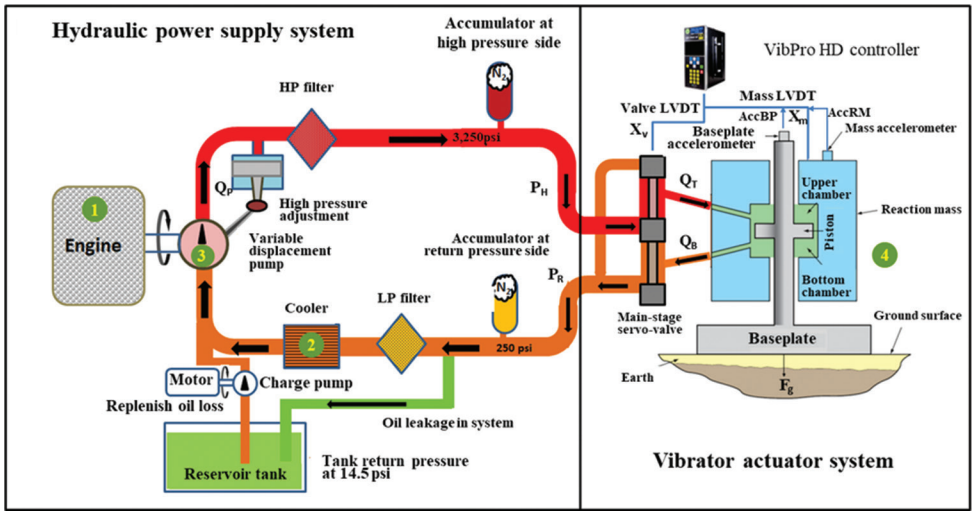


**Figure 2.** Schematic illustration of a hydraulic seismic vibrator
Abbreviations: AccBP: Accelerations of baseplate; AccRM: Accelerations of reaction mass; LP: Low pressure; LVDT: Linear variable differential transformer.

ready to leave the hydraulic power supply system and enter the vibrator actuator system.

The high-pressure fluid flows into the main-stage servo-valve. The displacement of the main-stage servo-valve is controlled by a vibrator controller. Specifically, the Vib Pro HD controller regulates the displacement of the main-stage servo-valve. In fact, it controls the current of the pilot servo-valve (not depicted in the diagram). The electrical current of the pilot servo-valve is proportional to the displacement of the main-stage servo-valve. For

simplicity, we assume that the vibrator controller directly controls the displacement of the main-stage servo-valve.

The high-pressure hydraulic fluid output from a control port of the main-stage servo-valve, $Q_T$, flows into the upper chamber of the reaction mass, rapidly increasing the pressure in the upper chamber. This increased pressure pushes the reaction mass upward. At the same time, the same pressure is applied to the top surface of the piston, causing the piston to move downward, resulting in a downward movement of the vibrator baseplate. Furthermore, the upward movement of the reaction mass and the downward movement of the baseplate combine to form a weighted-sum ground force ($F_g$), which is then transmitted into the deep ground.[16]

When the high-pressure oil fluid flows into the upper chamber of the reaction mass, the reaction mass moves upward, increasing the volume of the upper chamber while reducing the volume of the bottom chamber. The hydraulic oil fluid, $Q_B$, flows out of the bottom chamber and returns to the low-pressure side, or return side, of the hydraulic power supply system through another control port of the main-stage servo-valve. The oil flow leaves the vibrator actuator system and returns to the hydraulic power supply system. It also passes through a low-pressure accumulator to reduce pressure ripples and stabilize the return pressure. Typically, the return-side pressure is maintained at 250 psi. The return flow also passes through a low-pressure filter for filtration. The filtered low-pressure hydraulic oil then goes through a cooling system to dissipate heat. The cooled hydraulic oil is subsequently drawn into the pump again, and a new cycle begins.

During vibrator operation, some hydraulic oil loss is inevitable due to internal and external leakages in the hydraulic system. Therefore, a special hydraulic circuit is designed and added to allow the leaked oil fluid to flow back to a reservoir tank, effectively preventing environmental contamination. In addition, a small charge pump is added to the hydraulic circuit to compensate for the loss of hydraulic oil in the hydraulic system. As noted, in the vibrator system, hydraulic oil flow is an essential element that transfers energy, converting hydraulic energy into mechanical motion and ground force output.

### 2.3. Low-frequency limitations

In recent years, low-frequency vibroseis acquisition has become a routine practice in land seismic exploration.[17] Through years of field practice, field experience, and analysis have shown that the seismic vibrator ground force at low frequencies is severely limited due to constraints in the vibrator's mechanical and hydraulic systems. Wei[18] and Sallas[19] have studied the seismic vibrator extensively, concluding that the ground force at low frequencies is mainly limited by two key factors: the maximal travel distance of the reaction mass, also referred to as the mass stroke limit, and the vibrator's total flow, which is primarily determined by the hydraulic pumps (pump flow limit).[20]

Specifically, regarding the maximal travel distance of the reaction mass, **Equation 1** expresses the relationship between the maximal low-frequency ground force and the maximal reaction mass displacement, as well as the mass of the reaction mass.

$$F_{max1} = 4\pi^2 M_{rm} X_{rm} f^2 \tag{1}$$

Where $F_{max1}$ is the maximum force that can be theoretically generated by the vibrator mechanical system at low frequencies, $M_{rm}$ is the mass of the reaction mass, $X_{rm}$ is the maximum travel distance of the reaction mass, and $f$ is the frequency. Based on **Equation 1**, there is no parameter related to the vibrator hydraulic system. Thus, **Equation 1** expresses the low-frequency ground force limitation solely from the vibrator mechanical system.

**Equation 2** provides an expression based solely on the vibrator hydraulic system. For a given vibrator, the hydraulically limited low-frequency force scales with the available total flow.

$$F_{max2} = 9.87 \frac{M_{rm} Q}{A_p} f \tag{2}$$

Where $F_{max2}$ is the maximum force that can be theoretically generated by the vibrator oil flow at low frequencies, $A_p$ is the piston area in the reaction mass chambers, and $Q$ is the maximum vibrator oil flow, primarily contributed by the vibrator pump flow.

In summary, the vibrator ground force at low frequencies is determined by the reaction mass stroke for a given vibrator (**Equation 1**) and is also constrained by the vibrator's total flow (**Equation 2**). Given the specifications of a vibrator, a low-frequency force profile can be calculated using **Equations 1** and **2**.

Table 1 lists the key specifications of AHV-IV 364 (60,000-lbf) and AHV-IV 380 (80,000-lbf) vibrators. Using these specifications, their low-frequency force profiles can be obtained. Figure 3 shows the theoretical low-frequency force profiles for the AHV-IV 364 and AHV-IV 380 vibrators. The force curves at low frequencies (<10 Hz) were plotted using **Equations 1** and **2** with the specifications listed in Table 1. It can be clearly seen that the vibrator force curves at low frequencies are limited parabolically by the maximal reaction mass displacement and linearly by the vibrator total flow.

**Table 1. Specifications of AHV-IV vibrators**

| Parameters | AHV-IV 364 vibrator | AHV-IV 380 vibrator |
|---|---|---|
| Peak force (lbs) | 61,800 | 77,700 |
| Reaction-mass weight (*Mrm*; lbs) | 11,020 | 13,029 |
| Peak-to-peak useful mass stroke (*Xrm*; in) | 3.87 | 3.87 |
| Pumps (*Qp*; gallon/min) | Two P7; 164 gallon/min | Two P8; 187 gallon/min |
| Piston area (Ap; $in^2$) | 20.67 | 25.92 |

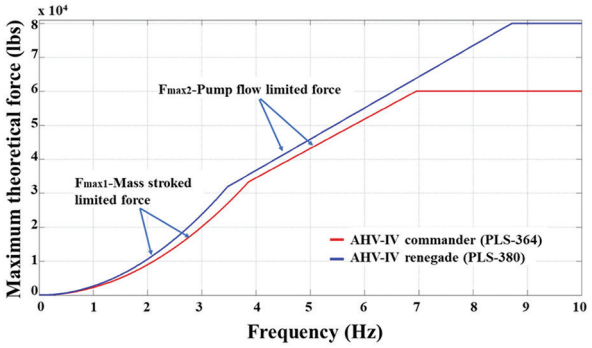


**Figure 3.** Theoretical low-frequency force profiles of AHV-IV vibrators

To overcome these limitations on the seismic vibrator ground force at low frequencies, several researchers, especially from vibrator manufacturers, have attempted to redesign the vibrator hydraulic and mechanical systems so that the vibrator mechanical system becomes more rigid and the hydraulic power supply system becomes more efficient and less noisy.[7,19-21] Field testing results have shown that at low frequencies, notable improvements in the vibrator ground force and reductions in harmonic distortion are observed. A remarkable improvement in the signal-to-noise ratio of the vibrator ground force is achieved. Thus, an extension of the vibroseis acquisition frequency bandwidth toward 1.5 Hz becomes achievable. However, these force improvements are still insufficient to meet the required force-energy in the frequency range below 5 Hz.

To meet the required force-energy, the low-dwell sweep is necessary. Several researchers[21-24] have explored different approaches, including low-frequency sweep design techniques, to supply extra force-energy so that the vibroseis acquisition bandwidth can be extended toward low frequencies (<5 Hz). These low-frequency sweep techniques aim to guide seismic vibrators to follow as closely as possible their low-frequency force profiles. Qi *et al.*[13] demonstrate how a low-frequency sweep is designed for a given mode of vibrator.

To date, with the most advanced vibrator technologies, combining the latest low-frequency seismic vibrator with customized low-dwell sweeps, the low-frequency vibroseis acquisition bandwidth has been extended to record seismic data as low as 1.5 Hz.[7] A good acquisition production rate is also achieved. However, challenges remain in preventing the complete failure of vibrator system components during vibroseis field operations. In other words, performing QC on seismic vibrator performance at low frequencies remains very challenging.

To address the limitation of the vibrator mechanical system, a reaction mass linear variable differential transformer (LVDT) sensor is mounted on the reaction mass to measure the reaction mass displacement in real-time. An LVDT is a type of sensor used for high-accuracy position or displacement measurements. Thus, the reaction-mass travel distance during a sweep becomes a known variable, and its real-time measurements are recorded in a vibrator QC report, for example, an extended QC text file.

Figure 4 illustrates the results of QC of the reaction-mass displacement. It can be clearly seen that the reaction-mass displacement between 3.5 s and 4.5 s, corresponding to frequencies from 3 Hz to 6 Hz, reaches its maximal stroke limit. For modern seismic vibrator control electronics, a limit control is embedded to prevent the vibrator reaction mass from reaching its maximal displacement limitation.

However, the vibrator oil flow or pump flow—a limitation of the vibrator hydraulic system—is not measured, as there is no flow sensor installed on seismic vibrators. Therefore, the status of the vibrator oil flow becomes a "black box." The vibrator flow status across the entire sweep bandwidth remains unknown, particularly in the low-frequency range. System reliability and complexity prevent the installation of flow sensors. Nonetheless, during a sweep, it is essential to understand how to obtain vibrator oil flow information. Thus, it is important to investigate the theoretical behavior of vibrator flow and develop a method to estimate the vibrator oil flow.

### 2.4. Theory: Total flow going to the reaction mass chamber

As shown in Figure 2, when the flow is output from the main-stage servo-valve, it goes to the reaction mass chamber (e.g., upper chamber). The vibrator oil flow in the reaction mass chamber follows the governing equation:

$$Q = V_{rm} A_p \tag{3}$$

Where $Q$ denotes the total flow going to the reaction mass chamber; $V_{rm}$ represents the reaction mass velocity—a relative velocity between the reaction mass and the baseplate; $A_p$ is the piston area in the reaction mass chambers.

Based on **Equation 3**, the vibrator oil flow can be estimated using the relative velocity of the reaction mass and the baseplate. The reaction mass and baseplate accelerations are measured in real-time for every vibrator sweep in field production. Hence, the relative velocity can be obtained by integrating the measured accelerations.

Figure 5A displays the measured reaction-mass and baseplate accelerations, where an AHV-IV 362 (60,000-lbf) vibrator performs a linear sweep from 1 to 21 Hz over a duration of 10 s, with a 1-s long cosine taper at the front end of the sweep on regular soil. This vibrator is equipped with two P7 pumps, and the maximal flow delivered by the two pumps is 167 gallons/min.

To evaluate the accuracy of the estimation algorithms, two accelerations are recorded with a sampling time interval of 0.25 ms, corresponding to a sampling frequency of 4,000 Hz. To obtain the relative velocity of the reaction mass, the accelerations are preprocessed to remove direct-current offsets, followed by application of a low-bandpass filter. Two acceleration curves shown in Figure 5A have had their direct-current offsets and high-frequency noise removed.

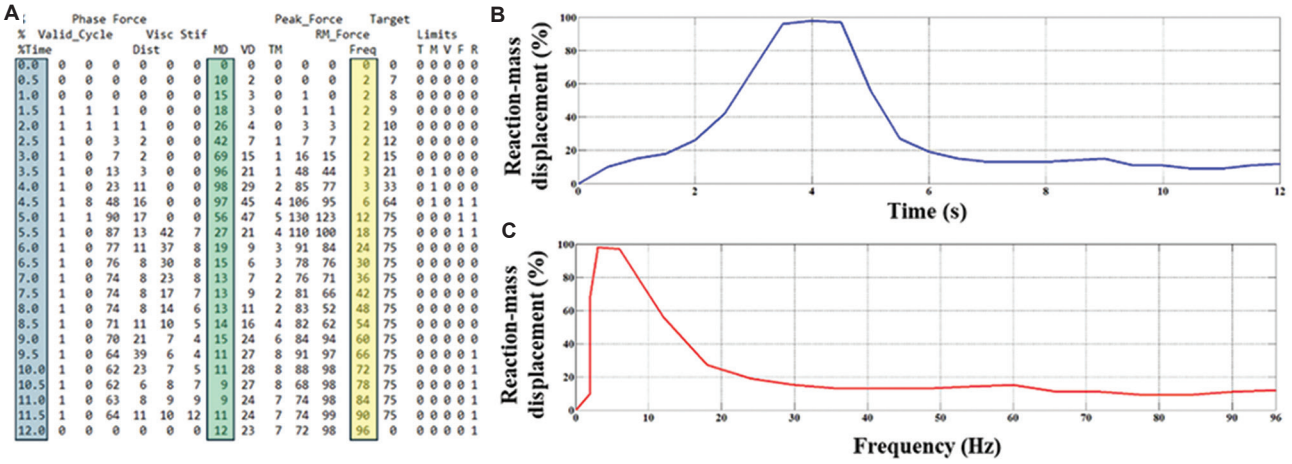


**Figure 4.** Reaction-mass displacement quality control. (A) Extended vibrator quality control data, with the blue bar indicating the sweep time series at 500 ms intervals, the yellow bar representing the corresponding frequencies of the first column, and the green bar showing the reaction-mass displacement during the sweep. (B) Reaction-mass displacement quality control data in the time domain. (C) Reaction-mass displacement quality control data in the frequency domain.

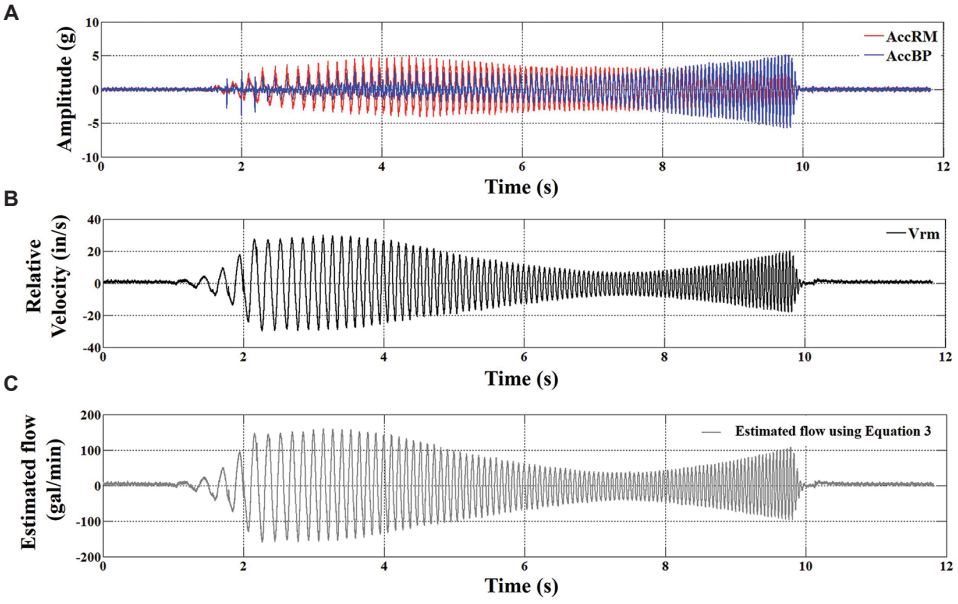


**Figure 5.** Signal display of (A) measured reaction-mass and baseplate accelerations on an AHV-IV 362 vibrator; (B) calculated reaction-mass velocity; and (C) estimated vibrator oil flow using **Equation 3**

After preprocessing, an integration operation is applied to both the reaction mass and baseplate acceleration. As a result, the relative velocity between the reaction mass and the baseplate is computed (Figure 5B). Finally, the vibrator oil flow is estimated using **Equation 3** and is plotted (Figure 5C).

It can be observed that the estimated vibrator oil flow remains at approximately 150 gallons/min between 2s and 4s, corresponding to the frequency range from 5 Hz to 9 Hz. During this time interval, the vibrator oil flow closely approaches the vibrator flow limitation of 167 gallons/min. In other words, the estimated vibrator flow curve indicates that the vibrator oil flow reaches approximately 90% of the hydraulic system's maximum flow capacity. This curve serves as an indicator and suggests that the vibrator hydraulic system components may be operating under potentially harmful vibration conditions. At this point, the question becomes, "How do we know whether the estimation using **Equation 3** is reasonable?" In practice, direct flow measurement is not available because flow sensors are not installed on the seismic vibrator, due to system complexity and extensive hardware modifications required for installation. Consequently, direct flow measurement is unrealistic in real vibroseis acquisition. Nevertheless, an alternative method based on the main-stage servo-valve can be used to calculate the vibrator oil flow. This method is presented in this study as an indirect validation of the estimation approach derived from **Equation 3**.

## 3. Solution and verification

### 3.1. Main-stage servo-valve total flow verification

As illustrated in Figure 2, the vibrator oil flow going to the reaction-mass upper chamber is equivalent to the flow output from the main-stage servo-valve. A modern seismic vibrator actuator is driven by a hydraulic servo-valve assembly consisting of a Moog 760-928A pilot servo-valve and an Atlas 240H main-stage servo-valve. When supported by vibrator control electronics (e.g., Vib Pro HD controllers), an optional Pelton DR-valve can be installed between the pilot servo-valve and the main-stage servo-valve.

Figure 6 shows an example of a servo-valve assembly mounted on a modern seismic vibrator. The main-stage servo-valve, specifically the Atlas 240H, alternately outputs oil flow to drive the seismic vibrator actuator. The governing equation for the servo-valve flow is expressed in **Equation 4**. Merritt[25] is a valuable source, offering comprehensive knowledge and a thorough treatment of servo-valve technology.[25] The governing equation is as follows:

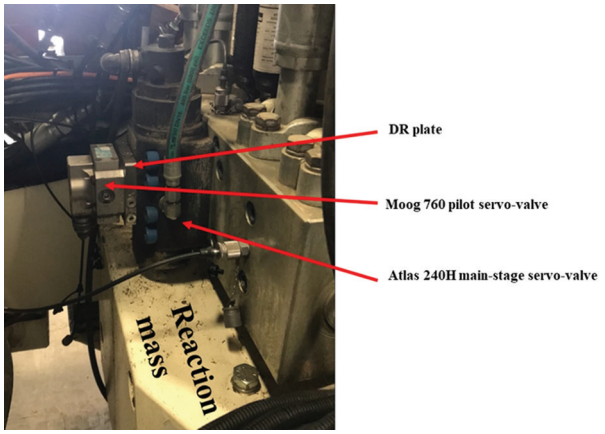


**Figure 6.** Servo-valve assembly installed on a modern seismic vibrator

$$Q = Kx_v\sqrt{P_s - \frac{x_v}{|x_v|}P_d} \quad \text{(IV)}$$

Where:

(i) $Q$ denotes the total flow output from the main-stage servo-valve control ports A and B ($in^3/s$).

(ii) $K$ is the flow–pressure coefficient ($in^2/s/\sqrt{psi}$).

(iii) $x_v$ represents the displacement of the main-stage servo-valve (in).

(iv) $P_s$ is the supply pressure to the main-stage servo-valve (psi).

(v) $P_d$ represents the differential pressure across control ports A and B of the main-stage servo-valve (psi).

The supply pressure is equivalent to the system high pressure minus the system return pressure. Typically, the system high pressure is set at 3,250 psi, and the system return pressure is set at 250 psi. Thus, the supply pressure is 3,000 psi. The hydraulic oil flow is delivered through the main-stage servo-valve control ports, resulting in a differential pressure across control ports A and B on the main-stage servo-valve. This differential pressure theoretically corresponds to the differential pressure across the piston in the reaction-mass chamber. By controlling the displacement of the main-stage servo-valve spool, the differential pressure across the piston can therefore be controlled.

Based on **Equation 4**, the oil flow from the main-stage servo-valve, $Q$, can be estimated if the supply pressure, the displacement of the main-stage servo-valve, and the differential pressure across the piston in the reaction-mass chamber are known. To estimate the vibrator flow using **Equation 4**, four pressure sensors were installed on the main-stage servo-valve of the AHV-IV 362 vibrator to measure the system high pressure, system return pressure, and the differential pressure at control A and B,

respectively. During the tests, a Vib Pro controller drove the vibrator with a linear sweep from 1 to 21 Hz over 10 s at a 70% force level (42,000 lbs). The sweep rate was 2 Hz/s, the start taper was 1 s, and the end taper was 0.2 s.

Figure 7 illustrates the supply pressure measurements, illustrating the system high pressure and system return pressure. In general, the high pressure remains around 3,250 psi, and the return pressure remains at 250 psi. Pressure ripples or spikes are observed on the high- and return-pressure signals.

The pressure fluctuation is more pronounced in the supply pressure. Figure 8 presents the differential pressure measurements, illustrating the pressures measured at control ports A and B. The differential pressure was calculated as the pressure measured at control port A minus the pressure measured at control port B. Since the main-stage servo-valve is equipped with an LVDT transducer to measure its displacement for servo-valve feedback position control, the displacement of the main-stage servo-valve was measured and recorded by the vibrator controller in real time. Figure 9 displays the measured displacement of the main-stage servo-valve during this sweep.

By incorporating all measurements into **Equation 4**, where the flow-pressure coefficient (K) was set to 292, the total vibrator oil flow was estimated for this sweep.

Figure 10A illustrates the estimated flow responses using **Equations 3** and **4**. In general, it can be seen that the flow curves show a strong similarity. To better demonstrate the similarity between the two flow curves, a similarity line was constructed using the $x$–$y$ coordinates and is

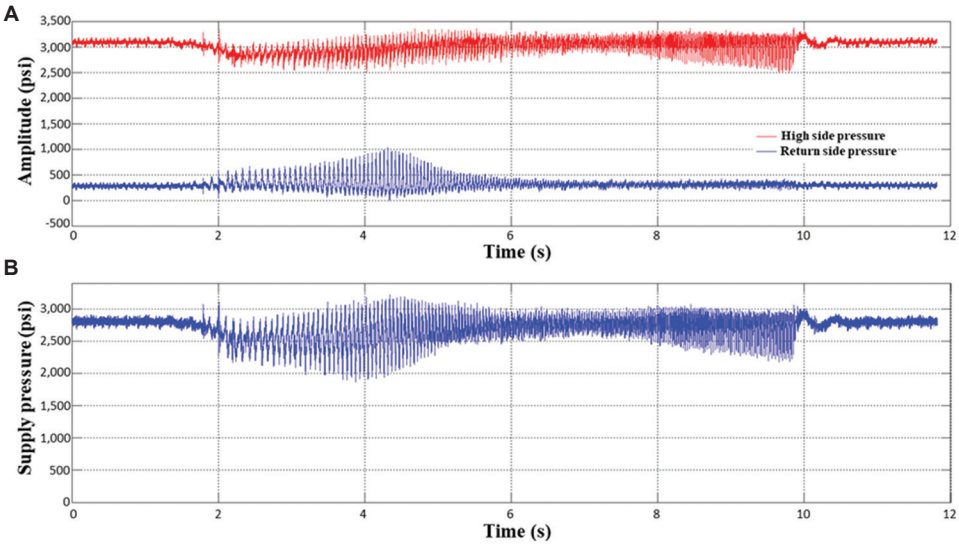


**Figure 7.** Measured system high pressure and system return pressure on an AHV-IV 362 vibrator

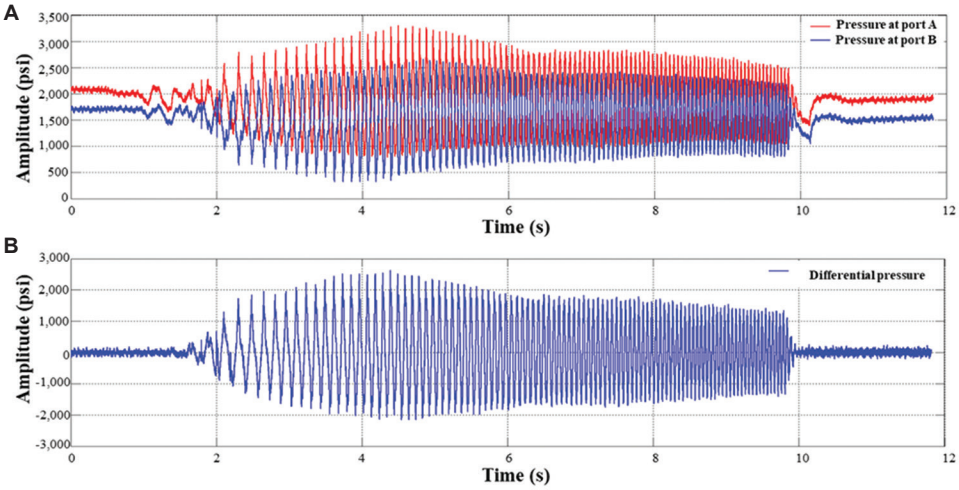


**Figure 8.** Measured differential pressure at control ports A and B on an AHV-IV 362 vibrator

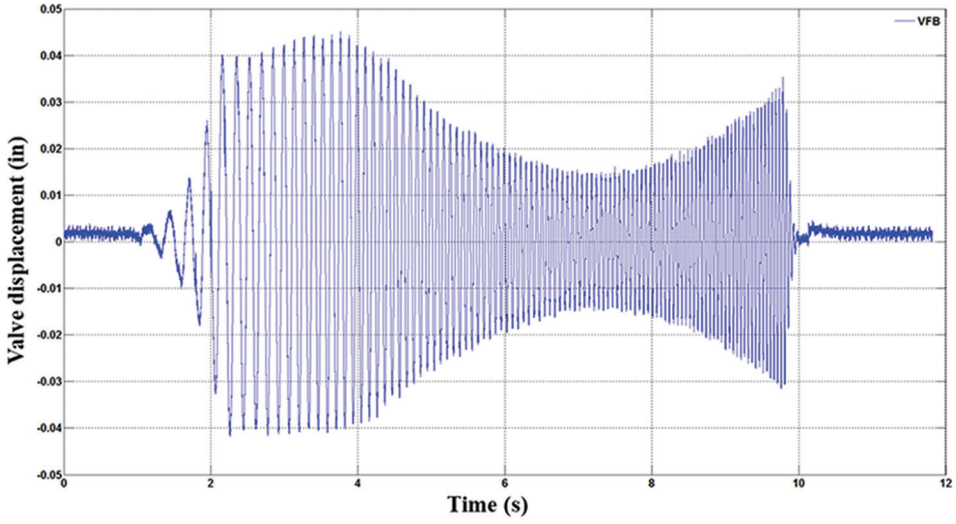


**Figure 9.** Measured displacement of the Atlas 240 H main-stage servo-valve on an AHV-IV 362 vibrator
Abbreviations: VFB: Valve feedback.

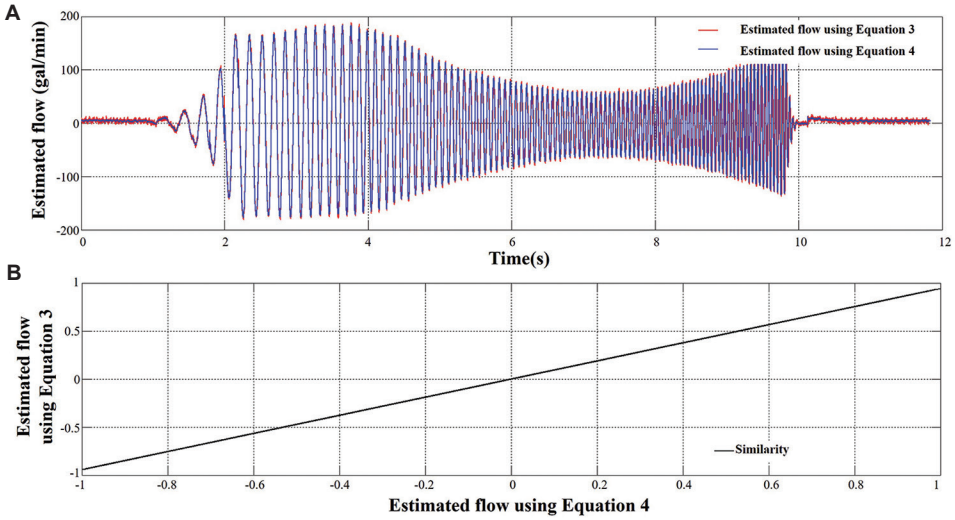


**Figure 10.** Estimated (A) vibrator oil flow and (B) comparison of flow similarity using **Equations 3** and **4**

shown in Figure 10B. The flow samples estimated using **Equation 4** were assigned to the x-coordinate, while the flow samples estimated using **Equation 3** were assigned to the *y*-coordinate. Together, they form ordered pairs ($x$, $y$) that locate points on a coordinate plane.

Theoretically, if the similarity line appears as an oblique line, the data samples in the *x*-coordinate are in-phase with those in the *y*-coordinate, and the two datasets are similar. If the similarity line has a 45° inclination, the data samples in the *x*-coordinate match perfectly with those in the *y*-coordinate in both amplitude and phase.

Figure 10B shows a very strong similarity between the flow curves estimated using **Equations 3** and **4**, although a slight amplitude difference is observed. This amplitude discrepancy is clearly visible near the ordered pairs of (1, 1) and (−1, −1) and is approximately 5%. **Equation 4** provides a method to estimate the vibrator oil flow for any sweep; however, this estimation requires multiple measurements that cannot be obtained during field production. In vibroseis acquisition operations, no pressure sensors are installed; therefore, the supply pressure and the differential pressure are not measured.

In summary, for the estimation of the vibrator oil flow, the two estimation methods based on **Equations 3** and **4** produce highly similar flow curves. This similarity implies that both estimation methods provide reasonable estimates

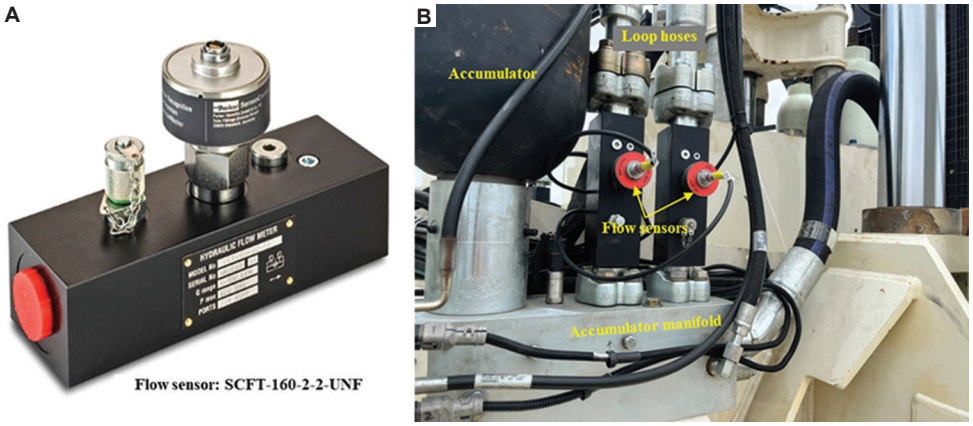


**Figure 11.** Flow sensor used in the experimental test: (A) sensor model and (B) installation of the flow sensors on the vibrator

of the vibrator oil flow. The two approaches cross-validate each other, demonstrating that each is capable of producing a valid flow estimation.

Based on Figure 10A, the estimated flow approaches the pump maximum capacity of 167 gallons/min between 2 s and 4 s, corresponding to the frequency range from 5 Hz to 9 Hz. Outside this frequency range, the flow demand decreases as the vibrator operates.

For vibrator QC, during the reference or pilot sweep, the reaction mass and baseplate accelerations were measured and recorded for each vibrator sweep. Therefore, the oil-flow estimation method using **Equation 3** is practical for field QC, and its estimated result, as shown in Figure 10, is considered reliable.

### 3.2. Additional tests for flow estimation verification

To further test the validity of the flow estimation using **Equation 3**, a field test was performed on a vibrator in the Middle East desert. In this test, two flow sensors were successfully installed on the accumulator manifold, enabling direct measurement of the vibrator oil flow.

Figure 11 illustrates the flow sensor model (Figure 11A) used in the experimental test and its installation on the vibrator (Figure 11B). This type of flow sensor can measure flows of up to 160 gallons/min with minimal flow resistance. One side of the flow sensors was installed on the accumulator manifold, and the other side was connected to the loop hoses leading directly to the main-stage servo-valve.

The vibrator performed a linear sweep from 1 Hz to 11 Hz in 20 s at 70% force level, with the sweep frequency increasing linearly at a slow sweep rate of 0.5 Hz/s. This slow sweep rate allowed the vibrator to operate in a steady state, enabling accurate measurement of the vibrator oil flow at low frequencies.

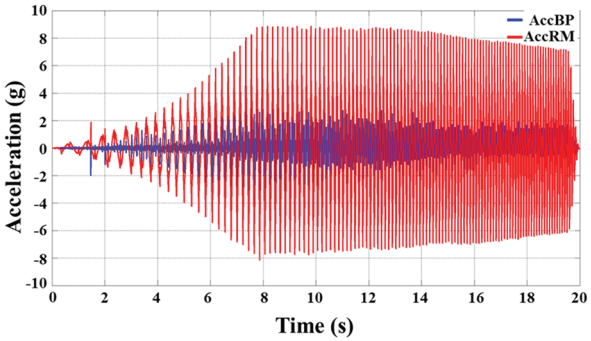


**Figure 12.** Measured reaction-mass (AccRM) and baseplate (AccBP) accelerations of the vibrator
Abbreviations: AccBP: Accelerations of baseplate; AccRM: Accelerations of reaction mass.

Figure 12 displays a set of measured accelerations of the reaction mass and baseplate. From this set of accelerations, the relative velocity was obtained through an integration operation. Then, the estimated flow was calculated using **Equation 3**. The estimated flow forms a sinusoidal waveform, which is very similar to what is shown in Figure 10A.

For better comparison, a processing algorithm was applied to extract the maximal envelope of the estimated flow. This maximal envelope of the estimated vibrator oil flow is illustrated in Figure 13. For comparison, the measured vibrator oil flow, as shown in Figure 13, was obtained from the raw measured data and smoothed to remove high-frequency spiky noise. In general, the estimated vibrator flow using **Equation 3** agrees well with the measured vibrator flow, although some discrepancies remain.

The estimated flow curve reaches its peak value of 152 gallons/min at 7.9 s, corresponding to a frequency of 5 Hz, while the measured flow reaches its peak value of

155 gallons/min at 8.5 s, corresponding to a frequency of 5.25 Hz. Figure 13 demonstrates that **Equation 3** can be used to estimate the actual vibrator oil flow.

To demonstrate the generalizability of these findings, the estimated flow method based on **Equation 3** was applied in production, where the vibrator operated on the sandy ground surface. This ground surface is a mixture of loose sand and gravel, and it is poorly consolidated. Figure 14 shows an example illustrating the production use of the estimated method based on **Equation 3**. In this case, a low-dwell sweep from 1.5 Hz to 96 Hz in 12 s was applied to shake the AHV-IV 364 vibrator.

Figure 14A illustrates the vibrator ground force, Figure 14B shows the accelerations of the reaction mass and baseplate, and Figure 14C shows the vibrator oil flow estimated using **Equation 3**. It can be observed that the estimated vibrator oil flow is severely asymmetrical.

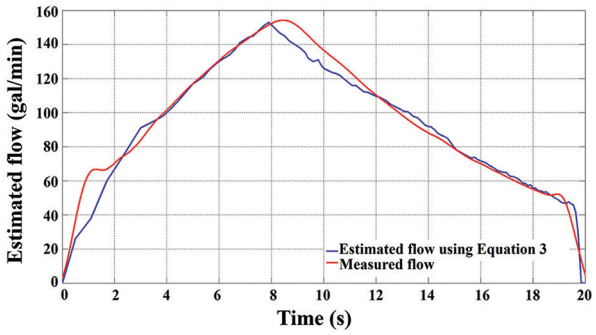


**Figure 13.** Comparison of estimated and measured vibrator oil flow

Between 4 s and 5 s, corresponding to a frequency range from 5 Hz to 7 Hz, the vibrator flow reaches its maximum with a peak-to-peak value of 250 gallons/min. This indicates that the average flow usage is 125 gallons/min, lower than the maximal pump flow limit of 164 gallons/min.

The estimated vibrator flow curve in Figure 14 provides a QC indication that this low-dwell sweep is compatible with the vibrator hydraulic system, and the vibrator hydraulic system components remain within a safe range. This gentle usage of vibrator oil flow results in no spiky noise in the vibrator ground force, especially at approximately 5 s, when the sweep amplitude changes from the non-linear portion (<5 s) to the linear portion (>5 s), as shown in Figure 14A. With such smooth low-frequency force, less noisy seismic records (Figure 15) are obtained. In addition, the estimated vibrator oil flow can help evaluate the low-frequency sweep design, allowing an optimal low-frequency sweep to be achieved.

## 4. Discussion

The theoretical framework of this study addresses an unmet need in low-frequency seismic vibrator performance monitoring by proposing methods to estimate vibrator oil flow, which is crucial for QC in seismic data acquisition. The validation of these methods through experimental tests on an AHV-IV 362 vibrator demonstrates good agreement with measurements. The consistency between the estimated and measured oil flows confirms the validity of the theoretical model, highlighting its potential for practical application. This

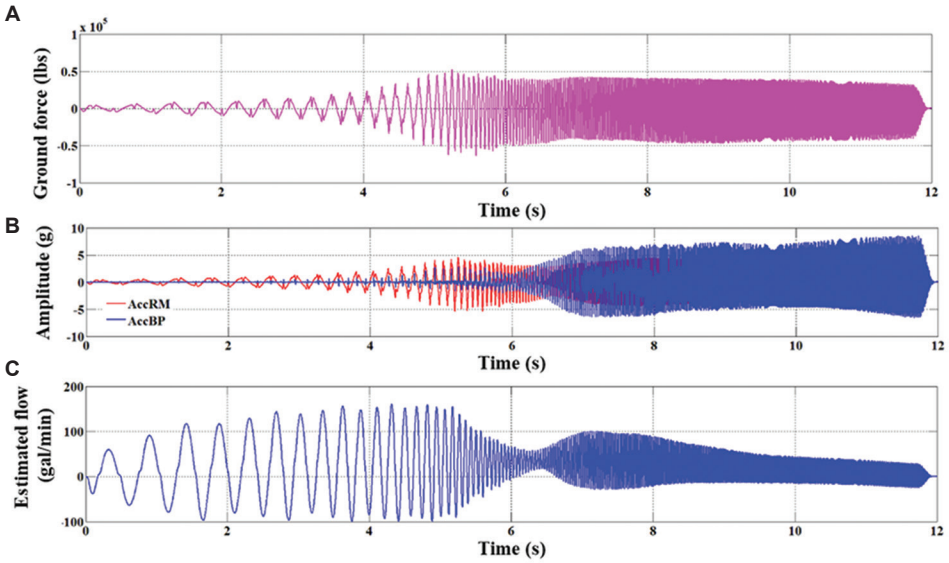


**Figure 14.** Estimated vibrator oil flow on an AHV-IV 364 vibrator. (A) Vibrator ground force. (B) The accelerations of the reaction mass (AccRM) and baseplate (AccBP). (C) Estimated vibrator oil flow.
Abbreviations: AccBP: Accelerations of baseplate; AccRM: Accelerations of reaction mass.

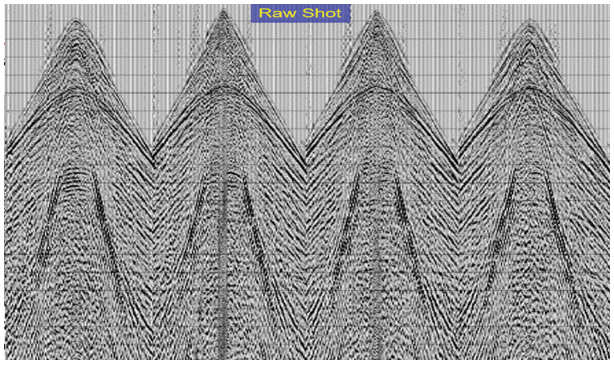


**Figure 15.** Normal shot records

validation is further supported by tests on an AHV-IV 364 vibrator, reinforcing the methods' robustness across different vibrator models.

Although some discrepancies remain between the two sets of results, they exhibit high consistency, and the level of precision is sufficient to meet production requirements. This demonstrates that the proposed method is theoretically sound and practically feasible. However, it is important to acknowledge certain limitations, such as reliance on sensor accuracy and assumptions embedded in the model. Further refinement and validation under more diverse conditions should be conducted to enhance the robustness and generalizability of the method.

## 5. Conclusion

Low-frequency vibroseis acquisition has become a routine practice in land seismic operations. At low frequencies, the limitations of vibrator mechanical and hydraulic systems on ground force output are well recognized. During a vibrator low-dwell sweeping, the travel distance of the reaction mass is recorded and monitored. The reaction mass displacement is incorporated into vibrator QC. However, the vibrator oil flow is not measured and, therefore, is not included in vibrator QC. The methods presented in this paper provide an estimation of the vibrator oil flow, enabling real-time QC of the vibrator oil flow. Major failures in vibrator hydraulic system components, such as pilot servo-valves, can be avoided, thereby maintaining high acquisition productivity. Furthermore, the estimated vibrator oil flow can help derive a more practical vibrator force profile at low frequencies, thereby optimizing the low dwell sweep design.

## Acknowledgments

We thank BGP for providing the seismic data used in this study and granting permission for the data to be published.

## Funding

This study was financially supported by the science and technology project "Research on Multi-physical Field High-Precision Oil and Gas Geophysical Exploration Technology and Equipment" (No.2023ZZ05) of the China National Petroleum Corporation, titled *Theory, Key Technologies,* and *Core Equipment of Full Wave Field Seismic Acquisition*.

## Conflict of interest

The authors declare that they have no competing interests.

## Author contributions

*Conceptualization:* Mingtao Nie, Zhouhong Wei
*Formal analysis:* Mingtao Nie, Zhouhong Wei, Yang Liu
*Funding acquisition:* Mingtao Nie,Yongfei Qi
*Investigation:* Tao Fang, Xiaolong Jiang, Yongan Xu
*Methodology:* Mingtao Nie, Zhouhong Wei
*Validation:* Zhouhong Wei, Yang Liu
*Writing–original draft:* Mingtao Nie, Zhouhong Wei, Yongfei Qi
*Writing–review* and *editing:* All authors

## Availability of data

All data analyzed are presented in the paper.

## References

1. Rozemond HJ. Slip-Sweep Acquisition. In: *66th Annual International Meeting*. SEG Expanded Abstracts; 1996. p. 64-67.

   doi: 10.1190/1.1826730

2. Allen KP, Johnson ML, May JS. High Fidelity Vibratory Seismic (HFVS) Method for Acquiring Seismic Data. In: *68th Annual International Meeting*. SEG Expanded Abstracts; 1998. p. 140-143.

   doi: 10.1190/1.1820171

3. Bouska J. *Distance Separated Simultaneous Sweeping: The World's Fastest Vibroseis Technique. EAGE Vibroseis Workshop*. Prague, Czech Republic, Extended Abstract; 2008. p. 15983.

4. Howe D, Foster M, Allen A, Jack I, Taylor B. Independent Simultaneous Sources: A Method to Increase Productivity of Land Seismic Crews. In: *78th Annual International Meeting*. SEG Expanded Abstracts; 2008. p. 2826-2830.

5. Wei Z. Design of a P-wave seismic vibrator with advanced performance. *GeoArabia*. 2008;13:123-136.

   doi: 10.2113/geoarabia1302123

6. Wei Z, Hall MA, Phillips TF. Geophysical benefits from an improved seismic vibrator. *Geophys Prospect*. 2012;60:466-479.

doi: 10.1111/j.1365-2478.2011.01008.x

7. Wei Z, Criss J, Wang R, Clow A. A new generation low-frequency seismic vibrator. *Geophysics*. 2022;87(4):P29-P38.

   doi: 10.1190/geo2022-0010.1

8. Peng X, Sun J, Li Y, Teng Z, Hao L. Modeling and analysis of a shear-wave vibrator-ground coupled system dynamics. *Int J Mech Sci*. 2025;289:110064.

   doi: 10.1016/j.ijmecsci.2025.110064

9. Rowse SL, Heath B. The vibrator and its interaction with the ground. *First Break*. 2025;43(1):75-81.

   doi: 10.3997/1365-2397.fb2025007

10. Robin A, Secker S. Source Motion Corrections for Marine Vibrator Data: Who's Who and What They're Not. In: *86th EAGE Annual Conference* and *Exhibition*. Vol. 1. European Association of Geoscientists and Engineers; 2025. p. 1-5.

11. Xiao Y. Nonlinear sweeping signal design of vibrator based on spectral characteristics. *Progress in Geophysics*. 2021;36(1):300-309. [Article in Chinese].

    doi: 10.6038/pg2021ee0127

12. Wei T, Zhu Y, Liu Z,Wang D, Wei G, Nie M. Design of Low Frequency Sweep Signals for Conventional Vibrators. In: *SEG International Exposition* and *Annual Meeting*. SEG; 2024. p. 4090586.

    doi: 10.1190/image2024-4090586.1

13. Qi YF, Wei ZH, Nie MT, *et al*. Low-frequency sweep design-a case study in middle east desert environments. *Appl Geophys*. 2024;22(1):71-83.

    doi: 10.1007/s11770-024-1126-3

14. Liu Y, Wen X, Li B, An Z, Wu D. Designing nonlinear sweep signal to improve the resolution of vibroseis acquisition. *Geophysics*. 2025;90(5):P73-P86.

    doi: 10.1190/geo2024-0490.1

15. Sallas JJ. How do hydraulic vibrators work? A look inside the black box. *Geophys Prospect*. 2010;58(1):3-18.

    doi: 10.1111/j.1365-2478.2009.00837.x

16. Sallas JJ. Seismic vibrator control and the downgoing P-wave. *Geophysics*. 1984;49:732-740.

    doi: 10.1190/1.1441701

17. Mahrooqi S, Rawahi S, Yarubi S, *et al*. Land Seismic Low Frequencies: Acquisition, Processing and Full Wave Inversion of 1.5-86 Hz. In: *82nd Annual International Meeting*, *SEG Exp*and*ed Abstracts*; 2012.

    doi: 10.1190/segam2012-0961.1

18. Wei Z. Pushing the vibrator ground-force envelope towards low frequencies. *Geophys Prospect*. 2009;57(1):151-161.

    doi: 10.1111/j.1365- 2478.2008.00738.x

19. Wei Z. A new generation low frequency seismic vibrator. In: *85th Annual International Meeting*. SEG Expanded Abstracts; 2015. p. 211-215.

    doi: 10.1190/segam2015-5713173.1

20. Wei Z, Criss J, Bull A, Liang F, Wu Y. The low-frequency seismic vibrator: Design and experimental verification. *First Break*. 2018;36(1):77-84.

    doi: 10.3997/1365-2397.n0066

21. Bagaini C, Dean T, Quigley J, Tite G, Inventors. Westerngeco LLC, Assignee. *Systems and Methods for Enhancing Low-Frequency Content in Vibroseis Acquisition*. US Patent US 7,327,633 B2. 2008.

22. Phillips TF, Wei Z, Inventors. INOVA LTD., Assignee. *Seismic Frequency Sweep Enhancement*. US Patent US 9,121,961 B2. 2015.

23. Sallas JJ, Inventors. CGG VERITAS, Assignee. *System and Method for Determining a Frequency Sweep for Seismic Analysis.* US Patent US 9,535,178 B2. 2017.

24. Dellinger JA, Harper M, Inventors. BP Corporation North America Inc., Assignee. Harper M. *System and Method for Performing Seismic Surveys with a Controlled Source using Maximum-Power Sweeps* . US Patent US 9,702,991 B2. 2017.

25. Merritt HE. *Hydraulic Control Systems*. United States: John Wiley and Sons, Inc.; 1967.

ACCSCIENCE PUBLISHING

Journal of Seismic Exploration

ARTICLE

# Fault identification and enhancement using residual U-Net: Application to field seismic data

**Jianhua Wang[1]*, Cong Niu[1], Yandong Wang[1], Yun Ling[1], Di Wang[1], Xiuping Jiang[2,3,4], and Chenshuo Yuan[2]**

[1]CNOOC Research Institute Co., Ltd., Beijing, China

[2]College of Marine Geo-sciences, Ocean University of China, Qingdao, Shandong, China

[3]Qingdao National Laboratory for Marine Science and Technology, Qingdao, Shandong, China

[4]Key Laboratory of Submarine Geosciences and Prospecting Techniques, Ministry of Education, Ocean University of China, Qingdao, Shandong, China

## Abstract

Fault identification is a critical step in seismic data interpretation. Traditional fault identification methods rely heavily on manual interpretation, which is inefficient and significantly influenced by subjective factors. This paper proposes a fault identification algorithm based on a Residual U-Net–curvelet hybrid framework. By introducing residual learning strategies and applying batch normalization and skip connection techniques, the generalization ability and convergence speed of the network are enhanced, thereby improving the accuracy and efficiency of fault identification. Results from field data processing demonstrate that this method achieves high identification accuracy under complex geological structures and low signal-to-noise ratio conditions, providing reliable fault identification results for efficient seismic data interpretation.

***Keywords:*** Fault identification and enhancement; Deep learning; Residual U-Net; Random noise suppression

***Corresponding author:**
Jianhua Wang
(wangjh7@cnooc.com.cn)

**Citation:** Wang J, Niu C, Wang Y, *et al.* Fault identification and enhancement using residual U-Net: Application to field seismic data. *JSeismicExplor.*2026;35(1):184-199. doi: 10.36922/JSE025360067

**Received:** September 3, 2025

**1st revised:** November 6, 2025

**2nd revised:** November 17, 2025

**Accepted:** November 27, 2025

**Published online:** January 20, 2026

**Copyright:** © 2026 Author(s). This is an Open-Access article distributed under the terms of the Creative Commons Attribution License, permitting distribution, and reproduction in any medium, provided the original work is properly cited.

**Publisher's Note:** AccScience Publishing remains neutral with regard to jurisdictional claims in published maps and institutional affiliations.

## 1. Introduction

Fault identification is a critical aspect of seismic data interpretation, particularly in oil and gas exploration and development. Accurate fault identification holds significant importance for structural interpretation, reservoir prediction, and analysis of hydrocarbon migration pathways.

However, traditional fault identification methods rely heavily on the experience of interpreters and use seismic attributes or structural features for recognition, which are labor-intensive, highly subjective, and sensitive to noise. These limitations make it difficult to meet the demands of detailed interpretation, particularly in complex geological settings or in seismic data with low signal-to-noise ratios (SNR), where the ability to identify small faults is often inadequate. Therefore, achieving automated, rapid, and high-precision fault identification has become an urgent research problem.

With the advancement of seismic-attribute technology, fault-identification methods include attribute-based classifiers, such as coherence cubes,[1,2] variance cubes,[3] curvature

attributes,[4,5] the C3-coherence technique,[2] and fault-likelihood measures;[6,7] fault-enhancement approaches, such as ant tracking,[8] structure-oriented filtering,[9] and optimal surface voting;[10] as well as hybrid workflows that combine variance cubes with high-definition ant tracking. However, these approaches are highly dependent on data quality: While they can be effective in shallow sections, their performance degrades for deep, low-quality seismic data and in structurally complex or heavily faulted areas, where inferred fault continuity is poor, and the solutions are strongly non-unique, often diminishing their interpretational value.

In recent years, with the rapid development of artificial intelligence (AI) technology, the application of AI to achieve automatic, fast, and accurate fault identification—overcoming the subjective influence of manual interpretation—has gradually become an important research direction in the field of oil and gas geophysical exploration and development.

Early studies primarily adopted relatively simple architectures, such as AlexNet and VGGNet,[11] but their accuracy in fault identification was limited. Later, researchers introduced residual network (ResNet)-based models[12]—by leveraging residual learning to mitigate deep-network degradation and vanishing gradients, these models improved fault-detection accuracy. Nevertheless, such approaches are constrained by fixed input-size requirements and a bias toward local feature extraction, resulting in poorer performance for small-scale faults. Wu *et al.*[13] employed a convolutional neural network for fault identification and subsequently constructed anisotropic Gaussian functions to estimate the fracture dip and azimuthal extent. However, because the model is trained on local image patches and extracts features only within small-scale neighborhoods, its computational efficiency is significantly limited.

Fully convolutional neural networks achieved the first end-to-end breakthrough in image recognition.[14] U-Net[15,16] introduced an architectural innovation that couples multi-scale feature extraction in the encoder with precise localization in a symmetric decoder and, via skip connections, enables cross-level fusion of shallow details and deep semantic features,[17] thereby markedly improving fault-identification accuracy. Moreover, integrating U-Net with ResNet to form residual U-Net (ResU-Net) increases network depth and further enhances fault-detection performance.[18] Unlike the classical U-Net—which adopts a symmetric encoder–decoder built from convolution–batch normalization–rectified linear unit (ReLU) stacks and conveys spatial details via skip connections—the residual U-Net introduces residual blocks within each stage. While preserving U-Net's original skip connections and precise localization capability, it significantly improves gradient flow and feature reuse, making the network easier to deepen and more stable to train. Consequently, it is more robust under low-SNR and complex structural settings: It converges faster, is more sensitive to weak/narrow faults, reduces false positives, and improves generalization and fault identification/detection accuracy.

To further reduce the subjectivity of manual fault identification and enhance the accuracy of identifying micro-faults, this study develops a fault detection model utilizing a ResU-Net architecture–curvelet hybrid framework, designed to learn the complex non-linear mapping between seismic amplitude data and fault probability distributions. In addition, fault information is enhanced using multi-scale component extraction and curvelet domain filtering techniques, thereby providing a solid foundation for subsequent interpretation and analysis.

## 2. Fault identification based on residual U-Net

### 2.1. Residual learning strategy for fault identification

By employing a residual U-Net, the sample space formed by fault-related seismic data is explored to construct a fault identification model that characterizes the mapping between seismic data and faults. In the fault identification task, the ResU-Net is trained with a hybrid loss function that combines cross-entropy and the Dice coefficient, and the evaluation metric is identification accuracy.

Compared to traditional fault-identification methods based on the U-Net convolutional neural network, the ResU-Net-based method not only adopts a different network architecture but also incorporates an improved loss function. The mathematical expression of the combined loss function is as follows:

$$\mathrm{Dice} = \frac{2\times\sum y\times\hat{y}}{\sum y+\sum\hat{y}} \tag{1}$$

$$\hat{L} = -\frac{1}{2}\left[y\log\hat{y} + (1-y)\log(1-\hat{y})\right] - \mathrm{Dice} \tag{2}$$

Where $\hat{L}$ represents the combined loss function, $y$ denotes the fault labels of the true data, and $\hat{y}$ represents the predicted faults.

From a theoretical standpoint, the hybrid loss (cross-entropy/binary cross-entropy [BCE] + Dice coefficient) combines probability calibration with set-overlap optimization. BCE treats segmentation as per-pixel

log-likelihood maximization, yielding well-calibrated probabilities and sharp boundaries; because the Dice coefficient is normalized by the sizes of the foreground and the prediction, it is inherently robust to the class imbalance between thin fault traces and the vast background. Adding BCE provides stable, non-vanishing gradients in the early stage of training (when predictions are near zero) and helps prevent foreground over-expansion, thereby improving the precision–recall trade-off. In addition, in the ResU-Net-based fault-identification method, the neural network uses a sigmoid activation at the output layer and ReLU activations in the hidden layers.

### 2.2. Architecture of residual U-Net

This study employed the U-Net main structure, combined with batch normalization and residual learning concepts, to construct the ResU-Net, as shown in Figure 1. The network consists of four layers of upsampling and four layers of downsampling, each containing convolutional operations and batch normalization layers. The specific structural parameters vary slightly at different depths of the network. Each convolutional layer is immediately followed by batch normalization to optimize network performance and accelerate convergence. To maintain dimensional consistency between input and output tensors throughout the architecture, zero-padding is implemented in each convolutional layer to ensure that the input and output data dimensions remain the same.

The ResU-Net implements the residual learning strategy by adding an identity mapping (shown as "identity mapping" in Figure 1) between the input and output layers. In addition, to ensure rapid network convergence and avoid potential numerical issues, amplitude normalization is applied, scaling the seismic record amplitudes to the range [0, 1]. Consequently, the output layer of the neural network employs the sigmoid activation function, whose value range is [0, 1], with its mathematical expression provided in **Equation 3**. Furthermore, we applied a morphological dilation algorithm when creating the fault labels to make the fault locations more prominent, thereby improving the neural network's training efficiency. For the remaining layers, the ReLU activation function is used, and its mathematical expression is given in **Equation 4**. The loss function $\hat{L}$ of the ResU-Net is described in **Equation 2**, and the optimizer chosen is the adaptive gradient algorithm (Adagrad), which prevents oscillation during the later stages of training by adaptively reducing the learning rate.

$$S(x)=\frac{1}{1+e^{-x}} \tag{3}$$

$$R(x)=\begin{cases} x & x>0 \\ 0 & x\le 0 \end{cases} \tag{4}$$

In the ResU-Net structure, each upsampling or downsampling stage is treated as a separate module. Skip connections link encoder and decoder modules that share the same spatial resolution, enabling direct transfer of corresponding feature maps. By channeling input image characteristics directly into the upsampling pathway, this structure enables precise spatial information transfer across network levels, thereby aiding in information reconstruction and accelerating convergence speed. The residual connections bridging input and output layers fundamentally modify the network's optimization objective, transitioning the learning paradigm from direct label prediction to residual mapping. This architectural innovation significantly enhances model performance by

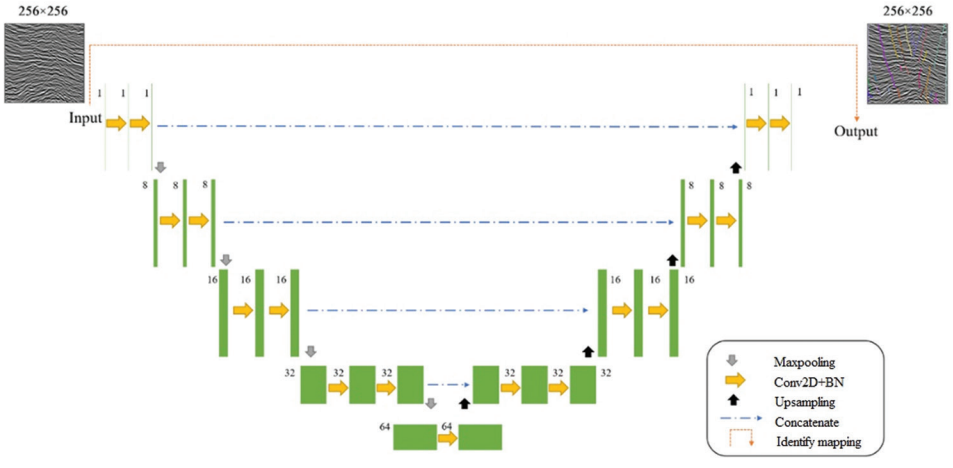


**Figure 1.** Residual U-Net structure
Abbreviations: BN: Batch normalization; Conv2D: 2D convolutional layer.

reducing the network's reliance on direct label fitting. As a result, the network captures more fault-related features, improving its generalization performance and mitigating overfitting.

We evaluated the computational complexity of the ResU-Net, as shown in Figure 1—input: 1 × 256 × 256; channel progression: 1→8→16→32→64→32→16→8; each stage uses a residual block with two 3×3 convolutions followed by batch normalization; the decoder adopts bilinear upsampling and concatenates with encoder features. Based on standard formulas, the model contains approximately 0.20 M parameters (including batch normalization), with FP32 weights requiring about 0.8 MB, and it requires approximately 0.69 GFLOPs per forward pass per sample. Training uses the Adagrad optimizer; the parameter-related memory footprint is approximately four times the weight size (including weights, gradients, and optimizer statistics), totaling approximately 3.2 MB. Under FP32 with a batch size of $B = 4$, activation maps dominate memory usage at 35 ivatB; when framework caches and intermediate tensors are included, the peak training memory typically reaches 50ach0 MB. Overall, complexity scales approximately as O(HW) with input resolution and grows roughly linearly with channel width and depth, while residual shortcuts and bilinear upsampling introduce only negligible additional overhead.

The ResU-Net deep neural network, whose core structure relies on skip connections between the encoder and decoder, utilizes cropped seismic profiles as inputs and their corresponding interpreted fault images as labels. During the training phase, the model parameters undergo optimization, yielding a pre-trained network that subsequently performs comprehensive fault detection across all seismic profiles. Subsequently, the fault images undergo vectorization processing, which involves extracting a list of fault points ($x_i$, $t_i$), describing the fault location information based on the amplitude values of the sample points in the image. Here, $i$ is the breakpoint index, $x_i$ and $t_i$ represent the spatial coordinates and travel time of the $i$-th breakpoint (where $1 \le i \le I$), and $I$ denotes the total number of fault points.

To clarify the configuration of the neural network, Table 1 presents the detailed parameter settings of the ResU-Net used in this study, including the kernel size, number of channels, stride, and activation function for each layer. The network consists of four downsampling and four upsampling modules, each comprising convolutional operations followed by batch normalization. Skip connections are incorporated between corresponding encoder and decoder layers to enhance the reconstruction capability of fault structures. To maintain consistent input and output dimensions, all convolutional layers adopt zero-padding (padding = "same"). In addition, residual connections are introduced to improve the stability and generalization ability of the model.

The process of fault identification based on the migrated data volume is described as follows: First, a ResU-Net deep neural network, as shown in Figure 1, is constructed, and a sample set is generated using the partial seismic profile and the corresponding interpreted fault image depicted in Figure 2, after which the neural network is trained. The number of training iterations was set to 5,000, and the Adagrad optimizer was used. A subset of 2,000 samples was randomly selected from the sample set and used for training. All experiments in this study were implemented using the PyTorch framework.

At this stage, the correlation between the predicted fault probabilities and the reference labels exceeds 80%, indicating effective fault identification with a compact network architecture and good computational efficiency. The correlation versus iteration curve is shown in Figure 3.

**Table 1. Network structure parameters**

| Module number | Kernel size | Convolution depth | Activation function | Normalization method | Skip connection | Up/downsampling | Image size |
|---|---|---|---|---|---|---|---|
| 1 | 3×3 | 1 | ReLU | BN | 9 | Downsampling | 256×256 |
| 2 | | 8 | ReLU | | 8 | Downsampling | 128×128 |
| 3 | | 16 | ReLU | | 7 | Downsampling | 64×64 |
| 4 | | 32 | ReLU | | 6 | Downsampling | 32×32 |
| 5 | | 64 | ReLU | | None | None | 16×16 |
| 6 | | 32 | ReLU | | 4 | Upsampling | 32×32 |
| 7 | | 16 | ReLU | | 3 | Upsampling | 64×64 |
| 8 | | 8 | ReLU | | 2 | Upsampling | 128×128 |
| 9 | | 1 | Sigmoid | | 1 | Upsampling | 256×256 |

Abbreviations: BN: Batch normalization; ReLU: Rectified linear unit.

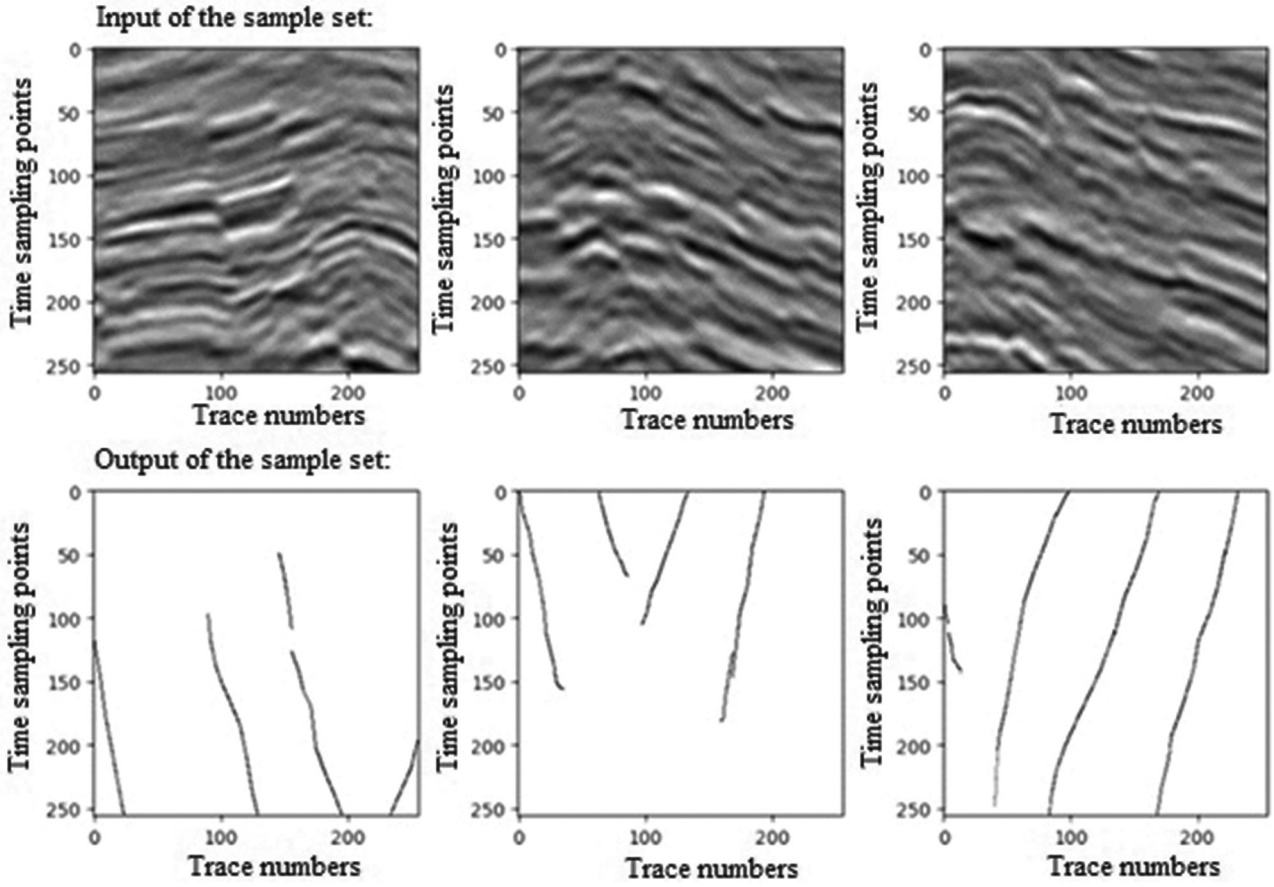


**Figure 2.** Example of input and output of the sample set for neural network training

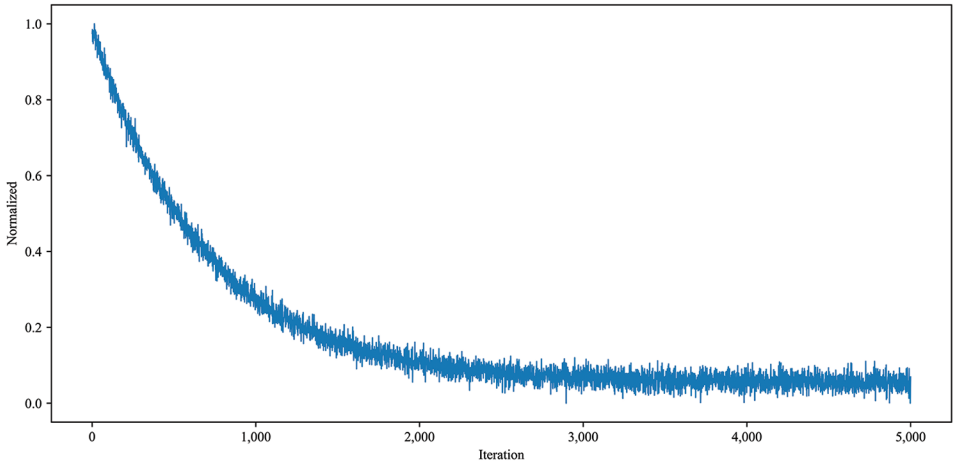


**Figure 3.** Correlation curve

## 3. Fault enhancement method based on multi-scale component extraction and filtering

During the acquisition process, seismic data are inevitably affected by factors, such as sensor sensitivity. The presence of noise and quantization errors during analog-to-digital conversion typically yields a diminished SNR. In seismic data processing, the limited spatial resolution of migration imaging methods and the difficulty of accurately positioning fault reflections often lead to "blurred fault points and

overlapping wavelets" in the migrated profiles. These issues significantly increase the difficulty of fault identification.

Directional filtering and edge-preserving filtering are commonly used techniques in image enhancement. The physical process involves smoothing the image using filters aligned with the local direction of the image, suppressing noise, and enhancing the continuity along the texture lines. The role of edge-preserving filtering is to protect the image edges during the filtering process, preventing edge information from becoming blurred due to filtering. These methods have been introduced into seismic data optimization, where directional filtering enhances the SNR and continuity of seismic wavelets. In addition, edge-preserving filtering preserves fault information, avoiding the blurring of faults caused by smoothing using data points on both sides of the fault. However, fundamentally, these methods belong to fault-preserving optimization techniques and cannot truly improve the imaging quality of fault structures. Therefore, they exhibit significant limitations in fault enhancement processing.

To address this issue, this study proposes a fault enhancement method based on multi-scale component extraction and filtering. The approach combines fault identification based on ResU-Net, calculation of fault enhancement filtering factors, and fault enhancement of multi-scale component data. It not only improves the accuracy of fault identification but also achieves high-precision fault enhancement processing for the imaging data volume, laying a solid foundation for subsequent interpretation and analysis.

### 3.1. Random noise suppression based on curvelet transform

The curvelet transform is composed of anisotropic curve-like basis elements, which can sparsely represent seismic data features. By applying thresholding to the coefficients in the curvelet domain, random noise can be effectively suppressed. This processing step significantly improves the SNR, making fault structures in the data more distinct. The curvelet transform is defined as the inner product between the seismic profile $s(x,t)$ and the curvelet function $\phi_{i,j,k}(x,t)$, and can be expressed as:

$$c(j,l,k)=\left\langle s,\varphi_{j,l,k}\right\rangle=\int_{x,t}s(x,t)\overline{\varphi_{j,l,k}(x,t)}dxdt \tag{5}$$

Where $\left\langle\cdot,\cdot\right\rangle$ represents the inner product, $\phi_{j,l,k}(x)$ denotes the curvelet basis function at scale $j$, direction $l$, and position $k$, and $c(j,l,k)$ represents the curvelet coefficients obtained from the curvelet transform.

Among the obtained curvelet coefficients $c(j,l,k)$, a small number of large-amplitude coefficients represent the effective signal, while the majority of smaller-value coefficients indicate noise interference. Therefore, by zeroing out the smaller-amplitude coefficients and transforming back to the time–space domain, noise suppression can be achieved. By comparing the coefficients point by point, the maximum value $c_{max}$ in $c(j,l,k)$ is obtained. Given a threshold parameter $\lambda$ (where $0<\lambda<c_{max}$), let:

$$c'(j,l,k)=\begin{cases}c(j,l,k), & |c(j,l,k)|\geq\lambda\\ 0, & |c(j,l,k)|<\lambda\end{cases} \tag{6}$$

Where $\lambda$ represents the threshold parameter.

To avoid damaging the effective signal, $\lambda$ is generally chosen within the range $\lambda\in[0.01c_{max},0.1c_{max}]$.

The curvelet transform is a reversible mathematical transformation. Using the curvelet coefficients $c'(j,l,k)$, the noise-eliminated profile data $s'(x,t)$ can be reconstructed, expressed as:

$$s'(x,t)=\sum_{j,l,k}c'(j,l,k)\varphi_{j,l,k}(x,t) \tag{7}$$

### 3.2. Fault information recovery in the migrated section

After attenuating random noise using the curvelet transform, fault information in the data is often compromised. To address this, it is necessary to restore the fault information based on the extracted breakpoint list $(x_i,t_i)$. Since faults are large-angle structures, an interpolation method along the x-direction is employed to ensure a natural transition in the processed results. Let the interpolation width be $\Delta x$; then, the weighting factor for restoring fault information can be calculated as:

$$f(x,t_i)=\begin{cases}\dfrac{1}{\Delta x}|x-x_i|, & |x-x_i|<\Delta x\\ 1, & |x-x_i|\geq\Delta x\end{cases} \tag{8}$$

Where $f(x,t_i)$ represents the weighting factor for fault information recovery.

The fault recovery result is obtained by performing a weighted summation of the filtered data and the original data using the weighting factor $f(x,t_i)$.

$$\tilde{s}(x,t_i)=s(x,t_i)\left[1-f(x,t_i)\right]+s'(x,t_i)f(x,t_i) \tag{9}$$

Where $\tilde{s}(x,t_i)$ represents the fault recovery result specifically for the breakpoint $(x_i,t_i)$. By applying the weighted processing of **Equation 9** to all fault points in the

breakpoint list $(x_i,t_i)$, the final fault recovery profile $\tilde{s}(x,t)$ is obtained.

### 3.3. Fault enhancement based on multi-scale components

Building on the multi-scale property of the curvelet transform, the profile data are further decomposed by scale. Let $\tilde{s}_n(x,t)$ denote the component obtained at scale $n$ by retaining the corresponding curvelet coefficients and performing the inverse transform based on **Equation 7**.

By setting the scale factor $g_n$ (where $0 \le g_n \le 1$) related to scale $n$, the filtering factor for the breakpoint list $(x_i,t_i)$ can be defined as follows:

$$f_n(x,t_i)=\begin{cases}1-\dfrac{1-g_n}{\Delta x_n}\left|x-x_i\right|, & \left|x-x_i\right|<\Delta x_n\\ 1, & \left|x-x_i\right|\ge\Delta x_n\end{cases} \tag{10}$$

Where $f_n(x,t_i)$ represents the filtering factor for fault enhancement.

By applying the filtering factor $f_n(x,t_i)$ to the profile component $\tilde{s}_n(x,t)$ at scale $n$, fault-enhancement filtering can be performed, resulting in:

$$\tilde{s}'_n(x,t_i)=\tilde{s}_n(x,t_i)f_n(x,t_i) \tag{11}$$

Where $\tilde{s}'_n(x,t_i)$ represents the fault enhancement result specifically for the breakpoint $(x_i,t_i)$. By applying the weighted processing of **Equation 12** to all fault points in the breakpoint list $(x_i,t_i)$, the final processed result $\tilde{s}'_n(x,t)$ is obtained.

By synthesizing the multi-scale component data of fault enhancement into a single profile, the final fault enhancement result is obtained, expressed as:

$$\tilde{s}'(x,t)=\sum_{n=1}^{N}\tilde{s}'_n(x,t) \tag{12}$$

Where $\tilde{s}'(x,t)$ represents the fault-enhanced profile

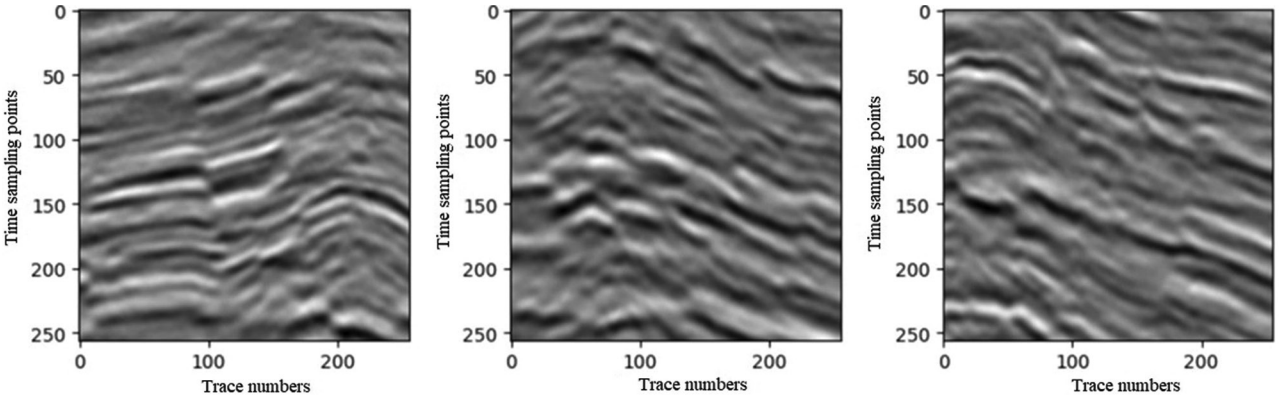


**Figure 4.** Input of the sample set (neural network inputs)

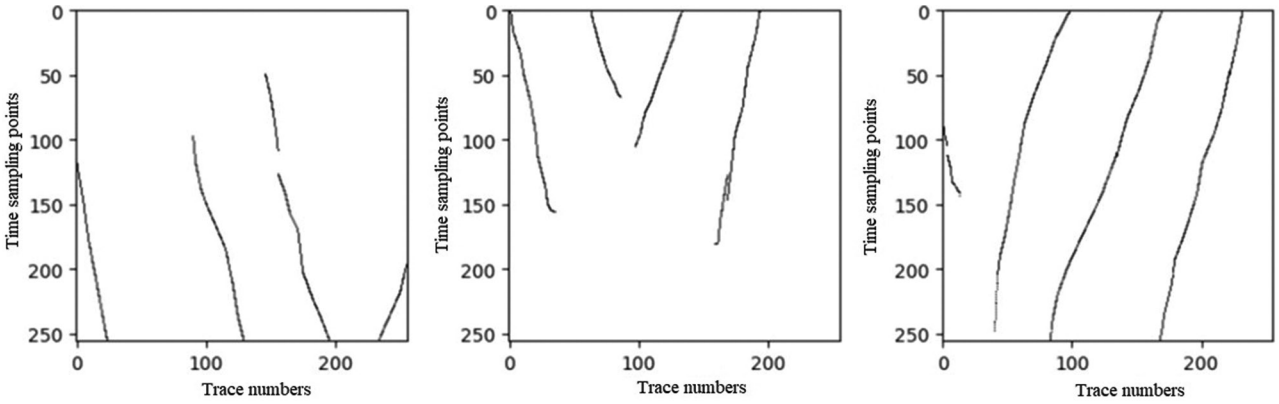


**Figure 5.** Output of the sample set, with the black lines indicating the fault area

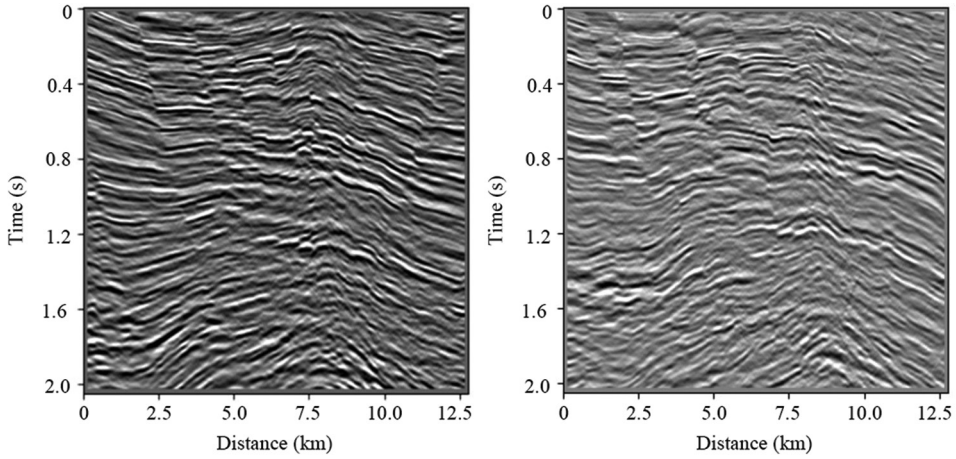


**Figure 6.** Example seismic profile used for fault prediction (neural network inputs)

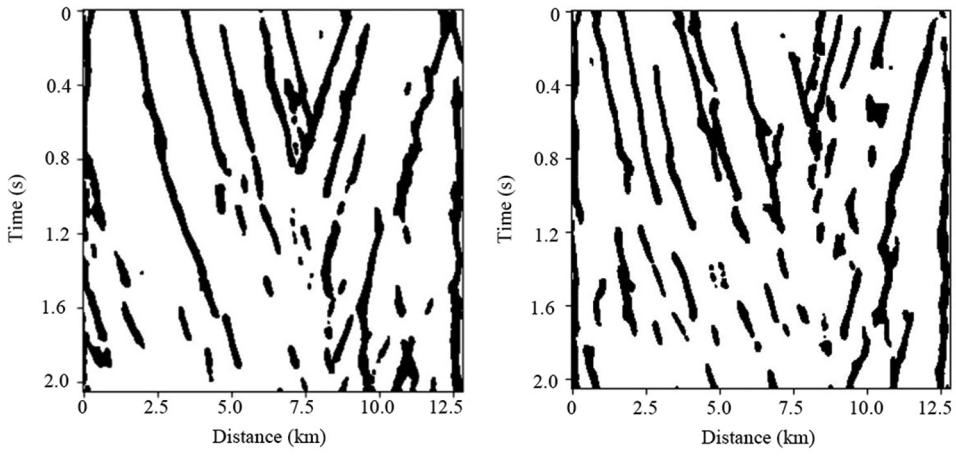


**Figure 7.** Predicted fault probability image based on the input profile shown in Figure 6

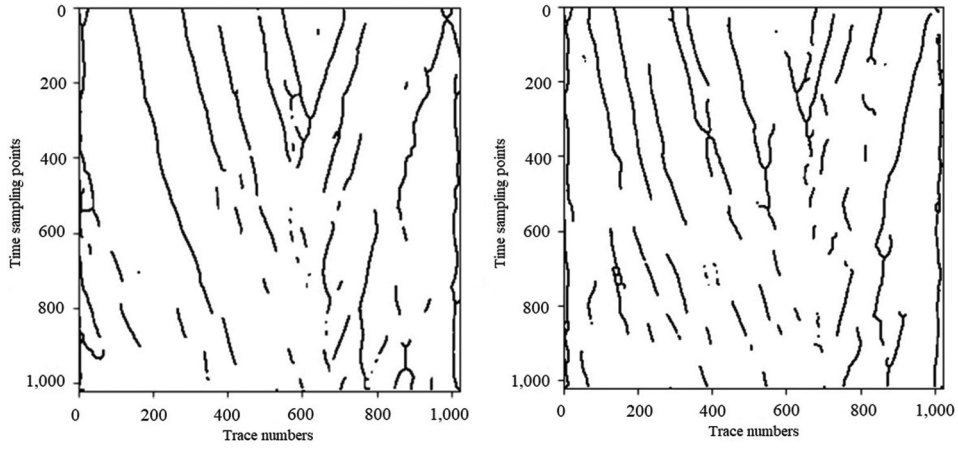


**Figure 8.** Fault skeleton image extracted via multi-scale analysis in the curvelet domain, with the black lines indicating the fault skeleton

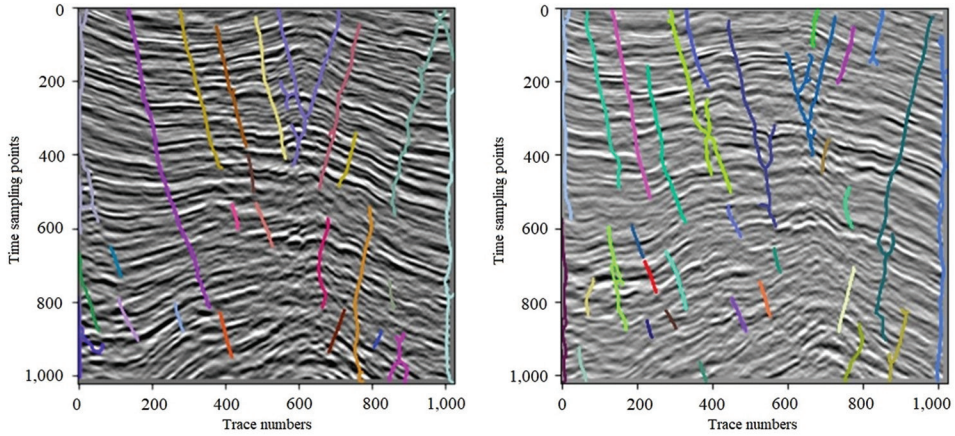


**Figure 9.** Fault spatial location information extracted via contour tracing technology, with the colored lines indicating the fault traces

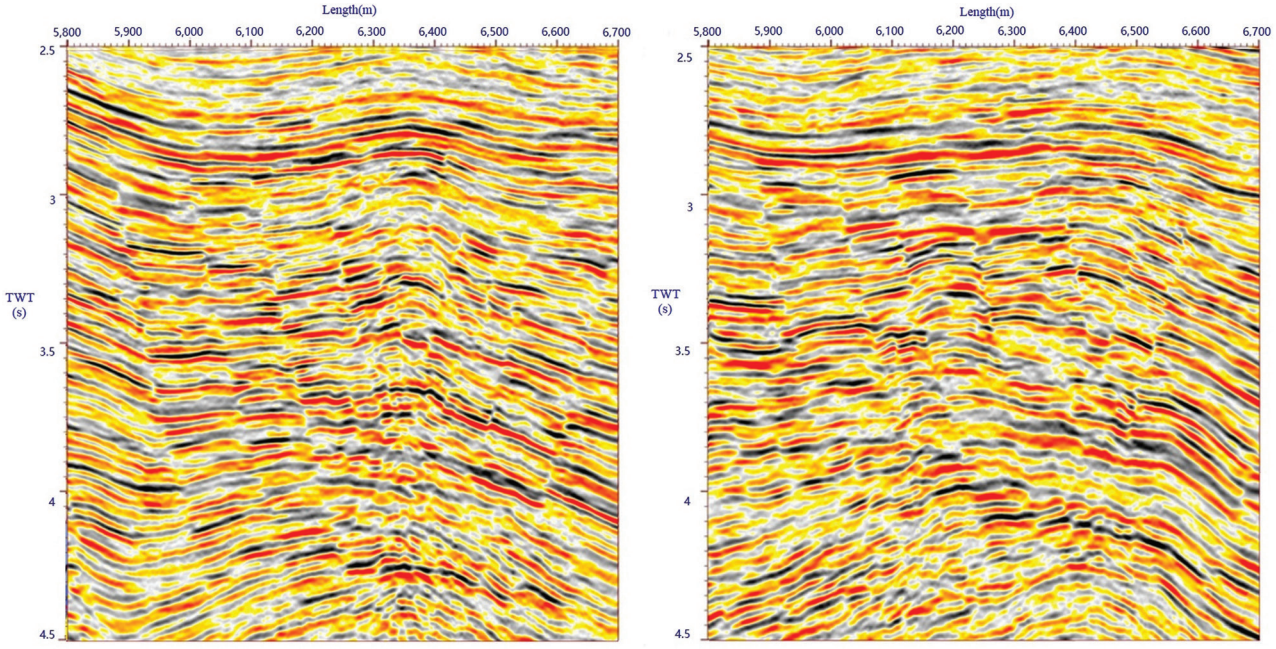


**Figure 10.** Imaging profile
Abbreviation: TWT: Two-way travel time.

obtained after multi-scale component extraction and filtering.

## 4. Effect analysis

### 4.1. Fault identification effect analysis of work area data

To assess performance on field data, a structural area in the East China Sea was employed as a case study. The imaging profiles and manually picked faults in this area were cropped into 256 × 256 patches to construct the sample set for training and evaluation (representative samples are shown in Figures 4 and 5).

A training dataset comprising 2,000 samples was randomly selected from the original sample set. After training and fine-tuning the neural network parameters, the optimized pre-trained model was applied to detect faults in the migrated section data of the target work area. The input seismic profiles and the corresponding fault predictions are illustrated in Figures 6 and 7, respectively.

Subsequently, fault skeleton extraction based on multi-scale analysis in the curvelet domain was performed on the fault probability image, resulting in the fault skeleton image as shown in Figure 8. To obtain the spatial location information of fault development, digital extraction based on

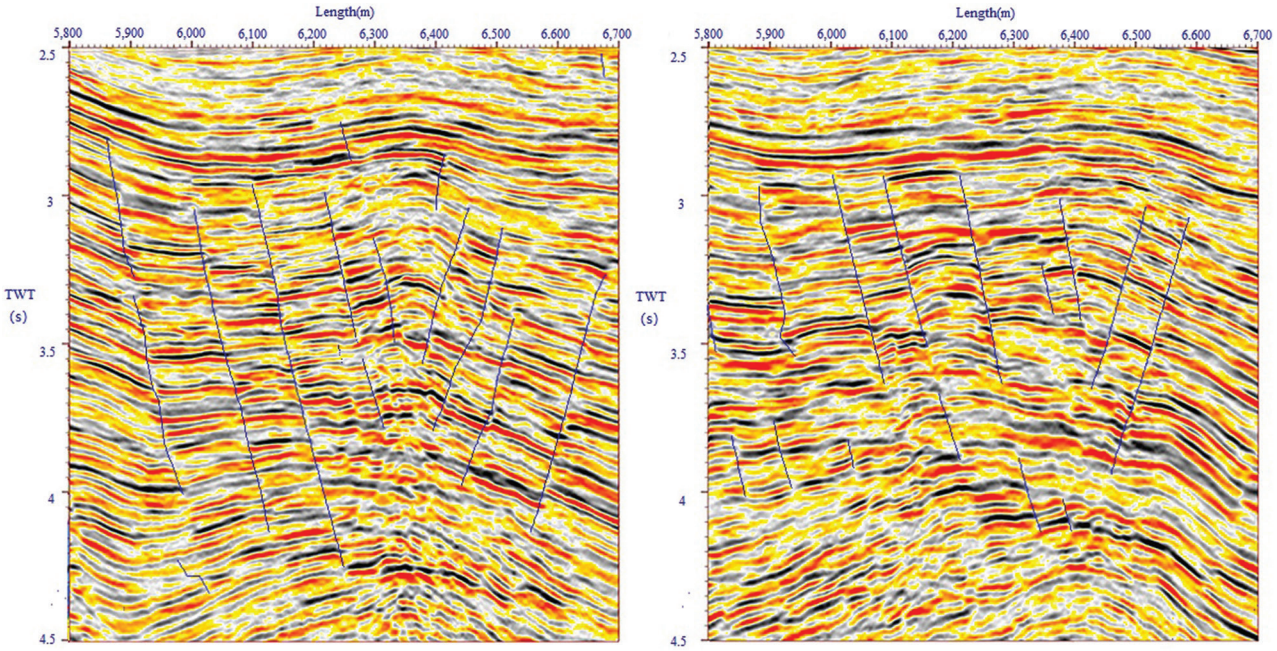


**Figure 11.** Imaging profile with manually picked fault curves
Abbreviation: TWT: Two-way travel time.

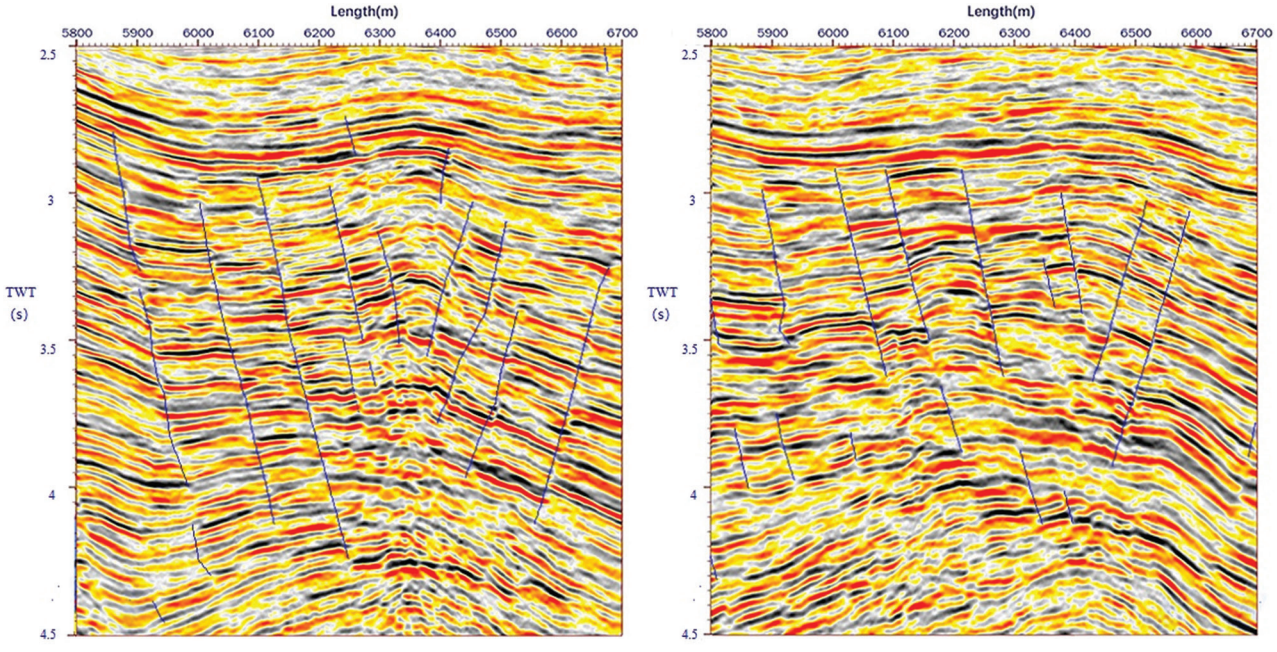


**Figure 12.** Imaging profile with loaded fault curves
Abbreviation: TWT: Two-way travel time.

contour tracing technology was implemented, as illustrated by the colored curves on the profile shown in Figure 9.

For clarity, Figures 10-12 present the imaging profile, the manually picked fault curves, and the overlaid fault curves, respectively. A comparison shows that the main faults in the original profile have been effectively identified, and the fault curves picked by the proposed method are generally consistent with the manually picked ones in the vicinity of the fault structures, demonstrating the effectiveness

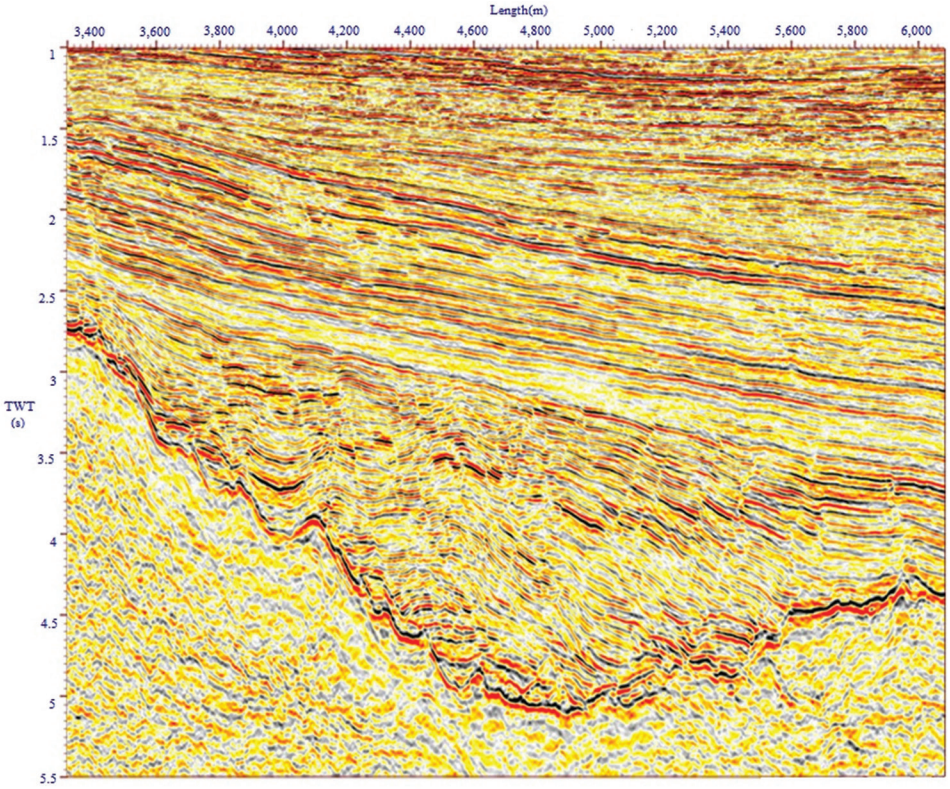


**Figure 13.** The original migrated section with unclear fault structures
Abbreviation: TWT: Two-way travel time.

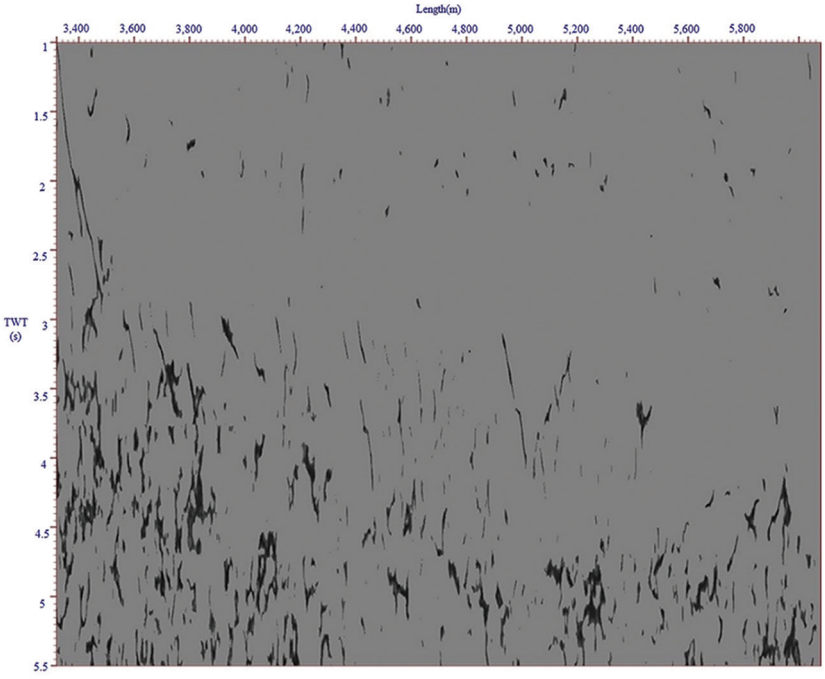


**Figure 14.** Identified fault image
Abbreviation: TWT: Two-way travel time.

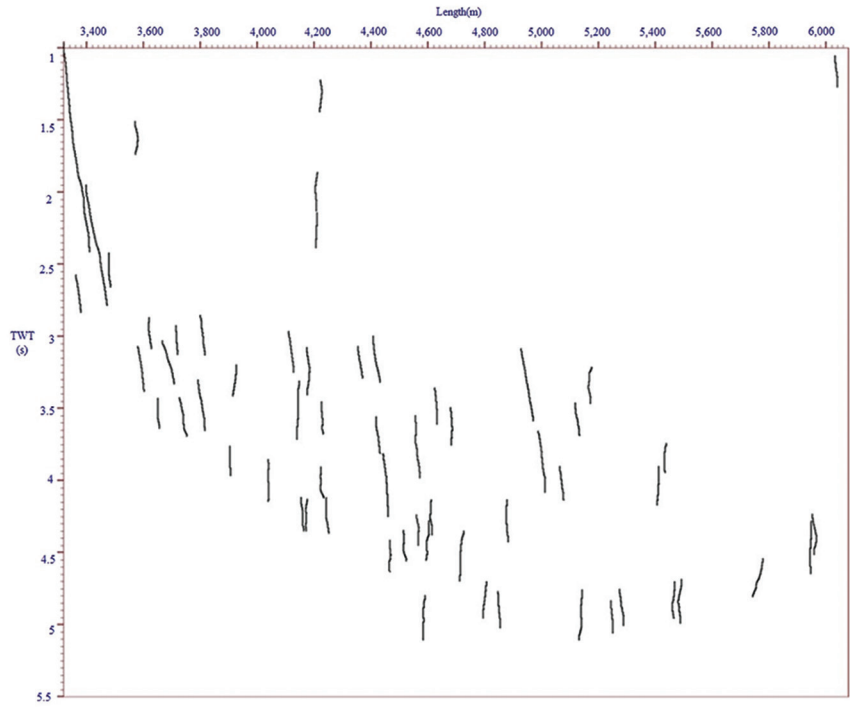


**Figure 15.** Image of breakpoint list describing fault skeleton information
Abbreviation: TWT: Two-way travel time.

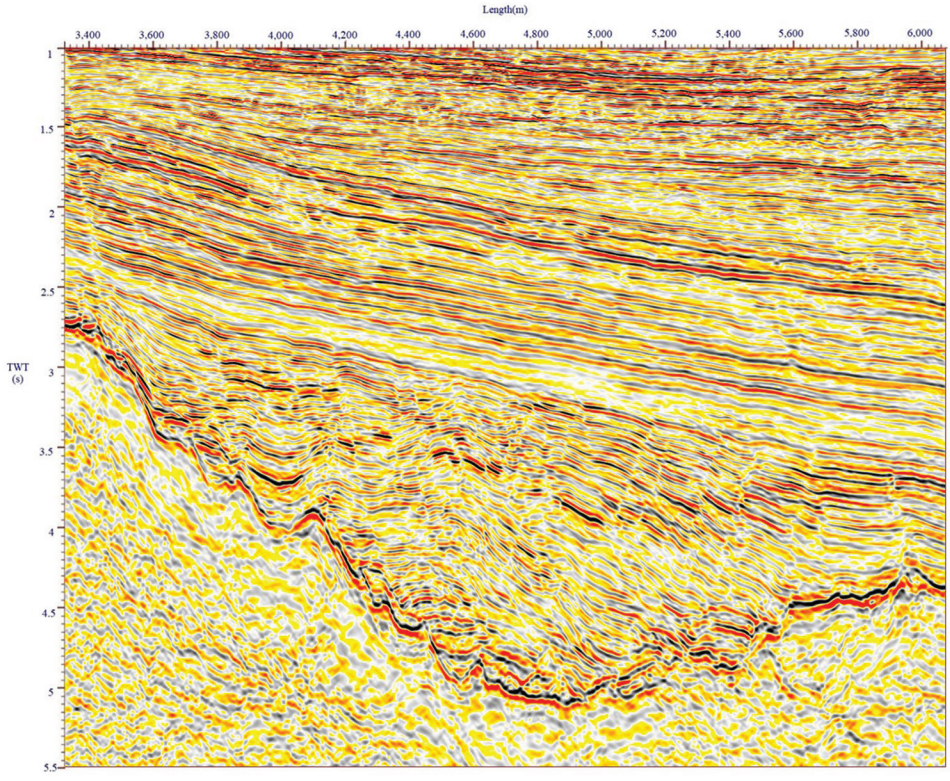


**Figure 16.** Example of a denoised profile obtained using the curvelet transform
Abbreviation: TWT: Two-way travel time.

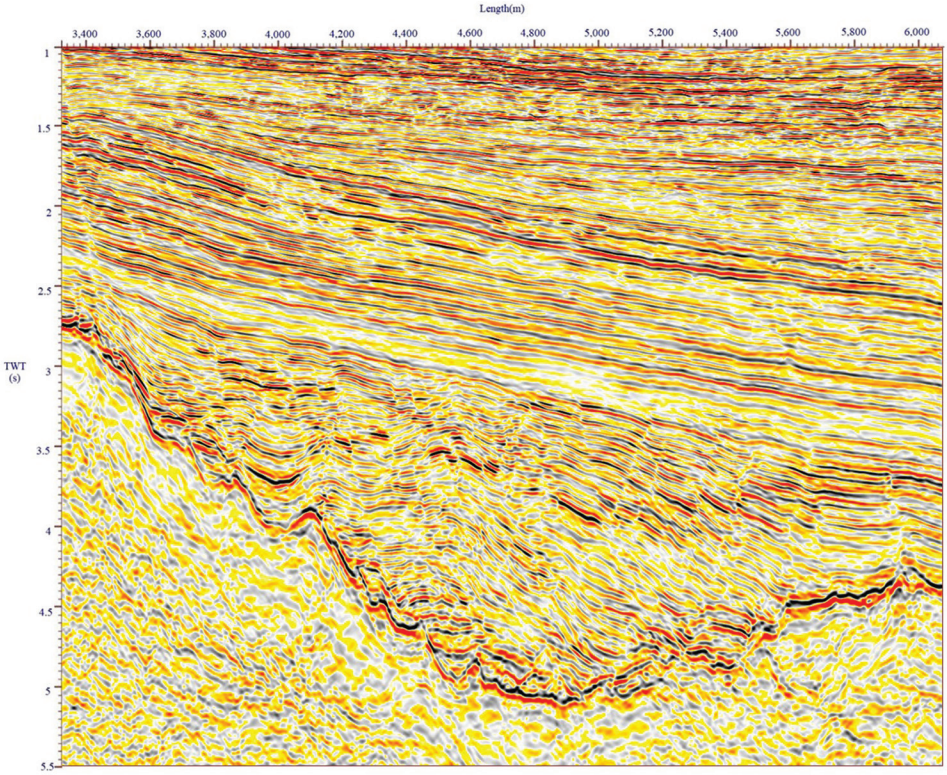


**Figure 17.** Denoised profile with restored fault information
Abbreviation: TWT: Two-way travel time.

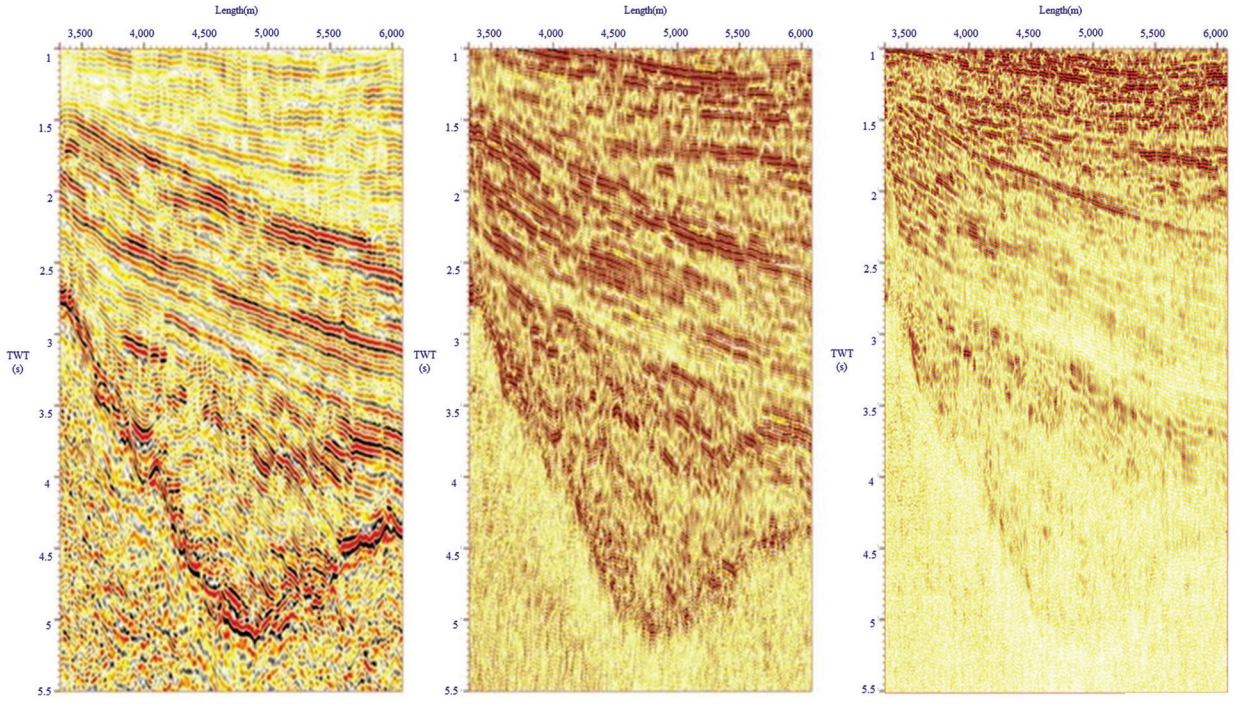


**Figure 18.** Migrated the section of each scale component
Abbreviation: TWT: Two-way travel time.

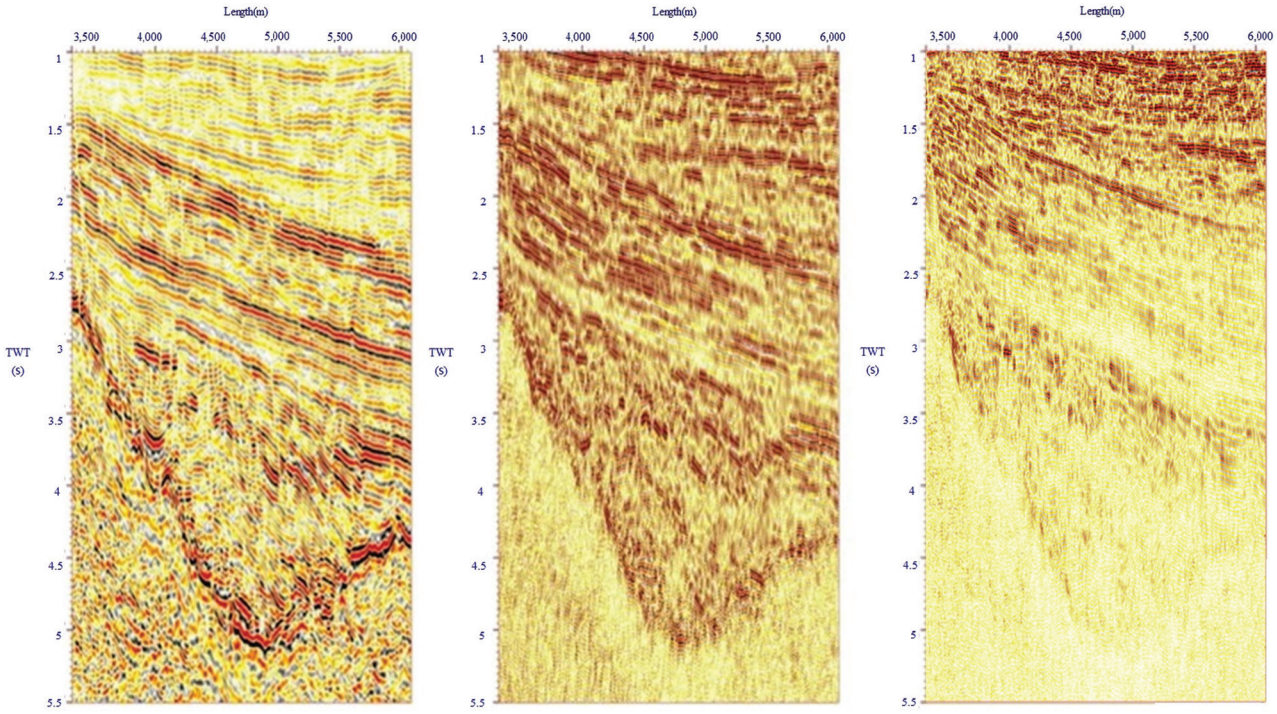


**Figure 19.** Fault enhancement results for each scale component profile
Abbreviation: TWT: Two-way travel time.

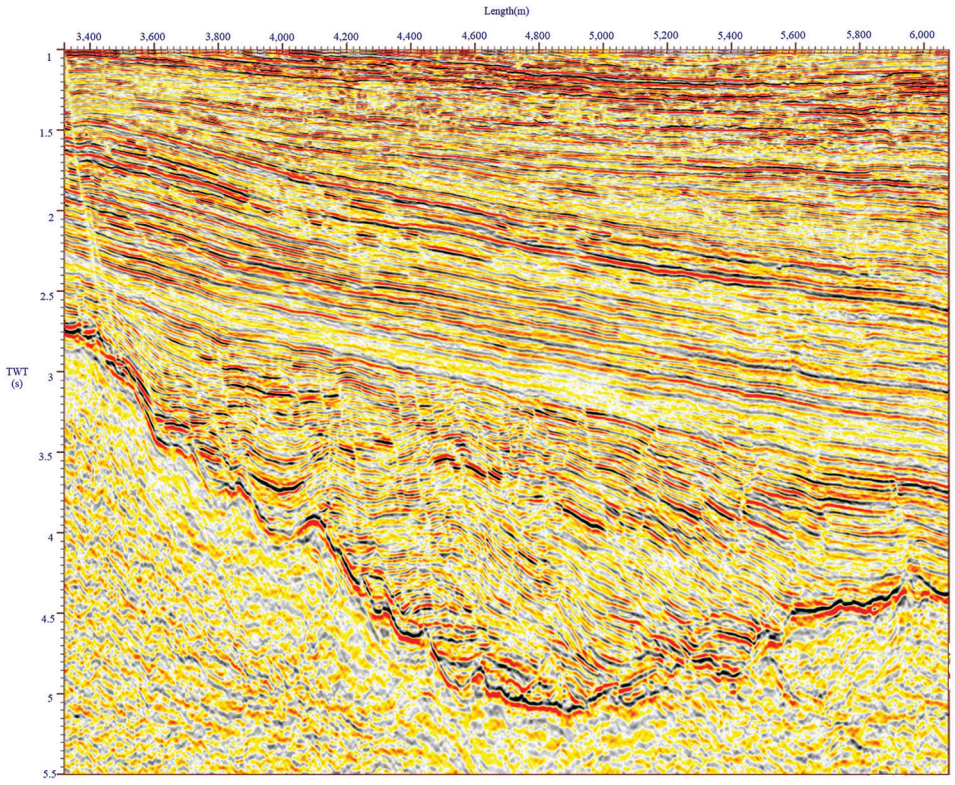


**Figure 20.** Migrated section after fault enhancement
Abbreviation: TWT: Two-way travel time.

of the method. Our method achieved an accuracy of 97.63%, an F1 score of 93.24%, and an intersection over union of 80.64%. Overall, most metrics achieved the best performance among the compared methods, further demonstrating the reliability of the proposed approach.

To demonstrate the generalization performance of the trained neural network, we applied it to another work area for fault identification. The original migrated seismic section of the new work area, where the fault structures are not clearly visible, is shown in Figure 13. Using the trained neural network for identification, the resulting fault image is shown in Figure 14. Finally, the fault image was vectorized to obtain a profile describing the fault skeleton, as shown in Figure 15, for subsequent interpretation and analysis. The curves in the profile accurately indicate the spatial locations of fault development, demonstrating that our trained neural network has strong generalization capabilities.

### 4.2. Fault enhancement effect analysis of work area data

Based on **Equation 5**, the migrated section (Figure 13) was transformed into the curvelet domain. By setting the threshold parameter, the curvelet coefficients with values smaller than 0.1 were set to zero. Then, using **Equation 7**, the filtered result was transformed back to the time–space domain, resulting in the migrated section with attenuated random noise, as shown in Figure 16.

For the denoised migrated section shown in Figure 16, the fault information was restored based on the extracted breakpoint list (Figure 15) using **Equations 8** and **9**. The resulting profile is shown in Figure 17, where the discontinuities associated with the fault events are enhanced to a certain extent.

The denoised profile shown in Figure 17 was used, with the number of scales and directions for the curvelet transform set to 3 and 16, respectively. Using **Equation 11**, it was transformed into the curvelet domain. Subsequently, a single-scale component inverse transform was performed on the curvelet-domain records for scale indices $n$ = 1,2, or 3, resulting in the scale-component profiles shown in Figure 18. Through analysis, it can be observed that as the scale index $n$ increases, the resolution of the component profiles improves, while the continuity of the faults gradually decreases.

For the migrated section of the three scale components shown in Figure 18, let $g_1$, $g_2$, and $g_3$ be 0, 0, and 0.5, respectively, and $\Delta x_1$, $\Delta x_2$, and $\Delta x_3$ be 225 m, 187.5 m, and 150 m, respectively. Based on **Equation 11**, the corresponding filtering factors were calculated. These factors were then used to perform fault-enhancement processing, and the resulting profiles are shown in Figure 19. Overall, as the scale index $n$ increases, the degree of fault filtering gradually decreases, achieving fault enhancement while preserving information.

The profile component data processed with differentiated parameters, as shown in Figure 19, were merged into a single migrated section. The resulting profile is shown in Figure 20. Compared to the original profile (Figure 13), the faults are significantly enhanced, providing a solid foundation for subsequent interpretation and analysis.

## 5. Conclusion

Our present focus is to demonstrate the feasibility and practical effectiveness of this U-Net–curvelet hybrid framework. The findings demonstrate that the hybrid framework effectively suppresses random noise and enhances the clarity of fault information, thereby further improving fault-identification accuracy. Applications to field data demonstrate that the method performs excellently under complex structural settings and low SNR conditions, enabling efficient and accurate fault identification, significantly improving fault imaging, and providing a reliable automated solution for seismic data interpretation.

However, direct quantitative comparisons with more complex architectures, such as U-Net–transformer models (e.g., MCA-SCUNet) were not conducted in this study. Nonetheless, we fully agree that further benchmarking with transformer-based models would provide valuable insight, and we consider this a key direction for future research. Future research should further optimize the network structure and explore more methods for integrating seismic attributes to address more complex geological conditions and exploration needs. Although the hybrid framework performs robustly on field data, challenges remain under very low SNR conditions: strong random/coherent noise tends to trigger false positives and obscure weak faults. Moreover, this method can be extended to the identification and enhancement of other geological features, further enhancing its applicability and practicality in geophysical exploration.

## Acknowledgments

None.

## Funding

This research is jointly funded by the National Natural Science Foundation of China (U23B20158) and the Major Science and Technology Project of China National Offshore Oil Corporation (CNOOC) during the "14th Five-Year Plan" (KJGG2022-0104).

## Conflict of interest

The authors declare no conflict of interest.

## Author contributions

*Conceptualization:* All authors
*Formal analysis:* Jianhua Wang, Cong Niu, Yandong Wang, Yun Ling, Di Wang
*Investigation:* Jianhua Wang, Cong Niu, Yandong Wang, Yun Ling, Di Wang
*Methodology:* Jianhua Wang, Cong Niu, Yandong Wang, Yun Ling, Di Wang
*Writing–original draft:* Jianhua Wang, Cong Niu, Yandong Wang
*Writing–review & editing:* All authors

## Availability of data

All data generated and analyzed during this study are included in this published article.

## References


1. Marfurt KJ, Kirlin RL, Farmer SL, *et al*. 3-D seismic attributes using a semblance-based coherency algorithm. *Geophysics*. 1998;63(4):1150.

   doi: 10.1190/1.1444415

2. Gersztenkorn A, Marfurt KJ. Eigenstructure-based coherence computations as an aid to 3-D structural and stratigraphic mapping. *Geophysics*. 1999;64(5):1468-1479.

   doi: 10.1190/1.1444651

3. Li X, Yang P, Yan H, *et al*. Identification of minor fault and its applications on the development of offshore oil fields. *Comput Techn Geophys Geochem Explor*. 2014;36(2):222-227.

4. Roberts A. Curvature attributes and their application to 3D interpreted horizons. *First Break*. 2001;19(2):85-100.

   doi: 10.1046/j.0263-5046.2001.00142.x

5. Al-Dossary S, Marfurt KJ. 3D volumetric multispectral estimates of reflector curvature and rotation. *Geophysics*. 2006;71(5):P41-P51.

   doi: 10.1190/1.2242449

6. Hale D. Methods to compute fault images, extract fault surfaces, and estimate fault throws from 3D seismic images. *Geophysics*. 2013;78(2):O33-O43.

   doi: 10.1190/geo2012-0331.1

7. Wu X, Hale D. 3D seismic image processing for faults. *Geophysics*. 2016;81(2):IM1-IM11.

8. Pedersen SI, Randen, T, Sønneland L, *et al*. Automatic Fault Extraction using Artificial Ants. In: *SEG Technical Program Expanded Abstracts 2002, SEG-2002-0512*. Salt Lake City: SEG; 2002.

9. Lavialle O, Pop S, Germain C, *et al*. Seismic fault preserving diffusion. *J Appl Geophys*. 2007;61(2):132-141.

   doi: 10.1016/j.jappgeo.2006.06.002

10. Wu X, Fomel S. Automatic fault interpretation with optimal surface voting. *Geophysics*. 2018;83(5):O67-O82.

    doi: 10.1190/geo2018-0115.1

11. Chen G, Liu Y. Research progress of automatic fault recognition based on artificial intelligence. *Prog Geophys*. 2021;36(1):119-131.

12. He K, Zhang X, Ren S, Sun J. Deep Residual Learning for Image Recognition. In: *2016 IEEE Conference on Computer Vision and Pattern Recognition (CVPR)*; 2016. IEEE. p. 770-778.

    doi: 10.1109/CVPR.2016.90

13. Wu X, Shi Y, Fomel S, *et al*. Convolutional Neural Networks for Fault Interpretation in Seismic Images. In: *2018 SEG International Exposition and Annual Meeting*. Anaheim: SEG, 2018.

14. Long J, Shelhamer E, Darrell T. Fully convolutional networks for semantic segmentation. In: *2015 IEEE Conference on Computer Vision and Pattern Recognition (CVPR)*. IEEE; 2015. p. 3431-3440.

    doi: 10.1109/cvpr.2015.7298965

15. Ronneberger O, Fischer P, Brox T. *U-Net: Convolutional Networks for Biomedical image Segmentation[C]// Medical Image Computing and Computer-Assisted Intervention - MICCAI 2015*. Cham: Springer, 2015. p. 234-241.

    doi: 10.1007/978-3-319-24574-4_28.

16. Wu X, Liang L, Shi Y, *et al*. FaultSeg3D: Using synthetic data sets to train an end-to-end convolutional neural network for 3D seismic fault segmentation. *Geophysics*. 2019;84(3):IM35-IM45.

    doi: 10.1190/geo2018-0646.1

17. Zhao M, Zhao Y, Shen D, Wang J, Dai X. High-resolution processing of seismic data using adaptive attention mechanism U-net. *Oil Geophys Prospect*. 2024;59(4):675-683.

    doi: 10.13810/j.cnki.issn.1000-7210.2024.04.003

18. He T, Liu NH, Wu BY, *et al*. ResU-net based three-dimensional fault identification method and application. *Chin J Eng Math*. 2023;40(1):1-19.

    doi: 10.3969/j.issn.1005-3085.2023.01.001

ACCSCIENCE PUBLISHING

Journal of Seismic Exploration

ARTICLE

# Generalized Gaussian distribution-based pre-stack inversion: A case study of channel sands in the Lianggaoshan Formation, Sichuan Basin

**Meng Yuan*, Zhiwei Miao, Lei Pan, Jianlong Su, and Chang Sun**

Exploration and Research Institute, Sinopec Exploration Company, Chengdu, Sichuan, China

(This article belongs to the *Special Issue: Geophysical Inversion and Intelligent Prediction Technologies for Complex Hydrocarbon Reservoirs*)

## Abstract

Tight sandstone channel systems occur in the second member of the Lianggaoshan Formation in the Sichuan Basin. These channels predominantly exhibit single bright-spot reflections on seismic sections. Due to the limited resolution of post-stack data and the constraints of attribute dimensionality, drilling results reveal complex internal lithological assemblages and pronounced lateral heterogeneity within these channels. Traditional post-stack methods struggle to effectively characterize internal channel details, thereby hindering subsequent exploration planning and reserve evaluation. To address these challenges, this study develops a pre-stack seismic inversion workflow based on generalized Gaussian distribution (GGD) prior constraints, aiming to enhance the identification and prediction of complex channel sand bodies. First, pre-stack amplitude versus offset (AVO) response analysis was conducted using typical wells to determine the effective incident angle range. By integrating optimal angle stacked data and AVO attribute extraction, the accuracy of characterizing the lateral distribution of channels was improved. Subsequently, a low-frequency facies-controlled model was constructed by integrating AVO attributes with elastic parameters. GGD prior constraints were incorporated into the pre-stack elastic parameter inversion, enabling detailed prediction of internal channel architecture. This technique yielded promising results in the Fuxing Block and was successfully validated in the Bazhong Block. It effectively enhanced the accuracy of identifying and predicting complex channels, providing technical support for the exploration, deployment, and resource evaluation of Jurassic tight sandstone channels in the Sichuan Basin.

***Keywords:*** Channel sandstone; Lianggaoshan Formation; Amplitude versus offset attribute; Generalized Gaussian distribution; Low-frequency facies-controlled model

***Corresponding author:**
Meng Yuan
(yuanm.ktnf@sinopec.com)

**Citation:** Yuan M, Miao Z, Pan L, Su J, Sun C. Generalized Gaussian distribution-based pre-stack inversion: A case study of channel sands in the Lianggaoshan Formation, Sichuan Basin. *JSeismicExplor.*2026;35(1):200-220. doi: 10.36922/JSE025450105

**Received:** November 06, 2025

**Revised:** December 19, 2025

**Accepted:** December 22, 2025

**Published online:** January 26, 2026

**Copyright:** © 2026 Author(s). This is an Open-Access article distributed under the terms of the Creative Commons Attribution License, permitting distribution, and reproduction in any medium, provided the original work is properly cited.

**Publisher's Note:** AccScience Publishing remains neutral with regard to jurisdictional claims in published maps and institutional affiliations.

## 1. Introduction

The Jurassic tight sandstones in the Sichuan Basin host substantial oil and gas resources.[1] Fluvial sandstone reservoirs in Jurassic continental strata have become a key target for recent hydrocarbon exploration. Both the China National Petroleum Corporation and Sinopec have reported large-scale geological reserves in this area, confirming promising

exploration prospects and significant resource potential in Jurassic tight sandstones.[2] The Lianggaoshan Formation, a Middle Jurassic ($J_2l$) sedimentary unit, is characterized by a delta-lacustrine depositional system. During the middle to late depositional stages of its second member ($J_2l^2$) through the third member ($J_2l^3$), the basin experienced continuous lacustrine regression, dominated by delta-front deposits. This period resulted in the development of multiple episodes of subaqueous distributary channel sand bodies, which are vertically stacked, laterally interconnected, and exhibit a banded distribution pattern. These sand bodies are widely distributed in the Fuxing Block (southeastern Sichuan) and the Bazhong Block (northeastern Sichuan).

As critical reservoirs for hydrocarbon accumulation, channel sand bodies have long been a primary focus of seismic exploration due to their distinct sedimentary features and distribution patterns.[3] To better understand the seismic response of channel sands, Li *et al*.[4] developed numerous thin-interbed convolution models based on typical channel sedimentary patterns to investigate the seismic reflection characteristics of sand-mud interbeds. Similarly, Li *et al*.[5] applied wave equation-based methods to analyze the seismic reflection characteristics of channel sandstones, examining the relationship between seismic reflections and sedimentation patterns from the perspective of wavelength interference. Other researchers have systematically studied the response characteristics of various continental thin-interbed configurations, revealing that post-stack seismic reflections vary significantly with changes in sandstone-to-mudstone stacking patterns, relative position, and thickness.[6,7] Collectively, these studies have advanced the understanding of seismic responses of channel systems under different sedimentary backgrounds by analyzing how sand-mud combinations and thickness variations manifest in post-stack seismic data.

For channels characterized by substantial width, thick individual sand bodies, and distinct seismic responses, post-stack seismic methods remain effective for delineating their planar distribution. Various techniques applied to channel sand prediction have yielded satisfactory results.[8,9] In terms of seismic identification, approaches such as spectral decomposition and waveform clustering based on post-stack data have been successfully employed to map channel distribution.[10,11] The seismic expression of thin-interbed sand bodies has been enhanced through 90° phase rotation or phase spectrum decomposition, while post-stack inversion methods, including sparse pulse and waveform indication inversion, have been utilized for channel sand prediction through P-impedance inversion.[12] Amplitude versus offset (AVO) characteristic analysis has enabled the identification of incident angles favorable for channel sand detection, with partial stacking techniques improving the identification of subtle channels.[13-15] The development and implementation of these identification and prediction technologies have demonstrated their effectiveness across multiple blocks, showing broad applicability.

With the progression of channel sandstone exploration from simple to complex types, growing evidence suggests that post-stack seismic data face inherent limitations in resolving the detailed response characteristics of intricate channel systems due to constraints in seismic resolution. Conventional post-stack seismic attributes likewise show limited capability in enhancing the identification accuracy of internal architectural details within such complex channels.[16] Post-stack inversion methods are often inadequate for quantitatively characterizing the heterogeneity and spatial complexity of these channels, typically exhibiting low resolution in predicting sand-mud interbedded intervals. In response, significant research efforts have been directed toward AVO inversion to improve the accuracy of lithology and reservoir prediction.[17-25] However, AVO inversion itself is susceptible to noise contamination, leading to considerable uncertainties in results and challenges in achieving reliable and stable solutions.[26] To mitigate this, AVO inversion commonly integrates prior information within a Bayesian framework to enhance stability. Currently adopted prior distributions include Gaussian, Cauchy, Huber, and modified Cauchy distributions. Applications based on these prior assumptions have demonstrated positive outcomes across various blocks, showing appreciable applicability in practice.[27]

Horizontal well drilling from Fuxing Block in the Sichuan Basin reveals that the Lianggaoshan Formation channels exhibit multi-phase vertical stacking, extensive sandstone-mudstone interbedding, and pronounced lateral heterogeneity. The tuning effect further destabilizes the seismic response of single bright-spot channels, while the limited resolution of post-stack seismic data proves inadequate for detailed reservoir characterization. These limitations result in significant multi-solution uncertainty in channel prediction, consequently constraining optimal horizontal well placement and impeding efficient reserve development in the block.

To address these challenges, this study develops a comprehensive pre-stack seismic workflow for characterizing complex channel systems in the Jurassic Lianggaoshan Formation. The methodology comprises three key stages. First, pre-stack AVO analysis of horizontal well data from the Fuxing Block is employed to identify the optimal incident angle range for detecting lithological variations. Selective angle stacking within this range

enhances the response characteristics of single bright-spot channels and improves channel distribution mapping. Second, AVO attribute analysis identifies gradient attributes as particularly sensitive to lithological changes. Extraction of these attributes significantly improves the accuracy of channel characterization. Finally, within a Bayesian framework, we extend the conventional Gaussian before a more adaptable generalized Gaussian distribution (GGD). After validating its statistical suitability with well data, we integrate the pre-stack angle gathers with AVO attributes to construct a geologically constrained low-frequency model. This facilitates pre-stack inversion that effectively resolves internal channel architecture. Application of this workflow to the $J_2l^2$ reservoirs in the Fuxing Block yielded significant improvements in channel prediction, with subsequent successful validation in the Bazhong Block confirming its robustness. This approach provides reliable technical support for reservoir evaluation and development optimization of complex channel systems in the Sichuan Basin.

## 2. Overview of the study area

Recent exploration studies confirmed that the Jurassic Lianggaoshan Formation in both the Fuxing Block (southeastern Sichuan Basin) and Bazhong Block (northeastern Sichuan Basin) developed under sedimentary conditions favorable for deltaic meandering river channel sandstones. Vertically, the formation comprises three distinct members: from base to top, the first ($J_2l^1$), second ($J_2l^2$), and third ($J_2l^3$) members. This vertical succession records a complete transgressive-regressive cycle, which promoted the development of multiple phases and types of vertically superimposed channel systems. In addition, the presence of numerous hydrocarbon source centers within the formation provides favorable conditions for near-source hydrocarbon accumulation (Figure 1).

In the absence of dedicated exploration wells targeting channel sandstones in the Lianggaoshan Formation, Sinopec drilled Well FL1 in the Fuxing Block to evaluate the second member ($J_2l^2$). The well penetrated a 26.5-m sandstone interval, and production testing yielded promising results, with an average daily output of 13,100 $m^3$ of gas and 10.4 $m^3$ of oil. This success confirms the presence of large-scale channel sandstone development in the $J_2l^2$ and highlights the reserve potential of the Lianggaoshan Formation. To further assess the scale of accumulation in this channel system, Well FL101 was subsequently drilled, encountering a 21.9-m sandstone layer in the same member. Well-seismic calibration confirmed that the sandstone in Well FL101 belongs to the same channel phase as that encountered in Well FL1. Post-stack seismic profiles across both wells showed a consistent "peak-top and trough-bottom" reflection configuration, characterized by a single bright-spot wavelet, indicating relatively uniform lithology and lateral continuity of the channel sandstone (Figure 2).

To enable effective production from the $J_2l^2$ channel sandstones, a sidetracked horizontal well (FL101HF) was drilled from the Well FL101 platform along a favorable azimuth targeting distinct bright-spot anomalies. The actual trajectory largely traversed the flanks of these seismic amplitude features. Drilling results revealed predominantly pure sandstone in the first half of the horizontal section, transitioning to pronounced sand-mud interbedding in the second half. This marked lateral lithological variation diverges significantly from pre-drill seismic interpretations (Figure 3), demonstrating substantial heterogeneity within the channel system. The integration of data from vertical Well FL101 and horizontal sidetrack FL101HF confirms that the uniform bright-spot channel contains significant internal heterogeneity, with laterally discontinuous sandstone distribution. This complexity remained unresolved in conventional post-stack seismic data due to its limited vertical resolution, which proves inadequate for characterizing the intricate lithological variations and internal architecture of the channel fill.

## 3. Methodology

To address the limitations of post-stack seismic data in characterizing complex channel sandstones within the $J_2l^2$ member, this study developed a dedicated pre-stack seismic prediction workflow. The methodology, outlined below, comprised three sequential steps designed to leverage the full information content of pre-stack data for enhanced lithological discrimination.

(i) AVO response analysis. AVO forward modeling of various lithological intervals, calibrated with horizontal well data, was performed. The comparative analysis of synthetic and actual seismic gathers revealed the amplitude-variation-with-angle behavior, pinpointing the incident angle range that is diagnostic of lithological changes.

(ii) AVO attribute extraction: Guided by the AVO response, an optimal approximation of the Zoeppritz equation was applied to the $J_2l^2$ seismic data. The resultant intercept or gradient attribute that most effectively characterized channel internal geometry was extracted for subsequent analysis.

(iii) Pre-stack seismic inversion: A low-frequency, facies-controlled model was constructed by integrating the well-derived interpolation model with the diagnostic AVO attributes, thereby reconciling vertical detail with lateral trends. Finally, a pre-stack inversion employing GGD prior constraints was implemented to produce

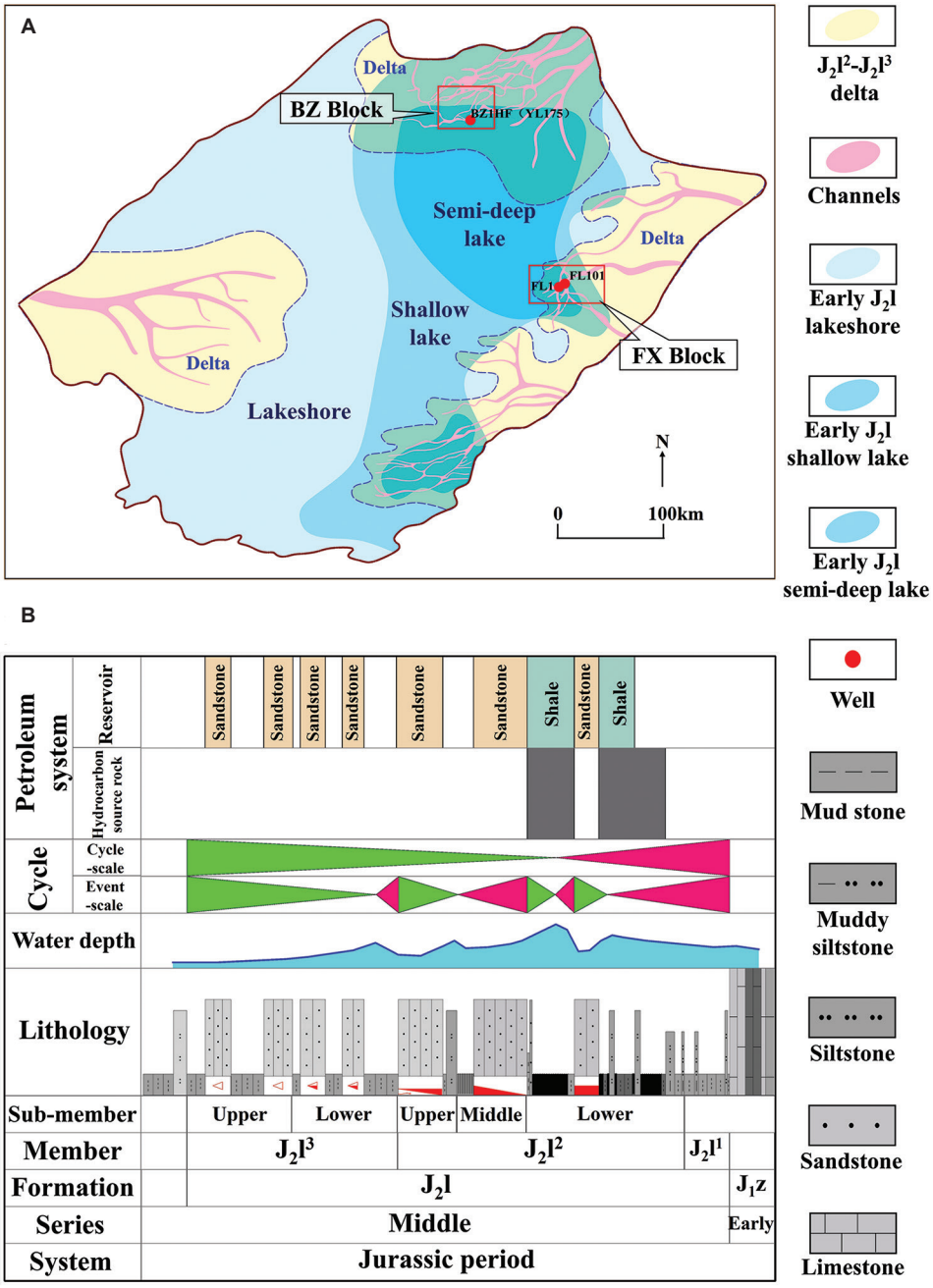


**Figure 1.** Hydrocarbon exploration and evaluation map of Lianggaoshan Formation, Sichuan Basin. (A) The hydrocarbon source rocks and channel overlay map from the Lianggaoshan Formation in the Sichuan Basin. (B) The lithostratigraphic column of the Jurassic system.
Abbreviations: BZ: Bazhong; FX: Fuxing.

a high-fidelity elastic parameter model, significantly enhancing prediction accuracy both vertically and laterally.

### 3.1. AVO response analysis and attribute extraction

While post-stack seismic data provided a consolidated view by stacking pre-stack gathers across all incident angles, this process averages out critical AVO information, thereby masking lithological anomalies.[28] Pre-stack data analysis, however, leverages this very AVO information to delineate lithological changes and fluid effects, proving highly effective for identifying channel features.

This study leveraged AVO theory to characterize the seismic response of multi-phase channel sand

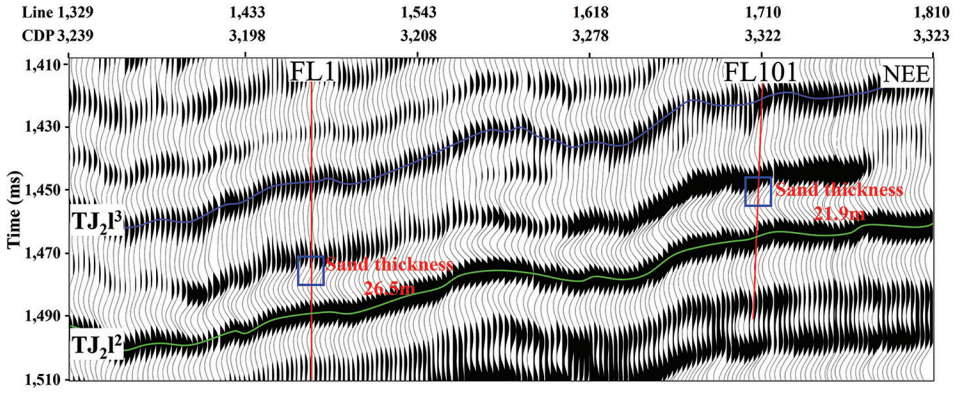


**Figure 2.** Post-stack seismic profile across Wells FL1 and FL101
Abbreviations: CDP: Common depth point; NEE: North-east-east direction.

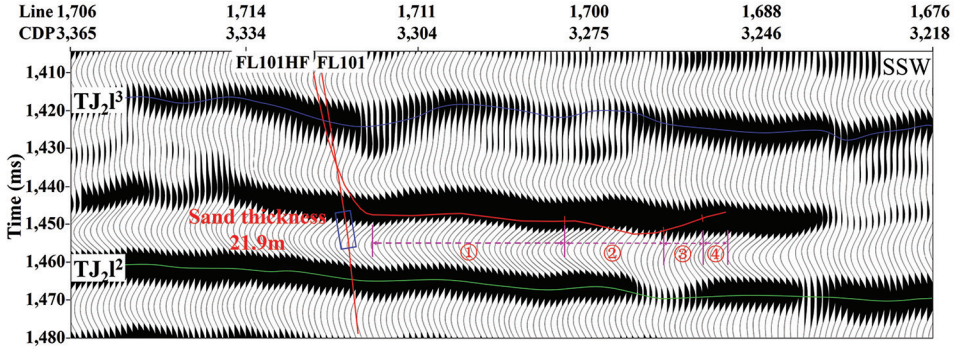


**Figure 3.** Post-stack seismic profile along the trajectory of Well FL101HF. ①, ②, ③, and ④ respectively represent the interval of sandstone, sand-mud interbedded, calcareous fine sandstone, and mudstone.
Abbreviations: CDP: Common depth point; SSW: South-south-west direction.

bodies encountered by horizontal well FL101HF. The well's trajectory intersected a sandstone interval, a sand-mud interbedded interval, and a calcareous fine sandstone interval before penetrating the overlying mudstone. A detailed analysis of pre-stack gathers at three representative common depth points (Table 1) revealed a common trend of amplitude reduction with increasing angle. The defining characteristic, however, is the markedly rapid amplitude decay in the sand-mud interbedded interval at far offsets (30–40°), creating a clear AVO response distinction from the other two intervals (Figure 4).

Based on the aforementioned AVO response analysis, this study demonstrated that AVO attributes can effectively reveal internal lithological variations within $J_2l^2$ channels. These attributes are typically extracted through fundamental pre-stack seismic inversion methods, which decode the implicit information in seismic data to characterize AVO anomaly variations.[29]

**Table 1. Forward modeling parameters table for the main lithological intervals encountered in the horizontal section of well FL101HF**

| Lithological intervals | P-wave velocity (m/s) | S-wave velocity (m/s) | Density (g/cm³) |
|---|---|---|---|
| Sandstone | | | |
| Mudstone | 4,834 | 2,685 | 2.610 |
| Sandstone | 5,424 | 3,191 | 2.640 |
| Sand-mud interbedded | | | |
| Mudstone | 4,834 | 2,685 | 2.610 |
| Mudstone | 5,022 | 2,870 | 2.564 |
| Calcareous fine sandstone | | | |
| Mudstone | 4,834 | 2,685 | 2.610 |
| Calcareous fine sandstone | 5,531 | 3,253 | 2.654 |

Analysis of Figure 4 indicates that the channel sandstones in the $J_2l^2$ generally exhibited a Class I AVO

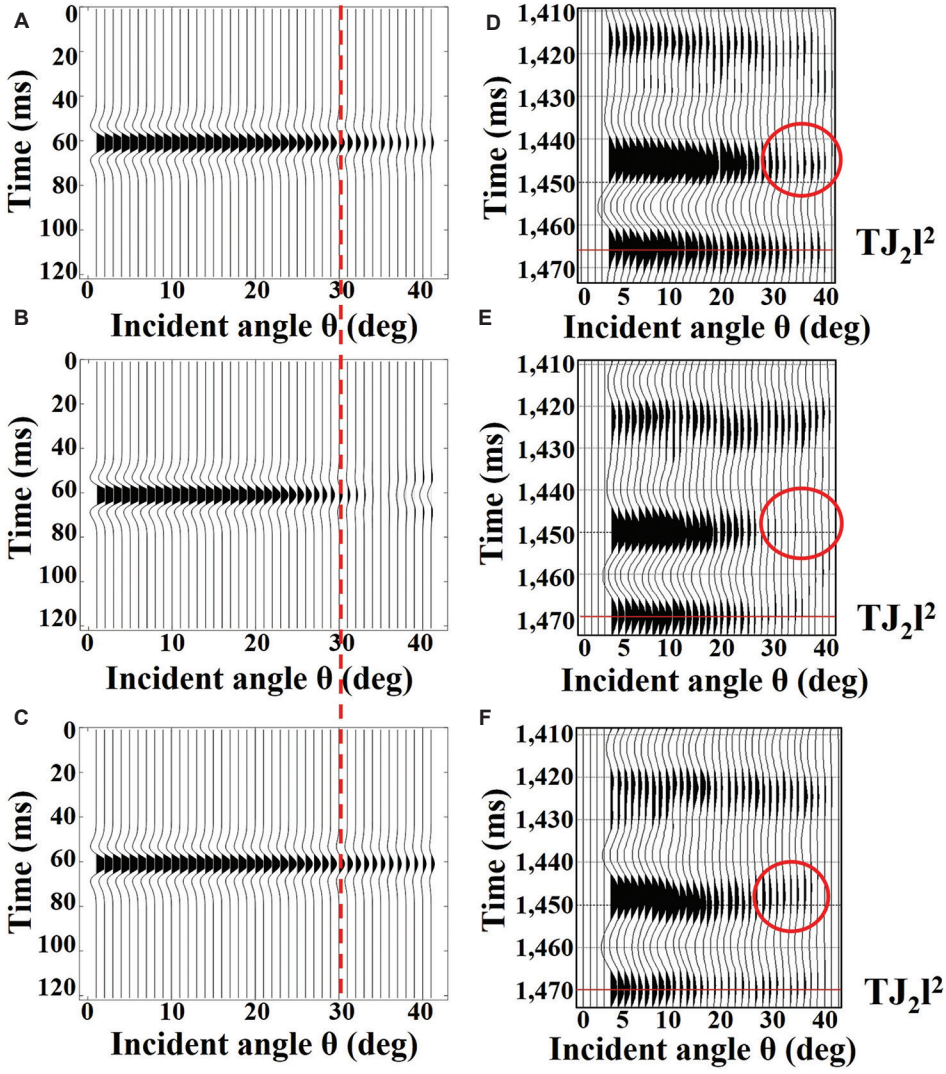


**Figure 4.** Comparison of (A-C) AVO forward modeling and (D-F) actual seismic gathers for different lithologies in Well FL101HF

response. Notably, within the 30–40° incident angle range, the sand-mud interbedded interval displayed significantly stronger amplitude variation with angle compared to other lithologies. Therefore, the gradient attribute was identified as the most sensitive parameter for highlighting intra-channel lithological variations.

### 3.2. AVO inversion method with GGD prior constraints

Conventional Bayesian inversion often employs the Gaussian distribution, the Laplace distribution, and the Huber distribution as priors. These prior constraints have relatively low precision and lack universality. To achieve a more accurate prediction of pre-stack elastic parameters, this study generalized the traditional Gaussian distribution and constructed a GGD with stronger adaptability. The probability density function of its observed samples is as follows in **Equation 1**:

$$g(x;\alpha,\mu,\sigma)=\left[\frac{\alpha}{2\sigma\Gamma\left(\frac{1}{\alpha}\right)\sqrt{\Gamma\left(\frac{1}{\alpha}\right)\Big/\Gamma\left(\frac{3}{\alpha}\right)}}\right]e^{-\left[\frac{|x-\mu|}{\sigma\sqrt{\Gamma\left(\frac{1}{\alpha}\right)\Big/\Gamma\left(\frac{3}{\alpha}\right)}}\right]^{\alpha}} \quad (1)$$

where $\mu$ and $\sigma$ represent the mean and variance, respectively. $\alpha$ controls the shape of the probability density function and is defined as the degree of freedom of the GGD. The function $\Gamma(\bullet)$ satisfies $\Gamma(1/\alpha)=\int_0^{+\infty}e^{-x}x^{1/\alpha-1}dx$.

The shape of the generalized Gaussian probability distribution is strongly influenced by the parameter $\alpha$: when the value of $\alpha$ is close to 0, the overall probability distribution values tend to be closer to the vicinity of the mean; when $\alpha = 1$, this probability distribution function is consistent with the Laplace probability distribution; when $\alpha = 2$, the shape of this probability distribution function is completely identical to that of the Gaussian probability distribution function; when $\alpha = +\infty$ (positive infinity), the probability distribution approximates a uniform distribution (Figure 5). Thus, the GGD can transition between several common probability distributions by adjusting the parameter $\alpha$, which unifies the common probability distribution functions to a certain extent and has stronger adaptability.

### 3.3. AVO inversion objective equation

Building on the analysis of AVO response characteristics and attribute extraction, this study further explored AVO inversion methods. Unlike post-stack inversion, pre-stack seismic inversion requires the use of angle information from pre-stack gathers and well logging data to conduct petrophysical crossplot analyses, aiming to obtain elastic parameters sensitive to lithology and reservoirs.[30,31] Recent studies have also demonstrated the effectiveness of pre-stack inversion based on the exact Zoeppritz equation for direct estimation of fluid properties and brittleness, which is crucial for predicting the sweet spot in unconventional reservoirs.[32]

#### 3.3.1. AVO forward modeling equation

To fully utilize the amplitude information across all incident angles in pre-stack gathers, this study employed the exact Zoeppritz equation to generate synthetic gathers in the pre-stack, full-angle domain, thereby comprehensively capturing the AVO characteristics.[33] The expression is given in **Equation 2**:[34]

$$\begin{bmatrix} \sin\theta_1 & \cos\theta_3 & \sin\theta_2 & \cos\theta_4 \\ \cos\theta_1 & \sin\theta_3 & \cos\theta_2 & \sin\theta_4 \\ \sin 2\theta_1 & \frac{V_{P1}}{V_{S1}}\cos 2\theta_2 & \frac{V_{P1}V_{S2}^2\rho_2}{V_{P2}V_{S1}^2\rho_1}\sin 2\theta_2 & -\frac{V_{P1}V_{S2}\rho_2}{V_{S1}^2\rho_1}\cos 2\theta_4 \\ \cos 2\theta_3 & -\frac{V_{S1}}{V_{P1}}\sin 2\theta_3 & -\frac{V_{P2}\rho_2}{V_{P1}\rho_1}\cos 2\theta_2 & -\frac{V_{S2}\rho_2}{V_{P1}\rho_1}\sin 2\theta_4 \end{bmatrix} \begin{bmatrix} \mathbf{R}_{PP} \\ \mathbf{R}_{PS} \\ \mathbf{T}_{PP} \\ \mathbf{T}_{PS} \end{bmatrix} = \begin{bmatrix} \sin\theta_1 \\ \cos\theta_1 \\ \sin 2\theta_1 \\ -\cos 2\theta_3 \end{bmatrix} \quad (2)$$

The angles $\theta_1$, $\theta_2$, $\theta_3$, and $\theta_4$ correspond to the P-wave reflection, P-wave transmission, S-wave reflection, and S-wave transmission angles, respectively. These angles satisfy Snell's law in relation to the P-wave and S-wave velocities of the medium. The upper and lower layers are characterized by P-wave velocities $V_{P1}$ and $V_{P2}$, S-wave velocities $V_{S1}$ and $V_{S2}$, and densities $\rho_1$ and $\rho_2$, respectively. The terms $R$ and $T$ denote reflection and transmission coefficients, with subscripts $PP$ and $PS$ indicating P-wave and converted-wave (S-wave) components, respectively.

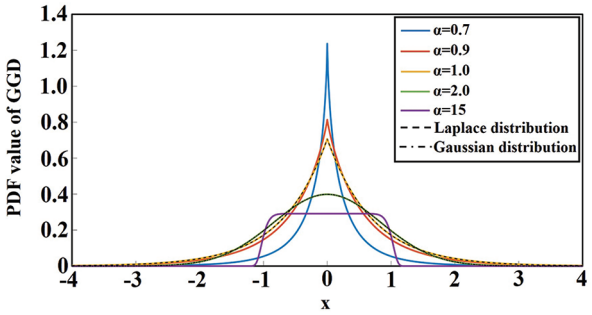


**Figure 5.** Probability density plot of the generalized Gaussian distribution
Abbreviation: GGD: Generalized Gaussian distribution.

Following generalized linear inversion theory, the P-wave reflection coefficient $R_{PP}$ in **Equation 2** was expanded using a first-order Taylor series approximation, yielding the linearized expression in **Equation 3**:

$$\mathbf{R}_{PP} = \mathbf{R}_{PP}^{Int} + \frac{\partial \mathbf{R}_{PP}^{Int}}{\partial \mathbf{R}_{VP}}\Delta\mathbf{R}_{VP} + \frac{\partial \mathbf{R}_{PP}^{Int}}{\partial \mathbf{R}_{VS}}\Delta\mathbf{R}_{VS} + \frac{\partial \mathbf{R}_{PP}^{Int}}{\partial \mathbf{R}_{D}}\Delta\mathbf{R}_{D} \quad (3)$$

Where $R_{PP}^{Int}$ is the reflection coefficient of the initial model parameters; the reflection coefficients of $V_P$, $V_S$, and $\rho$ correspond to $R_{VP}$, $R_{VS}$, and $R_D$ in the above formula, respectively.

By setting $\mathbf{m} = \begin{bmatrix} \mathbf{R}_{VP} & \mathbf{R}_{VS} & \mathbf{R}_{D} \end{bmatrix}^T$ and $\mathbf{L} = \begin{bmatrix} \frac{\partial \mathbf{R}_{PP}^{Int}}{\partial \mathbf{R}_{VP}} & \frac{\partial \mathbf{R}_{PP}^{Int}}{\partial \mathbf{R}_{VS}} & \frac{\partial \mathbf{R}_{PP}^{Int}}{\partial \mathbf{R}_{D}} \end{bmatrix}$, we can obtain the following formula (**Equation 4**):

$$\boldsymbol{R_{PP} = Lm} \quad (4)$$

In addition, the seismic synthetic record $S$ can be expressed as the product of the wavelet matrix and the reflection coefficient matrix, shown in **Equation 5**:

$$\boldsymbol{S = WR_{PP}} \quad (5)$$

#### 3.3.2. Inversion objective function

According to Bayes' theorem, the model parameters $m$ and the observed seismic data $D$ satisfy the following statistical law:[35]

$$P(\mathbf{m}|\mathbf{D}) = \frac{P(\mathbf{D}|\mathbf{m})P(\mathbf{m})}{P(\mathbf{D})} \propto P(\mathbf{D}|\mathbf{m})P(\mathbf{m}) \quad (6)$$

Among them, $P$(m) is the marginal probability distribution of the actual data, which is generally assumed

to be a constant; therefore, the integral of the posterior probability distribution function P(m|D) equals 1. In general, it is assumed that the noise in seismic data follows a Gaussian distribution, and $P(D|M)$ as the likelihood function of model parameters and observed data, can be written as:

$$P(\mathbf{D}|\mathbf{m}) = \frac{1}{\left[(2\pi)^N \mathbf{C}_d\right]^2} e^{\left[-\frac{1}{2}(\mathbf{D}-\mathbf{Gm})^T \mathbf{C}_d^{-1}(\mathbf{D}-\mathbf{Gm})\right]} \tag{7}$$

In **Equation 7**, $C_d$ is the covariance matrix of error data between synthetic records and observed data, $N$ is the number of time samples of the observed records, and G = WL. If we follow a GGD, $P(m)$ can be written as:

$$P(\mathbf{m}) = k_1 e^{\left[-\left(\frac{|\mathbf{m}|}{k_2}\right)^\alpha\right]} \tag{8}$$

In **Equation 8**,

$$k_1 = \frac{\alpha}{2\sigma\Gamma\left(\frac{1}{\alpha}\right)\sqrt{\Gamma\left(\frac{1}{\alpha}\right)/\Gamma\left(\frac{3}{\alpha}\right)}} \tag{9}$$

$$k_2 = \sigma\sqrt{\Gamma\left(\frac{1}{\alpha}\right)/\Gamma\left(\frac{3}{\alpha}\right)} \tag{10}$$

In general, when $\alpha$ is a fixed value, and $k_1$, $k_2$ are constants, the posterior probability density can be obtained as **Equation 11**:

$$P(\mathbf{D}|\mathbf{m}) = \frac{1}{\left[(2\pi)^N \mathbf{C}_d\right]^2} e^{\left[-\frac{1}{2}(\mathbf{D}-\mathbf{Gm})^T \mathbf{C}_d^{-1}(\mathbf{D}-\mathbf{Gm})\right]} \times k_1 e^{\left[-\left(\frac{|\mathbf{m}|}{k_2}\right)^\alpha\right]} \tag{11}$$

By omitting the constant terms in the above formula and calculating the maximum a posteriori solution of the model parameters, the following objective function (**Equation 12**) was constructed:

$$J_\sigma(m) = \frac{1}{2}(\mathbf{D}-\mathbf{Gm})^T(\mathbf{D}-\mathbf{Gm}) + \lambda\left(|\mathbf{m}|\right)^\alpha \tag{12}$$

In **Equation 12**, $\lambda = \mathbf{C}_d / k_2^\alpha$ is related to the degrees of freedom and the background noise of seismic signals.

To further improve the inversion accuracy of the model parameters in **Equation 12**, this study added a background constraint term to the equation. The new objective function is as follows in **Equation 13**:

$$J(m) = J_\alpha(m) + \beta(\mathbf{m}-\mathbf{m}_{ref})^T(\mathbf{m}-\mathbf{m}_{ref}) \tag{13}$$

Where, $m_{ref}$ is the background trend of model parameters, which can be obtained from existing logging data or geological knowledge, and $\beta$ is the regularization parameter for this constraint term.

#### 3.3.3. Algorithms for solving the objective function

**Equation 13** contains multiple regularization constraint terms and can be solved using the Alternating Direction Method of Multipliers.[36] First, the equation is decomposed into a subproblem $J_1(m)$ as follows in **Equation 14**,

$$J_1(\mathbf{m}) = \min_{\mathbf{m}}\left[\frac{1}{2}\|\mathbf{D}-\mathbf{Gm}\|_2^2 + \lambda|\mathbf{m}|^\alpha\right] \tag{14}$$

and subproblem $J_2(m)$ as follows in **Equation 15**:

$$J_2(\mathbf{m}) = \frac{1}{2}\|\mathbf{D}-\mathbf{Gm}\|_2^2 + \beta\|\mathbf{m}-\mathbf{m}_{ref}\|_2^2 \tag{15}$$

Finally, subproblem $J_1(m)$ and subproblem $J_2(m)$ can be solved by the soft-thresholding algorithm and least-squares inversion, respectively. The detailed process for solving the objective function is given in Appendix 1.

### 3.4. Testing of the model

To verify the applicability of the proposed method, we performed a statistical analysis on the probability distributions of the three model parameters to be inverted for Wells FL1 and FL101 within the study area, namely the reflectivity series of P-wave velocity, S-wave velocity, and density. The results indicated that all three types of distributions derived from these two wells were in high agreement with the GGD ($\alpha = 0.83$), as illustrated in Figure 6.

As illustrated in Figure 7, we conducted a single-well inversion test using Well FL101 as a case study. The inversion results, constrained by both the Gaussian distribution and the GGD, exhibited a consistent overall trend. However, the GGD-constrained inversion demonstrated superior performance, with its P-wave and S-wave velocity results showing a higher degree of consistency with the original well log curves. Although both methods produced noticeable errors in density estimation, the GGD-derived density was more stable and aligned more closely with the actual well values. Consequently, the single-well test confirmed that the GGD-based inversion of the $J_2l^2$ target interval achieved satisfactory consistency with the drilling data, meeting the accuracy prerequisites for subsequent channel sandstone prediction.

While the proposed pre-stack seismic inversion method theoretically enhances vertical resolution and stability—a benefit supported by single-well test results—it remains challenging to apply directly to three-dimensional volume prediction. Relying solely on high-frequency well information to build an interpolation model and extrapolating it laterally to form a low-

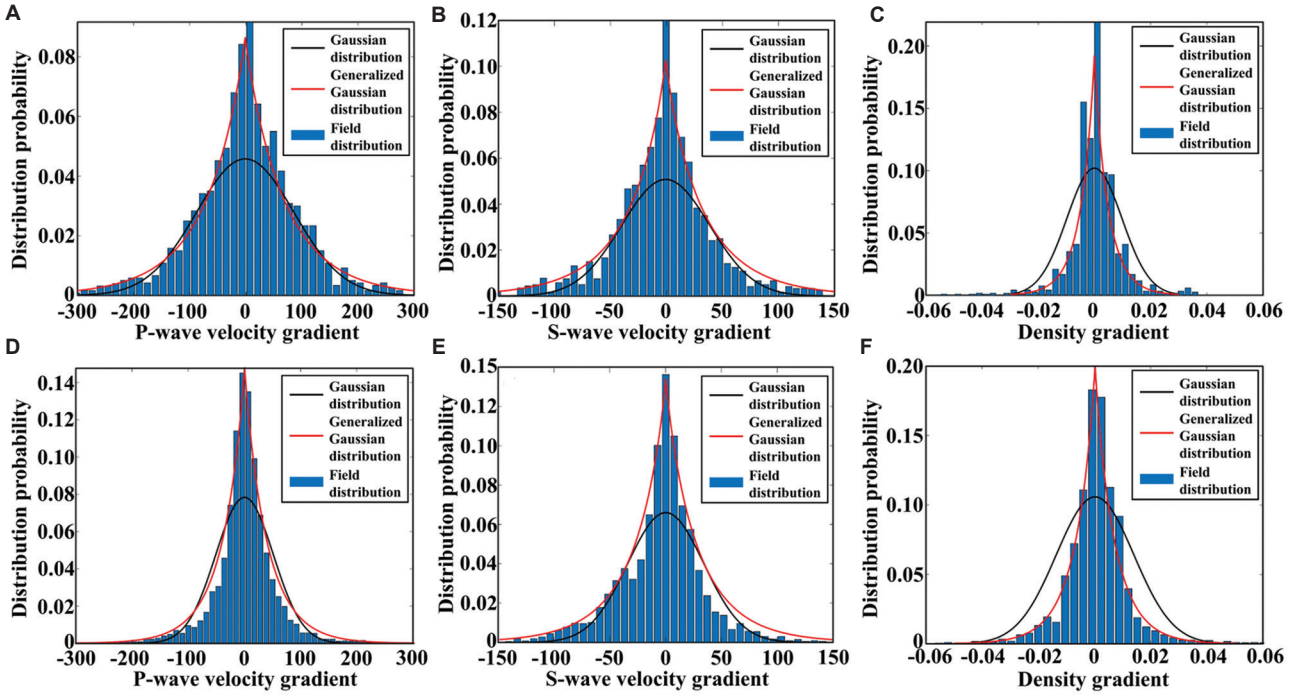


**Figure 6.** Probability distribution map (P-wave velocity, S-wave velocity, and density) from actual drilled wells to be inverted in (A-C) Wells FL101 and (D-F) FL1

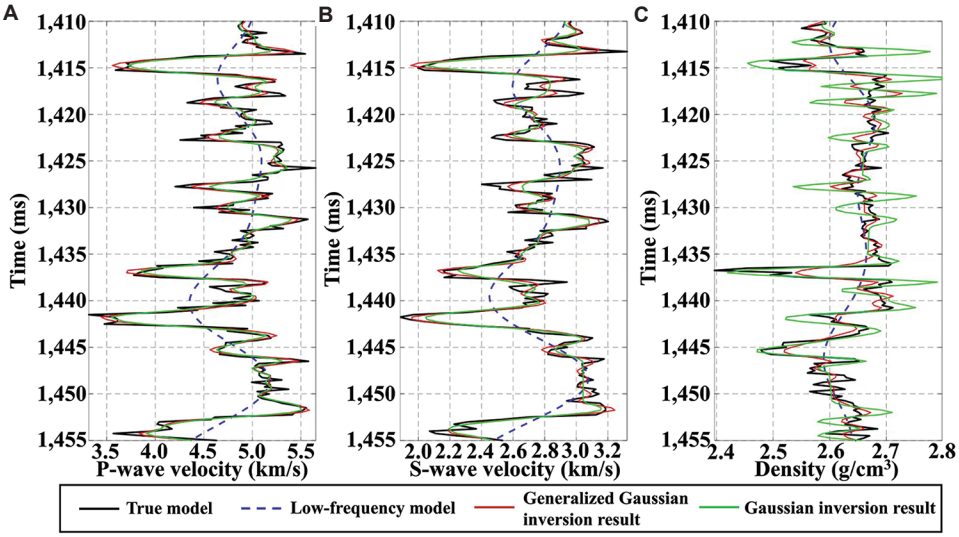


**Figure 7.** Comparison chart of inversion results and original curves for the target interval of the $J_2l^2$ in Well FL101. (A) P-wave velocity (km/s), (B) S-wave velocity (km/s), and (C) density (g/cm$^3$).

frequency model often leads to significant discrepancies with actual seismic lateral variations. This approach tends to overemphasize well control and vertical resolution, resulting in strongly model-driven outcomes that compromise the accuracy of lateral geological anomaly resolution and obscure the spatial outlines of such anomalies.

For the complex $J_2l^2$ channels in the Fuxing Block, reference to existing studies confirms that inversion based exclusively on well data is inadequate for reliable characterization of these channels. Taking the P-wave velocity as an example, since the initial model constructed by means of well interpolation in the early stage yielded poor prediction results after extrapolation inversion and

exhibited low lateral resolution, the inversion results of the $J_2l^2$ channel in the lateral direction exhibited a model-driven effect, and the consistency with seismic waveforms was low. Thus, incorporating lateral resolution as a constraint is essential, though it remains a major challenge in conventional well-driven workflows.[37-41] As established earlier, the AVO gradient attribute effectively reflects intra-channel lithological changes. To improve lateral prediction accuracy, we constructed a low-frequency facies-controlled model by fusing the well-interpolated initial model with AVO gradient attributes in the frequency domain, using differentiated weights to construct a low-frequency facies-controlled model for inversion calculations. This approach aims to balance the vertical and lateral resolution of the prediction results as much as possible. After a series of experiments (Figure 8), it was found that when the fusion weight of the well-interpolated initial model reaches or exceeds 50%—on the premise that a certain proportion of AVO attribute weight is incorporated—the inversion results can not only well delineate the distribution of channel sandstones in $J_2l^2$, but also identify the thin sand bodies developed in the upper strata of the $J_2l^2$ around the Well FL101.

Based on the above analysis, this study explored and summarized that the implementation of the low-frequency facies-controlled model mainly consists of two

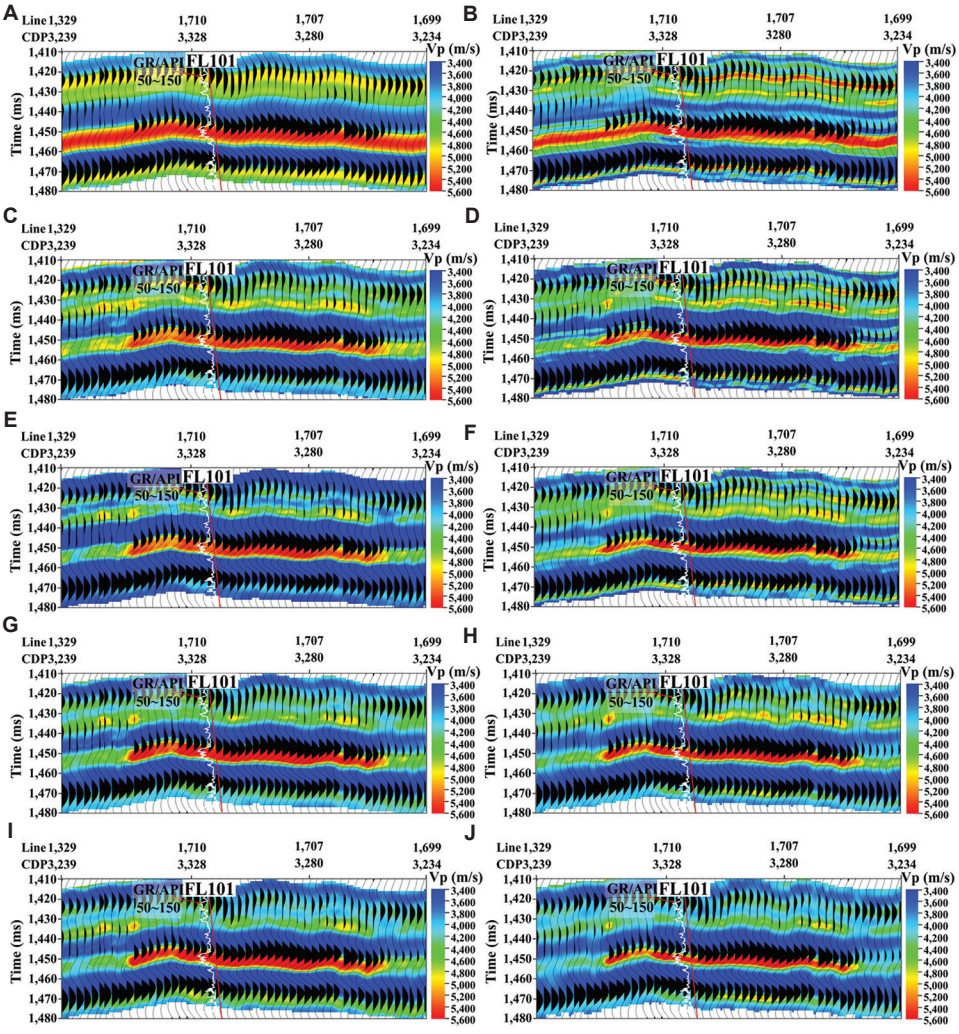


**Figure 8.** Fusion effects of the well-interpolated initial P-velocity (Vp) model and AVO gradient attributes under different weights, and their corresponding inversion results. (A and B) The initial model from a well-interpolated model, and its inversion results. (C and D) Fusion model with 60% weight of the well-interpolated model and 40% weight of the AVO gradient attributes, and its inversion results. (E and F) Fusion model with 50% weight of the well-interpolated model and 50% weight of the AVO gradient attributes, and its inversion results. (G and H) Fusion model with 40% weight of the well-interpolated model and 60% weight of the AVO gradient attributes, and its inversion results. (I and J) Initial model from AVO gradient attributes, and its inversion results.

Abbreviations: AVO: Amplitude versus offset; CDP: Common depth point; Vp: P-wave velocity.

key steps: first, normalizing the AVO attributes according to the value range of relevant elastic parameters; second, fusing the normalized attributes with the inter-well interpolation model. This operation ensured that the low-frequency facies-controlled model could preserve the lateral variation trend of AVO attributes during spatial extrapolation. When applied to subsequent inversion iterations, the model effectively balanced the vertical and lateral resolution of the inversion results. Taking P-wave velocity as an example, Figure 9 separately displays the inter-well interpolation model, AVO attributes, and the fused low-frequency facies-controlled model derived from their integration.

## 4. Application examples

### 4.1. Application result of Well FL101HF

Pre-stack AVO analysis of Well FL101HF identified the 30–40° incident angle range as the optimal window for detecting lithological variations within the horizontal section. By applying far-offset partial stacking within this range, internal response variations of the single bright-spot channel in the $J_2l^2$ were effectively enhanced. As demonstrated in Figure 10, the far-offset stacked section showed significantly attenuated amplitudes in sand-shale interbedded intervals, whereas sandstone and calcareous fine sandstone intervals maintained strong bright-spot

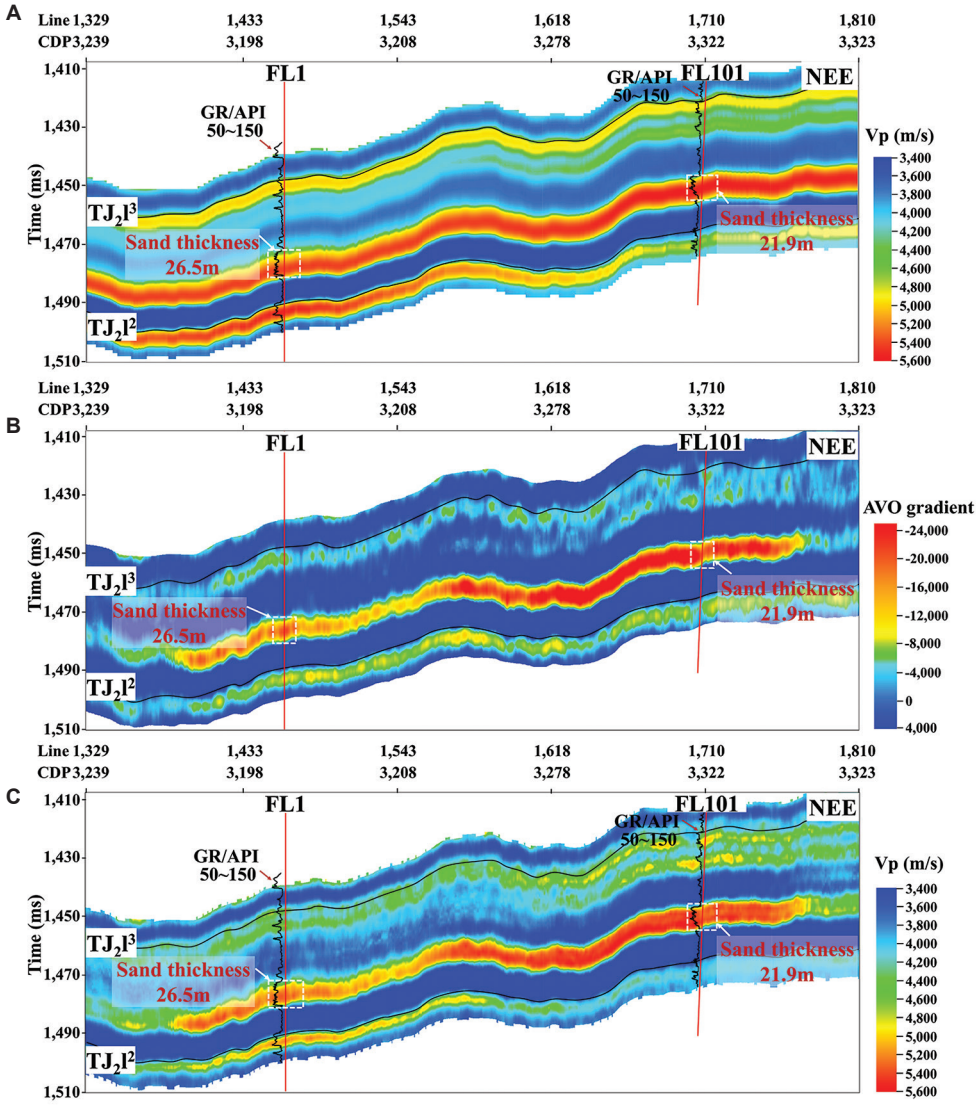


**Figure 9.** Cross-well profile through Wells FL1 and FL101. (A) Inter-well interpolation model of P-wave velocity. (B) AVO gradient attribute. (C) Facies-controlled model fused from an inter-well interpolation model and AVO attributes.
Abbreviations: AVO: Amplitude versus offset; CDP: Common depth point; NEE: North-east-east direction.

reflections. This result is consistent with actual drilling data and provides a more accurate lithological representation than conventional post-stack seismic data.

The observed amplitude variations confirm that lateral lithological changes produce distinct AVO responses, primarily manifested as differential rates of amplitude change with incident angle (gradient) across lithological units. This demonstrates that partial stacking effectively suppresses the dominant influence of small-to-medium angle amplitudes inherent in full-stack data, thereby accentuating the diagnostic amplitude characteristics of channel bright-spot reflections.

Based on the far-offset stacked seismic data (incident angle range: 30–40°), we conducted an isochronous slice analysis of bright-spot reflection characteristics using along-layer slicing. The advantage of along-layer slicing lies in its ability to extract the seismic response characteristics of specific phases of channels through horizon tracking and interpretation, thereby accurately delineating the distribution variation patterns of the sedimentary facies within the same-stage channels (Figure 11A). This effectively avoids the diachronism issue that arises when horizon-based slices are extracted using conventional isochronous framework models (Figure 11B). The results

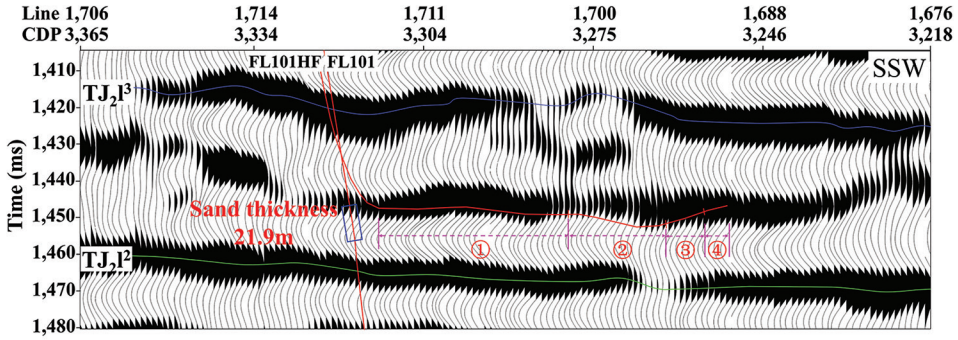


**Figure 10.** Far-offset (from 30° to 40°) stacked seismic profile through Well FL101HF. ①, ②, ③, and ④ respectively represent the interval of sandstone, sand-mud interbedded, calcareous fine sandstone, and mudstone, respectively.
Abbreviations: CDP: Common depth point; SSW: South-south-west direction.

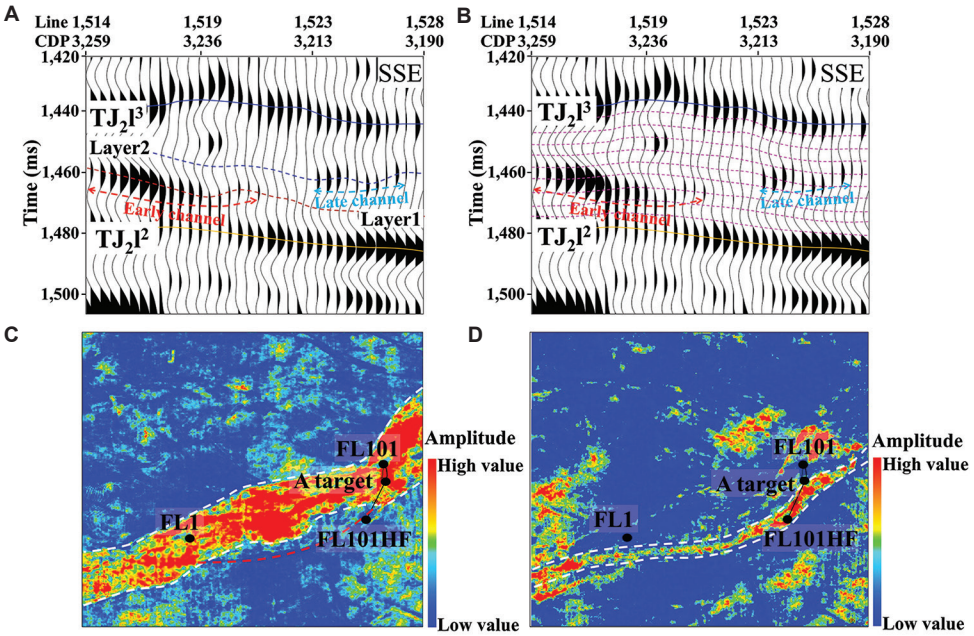


**Figure 11.** Seismic profiles perpendicular to channels and amplitude of channels using along-layer slicing around Well FL101HF. (A) Along-layer slicing based on the horizon tracking method. (B) Along-layer slicing from an isochronous framework model. (C) Early-channel slice and (D) late-channel slice around Well FL101, which are based on the far-offset stacked seismic data.
Abbreviation: CDP: Common depth point.

indicate that the horizontal section of Well FL101HF penetrated two phases of superimposed channels (Figure 11C and D), resulting in a sand-shale interbedded lithology, which suggests a location near the channel margin. Specifically, the first half of the horizontal section primarily traversed early-stage channel deposits dominated by fine sandstone, whereas the latter half encountered late-stage channel facies characterized by calcareous fine sandstone, influenced by progressive lateral channel migration. During the migration between the two channel phases, a transitional zone featuring sand-shale interbedding developed along their margins.

Based on the GGD-constrained pre-stack inversion approach and the low-frequency facies-controlled modeling strategy, this study performed inversion tests in the Well FL101 area of the Fuxing Block. Petrophysical crossplot analysis confirms Young's modulus as a sensitive discriminator for channel sandstones in the Lianggaoshan Formation, with sandstone intervals exhibiting significantly higher values than mudstone intervals (Figure 12). This distinct contrast enables effective lithology differentiation within the $J_2l^2$ member. For the inversion process, an inter-well interpolation model derived from Wells FL1 and FL101 was integrated with AVO gradient attributes to construct a low-frequency facies-controlled model, providing essential geological constraints for the pre-stack seismic inversion.

Given the complex lithological conditions encountered by Well FL101HF in the $J_2l^2$ formation, Young's modulus was selected as the key lithology-sensitive parameter for pre-stack seismic inversion to validate prediction effectiveness. To verify the inversion performance of the proposed method, we compared its prediction results with those derived from the conventional pre-stack inversion method. Specifically, the prediction results of the conventional pre-stack inversion method (constrained by the Gaussian prior distribution) were generated using Conver (version 3.1.0.1), a professional geophysical

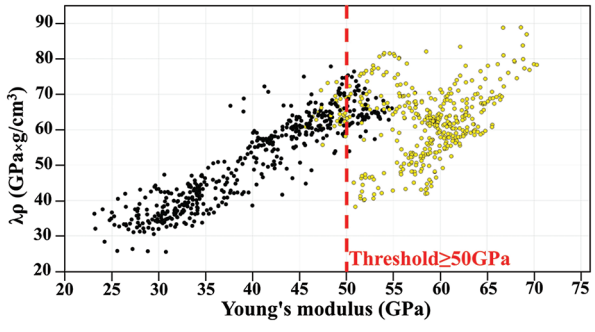


**Figure 12.** Crossplot of Young's modulus vs. lambda-rho in the second member of the Fuxing Block

data processing software.[26] The prediction results of the conventional pre-stack inversion method exhibited relatively high Young's modulus values in the sand-mud interbedded intervals (Figure 13A), which are inconsistent with the actual drilling data (Figure 13C). Consequently, the lateral lithological variations in the horizontal section were not accurately characterized. Comparison with conventional pre-stack inversion results confirmed that the proposed method achieved superior consistency with actual drilling data (Figure 13B): sandstone intervals exhibited high Young's modulus values, while mudstone sections showed significantly lower values. Sand-mud interbedded intervals displayed characteristic alternating high-low modulus responses, and calcareous fine sandstone intervals showed markedly elevated modulus values. As the well trajectory exited the channel and entered the overlying mudstone near the bottom, Young's modulus decreased substantially. The prediction results demonstrate that the proposed method yielded markedly higher prediction accuracy for both vertical and lateral lithological variations.

Exploration results indicate that the $J_2l^2$ in the Fuxing Block contains delta-front subaqueous distributary channel sands, representing favorable reservoir facies. Within these main channels, sand bodies displayed vertical multi-phase superposition and lateral avulsion and migration patterns. The channel prediction plan derived from pre-stack inversion results (Figure 14) revealed multiple overlapping and migrating channel branches, with enhanced migration complexity in high-sinuosity segments. This confirms significant heterogeneity in sand body distribution, though stable sand development segments within main channels remain optimal targets for horizontal drilling.

Following segmented fracturing, a production test in Well FL101HF yielded an oil flow rate of 26.88 $m^3/d$, demonstrating the substantial exploration potential of channel sandstones in the Jurassic Lianggaoshan Formation of the Sichuan Basin.

### 4.2. Promotion effect in Bazhong Block

Following the successful application in the Fuxing Block, the methodology was extended to the Bazhong Block. Geological evaluation confirmed the development of large-scale channel systems in the Jurassic $J_2l^2$ member of this region. Building on the exploration insights gained from the Fuxing Block and based on the stacking patterns of intra-channel sand bodies, the channel sedimentary models in the Bazhong Block were categorized into three distinct types: isolated, migratory, and superimposed. These classifications reflect the inherent heterogeneity within the channel complexes. Among these, the superimposed

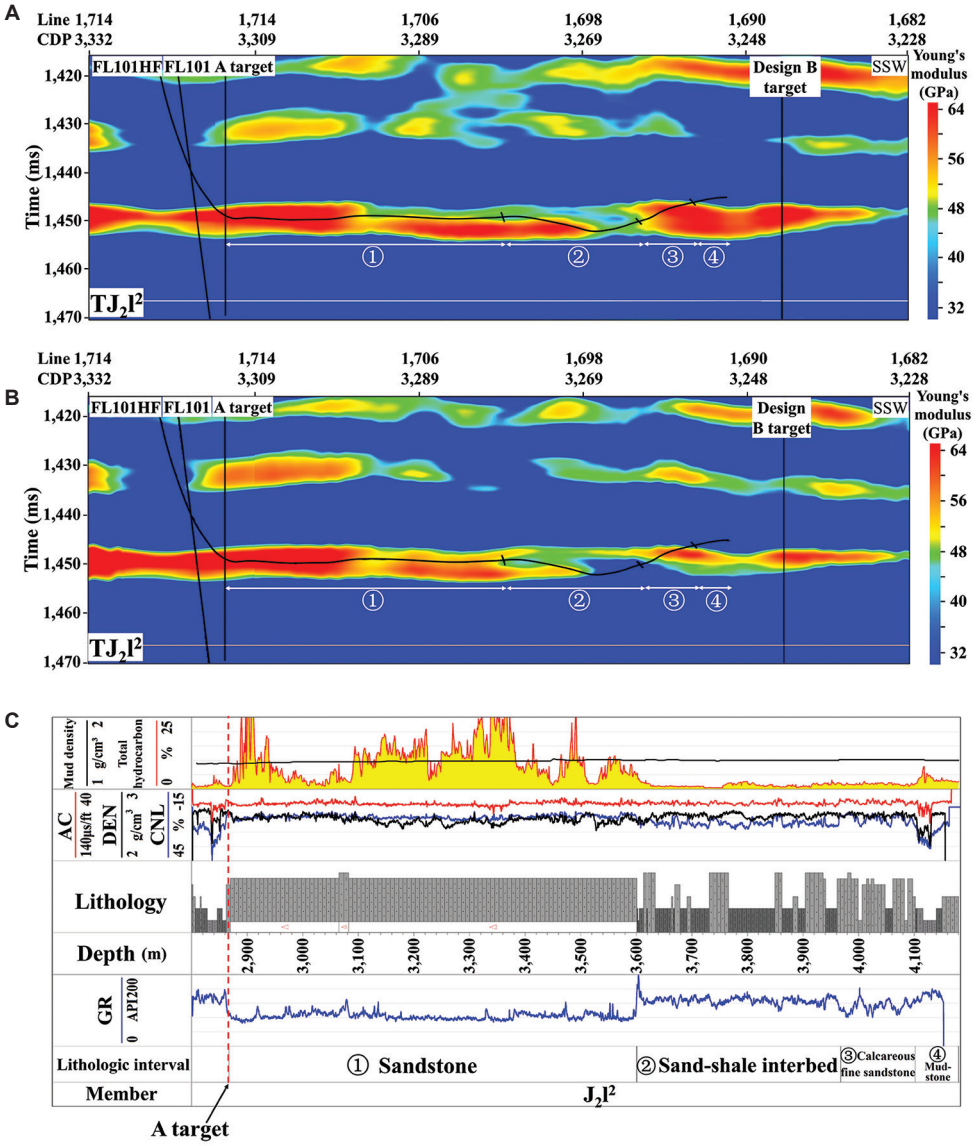


**Figure 13.** Pre-stack inversion prediction profile through Well FL101HF. (A) Gaussian distribution prior constraint method. (B) Generalized Gaussian prior constraint inversion method. (C) Comprehensive histogram of Well FL101HF.
Abbreviations: CDP: Common depth point; SSW: South-south-west direction.

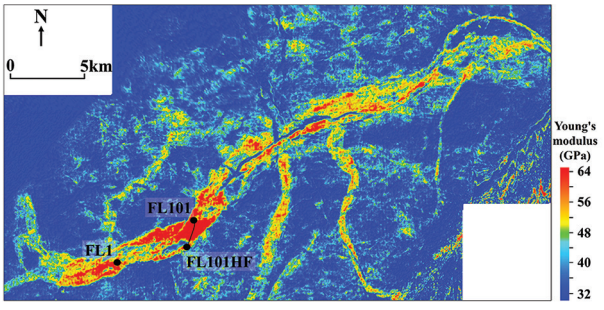


**Figure 14.** Channel prediction plan of the second member of the Fuxing Block

type—characterized by thick, large-scale sand bodies—was identified as the most favorable exploration target (Figure 15).

To assess the exploration potential of tight sandstone channels in the Bazhong Block's Lianggaoshan Formation, a horizontal well was sidetracked from the original Well YL175. Drilling results confirmed complex lithological variations in the horizontal section, demonstrating significant vertical and lateral heterogeneity within the $J_2l^2$ channels. For detailed analysis, AVO gradient attributes were extracted to characterize internal channel architecture.

As shown in Figure 16, these attributes revealed substantial heterogeneity across the study area.

Given the strong trough-bright-spot characteristics exhibited by $J_2l^2$ channel sandstones in post-stack seismic data, reversed-polarity seismic profiles were compared with AVO attributes to delineate lateral sand body superposition relationships. Well YL175, positioned in the southern straight segment of the channel system, encountered 25-meter-thick sandstones interpreted as the superimposed type based on AVO gradient attributes (Figure 16A). North of this segment, the channel morphology was more sinuous, exhibiting clear evidence of lateral migration in the curved sections (Figure 16C). Cross-sectional views perpendicular to these curved segments consistently displayed migratory patterns in AVO gradient attributes, confirming the coexistence of multiple sand body superposition patterns within the channel system near Well YL175.

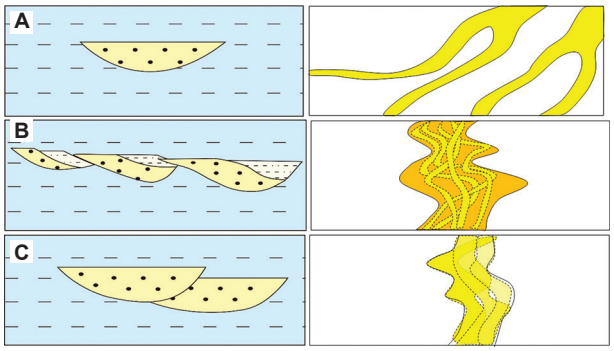


**Figure 15.** Main sedimentary models of channels from the second member of the Bazhong Block. (A) Isolated type, (B) migratory type, and (C) superimposed type.

Well BZ1HF, a horizontal well drilled from the YL175 platform, encountered similarly complex lithological conditions in its horizontal section as those observed in Well FL101HF from the Fuxing Block, primarily resulting from dynamic variations in the well trajectory (Figure 17A). In this study, the P-wave velocity/S-wave velocity (Vp/Vs) ratio was employed as a sensitive diagnostic parameter for distinguishing sandstone and mudstone lithologies. A low-frequency facies-controlled model, constructed using AVO gradient attributes, was utilized to constrain the pre-stack seismic inversion.

The inversion results demonstrated a strong correlation between the predicted Vp/Vs profile and the actual drilling data (Figure 17A): mudstone intervals were characterized by high Vp/Vs ratios, sandstone intervals by low ratios, and sand-shale interbeds exhibited intermediate values. The inversion-based plan view (Figure 17B) further confirms that Well BZ1HF is situated within the southern straight segment of the channel system, where laterally extensive, thick superimposed sand bodies—similar to those encountered in Well YL175—are well developed. These consistent results validate the effectiveness and reliability of the proposed pre-stack seismic prediction methodology.

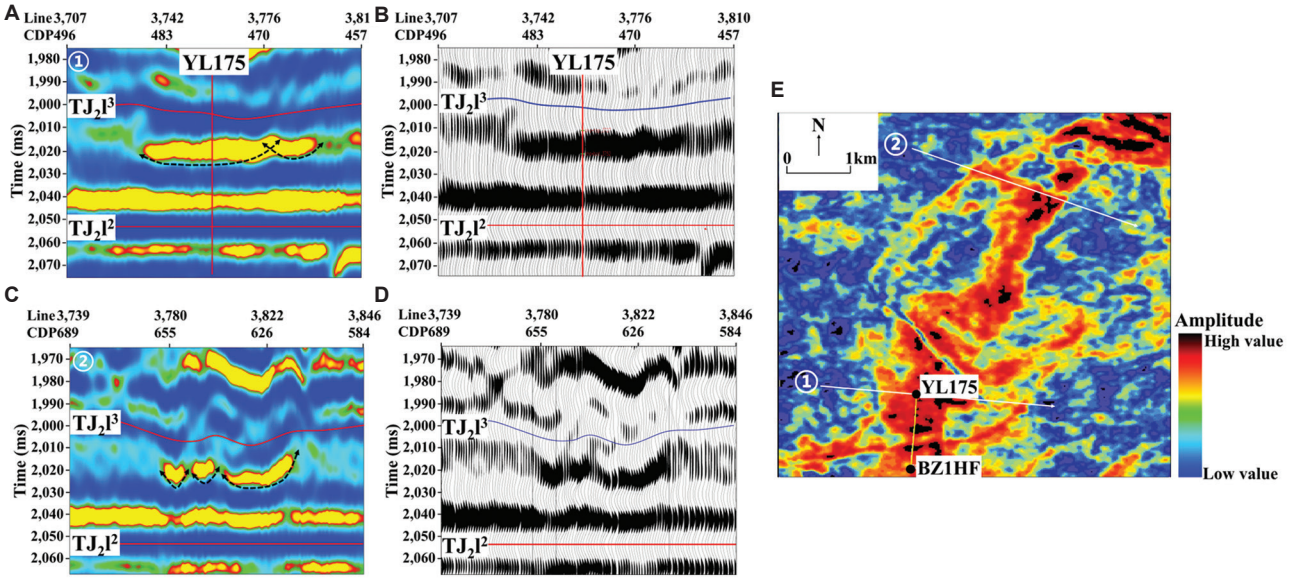


**Figure 16.** AVO gradient attribute plane and profile of the second member in the Bazhong block. (A and B) AVO gradient attribute profile and anti-polar seismic profile of well YL175. (C and D) AVO gradient attribute profile and anti-polar seismic profile of channel north section of the second member. (E) AVO gradient attribute plane.
Abbreviations: AVO: Amplitude versus offset; CDP: Common depth point.

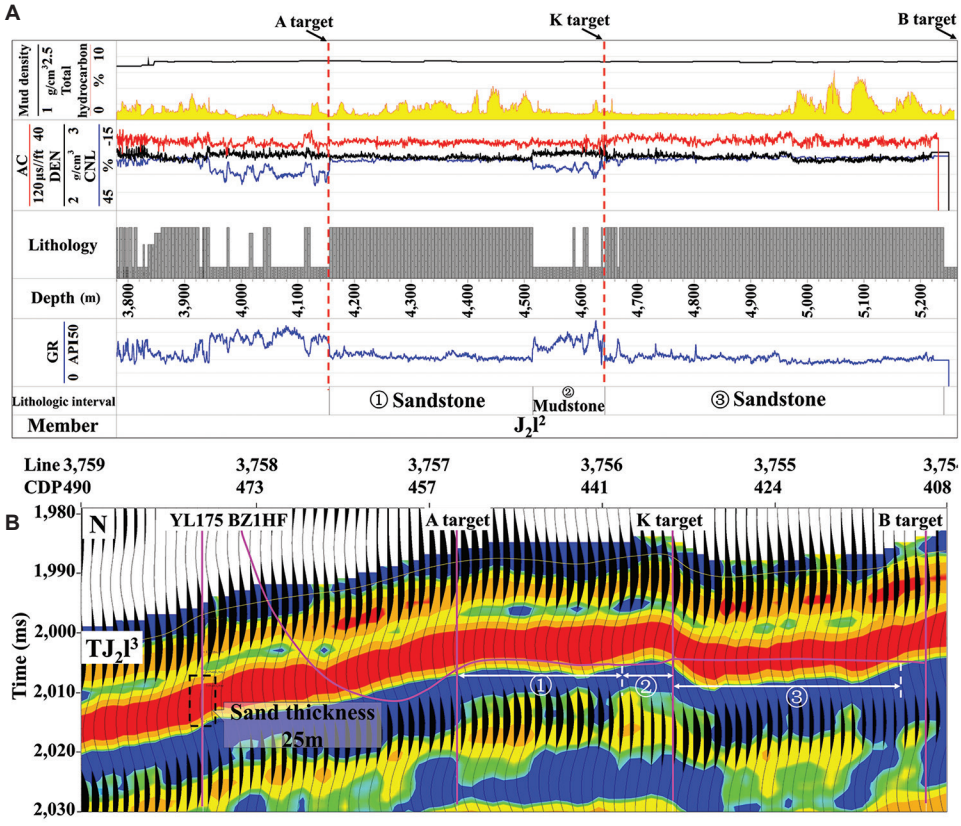


**Figure 17.** Comparison diagram of inversion and actual drilling results in the second member, through Well BZ1HF, Bazhong Block. (A) Comprehensive lithological histogram of Well BZ1HF. (B) Inversion prediction profile of P-wave/S-wave velocity (Vp/Vs) ratio through Well BZ1HF.
Abbreviation: CDP: Common depth point.

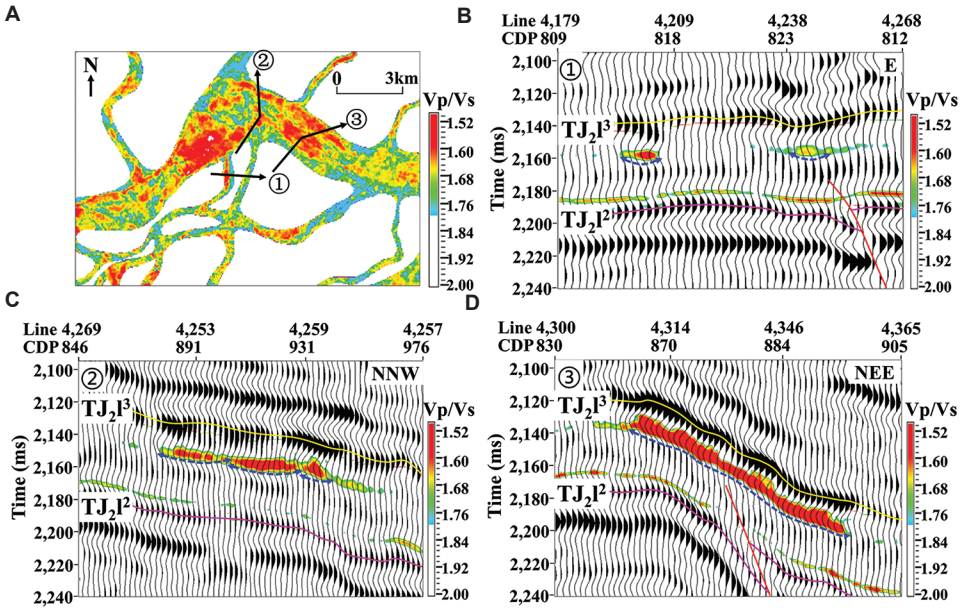


**Figure 18.** Pre-stack inversion prediction map of second member channels, Bazhong Block. (A) Channel prediction plan. (B) Isolated type. (C) Migratory type. (D) Superimposed type.
Abbreviations: CDP: Common depth point; E: East direction; NEE: North-east-east direction; NNW: North-north-west direction; Vp/Vs: P-wave velocity/S-wave velocity.

Building on the inversion results, this study further investigated the spatial distribution characteristics of $J_2l^2$ channels across different geomorphological segments. By applying the geological classification model established in Figure 15, three distinct channel types were analyzed: narrow, straight-wide, and high-sinuosity segments (Figure 18). The analysis revealed a systematic distribution pattern: isolated channel sand bodies of limited scale predominantly occurred in narrow segments; migratory sand bodies with strong lateral heterogeneity developed mainly in high-sinuosity segments; while thick, large-scale superimposed sand bodies characterized the straight-wide segments.

The production performance of Well BZ1HF, yielding 126.00 $m^3$/d of oil and 57,700 $m^3$/d of gas, confirmed that straight-wide segments represent the most favorable exploration targets. The methodology demonstrated in this study successfully captured the internal architectural complexity of $J_2l^2$ channels and provides reliable technical support for subsequent exploration and reservoir evaluation.

## 5. Conclusion

This study presents a pre-stack seismic workflow centered on GGD prior constraints to enhance the characterization of complex channel sandstones in the $J_2l^2$ member. Key findings demonstrated that pre-stack AVO analysis effectively identified an optimal incident angle range (30–40°), which, when applied through partial stacking, resolved the complex lithological heterogeneities encountered in Well FL101HF. Furthermore, AVO gradient attributes were established as a highly sensitive indicator for delineating lateral lithological variations within the channels, a finding validated across both the Fuxing and Bazhong Blocks. Integrating these AVO attributes with inter-well models to construct a low-frequency facies-controlled model significantly improved the lateral predictive capability of the subsequent GGD-constrained pre-stack inversion. This method provides a robust approach for fine-scale vertical and lateral prediction of complex channels, offering critical technical support for tight sandstone exploration and development.

## Acknowledgments

None.

## Funding

None.

## Conflict of interest

The authors declare no potential conflict of interest.

## Author contributions

*Conceptualization:* Meng Yuan
*Formal analysis:* Chang Sun
*Investigation:* Jianlong Su
*Methodology:* Zhiwei Miao
*Visualization:* Lei Pan
*Writing–original draft:* Meng Yuan
*Writing–review & editing:* Meng Yuan

## Availability of data

All data analyzed have been presented in the paper.

## References

1. Wu XY, Liu TY. Analysis of seismic spectral attenuation based on Wigner-Ville distribution for sandstone reservoir characterization-a case study from West Sichuan Depression, China. *J Seismic Explor*. 2010;19(1):69-85.

2. Zhang DW, Yang Y. Exploration potential and development direction of continental tight sandstone gas in the Sichuan basin. *Natural Gas Industry*. 2022;42(1):1-11.

   doi: 10.3787/j.issn.1000-0976.2022.01.001

3. Liu H, Lei X, Mao C, Li S. Improving reservoir thickness prediction using seismic attributes and attributes fusion. *Acta Geophysica*. 2014;62(3):544-563.

   doi: 10.2478/s11600-013-0174-5

4. Li QZ. Discussion on seismic exploration of lithologic reservoirs. *Litholgic Reserv*. 2008;20(2):45-54.

   doi: 10.3969/j.issn.1673-8926.2008.02.001

5. Li GF, Xiong JL, Zhou H, Zhai TL. Seismic reflection characteristics of fluvial sand and shale interbedded layers. *Appl Geophys*. 2008;5(3):219-229.

   doi: 10.1007/s11770-008-0025-3

6. Bi J, Gu H, Liu S, Guan X. Analysis on seismic response characteristics of channel sands and its influence factors: Case study of Upper Guantao Formation in KD1 area. *Geophys Prospect Petrol*. 2013;52(1): 97-103. [Article in Chinese].

   doi: 10.3969/j.issn.1000-1441.2013.01.015

7. Zhang X, Hu G, Fan T, Jing Y, Wang H, Yu B. Seismic response analysis and prediction for fluvial reservoir architecture. *China Offshore Oil Gas*. 2018;30(1):110-117. [Article in Chinese].

   doi: 10.11935/j.issn.1673-1506.2018.01.013

8. Li HH, Yue DL, Li W, Guo CC, Li X, Lyu M. Identification of point bar and abandoned channel of meandering river by spectral decomposition inversion based on machine learning. *Oil Geophys Prospect*. 2023;58(2):358-368.

   doi: 10.13810/j.cnki.issn.1000-7210.2023.02.013

9. Zhang JL, Cheng BJ, Xu TJ, Yong L. Identification of paleochannels by seismic attribute principal component analysis. *Oil Geophys Prospect*. 2023;58(1):190-195.

   doi: 10.13810/j.cnki.issn.1000-7210.2023.01.020

10. Xu H, Du X, Gao J, *et al*. Quantitative interpretation of sedimentary microfacies based on waveform clustering: A case study of X oilfield, Middle East. *Geophys Prospect Petrol*. 2018;57(5):744-755. [Article in Chinese]

    doi: 10.3969/j.issn.1000-1441.2018.05.014

11. Lu M, Bai JH, Jiao YL, *et al*. A PCA and wavelet packet transform integrated method for high-precision identification of abandoned channels in large meandering river systems. *J Geophys Eng*. 2025;22(5):1392-1405.

    doi: 10.1093/jge/gxaf082

12. Qian YL, Hu QX, Wang XH, Wang KP, Shi QD. Application of seismic waveform indicator inversion in thin sandstone prediction technology. *J Chongqing Univ Sci Technol (Nat Sci Ed)*. 2017;19(6):17-20.

    doi: 10.19406/j.cnki.cqkjxyxbzkb.2017.06.005

13. Gui PJ, Gao ZP, Cao SH, Wen LF. Application of AVO based on pre-stack seismic data in subtle channel identification of Dongsheng gas field. *Petrol Geol Eng*. 2022;36(6):1-7.

    doi: 10.3969/j.issn.1673-8217.2022.06.001

14. Liu XY, Li MH, Ye TR. Fine characterization of complicated channels in Western Sichuan and identification of sedimentary facies. *Geophys Prospect Petrol*. 2019;58(05):750-757.

    doi: 10.3969/j.issn.1000-1441.2019.05.014

15. Sun ZT, Yin XY, Ji YZ. Angle-dependent seismic attenuation-based gas-bearing detection of a sandstone river channel reservoir in the western Sichuan basin. *J Geophys Eng*. 2024;21(3):913-921.

    doi: 10.1093/jge/gxae042

16. Sotelo V, Almanza O, Montes L. Post-stack seismic inversion through probabilistic neural networks and deep forward neural networks. *Earth Sci Inform*. 2024;17(3):1957-1966.

    doi: 10.1007/s12145-024-01251-4

17. Yang T, Wang PQ, Li QC, Huo KY, Li W, He XK. A pre-stack nonlinear inversion method for joint PP-PS wave based on exact Zoeppritz equation. *Oil Geophys Prospect*. 2025;60(1):152-203.

    doi: 10.13810/j.cnki.issn.1000-7210.20240015

18. Wang J, Wu YN, Wang T, Jia WL, Bao YF, Liu LF. Multi-level sparse regularization inversion method for seismic frequency division: A case study from the second member of paleogene dongying formation in shijiutuo uplift, bozhong sag. *Litholgic Res*. 2025;37(4):38-49.

    doi: 10.12108/yxyqc.20250404

19. Chen K, Dai JC, Wei W, *et al*. Lithofacies classification of tight sandstone based on bayesian facies-AVO attributes: A case study of the first member of jurassic shaximiao formation in central sichuan basin. *Litholgic Res*. 2024;36(5):111-121.

    doi: 10.12108/yxyqc.20240511

20. Yang WY, Wei XJ, Li HS. The past, present and future of intelligent geophysical technology. *Lithologic Res*. 2024;36(2):170-188.

    doi: 10.12108/yxyqc.20240216

21. Zhang SH, Liu YJ, Liu XH. Prediction technique of high-quality reservoir in tight reservoir of the sixth member of Xujiahe formation in Jiannan area. *Lithologic Reserv*. 2015;27(3):98-102.

    doi: 10.3969/j.issn.1673-8926.2015.03.015

22. Zhou ZQ. Simulation and prediction of tight sandstone reservoirs based on waveform facies-controlled inversion: A case study from the second member of Paleogene Kongdian Formation in Southern Cangdong sag. *Lithologic Reserv*. 2024;36(5):77-86.

    doi: 10.12108/yxyqc.20240508

23. Niu LP, Hu HF, Zhou D, Zheng XD, Geng JH. Bayesian prestack seismic stochastic inversion based on the exact Zoeppritz equation. *Geophys Geochem Explor*. 2024;48(1):77-87.

    doi: 10.11720/wtyht.2024.2572

24. Cao YM, Zhou H, Yu B, Zhang YG, Dai SL. Prestack seismic stochastic inversion method based on spatial co-simulation. *Oil Geophys Prospect*. 2024;59(2):268-278.

    doi: 10.13810/j.cnki.issn.1000-7210.2024.02.009

25. Wu S, Han B, Ji LX, Sun ZX. Pre-stack AVO inversion for estimating effective pressure in sandstone reservoirs. *Oil Geophys Prospect*. 2024;59(5):1165-1173.

    doi: 10.13810/j.cnki.issn.1000-7210.2024.05.020

26. Huang HD, Yuan S, Zhang Y, Zeng J, Mu W. Use of nonlinear chaos inversion in predicting deep thin lithologic hydrocarbon reservoirs: A case study from the Tazhong oil field of the Tarim Basin, China. *Geophysics*. 2016;81(6):B221-B234.

    doi: 10.1190/geo2015-0705.1

27. Yin XY, Zhou QC, Zong AY, Liu HQ. AVO inversion with t-distribution as priori constraint. *Geophys Prospect Petrol*. 2014;53(1):84-92.

    doi: 10.3969/j.issn.1000-1441.2014.01.012

28. Zhang J, Gao J, Wang L, Dong B, Cai Z, Cheng R. Study on multicomponent amplitude versus offset forward modelling of thin layer gas hydrate using the Brekhovskikh equation. *Geophys Prospect*. 2023;72(4):1350-1361.

    doi: 10.1111/1365-2478.13375

29. Rutherford SR, Williams RH. Amplitude-versus-offset variations in gas sands. *Geophysics*. 1989;54(6):680.

doi: 10.1190/1.1442696

30. Chen X, Li S, Wei Z, Ning J, Yang X, Pre-stack seismic inversion based on one-dimensional GRU combined with two-dimensional improved ASPP. *J Geophys Eng*. 2024;21(6):1791-1809.

doi: 10.1093/jge/gxae106

31. Yang YM, Yin XY, Li K, Zhang F, Gao JH. Fast pre-stack multi-channel inversion constrained by seismic reflection features. *Petrol Sci*. 2023;20(4):2060-2074.

doi: 10.1016/j.petsci.2023.02.009

32. Zhang S, Huang HD, Dong YP, Yang X, Wang C, Luo YN. Direct estimation of the fluid properties and brittleness via elastic impedance inversion for predicting sweet spots and the fracturing area in the unconventional reservoir. *J Nat Gas Sci Eng*. 2017;45:415-427.

doi: 10.1016/j.jngse.2017.04.028

33. Wu S, Wang Y, Li Q, He Z, Geng J. Joint data-driven and physics-driven prestack amplitude-variation-with-angle elastic parameter inversion. *Geophysics*. 2024;89(1):R17-R32.

doi: 10.1190/geo2023-0135.1

34. Zuo Y, Zong Z, Li K, Luo K. Bayesian AVOAz inversion of fluid and anisotropy parameters using Gibbs sampling with AISM algorithm. *IEEE Trans Geosci Remote Sens*. 2024;62:1-15.

doi: 10.1109/tgrs.2024.3484435

35. Wang C, Yin X, Shi XW, Pan SL, Gou QY. Direct prediction method of fracturing ability in shale formations based on pre-stack seismic inversion. *J Seism Explor*. 2022;31(5):407-424.

36. Gao B, Ma F. Symmetric alternating direction method with indefinite proximal regularization for linearly constrained convex optimization. *J Optimiz Theor Applic*. 2017;176(1):178-204.

doi: 10.1007/s10957-017-1207-z

37. Zhang X, Li YW, Guan X, Long JY, Xiong Y. Research and application of pre-stack fast inversion technology based on lithology data reconstruction. *Oil Geophys Prospect*. 2024;59(5):1141-1154.

doi: 10.13810/j.cnki.issn.1000-7210.2024.05.018

38. She YW, Zhang MB, Wang YG, Zhang Y, Li F. Application of phase-controlled pre-stack inversion technique based on rock physics analysis in bauxite reservoir prediction: A case study of the Qingcheng district in the Ordos Basin. *Nat Gas Geosci*. 2024;35(8):1432-1440.

doi: 10.11764/j.issn.1672-1926.2024.05.001

39. Zhang S, Chang S, Huang H, *et al*. Prediction of favorable carbonate reservoirs under extremely thick salts via poststack facies-controlled and prestack zoeppritz equation inversions in the Santos basin of Brazil. *Geofluids*. 2020;2020(1):6205185.

doi: 10.1155/2020/6205185

40. Zhang S, Huang H, Zhu B, Li H, Zhang L. Seismic facies-controlled prestack simultaneous inversion of elastic and petrophysical parameters for favourable reservoir prediction. *Explor Geophys*. 2018;49(5):655-668.

doi: 10.1071/EG17048

41. Jia W, Zong Z, Lan T. Elastic impedance inversion incorporating fusion initial model and kernel Fisher discriminant analysis approach. *J Petrol Sci Eng*. 2023;220:111235.

doi: 10.1016/j.petrol.2022.111235

42. Lyu Q, Lin Z, She Y, Zhang C. A comparison of typical ℓp minimization algorithms. *Neurocomputing*. 2013;119:413-424.

doi: 10.1016/j.neucom.2013.03.017

## Appendix 1

### Appendix: Solution methods for Equation 13

**Equation 14** in the original manuscript is written in the vector form as follows:

$$\mathrm{J}(\mathbf{m}) = \min_{\mathbf{m}} \left( \frac{1}{2} \left\| \mathbf{D} - \mathbf{G}\mathbf{m} \right\|_2^2 + \lambda \left\| \mathbf{D}\mathbf{m} \right\|_\alpha^\alpha + \beta \left\| \mathbf{m} - \mathbf{m}_{\mathrm{ref}} \right\|_2^2 \right) \tag{A1}$$

A Lagrangian operator term was introduced into the above formula. H = Lm converts the above formula into an unconstrained optimization problem. The new formula is as follows:

$$\mathrm{J}(\mathbf{m}) = \min_{\mathbf{m}} \left( \frac{1}{2} \left\| \mathbf{D} - \mathbf{G}\mathbf{m} \right\|_2^2 + \lambda \left\| \mathbf{H} \right\|_\alpha^\alpha + \beta \left\| \mathbf{m} - \mathbf{m}_{\mathrm{ref}} \right\|_2^2 + \gamma \left\| \mathbf{H} - \mathbf{L}\mathbf{m} \right\|_2^2 - 2\gamma\mu^{\mathrm{T}} \left( \mathbf{H} - \mathbf{L}\mathbf{m} \right) \right) \tag{A2}$$

Here, γ denotes the regularization parameter term of the Lagrange multiplier, and is the Lagrange multiplier corresponding to the constraint term in **Equation A2**. Based on the framework of the Alternating Direction Method of Multipliers, the objective function is decomposed into sub-functions related to m and H, respectively. Among them, the objective function associated with m is the same as **Equation 14** in the manuscript, which is expressed as follows:

$$\mathrm{J}(\mathbf{m}) = \min_{\mathbf{m}} \left( \frac{1}{2} \left\| \mathbf{D} - \mathbf{G}\mathbf{m} \right\|_2^2 + \beta \left\| \mathbf{m} - \mathbf{m}_{\mathrm{ref}} \right\|_2^2 + \gamma \left\| \mathbf{H} - \mathbf{L}\mathbf{m} \right\|_2^2 - 2\gamma\mu^{\mathrm{T}} \left( \mathbf{H} - \mathbf{L}\mathbf{m} \right) \right) \tag{A3}$$

**Equation A3** is a conventional optimization problem, and the update rule for m can be directly derived using the least squares method for solution using **Equation A4**:

$$\mathbf{m}^{i+1} = \left( \mathbf{G}^{\mathrm{T}}\mathbf{G} + \beta\mathbf{I} + \gamma\mathbf{L}^{\mathrm{T}}\mathbf{L} \right)^{-1} \left( \mathbf{G}^{\mathrm{T}}\mathbf{L} + \beta\mathbf{m}_{\mathrm{ref}} + \gamma\mathbf{L}^{\mathrm{T}} \left( \mathbf{H}^i - \mu^i \right) \right) \tag{A4}$$

where I denotes the identity matrix. After obtaining the updated m, the sub-function in the following formula can be solved using **Equation A5**:

$$\mathrm{J}(\mathbf{H}) = \min_{\mathbf{H}} \left( \lambda \left\| \mathbf{H} \right\|_\alpha^\alpha + \gamma \left\| \mathbf{H} - \mathbf{L}\mathbf{m} \right\|_2^2 - 2\gamma\mu^{\mathrm{T}} \left( \mathbf{H} - \mathbf{L}\mathbf{m} \right) \right) \tag{A5}$$

In **Equation A5**, the objective function is an optimization problem analogous to the one based on the Lp quasi-norm, and the soft-thresholding shrinkage algorithm is introduced herein for its solution:[42]

$$\mathbf{X}^{k+1} = \mathbf{L}\mathbf{m}^{i+1} + \mu^i \tag{A6}$$

By substituting **Equation A6** into **Equation A5**, we can obtain

$$\mathbf{H}^{i+1} = \underset{\mathbf{Q}}{\operatorname{argmin}} \ \gamma \left\| \mathbf{H} - \mathbf{X}^{i+1} \right\|_2^2 + \lambda \left\| \mathbf{H} \right\|_p^p \tag{A7}$$

From the iterative reweighted algorithm, the approximate solution of each iteration can be obtained as follows (**Equation A8**):

$$\mathbf{H}^{k+1} = \min_{\mathbf{V}} \ \gamma \left\| \mathbf{H} - \mathbf{X}^{i+1} \right\|_2^2 + \sum_{k=1}^{n} \lambda p \left( \left| H_k^i \right| + \varepsilon \right)^{p-1} \left| \mathbf{H}_k \right| \tag{A8}$$

In **Equation A8**, by setting $t_i^{k+1} = \lambda p \left( \left| H_i^k \right| + \varepsilon \right)^{p-1}$, it can be further rewritten into the form of the L1-norm, which can be solved via soft-thresholding calculation, as shown in **Equation A9**:

$$\mathbf{H}^{k+1} = \min_{\mathbf{V}} \ \gamma \left\| \mathbf{H} - \mathbf{X}^{i+1} \right\|_2^2 + \sum_{k=1}^{n} t_k^{i+1} \left| H_k \right| \tag{A9}$$

The above **Equation A9** can be calculated using the one-dimensional soft-thresholding function, and the result is obtained as follows (**Equation A10**):

$$\begin{aligned}\mathbf{H}^{i+1} &= \text{shrink}\left(\mathbf{X}^{k+1}, \frac{\mathbf{t}^{i+1}\gamma}{\lambda}\right) \\ &= \max\left\{\mathbf{X}^{i+1} - \frac{\mathbf{t}^{i+1}\gamma}{\lambda}, 0\right\} \bullet \text{sign}\left(\mathbf{X}^{i+1}\right)\end{aligned} \tag{A10}$$

Where $\text{sign}(\bullet)$ is the sign function.

The solution for $\mu$ in **Equation A2** can be directly obtained using the gradient descent method in **Equation A11**.

$$\mu^{i+1} = \mu^{i} + \left(\mathbf{L}\mathbf{m}^{i+1} - \mathbf{H}^{i+1}\right) \tag{A11}$$

ACCSCIENCE PUBLISHING

Journal of Seismic Exploration

ARTICLE

# Convolutional autoencoder with local wavefield characteristic constraint for suppressing near-surface seismic scattered waves

**Daling Hou, Jixiang Xu*, and Meng Li**

Institute of Oil and Gas Geophysics, Research Institute of Petroleum Exploration and Development, Beijing, China

## Abstract

In mountainous seismic exploration, complex near-surface environments cause strong wave scattering, reducing the signal-to-noise ratio and complicating data processing. Therefore, suppressing scattered waves is crucial. To address this issue, this study proposes a convolutional autoencoder constrained by local scattered wave characteristics to suppress near-surface scattered waves (NSWs) in full-wavefield seismic data. This method uses the scattered waves predicted by seismic interferometry as the network input, and the original seismic records containing true scattered waves as the label. Since there are differences in amplitude and phase between the predicted scattered waves and the true scattered waves, the network introduces local wavefield features of the scattered waves for constraint, and adds a smoothness regularization term in the loss function to ensure the continuity of the output waveform. After training, the network maps the energy of predicted scattered waves into the actual seismic records, thereby accurately extracting scattered waves. Finally, by subtracting the network output from the original records, clean data with scattered waves removed can be obtained. This method is a self-supervised learning strategy and does not require additional clean signal samples. During training, the weights of each item in the loss function can be dynamically adjusted to guide the network to focus on local scattered-wave features, avoid learning effective wave information, and ensure that only scattered-wave components are retained in the output. Practical application results show that this method can effectively suppress NSWs and improve the signal-to-noise ratio of seismic data.

***Keywords:*** Near-surface scattered waves; Convolutional autoencoder; Interferometry; Wavefield characteristics

***Corresponding author:**
Jixiang Xu
(xjx6611@petrochina.com.cn)

**Citation:** Hou D, Xu J, Li M. Convolutional autoencoder with local wavefield characteristic constraint for suppressing near-surface seismic scattered waves. *JSeismicExplor.* 2026;35(1):221-236. doi: 10.36922/JSE025470112

**Received:** November 17, 2025

**Revised:** December 23, 2025

**Accepted:** December 26, 2025

**Published online:** January 27, 2026

**Copyright:** © 2026 Author(s). This is an Open-Access article distributed under the terms of the Creative Commons Attribution License, permitting distribution, and reproduction in any medium, provided the original work is properly cited.

**Publisher's Note:** AccScience Publishing remains neutral with regard to jurisdictional claims in published maps and institutional affiliations.

## 1. Introduction

When seismic waves propagate underground, variations caused by three-dimensional spatial heterogeneity are referred to as scattered waves. In complex regions, especially in the near-surface, medium heterogeneity is the greatest. The widespread presence of small-scale heterogeneities, strong velocity and density contrasts, and irregular interfaces leads to significant impedance contrasts along the wave propagation path, thereby generating wave "reflections." Because these heterogeneities are much smaller in scale and more irregular in geometry than subsurface reflecting interfaces, the resulting

wavefield response mainly manifests as scattering. These scattered waves overlap with the effective waves in time, space, and frequency, reducing the signal-to-noise ratio (SNR) of seismic data and affecting the accuracy of subsequent inversion and imaging. Wu *et al.*[1] pointed out that the primary cause of low SNR in seismic data is the influence of near-surface scattered waves (NSWs). Therefore, suppressing NSWs is a critical step in obtaining high-quality seismic data.

Scattered-wave suppression is a complex task that involves not only analyzing the properties of scattered waves but also developing advanced processing techniques.[2] Traditional filtering methods often remove scattered waves at the cost of losing effective waves. Thus, an alternative approach—analyzing the characteristics of scattered waves, predicting the true scattered wavefield, and subtracting it from seismic data—minimizes the impact on effective waves and is widely applied in practice. Campman *et al.*[3] introduced impedance functions to model and suppress NSWs. Liu *et al.*[4] estimated and removed scattered waves from radial and vertical components using filtering and correlation analysis based on transverse component assumptions, thereby improving data SNR. Almuhaidib and Toksöz[5] employed controllable filters to estimate spatial variations in noise and used directional non-linear filters for noise separation. In recent years, seismic interferometry has been effectively applied to suppress scattered waves. Xu *et al.*[6] provided a detailed discussion on NSW characteristics and the principles of scattered-wave interferometry, enhancing the coherence of scattered waves to separate them from true records. Halliday *et al.*[7] proposed a model-driven seismic interferometry approach, using models as inputs to estimate scattered surface waves between sources and receivers. Xu *et al.*[8] applied an improved source–receiver interferometry method to reconstruct NSW fields from pre-stack data and then adaptively subtracted the predicted scattered waves using matched filtering, effectively suppressing NSWs.

Deep learning, a subfield of machine learning, has been the fastest-growing branch in the past decade.[9] Deep neural networks construct multi-layer networks to represent targets at multiple levels, aiming to use hierarchical features to capture abstract semantic information from data. Among them, convolutional neural networks (CNNs) leverage local connectivity and weight sharing to effectively capture local features while reducing the number of parameters. In recent years, deep neural networks have shown promising applications in seismic denoising. Through synthetic and real-data demonstrations, deep learning has exhibited significant potential in attenuating random noise, linear noise, and multiple reflections.[10] Yu *et al.*[11] used a denoising CNN to suppress surface waves in synthetic data and transferred the trained network to real seismic data. Liu *et al.*[12] trained a convolutional autoencoder (CAE) using synthetic noise and standard induced polarization signals to denoise continuous random noise in induced polarization signals. Sui *et al.*[13] developed data-adaptive dictionaries through deep unfolding dictionary learning to construct training networks suitable for different noise levels. Li *et al.*[14] designed an automated training data generation workflow based on the noise characteristics of nodal seismic acquisition systems, achieving superior performance in suppressing environmental noise compared to traditional methods. In practical seismic denoising, obtaining noise-free sample data is challenging. Supervised learning often uses traditional denoised data or synthetic data as labels, whereas self-supervised and unsupervised learning methods eliminate the need for clean labels. As a result, deep learning applications in seismic denoising are shifting from supervised to self-supervised and unsupervised approaches, which better align with seismic processing workflows. Song *et al.*[15] employed a CAE for unsupervised random noise suppression. Shao *et al.*[16] applied the Noisy2Noisy framework to remove random noise, achieving supervised learning-level denoising performance without labeled data. Wu *et al.*[17] proposed a self-supervised deep learning approach based on the Neighbor2Neighbor framework to suppress random noise. For coherent noise suppression, a series of self-supervised denoising networks was introduced to remove surface-related multiples, demonstrating promising results;[18-21] Sun *et al.*[22] proposed a multi-channel U-Net with multi-mode and multi-model capabilities for suppressing multiples; Qi *et al.*[23] introduced an interpretable Fast Iterative Shrinkage-Thresholding Algorithm Network for adaptive multiple suppression. Despite significant progress and breakthroughs in seismic denoising using deep learning, research and applications targeting NSW suppression remain largely unexplored.

In image processing and computer vision, commonly used image quality assessment methods are often based on error visibility, such as mean-squared error (MSE) and Peak SNR. While these methods effectively quantify image differences, they fail to accurately reflect human visual perception of image quality. To address this, Wang and Bovik[24] proposed the structural similarity index (SSIM), which evaluates image similarity by considering luminance, contrast, and structure, thereby aligning more closely with human visual perception. SSIM has been widely applied in image denoising and reconstruction. In recent years, SSIM has also been adopted in seismic denoising, seismic interpolation, and velocity modeling. Almadani *et al.*[25] used SSIM to evaluate the denoising performance

of convolutional sparse coding. Sun and Williamson[26] applied SSIM to assess the advantages of frequency-constrained neural networks in seismic interpolation. Simon *et al.*[27] employed SSIM to evaluate the effectiveness of transfer learning in seismic velocity modeling. In this study, we modify and extend SSIM to better capture the characteristics of seismic wavefields and incorporate it into the loss function to enhance network performance.

To more effectively suppress NSWs, this study proposes a CAE constrained by local scattered wave characteristics (LSC-CAE). This method does not rely on additional clean data as labels but instead constructs a self-supervised denoising process. The core idea is to predict the scattered-wave structures, restore their energy to the real-data level, and suppress them by subtraction from the full-wavefield data. Specifically, NSWs are first predicted using seismic interferometry and then used as the input of the CAE; at the same time, full-wavefield data containing scattered waves are used as labels to guide the network in learning the spatial and temporal characteristics of scattered waves. To enable effective training, we designed a composite loss function composed of MSE, a local scattered-wave feature loss, and a waveform-smoothing regularization term, thereby encouraging the network to focus on the structural and energy features of scattered waves and achieve energy matching with real scattered waves. Finally, by subtracting the network output from the full-wavefield data, the denoised seismic record was obtained. In addition, to enhance the network's ability to model complex wavefield structures, a multi-head self-attention mechanism was introduced in the intermediate layers of the CAE to improve the network's perception of global scattered-wave features. Meanwhile, residual structures were introduced to accelerate training and enhance network stability. Application results on real seismic data show that the proposed method can effectively suppress scattered waves while preserving the integrity of effective waveforms, demonstrating good denoising performance and practical value.

## 2. Methods

### 2.1. Near-surface interferometry

Seismic interferometry is a wavefield reconstruction technique based on wave theory that extracts intercorrelation information from seismic data to reconstruct seismic wave propagation paths. The theoretical foundation of seismic interferometry lies in the Green's function, which allows the cross-correlation of wavefields between two points to be reconstructed as the seismic response of one point acting as a virtual source and the other as a receiver. Schuster[28] first introduced the concept of seismic wave interferometry in 2001 and subsequently conducted a series of studies exploring its principles.[29-33] Following this, several studies provided comprehensive analyses of the principles, advancements, and applications of seismic interferometry.[34-36] Today, seismic interferometry has been widely applied in seismic imaging and seismic monitoring, playing a crucial role in enhancing subsurface characterization and detecting temporal changes in the Earth's structure.

Under the high-frequency and far-field approximations, the source imaging and seismic monitoring, playing a crucial **Equation 1**:[37]

$$G(y_1,x_1;\omega)+G^*(y_1,x_1;\omega)\approx\frac{4}{(\rho c)^2}\times \oint_{S_1}G(y_1,x;\omega)dS_1\oint_{S_2}G^*(y,x;\omega)G(y,x_1;\omega)dS_2 \quad (1)$$

Where $\omega$ is the angular frequency, $\rho$ and $c$ represent density and velocity, * denotes the complex conjugate, and $G(y_1,x_1;\omega)$ represents the wavefield generated by point source $x_1$ at point $y_1$, and similarly for $G(y_1,x;\omega)$ and $G(y,x_1;\omega)$.

When intersource interferometry is computed using correlation, it introduces wavelet distortion in the frequency domain. The amplitude spectrum of the reconstructed virtual wavelet becomes the cube of the original wavelet spectrum, leading to amplitude distortion and peak-like features. Deconvolutional interferometry can effectively remove wavelet effects from seismic records. Therefore, this study employed the improved source–receiver interferometry method[8], expressed as **Equation 2**:

$$G(y_1,x_1;\omega)+G^*(y_1,x_1;\omega)\approx\frac{4}{(\rho c)^2}\times \oint_{S_1}G(y_1,x;\omega)dS_1\oint_{S_2}\frac{G(y,x_1;\omega)}{G(y,x;\omega)}dS_2 \quad (2)$$

We used deconvolution to replace cross-correlation calculations, making the reconstructed wavelet closer to the original in shape and relative amplitude, and reducing nonphysical artifacts and spurious energy generated by source interference. Then, a convolution-based shot-receiver interferometry method compensated for the common path between the near-surface scatterers and common shot points, restoring the wavefield's propagation characteristics. This procedure effectively suppressed the influence of the source wavelet and improved the quality of the reconstructed wavefield. Applying this method to predict the NSWs in the actual seismic data (Figure 1A), a wavefield dominated by scattered-wave energy was obtained (Figure 1B).

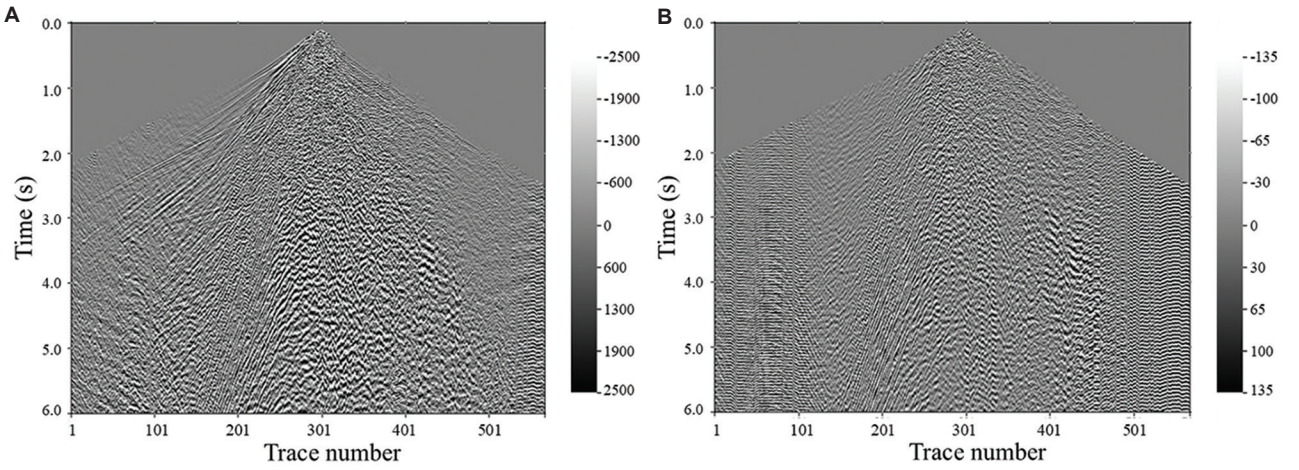


**Figure 1.** Single-shot record. (A) Full-wavefield data. (B) Interferometric predicted data.

### 2.2. Improved CAE

A CAE is a deep learning model that combines the concept of an autoencoder with the characteristics of CNNs. It replaces the fully connected layers in traditional autoencoders with convolutional and pooling layers, enabling the CAE to reduce the dimensionality and compress input data with fewer parameters while retaining important spatial features. This makes it well-suited for handling high-dimensional data. The CAE consists of an encoder and a decoder. The encoder, which includes convolutional and pooling layers, extracts invariant features and compresses the input into a latent space representation. The decoder uses deconvolutional layers to reconstruct the input from the latent-space representation. The network architecture is summarized in Figure 2.

During training, the CAE adjusted the hyperparameters of the convolutional and pooling layers to minimize the difference between the reconstructed image (obtained by adjusting the hyperparameters) and the original image. Ultimately, an optimal basic framework was identified, consisting of one convolutional layer, one pooling layer, and their corresponding hyperparameters. Additional convolutional and pooling layers were then stacked to form a large neural network, with a fully connected layer added at the end to create a CNN-based architecture. The learning process of the CAE is represented as **Equation 3**:

$$y = F(x,\theta) \tag{3}$$

where $x$ and $y$ represent the network's input and output, respectively. θ refers to the parameters that the network needs to learn, which include the weights $w_i$ and biases $b_i$ of each convolutional layer in the encoder, and the weights $w_d$ and biases $b_d$ of the deconvolutional layer in the decoder.

For seismic data, deep networks are typically required to extract complex waveform features, thereby providing a better and more comprehensive description of the target. However, when the network depth reaches a certain level, increasing it can degrade network performance due to the accumulation of errors during information transfer. To address this, He *et al.*[38] proposed a residual structure with identity mapping to avoid issues, such as gradient vanishing and model degradation, when the network depth increases. The residual structure adds the input to the learning result before passing it to the next learning unit, enabling deep networks to retain the complete information from previous layers. The information from identity mapping in the previous layer can be viewed as pre-learned knowledge, so each layer only needs to learn the difference between the existing knowledge and the ideal model. This can be expressed as **Equation 4**:

$$y_{i+1} = h(x_i)+F(x_i,\theta_i) \tag{4}$$

where $x_i$ is the input, the output $y_{i+1}$ is the result of adding the identity mapping $h(.)$ and the transformation function $f(.)$, where the transformation function may include multiple operations, such as convolution, normalization, and activation.

In seismic data, signals at different spatiotemporal locations may exhibit complex dependencies. Compared to the local receptive field of CNNs, the multi-head self-attention mechanism can directly capture global-scale features.[39] The core idea of self-attention is to compare each element in a sequence with all others and assign weights that reflect the degree of correlation between them. To further enhance feature extraction, this study employed a multi-head self-attention module. Specifically, eight independently learned linear

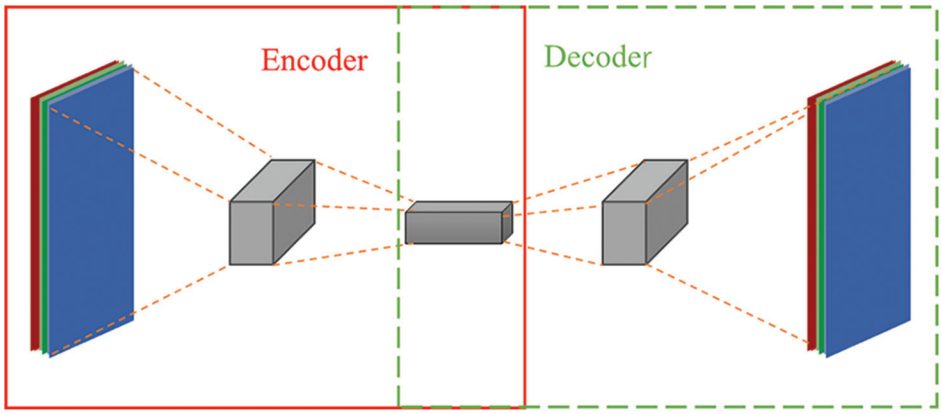


**Figure 2.** Convolutional autoencoder structure

projections were used to represent queries, keys, and values in different subspaces. The attention of each head was computed in parallel and then concatenated to generate the final output. The core principle and detailed computational process of the multi-head self-attention mechanism were as follows:

i) Project input feature matrix $\mathbf{X} \in \mathbb{R}^{n \times d_{model}}$ into queries, keys, and values.
Q=XW$^{Q}$, K=XW$^{K}$, V=XW$^{V}$, where $W^{Q}, W^{K}, W^{V} \in R^{d_{model} \times d_k}$, $d_k$ represents the dimension of the $Q/K$, which is typically set as $d_k = d_{model}/h$, where $h$ is the number of attention heads.

ii) Dimension splitting: The matrices $Q$, $K$, and V were split along the feature dimension $d_k$ into $h$ independent submatrices, each with a dimension of $d_k$:

$$Q=[Q_1,Q_2,\ldots.Q_h]$$
$$K=[K_1,K_2,\ldots.K_h]$$
$$V=[V_1,V_2,\ldots.\ V_h]$$

iii) Multi-head parallel computation: For each submatrix triplet $(Q_i,K_i,V_i)$, an independent single-head self-attention operation was performed to obtain $h$ output results:

$$Output_i = Soft\max\left(\frac{Q_i K_i^T}{\sqrt{d_k}}\right)V_i, i = 1,2,\ldots\ldots h$$

iv) Concatenation: The $h$ output results were concatenated along the feature dimension to obtain the output:

$$Output_{concat} = [Output_{1,}\ Output_{2,\ldots.}\ Output_{h}]$$

v) Then, a linear layer $W_O \in \mathbb{R}^{d_{model} \times d_{model}}$ was applied for feature fusion, resulting in the final multi-head self-attention output:

$$Output = Output_{contact} W_o$$

As shown in Figure 3, the proposed network with residual connections and a multi-head self-attention mechanism is referred to as the residual self-attention convolutional autoencoder (RS-CAE). The model adopted a U-Net style encoder-decoder framework, where both the encoder and decoder consisted of multiple stacked residual blocks. A multi-head self-attention module was inserted at the bottleneck layer to enable a more comprehensive representation of the global wavefield structure. This design enabled the network to capture both short- and long-range dependencies, establish long-distance relationships in higher-order features, and restore structural details of the wavefield, thereby enhancing the network's ability to distinguish scattered waves from other wavefield components.

The detailed configuration of the proposed RS-CAE is listed in Table 1.

## 2.3. Loss function

### *2.3.1. Local scattered-wave feature loss*

The SSIM was first proposed by Wang *et al.*[40] and was used for image denoising and reconstruction. The original image information was almost completely recovered through a simple point-to-point inverse linear brightness transformation, while the structural information of the reference image was well preserved. The SSIM primarily measures the luminance $l(x,x')$, contrast $c(x,x')$, and structure $s(x,x')$ of the input data and the output data, and the final similarity is a function of these three components, expressed as **Equation 5**:

$$S(x,x') = f(l(x,x'),c(x,x'),s(x,x')) \quad (5)$$

For seismic data, luminance reflects the difference in the mean amplitude between the input and output

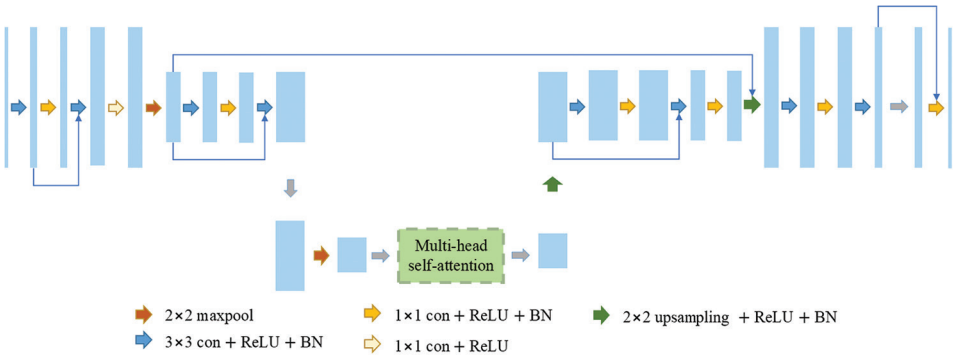


**Figure 3.** Structure diagram of the improved convolutional encoder
Abbreviations: BN: Batch normalization; ReLU: Rectified linear unit.

**Table 1. Parameters of residual-self-attention convolutional autoencoder (RS-CAE)**

| Module | Layer type | Kernel size | Channels | Output size | Activation |
|---|---|---|---|---|---|
| Encoder block 1-1 | Conv2D+BatchNorm | 3×3 | 1atc | 256×256 | ReLU |
| Encoder block 1-2 | Conv2D+BatchNorm | 1×1 | 64→64 | 256×256 | ReLU |
| Encoder block 2 | Conv2D+MaxPool+BatchNorm | 3×3/1×1/2×2 | 64 chN | 128×128 | ReLU |
| Encoder block 3 | Conv2D+BatchNorm | 3×3/1×1 | 128chNo | 128×128 | ReLU |
| Encoder block 4 | Conv2D+MaxPool+BatchNorm | 3×3/1×1/2×2 | 128ch56 | 64×64 | ReLU |
| Bottleneck (attention) | Multi-head self-attention (eight heads) | - | 256ads) | 64×64 | - |
| Decoder block 1-1 | ConvTranspose2D+BatchNorm | 3×3 | 256chNo | 128×128 | ReLU |
| Decoder block 1-2 | Conv2D+BatchNorm | 3×3/1×1 | 256chNo | 128×128 | ReLU |
| Decoder block 2 | Conv2D+BatchNorm | 3×3/1×1 | 256chNo | 128×128 | ReLU |
| Decoder block 3 | ConvTranspose2D+Conv2D+BatchNorm | 3×3/1×1 | 128chN | 256×256 | ReLU |
| Decoder block 4 | Conv2D+BatchNorm | 1×1 | 64 ch | 256×256 | ReLU |
| Output layer | Conv2D | 1×1 | 64 v | 256×256 | - |

Abbreviation: ReLU: Rectified linear unit.

data, indicating the consistency of the average energy distribution between the two datasets. Contrast measures the amplitude differences between the two datasets and evaluates whether the output data can preserve the relative amplitude variations of the input in the output, using the standard deviation as an estimate. Structural similarity reflects the differences in seismic waveform and phase between the input data and the network output, estimated using the value normalized by the standard deviation of the signal itself.

During the interferometric process, coherent signals are enhanced, resulting in a significant overall energy difference between the predicted scattered wave $x$ and the real data $y$. Therefore, directly applying the luminance term of SSIM is not suitable for scattered-wave analysis, while the relative amplitude and phase differences of the waveform are relatively small. Inspired by the SSIM, we defined a scattered-wave feature loss that constrained the network output's amplitude and waveform based on the contrast and structural differences among the predicted scattered waves, the true scattered waves, and the full-wavefield data, thereby guiding the network to suppress scattered waves without compromising effective waveforms.

The similarity of scattered-wave features is described using standard deviation and covariance, with the calculation formula as shown in **Equation 6**:

$$S_{SS} = \frac{2\sigma_{xx'} + 2C_1}{\sigma_x^2 + \sigma_{x'}^2 + C_1} \tag{6}$$

Where $C_1$ is a constant to prevent the denominator from being zero during the calculation, defined as **Equation 7**:

$$C_1 = (K_1 L)^2 \tag{7}$$

Typically, $K_1$ << 1and taken as 0.001–0.003, $L$ representing the range of normalized input data. $\sigma_x$ and $\sigma_{x'}$

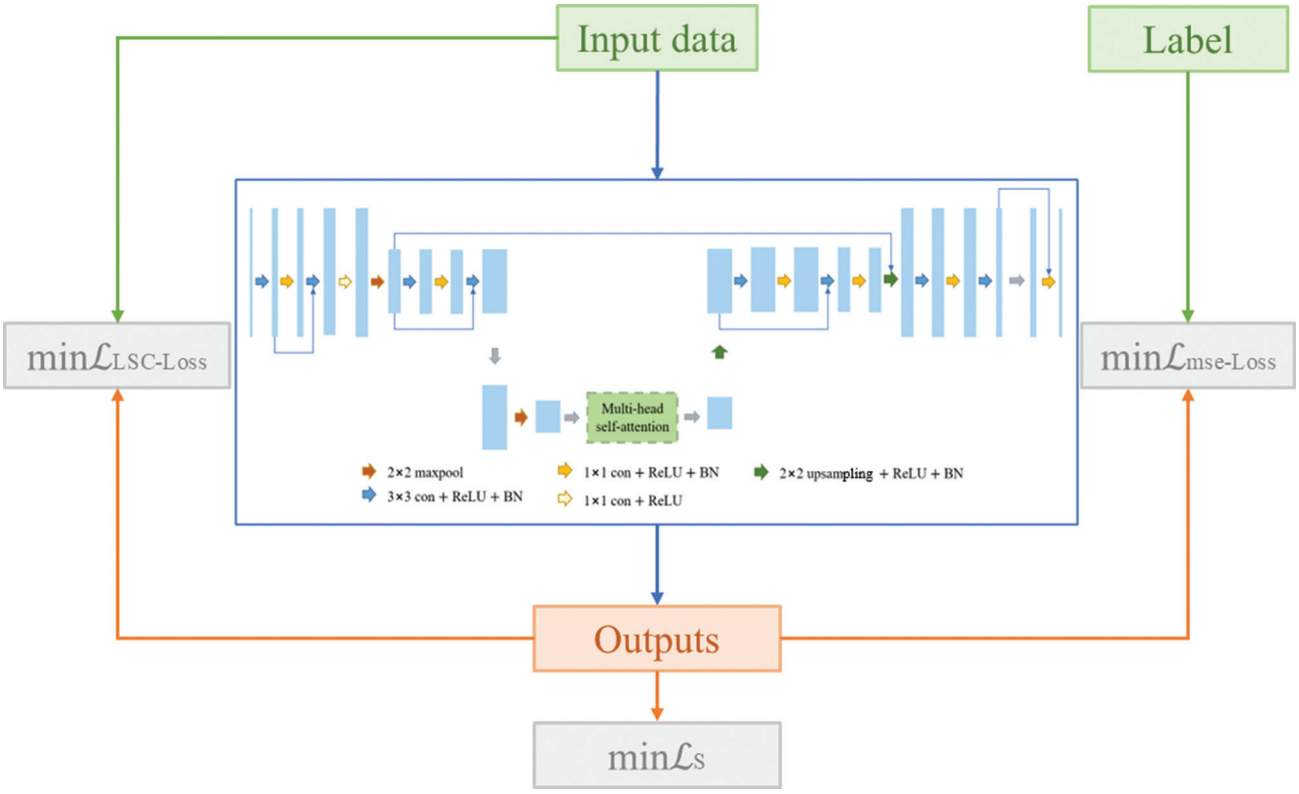


**Figure 4.** Construction of the loss function

are the standard deviations of the input and output data, defined as **Equations 8 and 9**:

$$\sigma_x = \left( \frac{1}{N-1} \sum_{i=1}^{N} \left( x_i - \mu_x \right)^2 \right)^{\frac{1}{2}} \tag{8}$$

$$\sigma_{x'} = \left( \frac{1}{N-1} \sum_{i=1}^{N} \left( x_i' - \mu_{x'} \right)^2 \right)^{\frac{1}{2}} \tag{9}$$

$\sigma_{xx'}$ is the covariance of $x$ and $x'$ that reflect the covariance of signals in structure, and is used to measure the similarity of data in local structure, that is, shape and phase. The calculation formula is shown in **Equation 10**:

$$\sigma_{xx'} = \frac{1}{N-1} \sum_{i=1}^{N} \left( x_i - \mu_x \right) \left( y_i - \mu_y \right) \tag{10}$$

$\mu_{x'}$ and $\mu_{y'}$ represent the mean values of the output data and the label data, respectively. $S_{SS}$ evaluates the similarity between the network output and the input. The training objective is to minimize the difference, so it needs to be transformed into a difference value to obtain the final local scattered-wave feature loss, which is given by **Equation 11**:

$$L_{LSC} = 1 - S_{SS} \tag{11}$$

### 2.3.2. Smoothing regularization

In 2017, Goodfellow *et al.*[41] stated in the book *Deep Learning* that any modifications that can improve the model's accuracy during testing and enhance the model's generalization ability can be considered regularization. The application of regularization terms is achieved by adding a penalty term to the model's loss function to enhance the model's generalization ability, such as $L_1$ and $L_2$ regularizations. Unlike the loss function, the added regularization term is independent of the label data, imposing certain prior knowledge constraints on the data to improve the model's denoising effectiveness. During the self-supervised denoising process, coherent scattered noise data exhibits good local continuity. Therefore, a smoothing regularization term is added to the loss function to constrain waveform continuity, using the first derivative differences of adjacent points in the network output to measure waveform continuity, as shown in **Equations 12 and 13**:

$$Loss_t = \frac{1}{N}\sum_{i=1}^{N}\sum_{j=1}^{M}\left(u(i+1,j)-u(i,j)\right)^2 \quad (12)$$

$$Loss_x = \frac{1}{M}\sum_{i=1}^{N}\sum_{j=1}^{M}\left(u(i,j+1)-u(i,j)\right)^2 \quad (13)$$

where $N$ and $M$ represent the time dimension and spatial dimension, respectively. **Equations 12 and 13** represent the squared differences of adjacent points in the two dimensions. Combining these two terms yields the final smoothing regularization term, as in **Equation 14**:

$$L_S = Loss_t + Loss_x \quad (14)$$

### 2.3.3. Composite loss function

The local scattered-wave characteristics loss is combined with the MSE loss, and a smoothing regularization term is added to guide the network in learning the scattered waves of the label data while avoiding excessive attention to effective waves, as shown in Figure 4. Specifically, MSE Loss serves as the reconstruction loss, minimizing the difference between the network output and the label data, ensuring the predicted scattered-wave energy closely matches the true values. In addition, to ensure that the network focuses on learning scattered-wave characteristics and ignores other wavefields, including reflected waves, a term $L_{LSC}$ is introduced to minimize the structural differences between the network output and the input data wavefield. This helps the network output retain the waveform and location information of the scattered waves. Seismic coherent noise and reflected waves differ from random noise, typically exhibiting continuity and specific shapes. Deep learning methods are data-driven and often lack interpretability in complex workflows, such as seismic signal denoising. Therefore, adding a regularization term to the loss function ensures the continuity of coherent noise wavefields, calculates the network output, and ensures the data conforms to wavefield characteristics, standardizing the learning process and enhancing the physical rationality of the network.

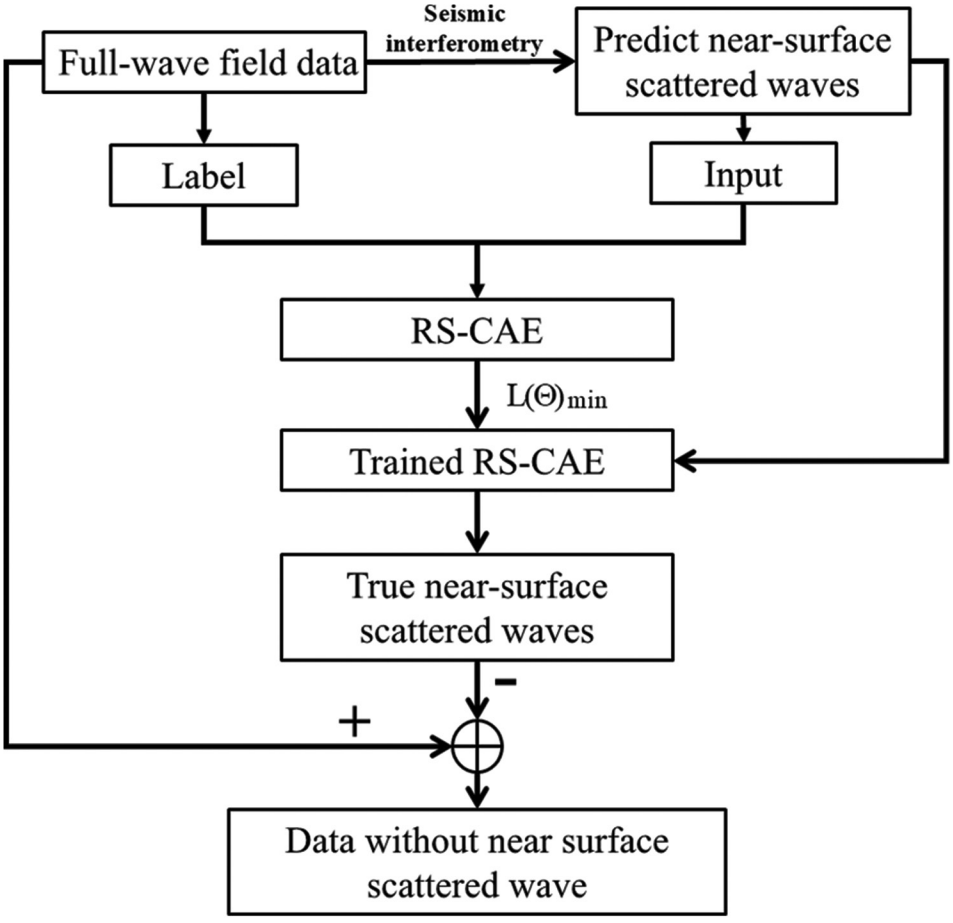


**Figure 5.** Flow chart of denoising
Abbreviation: RS-CAE: Residual-self-attention convolutional autoencoder.

Finally, the expression for the total loss function is as in **Equation 15**:

$$L = \lambda_1 L_{mse} + \lambda_2 L_{LSC} + \lambda_3 L_s \quad (15)$$

where $\lambda_1$, $\lambda_2$, and $\lambda_3$ are the weight coefficients for the three types of losses, satisfying the condition: $\lambda_1+\lambda_2+\lambda_3=1$, $L_{mse}$ is the MSE loss, expressed as **Equation (16)**:

$$L_{mse} = \frac{1}{N}\sum_{i=1}^{N}\left(x_i' - y_i\right)^2 \quad (16)$$

### 2.4. Near-surface scattered-wave suppression

In the process of NSW suppression, seismic interferometry reconstructs the predicted scattered-wave data $X$, whereas the original wavefield data $Y$ serves as the network label. Using the learning process of CAEs, the loss function $L$ is minimized to obtain the true scattered-wave data, which is then subtracted from the original data to achieve denoising. The specific denoising process is shown in Figure 5. Before training, both synthetic and field data were divided into training and test sets at an 8:2 ratio, with the latter used for final model performance evaluation. Meanwhile, to make the model easier to train and converge, it is necessary to normalize both the predicted scattered waves and the original wavefield data so that their ranges are similar. The normalization was applied to single-shot data, and due to the large amplitude differences, mean-variance normalization was used to process the data, resulting in the predicted scattered wave $x$ and label $y$ for the network input (**Equations 17 and 18**):

$$x = \frac{X - \mu_1}{\sigma_1} \quad (17)$$

$$y = \frac{Y - \mu_2}{\sigma_2} \quad (18)$$

where $\mu$ and $\sigma$ represent the mean and standard deviation of the data, respectively.

To preserve more local waveform characteristics, the normalized seismic data were divided into equally-sized blocks to create a training dataset for the network. During the learning process, a dynamic learning rate was used, which was reduced by half every 200 iterations. As the learning rate decreased, $L$ continuously dropped, and when it reached its lowest value and stabilized, it indicated that the network learned the feature parameters of the input and label data. Finally, the test data were used as input to obtain the true NSW, which can be directly subtracted from the full-wavefield data. All experiments were implemented using PyTorch (Version 2.5.1, Meta Platforms, Inc., United States of America) and conducted on a workstation equipped with an NVIDIA RTX 4090 GPU with 16 GB memory.

**Table 2. Parameter design of the loss function**

| Iterations | 0–200 | 201–400 | 401–500 |
|---|---|---|---|
| Parameter ($\lambda_1$,$\lambda_2$,$\lambda_3$) | (0.7, 0.25, 0.05) | (0.5, 0.4, 0.1) | (0.3, 0.5, 0.2) |
| $L_{min}$ | 0.1512 | 0.1704 | 0.1811 |

## 3. Results and discussion

### 3.1. Training process

For the model dataset, the training process consisted of 500 iterations (Table 2). In the early stage, restoring the energy of the predicted scattered waves was the primary objective. Because there were significant discrepancies between the predicted and true scattered waves, especially for field data, the loss term associated with energy matching was assigned a relatively higher weight to ensure that the network prioritized alignment with the energy distribution of the original data. After 200 iterations, the loss decreased and stabilized at 0.1512, indicating that the network had successfully learned the energy discrepancy between data pairs and had compensated for it accordingly. Subsequently, the weight of $L_{mse}$ was gradually reduced, shifting the network's focus from energy recovery to learning the structural characteristics of waveforms. However, increasing $\lambda_2$ may lead to a slight reduction in energy-matching accuracy, highlighting the need for a trade-off between these two aspects.

The training loss curve of the model dataset over 500 iterations is shown in Figure 6. The loss decreased rapidly in the early stage, indicating that the network quickly learned the energy features. Around iteration 200, the curve began to stabilize, eventually reaching approximately 0.15, indicating that the network successfully converged. During

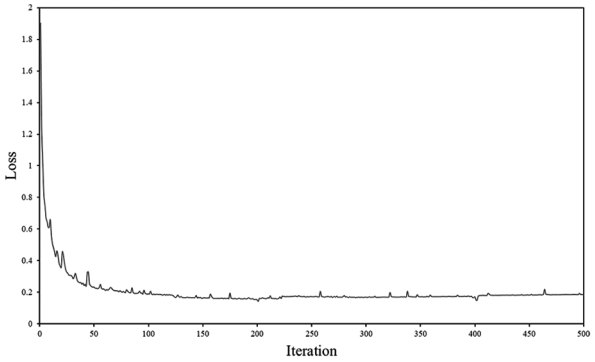


**Figure 6.** Training loss curve on the model dataset

training, weight adjustments were applied to balance the contributions of different loss components, causing minor fluctuations. Overall, the curve demonstrated that the network effectively captured both the energy and waveform characteristics of the training data.

Figure 7 illustrates the performance of synthetic data at different training stages. For comparison, the network was trained with $\lambda_1$ = 1 for 500 iterations, yielding the result as shown in Figure 7A. In complex wavefields, the network primarily focused on simple energy recovery. When adopting

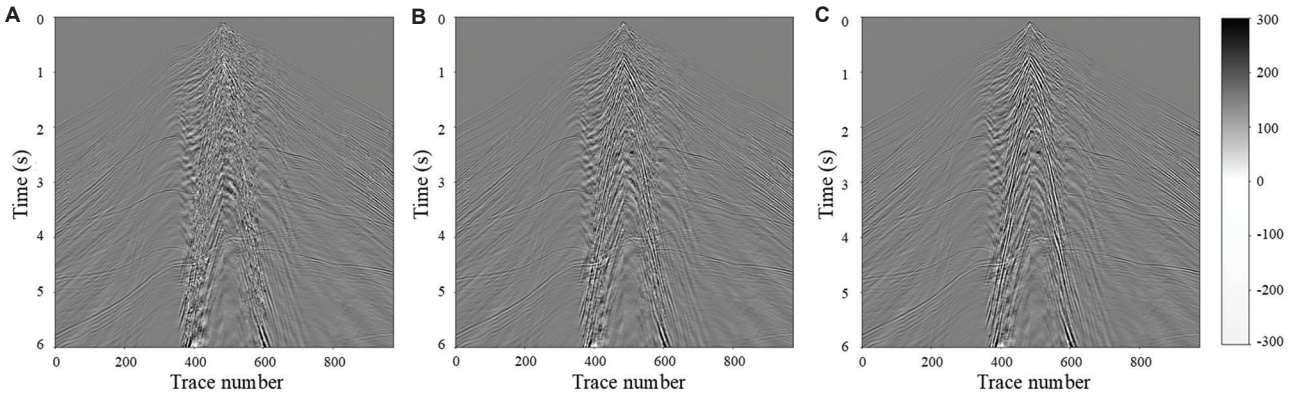


**Figure 7.** Results of synthetic data processed with different parameters. (A) Results with $\lambda_1$=1 after 500 iterations. (B) Result with dynamically adjusted weights after 300 iterations. (C) Result with dynamically adjusted weights after 500 iterations.

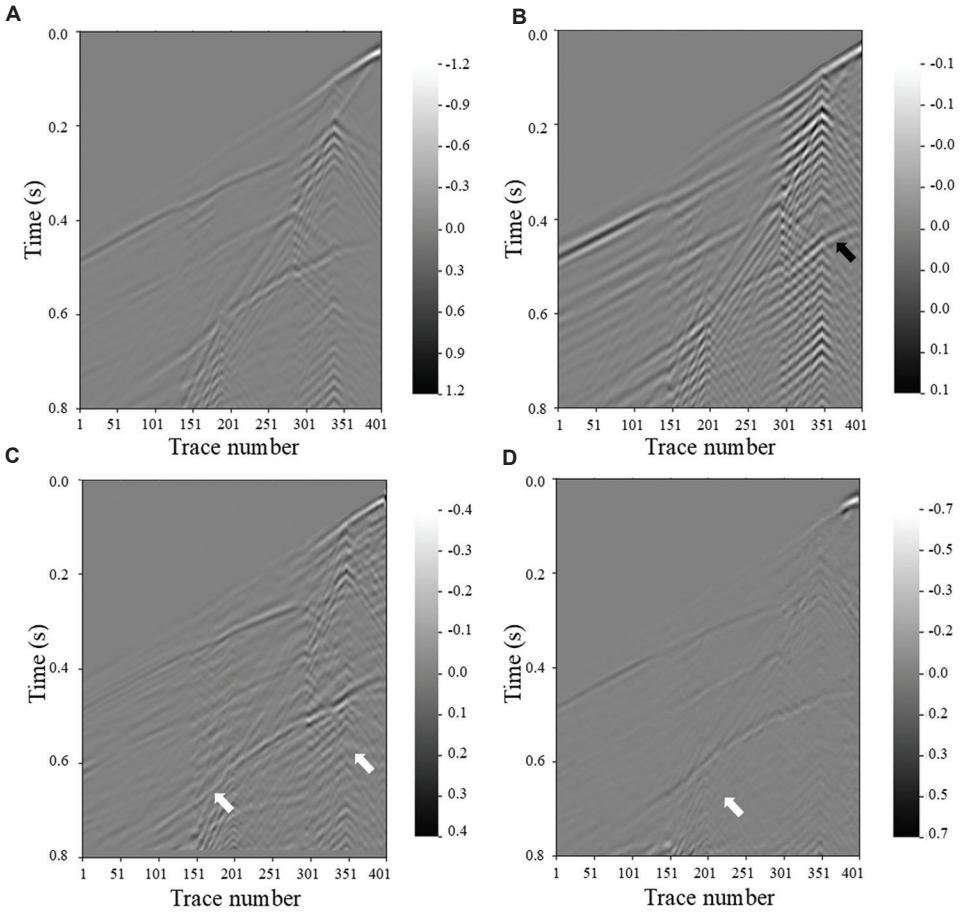


**Figure 8.** Denoising results of synthetic data 1. (A) Original data. (B) Interferometric data. (C) Results after matched filtering. (D) Denoising results of a convolutional autoencoder constrained by local scattered wave characteristics (LSC-CAE).

a dynamic parameter adjustment strategy to gradually increase $\lambda_2$ and $\lambda_3$, as shown in Figure 7B and 7C, the waveform characteristics of the test data were better preserved on the basis of energy recovery, demonstrating the effectiveness of LSC-CAE in suppressing noise in seismic data.

### 3.2. Application of synthetic data

To validate the effectiveness of the proposed method, LSC-CAE was applied to synthetic seismic records to suppress noise. The simple model consisted of two horizontal layers, with a velocity anomaly introduced near the surface to generate scattered waves. A total of 70 shot records were simulated. The predicted scattered-wave data were obtained through interferometric processing. Figure 8A and B shows the original data and the predicted scattered-wave data that served as the network's labels and inputs, respectively. However, due to the limited aperture effect in the simulation, the interferometric processing could not entirely eliminate body waves, leaving residual reflection signals in the predicted data (black arrow). Figure 8C and D shows the denoised results obtained using matched filtering and LSC-CAE, respectively. Compared to matched filtering, the network-based denoising not only better preserved the reflection signals but also more effectively suppressed scattered waves (white arrows). Moreover, the computational time for network-based denoising was only a few seconds, demonstrating significantly higher efficiency than matched filtering.

To further verify the effectiveness of the network-based denoising, a more complex undulating surface model was constructed for forward modeling, generating 70 synthetic shot records. Figure 9A and B shows the original data and the predicted scattered-wave data, respectively. In the original data, the reflection signals were overwhelmed by noise. The interferometric processing results demonstrate that surface and scattered waves were well predicted, with waveform amplitude and phase closely matching the original data, providing high-quality training samples for the network.

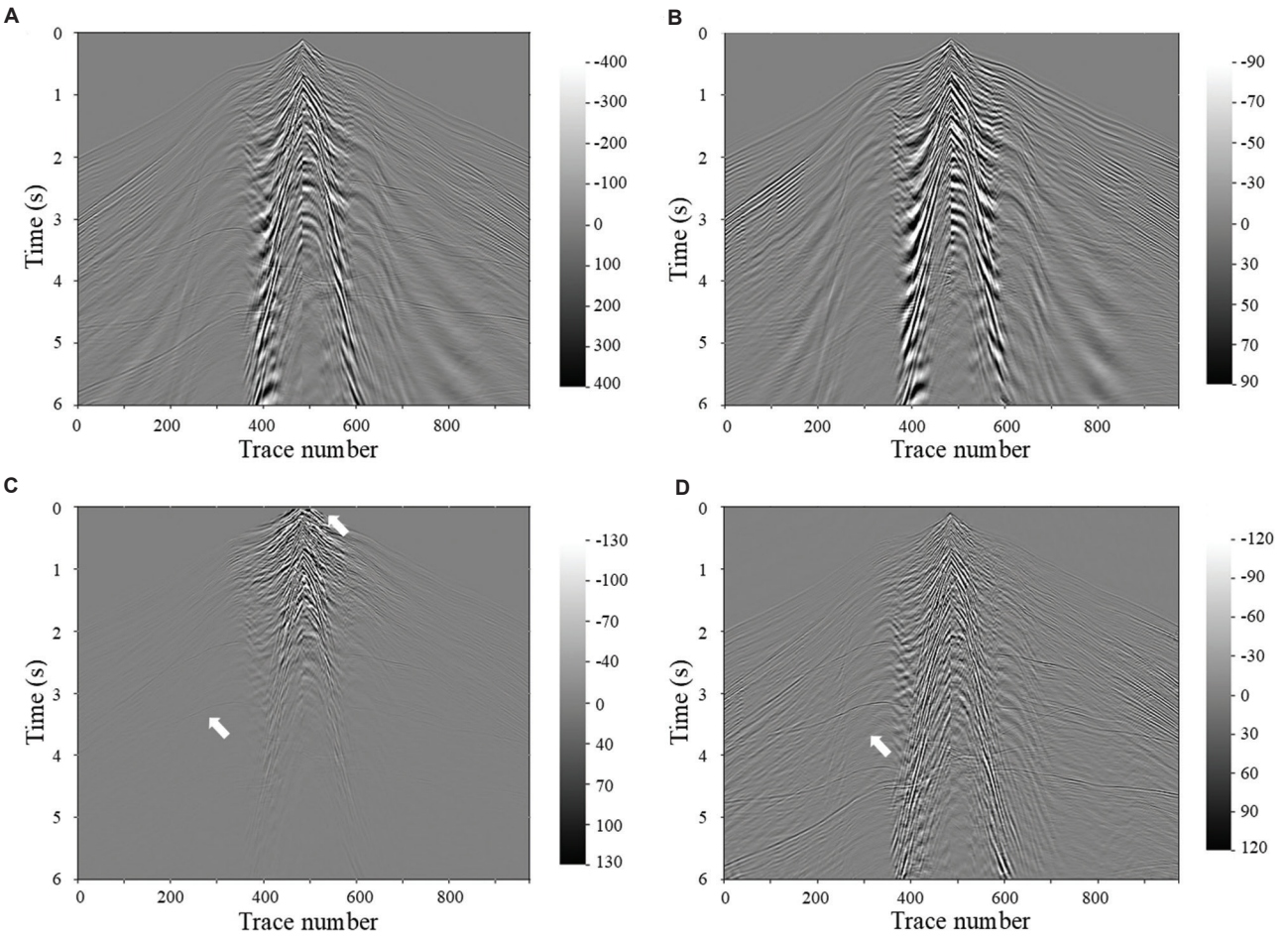


**Figure 9.** Denoising results of synthetic data 2. (A) Original data. (B) Interferometric data. (C) Results after matching filtering. (D) Denoising results of a convolutional autoencoder constrained by local scattered wave characteristics (LSC-CAE).

After applying the matched filter for noise suppression (Figure 9C), the SNR improved slightly. However, a portion of the body waves was attenuated during the filtering process (white arrows). When processed using LSC-CAE (Figure 9D), the body wave energy was effectively restored, the SNR was further enhanced, and both waveform continuity and phase information were preserved, demonstrating the effectiveness of the proposed method.

### 3.3. Field data application

The synthetic data experiments demonstrated that the proposed self-supervised learning approach enabled the predicted scattered waves to match the energy of the true wavefield. The LSC-CAE was then applied to field seismic data following the workflow described in Section 2.4. Due to the complexity of real seismic data, a larger dataset was required to capture the data characteristics effectively. Therefore, 60-shot records from mountainous terrain were selected as training samples for the network. First, shot-receiver interferometry was performed to obtain the predicted scattered waves. The 60-shot records were then partitioned into 15,000 data pairs, each of size 256 × 256. These predicted scattered wavefield slices and full-wavefield data slices were used as network inputs and labels, respectively, for training.

Unlike synthetic data, the predicted scattered waves generated during field seismic data processing exhibit significant energy differences compared to the full-wavefield data. Thus, when selecting coefficients in the loss function, it was crucial to consider energy recovery and maintain a proper balance among the different loss components. The denoising results for the first field dataset are shown in Figure 10. Figure 10A and F displays the original data and the predicted scattered waves. The shot data shows typical high-frequency scattering and low-frequency, large-curvature side NSWs (black arrow in Figure 10A). The interferometric results demonstrate that structured external interferences and scattered surface waves were well predicted without introducing additional noise. To comprehensively demonstrate the denoising superiority of the LSC-CAE, we compared its denoised results (Figure 10B) and the extracted noise (Figure 10G) with those obtained from the RS-CAE trained with a conventional MSE loss (Figure 10D and 10I), the matched-filtering method (Figure 10E and 10J), and the CAE using a composite loss function (Figure 10C and 10H). The results demonstrate that the LSC-CAE produced cleaner denoised sections and almost completely suppressed the scattered-wave groups (red arrows). In contrast, the conventional CAE and matched filtering approach failed to recover the predicted noise to its original amplitude,

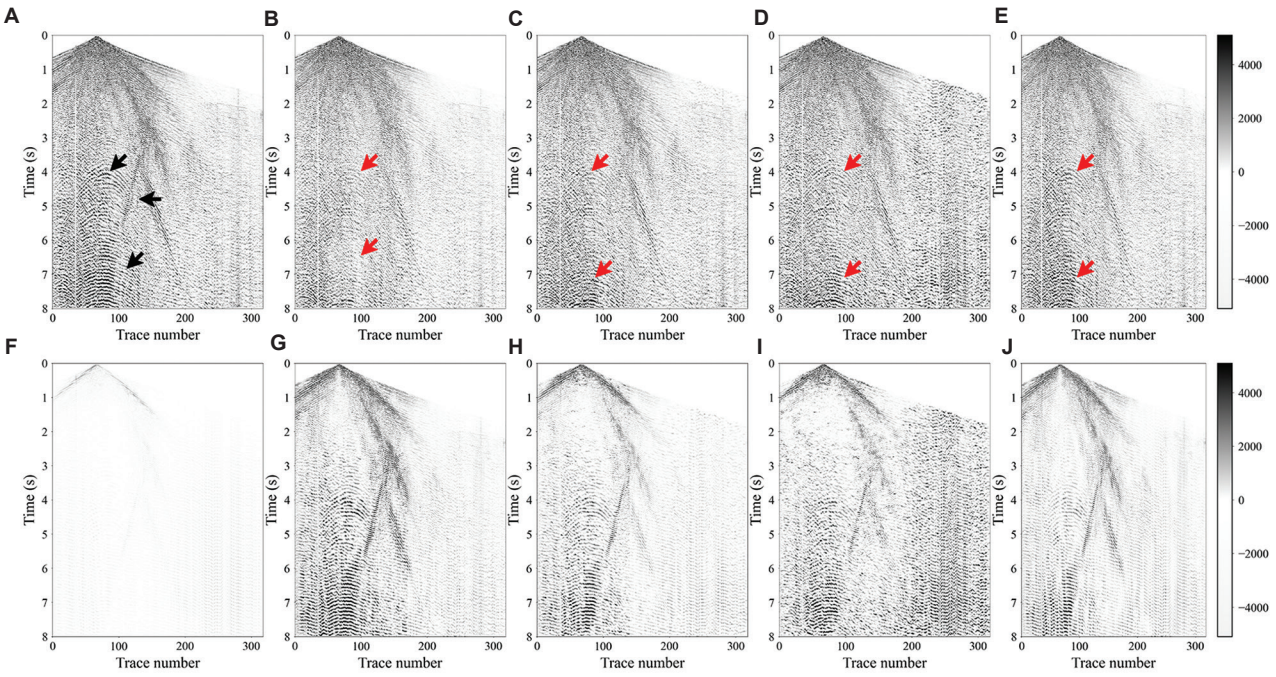


**Figure 10.** Denoising results of field data 1. (A) Original data. (B) LSC-CAE denoising result (dynamic parameter adjustment strategy). (C) CAE denoising result (dynamic parameter adjustment strategy). (D) LSC-CAE denoising result ($\lambda_1$=1). (E) Matched filtering result. (F) Interferometric data. (G) Noise removed by the LSC-CAE. (H) Noise removed by the CAE. (I) Noise removed by the LSC-CAE ($\lambda_1$=1). (J) Noise removed by matched filtering
Abbreviations: CAE: Convolutional autoencoder; LSC: Local scattered wave.

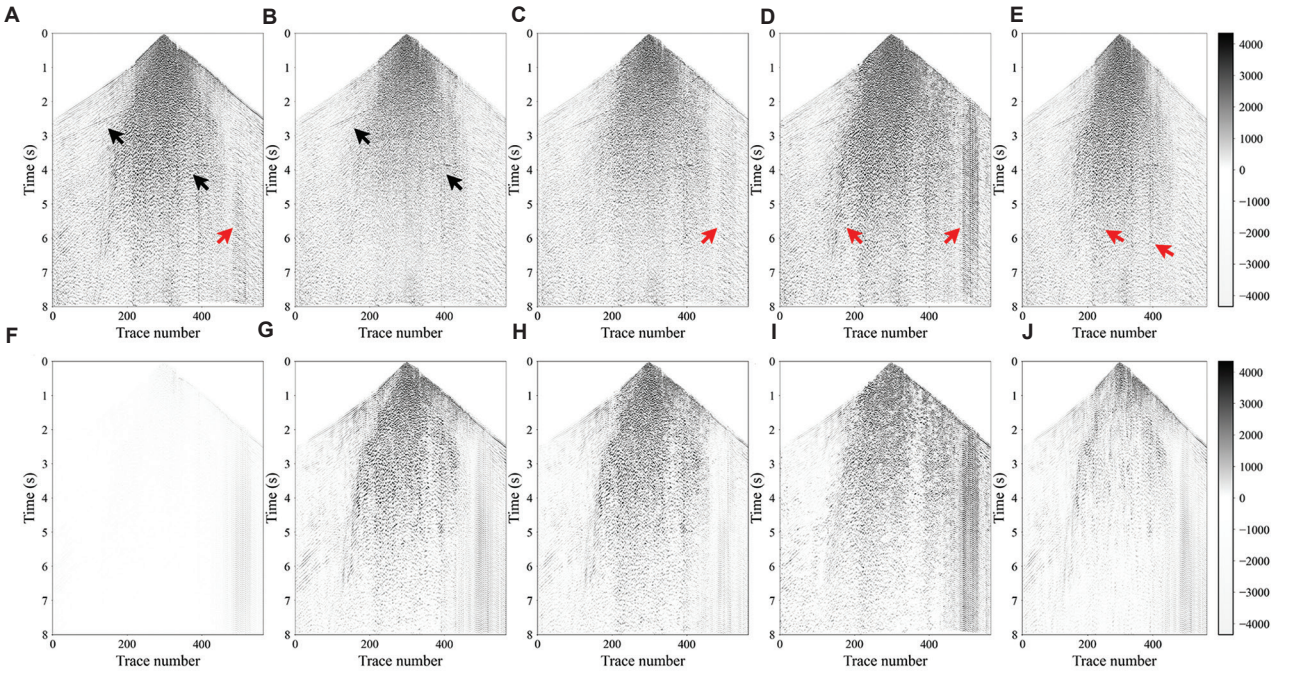


**Figure 11.** Denoising results of field data 2. (A) Original data. (B) LSC-CAE denoising result (dynamic parameter adjustment strategy). (C) CAE denoising result (dynamic parameter adjustment strategy). (D) LSC-CAE denoising result ($\lambda_1$=1). (E) Matched filtering result. (F) Interferometric data. (G) Noise removed by the LSC-CAE. (H) Noise removed by the CAE. (I) Noise removed by the LSC-CAE ($\lambda_1$=1). (J) Noise removed by matched filtering
Abbreviations: CAE: Convolutional autoencoder; LSC: Local scattered wave.

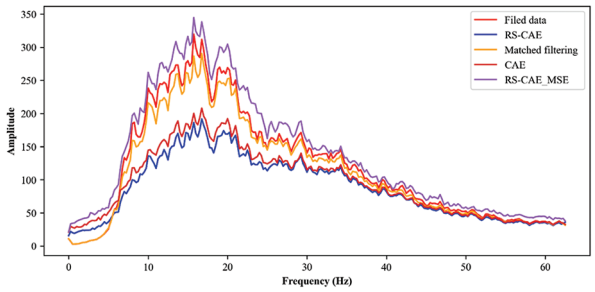


**Figure 12.** Spectral analysis of the surface wave region after denoising using different methods
Abbreviations: CAE: Convolutional autoencoder; RS-CAE: Residual-self-attention convolutional autoencoder; MSE: Mean squared error.

leaving significant scattered-wave energy in their denoised outputs. Moreover, when only the traditional MSE loss was used ($\lambda_1$=1), the network tended to focus primarily on amplitude restoration while neglecting the underlying structural characteristics of the waveforms, ultimately limiting its denoising performance.

For the second field dataset (Figure 11), the data denoised by the LSC-CAE (Figure 11B and 11G) showed a more pronounced attenuation of surface-wave energy compared with the CAE using only a dynamic loss function (Figure 11C and 11H), the LSC-CAE with $\lambda_1$=1 (Figure 11D and 11I), and the matched filter (Figure 11E and 11J). Since the scattered-wave energy in field data primarily originates from surface waves, this result indicates that, in addition to effectively suppressing large-curvature low-frequency scattering, the LSC-CAE performed better in complex scenarios where multiple scattered waves were superimposed. Furthermore, the regular interference near trace 500 was also effectively suppressed.

A spectral analysis was performed on the surface wave region to evaluate the capability of different denoising methods in suppressing NSWs. The surface wave energy was mainly concentrated in the 10-30 Hz frequency range, with a peak at 20 Hz. As shown in Figure 12, the RS-CAE method achieved the best performance, reducing the peak amplitude from 320 to 190, corresponding to a denoising rate of approximately 40%. The CAE method with local wavefield feature constraints performed moderately, while the network trained with only MSE ($\lambda_1$=1) failed to effectively suppress the surface-wave noise. These results indicate that the RS-CAE network, incorporating residual structures and self-attention mechanisms along with local wavefield characteristic constraints, exhibited a significant advantage in NSW suppression.

Both synthetic and field data examples demonstrated that introducing the local scattered-wave characteristics

loss enhances the network's ability to extract features in complex wavefields. During the training process, the weights of $L_{mse}$, $L_{LSC}$, and $L_S$ were dynamically adjusted in phases to meet the learning objectives of each stage. This strategy guided the network to gradually balance energy-related features and waveform structural characteristics while maintaining training stability.

## 4. Conclusion

We proposed a self-supervised deep learning strategy that eliminated the need for additional clean sample data as labels. During dataset preparation, seismic interferometry was utilized to predict noise from the original noisy data, generating high-quality training samples for the network. Throughout the network training process, a local scattered-wave feature loss term and regularization terms were integrated with the conventional MSE, allowing the network to autonomously focus on waveform characteristics. A dynamic adjustment strategy was employed to control the network's feature extraction priorities at different stages, ultimately enabling the model to learn both energy discrepancies and the waveform characteristics of scattered waves.

Traditional matched filters, relying on fixed parameters, often struggle to achieve satisfactory results in complex survey areas, whereas a trained network can adaptively handle varying noise conditions, providing stable denoising performance. Although network training can be time-consuming, once completed, inference is extremely fast, with a single-shot gather taking less than a second, substantially improving overall efficiency. During training, only a small portion of data from each survey area or model is needed to satisfy the network's sample requirements. Tests on both synthetic and field seismic data show that incorporating local scattered-wave characteristic constraints enables the network to effectively achieve the intended denoising objectives.

## Acknowledgment

None.

## Funding

This work is supported by the China National Petroleum Corporation Science and Technology Project, "Key Technologies for Seismic Physical Modeling, Acquisition, and Processing in the Tajik Basin" (2024DJ9905).

## Conflict of interest

The authors declare that they have no conflict of interest.

## Author contributions

*Conceptualization:* Daling Hou
*Formal analysis:* Daling Hou
*Funding acquisition:* Meng Li
*Investigation:* Daling Hou
*Methodology:* Daling Hou
*Visualization:* Daling Hou
*Writing–original draft:* Daling Hou
*Writing–review & editing:* Daling Hou, Jixiang Xu

## Availability of data

The data used in this study are available from the corresponding author upon reasonable request.

## References

1. Wu X, Li Y, Zhang M, He J, Long Z. Causes and countermeasures for low signal-to-noise ratio in seismic data in complex areas (part 1) - surface scattered waves are the root cause of low signal-to-noise ratio in seismic data. *Nat Gas Ind*. 2012;32(1):27-32. [Article in Chinese].

   doi: 10.3787/j.issn.1000-0976.2012.01.005

2. Shao J, Tang J, Sun C. Progress of seismic wave scattering theory and application. *Prog Geophys*. 2016;31(1):334-343.

   doi: 10.6038/pg20160139

3. Campman XH, Wijk Kvan, Scales JA, Herman GC. Imaging and suppressing near-receiver scattered surface waves. *Geophysics*. 2005;70(2):V21-V29.

   doi: 10.1190/1.1884831

4. Liu Y, Hu G, Fan T. Suppression of strong scattered waves using the transverse component. *J Appl Geophys*. 2015;112:226-235.

   doi: 10.1016/j.jappgeo.2014.11.021

5. Almuhaidib AM, Toksöz MN. Suppression of near-surface scattered body-to-surface waves: A steerable and nonlinear filtering approach. *Geophys Prospect.* 2016;64(2):392-405.

   doi: 10.1111/1365-2478.12275

6. Xu J, McLean JX, Song J. A near-surface seismic scattered wave separation method. *Pet Explor Dev*. 2014;41(6):771-777.

   doi: 10.1016/S1876-3804(14)60091-4

7. Halliday D, Bilsby P, West L, Kragh E, Quigley J. Scattered ground-roll attenuation using model-driven interferometry. *Geophys Prospect*. 2015;63(1):116-132.

   doi: 10.1111/1365-2478.12165

8. Xu J, Dong S, Cui H, Zhang Y, Hu Y, Sun X. Near-surface scattered waves enhancement with source-receiver interferometry. *Geophysics*. 2018;83(6):Q49-Q69.

   doi: 10.1190/geo2017-0806.1

9. Zhou P, Li P, Wang Y, Wei Z. *Principle and Practice of Deep Convolution Neural Network*. Beijing, China: Publishing House of Electronics Industry. 2020. p. 17-18.

10. Yu S, Ma J, Wang W. Deep learning for denoising. *Geophysics*. 2019;84:V333-V350.

doi: 10.1190/geo2018-0668.1

11. Yu S, Yang W, Li H, Wang H, Ma H. Scattered ground roll intelligent attenuation based on deep learning. *Chin Sci Bull (Chinese Version)*. 2021;66(18):2343-2354.

doi: 10.1360/TB-2020-0564

12. Liu W, Lü Q, Chen Q, *et al*. A synthetic denoising algorithm for full-waveform induced polarization based on deep learning. *Geophysics*. 2023;88(1):WA267-WA279.

doi: 10.1190/geo2022-0234.1

13. Sui Y, Wang X, Ma J. Deep unfolding dictionary learning for seismic denoising. *Geophysics*. 2023;88(1):WA129-WA147.

doi: 10.1190/geo2022-0198.1

14. Li X, Qi Q, Yang Y, Duan P, Cao Z. Removing abnormal environmental noise in nodal land seismic data using deep learning. *Geophysics*. 2024;89(1):WA143-WA156.

doi: 10.1190/geo2023-0143.1

15. Song H, Gao Y, Chen W, Zhang X. Seismic data denoising based on convolutional autoencoder. *Oil Geophys Prospect.* 2020;55(6):1210-1219+1160-1161. [Article in Chinese].

doi: 10.13810/j.cnki.issn.1000-7210.2020.06.006

16. Shao D, Zhao Y, Li Y, Li Y. Noisy2Noisy: Denoise pre-stack seismic data without paired training data with labels. *IEEE Geosci Remote Sens Lett.* 2022;19:1-5.

doi: 10.1109/lgrs.2022.3145835

17. Wu T, Meng T, Liu H, Li T. A seismic random noise suppression method based on self-supervised deep learning and transfer learning. *Acta Geophys*. 2024;72:655-671.

doi: 10.1007/s11600-023-01105-5

18. Wang K, Hu T, Wang S, Wei J. Seismic multiple suppression based on a deep neural network method for marine data. *Geophysics*. 2022a;87(4):V341-V365.

doi: 10.1190/geo2021-0206.1

19. Wang K, Hu T, Zhao B. An unsupervised deep neural network approach based on ensemble learning to suppress seismic surface-related multiples. *IEEE Trans Geosci Remote Sens*. 2022b;60:1-14.

doi: 10.1109/TGRS.2022.3225809

20. Wang K, Hu T, Zhao B, Wang S. Surface-related multiple attenuation based on a self-supervised deep neural network with local wavefield characteristics. *Geophysics*. 2023a;88(5):V387-V402.

doi: 10.1190/geo2022-0599.1

21. Wang K, Hu T, Zhao B, Wang S. An unsupervised learning method to suppress seismic internal multiples based on adaptive virtual events and joint constraints of multiple deep neural networks. *IEEE Trans Geosci Remote Sens*. 2023b;61:1-18.

doi: 10.1109/tgrs.2023.3243106

22. Sun K, Li Z, Wang Y, Ma J, Dai X, Li B. Adaptive subtraction based on expanded multichannel U-Net with multi-pattern multiple model for surface-related multiple removal. *IEEE Trans Geosci Remote Sens*. 2025;63:5912511.

doi: 10.1109/tgrs.2025.3565358

23. Qi Z, Li Z, Sun N, Li X, Li B, Wang Y. Semi-supervised interpretable FISTA-Net for adaptive subtraction and removal of seismic multiples. *IEEE Trans Geosci Remote Sens*. 2025;63:5912214.

doi: 10.1109/tgrs.2025.3564071

24. Wang Z, Bovik AC. A universal image quality index. *IEEE Signal Proc Let*. 2005;9(3):81-84.

doi: 10.1109/97.995823

25. Almadani M, Waheed U, Masood M, Chen Y. Dictionary learning with convolutional structure for seismic data denoising and interpolation. *Geophysics*. 2021;86(5):V361-V374.

doi: 10.1190/geo2019-0689.1

26. Sun Y, Williamson P. Seismic data interpolation via frequency-constrained 3D inception Unet. In: *Second International Meeting for Applied Geoscience and Energy*; 2022. p. 1679-1683.

doi: 10.1190/image2022-3751145.1

27. Simon J, Fabien-Ouellet G, Gloaguen E, Khurjekar I. Hierarchical transfer learning for deep learning velocity model building. *Geophysics*. 2023;88(1):R79-R93.

doi: 10.1190/geo2021-0470.1

28. Schuster GT. Theory of Daylight/Interferometric Imaging: Tutorial. In: *63rd EAGE Annual International Conference and Exhibition*, Amsterdam, Netherlands; 2001.

doi: 10.3997/2214-4609-pdb.15.A-32

29. Schuster GT. Imaging the Most Bounce out of Multiples. In: *65th EAGE Conference and Exhibition*, Stavanger, Norway; 2003.

doi: 10.3997/2214-4609.201405725

30. Schuster GT, Yu J, Sheng J, Rickett J. Interferometric/daylight seismic imaging. *Geophys J Int*. 2004;157(2):838-852.

doi: 10.1111/j.1365-246X.2004.02251.x

31. Schuster GT. Fermat's interferometric principle for multiple reflection tomography. *Geophys Res Lett*. 2005a;32(12):L12303.

doi: 10.1029/2005gl022351

32. Schuster GT. Fermat's interferometric principle for target-oriented traveltime tomography. *Geophysics*. 2005b;70(4):U47-U50.

doi: 10.1190/1.1997368

33. Schuster GT, Zhou M. A theoretical overview of model-based and correlation-based redatuming methods. *Geophysics*. 2006;71(4):103-110.

doi: 10.1190/1.2208967

34. Wapenaar K, Draganov D, Snieder R, Campman X, Verdel A. Tutorial on seismic interferometry: Part 1-basic principles and applications. *Geophysics*. 2010a;75(5):75A195-75A209.

doi: 10.1190/1.3457445

35. Wapenaar K, Slob E, Snieder R, Curtis A. Tutorial on seismic interferometry: Part 2-Underlying theory and new advances. *Geophysics*. 2010b;75(5):75A211-75A227.

doi: 10.1190/1.3463440

36. Wapenaar K, Ruigrok E, Neut J, Draganov D. Improved surface-wave retrieval from ambient seismic noise by multidimensional deconvolution. *Geophys Res Lett*. 2011;38(1):L01313.

doi: 10.1029/2010GL045523

37. Curtis A, Halliday D. Source-receiver wave field interferometry. *Phys Rev E Stat Nonlin Soft Matter Phys*. 2010;81(4):046601.

doi: 10.1103/physreve.81.046601

38. He K, Zhang K, Ren S. Deep Residual Learning for Image Recognition. In: *Proceedings of IEEE Conference on Computer Vision and Pattern Recognition*. IEEE Computer Society; 2016. p. 770-778.

doi: 10.1109/CVPR.2016.90

39. Vaswani A, Shazeer N, Parmar N, *et al.* Attention is All You Need. In: *Advances in Neural Information Processing Systems* [Preprint]. Vol. 30; 2017. p. 5998-6008.

doi: 10.48550/arXiv.1706.03762

40. Wang Z, Bovik AC, Sheikh HR, Simoncelli EP. Image quality assessment: From error visibility to structural similarity. *IEEE Trans Image Process*. 2004;13(4):600-612.

doi: 10.1109/TIP.2003.819861

41. Goodfellow I, Bengio Y, Courville A. *Deep Learning*. Cambridge, MA: MIT Press; 2016.

ACCSCIENCE PUBLISHING

Journal of Seismic Exploration

ARTICLE

# Unscaled generalized S-transform and its applications on seismic attenuation delineation: A case study in the Ordos Basin, Northwest China

**Wenlong Jiao[1], Naihao Liu[2]*, Yongxiang Jiang[1], Jun Yang[3], and Wei Zhao[3]**

[1]Department of Geophysics, PetroChina Yumen Oilfield Company, Jiuquan, Gansu, China

[2]School of Information and Communications Engineering, Xi'an Jiaotong University, Xi'an, Shaanxi, China

[3]Exploration and Development Research Institute, PetroChina Yumen Oilfield Company, Jiuquan, Gansu, China

(This article belongs to the *Special Issue: Advanced Artificial Intelligence Theories and Methods for Seismic Exploration*)

## Abstract

Seismic attenuation estimation is an important tool for hydrocarbon identification and reservoir characterization. Conventional time–frequency (TF) methods, particularly the S-transform (ST), are widely applied but suffer from a systematic dominant-frequency shift and fixed TF resolution, which may reduce the accuracy of attenuation analysis. To address these limitations, we introduce the unscaled generalized ST (UGST) and apply it to field seismic data from the Ordos Basin in Northwest China to qualitatively estimate attenuation. The UGST corrects the frequency shift inherent in the standard ST and introduces two tunable parameters that enable flexible adjustment of TF resolution to better match local seismic responses. Application to a three-dimensional seismic dataset demonstrates that the UGST produces TF spectra with improved readability and accurate frequency localization, resulting in a reduction of approximately 10 Hz in dominant frequency error compared to ST. The attenuation attributes derived from UGST show strong correspondence with known gas-bearing intervals, as verified by well-log data. The derived attenuation attributes show strong correspondence with gas-bearing intervals, with anomaly overlap rates exceeding 85% relative to well-log fluid indicators. These results indicate that the UGST provides a robust and effective approach for delineating seismic attenuation, offering practical value for reservoir characterization in exploration geophysics.

***Keywords:*** Seismic attenuation estimation; Time–frequency analysis; Unscaled generalized S-transform; Reservoir characterization

***Corresponding author:**
Naihao Liu
(naihao_liu@mail.xjtu.edu.cn)

**Citation:** Jiao W, Liu N, Jiang Y, Yang J, Zhao W. Unscaled generalized S-transform and its applications on seismic attenuation delineation: A case study in the Ordos Basin, Northwest China. *JSeismicExplor.*2026;35(1):237-250. doi: 10.36922/JSE025450106

**Received:** November 7, 2025

**Revised:** January 7, 2026

**Accepted:** January 12, 2026

**Published online:** February 10, 2026

**Copyright:** © 2026 Author(s). This is an Open-Access article distributed under the terms of the Creative Commons Attribution License, permitting distribution, and reproduction in any medium, provided the original work is properly cited.

**Publisher's Note:** AccScience Publishing remains neutral with regard to jurisdictional claims in published maps and institutional affiliations.

## 1. Introduction

In hydrocarbon exploration, seismic attenuation analysis is an essential technique for fluid identification and reservoir characterization.[1-3] The physical basis of this approach

lies in the observation that when seismic waves propagate through hydrocarbon-bearing formations, high-frequency components generally undergo greater energy attenuation than low-frequency ones.[4,5] This frequency-dependent amplitude loss provides a useful indicator for direct hydrocarbon detection, particularly in gas-saturated porous media.[6-8] Conventional qualitative attenuation analysis methods typically employ time–frequency (TF) analysis techniques, in which attenuation anomalies are identified by comparing energy variations across different frequency components.[9,10]

The development of qualitative attenuation estimation has advanced in parallel with improvements in TF analysis.[11,12] Early studies used basic spectral decomposition methods, comparing amplitude spectra within selected time windows to detect frequency anomalies. Although conceptually simple, these approaches suffered from limited resolution and an inability to effectively track temporal changes in spectral content. Advances in TF analysis led to sophisticated techniques, including the continuous wavelet transform and various adaptive TF representations. These methods offer improved capabilities for visualizing and quantifying frequency-dependent amplitude variations.[13-15] Moreover, excellent TF analysis tools have been proposed in recent years to address various practical issues, such as the synchrosqueezing transform[16] and sparse transform.[17,18] Although they can improve the TF resolution, these methods have various limitations in real applications, such as the difficult parameter selection, the high computational cost, and the high requirements for actual data.[18,19] Similar challenges are encountered in other signal processing domains, where advanced techniques are developed for weak-signal enhancement[20] and adaptive noise suppression.[21] These approaches, while promising, often involve complex parameterization that may limit their direct applicability to large-scale seismic datasets.

Among various TF analysis methods, the S-transform (ST) has attracted considerable attention for its distinctive TF resolution characteristics.[22,23] Unlike the fixed window length in the short-time fourier transform, the ST employs a frequency-adaptive Gaussian window, providing higher frequency resolution at low frequencies and better time resolution at high frequencies. This property of progressive resolution has led to its wide application in seismic signal analysis, especially for detecting thin beds and characterizing complex stratigraphic features.[9,24] Its ability to provide frequency-dependent resolution makes it particularly suitable for seismic attenuation analysis, where both temporal precision and frequency discrimination are essential.[23,25] Furthermore, it can benefit from several fast algorithms, significantly promoting its practical applications.[26-29]

However, the conventional ST exhibits a dominant frequency shift, in which the peak frequency in the computed spectrum deviates from the true frequency. This shift, caused by the frequency scaling of the Gaussian window, can affect the accuracy of attenuation estimation.[30] When comparing high- and low-frequency components for attenuation analysis, such frequency shifts may introduce systematic errors, leading to misinterpretation of attenuation anomalies or failure to detect subtle hydrocarbon indicators.[19,31] To mitigate this problem, researchers proposed the unscaled ST (UST). The UST modifies the Gaussian window function to correct the dominant frequency shift while preserving the adaptive nature of the original ST.[30] This adjustment ensures that the estimated frequencies more accurately represent the true spectral content of the signal. Nevertheless, the UST retains the same resolution characteristics as the conventional ST, which cannot be flexibly tuned for different geological targets or data types. This limitation becomes critical in complex reservoir characterization, where geological targets often demand varying TF resolutions for optimal interpretation. For example, detecting thin layers may require higher temporal resolution, whereas distinguishing subtle stratigraphic features benefits from improved frequency resolution.[32,33] The inability to adapt transform parameters to specific geological contexts constrains practical applications, particularly in heterogeneous reservoirs where attenuation behavior can vary significantly.[34,35]

The study area, located at the Ordos Basin, Northwest China, presents a compelling case for testing advanced attenuation estimation methods. This region contains complex fluvial-deltaic systems characterized by thin interbedded sandstones and shales, with reservoir thickness often below the tuning thickness. Extensive faulting complicates the structural setting, creating compartmentalized reservoirs with varying fluid contacts. Although previous exploration has confirmed the commercial hydrocarbon accumulations, reservoir delineation remains challenging. This is primarily due to complex pore-fluid distributions and subtle seismic responses, which necessitate advanced analytical techniques. These geological complexities necessitate advanced analytical techniques capable of resolving subtle attenuation anomalies associated with hydrocarbon presence.

In this context, we propose applying the unscaled generalized ST (UGST) to estimate attenuation qualitatively in these challenging seismic data. The UGST maintains frequency accuracy while enabling flexible control of TF resolution through adjustable parameters. This enhanced flexibility allows for optimization of the TF representation

according to specific geological objectives and data characteristics. We established a comprehensive workflow for qualitative attenuation analysis using the UGST, incorporating optimized parameter selection, frequency-component extraction, and attenuation calculation. The workflow is validated using comprehensive three-dimensional (3D) seismic data from the Ordos Basin, Northwest China, supported by well log information and production data for verification. Practical applications demonstrate that, compared to conventional methods, UGST yields more interpretable TF spectra and more reliable attenuation estimations. The method identifies attenuation anomalies in known hydrocarbon-bearing zones and provides improved resolution of thin reservoir units. This approach offers an effective technical solution for reservoir characterization under complex geological conditions, particularly in challenging exploration settings where conventional attributes provide ambiguous results. The successful application of UGST-based attenuation analysis in this study highlights its potential as a robust tool for reservoir characterization and reduction of exploration risk in geologically complex areas.

## 2. Methodology

### 2.1. Theoretical foundation of UGST

The UGST represents a significant advancement in TF analysis, specifically designed to overcome the limitations of conventional methods while preserving accurate frequency representation. The development of UGST builds upon the foundation of the standard ST, which itself marked an important evolution in TF analysis methodology.

The conventional ST of a seismic signal $x(t)$ is defined as **Equation 1:**

$$ST(\tau,f)=\int_{-\infty}^{+\infty}x(t)\frac{|f|}{\sqrt{2\pi}}e^{-\frac{(t-\tau)^2f^2}{2}}e^{-i2\pi ft}dt \tag{1}$$

Where $f$ and $t$ represent frequency and time variables, and $\tau$ denotes the time shifting variable. While ST provides a frequency-adaptive analysis window, it suffers from a systematic dominant frequency shift due to the scaling factor $|f|$ in the Gaussian window.

To address this frequency shift issue, the UST is introduced with the modified formulation,[30] written as **Equation 2**:

$$UST(\tau,f)=\int_{-\infty}^{+\infty}x(t)\frac{1}{\sqrt{2\pi}}e^{-\frac{(t-\tau)^2f^2}{2}}e^{-i2\pi ft}dt \tag{2}$$

The UST removes the frequency scaling factor from the normalization term $|f|/\sqrt{2\pi}$ of the window function based on the conventional ST. This modification prevents a shift in the dominant frequency toward higher frequencies. Meanwhile, the UST retains the frequency scaling in the exponential term, preserving its ability to adaptively adjust TF localization characteristics. The removal of the scaling factor $|f|$ in UST's normalization term addresses a fundamental limitation of standard ST. In conventional ST, this frequency-dependent scaling introduces a systematic bias in spectral localization, shifting estimated frequencies upward. UST eliminates this bias by decoupling the normalization from frequency scaling, thereby providing accurate frequency representation while preserving the adaptive window mechanism.

Building on UST, we propose the UGST, which incorporates additional parameters to enable flexible adjustment of TF resolution while maintaining frequency accuracy. The UGST is defined as **Equation 3**:

$$UGST(\tau,f)=\int_{-\infty}^{+\infty}x(t)\frac{1}{\sqrt{2\pi}}e^{-\frac{(t-\tau)^2(kf^p)^2}{2}}e^{-i2\pi ft}dt \tag{3}$$

Where $k$ and $p$ are two tunable parameters to control the window of our transform. Next, we also have the UGST in the frequency domain, denoted as **Equation 4**:

$$\begin{aligned}UGST(\tau,f)&=\int_{-\infty}^{+\infty}x(t)\frac{1}{\sqrt{2\pi}}e^{-\frac{(t-\tau)^2(kf^p)^2}{2}}e^{-i2\pi ft}dt\\&=x(\tau)e^{-i2\pi f\tau}\circledast g(\tau)\\&=IFT\left\{\hat{x}(\xi+f)\hat{g}(\xi)\right\}\\&=\int_{-\infty}^{+\infty}\hat{x}(\xi+f)\frac{1}{k|f|^p}e^{-\frac{2\pi^2\xi^2}{(kf^p)^2}}e^{i2\pi\xi\tau}d\xi\end{aligned} \tag{4}$$

Through this systematic approach, UGST leverages both accurate frequency localization and flexible resolution control to generate reliable attenuation estimates. By integrating geological constraints through reference-layer normalization, the method effectively distinguishes fluid-related attenuation from lithological effects, providing a robust tool for reservoir characterization.

### 2.2. Qualitative attenuation estimation workflow

We developed a workflow for qualitative attenuation characterization based on the proposed UGST, as shown in Figure 1. The workflow leverages the stronger attenuation of the high-frequency component relative to the low-frequency component and compares the difference between the two components to directly indicate the region of strong attenuation.[36,37]

We first denoted the two-dimensional seismic data with $d(x,t)$, where $x$ and $t$ represent the CDP number and

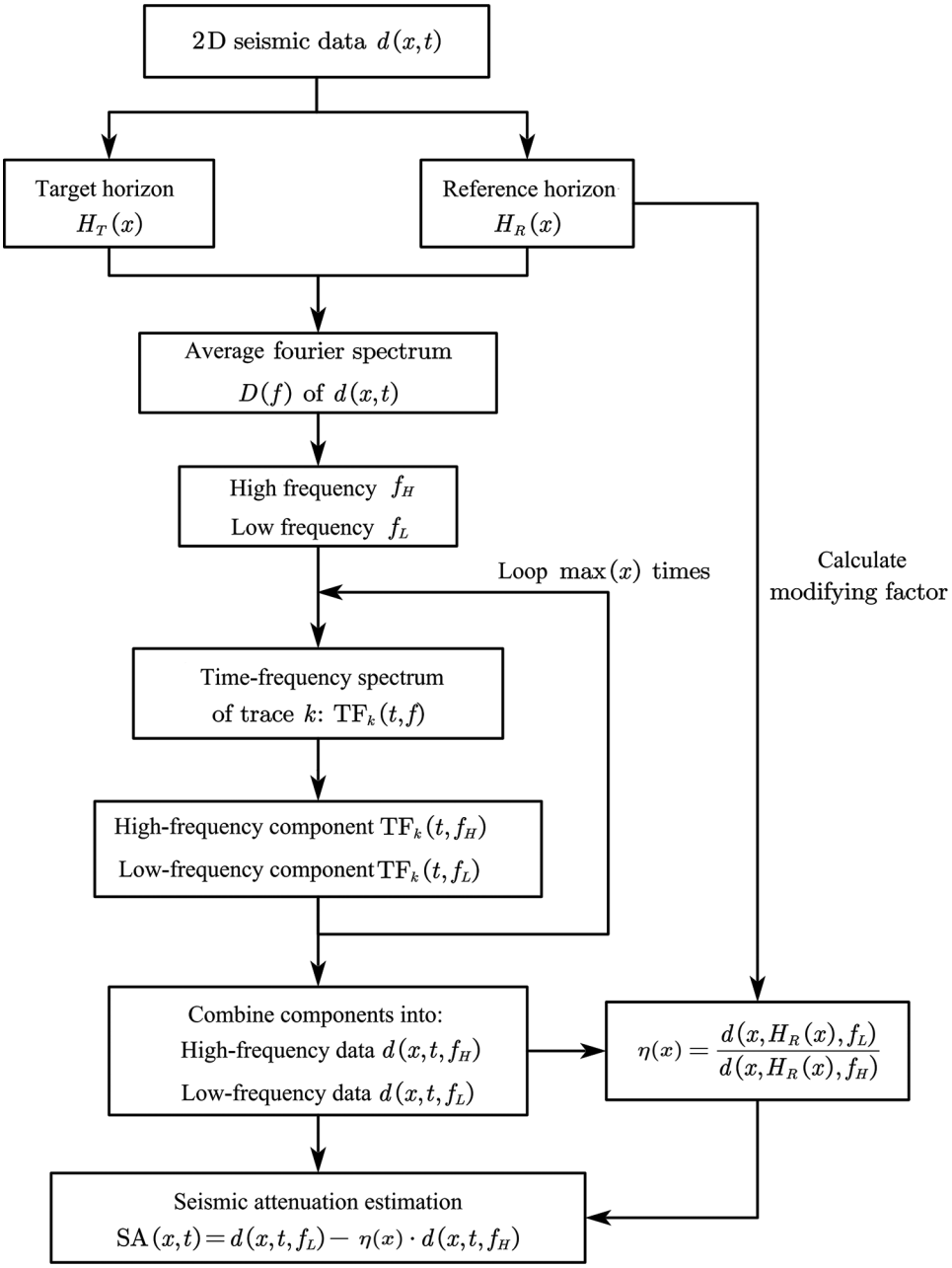


**Figure 1.** The proposed workflow of seismic attenuation characterization based on the proposed unscaled generalized S-transform
Abbreviations: 2D: Two-dimensional; SA: Seismic attenuation.

the time index. $H_T(x)$ is the target layer and $H_R(x)$ is the reference layer. Next, we selected the high frequency and the low frequency based on the average Fourier spectrum $D(f)$ of $d(x,t)$. Notably, $f$ should be included in the effective frequency band. Then, we adopted our proposed UGST to obtain the low-frequency component $d(x,t,f_L)$ and high-frequency component $d(x,t,f_H)$. Finally, we utilized the difference between them to estimate the seismic attenuation result $\mathrm{SA}(x,t)$ qualitatively at the target layer $H_T(x)$, which is defined as **Equation 5**:

$$\mathrm{SA}(x,t) = d(x,t,f_L) - \eta(x) \times d(x,t,f_H) \quad (5)$$

Where $\eta(x) = d(x,H_R(x),f_L)/d(x,H_R(x),f_H)$ is a scale-modified factor to remove the error behind the target layer. To enhance numerical stability when the high-frequency component amplitude is small, we applied a simple thresholding procedure. Before computing $\eta(x)$, the high-frequency amplitude was compared against a noise-level threshold T, which was derived from the average amplitude in non-reservoir intervals. If the amplitude fell below T, it

was replaced by T. This prevented division by near-zero values while maintaining the attenuation contrast essential for reservoir characterization. In this way, benefiting from the TF spectrum with high TF readability achieved by the proposed UGST, we effectively delineated seismic attenuation. In addition, the proposed UGST mitigates the frequency shift issue, which is beneficial to accurately characterize seismic attenuation.

## 3. Experimental setup

### 3.1. Field data and geological setting

The proposed UGST workflow was validated using 3D post-stacked seismic data from the Ordos Basin, Northwest China. This region represented a complex fault-block reservoir system developed in a fluvial-deltaic sedimentary environment. The target formation consisted of a series of thin interbedded sandstones and shales, with reservoir thickness typically below seismic tuning thickness, making it particularly challenging for conventional seismic interpretation methods. Understanding such complex reservoir systems benefited from insights gained in related geological studies, including investigations of pore-fracture connectivity in shale reservoirs[38] and fluid-rock interactions at the molecular scale.[39] These studies highlighted the importance of micro-scale features that influenced macro-scale seismic responses, providing context for interpreting the attenuation anomalies observed in our study. The structural framework was characterized by a series of northeast-southwest-trending normal faults that compartmentalize the reservoir into several isolated blocks.

The dataset covered an area of approximately 108 km$^2$ with a bin size of 20 m × 20 m, as indicated in Figure 2. The target interval spanned 2,000–3,022 ms, with a 2 ms sample interval providing sufficient temporal resolution for detailed spectral analysis. Figure 3 presents the normalized Fourier spectrum of the whole seismic data at the target layers. It is evident that the effective frequency bandwidth of the seismic data ranged from 5 Hz to 50 Hz, as determined from spectral analysis of multiple representative traces across the survey area. This comprehensive spectral analysis ensured that the selected frequency components for attenuation calculation fall within the reliable signal band, thereby enhancing the robustness of our attenuation estimation. Four key wells, spanning different structural positions, were selected for method validation (W1, W2, W3, and W4; Table 1). These wells provided comprehensive logging data, including gamma-ray, resistivity, and density logs, along with production test results that served as ground truth for validation of attenuation analysis.

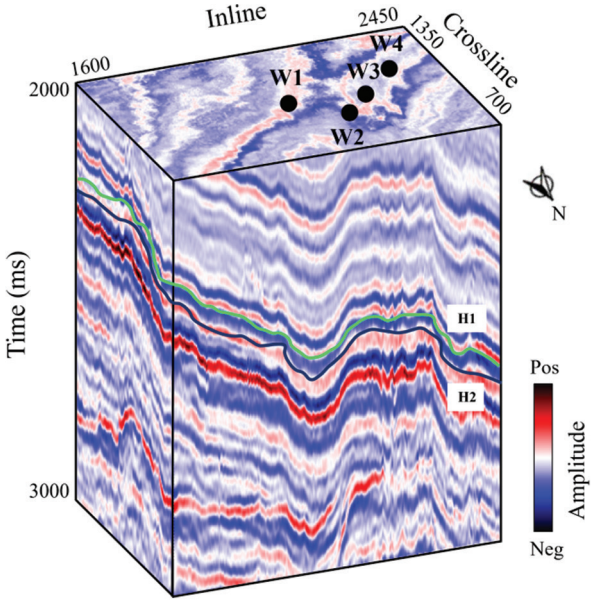


**Figure 2.** The three-dimensional post-stacked seismic data, located at the Ordos Basin, Northwest China, where W1, W2, W3, and W4 indicate four productive wells. The green and dark blue solid curves present two interpreted horizons: H1 and H2.

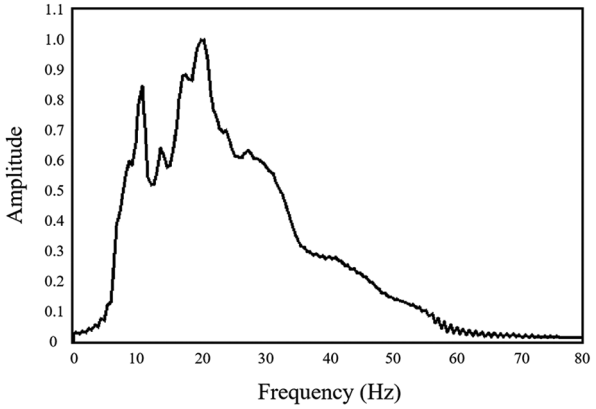


**Figure 3.** The normalized Fourier spectrum of the whole field data at the target layers

**Table 1. Summary of well–borehole data used for validation**

| Well | Depth to reservoir (m) | Production rate ($10^4$ m$^3$/d) | Fluid type |
|---|---|---|---|
| W1 | 3,150–3,210 | 10.02 | Gas |
| W2 | 3,190–3,220 | 6.45 | Gas |
| W3 | 3,175–3,205 | 6.35 | Gas |
| W4 | 3,200–3,220 | 1.73 | Gas |

### 3.2. Data preprocessing and parameter configuration

A comprehensive preprocessing sequence was applied to the seismic data before UGST analysis to ensure data quality

and interpretation reliability. Structural smoothing using dip-steered filtering was implemented to enhance lateral continuity while carefully preserving fault structures and stratigraphic terminations. This was particularly important given the complex fault network presented in the study area. Surface-consistent amplitude compensation was applied to normalize amplitude variations caused by near-surface effects and acquisition geometry, ensuring uniform seismic response across the entire survey area. Random noise suppression via FX-deconvolution improved the signal-to-noise ratio, a crucial for reliable TF analysis.

The design and parameterization of these preprocessing steps were carefully considered to balance noise suppression with the preservation of geological features. Specifically, dip-steered smoothing was applied with a conservative operator length (3 traces laterally, 5 ms vertically) to improve lateral continuity without blurring fault boundaries or stratigraphic terminations. This step was particularly critical in the fault-compartmentalized reservoirs of the Ordos Basin, where maintaining structural integrity was essential for reliable anomaly mapping. FX-deconvolution was employed to suppress random noise while preserving amplitude variations related to fluid content. Its parameters were calibrated to avoid over-smoothing, which could otherwise mask subtle attenuation anomalies associated with thin gas-bearing layers. The effectiveness of these preprocessing steps was validated by comparing raw and processed sections along key horizons, confirming that attenuation anomaly boundaries remained geologically consistent and aligned with well-based fluid indicators. Together, these preprocessing measures ensured that the input data to UGST were both interpretable and representative of true subsurface responses, thereby enhancing the reliability of the subsequent attenuation estimation without introducing artifacts or unrealistic smoothing.

The UGST parameters were optimized through an iterative testing process focused on achieving optimal TF resolution for the specific geological objectives. The window parameter $k$ was set to 1.2 after testing values ranging from 0.5 to 2.0, with this value providing the best compromise between time and frequency resolution for the target thin-bed reservoirs. The scaling parameter $p$ was established at 0.8, which was found to provide enhanced resolution in the low-frequency range while maintaining adequate time localization. Frequency selection was based on comprehensive spectral analysis of the entire seismic volume, as indicated in Figure 3, with the low frequency $F_L$ set at 8 Hz and high frequency $F_H$ at 34 Hz, both falling within the effective bandwidth of the data while providing sufficient separation for attenuation analysis. The careful selection of these frequencies, guided by the global spectrum, ensured that the attenuation calculation captured meaningful spectral variations related to reservoir properties. A continuous shale layer immediately above the target reservoir interval was selected as the reference horizon for amplitude normalization, ensuring that the resulting attenuation anomalies primarily reflected fluid-related effects rather than lithological variations.

The parameters $k$ and $p$ in the UGST formulation served distinct yet complementary roles in shaping the TF representation. $k$ primarily controlled the width of the Gaussian window in the time domain, influencing the trade-off between temporal sharpness and frequency localization. $k$ = 1.2 was selected after iterative testing across a range of 0.5–2.0. This choice was driven by the need to balance two competing demands in the Ordos Basin reservoirs: Sufficient temporal resolution to delineate thin interbedded layers (often below tuning thickness) and adequate frequency stability to reliably track attenuation trends. Lower $k$ values (<1.0) improved temporal resolution but introduced undesirable spectral smearing in the low-frequency range, while higher $k$ values (>1.5) enhanced frequency discrimination at the expense of blurring subtle temporal boundaries associated with fluid contacts. On the other hand, $p$ modulated the window's shape in the frequency domain, effectively controlling how the window scaled with frequency. Setting $p$ = 0.8 was found to optimize the representation of the seismic bandwidth relevant to attenuation analysis (approximately 5–50 Hz in this dataset). This value enhanced resolution in the lower frequency band (8–20 Hz), where gas-related attenuation anomalies were often most diagnostic, without over-compressing the window at higher frequencies where noise may dominate.

Together, these parameter choices reflected a tailored approach to the specific seismic response and geological complexity of the study area. The selection was further validated by comparing UGST outputs with well-log indicators across multiple representative traces, confirming that the chosen parameter set yielded TF spectra that were both interpretable and geologically consistent. While these values were optimized for the Ordos Basin dataset, the same methodological framework—iterative testing guided by local seismic character and geological objectives—could be applied to adapt UGST to other basin settings or data types.

### 3.3. Validation methodology

A multi-faceted validation approach was implemented to assess the reliability and geological consistency of the UGST-derived attenuation results. Well-based validation involved direct comparison of attenuation anomalies with known fluid contacts identified from well logs, with

particular focus on the gas–water contacts identified in W1 and W2. Production data correlation examined the relationship between attenuation strength and actual production performance, providing a practical measure of the method's predictive capability. Geological consistency assessment evaluated the spatial correlation between attenuation anomalies and structural features, ensuring that the observed patterns aligned with the understood petroleum system dynamics. Comparative analysis with conventional ST and UST implementations provided a baseline for evaluating the added value of the UGST approach, with particular attention to resolution improvement and frequency fidelity.

## 4. Results and discussions

### 4.1. TF analysis comparisons

To ensure a fair comparison among the TF methods, all transforms were implemented under consistent computational conditions. The standard ST and UST were implemented using their conventional formulations with Gaussian windows, matching the temporal sampling (2 ms) and frequency range (0–80 Hz) of UGST. No amplitude-preserving adjustments were applied to any method, ensuring that input data and processing conditions remained identical for all analyses. The TF characteristics of different transforms were examined using a representative seismic trace located near W1 (Figure 4A), which penetrated a known gas-bearing zone. The conventional ST result in Figure 4B displays a noticeable frequency shift phenomenon, with the dominant frequency appearing at approximately 45 Hz compared to the actual 35 Hz characteristic of the seismic wavelet. This systematic deviation introduced significant uncertainty in subsequent spectral decomposition and attenuation analysis. The UST result in Figure 4C successfully corrected this frequency shift but exhibited smeared TF representation, particularly in the critical 20–30 Hz range where important stratigraphic information was contained. The reduced concentration of spectral energy made it difficult to identify subtle features associated with thin bedding and fluid effects. In contrast, the UGST provided both accurate frequency localization and superior energy concentration (Figure 4D), clearly resolving the subtle spectral variations associated with thin layers and fluid contacts. The superior performance of UGST was particularly evident in the precise delineation of the frequency components around 30–40 Hz, which corresponded to the primary reservoir response, a feature that was blurred in both ST and UST results. The adjustable parameters enable optimal balancing of time and frequency resolution, revealing detailed features that are obscured in both ST and STFT representations.

### 4.2. Geological interpretation and discussions

Figure 5 displays the two-dimensional post-stacked seismic profile with four borehole locations (W1, W2, W3, and W4), where the yellow blocks clearly mark the reservoirs between two interpreted horizons: H1 and H2. All four wells penetrated gas-bearing reservoirs within

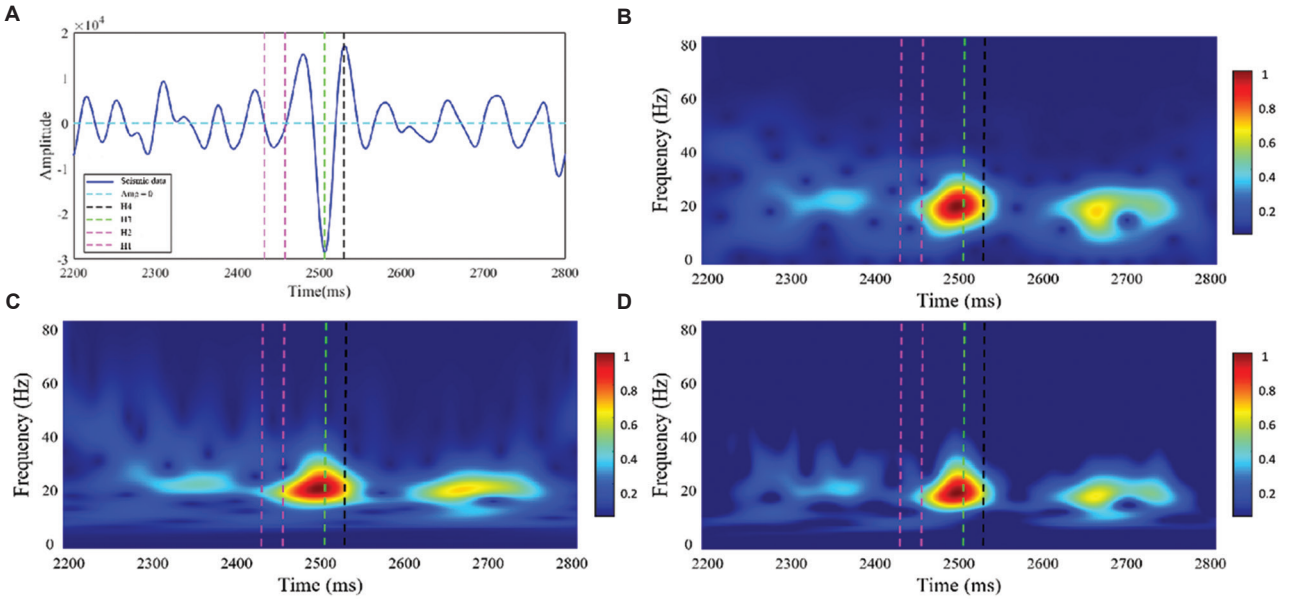


**Figure 4.** A representative seismic trace and its time-frequency spectra. (A) A representative seismic trace located near Well A and its time–frequency transform results calculated using (B) S-transform, (C) Unscaled S-transform, and (D) Unscaled generalized S-transform. The black, green, and two pink dashed lines indicate horizon H4, H3, H2, and H1, where the interpreted reservoir is located between H1 and H2.

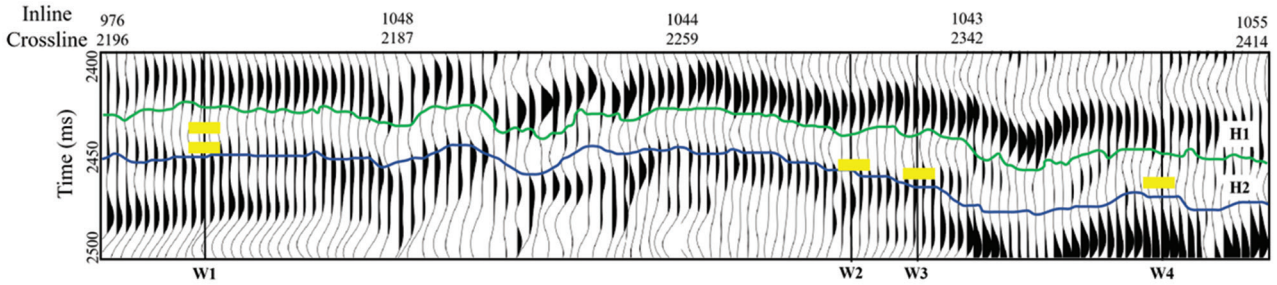


**Figure 5.** Two-dimensional post-stacked field data with four borehole locations. The green and dark blue solid curves present two interpreted horizons: H1 and H2. The yellow blocks indicate the location of the interested reservoirs.

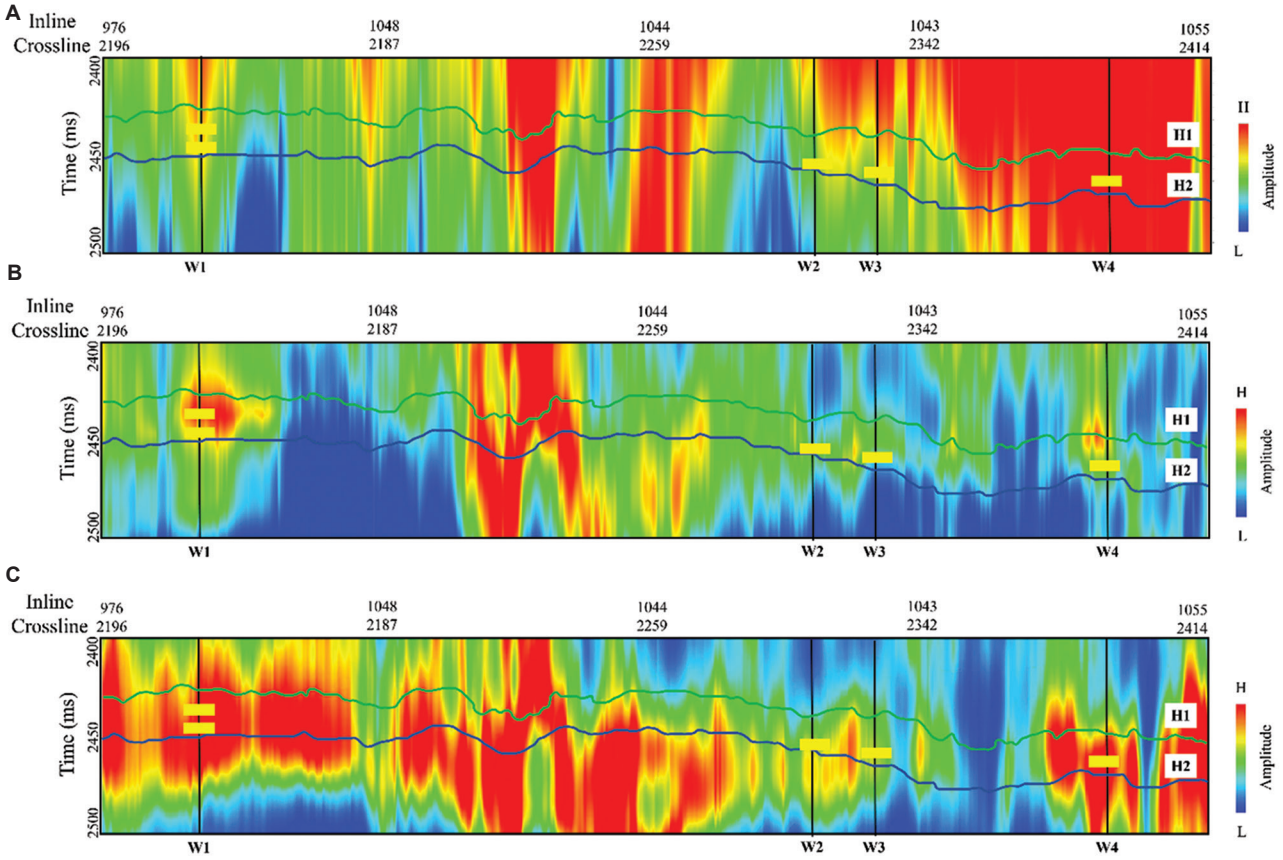


**Figure 6.** Seismic attenuation estimation for two-dimensional post-stacked field data in Figure 4, calculated by using (A) S-transform, (B) Unscaled S-transform, and (C) Unscaled generalized S-transform

these marked intervals, providing a robust dataset for method validation. The seismic profile shows characteristic reflection patterns typical of fluvial-deltaic depositional systems, with complex stratigraphic relationships and fault structures that pose challenges for conventional interpretation methods.

The qualitative attenuation profiles along target reservoirs demonstrated distinct characteristics among the three methods, as shown in Figure 6. The ST-based attenuation result in Figure 6A exhibits scattered anomalies with discontinuous spatial distribution, showing limited correlation with the known reservoir positions marked by yellow rectangles. The anomaly patterns appeared fragmented and lacked geological consistency, making it difficult to establish meaningful relationships with the reservoir distribution. The persistent frequency shift in ST likely contributed to this inconsistent performance, as the inaccurate spectral representation affected both the

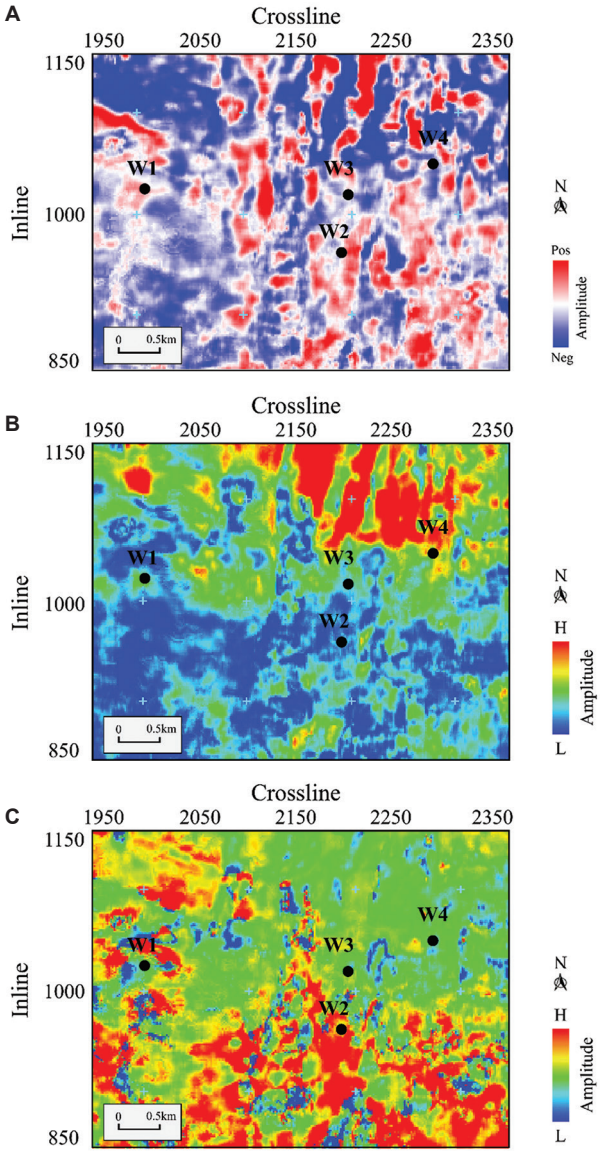


**Figure 7.** Seismic attribute slices extracted along H1 based on the post-stacked field data. (A) Seismic amplitude attribute. (B) Root mean square attribute. (C) Instantaneous frequency attribute.

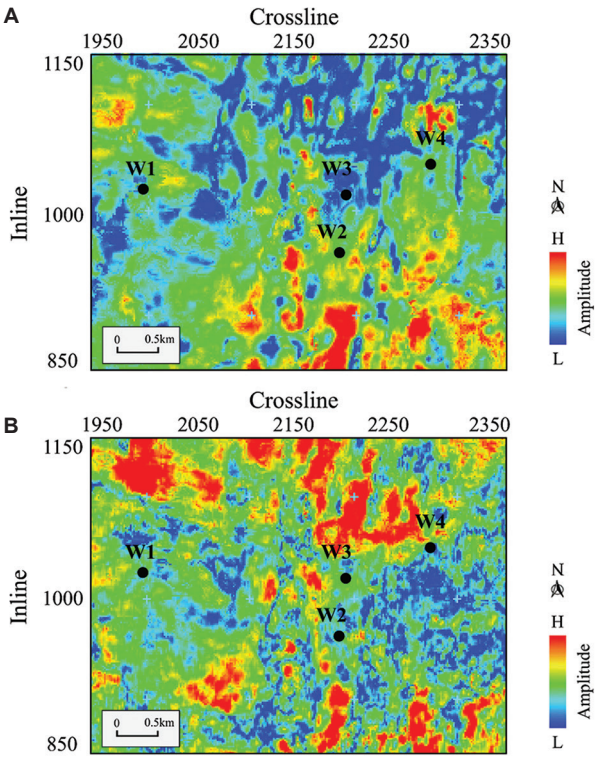


**Figure 8.** Constant frequency components extracted along H1 by using the S-transform; (A) low-frequency component and (B) high-frequency component.

low- and high-frequency components used in attenuation calculation. The UST-derived attenuation profile in Figure 6B shows improved spatial continuity compared to ST, with better-defined anomaly patterns that began to correlate with the reservoir positions. However, the resolution remained limited, particularly in delineating the detailed spatial variation of attenuation strength within the reservoir intervals. The anomalies appeared somewhat smoothed and lacked the sharp boundaries expected from geological considerations, suggesting that UST's fixed resolution limited its ability to capture fine-scale attenuation variations. The UGST-derived attenuation profile in Figure 6C reveals the most coherent and geologically consistent anomaly patterns among the three methods. The attenuation anomalies showed clear spatial correspondence with the reservoir positions marked by yellow rectangles, demonstrating strong correlation with all four gas-bearing wells (W1, W2, W3, and W4). The enhanced resolution of UGST effectively captured the attenuation variations within the reservoir units, showing well-defined anomaly boundaries that aligned with the structural and stratigraphic features observed in the seismic data. This improved performance was particularly evident in the areas between major faults, where UGST successfully identified continuous attenuation patterns that reflected the reservoir connectivity. Meanwhile, it is worth noting that the clear distinction between target and reference horizons in this study suggests a certain layer thickness, which typically improve detectability of gas-related attenuation contrasts. Nevertheless, the tunable resolution of UGST enabled it to capture subtle attenuation anomalies even in thinner reservoirs near or below seismic tuning thickness. This adaptability makes the method applicable not only to thick gas-bearing intervals but also to challenging thin-bed environments where conventional methods often struggle.

A comparative summary of the three methods highlights the quantitative improvements UGST offered. In terms of frequency fidelity, both UST and UGST fully corrected the approximately 10 Hz systematic shift observed in ST (Figure 4). Regarding the spatial consistency of anomalies, visual analysis of the attenuation profiles (Figure 6) indicated that UGST produced continuous anomalies that corresponded to all four validation wells, a level of alignment not achieved by the fragmented ST result. Furthermore, UGST demonstrated superior resolution in delineating reservoir boundaries within the target interval, as evidenced by sharper attenuation anomaly definition compared to the smeared responses of ST and UST. While formal cross-well correlation coefficients are beyond the scope of this qualitative case study, the consistent and enhanced performance of UGST across these multiple, observable criteria strongly supports its practical utility for attenuation-based reservoir characterization.

For the 3D seismic analysis, all attribute extractions were performed along the H1 horizon. H1 was selected for 3D attribute extraction because it corresponded to the top of the main reservoir unit within the 2,000–3,022 ms target interval. Seismic interpretation confirmed that the primary gas-bearing reservoirs are predominantly developed immediately beneath this surface, making H1 the most suitable reference for mapping reservoir–related attenuation anomalies throughout the 3D volume. This alignment ensured that the observed attenuation patterns were directly linked to the primary reservoir development zone, enhancing the geological relevance of our interpretations. This approach was adopted because seismic interpretation confirmed that the main reservoir units were predominantly developed adjacent to the H1 surface, making it the most suitable reference for mapping reservoir-related attenuation anomalies throughout the 3D volume. The choice of H1 for 3D attribute extraction thus directly linked the observed attenuation anomalies to the primary reservoir development zone, improving the geological relevance of our interpretations. Further analysis of seismic attribute slices along horizon H1 provided additional geological context for interpreting the attenuation results, as shown in Figure 7. The seismic amplitude attribute in Figure 7A reveals the basic structural framework, showing fault patterns and stratigraphic features that control the reservoir distribution. The root-mean-square amplitude attribute in Figure 7B enhances

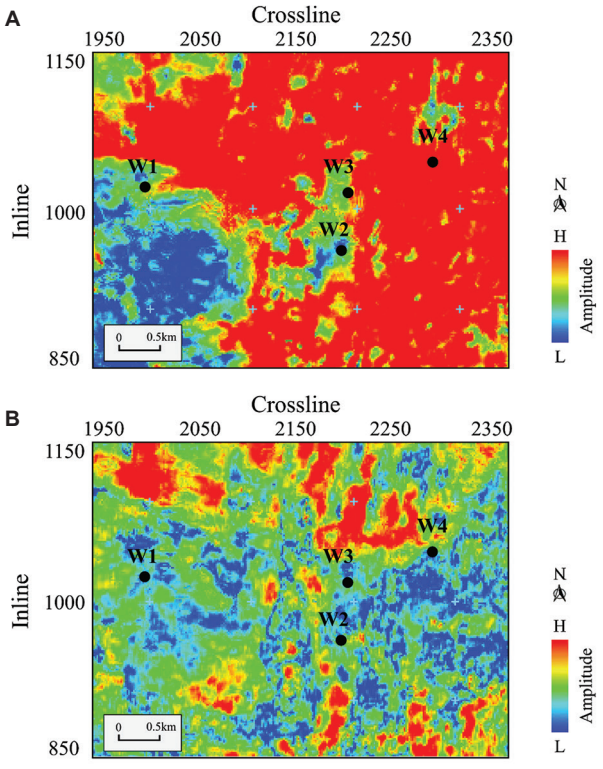


**Figure 9.** Constant frequency components extracted along H1 by using the unscaled S-transform; (A) low-frequency component and (B) high-frequency component

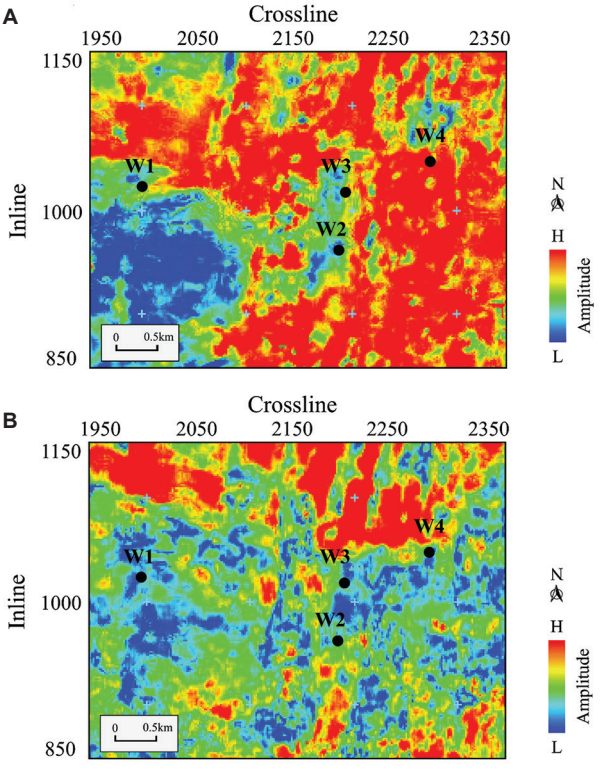


**Figure 10.** Constant frequency components extracted along H1 by using the unscaled generalized S-transform; (A) low-frequency component and (B) high-frequency component

the identification of amplitude anomalies associated with reservoir properties, showing good correlation with the known gas-bearing zones. The instantaneous frequency attribute in Figure 7C shows complementary spectral characteristics that supported the attenuation analysis, with frequency anomalies that corresponded well to the attenuation patterns identified by UGST.

We extracted and compared the constant-frequency components calculated using ST, UST, and UGST, as indicated in Figures 8-10, respectively. The subplots (A) and (B) denote the low- and high-frequency components extracted along the interpreted horizon H1.

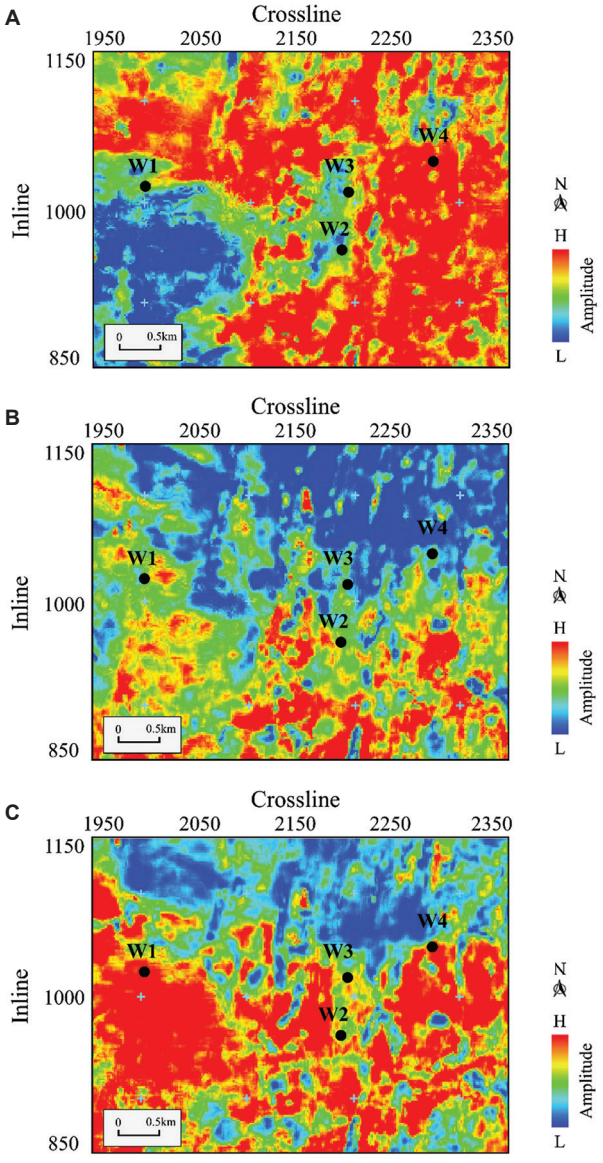


**Figure 11.** Seismic attenuation slices of H1 in 3D field data calculated by using (A) S-transform, (B) unscaled S-transform, and (C) unscaled generalized S-transform, respectively

We selected 8 Hz and 34 Hz as the low- and high-frequency bands in this study based on the Fourier spectrum of the whole field data. By comparing these images, we found that the components extracted using ST in Figure 8 showed significant spectral smearing and resolution limitations, particularly in the high-frequency component, where geological details were obscured by the method's inherent limitations. The UST-derived components in Figure 9 provided improved frequency fidelity, but resolution was limited in complex areas, limiting the ability to separate thin layers and subtle features. In contrast, our UGST method Figure 10 delivered superior component separation with enhanced resolution, clearly delineating the reservoir boundaries and internal heterogeneities that are critical for accurate reservoir characterization. It can be concluded that the constant-frequency component analysis demonstrated UGST's advantage in reservoir characterization through detailed comparisons of the extracted low- and high-frequency components.

Finally, we calculated and extracted the comprehensive 3D attenuation results as shown in Figure 11. Figure 11A-C correspond to the results calculated using ST, UST, and UGST, respectively. The UGST-derived attenuation slice showed well-defined anomaly patterns that correlated strongly with the reservoir distribution, whereas the results from ST and UST exhibited progressively poorer resolution and anomaly definition. The spatial continuity of UGST anomalies provided valuable insights into reservoir connectivity and compartmentalization, with attenuation patterns that reflected the complex interplay between structural elements and fluid distribution. The application of UGST for qualitative attenuation estimation in this complex reservoir confirmed its value for characterizing reservoirs under challenging geological conditions. The method's ability to accurately localize frequency while maintaining flexible resolution control addresses the fundamental limitations of conventional TF approaches. The strong correlation between UGST-derived attenuation anomalies and known reservoir positions, combined with the method's enhanced resolution, highlighted its potential to reduce exploration risk and improve reservoir characterization accuracy in similar complex reservoir settings. The consistent performance across different geological scenarios and the ability to reveal meaningful attenuation patterns that align with known geological features made UGST a valuable tool for integrated seismic interpretation and reservoir characterization workflows.

The UGST-derived attenuation maps provided high-resolution delineation of fluid-bearing zones, which can directly guide future well placement. For instance, areas with strong and continuous attenuation anomalies

along H1 (e.g., between W1 and W2) represent promising targets for infill drilling. In addition, the method's ability to resolve compartmentalization enabled optimization of injection strategies for enhanced oil recovery by identifying barriers and conduits within the reservoir. These insights reduced drilling uncertainty and support data-driven field development planning.

## 5. Conclusion

Our study presents the application of the UGST for qualitative estimation of seismic attenuation in a complex fault-block reservoir in the Ordos Basin, China. The proposed method effectively addressed two fundamental limitations of conventional TF analysis techniques: The systematic dominant-frequency shift inherent in the standard ST and the fixed resolution characteristics of the UST. By introducing tunable parameters into the Gaussian window function, UGST provides flexible control over TF resolution while maintaining accurate frequency representation, enabling enhanced analysis of non-stationary seismic signals.

The field application demonstrated that UGST generated TF spectra with superior readability and resolution compared to both conventional ST and UST methods. More importantly, the qualitative attenuation profiles derived from UGST showed strong correlation with known gas-bearing zones confirmed by well logs and production data. The method successfully identified attenuation anomalies associated with hydrocarbon presence while providing improved resolution of thin reservoir units and complex fault compartments. The geological consistency of the results, particularly the spatial alignment between attenuation anomalies and structural features, confirms the method's reliability for reservoir characterization in geologically complex settings.

The workflow developed in this study offers a robust approach for identifying fluid-related attenuation effects while minimizing interference from lithological variations. The identification of previously unrecognized prospective areas highlights UGST's potential to reduce exploration risk and optimize development strategies in similar complex reservoir environments. The principles underlying UGST-based attenuation analysis extend beyond hydrocarbon exploration to various geotechnical and engineering applications. In near-surface and engineering geophysics, similar TF approaches have been employed for tunnel seismic prospecting[40] and ground deformation monitoring using InSAR data.[41] Furthermore, in seismic hazard assessment, the accurate characterization of seismic signals is crucial for selecting appropriate ground motion models.[42] These diverse applications demonstrate the broad relevance of high-resolution signal analysis techniques across different scales and problem domains. The suggested UGST can be easily converted to a sparse version,[33] sacrificing computational efficiency for TF resolution. Due to our limited knowledge and the requirements of this research for efficient computation, we do not extend our suggested transform to the sparse version. Future work should focus on extending the method to the sparse version and on its application to quantitative attenuation estimation. We can also integrate it with other seismic attributes for comprehensive reservoir characterization. Moreover, the UGST method is not limited to the Ordos Basin and can be adapted to other sedimentary basins with complex reservoir architectures, such as fluvial-deltaic, turbidite, or carbonate systems. Its flexible parameterization allows customization for varying seismic data characteristics, including different frequency bandwidths, signal-to-noise ratios, and wavelet properties.

## Acknowledgments

None.

## Funding

This research was supported by the Science and Technology Projects of Yumen Oilfield Company for 2024–2025 (Grant No. YM2024-001).

## Conflict of interest

The authors declare that they have no competing interests.

## Author contributions

*Conceptualization:* Wenlong Jiao, Yongxiang Jiang
*Formal analysis:* Yongxiang Jiang
*Investigation:* Jun Yang, Wei Zhao
*Methodology:* Wenlong Jiao, Naihao Liu
*Validation:* Jun Yang, Wei Zhao
*Writing–original draft:* Wenlong Jiao, Wei Zhao
*Writing–review & editing: Naihao Liu*

## Availability of data

Data are available on request through naihao_liu@mail.xjtu.edu.cn.

## References

1. Li F, Verma S, Zhou H, Zhao T, Marfurt KJ. Seismic attenuation attributes with applications on conventional and unconventional reservoirs. *Interpretation*. 2016;4(1):SB63-SB77.

   doi: 10.1190/INT-2015-0105.1

2. Wang Z, Gao J, Wang D, Wei Q. 3D seismic attributes for a tight gas sand reservoir characterization of the eastern Sulige gas field, Ordos Basin, China. *Geophysics*. 2015;80(2):B35-B43.

doi: 10.1190/geo2014-0362.1

3. Ba J, Ba XY, Dong HJ, *et al*. Reservoir property estimation of interbedded sandstone and shale layers using segmented 3D rock-physics templates. *Appl Geophys*. 2025;22(3):1-17.

   doi: 10.1007/s11770-025-1263-3

4. Ashcroft W. Seismic input to mapping reservoir properties. In: *A Petroleum Geologist's Guide to Seismic Reflection*. United States: John Wiley and Sons; 2011. p. 127-145.

5. Liu S, Gu H, Yan Z, Li H, Wang H. Q-compensated beam migration with multiscale Gabor transform. *J Appl Geophys*. 2017;143:195-202.

   doi: 10.1016/j.jappgeo.2017.06.006

6. Ao Y, Li H, Zhu L, Ali S, Yang Z. Identifying channel sand-body from multiple seismic attributes with an improved random forest algorithm. *J Pet Sci Eng*. 2019;173:781-792.

   doi: 10.1016/j.petrol.2018.10.048

7. Ao Y, Li H, Zhu L, Yang Z. A SCiForest based semi-supervised learning method for the seismic interpretation of channel sand-body. *J Appl Geophys*. 2019;167:51-62.

   doi: 10.1016/j.jappgeo.2019.04.019

8. Wang Z, Gao J, Lei X, Cui X, Wang D. Application of 3D seismic attributes to optimize the placement of horizontal wells within a tight gas sand reservoir, Ordos Basin, China. *Geophysics*. 2016;81(3):B77-B86.

   doi: 10.1190/geo2015-0244.1

9. Chen Y, Liu T, Chen X, Li J, Wang E. Time-frequency analysis of seismic data using synchrosqueezing wavelet transform. In: *SEG Technical Program Expanded Abstracts 2014*. United States: Society of Exploration Geophysicists; 2014. p. 1589-1593.

   doi: 10.1190/segam2014-0034.1

10. Wang Y. The W transform. *Geophysics*. 2021;86(1):V31-V39.

    doi: 10.1190/geo2020-0316.1

11. Reine C, Van Der Baan M, Clark R. The robustness of seismic attenuation measurements using fixed-and variable-window time-frequency transforms. *Geophysics*. 2009;74(2):WA123-WA135.

    doi: 10.1190/1.3043726

12. Wang X, Gao J, Chen W, Zhao W, Jiang X, Zhu Z. Seismic attenuation qualitative characterizing method based on adaptive optimal-kernel time-frequency representation. *J Appl Geophys*. 2013;89:125-133.

    doi: 10.1016/j.jappgeo.2012.12.006

13. Wang B, Lu W. An efficient amplitude-preserving generalized S transform and its application in seismic data attenuation compensation. *IEEE Trans Geosci Remote Sens*. 2017;56(2):859-866.

    doi: 10.1109/TGRS.2017.2755666

14. Sinha S, Routh PS, Anno PD, Castagna JP. Spectral decomposition of seismic data with continuous wavelet transform. *Geophysics*. 2005;70(6):P19-P25.

    doi: 10.1190/1.2127113

15. Huang NE, Shen Z, Long SR, *et al*. The empirical mode decomposition and the Hilbert spectrum for nonlinear and non-stationary time series analysis. *Proc R Soc A*. 1998;454(1971):903-995.

    doi: 10.1098/rspa.1998.0193

16. Wang P, Gao J, Wang Z. Time-frequency analysis of seismic data using synchrosqueezing transform. *IEEE Geosci Remote Sens Lett*. 2014;11(12):2042-2044.

    doi: 10.1109/LGRS.2014.2317578

17. Liu N, Wei S, Li S, Yang Y, Zhang Y, Gao J. Sparse unscaled time-frequency transform and its application on seismic attenuation delineation. *Geophysics*. 2023;88(6):B355-B368.

    doi: 10.1190/geo2022-0522.1

18. Gholami A. Sparse time-frequency decomposition and some applications. *IEEE Trans Geosci Remote Sens*. 2012;51(6):3598-3604.

    doi: 10.1109/TGRS.2012.2220144

19. Liu N, Wei S, Liu R, Yang Y, Zhang N, Gao J. Seismic attenuation estimation via unscaled time-frequency representation and divergence. *IEEE Trans Geosci Remote Sens*. 2022;60:1-10.

    doi: 10.1109/TGRS.2022.3223721

20. Fu J, He T, Guo C, Bao Y, Li X, Liu X. An additional structure with power-law thickness for weak acoustic emission signal enhancement. *Thin Walled Struct*. 2025;211:113071.

    doi: 10.1016/j.tws.2025.113071

21. Li Z, Xie F, Ma J, Qi Z, Wang Y. CNN-based adaptive subtraction for the removal of seismic multiples. *J Seismic Explor*. 2023;32(2):169-184.

22. Liu N, Gao J, Zhang B, Wang Q, Jiang X. Self-adaptive generalized S-transform and its application in seismic time-frequency analysis. *IEEE Trans Geosci Remote Sens*. 2019;57(10):7849-7859.

    doi: 10.1109/TGRS.2019.2916792

23. Wang B. An amplitude preserving S-transform for seismic data attenuation compensation. *IEEE Signal Process Lett*. 2016;23(9):1155-1159.

    doi: 10.1109/LSP.2016.2586445

24. Verma AK, Cheadle BA, Mohanty WK, Routray A, Mansinha L. *Detecting Stratigraphic Discontinuities using Wavelet and S-Transform Analysis of Well Log Data*. In: *Proceedings of the GeoConvention 2012: Vision*; 2012. Calgary, Canada. Available from: https://geoconvention.

com/wp/content/uploads/abstracts/2012/163_gc2012_detecting_stratigraphic_discontinuities.pdf [Last accessed on 2026 Jan 16].

25. Shi Y, Zhou H, Niu C, Liu CC, Meng LJ. A variable gain-limited inverse Q filtering method to enhance the resolution of seismic data. *J Seismic Explor*. 2019;28:257-276.

26. Stockwell RG, Mansinha L, Lowe RP. Localization of the complex spectrum: The S transform. *IEEE Trans Signal Process*. 1996;44(4):998-1001.

doi: 10.1109/78.492555

27. Pinnegar CR, Eaton DW. Application of the S transform to prestack noise attenuation filtering. *J Geophys Res Solid Earth*. 2003;108(B9):2422.

doi: 10.1029/2002JB002258

28. Li D, Castagna J, Goloshubin G. Investigation of generalized S-transform analysis windows for time-frequency analysis of seismic reflection data. *Geophysics*. 2016;81(3):V235-V247.

doi: 10.1190/geo2015-0551.1

29. Beuter C, Oleskovicz M. S-transform: From main concepts to some power quality applications. *IET Signal Process*. 2020;14(3):115-123.

doi: 10.1049/iet-spr.2019.0042

30. Wu L, Castagna J. S-transform and Fourier transform frequency spectra of broadband seismic signals. *Geophysics*. 2017;82(5):O71-O81.

doi: 10.1190/geo2016-0679.1

31. Han C. Spectral decomposition AVO attributes for identifying potential hydrocarbon-related frequency anomalies. *First Break*. 2019;37(5):89-97.

doi: 10.3997/1365-2397.n0027

32. Li F, Zhou H, Zhao T, Marfurt KJ. Unconventional reservoir characterization based on spectrally corrected seismic attenuation estimation. *J Seismic Explor*. 2016;25(5):447-461.

33. Sattari H. High-resolution seismic complex trace analysis by adaptive fast sparse S-transform. *Geophysics*. 2017;82(1):V51-V67.

doi: 10.1190/geo2015-0425.1

34. Fomel S. Local seismic attributes. *Geophysics*. 2007;72(3):A29-A33.

doi: 10.1190/1.2437573

35. Liu J, Marfurt KJ. Instantaneous spectral attributes to detect channels. *Geophysics*. 2007;72(2):P23-P31.

doi: 10.1190/1.2428268

36. Yang Y, Gao J, Wang Z, Li Z. Seismic absorption qualitative indicator via sparse group-lasso-based time-frequency representation. *IEEE Geosci Remote Sens Lett*. 2021;18(9):1680-1684.

doi: 10.1109/LGRS.2020.3006340

37. Tary JB, Van Der Baan M, Herrera RH. Applications of high-resolution time-frequency transforms to attenuation estimation. *Geophysics*. 2017;82(1):V7-V20.

doi: 10.1190/geo2016-0022.1

38. Sun M, Duan X, Liu Q, *et al*. The importance of pore-fracture connectivity in overmature marine shale for methane occurrence and transportation. *Mar Pet Geol*. 2023;157:106495.

doi: 10.1016/j.marpetgeo.2023.106495

39. Yan Z, Wang F, Liu Y, Zhang J, Liu L, Gao M. Effects of $CO_2$ pressure on the dynamic wettability of the kerogen surface: Insights from a molecular perspective. *Appl Surf Sci*. 2025;694:162822.

doi: 10.1016/j.apsusc.2025.162822

40. Jia C, Cheng S, Li L, Chen Y. Seismic ahead-prospecting method based on delayed blasting excitation in the tunnel face: A case study. *Tunnell Undergr Space Technol*. 2025;161:106577.

doi: 10.1016/j.tust.2025.106577

41. Liang Y, Qiu H, Wang J, *et al*. Automated identification of ground kinematic patterns based on InSAR time series displacement and K-SC clustering. *Eng Geol*. 2025;357:108367.

doi: 10.1016/j.enggeo.2025.108367

42. Li B. Selecting hazard-consistent ground motions for seismic risk analysis: An equivalent earthquake-based methodology. *Bull Earthq Eng*. 2025;23:5275-5299.

doi: 10.1007/s10518-025-02228-4

ACCSCIENCE PUBLISHING

Journal of Seismic Exploration

ARTICLE

# Adaptive learned iterative shrinkage-thresholding algorithm combined with a physics-driven self-supervised method for sparse spike deconvolution

**Shunhao Hu[1,2], Shulin Pan[1]*, Ziyu Qin[1,3], Yinghe Wu[4]*, and Yaojie Chen[2]**

[1]State Key Laboratory of Oil and Gas Reservoir Geology and Exploitation, Southwest Petroleum University, Chengdu, Sichuan, China

[2]Reservoir Geophysical Laboratory, School of Geoscience and Technology, Southwest Petroleum University, Chengdu, Sichuan, China

[3]Department of Software Engineering, School of Computer Engineering, Chengdu Technological University, Chengdu, Sichuan, China

[4]State Key Laboratory of Lithospheric Evolution, Institute of Geology and Geophysics, Chinese Academy of Sciences, Beijing, China

***Corresponding author:**
Shulin Pan
(shulinpan@swpu.edu.cn)
Yinghe Wu
(yinghe1999@mail.iggcas.ac.cn)

**Citation:** Hu S, Pan S, Qin Z, Wu Y, Chen Y. Adaptive learned iterative shrinkage-thresholding algorithm combined with a physics-driven self-supervised method for sparse spike deconvolution. *J Seismic Explor*. 2026;35(1):251-268.
doi: 10.36922/JSE025460111

**Received:** November 16, 2025

**Revised:** January 6, 2026

**Accepted:** January 20, 2026

**Published online:** February 23, 2026

**Copyright:** © 2026 Author(s). This is an Open-Access article distributed under the terms of the Creative Commons Attribution License, permitting distribution, and reproduction in any medium, provided the original work is properly cited.

**Publisher's Note:** AccScience Publishing remains neutral with regard to jurisdictional claims in published maps and institutional affiliations.

## Abstract

The conventional iterative shrinkage-thresholding algorithm (ISTA) faces several limitations, such as dependence on manual parameter tuning and limited ability to recover weak reflections. Hence, this study proposes a sparse spike deconvolution method based on an adaptive learned ISTA (Ada-LISTA) and a self-supervised physics-driven objective function to overcome these challenges. First, using Ada-LISTA as the backbone, the threshold and step size in the iterative process were dynamically adjusted through its adaptive parameter learning, and the seismic wavelet dictionary was used as the model input to enhance the adaptability to different complex geological scenarios. Then, a self-supervised physics-driven objective function was introduced to jointly optimize the residual of seismic records and the sparsity of reflection coefficients, further improving the interpretability of the model. Finally, comparative experiments were carried out using theoretical simulation data and actual seismic data from the Bohai Bay Basin, China, to evaluate the inversion performance of the proposed method. The experimental results indicate that, compared to the traditional ISTA algorithm, the proposed method achieved marked enhancements in reflection coefficient inversion accuracy, seismic resolution, and robustness against noise. Overall, the proposed method offers an efficient and reliable technical solution for high-resolution seismic inversion and effective recovery of weak reflection signals, providing practical support for interpreting complex subsurface geological structures.

***Keywords:*** Sparse spike deconvolution; Seismic resolution; Weak reflection; Adaptive learned iterative shrinkage-thresholding algorithm; Physics-driven self-supervised method

## 1. Introduction

Sparse spike deconvolution, which inverts the underground reflection coefficient sequence using seismic records with limited bandwidth, is a common processing approach to enhance seismic data resolution.[1] The spectral sparse reconstruction proposed by Levy and Fullagar[2] and the two-dimensional Bayesian inversion framework by Lavielle[3] have collectively laid the foundation for the theoretical development of sparse spike deconvolution. Studies of well-log data have shown that primary reflection coefficients typically exhibit spectral non-whiteness[4] and amplitude distributions that are distinctly non-Gaussian, which fundamentally influence the design of effective deconvolution methods.[5] Based on these observations, the core principle of sparse spike deconvolution is to formulate seismic inversion as a linear inverse problem in which the reflectivity is modeled as a sparse impulse sequence and L1 regularization is used to promote sparsity.[6] The solution methods can be categorized into two groups, namely convex optimization methods founded based on pursuit[7] and greedy iterative algorithms derived from matching pursuit.[8,9] Among these, the iterative shrinkage-thresholding algorithm (ISTA) introduced by Beck and Teboulle[10] converts the non-smooth L1 regularization problem into an iteratively solvable optimization problem by introducing a soft-thresholding operator, thus becoming a widely used standard numerical solution in the field of sparse spike deconvolution. However, the traditional ISTA algorithm exhibits numerous limitations in practical applications. Specifically, its threshold and step size parameters rely heavily on manual adjustment.[11] Moreover, it is highly sensitive to the initial dictionary,[12] struggles to process complex seismic data,[13] and performs poorly in recovering weak reflection coefficients.[14]

To overcome these limitations, researchers have started to develop novel algorithmic frameworks using deep learning techniques.[15-17] In contrast to traditional methods that rely on manually designed iterative rules, these new approaches enable algorithms to automatically learn efficient solution strategies in a data-driven manner.[18] Gregor and LeCun[19] developed the learned ISTA (LISTA) by unfolding the iterative process of ISTA into a neural network structure, enabling end-to-end learning of parameters to adapt to signal distributions, accelerate convergence, and achieve automatic parameter optimization. Inspired by this, researchers have conducted extensive explorations on deep learnable sparse solver methods in fields such as seismic exploration and high-resolution imaging. In recent years, focusing on LISTA and its iteratively unfolded networks, researchers have proposed various variants. Analytic LISTA[20] adopts analytical parameters to simplify training while ensuring theoretical convergence. Gated LISTA[21] introduces gating and compensation mechanisms to enhance the expressive ability in adjusting sparse components and step sizes. Hybrid LISTA[22] realizes a more flexible network structure design through a hybrid form of iterative unfolding architecture. Step-LISTA[23] achieves step size learning to accelerate convergence. Extragradient-based LISTA[24] enhances the network recovery performance through residual structures and improved threshold functions. LISTA with adaptive thresholds[25] employs element-wise adaptive thresholds to improve the algorithm's adaptability to different sparse signals. Extragradient analytic LISTA and fast analytic LISTA,[26] respectively, enhance the robustness and accuracy of inversion under limited observations by introducing residual connections and momentum acceleration. LISTA with coupled weights and support selection[27] optimizes convergence efficiency through a support selection structure. Adaptive threshold analytic LISTA-based sparse imaging network[28] has shown excellent performance in high-resolution imaging tasks such as high-resolution synthetic aperture radar tomography and three-dimensional reconstruction, effectively improving spatial resolution under limited observation conditions. These methods have made significant progress in parameter adaptability, convergence speed, and complex signal expression, but they still rely on fixed dictionaries, making it difficult to adapt to complex environments. To address this limitation, Aberdam *et al.*[29] developed the adaptive LISTA (Ada-LISTA), which improves the model's adaptability to different scenarios by taking the dictionary as input. However, Ada-LISTA currently mainly targets general signal processing tasks and adopts a supervised learning approach, which has high demands on prior labels. It has not yet been effectively applied in the field of geophysics, especially in the recovery of weak reflection signals.

The traditional ISTA, which relies on global static thresholds and fixed dictionaries, frequently results in excessive suppression of low-amplitude reflection coefficients and consequently impedes the effective recovery of weak signals. Meanwhile, although supervised learning models perform excellently under ideal label conditions, the number of on-site logging labels is limited,[30] resulting in insufficient generalization performance.[31] In recent years, unsupervised and semi-supervised frameworks have gradually become new trends in seismic inversion.[32] On one hand, researchers have widely incorporated physical constraints, such as the seismic wave equation[33] and forward modeling,[34] constructed physically consistent losses,[35] and trained networks in an unsupervised manner to achieve effective recovery of weak seismic reflections and high-resolution structural information.[36] On the other

hand, they have adopted semi-supervised and multi-task learning frameworks, combined attention mechanisms[37] to enhance the feature expression of high-frequency and weak components, employed domain-adaptive adversarial training[38] to effectively improve the generalization ability of models to complex structures and unknown environments, and introduced amplitude versus angle physical priors[39] to strengthen the physical consistency and interpretability of models. These measures have significantly alleviated the generalization bottleneck caused by scarce labels in seismic inversion[40] and achieved remarkable improvements in the identification of complex seismic records and thin-layer weak reflection signals.[41] These research advances verify the advantages of physics-driven unsupervised methods and provide an important basis for the construction of the objective function in this study.

Given the limitations of the traditional ISTA algorithm in recovering weak reflection signals and the reliance of existing learning-based methods on fixed dictionaries and labeled data, this study proposes a self-supervised Ada-LISTA-based sparse inversion method for weak reflection signals. Through a hierarchical iterative optimization structure, adaptive learning of parameters and dynamic adaptation of the dictionary are achieved. The physics-driven self-supervised method is employed to ensure that inversion results conform to geophysical laws, and seismic record reconstruction is performed. The proposed method is tested using theoretical model data and actual oilfield data.

## 2. Methodology

### 2.1. ISTA

Under the assumptions of the convolutional model in seismic exploration, *y(t)* let y denote the seismic record, *d(t)* denote the seismic wavelet and *x(t)* denote the reflection coefficient. The relationship among the three can be expressed as **Equation 1**:

$$y(t) = d(t) * x(t) + n(t) \tag{1}$$

where *n(t)* is random noise.

Based on **Equation 1**, sparse spike deconvolution can be expressed as **Equation 2**:

$$\underset{x}{\operatorname{argmin}}\left(\frac{1}{2}Dx - y_2^2 + \lambda x_1\right) \tag{2}$$

Where $y$ is the seismic record vector, $D$ denotes the dictionary composed of seismic wavelets, $x$ denotes the reflection coefficient vector to be solved, $\lambda$ is the regularization parameter, $\|\cdot\|_2^2$ denotes the square of the Euclidean norm, and $\|x\|_1$ is the sum of the absolute values of all components of $x$.

**Equation 2** can be solved using the ISTA algorithm,[10] and the result is expressed as **Equation 3**:

$$x_{k+1} = S_\theta\left(x_k - \frac{1}{L}D^T\left(Dx_k - y\right)\right) \tag{3}$$

Where $D^T$ is the transpose matrix of $D$, $L$ ($L$>0) is the Lipschitz constant, $\gamma = 1/L$ is the step size parameter, $x_{k+1}$ and $x_k$ are the optimal reflection coefficients of the k+1-th and k-th iterations, respectively, $\theta$ is the threshold, and $S_\theta$ ($p$) is the soft thresholding function, defined as **Equation 4**:

$$S_\theta\left(p\right) = \begin{cases} p + \theta . p \le -\theta \\ 0, |p| < \theta \\ p - \theta, p \ge \theta \end{cases} \tag{4}$$

Let $U = \frac{1}{L}D^T, H = I - \frac{1}{L}D^T D$, and $I$ be identity matrices, then **Equation 3** can be simplified as **Equation 5**:

$$x_{k+1} = S_\theta\left(Uy + Hx_k\right) \tag{5}$$

The iterative flow chart of ISTA is shown in Figure 1. In actual calculations, both threshold $\theta$ and step size parameter $\gamma$ need to be set manually. In the actual experimental process, it is necessary to repeatedly try different values to optimize the results. In addition, ISTA relies on a fixed threshold, and weak reflection coefficients are prone to excessive compression.

### 2.2. LISTA

To simplify the cumbersome parameter tuning problem caused by fixed parameters in ISTA, Gregor and LeCun[19] developed the LISTA. Its core is to reconstruct the iterative process of ISTA into a deep neural network architecture. The k-th iteration of ISTA corresponds to the k-th layer of the network, and the iteration formula for each layer is expressed as **Equation 6**:

$$x_{k+1} = S_{\theta_k}\left(U_k y + H_k x_k\right), k = 0,1,\cdots,k-1 \tag{6}$$

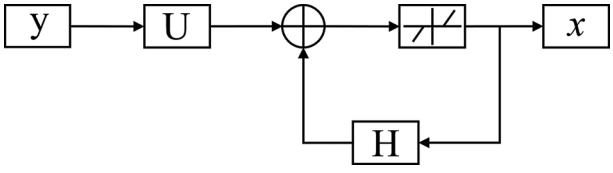


**Figure 1.** The iterative shrinkage-thresholding algorithm architecture

Where $\theta_k$ is the learnable threshold parameter of the k-th layer, and $U_k$ and $H_k$ are learnable matrices of the k-th layer. During initialization, $U_k = \frac{1}{L}D^T$, and $H_k = I - \frac{1}{L}D^T D$.

Figure 2 shows the network architecture of LISTA. The seismic record $y$ is multiplied by matrix $U$, then added to $Hx$, and processed by a soft-thresholding function. This result serves as the input to the next layer, and the process is repeated. After multi-layer cascaded operations, the reflection coefficient $x$ is finally obtained.

A comparison of Figures 1 and 2 reveals a clear structural connection between ISTA and LISTA. Each iteration in ISTA can be regarded as a network layer in LISTA. The input and output of each layer are computed using learnable matrices and thresholds. Unlike ISTA, the parameters of each layer in LISTA are automatically adjusted based on data during training without manual setting. Through an end-to-end learning approach, LISTA converts the ISTA algorithm into a trainable network structure, thereby improving the recovery performance of reflection coefficients.

### 2.3. Ada-LISTA

Although LISTA significantly optimizes the training process of ISTA through learnable parameters, it is still limited by its reliance on a fixed dictionary during the training phase. Due to the lack of dynamic adaptability in the fixed dictionary, it is difficult to accurately identify reflection signals with weak energy and sparse features. Such signals are easily misjudged as noise and incorrectly suppressed.

To break through this bottleneck, this study introduces the Ada-LISTA[29] framework proposed by Aberdam *et al.*[29] This framework is improved based on LISTA. It not only takes the dictionary as the model input, but also introduces two auxiliary weight matrices $W$ and $M$, enabling the model to dynamically adjust parameters according to different signals and dictionaries, thereby enhancing the flexibility of inference.

Specifically, the Ada-LISTA iteration formula is defined as **Equation 7**:

$$x_{k+1} = S_{\theta_k}\left(\left(I - \gamma_k D^T W_k{}^T W_k D\right)x_k + \gamma_k D^T M_k{}^T y\right) \quad (7)$$

Where $\theta_k$, $\gamma_k$, $W_k$, and $M_k$ are learnable parameters, $\theta_k$ is the threshold parameter of the k-th layer, $\gamma_k$ is the step size parameter of the k-th layer, $W_k, M_k \in \mathbb{R}^{n\times n}$ is an auxiliary weight matrix, $I$ is the identity matrix.

A comparison of **Equations 3**, **5**, **6**, and **7** shows that ISTA, LISTA, and Ada-LISTA present an obvious progressive relationship in structure. ISTA (**Equations 3** and **5**) adopts fixed parameter matrices $U$ and $H$ to solve input signals iteratively. Its parameters need to be manually specified, making it difficult to adapt to the characteristics of different signals. LISTA (**Equation 6**) unfolds the iterative process of ISTA into a multi-layer network structure and treats $U$ and $H$ as learnable parameter matrices. It realizes automatic parameter adjustment through adaptive optimization with training data. Ada-LISTA (**Equation 7**) further refines the parameter structure and uses weight matrices $W$ and $M$ to construct the original $U$ and $H$ more elaborately. It adjusts $U_k = \frac{1}{L}D^T = \gamma_k D^T$ in LISTA to $\gamma_k D^T M_k{}^T$ through $M$ in Ada-LISTA, and adjust $H_k = I - \frac{1}{L}D^T D = I - \gamma_k D^T D$ to $I - \gamma_k D^T W_k{}^T W_k D$ through $W$. This enables each layer to fine-tune the dictionary via weight matrices $W$ and $M$, enhancing adaptability to different seismic data. In general, these three methods gradually improve in parameter expression, structural setting, and adaptability, fully reflecting the development process of the model from fixed parameters to learnable parameters and then to dynamically adaptive parameters.

As shown in Figure 3, Ada-LISTA further extends the design of LISTA in the network structure. By introducing weight matrices $W$ and $M$, Ada-LISTA can achieve hierarchical adaptive adjustment of input signals and dictionary information. Compared with LISTA, Ada-LISTA maintains the benefit of learnable parameters while improving adaptability to varying seismic data conditions through dynamic dictionary adjustments. This structure

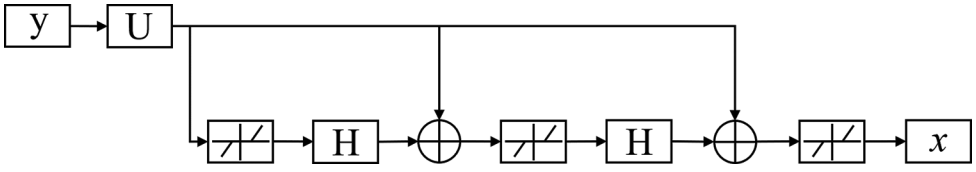


**Figure 2.** The learned iterative shrinkage-thresholding algorithm architecture

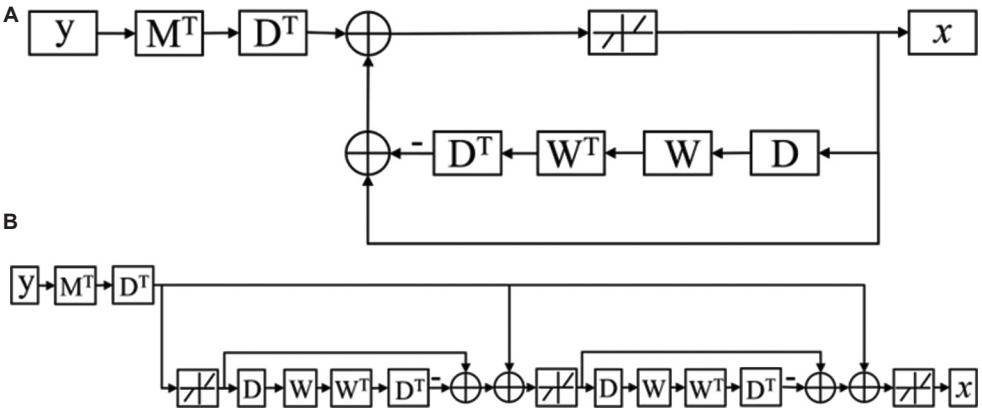


**Figure 3.** Adaptive learned iterative shrinkage-thresholding algorithm architecture. (A) Iterative model. (B) Unfolded model.

effectively improves the ability to identify weak reflection signals within complex geological settings and enhances overall flexibility and adaptability.

### 2.4. Objective function

In the task of seismic sparse spike deconvolution, the insufficiency of model prior information makes it difficult to directly apply the traditional deep learning end-to-end objective function. This study introduces a self-supervised objective function to overcome this limitation. This objective function skillfully incorporates geophysical features, enabling full utilization of the inherent structure of input data for model optimization, while significantly enhancing the interpretability of deep learning models for geophysical applications. Specifically, the objective function is defined as **Equation 8**:

$$L = A \cdot \frac{1}{2}\left\|D \cdot x - y\right\|_2^2 + B \cdot \left\|x\right\|_1 \tag{8}$$

In **Equation 8**, $A$ and $B$ are coefficients used to balance the data fitting term and the sparse regularization term. $D$ is a dictionary composed of seismic wavelets and is represented by a Toeplitz-type convolution matrix. The reflection coefficient result output by the model is denoted by $x$, and the input seismic record is denoted by $y$. This objective function ensures the consistency between the model output and the input data by minimizing the data fitting term $\left\|D \cdot x - y\right\|_2^2$, and at the same time uses the sparse regularization term $\left\|x\right\|_1$ to promote the model to output sparse reflection coefficients.

Compared with supervised training of Ada-LISTA, the proposed self-supervised objective improves applicability when labeled data or strong priors are unavailable, and can effectively capture the sparse features in seismic signals. This enables us to optimize the effect of sparse spike deconvolution without relying on a large amount of labeled data, thereby improving the seismic resolution.

### 2.5. Dataset construction and model optimization

To verify the performance of the model, this study conducted experiments using both synthetic data and actual seismic data. The synthetic dataset was produced by convolving Ricker wavelets with randomly generated reflection coefficient sequences. All data were normalized to facilitate parameter learning, optimization, and performance evaluation of the model. The actual seismic data were obtained from a seismic profile of an oilfield in the Bohai Bay Basin, China. For the field data, the statistical wavelet was extracted from the seismic profile based on the Wiener–Levinson process, adopting the autocorrelation method. The amplitude spectrum was derived from the autocorrelation of seismic traces, and a minimum phase spectrum was specified as the input parameter. After normalizing the extracted wavelet by its maximum absolute amplitude, it was used to construct the Toeplitz convolution matrix, forming the wavelet dictionary $D$ for inversion. The seismic data in this area are of poor quality, reflecting the complex geological structure of the oilfield and providing a realistic scenario for evaluating model performance. Seismic record reconstruction was performed to effectively enhance the resolution of actual seismic data, thereby revealing the details of underground geological structures more clearly.

In the model optimization stage, this study employed the Adam optimization algorithm with a learning rate of $1 \times 10^{-9}$ and a batch size of 8, leveraging its stability and fast convergence capability to update model parameters. To balance inversion accuracy and computational efficiency, the maximum number of iterations was set to 400, with an early stopping mechanism incorporated during the iterative process, where the iteration terminates when the Euclidean norm of the difference between successive

estimates is <0.1 for two consecutive iterations, avoiding redundant computations while ensuring inversion stability. To enhance the generalization capacity, an $L_1$ regularization term with a strength of 0.01 was introduced to constrain the complexity of model parameters and reduce the risk of overfitting. Meanwhile, an adaptive amplitude adjustment parameter was incorporated to dynamically regulate the amplitude range of model outputs, enabling better adaptation to the amplitude characteristics of different data and improving the model's adaptability to complex geological conditions. To further quantify the deconvolution performance of each method, relative error (Err) was introduced as an evaluation metric, calculated as **Equation 9**:

$$E_{rr} = \frac{\|\hat{r} - r\|}{\|r\|} \tag{9}$$

where $\hat{r}$ denotes the algorithm's deconvolved result, and $r$ represents the actual reflectivity coefficient. A smaller Err value indicates that the deconvolved result is closer to the actual reflectivity coefficient, signifying superior method performance.

## 3. Results

### 3.1. Simulation experiments

To evaluate the proposed sparse spike deconvolution method, a simulated seismic dataset was constructed based on the method introduced in **Section 2.5**, and comparative experiments were conducted. The simulated seismic signals were created through the convolution of a zero-phase Ricker wavelet, with a dominant frequency of 40 Hz, and randomly generated reflection coefficients with amplitudes distributed in the interval, thereby spanning both strong and weak reflections. Each trace of the reflection coefficients and seismic records in the final simulated dataset had a duration of 1300 ms, containing six reflection positions. To facilitate comprehensive feature extraction by the network, a total of 1000 traces of simulated data were generated, and one of them is shown in Figure 4.

The algorithm was used to test the simulated dataset with comparisons to the classical ISTA and LISTA algorithms (Figure 5). Quantitative results showed that the Err of ISTA, LISTA, and the proposed Ada-LISTA was 0.6237, 0.1479, and 0.0422, respectively. While all benchmark methods can achieve wavelet compression, ISTA suffers from significant amplitude loss and poor weak reflection recovery due to cumbersome manual parameter tuning. Additionally, although LISTA improved upon ISTA by adopting learnable parameters, our Ada-LISTA further outperformed both via adaptive adjustment to dynamically optimize thresholds and step sizes, thus achieving superior amplitude recovery and weak reflection identification.

### 3.2. Noise robustness evaluation

To further validate the efficacy of the algorithm, this study tested data with added random noise. Based on the synthetic seismic record shown in Figure 4B, random noise of different intensities was added to obtain three sets of noisy seismic records. The results are shown in Figure 6. These three models correspond to the high signal-to-noise ratio (SNR) theoretical model in Figure 6A, the medium SNR theoretical model in Figure 6B, and the low SNR theoretical model in Figure 6C.

When the SNR was 10 dB, as shown in Figure 7, the Err values for ISTA, LISTA, and the proposed Ada-LISTA were 0.7561, 0.1979, and 0.0526, respectively. When the SNR decreased to 3 dB, as presented in Figure 8, the Err values were 0.7640, 0.2312, and 0.0819 for the three methods. Traditional ISTA showed apparent amplitude attenuation and poor weak reflection recovery, with performance further deteriorating as SNR decreased. LISTA achieved certain improvements over ISTA by adopting learnable

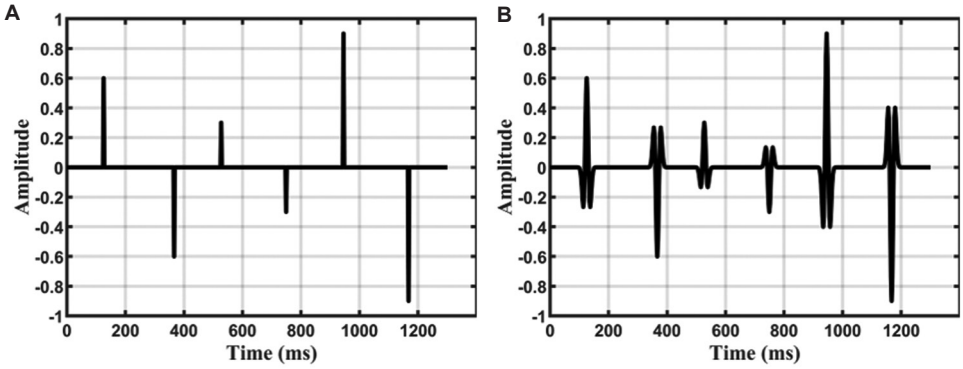


**Figure 4.** Theoretical model. (A) Reflection coefficient. (B) Synthetic seismogram.

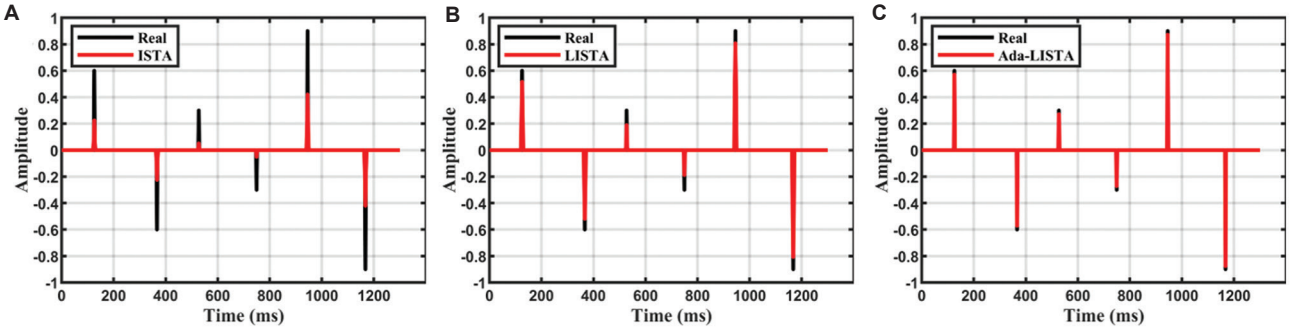


**Figure 5.** Deconvolution results on noise-free simulated data. (A) Iterative shrinkage-thresholding algorithm (ISTA). (B) Learned ISTA (LISTA). (C) Adaptive LISTA.

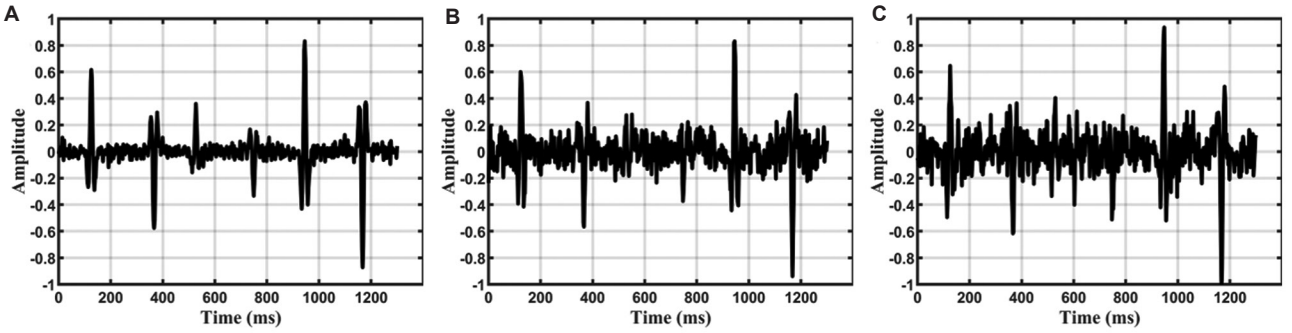


**Figure 6.** Noisy theoretical model. Signal-to-noise ratio of (A) 10 dB, (B) 3 dB, and (C) 1 dB.

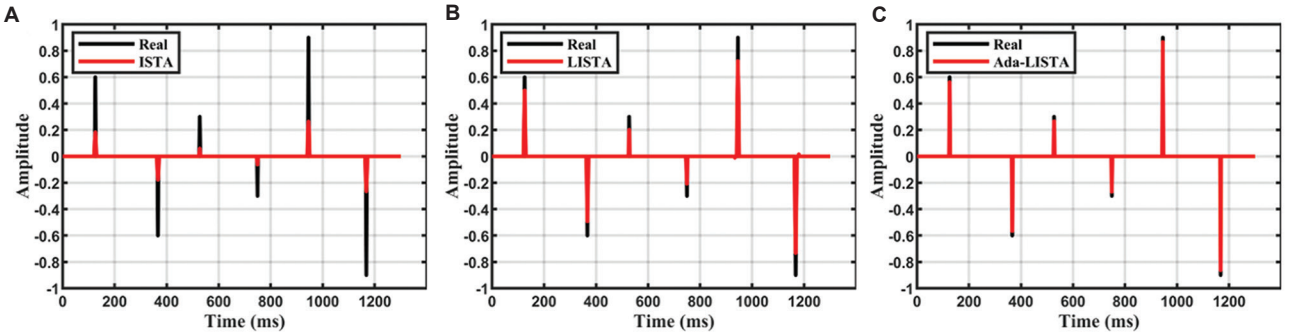


**Figure 7.** Deconvolution results at a signal-to-noise ratio of 10 dB. (A) Iterative shrinkage-thresholding algorithm (ISTA). (B) Learned ISTA (LISTA). (C) Adaptive LISTA.

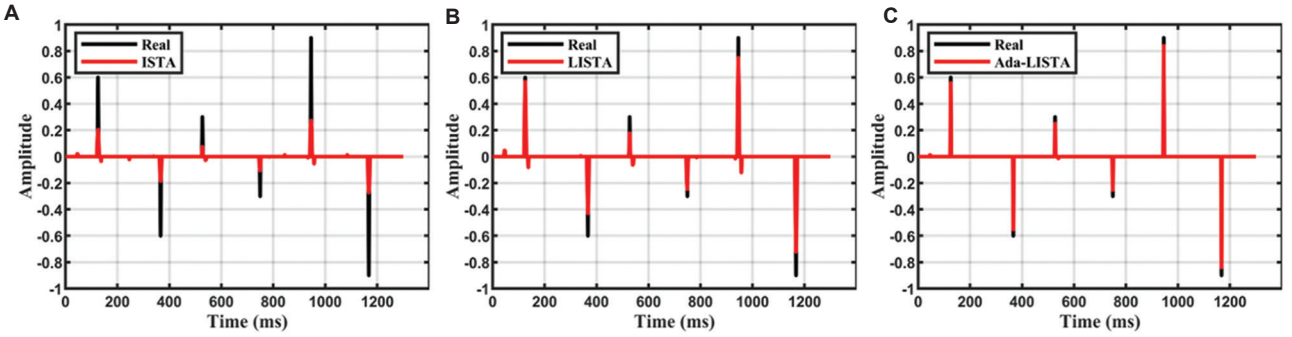


**Figure 8.** Deconvolution results at a signal-to-noise ratio of 3 dB. (A) Iterative shrinkage-thresholding algorithm (ISTA). (B) Learned ISTA (LISTA). (C) Adaptive LISTA.

parameters, whereas Ada-LISTA demonstrated superior noise robustness, realizing better amplitude recovery and maintaining higher accuracy in weak reflection coefficient recovery compared to both benchmarks.

When the SNR was as low as 1 dB, as depicted in Figure 9, the Err of ISTA, LISTA, and the proposed Ada-LISTA were 0.8007, 0.3582, and 0.1851, respectively. The deconvolution performance of the traditional ISTA algorithm degraded significantly. Amplitude attenuation was prominent, and weak reflection coefficients can hardly be accurately recovered. While LISTA achieved certain improvements over ISTA, it still struggled with severe noise interference. In comparison, although the method proposed in this study was affected by noise interference, its deconvolution results can still maintain a certain reliability under extremely low SNR conditions. It also outperformed the traditional ISTA and LISTA algorithms in both amplitude recovery effect and weak reflection coefficient identification ability. These results indicate that the method proposed in this study has stronger robustness and reflection coefficient recovery ability when processing low SNR data.

### 3.3. Application of real seismic data

Seismic data from the lower member of the Minghuazhen Formation in an oilfield within the Bohai Bay Basin, China, were chosen to evaluate the algorithm's applicability. The data has a sampling interval of 2 ms. Within the work area, structural undulations were small, faults were relatively well-developed, and strata were well-developed. The original seismic data of the target interval were of poor quality, with poor continuity of event axes, vague reflection interfaces, and low overall resolution. A local seismic profile of this target interval is shown in Figure 10, which did not meet the requirements for fine reservoir characterization and was suitable as actual data for verifying the effectiveness of the algorithm.

After processing with the traditional ISTA algorithm, the results in Figure 11A show that the continuity of

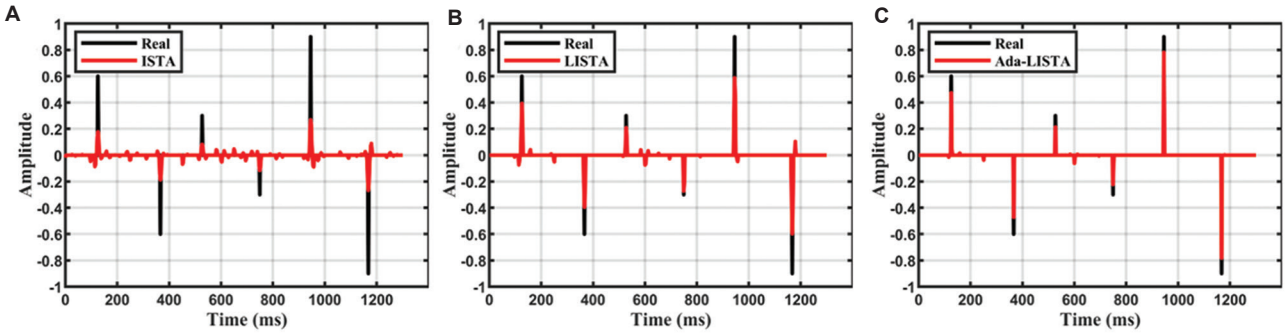


**Figure 9.** Deconvolution results at a signal-to-noise ratio of 1 dB. (A) Iterative shrinkage-thresholding algorithm (ISTA). (B) Learned ISTA (LISTA). (C) Adaptive LISTA.

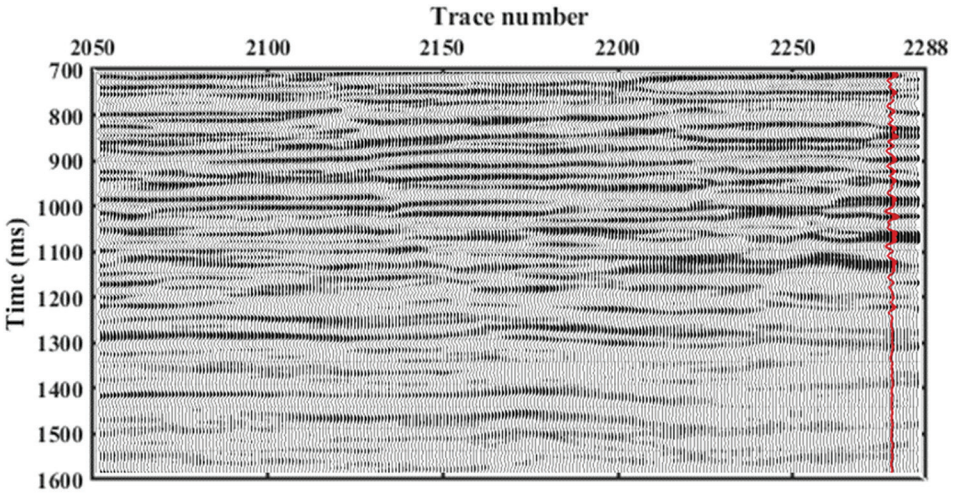


**Figure 10.** Field seismic data of the Minghuazhen Formation in an oilfield within the Bohai Bay Basin, China.

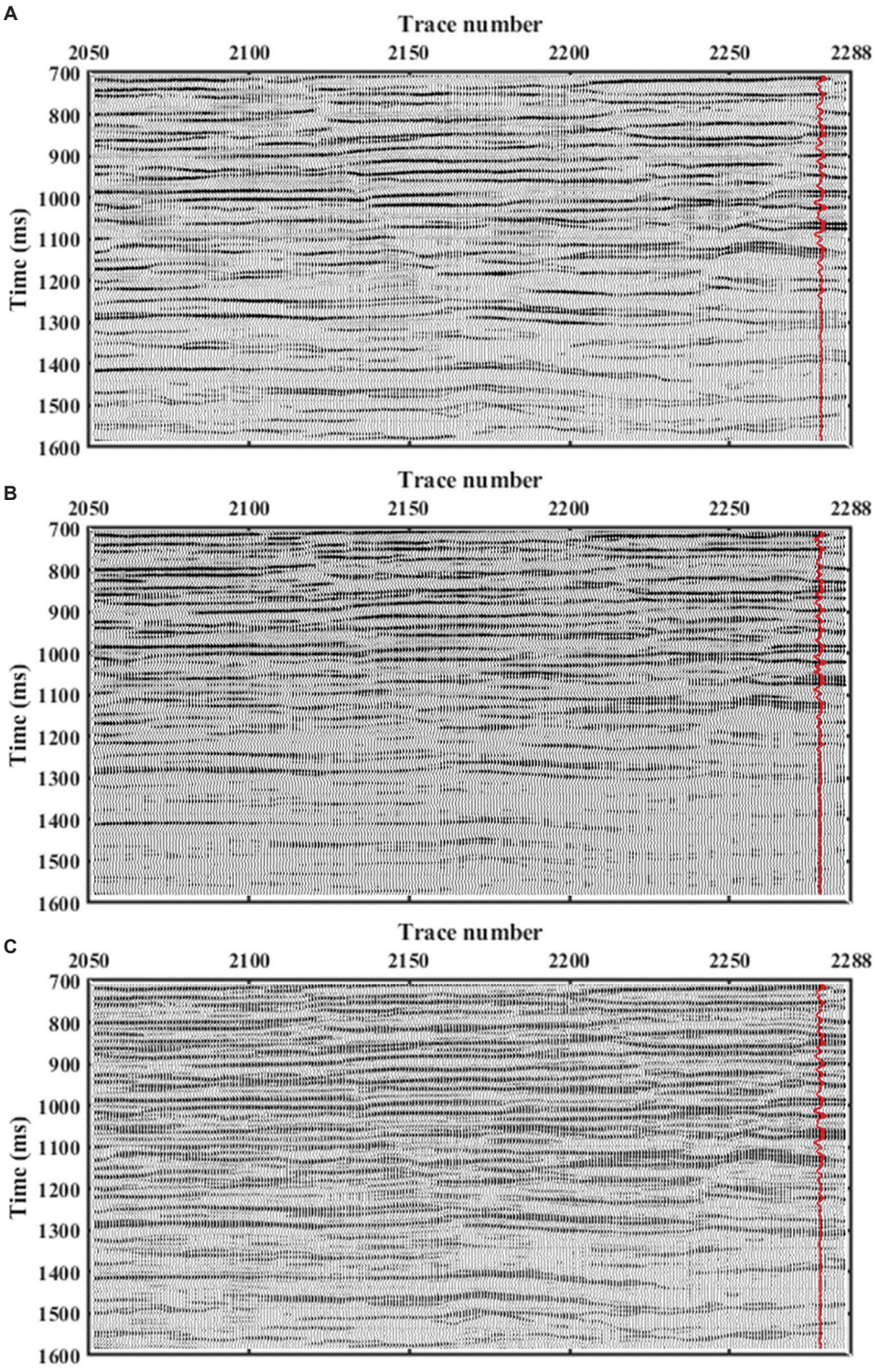


**Figure 11.** Deconvolution results of the Minghuazhen Formation in an oilfield within the Bohai Bay Basin, China. (A) Iterative shrinkage-thresholding algorithm (ISTA). (B) Learned ISTA (LISTA). (C) Adaptive LISTA.

seismic events in some regions of the seismic profile improved, with enhancements in the clarity of certain reflection interfaces. Compared with the original profile, the resolution increased, but the overall characterization

of details remained limited. Seismic events in some areas were still blurred, and the recovery of weak reflection signals was unsatisfactory. While LISTA outperformed ISTA in event continuity (Figure 11B), it still lacked sufficient weak reflection recovery due to its fixed dictionary. After processing with our method, the results in Figure 11C revealed a notable increase in the quantity of seismic events in the seismic profile. The distribution of interfaces was denser and more continuous. The clarity and detail characterization of seismic events were notably enhanced. Especially, the initially vague weak reflection zones were effectively strengthened. Reflection interfaces became sharper. Overall interpretability improved, with better agreement with the well log.

These results were further verified by Pearson correlation coefficient calculations. The correlation coefficient for the original profile and the well log was 0.6831, which increased to 0.8103 after ISTA processing and to 0.8369 after LISTA processing. The profile processed using the proposed method achieved the highest correlation with the well log, at 0.8783.

To further compare differences in the characterization of seismic profile details among various methods, a typical area within the aforementioned profile was selected for magnification of local information, as shown in Figure 12.

Comparisons revealed that in the detail area of the original profile, as presented in Figure 12A, the events were interleaved and reflections were blurred. After processing with the traditional ISTA, as shown in Figure 12B, some events were separated to a certain extent, but details remained limited. Although LISTA resolved more events than ISTA, the results in Figure 12C show that it failed to adequately distinguish weak reflections and thin layers. In contrast, after processing with our method, as depicted in Figure 12D, the events were continuous and detailed, and the thin-layer structures and weak reflection events were expressed more clearly. Specifically, weak reflection coefficients (marked by red arrows in Figure 12) were distinctly resolved, while the fidelity of the proposed method (indicated by blue arrows in Figure 12) was validated by the well-preserved strong reflections inherent to the original data. This aligns with changes in the overall profile and significantly enhances the identifiability of small-scale structures and thin interbeds within reservoirs.

The results of spectral analysis in Figure 13 indicate that, compared with the original seismic records and the traditional ISTA and LISTA methods, the method proposed in this study showed a gentler amplitude attenuation in the medium and high-frequency bands. The dominant frequency was progressively increased from 37.5 Hz for the original data to 47.5 Hz after ISTA, 52.5 Hz after LISTA, and 62.5 Hz after Ada-LISTA. Moreover, the effective bandwidth measured at −3 dB broadened from 42 Hz for the original records to 47 Hz after ISTA, 52.5 Hz after LISTA, and 60.5 Hz after Ada-LISTA. These quantitative improvements confirm that the proposed method significantly widened the effective frequency band and increased the dominant frequency, leading to a noticeable improvement in overall resolution. It also exhibited a stronger ability to recover high-frequency and weak signals.

To further validate the generalization capability of the method for more complex geological structures, this study tested it on actual seismic data from another work area. This area exhibited more intricate geology with significant lateral variations in stratigraphy. The field seismic data were characterized by a low SNR and poor resolution, featuring a dominant frequency of only 24 Hz and a narrow effective bandwidth. Consequently, this new dataset provided a more suitable test for evaluating the algorithm's adaptability and robustness under challenging low SNR and low-resolution conditions.

Figure 14 displays the field seismic data, which exhibited poor continuity of the event axes and vague reflection interfaces. These data were processed using the traditional ISTA, LISTA, and the proposed Ada-LISTA methods, with the results presented in Figure 15.

A comparison revealed that the ISTA-processed result (Figure 15A) only partially improved the continuity of the event axes, with a correlation coefficient of 0.5768 compared to 0.5055 for the field seismic data. Its ability to enhance weak reflections was limited, and the overall profile remained blurred. The LISTA-processed result (Figure 15B) showed an improvement over ISTA, yielding clearer event axes and achieving a higher correlation of 0.7550. However, its performance was constrained by a fixed dictionary, which limited its adaptability to complex geological structures. In contrast, the profile processed by the proposed Ada-LISTA method (Figure 15C) demonstrated superior performance, attaining the highest correlation coefficient of 0.8053. It exhibited significantly enhanced event continuity, successfully recovered more weak reflection events, presented sharper reflection interfaces, and ultimately revealed richer geological details.

To further compare the differences in detail rendering among the various methods, a typical region within the profile was selected for local magnification, as shown in Figure 16. The local details in the field seismic data (Figure 16A) exhibited cross-cutting events and disordered reflections. Although the ISTA-processed result (Figure 16B) demonstrated some separation effect, the details remained relatively coarse. The LISTA

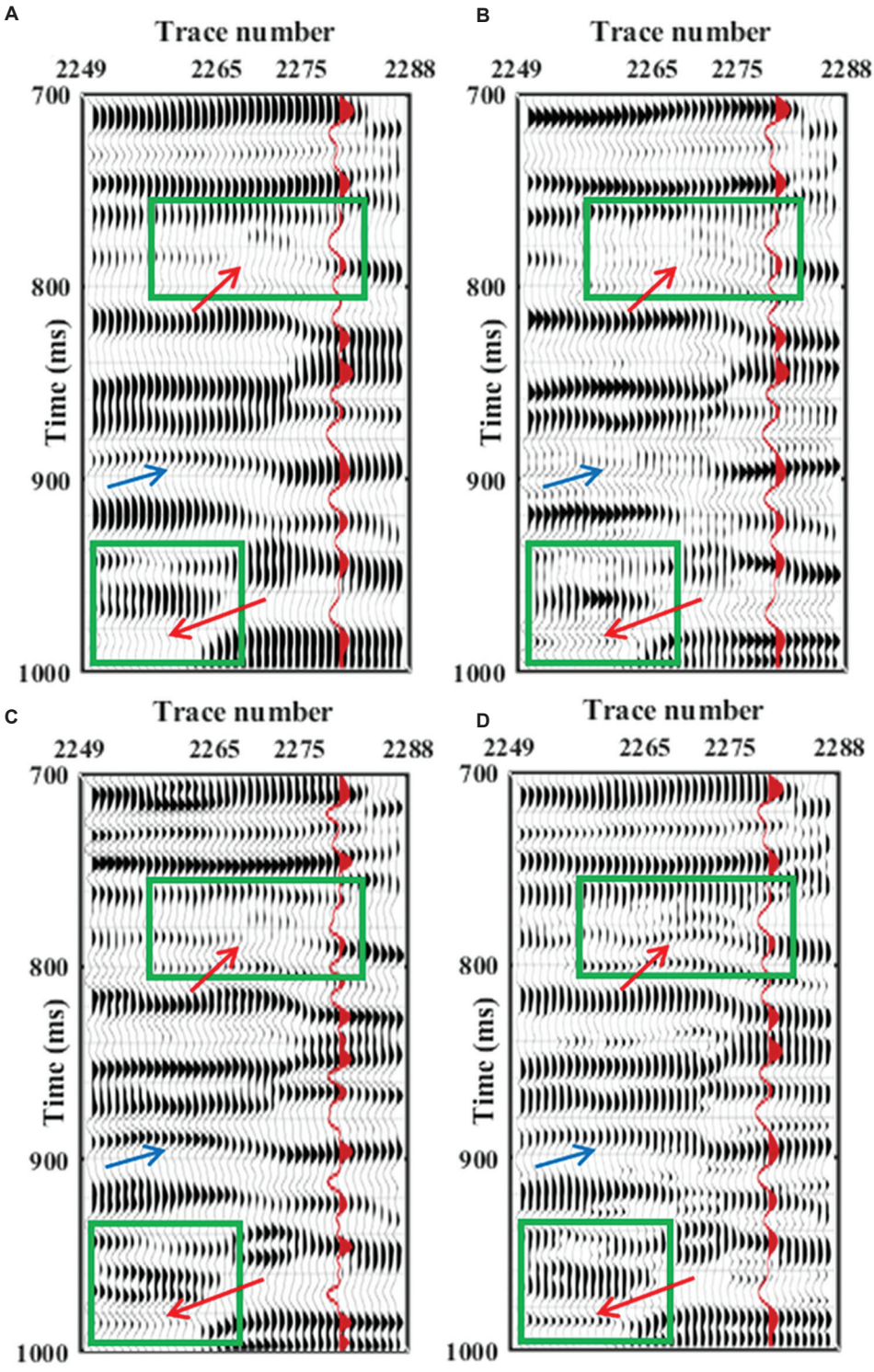


**Figure 12.** Amplified view of local details from the deconvolution results of the Minghuazhen Formation in an oilfield within the Bohai Bay Basin, China. (A) Field seismic data. (B) Iterative shrinkage-thresholding algorithm (ISTA). (C) Learned ISTA (LISTA). (D) Adaptive LISTA.

result (Figure 16C) resolved more seismic events but exhibited limited ability to distinguish thin interlayers and weak reflections. In contrast, the result from the method proposed in this study (Figure 16D) presented a continuous, clear arrangement of seismic events. Both thin-layer structures and weak reflection events were

clearly depicted, while strong reflection signals maintained fidelity consistent with the field data.

The spectral analysis results in Figure 17 further validated the significant effectiveness of this method in expanding the frequency band and enhancing the dominant frequency. The dominant frequency progressively increased from 24 Hz for the original data to 38 Hz after ISTA, 52 Hz after LISTA, and 58 Hz after Ada-LISTA. Moreover, the effective bandwidth measured at −3 dB broadened from 17.5 Hz for the original records to 29.5 Hz after ISTA, 54 Hz after LISTA, and 57 Hz after Ada-LISTA. This demonstrates that the method proposed in this paper can effectively broaden the effective frequency band, increase the dominant frequency, and significantly improve profile resolution and geological detail recognition capability even in work areas with more complex geological conditions.

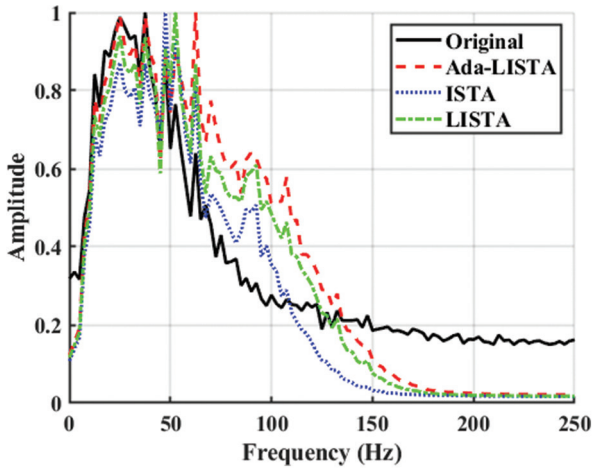


**Figure 13.** Spectrum analysis of the Minghuazhen Formation in an oilfield within the Bohai Bay Basin, China
Abbreviations: Ada: Adaptive; ISTA: Iterative shrinkage-thresholding algorithm; L: Learned.

The experimental results above demonstrate that the proposed sparse pulse deconvolution method, based on Ada-LISTA and a physics-driven self-supervised objective function, exhibited excellent generalization capability and stability across diverse geological backgrounds and resolution conditions. It effectively restored weak reflection signals and enhanced seismic data resolution, thereby possessing significant practical application value.

## 4. Discussion

This study developed a sparse spike deconvolution method based on the Ada-LISTA network architecture. The method effectively improved the shortcomings of the traditional ISTA algorithm in recovering weak reflection coefficients and notably boosted the algorithm's overall processing performance by introducing a self-supervised objective function and integrating an adaptive learning mechanism, based on the Ada-LISTA architecture. It dynamically adjusts threshold and step size parameters through an adaptive learning mechanism, thus effectively overcoming the deficiencies of traditional ISTA in recovering weak reflection coefficients. Meanwhile, in response to the actual needs of seismic data processing, the self-supervised objective function was incorporated into the model optimization process, enabling it to better express and recover weak reflection signals under complex geological conditions without the need for labeled data. Compared with LISTA and its variants, this method uses the dictionary as the network input, further enhancing the model's adaptability to different scenarios. It performed exceptionally well in processing weak reflection signals, demonstrating stronger generalization performance and practical effects.

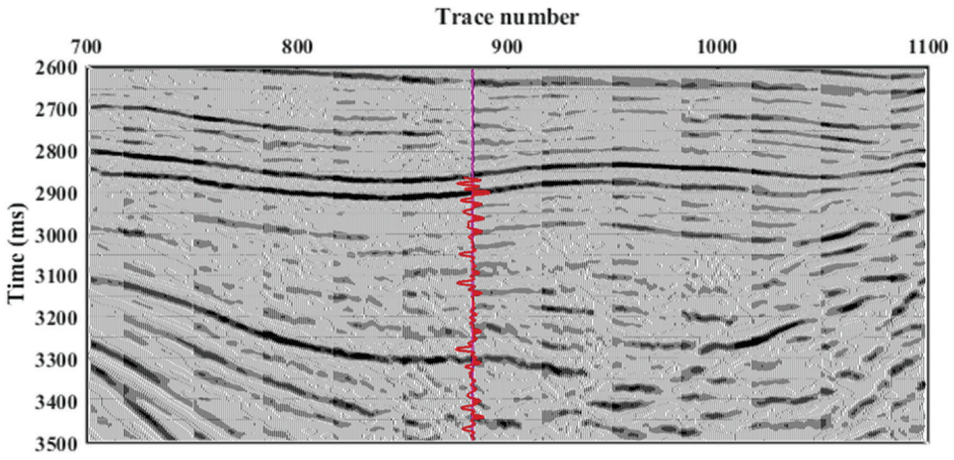


**Figure 14.** Field seismic data of the second work area.

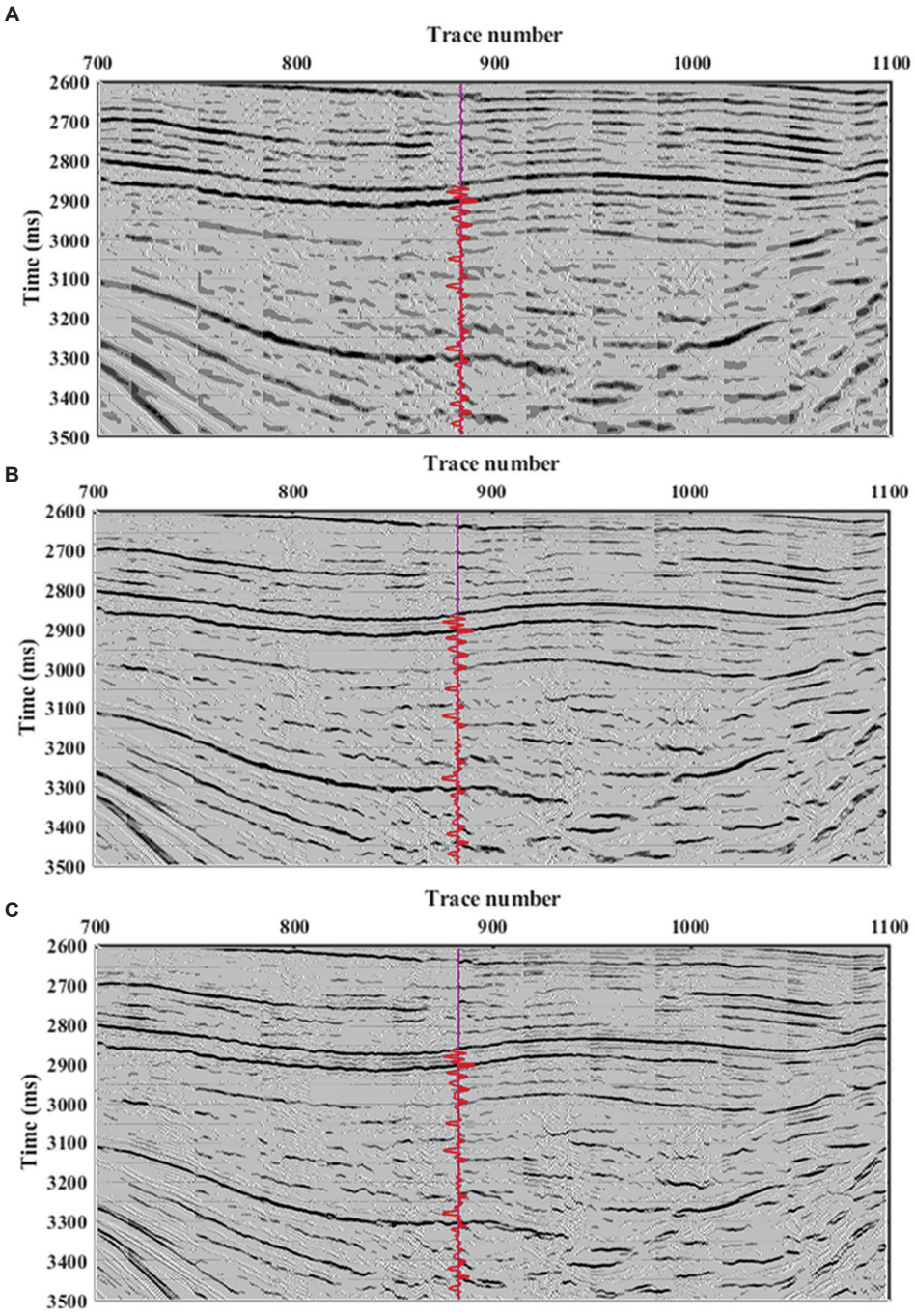


**Figure 15.** Deconvolution results of the second work area. (A) Iterative shrinkage-thresholding algorithm (ISTA). (B) Learned ISTA (LISTA). (C) Adaptive LISTA.

To evaluate the performance of the proposed approach, comparative experiments were conducted against traditional ISTA and LISTA. The results demonstrated that Ada-LISTA, which incorporated a self-supervised learning mechanism, exhibited superiority across multiple testing scenarios. In tests with simulated seismic data, this method not only enhanced the recovery accuracy of reflection coefficients but also performed excellently in thin layer identification and weak reflection signal enhancement. In noise resistance experiments, it can still effectively extract reflection coefficients even under low SNR conditions, showing stronger robustness and stability.

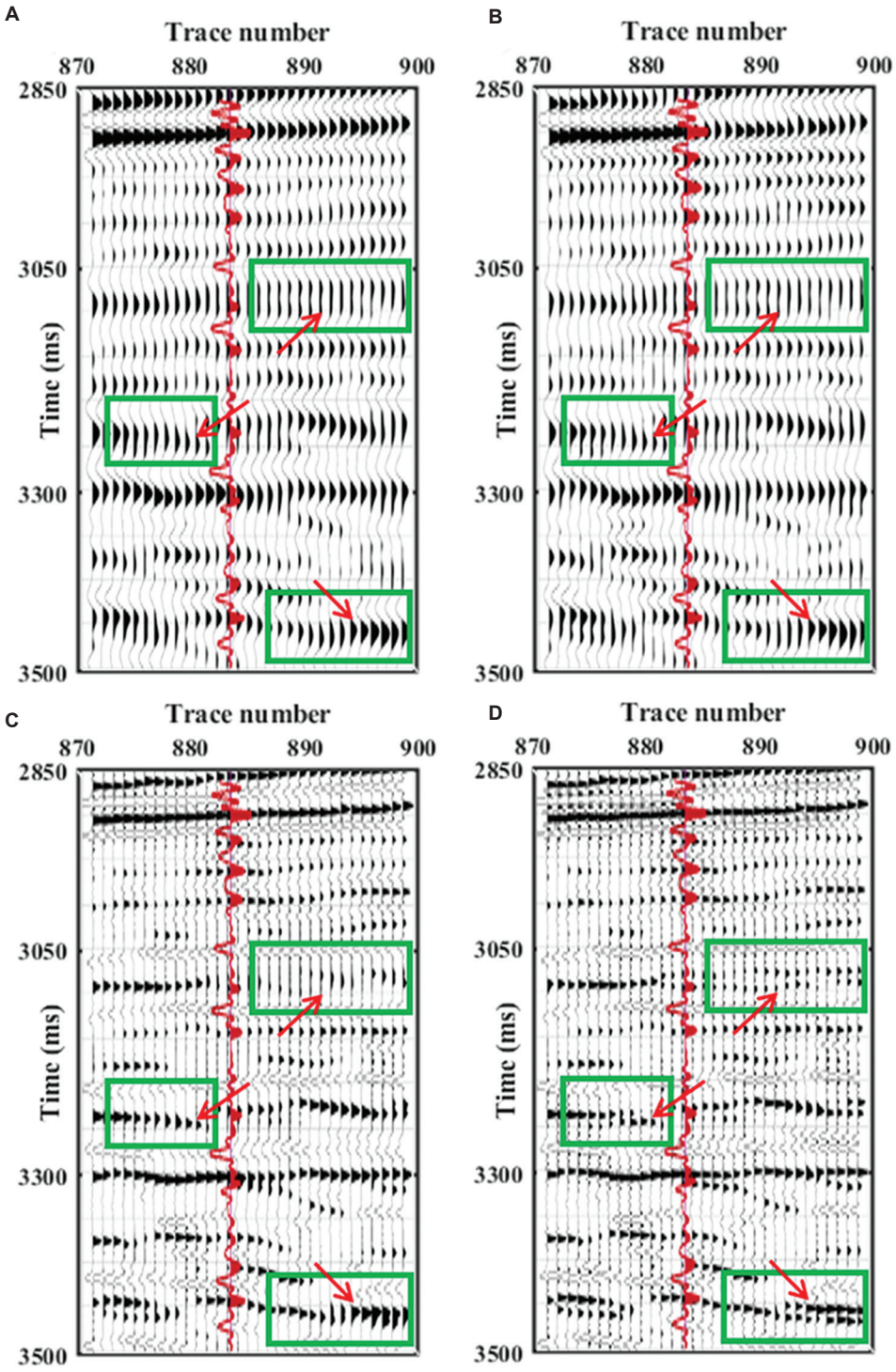


**Figure 16.** Amplified view of local details from the deconvolution results of the second work area. (A) Field seismic data. (B) Iterative shrinkage-thresholding algorithm (ISTA). (C) Learned ISTA (LISTA). (D) Adaptive LISTA.

These experimental findings robustly demonstrated the efficacy of the proposed approach when applied to complex seismic data.

The proposed method exhibited significant advantages in recovering weak reflection coefficients. Compared with the inversion with elastic-net regularization,[42] which relies

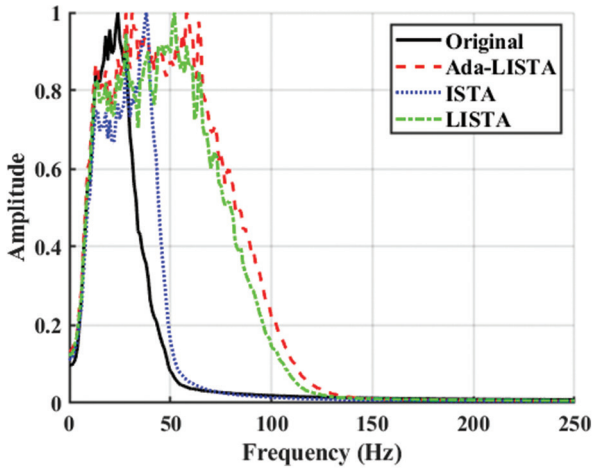


**Figure 17.** Spectrum analysis of the second work area
Abbreviations: Ada: Adaptive; ISTA: Iterative shrinkage-thresholding algorithm; L: Learned.

heavily on prior model constraints during the recovery of weak reflection signals, the method achieved accurate recovery of weak reflection coefficients without labeled data through a self-supervised objective function and an adaptive dictionary update strategy. Basis pursuit denoising in the joint time–frequency domain[43] improves time–frequency resolution via basis pursuit denoising technology, but suffers from high parameter sensitivity. In contrast, our proposed method adopted an adaptive learning mechanism to realize dynamic parameter adjustment, which effectively enhanced the ability to extract weak reflection signals under different geological scenarios. The seismic wavelet shape-oriented reflectivity inversion[44] method performs optimization based on prior assumptions of waveform shapes, and its performance is easily constrained. In contrast, the proposed approach integrated a deep-learning-based framework with geophysical prior knowledge and further improved recovery accuracy and adaptability through optimized objective function design. Extragradient-based LISTA[24] improves model performance through residual structures and modified threshold functions, but still has limitations under complex geological conditions. Our proposed method further integrated residual structures with deep learning methods, fully exploited geophysical prior information, and significantly enhanced the identification and recovery effects of weak reflection signals.

Application of the proposed method to real seismic data demonstrated that Ada-LISTA, combined with a self-supervised learning mechanism, significantly improved the resolution of seismic sections, thereby verifying its practical effectiveness. However, the method still has several limitations in practical applications. Wavelet phase shift can introduce non-negligible errors in deconvolution accuracy, especially when the zero-phase assumption deviates from actual conditions, leading to waveform distortion. To mitigate such errors and waveform distortion, Chen *et al.*[45] proposed that envelope-based sparse constraints can enhance wavelet stability, and also demonstrated that full-band data reconstruction is effective in addressing wavelet instability during inversion.[46]

The current noise robustness evaluation was limited to Gaussian random noise, which differs from real seismic scenarios where coherent noise and non-stationary noise are prevalent. These complex noise types can mask weak reflection signals and degrade inversion consistency more severely than Gaussian noise. Meanwhile, the balance coefficients A and B and adaptive parameters in the self-supervised objective function have demonstrated favorable performance for the actual seismic data used in this study. They may show reduced adaptability when applied to data with distinct geological backgrounds or signal characteristics due to the variability of subsurface structures. In addition, the multi-level iteration of Ada-LISTA requires adaptive updates of thresholds, step sizes, and weight matrices for each layer, which increases computational complexity for large-scale seismic surveys. Runtime comparison with ISTA and LISTA on the field data showed that Ada-LISTA takes approximately 1.5 times longer than LISTA due to adaptive parameter learning. High sampling rates can further amplify this burden, potentially limiting the method's practicality in time-sensitive large field projects. This runtime increase is manageable for medium-scale surveys but necessitates targeted optimization for field-scale applications.

Although the sparse spike deconvolution method constructed based on Ada-LISTA has achieved significant progress in several aspects, the model relies on the integrity and variety of the input datasets. Its computational efficiency may be affected when processing extremely high sampling rates or extremely complex geological structures. In this study, a self-supervised objective function was introduced into the Ada-LISTA framework, enabling the model to achieve adaptive optimization without labeled data and effectively expanding the application scope.

To address these limitations, future research should focus on multiple aspects. Researchers can integrate more sophisticated deep learning frameworks to enhance processing performance and computational efficiency. Adaptive parameter-tuning strategies, tailored to diverse data scenarios, can be explored to improve the model's generalization capability. Additionally, multi-task learning and transfer learning can be employed to increase the model's adaptability to different geological conditions. To

bolster robustness against various types of seismic noise, noise-specific suppression strategies can be integrated with adaptive learning mechanisms. Furthermore, lightweight network design and iterative pruning can be adopted to balance inversion performance with computational efficiency while maintaining high accuracy. Collectively, these advancements aim to address the challenges posed by the complexity and diversity of seismic data, which demand superior generalization from the model.

## 5. Conclusion

An enhanced seismic sparse spike deconvolution method was developed by integrating a self-supervised learning mechanism into the Ada-LISTA architecture. This method dynamically optimized threshold and step size parameters while refining the objective function by incorporating geophysical prior knowledge. It not only markedly strengthened the capability to recover weak reflection signals but also further elevated the model's interpretability and adaptability. Simultaneously, by utilizing the dictionary as input data, the model's adaptability to diverse geological scenarios was effectively enhanced, successfully surmounting the limitations of traditional methods when addressing complex geological conditions. Applied to real seismic data from the Bohai Bay Basin, China, this approach demonstrated significant advantages in enhancing the resolution of seismic profiles. It effectively remedied the deficiencies of the traditional ISTA algorithm in the recovery of weak reflection signals, offering reliable technical support for the detailed interpretation of complex geological bodies.

## Acknowledgments

None.

## Funding

This work was supported in part by the Deep Earth Probe and Mineral Resources Exploration–National Science and Technology Major Project (2025ZD1004600), in part by the Natural Science Foundation of Sichuan Province (2024NSFSC0808), and in part by the Talent Project of Chengdu Technological University (2024RC028).

## Conflict of interest

The authors declare they have no competing interests.

## Author contributions

*Conceptualization:* Shunhao Hu, Shulin Pan
*Formal analysis:* Ziyu Qin
*Investigation:* Shunhao Hu, Shulin Pan, Yaojie Chen
*Methodology:* Yinghe Wu
*Validation:* Shulin Pan
*Visualization:* Shunhao Hu, Yaojie Chen
*Writing–original draft:* Shunhao Hu
*Writing–review & editing:* Shunhao Hu, Shulin Pan, Yinghe Wu

## Availability of data

The data are available from the corresponding author on reasonable request.

## References

1. Pan S, Yan K, Lan H, Badal J, Qin Z. Adaptive step-size fast iterative shrinkage-thresholding algorithm and sparse-spike deconvolution. *Comput Geosci*. 2020;134:104343.

   doi: 10.1016/j.cageo.2019.104343

2. Levy S, Fullagar PK. Reconstruction of a sparse spike train from a portion of its spectrum and application to high-resolution deconvolution. *Geophysics*. 1981;46(9):1235-1243.

   doi: 10.1190/1.1441261

3. Lavielle M. 2-D bayesian deconvolution. *Geophysics*. 1991;56(12):2008-2018.

   doi: 10.1190/1.1443013

4. Walden AT, Hosken JWJ. An investigation of the spectral properties of primary reflection coefficients. *Geophys Prospect*. 1985;33(3):400-435.

   doi: 10.1111/j.1365-2478.1985.tb00443.x

5. Walden AT. Non-gaussian reflectivity, entropy, and deconvolution. *Geophysics*. 1985;50(12):2862.

   doi: 10.1190/1.1441905

6. Symes WW. The seismic reflection inverse problem. *Inverse Probl*. 2009;25(12):123008.

   doi: 10.1088/0266-5611/25/12/123008

7. Chen SS, Donoho DL, Saunders MA. Atomic decomposition by basis pursuit. *SIAM J Sci Comput*. 1998;20(1):33-61.

   doi: 10.1137/s1064827596304010

8. Mallat SG, Zhang Z. Matching pursuits with time-frequency dictionaries. *IEEE Trans Signal Process*. 1993;41(12):3397-3415.

   doi: 10.1109/78.258082

9. Cai TT, Wang L. Orthogonal matching pursuit for sparse signal recovery with noise. *IEEE Trans Inform Theory*. 2011;57(7):4680-4688.

   doi: 10.1109/tit.2011.2146090

10. Beck A, Teboulle M. A fast iterative shrinkage-thresholding algorithm for linear inverse problems. *SIAM J Imaging Sci*. 2009;2(1):183-202.

    doi: 10.1137/080716542

11. Zhang J, Ghanem B. ISTA-Net: Interpretable Optimization-Inspired Deep Network for Image Compressive Sensing. In: *2018 IEEE/CVF Conference on Computer Vision and Pattern Recognition (CVPR)*. Salt Lake City, UT, USA: IEEE; 2018. p. 1828-1837.

    doi: 10.1109/cvpr.2018.00196

12. Schnoor E, Behboodi A, Rauhut H. Generalization error bounds for iterative recovery algorithms unfolded as neural networks. *Inf Inference*. 2023;12(3):2267-2299.

    doi: 10.1093/imaiai/iaad023

13. Pan S, Yan K, Lan H, Badal J, Qin Z. A sparse spike deconvolution algorithm based on a recurrent neural network and the iterative shrinkage-thresholding algorithm. *Energies*. 2020;13(12):3074.

    doi: 10.3390/en13123074

14. Ito D, Takabe S, Wadayama T. Trainable ISTA for sparse signal recovery. *IEEE Trans Signal Process*. 2019;67(12):3113-3125.

    doi: 10.1109/tsp.2019.2912879

15. Hinton GE, Salakhutdinov RR. Reducing the dimensionality of data with neural networks. *Science*. 2006;313(5786):504-507.

    doi: 10.1126/science.1127647

16. Ranzato M, Boureau YL, LeCun Y. Sparse Feature Learning for Deep Belief Networks. In: Platt J, Koller D, Singer Y, Roweis S, editors. *Proceedings of the 21st Annual Conference on Neural Information Processing Systems(NIPS 2007)*. Vancouver, BC, Canada: Neural Information Processing Systems; 2007. p. 1185-1192.

17. Bengio Y, Lamblin P, Popovici D, Larochelle H. Greedy Layer-Wise Training of Deep Networks. In: Schölkopf B, Platt J, Hoffman T, editors. *Proceedings of the 20th Annual Conference on Neural Information Processing Systems(NIPS 2006)*. Vancouver, BC, Canada: Neural Information Processing Systems Foundation; 2006. p. 153-60.

18. Chai X, Tang G, Lin K, *et al*. Deep learning for multitrace sparse-spike deconvolution. *Geophysics*. 2021;86(3):V207-V218.

    doi: 10.1190/geo2020-0342.1

19. Gregor K, LeCun Y. Learning Fast Approximations of Sparse Coding. In: Furnkranz J, Joachims T, editors. *Proceedings of the 27th International Conference on Machine Learning*. Haifa, Israel; 2010. p. 399-406.

20. Liu J, Chen X, Wang Z, Yin W. Alista: Analytic Weights are as Good as Learned Weights in LISTA. In: *Proceedings of the 7th International Conference on Learning Representations (ICLR 2019)*. New Orleans, LA, United States: International Conference on Learning Representations (ICLR); 2019.

21. Wu K, Guo Y, Li Z, Zhang C. Sparse Coding with Gated Learned ISTA. In: *Proceedings of the 8th International Conference on Learning Representations (ICLR 2020)*. Addis Ababa, Ethiopia: International Conference on Learning Representations (ICLR); 2020.

22. Zheng Z, Dai W, Xue D, Li C, Zou J, Xiong H. Hybrid ISTA: Unfolding ISTA with convergence guarantees using free-form deep neural networks. *IEEE Trans Pattern Anal Mach Intell*. 2022;45(3):3226-3244.

    doi: 10.1109/tpami.2022.3172214

23. Ablin P, Moreau T, Massias M, Gramfort A. Learning Step Sizes for Unfolded Sparse Coding. In: Wallach H, Larochelle H, Beygelzimer A, D'Alché-Buc F, Fox E, Garnett R, editors. *Proceedings of the 33rd Annual Conference on Neural Information Processing Systems (NIPS 2019)*. Vancouver, BC, Canada: Neural Information Processing Systems Foundation; 2019.

24. Li Y, Kong L, Shang F, Liu Y, Liu H, Lin Z. Learned extragradient ISTA with interpretable residual structures for sparse coding. *Proc AAAI Conf Artif Intell*. 2021;35(10):8501-8509.

    doi: 10.1609/aaai.v35i10.17032

25. Kim D, Park D. Element-wise adaptive thresholds for learned iterative shrinkage thresholding algorithms. *IEEE Access*. 2020;8:45874-45886.

    doi: 10.1109/access.2020.2978237

26. Liang W, Liu J, Zhu J. Improved analytic learned iterative shrinkage thresholding algorithm and its application to tomographic synthetic aperture radar building object height inversion. *Mathematics*. 2024;12(10):1464.

    doi: 10.3390/math12101464

27. Chen X, Wang Z, Liu J, Yin W. Theoretical Linear Convergence of Unfolded ISTA and its Practical Weights and Thresholds. In: Bengio S, Wallach H, Larochelle H, Grauman K, Cesa-Bianchi N, Garnett R, editors. *Proceedings of the 32nd Conference on Neural Information Processing Systems*. Montreal, QC, Canada: Neural Information Processing Systems Foundation; 2018. p. 9061-9071.

28. Wang M, Zhang Z, Qiu X, Gao S, Wang Y. ATASI-Net: An efficient sparse reconstruction network for tomographic SAR imaging with adaptive threshold. *IEEE Trans Geosci Remote Sens*. 2023;61:1-18.

    doi: 10.1109/tgrs.2023.3268132

29. Aberdam A, Golts A, Elad M. Ada-LISTA: Learned solvers adaptive to varying models. *IEEE Trans Pattern Anal Mach Intell*. 2022;44(12):9222-9235.

    doi: 10.1109/tpami.2021.3125041

30. Abd Rahman AS, Elsheikh AH, Jaya MS. A deep semi-supervised learning approach for seismic reflectivity inversion. *IEEE Trans Geosci Remote Sens*. 2024;62:5927714.

    doi: 10.1109/tgrs.2024.3401768

31. Alfarraj M, AlRegib G. Semisupervised sequence modeling for elastic impedance inversion. *Interpretation*. 2019;7(3):SE237-SE249.

doi: 10.1190/int-2018-0250.1

32. Zhao Y, Li Y, Wang S, Yang B. Physical model and super-resolution theory-guided unsupervised deep learning deconvolution for seismic resolution enhancement. *IEEE Trans Geosci Remote Sens*. 2025;63:1-13.

doi: 10.1109/tgrs.2025.3531359

33. Liu B, Jiang P, Wang Q, Ren Y, Yang S, Cohn AG. Physics-driven self-supervised learning system for seismic velocity inversion. *Geophysics*. 2023;88(2):R145-R161.

doi: 10.1190/geo2021-0302.1

34. Zhang J, Sun H, Zhang G, Huang X, Han L. Simultaneous physics and model-guided seismic inversion based on deep learning. *IEEE Trans Geosci Remote Sens*. 2024;62:1-11.

doi: 10.1109/tgrs.2024.3443970

35. Schuster GT, Chen Y, Feng S. Review of physics-informed machine-learning inversion of geophysical data. *Geophysics*. 2024;89(6):T337-T356.

doi: 10.1190/geo2023-0615.1

36. Song C, Lu M, Li Y, *et al*. Spatial pattern learning: Dip structure constraint multi-view convolutional neural network for pre-stacked seismic inversion. *IEEE Trans Geosci Remote Sens*. 2023;61:1-16.

doi: 10.1109/tgrs.2023.3307897

37. Feng W, Liu Y, Li Y, Li H, Wang X. Acoustic impedance prediction using an attention-based dual-branch double-inversion network. *Earth Sci Inform*. 2025;18(1):70.

doi: 10.1007/s12145-024-01548-4

38. Zou B, Wang Y, Chen T, Liang J, Yu G, Hu G. The domain adversarial and spatial fusion semi-supervised seismic impedance inversion. *IEEE Trans Geosci Remote Sens*. 2024;62:1-15.

doi: 10.1109/tgrs.2023.3336392

39. Zhu L, Zhang F, Zhang S, Wu J. Semi-supervised intelligent inversion from prestack seismic attributes guided by geophysical prior knowledge. *J Appl Geophys*. 2025;233:105620.

doi: 10.1016/j.jappgeo.2025.105620

40. Shi Y, Zhang B, Xu J, Wang Y, Jin Z. Joint supervised and semi-supervised seismic velocity model building based on VGU network. *IEEE Trans Geosci Remote Sens*. 2025;63:1-14.

doi: 10.1109/tgrs.2025.3533548

41. Ge Q, Cao H, Yang Z, Yuan S, Song C. Deep-learning-based prestack seismic inversion constrained by AVO attributes. *IEEE Geosci Remote Sens Lett*. 2024;21:1-5.

doi: 10.1109/lgrs.2024.3373197

42. Dai R, Yin C, Peng D. An application of elastic-net regularized linear inverse problem in seismic data inversion. *Appl Sci*. 2023;13(3):1525.

doi: 10.3390/app13031525

43. Zhao X, Wu H, Li X, Peng Z, Li Y. Seismic reflection coefficient inversion using basis pursuit denoising in the joint time-frequency domain. *Energies*. 2020;13(19):5025.

doi: 10.3390/en13195025

44. Chen S, Fu X, Shi Y, Cao S. Seismic wavelet shape-oriented reflectivity inversion method. *J Geophys Eng*. 2024;21(4):1216-1229.

doi: 10.1093/jge/gxae065

45. Chen G, Yang W, Liu Y, Luo J, Jing H. Envelope-based sparse-constrained deconvolution for velocity model building. *IEEE Trans Geosci Remote Sens*. 2022;60:1-13.

doi: 10.1109/tgrs.2021.3063514

46. Chen G, Yang W, Wang H, Zhou H, Huang X. Elastic full waveform inversion based on full-band seismic data reconstructed by dual deconvolution. *IEEE Geosci Remote Sens Lett*. 2022;19:1-5.

doi: 10.1109/lgrs.2022.3178915

ACCSCIENCE PUBLISHING

Journal of Seismic Exploration

ARTICLE

# A physics-constrained autoencoder for full-waveform inversion using axial self-attention

**Yunbo Niu[1,2], Yingming Qu[1,2]*, and Zhenchun Li[1,2]**

[1]State Key Laboratory of Deep Oil and Gas, China University of Petroleum (East China), Qingdao, Shandong, China

[2]School of Geosciences, China University of Petroleum (East China), Qingdao, Shandong, China

(This article belongs to the *Special Issue: Full Waveform Inversion Methods and Applications for Seismic Data in Complex Media*)

## Abstract

Full-waveform inversion (FWI) is highly sensitive to the initial model and low-frequency content, and it often suffers from cycle skipping and degraded resolution in complex media. We propose a physics-constrained autoencoder-based FWI with axial self-attention (AxPCAE-FWI). In a unified encoder–decoder architecture, a differentiable acoustic wave-equation solver is explicitly embedded, and the data-domain waveform misfit is used as the primary objective, so that training is consistently governed by wave physics and does not rely on paired seismic–velocity labels. The encoder extracts inversion-relevant, low-dimensional features, while the decoder reconstructs physically admissible velocity models. To capture long-range spatiotemporal dependencies in the time–offset plane, axial multi-head self-attention is introduced in the encoder, where global attention is computed separately along the time and receiver axes; two one-dimensional global attentions approximate a single two-dimensional (2D) global attention, reducing the computational complexity relative to full 2D attention while preserving global context. This design improves the representation of complex wavefield phenomena, including multiples, converted waves, and far-offset reflections, thereby alleviating cycle skipping when low-frequency information is limited. Numerical experiments on the Marmousi2 and Society of Exploration Geophysicists salt-dome models demonstrate stable convergence and high structural similarity with improved geological plausibility. Compared to conventional physics-informed adaptive extended FWI under the same iteration budget, AxPCAE-FWI yields clearer salt-body boundaries and better imaging of structurally complex regions, with improved robustness to noise.

***Keywords:*** Full-waveform inversion; Deep learning; Self-attention; Physics-constrained autoencoder; Autoencoder

***Corresponding author:**
Yingming Qu
(20180041@upc.edu.cn)

**Citation:** Niu Y, Qu Y, Li Z. A physics-constrained autoencoder for full-waveform inversion using axial self-attention. *J Seismic Explor*. 2026;35(1):269-281. doi: 10.36922/JSE025480119

**Received:** November 24, 2025

**Revised:** January 9, 2026

**Accepted:** January 9, 2026

**Published online:** February 23, 2026

**Copyright:** © 2026 Author(s). This is an Open-Access article distributed under the terms of the Creative Commons Attribution License, permitting distribution, and reproduction in any medium, provided the original work is properly cited.

**Publisher's Note:** AccScience Publishing remains neutral with regard to jurisdictional claims in published maps and institutional affiliations.

## 1. Introduction

High-resolution imaging of the subsurface is a key step in improving the reliability of structural interpretation, reducing the overall cost of geophysical exploration, and enhancing the efficiency of resource development. As exploration targets have gradually shifted from simple structures to deeper, more complex formations and unconventional reservoirs, conventional imaging methods based on wave-equation migration and

ray theory have become increasingly inadequate in terms of resolution and quantitative inversion capability. Consequently, full-waveform inversion (FWI) has attracted widespread attention. By solving the forward wave equation and minimizing the waveform misfit between simulated and observed seismic records, FWI enables high-resolution reconstruction of subsurface medium parameters and is regarded as an important bridge between seismic imaging and subsurface property inversion.[1-4] In its classical framework, FWI typically adopts gradient-based or quasi-Newton optimization schemes to iteratively update the velocity model by minimizing a data-misfit objective function, and in theory can recover subsurface structures at wavelength or even subwavelength scales. In practical applications, however, acoustic FWI remains the most widely used form. It solves only the acoustic wave equation and inverts for the P-wave velocity model, simplifying the Earth as an isotropic, lossless scalar medium. This approximation is relatively effective in marine environments, but in complex onshore settings, the subsurface usually exhibits pronounced elastic behavior, anisotropy, and strong heterogeneity. Under such conditions, the acoustic approximation cannot explicitly account for S-waves and other elastic parameters, and it treats multiparameter coupling effects, such as those between velocity and density, in an oversimplified manner, thereby limiting the physical consistency and interpretational reliability of the inversion results. Mora[5] likened FWI to a combination of migration and tomography: the FWI process is equivalent to performing migration imaging and reflection tomography simultaneously, where tomography updates the background velocity field, and migration moves reflectors to their correct positions. Thus, the quality of an FWI result can be judged by how well the recovered model geometry matches the true reflector geometry. Nevertheless, FWI is intrinsically a strongly nonlinear inverse problem and faces multiple challenges. It is highly sensitive to the initial model: if the starting velocity field significantly deviates from the true subsurface, or if the observed data lack sufficient low-frequency content, large phase and cycle discrepancies arise between simulated and real wavefields. This leads to a highly multimodal objective function, making the inversion prone to being trapped in local minima, a phenomenon known as cycle skipping.[4] To provide a more suitable initial model for FWI, Xu *et al.*[6] proposed reflection waveform inversion, which fully exploits reflection data to simultaneously update the background velocity and delineate reflectors, and the resulting model can then serve as the initial model for FWI. Moreover, the computational cost of FWI is extremely high: large-scale forward and adjoint wavefield simulations must be repeatedly performed at high spatial and temporal resolution, imposing stringent demands on memory and computational resources.

In recent years, deep learning techniques have been successfully applied across numerous research fields.[7] In the field of geophysics, classical multilayer perceptron and convolutional neural network (CNN) architectures have been used for reflectivity inversion,[8,9] velocity inversion,[10-15] seismic tomography,[16-20] and impedance inversion.[21,22] In the context of velocity model building and waveform-based inversion, learning-based studies related to FWI can be described according to how neural networks are used with the physics-driven FWI workflow. A line of work targets data-driven seismic inversion, where a network learns a direct mapping from seismic waveforms to velocity models and produces rapid velocity estimates in a machine-learning paradigm.[23,24] These outputs are not necessarily generated using an iterative FWI update loop; however, the predicted models can be used to support FWI in a practical manner, for example, by providing profile- or model-level initialization for subsequent FWI iterations.[25] Another line of work uses deep learning to construct informative starting models for conventional physics-based FWI, such as CNN-based starting-model building for near-surface two-dimensional (2D) FWI.[26] In addition, deep learning can act within an iterative FWI procedure by introducing learned regularizers or plug-in refinement modules to improve stability and convergence, including diffusion-model-based learned regularization for multiparameter elastic FWI[27] and the "deep velocity generator" that refines starting or intermediate velocity models (together with migrated images) during FWI to mitigate cycle skipping and accelerate convergence.[28] Finally, a growing body of research couples neural networks more tightly with wave-equation physics, enabling training driven by data-domain waveform misfit and physical constraints without requiring paired seismic–model labels, such as physics-informed generative adversarial network-based FWI,[24] latent representation learning in physics-informed neural networks for FWI,[29] parametric CNN-domain FWI,[30] and deep neural network-based reparameterized FWI frameworks for regularization and uncertainty quantification.[31-33] Collectively, these developments indicate that integrating neural networks with wave-equation physics provides a viable route to stable, accurate velocity model building.

In this study, we propose a method that integrates the acoustic wave equation into an autoencoder architecture equipped with axial self-attention mechanisms. Physically, coherent reflections, multiples, and converted-wave arrivals follow kinematically consistent trajectories on the time–offset plane, governed by propagation paths and limited-aperture (Fresnel-zone) coherence. The axial self-attention exploits this structure by aggregating

information separately along time and offset: time-axis attention emphasized phase-consistent temporal patterns, while offset-axis attention adaptively selects an effective receiver aperture and downweights kinematically inconsistent energy. As a result, the network could better capture long-range spatiotemporal correlations and preserve event continuity and phase consistency in the time–offset domain. The acoustic wave equation was used to generate synthetic seismic data for a given velocity model, while the observed seismic records were used as inputs to the network. Under these physical constraints, the network was trained to infer the corresponding velocity model. The reconstructed velocity model was then input into an acoustic finite-difference partial differential equation forward simulator to generate synthetic seismic data. The network loss is defined as the discrepancy between the synthetic data predicted from the current velocity model and the reference (observed) seismic data. By backpropagating this misfit, we computed the gradients of the loss with respect to the network weights, enabling the network to learn how to transform latent features extracted from the observed data into an accurate velocity model. This physics-informed framework did not require an explicit initial model or low-frequency data to achieve convergence, thereby mitigating the cycle-skipping problem. We demonstrated the effectiveness of the proposed method on the Marmousi2 model and the Society of Exploration Geophysicists (SEG) salt model.

## 2. Methods

In conventional FWI, time-domain elastic velocity-stress equations are used for forward modeling to generate synthetic seismic data. The ultimate goal is to minimize the misfit between observed and synthetic data to invert for the velocity model. The data misfit is typically defined by the following objective function (**Equation 1**):

$$\min \mathcal{J}(m) = \sum_{k=1}^{N_s} \sum_{j=1}^{N_r} \sum_{n=1}^{N_t} \left\| d_{obs} - d_{pred} \right\|_2^2 \quad (1)$$

where $d_{obs}$ denotes the observed seismic data and $d_{pred}$ represents the synthetic data generated from the current model.

To minimize the objective function in **Equation 1**, the inversion is typically initialized with a starting model and then iteratively updated according to the following rule (**Equation 2**):

$$m^{k+1} = m^k - \alpha \nabla C(m^k) \quad (2)$$

Where $\alpha$ is the step size, and $\nabla C(m^k)$ denotes the gradient of the objective function with respect to the model parameters. The gradient is typically computed using the adjoint-state method,[34] which enables efficient evaluation of sensitivity kernels for updating the model.

We utilized the physics-constrained autoencoder-based FWI with axial self-attention (AxPCAE-FWI) network architecture as illustrated in Figure 1. We followed the optimization philosophy of conventional FWI and took the observed seismic records $d_{obs}$ as input. Through a data-driven, physics-constrained encoder–decoder framework, we obtained the subsurface parameter model $m$. The encoder was used to extract a low-dimensional latent representation that was most relevant to inversion from $d_{obs}$, while the decoder mapped the extracted latent features,

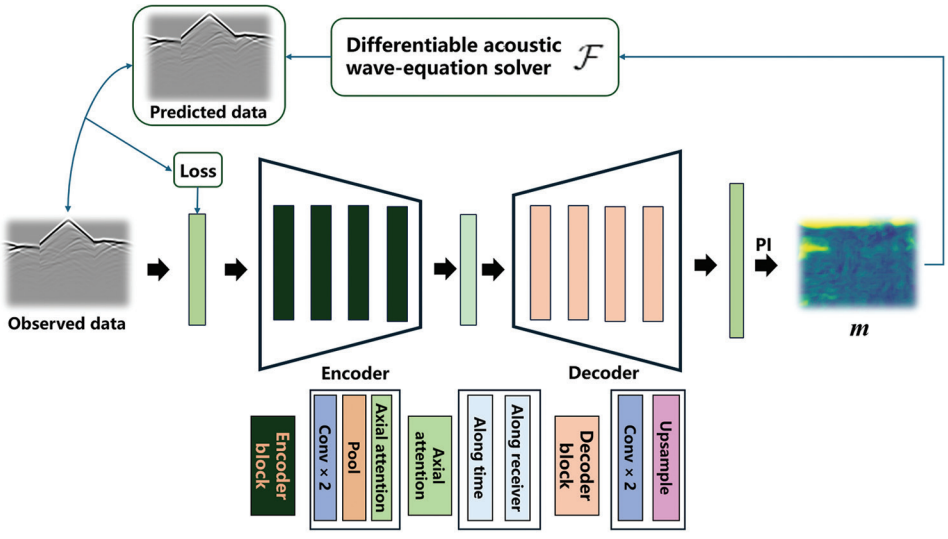


**Figure 1.** Architecture of the physics-constrained autoencoder-based full-waveform inversion with axial self-attention
Abbreviation: PI: Physics-informed.

under explicit physical constraints, to the desired velocity model. The predicted velocity model was then passed to a differentiable acoustic wave-equation solver $\mathcal{F}$ to generate synthetic seismic data $d_{pred}$ corresponding to the current model. A data-domain consistency loss was constructed between $d_{pred}$ and $d_{obs}$, thereby enforcing physical laws during network training.

Once the observed seismic data $d_{obs}$ were input to the network, they passed through four pooling layers in the encoder, where inversion-related features were progressively extracted and compressed into a latent representation, denoted as $\hat{z} \in (0,1)$. To enhance the modeling capability for long-range spatiotemporal correlations, we inserted axial multi-head self-attention blocks after selected pooling layers: scaled dot-product attention was computed independently along the time and receiver (offset) axes. The resulting attention features were fused with the backbone features via residual connections. The key idea was to approximate a full 2D global attention operation using two one-dimensional global attentions; compared to 2D global attention, axial multi-head self-attention substantially reduced computational cost. Meanwhile, for seismic records defined on the time–offset plane, which exhibited a strong one-dimensional sequential structure in time and were subjected to clear physical constraints along offset, axial self-attention was better suited than purely local convolutions for capturing long-range spatiotemporal dependencies associated with multiples, converted waves, and far-offset reflections, while preserving the continuity and phase consistency of reflection events in both time and space. Each attention block was followed by a point-wise feedforward network and residual connections to further enhance the representational power. The resulting feature maps were then fed into the decoder, which contained four upsampling layers that gradually restored the original spatial resolution of the latent representation. Finally, an affine transformation mapped the normalized network output to a physically admissible parameter interval [$m_{min}$, $m_{max}$], yielding the target model $m$ (**Equation 3**):

$$m = m_{\min} + \sigma(\hat{z}) \odot \left(m_{\max} - s m_{\min}\right) \tag{3}$$

Where $\sigma(\cdot)$ is the Sigmoid function and $\odot$ denotes element-wise (Hadamard) multiplication. This mapping was implemented using the Sigmoid layer followed by linear rescaling at the end of the decoder, which guaranteed that the output parameters fell within the prescribed physical bounds. The Sigmoid function is defined as **Equation 4**:

$$\sigma(x) = \frac{1}{1+e^{-x}} \tag{4}$$

The obtained model $m$ was then fed into the differentiable acoustic wave-equation solver $\mathcal{F}$ to generate the simulated seismic record $d_{pred}$, as shown in **Equation 5**:

$$d_{\text{pred}} = \mathcal{F}(m) \tag{5}$$

Accordingly, the objective function used in all experiments is the data-domain waveform-fitting loss (**Equation 6**):

$$\mathcal{L}_{\text{data}} = \frac{1}{N}\sum_{i=1}^{N}\left(\left\| d_{pred}(i) - d_{obs}(i)\right\|^2\right) \tag{6}$$

Notably, we did not introduce an explicit hidden/latent-space regularization term in this work; therefore, its weight was set to zero. The latent bottleneck and the physically admissible output mapping in **Equation 3** acted as implicit regularization.

The gradients of this loss with respect to the network weights were computed through backpropagation, and the Adam optimizer was then used to update $\omega$, as shown in **Equation 7**:

$$\omega_{t+1} = \omega_t - \alpha \cdot \frac{\partial \mathcal{L}_{data}}{\partial \omega} \tag{7}$$

Where $\alpha$ denotes the learning rate.

As the iterations progressed, the network learned to optimize a latent representation that could generate synthetic seismic records closely matching the observed data and to decode this representation into the velocity model, thereby yielding accurate FWI results.

We assessed the performance of the proposed AxPCAE-FWI framework using the structural similarity index (SSIM) and the peak signal-to-noise ratio (PSNR). SSIM quantifies perceptual similarity by jointly comparing luminance, contrast, and structural information between two images, and thus reflects how well edges and fine spatial details are preserved. The SSIM is defined as **Equation 8**:

$$\text{SSIM}(x,y) = \frac{(2\mu_x\mu_y + C_1)(2\sigma_{xy} + C_2)}{(\mu_x^2 + \mu_y^2 + C_1)(\sigma_x^2 + \sigma_y^2 + C_2)} \tag{8}$$

where $\mu_x$ and $\mu_y$ denote the mean values of the two images, $\sigma_x^2$ and $\sigma_y^2$ represent their variances, and $\sigma_{xy}$ is the covariance between them.

An SSIM value closer to 1 indicates a higher degree of structural similarity. The PSNR is defined as **Equation 9**:

$$\text{PSNR} = 10 \cdot \log_{10}\left(\frac{M^2}{\text{MSE}}\right) \tag{9}$$

Where M denotes the maximum possible (peak) value of the original image. A larger PSNR value indicates higher numerical fidelity and better reconstruction quality.

## 3. Results

### 3.1. Marmousi2 model

We evaluated the inversion performance of AxPCAE on the Marmousi2 model. The selected Marmousi2 model had a size of 1,790 × 1,410 grid points, with both horizontal and vertical grid spacing set to 10 m. The source was a Ricker wavelet with a dominant frequency of 20 Hz.

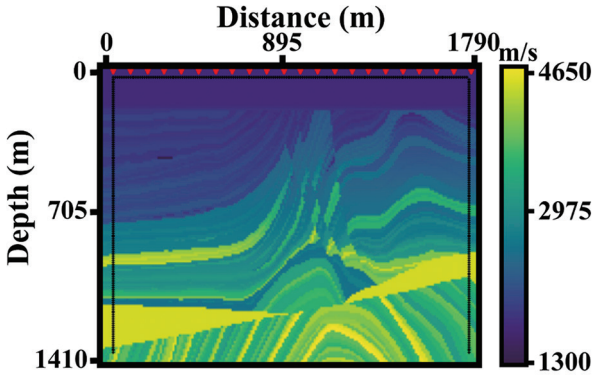


**Figure 2.** Marmousi2 model

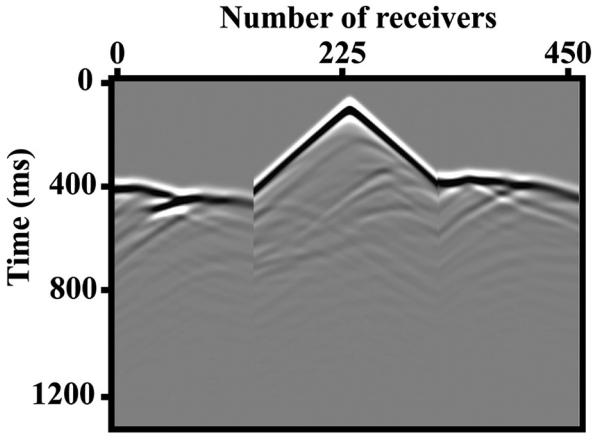


**Figure 3.** Seismic records of the Marmousi2 model

The acquisition geometry is shown in Figure 2, where red inverted triangles indicate source locations and black line denotes receiver positions. This acquisition configuration provides seismic records with richer information content (Figure 3).

The observed seismic records were then fed into AxPCAE, and the corresponding inversion results are shown in Figure 4. Figure 4A presents the result after the first iteration, Figure 4B after 100 iterations, and Figure 4C after 1,000 iterations. These results showed that the proposed method can perform FWI without requiring an explicit initial model. After 100 iterations (Figure 4B), the lateral velocity variations in the shallow and middle parts of the Marmousi2 model were clearly delineated: the continuity and geometry of several major reflectors were well reconstructed, and some high-wavenumber components began to be superimposed on the low-wavenumber background, making reflector boundaries sharper and structural undulations more distinct. At this stage, however, the deeper structures remained relatively smooth and several local features remained insufficiently resolved, indicating that the inversion was in a transition phase from predominantly low-frequency to mid–high-frequency updates, and that the multi-scale inversion had not yet fully converged.

When the number of iterations increased to 1,000 (Figure 4C), the model exhibited richer high-frequency details and finer lateral heterogeneities. Small-scale velocity fluctuations within the shallow sedimentary layers were clearly resolved, the undulations and bending of interfaces in structurally complex zones were well recovered, and the main deep reflectors together with underlying structures showed high resolution and good phase continuity. Meanwhile, the recovered velocity values remained within a physically plausible range, without obvious unphysical high-/low-velocity anomalies or strong striping artifacts. These observations demonstrate that, by incorporating axial self-attention and physical constraints, AxPCAE-FWI can progressively inject high-frequency information while preserving an accurate low-frequency background, thereby achieving consistent multi-scale

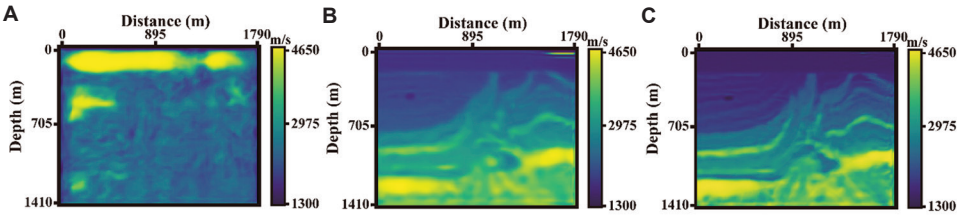


**Figure 4.** Physics-constrained autoencoder-based full-waveform inversion with axial self-attention inversion results for the Marmousi2 model. (A) Inversion result after the first iteration. (B) Inversion result after 100 iterations. (C) Inversion result after 1,000 iterations.

inversion that balances global convergence with high-resolution imaging capability.

Figure 5 presents single-trace velocity comparisons at x = 100 m and x = 600 m in the Marmousi2 model. For both profiles, the predicted curves closely followed the overall velocity gradient and the primary interface locations over the entire depth range, with only slight smoothing and mildly reduced amplitudes observed in structurally complex mid-to-deep sections. This indicates that AxPCAE exhibits strong inversion capability on the Marmousi2 model and can produce accurate inversion results.

Figure 6 compares the inversion results on the Marmousi2 model, where Figure 6A shows the physics-informed autoencoder (PIAE) result after 1,000 iterations and Figure 6B shows the AxPCAE result at the same iteration count. Due to the lack of high-wavenumber information, the PIAE result exhibited discontinuous undulations of shallow layered structures, blurred interface boundaries, and locally uneven layer thicknesses. Below the main reflector, extensive low-velocity patches and locally unrealistic velocity anomalies were observed within the high-velocity layer, breaking intra-layer continuity. In contrast, by introducing axial attention, AxPCAE could effectively constrain the focusing of wavefield energy along the true interfaces, thereby enhancing the imaging resolution and geological plausibility of the Marmousi2 model.

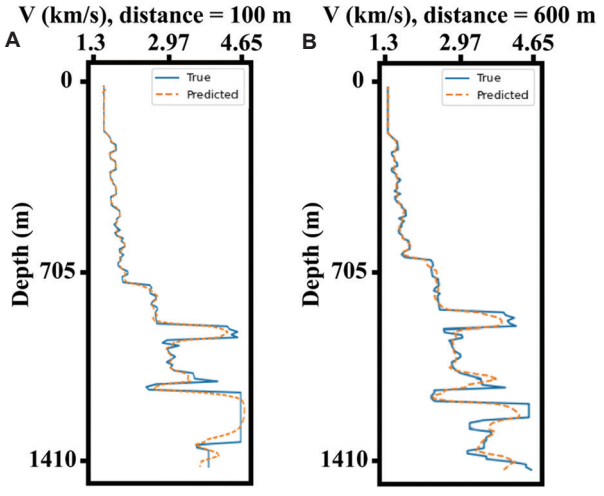


**Figure 5.** Trace-by-trace comparison between the inversion result of physics-constrained autoencoder-based full-waveform inversion with axial self-attention and the true model. (A) Single-trace comparison at x = 100 m. (B) Single-trace comparison at x = 600 m.

### 3.2. SEG's salt-dome model

We evaluated the performance of AxPCAE in the presence of strong overburden shielding using the SEG salt model (Figure 7). The model comprised 1,760 × 1,510 grid points, with both horizontal and vertical grid spacings set to 10 m. The source was a Ricker wavelet with a dominant frequency of 20 Hz, and the corresponding observed seismic records used as input are shown in Figure 8.

The inversion results obtained using AxPCAE-FWI for the SEG salt model are shown in Figure 9. Figure 9A presents the result after the first iteration, Figure 9B after 500 iterations, and Figure 9C after 1,000 iterations. As the iterations progressed to 500 steps, the overall geometry of the salt body was already well established (Figure 9B): the position and undulating features of the top-salt interface were reasonably recovered, the steeply dipping flanks on both sides of the salt-dome gradually emerged, and the velocity contrast within the overburden and parts of the subsalt region was enhanced, indicating that mid–high-wavenumber information began to be superimposed on the low-wavenumber background. However, a certain degree of subsalt under-illumination remained, and the resolution of some local structures remained limited, suggesting that, under strong velocity contrasts and complex multi-path wave propagation, the subsalt velocity field was still being progressively adjusted.

Examining the final inversion result (Figure 9C), AxPCAE-FWI achieved an accurate and high-resolution

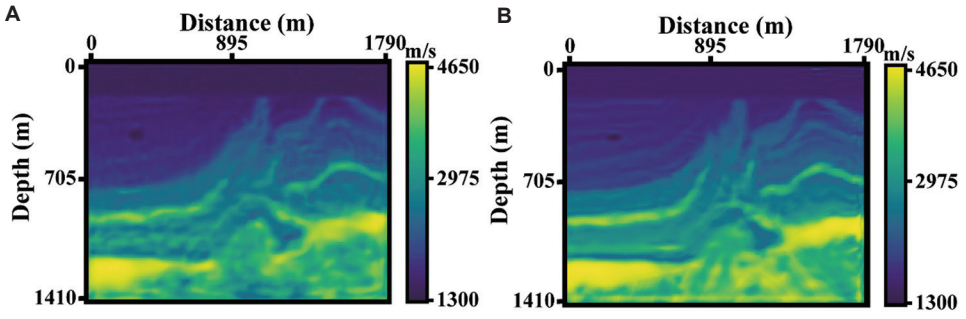


**Figure 6.** Comparison of inversion results for the Marmousi2 model obtained using (A) physics-informed autoencoder-full-waveform inversion and (B) physics-constrained autoencoder-based full-waveform inversion with axial self-attention after 1,000 iterations.

image of both the salt dome and subsalt structures in the presence of a strong shielding salt body. The top and base of the salt body, as well as the lateral flanks, were sharply delineated, and their geometry closely matched that of the target model. Layering within the overburden was well characterized, while the main subsalt reflectors and the underlying structures exhibited good phase continuity and a realistic description of lateral heterogeneities. The overall velocity distribution was smooth yet not overly smoothed, with no obvious nonphysical high- or low-velocity streaks or numerical oscillations. These results demonstrate that, in the challenging setting of a typical salt-body overburden, AxPCAE-FWI can build a stable low-wavenumber background and gradually compensate for wavefield distortion and illumination loss caused by the salt, thereby enabling effective inversion of subsalt targets and showcasing strong robustness and multi-scale imaging capability.

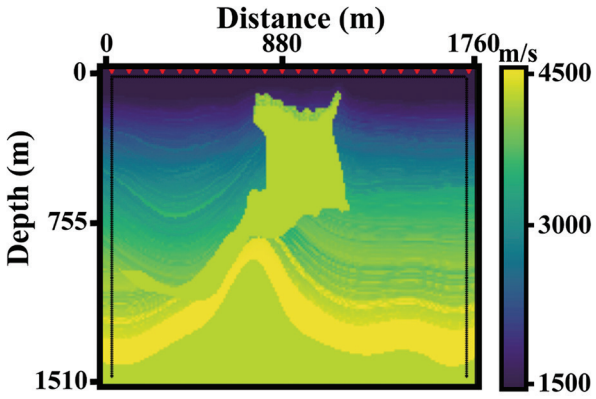


**Figure 7.** Society of Exploration Geophysicists salt-dome model

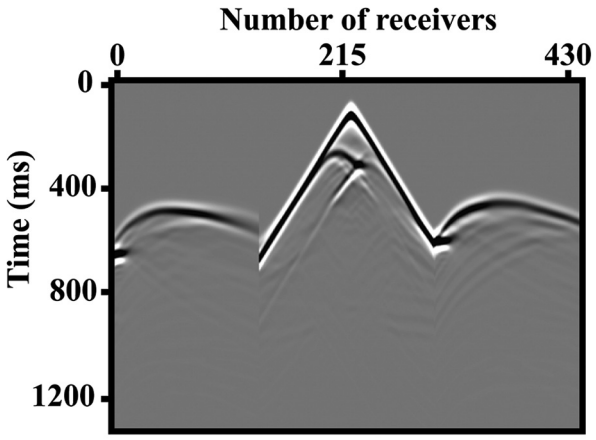


**Figure 8.** Seismic records of the Society of Exploration Geophysicists salt-dome model

Figure 10 shows single-trace velocity comparisons at x = 100 m (Figure 10A) and x = 600 m (Figure 10B). For the profile at 100 m, the inverted curve closely matched the true model over the entire depth range, with only slight smoothing observed in a few thin layers, indicating that both velocity gradients and fine-scale details could be accurately recovered in well-illuminated regions. In contrast, the profile at 600 m still aligned reasonably well with the true model in the shallow section, but exhibited pronounced discrepancies in the deeper subsalt zone: the sharp high-velocity contrasts were significantly smoothed, and their amplitudes were underestimated, reflecting that illumination loss induced by the overlying salt body continued to limit the inversion resolution in the subsalt region.

Similarly, we compared the proposed method with PIAE, and the results are shown in Figure 11. The PIAE-FWI result was clearly inferior (Figure 11A). The top-salt interface appeared relatively blurred, and the high-velocity anomaly diffused to varying degrees into the overlying sediments. The velocity transition zone between the salt body and the surrounding rocks was overly smoothed, resulting in insufficient constraints on the position and geometry of the interface. The imaging of the salt flanks exhibited trailing and smearing artifacts, and the high-wavenumber energy failed to adequately focus along the true boundaries. In the subsalt region, the velocity distribution contained numerous artifacts, showed poor lateral continuity, and had indistinct boundaries of the main structural units. Overall, the imaging quality was significantly lower than that of AxPCAE-FWI (Figure

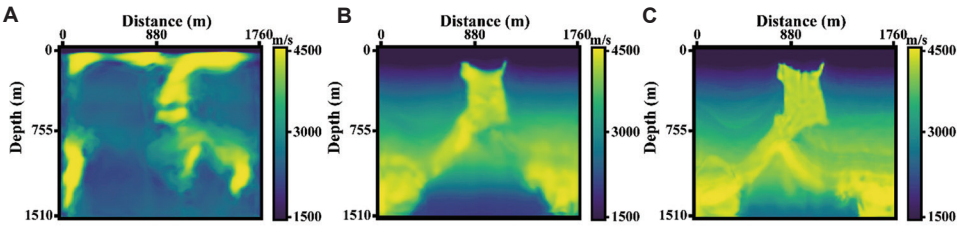


**Figure 9.** Physics-constrained autoencoder-based full-waveform inversion with axial self-attention results for the Society of Exploration Geophysicists salt-dome model. (A) Inversion result after the first iteration. (B) Inversion result after 500 iterations. (C) Inversion result after 1,000 iterations.

11B). These issues indicate that PIAE, which relied solely on convolutional architectures, faced difficulty capturing the long-range, anisotropic correlations of the wavefield under conditions of strong velocity contrasts and complex multi-path propagation.

Table 1 compares the SSIM and PSNR values of PIAE-FWI and AxPCAE-FWI for the Marmousi2 and SEG salt-dome models. The proposed method achieved significantly better recovery of the overall velocity gradient, interface locations, and fine structural textures than PIAE, resulting in higher structural similarity and numerical accuracy. Meanwhile, in the complex salt-dome environment characterized by strong velocity variations and severe illumination loss, AxPCAE effectively enhanced the imaging quality and structural consistency of the salt body and subsalt structures without increasing overall error, demonstrating stronger robustness and multi-scale imaging capability.

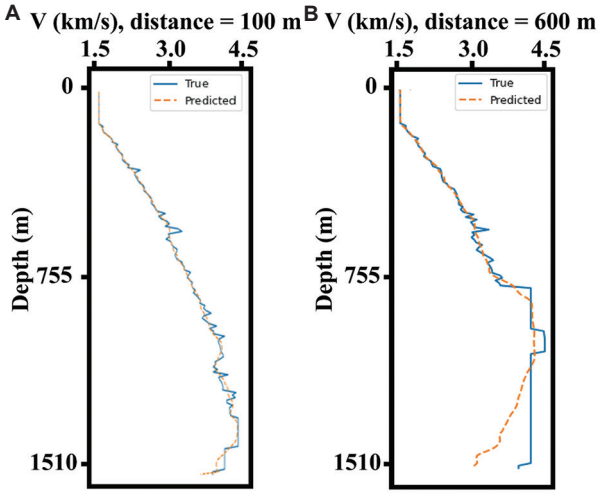


**Figure 10.** Trace-by-trace comparison between the physics-constrained autoencoder-based full-waveform inversion with axial self-attention result and the true model. (A) Single-trace comparison at x = 100 m. (B) Single-trace comparison at x = 600 m.

Table 2 compares the computational cost of PIAE and AxPCAE on the Marmousi2 and SEG salt-dome models. All experiments were conducted on an NVIDIA RTX 3090 GPU, and the reported runtimes correspond to the total wall-clock time for 1,000 iterations for each method. As shown, AxPCAE exhibited a runtime comparable to PIAE, with a slightly longer iteration time, while achieving superior inversion quality and improved recovery of complex structures. It should be emphasized that the "computational savings" referred to in this work were mainly relative to standard Transformers with full 2D global attention. By adopting axial self-attention, we substantially reduced the computational complexity of attention, thereby enhancing the representation of long-range spatiotemporal correlations at a manageable overall cost.

## 4. Discussion

We clarify here the key differences between AxPCAE-FWI and several closely related approaches. First, numerous deep learning–assisted FWI methods treat machine learning as a "plug-in" to a conventional update workflow,[32] for example, by generating an initial model or by providing an external regularization term to support a standard model-update loop. In contrast, AxPCAE-FWI embeds a differentiable acoustic wave-equation solver within a unified encoder–decoder framework and uses the data-domain waveform misfit as the primary constraint, thereby governing the optimization using wave-propagation physics. Second, supervised inversion networks typically learn an end-to-end mapping from seismic data to velocity models using paired "seismic–model" labels;[11] AxPCAE-FWI, however, does not require labeled velocity models. It is trained in an unsupervised manner by generating synthetic seismic records using the embedded differentiable solver and updating network parameters via backpropagation of the waveform misfit.[30] Third, physics-informed neural network-based or "neural-solver" variants often replace

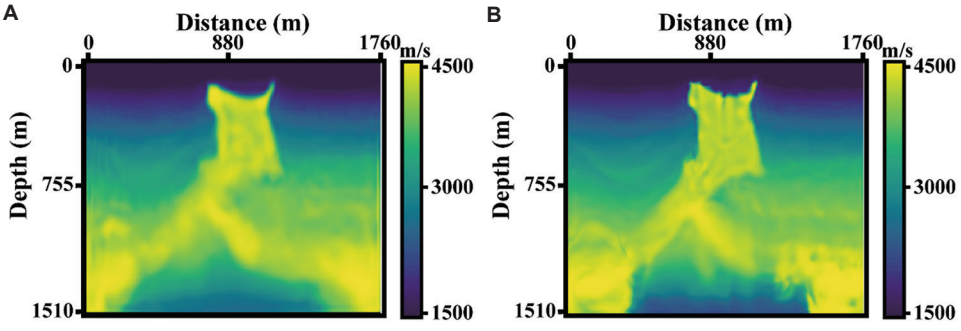


**Figure 11.** Comparison of inversion results for the SEG salt-dome model obtained using (A) physics-informed autoencoder-full-waveform inversion and (B) physics-constrained autoencoder-based full-waveform inversion with axial self-attention after 1,000 iterations

the numerical partial differential equation solver with a physics-informed network and may perform updates in a low-dimensional latent space while introducing an explicit latent-space regularization term.[29] In contrast, AxPCAE-FWI retains a conventional differentiable simulator and does not introduce explicit latent-space regularization; its stability mainly arises from implicit regularization provided by the latent bottleneck and the physically admissible output mapping, i.e., by limiting model capacity and constraining predictions to a feasible parameter range to mitigate ill-posedness. Finally, although AxPCAE-FWI is conceptually related to inversion methods that re-parameterize the model using a neural network generator,[31] our framework is explicitly data-conditioned: the encoder takes observed seismic records as input, and axial self-attention performs separable modeling along the temporal and offset axes to capture long-range correlations on the time–offset plane. This design enables effective representation of complex wave phenomena, such as multiples, converted waves, and far-offset reflections, while keeping the computational overhead manageable.

Building on these observations, we next investigated the robustness of AxPCAE-FWI under noise interference. Specifically, we contaminated the observed seismic records with substantial random noise and evaluated the corresponding inversion performance. We used the Marmousi2 and SEG salt-dome models, with model dimensions and acquisition geometry identical to those described above. The noisy observed data for the Marmousi2 model are shown in Figure 12, and the corresponding inversion results are presented in Figure 13.

**Table 1. Similarity comparison of inversion results obtained using PIAE-FWI and AxPCAE from different models**

| Models | SSIM | | PSNR (dB) | |
|---|---|---|---|---|
| | PIAE-FWI | AxPCAE-FWI | PIAE-FWI | AxPCAE-FWI |
| Marmousi2 | 0.545352 | 0.809973 | 22.87 | 28.07 |
| SEG salt-dome | 0.676215 | 0.728408 | 19.07 | 19.05 |

Abbreviations: AxPCAE-FWI: Physics-constrained autoencoder-based full-waveform inversion with axial self-attention; PIAE-FWI: Physics-informed autoencoder-full-waveform inversion; PSNR: Peak signal-to-noise ratio; SEG: Society of Exploration Geophysicists; SSIM: Structural similarity index.

**Table 2. Comparison of computational cost between AxPCAE-FWI and PIAE-FWI**

| Models | Average time per iteration (s) | | Total inversion time (h) | |
|---|---|---|---|---|
| | PIAE-FWI | AxPCAE-FWI | PIAE-FWI | AxPCAE-FWI |
| Marmousi2 | 39.98 | 69.54 | 11.11 | 19.32 |
| SEG salt-dome | 49.43 | 72.59 | 13.73 | 20.16 |

Abbreviations: AxPCAE-FWI: Physics-constrained autoencoder-based full-waveform inversion with axial self-attention; PIAE-FWI: Physics-informed autoencoder-full-waveform inversion; SEG: Society of Exploration Geophysicists.

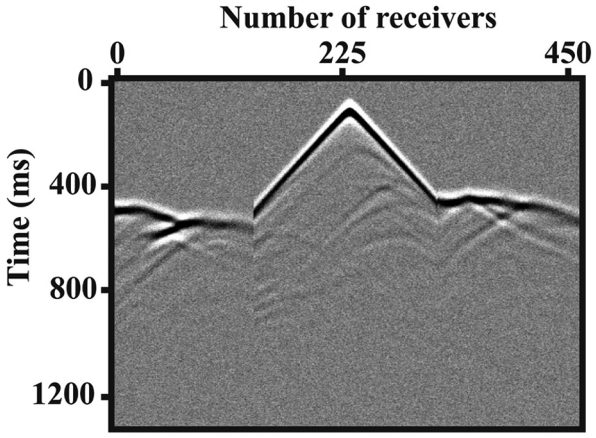


**Figure 12.** Seismic records for the Marmousi2 model contaminated with random noise

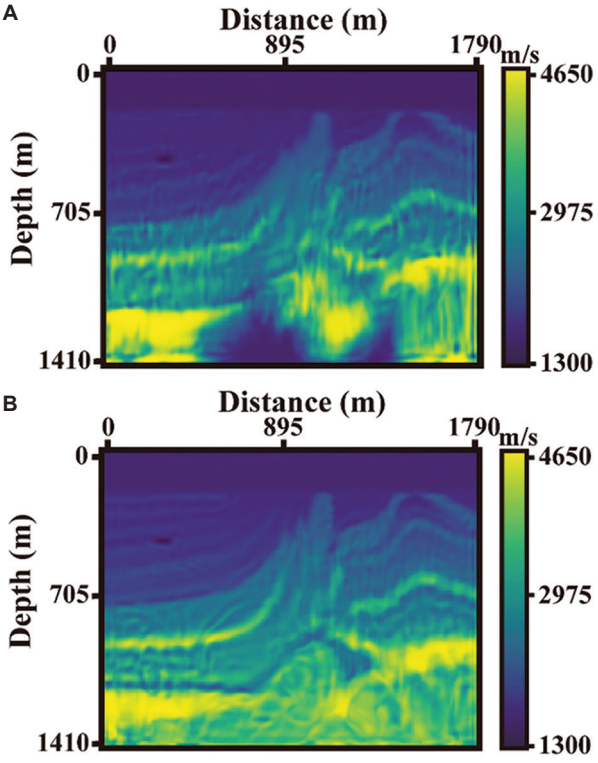


**Figure 13.** Comparison of Marmousi2 model inversion results under random noise after 1,000 iterations using (A) physics-informed autoencoder-full-waveform inversion and (B) physics-constrained autoencoder-based full-waveform inversion with axial self-attention

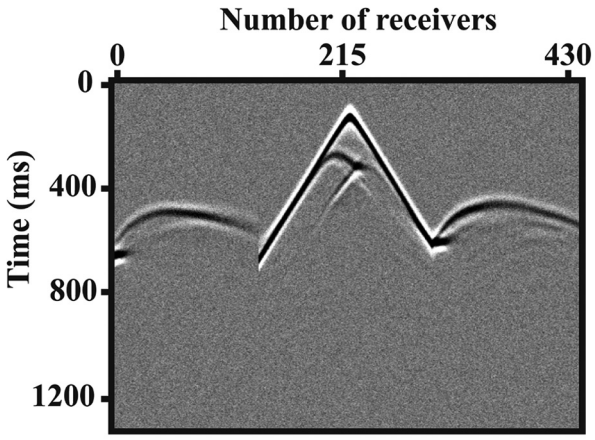


**Figure 14.** Seismic records for the Society of Exploration Geophysicists salt-dome model contaminated with random noise

In the Marmousi2 experiment with strong random noise, compared to the PIAE result (Figure 13A), the AxPCAE result (Figure 13B) achieved a more robust integration of low-wavenumber information, yielding a more stable macro-velocity trend and traveltime kinematics and mitigating noise-induced background undulation. Meanwhile, high-wavenumber details were selectively reinforced within the axial context, producing more concentrated interface gradients and narrower transition zones, thereby markedly improving the continuity and geometric fidelity of dipping strata and channelized structures. We attributed this to attention weights that adaptively aggregated coherent energy while suppressing incoherent speckle noise, thereby avoiding the bandwidth degradation in conventional results where "high-frequency edge spreading" coexisted with over-smoothing.

The noisy observed records for the SEG salt-dome model are shown in Figure 14, and the corresponding inversion results are presented in Figure 15.

Under strong random noise, the PIAE inversion in Figure 15A exhibited insufficient low-frequency constraints, leading to an unstable macro-velocity trend and traveltime kinematics. High-frequency information was obscured by noise due to amplitude compression; the continuity of subsalt wedge-shaped strata was poor, and speckle-like artifacts were observed. In contrast, the AxPCAE result in Figure 15B was more robust at both low- and high-wavenumber ends: gradients along the salt top and flanks were more concentrated with sharper contours, the base was better localized, subsalt layering was more coherent, and background texture noise was markedly reduced, yielding improved broadband consistency and noise robustness overall.

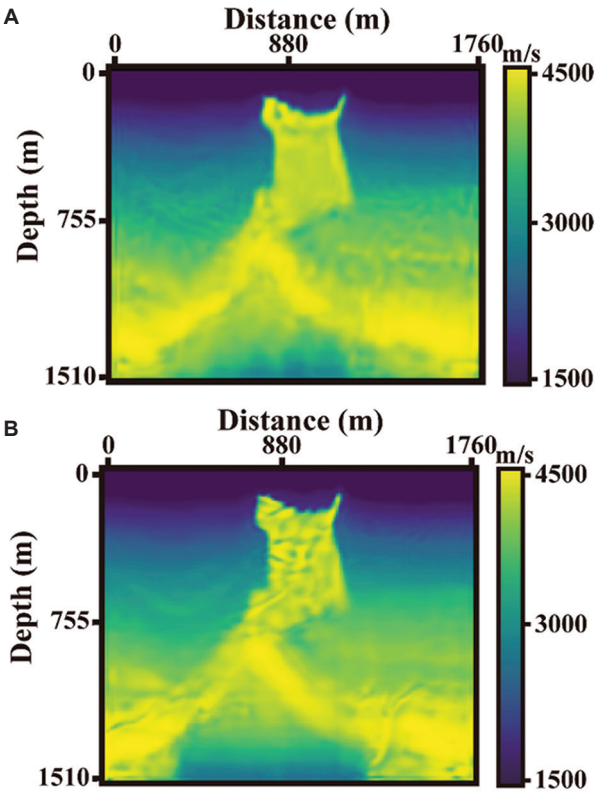


**Figure 15.** Comparison of SEG salt-dome model inversion results under random noise after 1,000 iterations using (A) physics-informed autoencoder-full-waveform inversion and (B) physics-constrained autoencoder-based full-waveform inversion with axial self-attention

Nevertheless, localized velocity discontinuities are observable within the salt body and its shadow zones, reflecting the anisotropy of axial attention that can amplify both noise and fine details at high frequencies. Overall, relative to PIAE, AxPCAE under high noise improves resolution and boundary delineation.

## 5. Conclusion

This study proposes AxPCAE-FWI, a physics-constrained autoencoder framework for FWI with axial self-attention. In a unified encoder–decoder framework, a differentiable acoustic wave-equation solver was explicitly embedded, and data-domain waveform fitting was used as the primary constraint, ensuring that the network training process was consistently governed using the wave equation rather than relying solely on empirical features or black-box fitting. In this way, the network automatically learned the nonlinear mapping from observed seismic records to subsurface velocity models. The encoder extracts low-dimensional latent features, while the decoder reconstructs the velocity model under a physically admissible constraint. A Sigmoid function followed by linear rescaling was applied to ensure

that the inverted parameters fell within a prescribed velocity range, thereby suppressing nonphysical anomalies at the implementation level.

In terms of network architecture, AxPCAE-FWI introduces axial multi-head self-attention modules in the encoding stage, where global attention is computed separately along the time and receiver axes. Two one-dimensional global attention operations were used to approximate a single two-dimensional global attention, enabling the method to capture long-range spatiotemporal correlations associated with multiples, converted waves, and far-offset reflections at a substantially reduced computational cost, and to enhance the representational capacity for complex wavefields. In contrast to conventional FWI, which performed gradient-based updates directly in the model space, the proposed approach conducted "implicit inversion" in the latent space and achieved stable convergence without requiring an explicit initial model or ultra-low-frequency data, thereby alleviating cycle skipping from a mechanistic perspective. Numerical experiments on the Marmousi2 and SEG salt-dome models show that, under complex structural settings and strong shielding from high-velocity bodies, AxPCAE-FWI achieves higher structural similarity and greater geological plausibility than conventional PIAE-FWI. It also demonstrates greater robustness to noise, confirming the effectiveness and practical promise of coupling axial self-attention with physical constraints for FWI.

## Acknowledgments

None.

## Funding

This study is supported by the National Natural Science Foundation of China (42574163), CNPC Science and Technology Innovation Foundation (Grant No. 2024DQ02-0135), and Taishan Scholars Program (Grant No. tsqn202312117).

## Conflict of interest

The authors declare that they have no known competing financial interests or personal relationships that could have influenced the work reported in this paper.

## Author contributions

*Conceptualization:* Yunbo Niu, Yingming Qu, Zhenchun Li
*Formal analysis:* Yunbo Niu
*Investigation:* Yunbo Niu
*Methodology:* Yunbo Niu, Yingming Qu
*Writing–original draft:* Yunbo Niu
*Writing–review & editing*: Yunbo Niu, Yingming Qu, Zhenchun Li

## Availability of data

All data are available upon reasonable request from the corresponding authors.

## References

1. Lailly P. The seismic inverse problem as a sequence of before stack migrations. In: Bednar JB, Redner R, Robinson E, Weglein A, editors. *Conference on Inverse Scattering: Theory and Application. Society for Industrial and Applied Mathematics*; 1983. p. 206-220.

2. Tarantola A, Valette B. Generalized nonlinear inverse problems solved using the least squares criterion. *Rev Geophys*. 1982;20(2):219-232.

   doi: 10.1029/RG020i002p00219

3. Tarantola A. Inversion of seismic reflection data in the acoustic approximation. *Geophysics*. 1984;49(8):1259-1266.

   doi: 10.1190/1.1441754

4. Virieux J, Operto S. An overview of full-waveform inversion in exploration geophysics. *Geophysics*. 2009;74(6):WCC1-WCC26.

   doi: 10.1190/1.3238367

5. Mora P. Inversion=migration+tomography. *Geophysics*. 1989;54(12):1575-1586.

   doi: 10.1190/1.1442625

6. Xu S, Wang D, Chen F, Lambaré G, Zhang Y. Inversion of reflected seismic waves. In: *SEG Technical Program Expanded Abstracts 2012*. Las Vegas, NV. Society of Exploration Geophysicists; 2012. p. 1-7.

   doi: 10.1190/segam2012-1473.1

7. LeCun Y, Bengio Y, Hinton G. Deep learning. *Nature*. 2015;521(7553):436-444.

   doi: 10.1038/nature14539

8. Kim Y, Nakata N. Geophysical inversion versus machine learning in inverse problems. *Lead Edge*. 2018;37(12):894-901.

   doi: 10.1190/tle37120894.1

9. Wu Y, McMechan GA, Wang Y. Adaptive feedback convolutional neural network-based high-resolution reflection-waveform inversion. *J Geophys Res Solid Earth*. 2022;127(6):e2022JB024138.

   doi: 10.1029/2022JB024138

10. Wang W, Yang F, Ma J. Velocity model building with a modified fully convolutional network. In: *SEG Technical Program Expanded Abstracts 2018; SEG International Exposition and 88th Annual Meeting*. Anaheim, CA: Society of Exploration Geophysicists; 2018. p. 2086-2090.

    doi: 10.1190/segam2018-2997566.1

11. Wu Y, Lin Y, Zhou Z. InversionNet: Accurate and efficient

seismic-waveform inversion with convolutional neural networks. In: *SEG Technical Program Expanded Abstracts 2018; SEG International Exposition and 88th Annual Meeting*. Anaheim, CA. Society of Exploration Geophysicists; 2018. p. 2096-2100.

doi: 10.1190/segam2018-2998603.1

12. Park MJ, Sacchi MD. Automatic velocity analysis using convolutional neural network and transfer learning. *Geophysics*. 2020;85(1):V33-V43.

doi: 10.1190/geo2018-0870.1

13. Li S, Liu B, Ren Y, Chen Y. Deep-learning inversion of seismic data. *IEEE Trans Geosci Remote Sens*. 2020;58(3):2135-2149.

doi: 10.1109/TGRS.2019.2953473

14. Wang W, Ma J. Velocity model building in a crosswell acquisition geometry with image-trained artificial neural networks. *Geophysics*. 2020;85(2):U31-U46.

doi: 10.1190/geo2018-0591.1

15. Lu J, Wu C, Zhang H, Qu Y, Xu Q, Zhu M. *Phi-Net: An Aggregation Network for Seismic Velocity Model Building. SSRN*; 2024. Available from: https://ssrn.com/abstract=5076729 [Last accessed on 2025 Nov 29].

doi: 10.2139/ssrn.5076729

16. Araya-Polo M, Jennings J, Adler A, Dahlke T. Deep-learning tomography. *Lead Edge*. 2018;37(1):58-66.

doi: 10.1190/tle37010058.1

17. Song C, Geng H, Wang Y, *et al.* Simultaneous P- and S-wave seismic traveltime tomography using physics-informed neural networks. *Geophys Prospect*. 2025;73(6):e70034.

doi: 10.1111/1365-2478.70034

18. Xue Z, Wang Y, Wu X, Ma J. Multi-geophysical information neural network for seismic tomography. *Geophysics*. 2025;90(3): R89-R100.

doi: 10.1190/geo2024-0039.1

19. Zhang X, Wang Y, Zhang H. Rapid probabilistic seismic tomography using graph mixture density networks. *J Geophys Res Solid Earth*. 2025;130(8):e2025JB031129.

doi: 10.1029/2025JB031129

20. Das V, Pollack A, Wollner U, Mukerji T. Convolutional neural network for seismic impedance inversion. *Geophysics*. 2019;84(6):R869-R880.

doi: 10.1190/geo2018-0838.1

21. Wu B, Meng D, Wang L, Liu N, Wang Y. Seismic impedance inversion using fully convolutional residual network and transfer learning. *IEEE Geosci Remote Sens Lett*. 2020;17(12):2140-2144.

doi: 10.1109/LGRS.2019.2963106

22. Taufik MH, Wang F, Alkhalifah T. Learned regularizations for multi-parameter elastic full waveform inversion using diffusion models. *J Geophys Res Machine Learn Comput*. 2024;1(1):e2024JH000125.

doi: 10.1029/2024JH000125

23. Kazei V, Ovcharenko O, Plotnitskii P, Peter D, Zhang X, Alkhalifah T. Mapping full seismic waveforms to vertical velocity profiles by deep learning. *Geophysics*. 2021;86(5):R711-R721.

doi: 10.1190/geo2019-0473.1

24. Yang F, Ma J. FWIGAN: Full-waveform inversion via a physics-informed generative adversarial network. *J Geophys Res Solid Earth*. 2023;128(4):e2022JB025493.

doi: 10.1029/2022JB025493

25. Zhang Z, Lin Y. Data-driven seismic waveform inversion: A study on the robustness and generalization. *IEEE Trans Geosci Remote Sens*. 2020;58(10):6900-6913.

doi: 10.1109/TGRS.2020.2977635

26. Yang Y, Engquist B, Sun J, *et al.* Application of optimal transport and the quadratic Wasserstein metric to full-waveform inversion. *Geophysics*. 2018;83(1):R43-R62.

doi: 10.1190/geo2016-0663.1

27. Vantassel JP, Kumar K, Cox BR. Using convolutional neural networks to develop starting models for near-surface two-dimensional full waveform inversion. *Geophys J Int*. 2022;231(1):72-90.

doi: 10.1093/gji/ggac179

28. Yang F, Ma J. Deep-learning inversion: A next-generation seismic velocity model building method. *Geophysics*. 2019;84(4):R583-R599.

doi: 10.1190/geo2018-0249.1

29. Taufik MH, Huang X, Alkhalifah T. Latent representation learning in physics-informed neural networks for full waveform inversion. *Earth Space Sci*. 2025;12(9):e2024EA004107.

doi: 10.1029/2024EA004107

30. Wu Y, McMechan GA. Parametric convolutional neural network-domain full-waveform inversion. *Geophysics*. 2019;84(6):R881-R896.

doi: 10.1190/geo2018-0224.1

31. Zhu W, Xu K, Darve E, *et al.* Integrating deep neural networks with full-waveform inversion: Reparameterization, regularization, and uncertainty quantification. *Geophysics*. 2022;87(1):R93-R109.

doi: 10.1190/geo2020-0933.1

32. Wang Y, Jiang B, Wei Z, *et al.* Deep velocity generator:

A plug-in network for FWI enhancement. *IEEE Trans Geosci Remote Sens*. 2023;61:1-17.

doi: 10.1109/TGRS.2023.3247880

33. He Q, Wang Y. Reparameterized full-waveform inversion using deep neural networks. *Geophysics*. 2021;86(1):V1-V13.

doi: 10.1190/geo2019-0382.1

34. Tromp J, Tape C, Liu Q. Seismic tomography, adjoint methods, time reversal and banana-doughnut kernels. *Geophys J Int*. 2005;160(1):195-216.

doi: 10.1111/j.1365-246X.2004.02453.x

ACCSCIENCE PUBLISHING

Journal of Seismic Exploration

ARTICLE

# A pre-trained dictionary learning framework combined with projections onto convex sets for seismic data reconstruction and denoising

**Jianlei Zhang[1,2,3], Bo Yang[4]*, Min Bai[4], Xilin Qin[4], Baobin Wang[2,3], Zhen Zou[2,3], and Boyuan Lv[4]**

[1]College of Geophysics, China University of Petroleum (Beijing), Beijing, China

[2]National Engineering Research Center for Computer Software for Oil & Gas Exploration, Research Institute of Petroleum Exploration and Development, Zhuozhou, Hebei, China

[3]BGPInc., China National Petroleum Corporation, Zhuozhou, Hebei, China

[4]Key Laboratory of Exploration Technologies for Oil and Gas Resources of Ministry of Education, Yangtze University, Wuhan, Hubei, China

## Abstract

The dictionary learning approach has proven effective in seismic data denoising and interpolation. Its core advantage lies in the ability to continuously update the initial dictionary, thereby adapting to the complex structural characteristics of seismic data. However, many existing implementations rely on predefined transforms (e.g., discrete cosine transform) for dictionary initialization. These fixed, data-agnostic bases often fail to fully capture the unique features of seismic signals, which may compromise the sparsity and fidelity of signal representation. Such a limitation can significantly degrade the performance of tasks requiring high-precision reconstruction or noise attenuation. To address this issue, we propose an innovative dictionary learning framework based on a variational sparse representation model. Specifically, this framework first extracts small data patches from arbitrary locations in seismic data, and then constructs a pre-training dataset using a windowing algorithm to preserve fine-grained data features. This process yields an initial dictionary that inherently encodes the intrinsic characteristics of the input seismic data. Subsequently, the initial dictionary is separately refined and updated through the K-singular value decomposition (K-SVD) and sequential generalization of K-means (SGK) algorithms, resulting in an optimized dictionary with more accurate and data-adaptive features. In addition, we integrate a multi-iteration projections onto convex sets algorithm to compensate for missing data features, ultimately achieving high-precision seismic data interpolation and noise attenuation. Numerical experiments demonstrate that the proposed methods (variational SGK and variational K-SVD) outperform the conventional K-SVD and SGK algorithms in both interpolation accuracy and denoising performance.

***Keywords:*** K-singular value decomposition; Sequential generalization of K-means; Variational sparse representation; Projections onto convex sets; Seismic data reconstruction and denoising

***Corresponding author:**
Bo Yang
(ycl2980738443@163.com)

**Citation:** Zhang J, Yang B, Bai M, *et al.* A pre-trained dictionary learning framework combined with projections onto convex sets for seismic data reconstruction and denoising. *J Seismic Explor*. 2026;35(1):282-299.
doi: 10.36922/JSE025440100

**Received:** October 31, 2025

**Revised:** January 5, 2026

**Accepted:** January 15, 2026

**Published online:** February 25, 2026

**Copyright:** © 2026 Author(s). This is an Open-Access article distributed under the terms of the Creative Commons Attribution License, permitting distribution, and reproduction in any medium, provided the original work is properly cited.

**Publisher's Note:** AccScience Publishing remains neutral with regard to jurisdictional claims in published maps and institutional affiliations.

## 1. Introduction

During the field data acquisition process, the complexity of geological and construction conditions can lead to incomplete data collection. To minimize costs, the acquisition system is often not dense enough, resulting in overly sparse datasets. In addition, the presence of restricted areas and obstacles can limit the deployment of receivers in certain locations, making it impossible to fully capture reflection information from these regions. Beyond the aforementioned issues, the raw data also contains numerous anomalous signals caused by environmental influences and unstable noise. Simply removing these anomalies may lead to significant losses in seismic data. Therefore, the raw data collected in the field must be processed to attenuate noise interference, reconstruct missing data, and restore complete seismic records. This will significantly improve the signal-to-noise ratio (SNR), resolution, and fidelity, thereby enabling more reliable analysis and evaluation of hydrocarbon reservoir characteristics in specified regions.

After years of research and development by numerous scholars in this field, the reconstruction methods can generally be categorized into several types. Wave equation-based seismic data reconstruction methods reconstruct data based on the characteristics of seismic wave propagation underground and often require substantial computational resources.[1,2] The method based on prediction filtering applies convolution operations between target data and prediction filters to estimate missing trace data corresponding to specific frequencies.[3,4] For regular or uniform sampling of seismic data, insufficient spatial sampling rates can often lead to spatial aliasing phenomena. Methods based on rank reduction optimization accomplish signal recovery through either Hankel matrix rank reduction or data dimension reduction techniques.[5,6] Nevertheless, the computational burden is significant for complex data. Seismic data reconstruction methods based on mathematical transforms can generally be categorized into fixed-basis methods and dictionary learning methods. Fixed-basis approaches (e.g., Fourier transform,[7] Radon transform,[8] Curvelet transform,[9] and Seislet transform[10,11]) rely on predefined transforms for sparse representation, and the reconstruction performance is inherently influenced by the chosen mathematical basis. Although these methods are computationally efficient and straightforward to implement, they cannot adaptively model diverse seismic structural features.[12] Representative methods, such as Curvelet-based reconstruction, enforce sparsity via thresholding in the Curvelet domain while applying projections onto convex sets (POCS)-based data consistency constraints, thereby achieving denoising and interpolation simultaneously and enhancing reflector continuity.[13] In contrast, dictionary learning methods suppress noise through sparse coding and iteratively learn a data-adaptive dictionary that better captures intrinsic structural characteristics, enabling unified interpolation and denoising, particularly with advantages in scenarios involving weak signals or high levels of missing data.[14]

The emergence of compressed sensing technology has driven significant progress in dictionary learning methods across multiple application fields. A novel statistical-based masking strategy has been proposed and applied to the compressed sensing framework for outlier denoising, offering new insights to enhance the applicability of compressed sensing in processing data contaminated with abnormal noise.[15] Building on this foundation, a new dictionary learning framework based on fully adaptive boundary empirical mode decomposition has been further developed and applied to seismic data denoising. The integration of this framework with dictionary learning improved the adaptability and noise removal efficacy for complex seismic data.[16] These approaches typically involve two key phases: performing sparse coding and then updating the dictionary, where iterative optimization between these stages yields an ideal sparse representation model.[17,18] Compared with signal transform methods, the advantage of dictionary learning methods lies in their ability to represent signals through a few sparse coefficients, which reduces computational costs and separates the desired components from other components. To address the problem of structured noise removal in seismic data, relevant studies have explored the combination of dictionary learning and atomic filtering, focusing on investigating the impact of atomic filtering operations on structured noise removal performance. These studies provide a reference for parameter optimization and strategy design of dictionary learning in handling specific types of noise.[19] The key difference between dictionary transforms and traditional transforms is that dictionary learning methods use a variable dictionary, whereas traditional transforms (such as wavelet transform) maintain a fixed dictionary.[20-22] Currently, such learned dictionaries with excellent representation performance are widely employed in interpolation and noise reduction applications.[23,24] Numerous overlapping small patches are segmented from the data and utilized to train the dictionary.[25] After a sufficient number of iterations, the resulting dictionary effectively captured reflection signals while attenuating noise. A dictionary with coherence constraints was introduced to facilitate learning without requiring any pre-existing information,[26] alleviating the issue of unstable noise prior information at different locations. An optimized approach for matrix rank reduction was utilized to simultaneously accomplish both

noise suppression and data interpolation.[27] An effective approach was adopted to extract leaked signals from noise; algebraic means were used for dictionary update instead of singular value decomposition (SVD),[28] addressing the high computational burden of training dictionaries in high-dimensional seismic data.

The K-singular value decomposition (K-SVD) algorithm ranks among the most traditional methods for dictionary learning.[29,30] This algorithm begins with a discrete cosine transform (DCT) dictionary as the initial dictionary and iteratively refines it to extract features. However, DCT dictionary atoms do not learn features, resulting in limited extraction of features, which in turn affects the accuracy of reconstruction and denoising.[31-34]

In this study, we introduce a novel dictionary learning framework derived from a variational sparse representation model, offering enhanced signal representation capabilities. First, we extract the features from seismic data using this model to obtain a preliminary dictionary. Subsequently, the traditional dictionary learning methods, such as K-SVD or sequential generalization of K-means (SGK), are applied to update the initial dictionary. We utilize the dictionaries updated by both algorithms for reconstructing and denoising. The POCS algorithm can effectively remove noise generated by missing traces through multiple iterations, thereby restoring the missing seismic traces. This approach effectively supplements the missing features in incomplete seismic datasets, enabling both reconstruction and denoising.

## 2. Theory

This section first introduces the variational sparse representation model, followed by an overview of the basic theories of the K-SVD and SGK methods. Finally, we introduce the reconstruction theory based on the POCS algorithm.

### 2.1. The variational sparse representation model

The general formula of this model is expressed in **Equation 1:**

$$\mathbf{b} = \sum_{\mathbf{i=1}}^{\mathbf{m}} \mathbf{z_i q_i} = \mathbf{Qz} \tag{1}$$

where the expression $\mathbf{z}^T = [\mathbf{z}_1,\mathbf{z}_2,\ldots,\mathbf{z}_m]$ represents a random vector, in which the components $\mathbf{z}_i$ correspond to their respective coefficients. Here, the vector $\mathbf{z}$ represents the orthogonal projection of $\mathbf{b}$ in the direction of $\boldsymbol{q}_i$. $\mathbf{Q}$ represents the extraction of data-driven basis functions and patches from the input data $\mathbf{Y}$.

The model extracts patches $\mathbf{Q}$ from the input data $\mathbf{Y}$ at arbitrary locations. Next, we constructed a series resembling **Equation 1** by the windowing algorithm to identify data features and establish a preliminary dictionary $\mathbf{D}_0$. Let $\mathbf{D}_0 = [\mathbf{d}_1,\mathbf{d}_2,\ldots,\mathbf{d}_k]$. We utilized the updated dictionary $\mathbf{D}$ derived from the dictionary learning approaches to reduce noise.

The pth window in the model is denoted as $\mathbf{I}_p$. Let $\mathbf{l}_p = \sum_{i=1}^{m} \mathbf{z}_{li}\mathbf{Q}_i$ denote the representation of $\mathbf{I}_p$ as an expansion using the patches $\mathbf{Q}_i$. This equation can be converted into **Equation 1**, where the window $\mathbf{I}_p$ corresponds to the pth implementation of $\mathbf{b}$ by mapping it according to lexicographical order. To implement this approach, k distinct windows must be extracted from the source dataset, with each window producing corresponding realizations of $\mathbf{b}$ and $\mathbf{z}$ that systematically map the patches $\mathbf{Q}_i$ to vectors $\mathbf{q}_i$ according to the lexicographic ordering specified in **Equation 1**.

### 2.2. The K-SVD algorithm

The K-SVD model can be described as an optimization problem as follows in **Equation 2**:

$$\min_{\mathbf{D},\mathbf{X}} \left\|\mathbf{Y} - \mathbf{DX}\right\|_F^2 \quad \text{s.t.}\forall i, \left\|\mathbf{x}_i\right\|_0 \le T \tag{2}$$

where the observed signal $\mathbf{Y}$ is expressed as the product of the dictionary matrix $\mathbf{D}$ and sparse coefficients $\mathbf{X}$, with $T$ indicating the desired sparsity.

When determining sparse coefficients, we employed the Orthogonal Matching Pursuit algorithm to find the solution. Furthermore, there are various other similar methods capable of achieving solutions, including Basis Pursuit and Bregman algorithms, among others. The approach updates the dictionary by updating it one column individually at each step. As an example, during the refinement process for the dictionary $t_{th}$ column, the corresponding vector is denoted as $\mathbf{d}_t$, referred to as an atom, while the corresponding $t_{th}$ row vector of $\mathbf{X}$ is recorded as $\mathbf{x}_t$. The mathematical derivation is presented through the subsequent formulation in **Equation 3**:

$$\begin{aligned}\left\|\mathbf{Y} - \mathbf{DX}\right\|_F^2 &= \left\|\mathbf{Y} - \sum_{j=1}^{t} \mathbf{d}_j\mathbf{x}_j\right\|_F^2 \\ &= \left\|\left(\mathbf{Y} - \sum_{j=1, j\neq t} \mathbf{d}_j\mathbf{x}_j\right) - \mathbf{d}_t\mathbf{x}_t\right\|_F^2 = \left\|\mathbf{E}_t - \mathbf{d}_t\mathbf{x}_t\right\|_F^2\end{aligned} \tag{3}$$

according to **Equation 3**, we can obtain **Equation 4**:

$$\mathbf{E}_t = \mathbf{Y} - \sum_{j=1, j\neq t} \mathbf{d}_j\mathbf{x}_j \tag{4}$$

where $\mathbf{E}_t$ represents the error matrix. Meanwhile, the optimization problem can be converted to **Equation 5**:

$$\min_{\mathbf{d}_t, \mathbf{x}_t} \left\| \mathbf{E}_t - \mathbf{d}_t \mathbf{x}_t \right\|_F^2 \tag{5}$$

To make the obtained sparse code as sparse as possible, we need to extract the position in $\mathbf{E}_t$ that is not zero for $\boldsymbol{x}_j$ to get the new $\mathbf{E}_t^{'}$. Here, we used the SVD method to solve this formula using **Equation 6**:

$$\mathbf{E}_t^{'} = \mathbf{U} \pounds \mathbf{V}^{\mathrm{T}} \tag{6}$$

The dictionary's $t_{th}$ column undergoes updating through the initial column of **U**, whereas $\mathbf{x}_t^{'}$ derives from multiplying the initial column of **V** with the initial diagonal element in **Σ**. This update enables the direct substitution of the resultin $\mathbf{x}_t^{'}$ into $\mathbf{x}_t$, effectively minimizing the value of **Equation 3**.

### 2.3. The sequential generalization of K-means algorithm

We introduce a dictionary learning model, as shown in **Equation 7**:

$$\forall_j \mathbf{x}_j = arg \min_{\mathbf{x}_j} \left\| \mathbf{Y} - \mathbf{DX} \right\|_F^2, s.t. \forall_j \mathbf{x}_j = \mathbf{e}_p \tag{7}$$

where $\mathbf{e}_p$ represents a unit vector that has a value of one for the $t_{th}$ element and is zero for all remaining elements. During the sparse coding process, we can consider the constraint on $\mathbf{x}_j$, specifically $\mathbf{x}_j = \boldsymbol{e}_p$. In the dictionary updating process, **D** needs to be updated in accordance with the K-SVD algorithm. While using K-SVD to address the same dictionary update problem is a common approach, we transitioned to an optimized approach by enforcing unit vector constraints on coefficients. The following optimization functions are defined as **Equation 8**:

$$J = \left\| \mathbf{E}_t^{'} - \mathbf{d}_t \mathbf{x}_t^{'} \right\|_F^2 \tag{8}$$

through computing the partial derivative of $J$ concerning the vector $\mathbf{d}_t$ and equating it to zero, we obtain **Equation (9)**:

$$\mathbf{d}_t = \mathbf{E}_t^{'} \left( \mathbf{x}_t^{'} \right)^T \left( \mathbf{x}_t^{'} \left( \mathbf{x}_t^{'} \right)^T \right)^{-1} \tag{9}$$

assuming that the row vector $\mathbf{x}_t^{'}$ has $N^t$ non-zero elements, then we obtain **Equation 10**:

$$\mathbf{x}_t^{'} \left( \mathbf{x}_t^{'} \right)^T = N^t \tag{10}$$

according to Wang *et al.*[35] we can get **Equation 11:**

$$\mathbf{d}_t = \frac{1}{N^t} \sum_{i=1}^{N^t} \mathbf{s}_i \tag{11}$$

**Equation 11** represents the dictionary optimization procedure within the SGK methodology. Notably, this approach replaces the conventional SVD-based iterative approximation of the dictionary element with a computationally efficient summation operation.

### 2.4. Reconstruction based on the POCS algorithm

The reconstruction problem may be mathematically formulated as **Equation 12**:

$$\mathbf{y} = \mathbf{Mp} \tag{12}$$

where **y** denotes the acquired incomplete data containing noise, **p** represents the target complete seismic data requiring reconstruction, while **M** stands for the stochastic sampling matrix.

The POCS algorithm is mainly divided into the following steps. First, we selected an appropriate threshold parameter $\lambda_i$ (i = 1, 2,…, $N$), $N$ representing the iteration number, and the initial input data were the noise data with random missing before reconstruction, which is defined as $\mathbf{y}_0 = \mathbf{y}$.

Then, the initial input data was subjected to curvelet transform, denoted as $\boldsymbol{\delta}_{i-1} = \boldsymbol{f}\boldsymbol{y}_{i-1}$, where $\boldsymbol{\delta}_{i-1}$ corresponds to the sparse representation of signal $\boldsymbol{y}_{i-1}$ within the transformation space **f**. Using a threshold parameter as a constraint, values less than the threshold $\lambda_i$ were removed and filled with 0, denoted as $\boldsymbol{\delta}_{i-1} = \mathbf{T}_{\boldsymbol{\lambda i}} \mathbf{f} \mathbf{y}_{i-1}$, where $\mathbf{T}_{\boldsymbol{\lambda i}}$ represents the threshold operator.

Next, we took the inverse of $\boldsymbol{\delta}_i$, which is shown in **Equation 13**:

$$\mathbf{y}_i = \mathbf{f}^{-1} \delta_i \tag{13}$$

After filling the non-missing data from the noisy data **y** with random missing into the $\mathbf{y}_i$, we get **Equation 14**:

$$\mathbf{y}_{i+1} = \left( \mathbf{I} - \mathbf{M} \right) \mathbf{y}_i + \mathbf{My} \tag{14}$$

After the updating $\mathbf{y}_i$, we continued the threshold iteration until the accuracy requirements were met. We performed the inverse transformation on the results $\boldsymbol{\delta}_N$ after the last iteration to acquire the reconstructed data. The selection of the threshold parameter had a significant impact on this process. An appropriately chosen threshold value reduces iteration counts and computational overhead without compromising solution precision.

We first used a variational sparse representation model to obtain an initial dictionary with partial features

learned from the seismic data. Then, the K-SVD and SGK algorithms were employed to update the dictionary. Using the updated dictionary and corresponding sparse coefficients, the data was reconstructed to obtain the initial results. Finally, the missing seismic data features were reconstructed using the POCS algorithm, completing the reconstruction and denoising.

## 3. Methodology

Figure 1 illustrates the overall workflow of the proposed seismic data denoising and reconstruction method based on POCS preprocessing and data-driven dictionary learning. First, a POCS preprocessing step was applied to the noisy and incomplete input seismic data. Through iterative thresholding and data-consistency projection, this step provided initial noise suppression and basic interpolation in missing regions, efficiently producing a structurally more coherent preliminary estimate. Subsequently, using this preprocessed result as input, dictionary initialization was performed through a variational sparse representation scheme, replacing the fixed DCT dictionary to better match the local structural characteristics of the data. Local image patches were then extracted using a sliding-window strategy, and sparse coding and dictionary updating were conducted using the SGK and K-SVD algorithms, respectively. The resulting sparse coefficients were further processed using a percentage-based complex thresholding scheme to suppress residual noise while retaining the dominant signal components. Finally, patch reconstruction and aggregation yielded the output seismic data with simultaneous denoising and reconstruction.

## 4. Results and discussion

We conducted validation tests using numerical experiments to evaluate the variational sparse representation SGK (VSGK) and variational sparse representation K-SVD (VK-SVD) algorithms' denoising and reconstruction performance. The assessment employed the SNR metric, mathematically expressed in **Equation 15**:

$$\mathrm{SNR} = 10\log_{10}\frac{\mathbf{Y}_{\mathrm{signal}}}{\mathbf{Y}_{\mathrm{noise}}} \tag{15}$$

where $\mathbf{Y}_{\mathbf{signal}}$ represents the power of the effective signal, and $\mathbf{Y}_{\mathbf{noise}}$ represents the power of the noise.

The assessment employed the structural similarity index measure (SSIM) metric, mathematically expressed in **Equation 16**:

$$SSIM = \frac{(2\mu_x\mu_y + C_1)(2\sigma_{xy} + C_2)}{(\mu_x^2 + \mu_y^2 + C_1)(\sigma_X^2 + \sigma_Y^2 + C_2)} \tag{16}$$

where $\mu_x$ represents the local mean of the true data, $\mu_y$ represents the local mean of the reconstructed data, $\sigma_x$ represents the local standard deviation of the true data, $\sigma_y$ represents the local standard deviation of the reconstructed data, $\sigma_{xy}$ represents the local covariance between the true

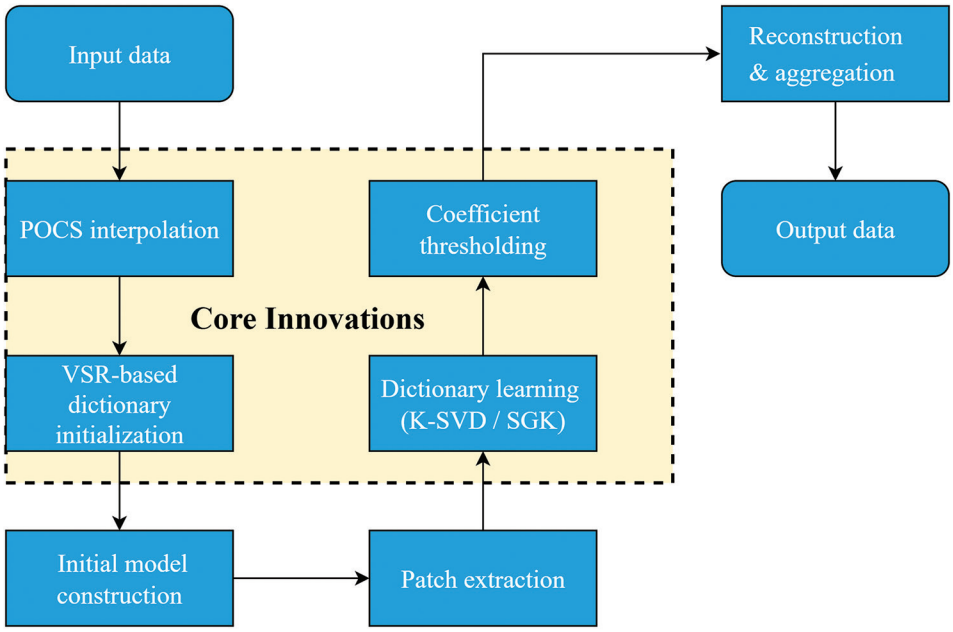


**Figure 1.** Flow chart of seismic data processing framework based on variational sparse representation
Abbreviations: K-SVD: K-singular value decomposition; POCS: Projections onto convex sets; SGK: Sequential generalization of K-means; VSR: Variational sparse representation.

and reconstructed data, $C_1$ represents a constant, and $C_2$ represents another constant.

The assessment employed the peak SNR (PSNR) metric, mathematically expressed as in **Equation 17**:

$$PSNR = 10\log_{10}\left(\frac{X_{\max}^2}{MSE}\right) \quad (17)$$

When $X_{max}$ represents the peak amplitude of the signal, and MSE represents the point-wise mean squared error between the reconstructed data and the true data.

### 4.1. Synthetic data

The synthetic data are shown in Figure 2, and the results of denoising and reconstruction using different methods are presented in Figure 3. SGK and K-SVD effectively removed random noise while partially recovering the seismic data at the missing locations, but some events are not very clear. Significant leakage of useful signals was observed in the areas indicated by the green arrows (Figure 3E and F). In Figure 3C, VSGK shows almost no residual background noise and exhibits better continuity of the events, with only a few useful signal losses in the region marked by the green arrow (Figure 3G). By comparison, the VK-SVD method exhibited less useful signal leakage.

Next, we examined the impact of the variational sparse representation model on overall performance using the data shown in Figure 2B. We replaced the initial dictionary in VSGK and VK-SVD with the DCT dictionary and compared it with the method that uses the dictionary trained by the variational sparse representation model as the initial dictionary. The initial dictionaries and the updated dictionaries for different methods are displayed in Figure 4. For the initial dictionaries, it can be seen that the atoms of the DCT dictionary are unrelated to the

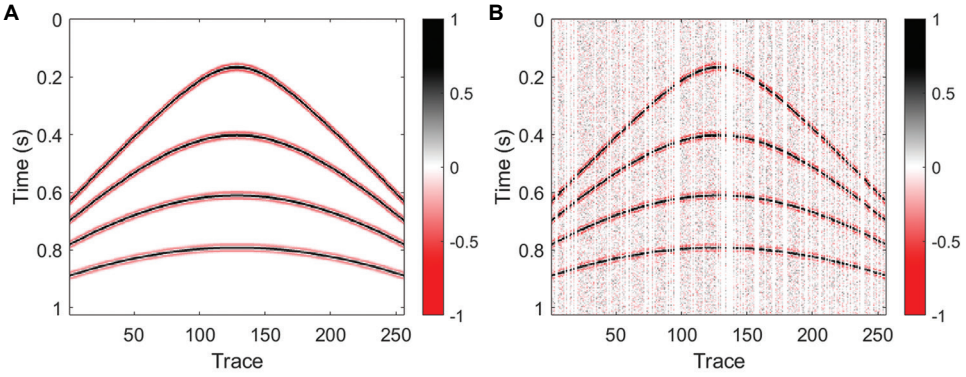


**Figure 2.** Original data and noisy data with random missing 0.3 data. (A) Original data, (B) noisy data with random missing 0.3 data.

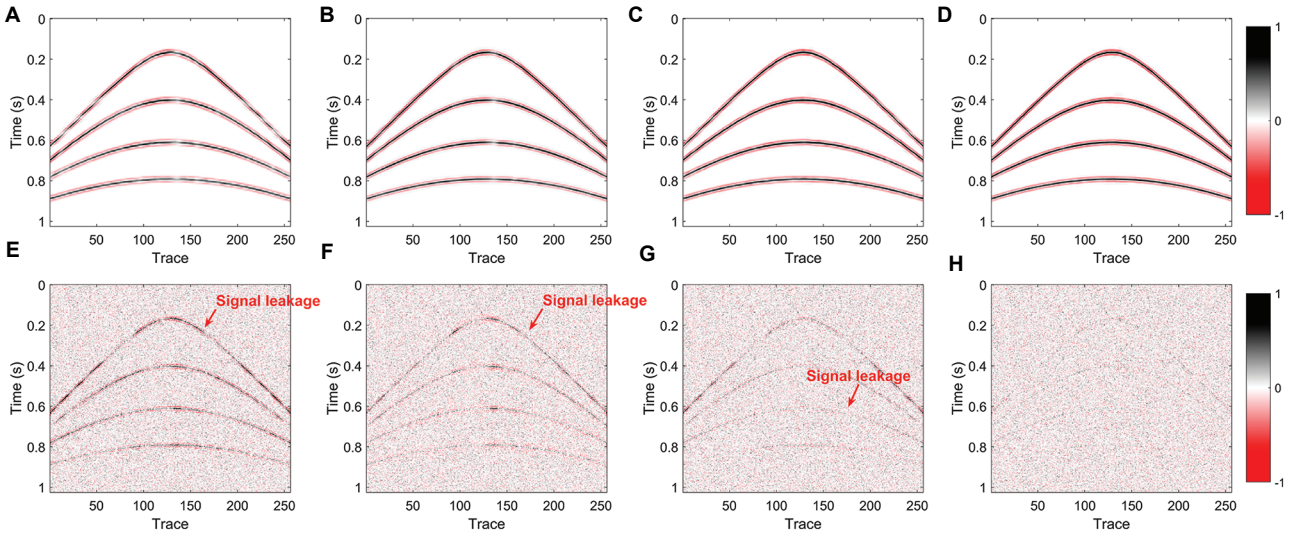


**Figure 3.** Comparison of results processed using various approaches. The result processed by (A) SGK, (B) K-SVD, (C) VSGK, and (D) VK-SVD. The noise that is removed by (E) SGK, (F) K-SVD, (G) VSGK, and (H) VK-SVD.
Abbreviations: K-SVD: K-singular value decomposition; SGK: Sequential generalization of K-means; V: Variational sparse representation.

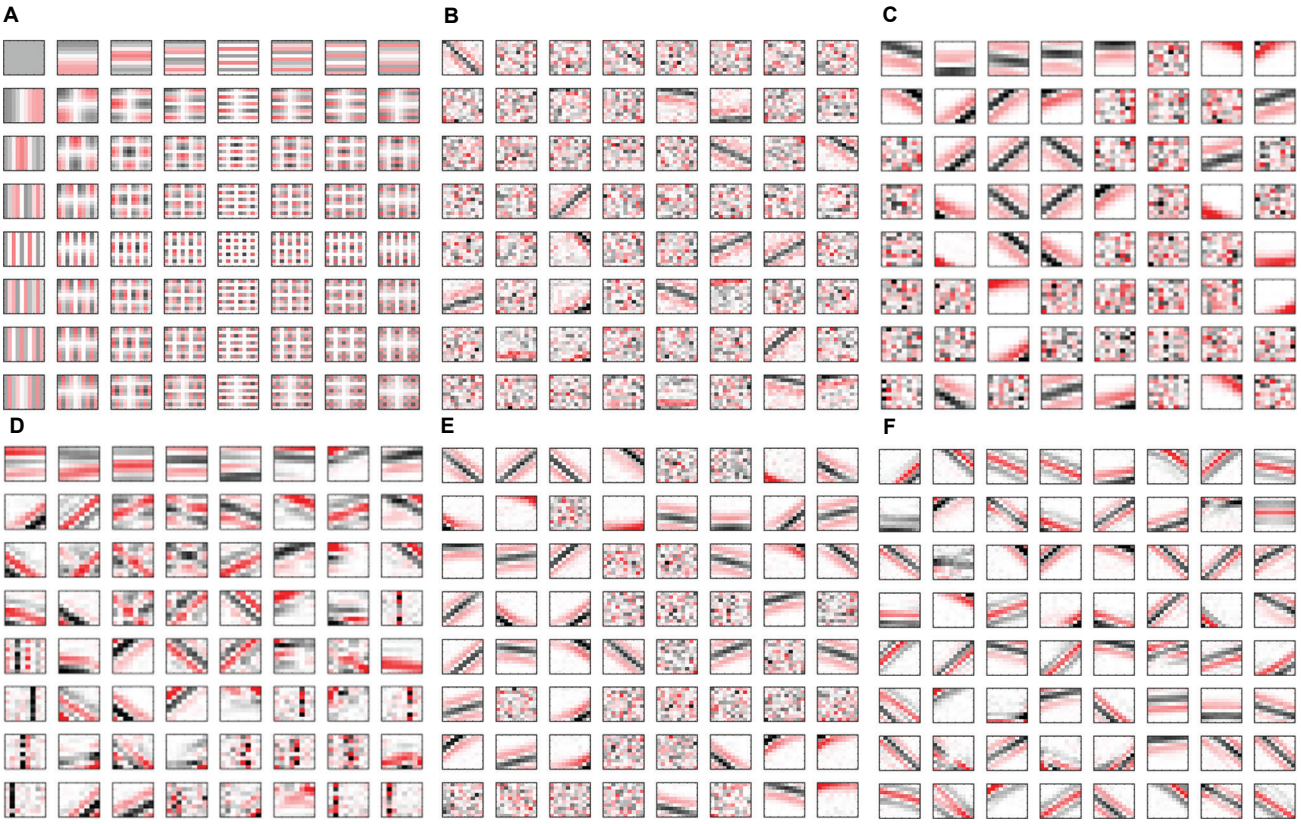


**Figure 4.** Dictionary comparison. (A) The DCT dictionary, (B) the dictionary obtained from the variational sparse representation (V) model, (C) the dictionary obtained after updating the DCT dictionary using the VSGK method, (D) the dictionary obtained after updating the DCT dictionary using the VK-SVD method, (E) the dictionary obtained after updating (B) using the VSGK method, and (F) the dictionary obtained after updating (B) using the VK-SVD method.
Abbreviations: D: Discrete cosine transform; K-SVD: K-singular value decomposition; SGK: Sequential generalization of K-means.

seismic data and have a fixed morphology, while the initial dictionary trained by the variational sparse representation model already captured some characteristics of the seismic data. Figure 4C and D shows the updated dictionaries after updating the DCT dictionary, whereas Figure 4E and F shows the updated dictionaries from the proposed method. The dictionary trained by the variational sparse representation model exhibited a richer morphology after updating and extracted more features from the seismic data. Figure 3 presents the results of reconstruction and denoising using different methods. We can observe that both VSGK and VK-SVD exhibited less effective signal loss compared to SGK and K-SVD, which used the DCT dictionary as the initial dictionary. These methods improved the SNR from 2.07 dB to 10.72 dB (SGK), 11.63 dB (K-SVD), 11.75 dB (VSGK), and 14.43 dB (VK-SVD).

To visualize the details, we conducted a spectrum analysis of the results processed by four methods (Figure 5). Figure 5A presents the spectrum corresponding to the clean data, while Figure 5B displays the spectrum of the noisy data after 0.3 random traces are missing. Figure 5C-F displays the spectrum corresponding to the denoising results from SGK, K-SVD, VSGK, and VK-SVD, respectively. From the figures, it can be seen that both SGK and K-SVD removed some useful signals, but K-SVD experienced slightly lower loss of useful signals. The spectrum obtained through the proposed method closely matches that of the original data. Figure 5G-J shows the difference in spectra between the original data and the processed results. It is evident that VSGK and VK-SVD exhibited fewer useful signals in their denoising residuals, with VK-SVD showing this more prominently.

To further evaluate the four methods, we extracted the 50$^{th}$ trace from the results of each method for single-trace analysis, as shown in Figure 6. In the area enclosed by the red box, it is clear that the curves of the useful signals from VSGK and VK-SVD closely match the clean data, further demonstrating that the proposed method performs better in recovering effective signals.

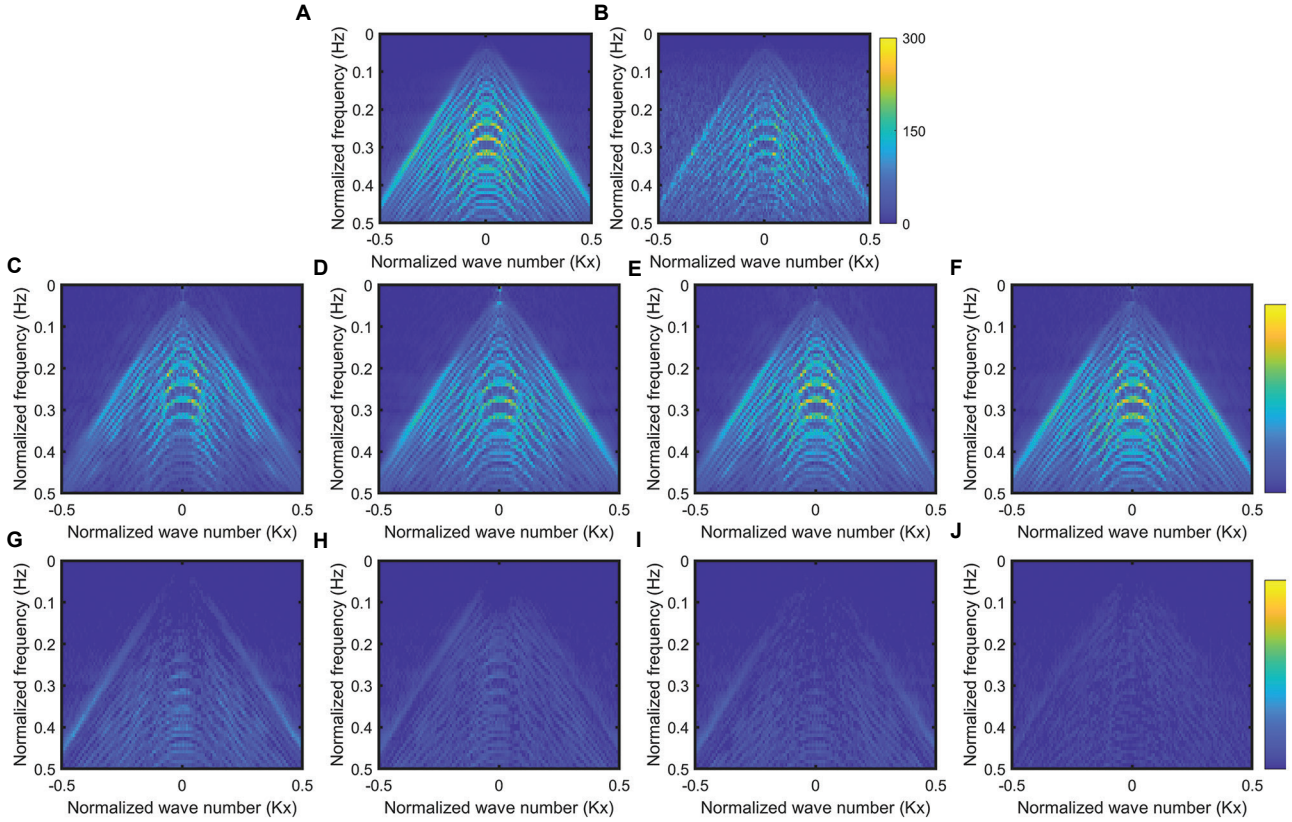


**Figure 5.** Frequency spectra comparison of various approaches. (A) Original data, (B) noisy data, (C) SGK, (D) K-SVD, (E) VSGK, and (F) VK-SVD. (G-J) The difference between processed data and original data.
Abbreviations: K-SVD: K-singular value decomposition; SGK: Sequential generalization of K-means; V: Variational sparse representation.

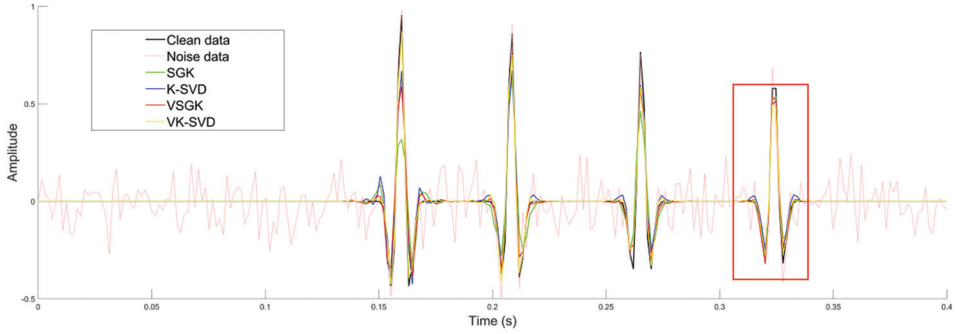


**Figure 6.** Single-channel seismic record analysis.
Abbreviations: K-SVD: K-singular value decomposition; SGK: Sequential generalization of K-means; V: Variational sparse representation.

### 4.2. Field data

This study evaluated the performance of the proposed method in seismic data reconstruction and noise suppression under practical scenarios, utilizing both pre-stack and post-stack field seismic datasets for testing and validation. Among these datasets, Figure 7 shows a pre-stack shot gather, which was acquired using the observation configuration of central-source excitation with bilateral geophone deployment. The propagation characteristics of seismic events and the spatial distribution pattern of noise can be clearly identified from the gather, which was thus employed as the baseline model for real seismic data testing. Figure 7 presents the pre-stack data used in the experiment, which not only exhibited 0.3 random trace missing but also contained significant background noise. To compare the processing effectiveness, four methods—SGK, K-SVD, VSGK, and

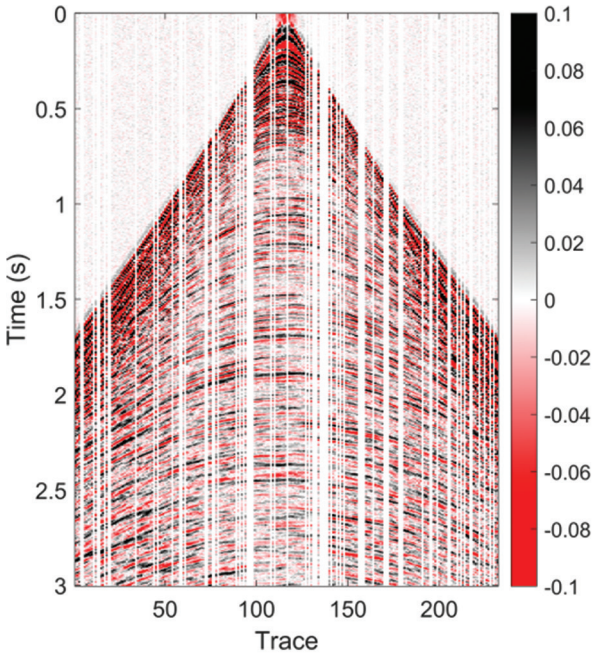


**Figure 7.** The first field data.

VK-SVD—were applied to this pre-stack data, with the results shown in Figure 8. The experimental results demonstrate that the SGK and K-SVD methods yielded unsatisfactory recovery of the missing traces, leading to noticeable degradation in the spatial continuity of seismic events. In contrast, the proposed VSGK and VK-SVD methods effectively reconstructed the missing seismic traces, significantly enhancing data integrity. However, during the noise suppression process, both methods exhibited a slight leakage of useful signals.

Figure 9 presents a post-stack seismic section in a tilted structural setting. The region with the most complex geological structures within this section was selected as the test target; the distinct tilted structural features of the section are suitable for verifying the applicability of the proposed method in scenarios with complex geological structures. The original data contains different types of events and has 0.3 randomly missing traces, along with a significant amount of noise near the events. Figure 10 displays the results processed by four methods. The results of SGK and K-SVD showed many missing seismic

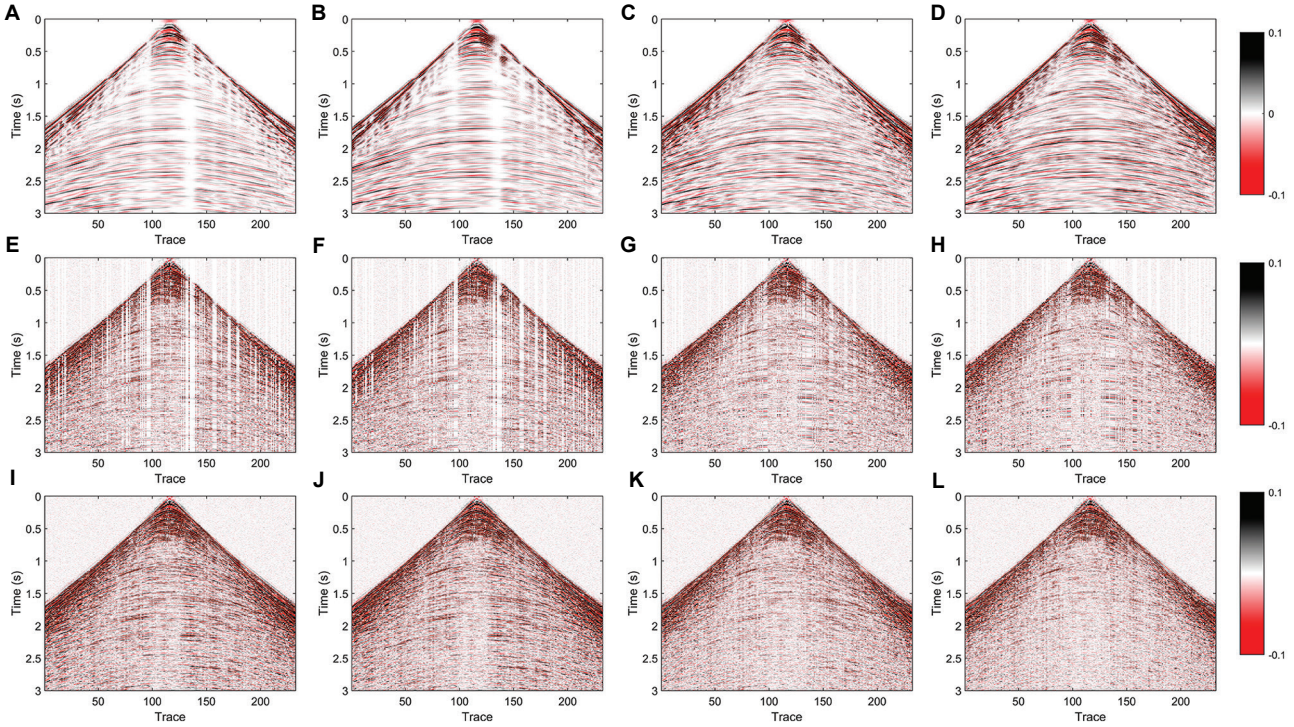


**Figure 8.** Comparison of the first field data results processed using various approaches. The result processed by (A) SGK, (B) K-SVD, (C) VSGK, and (D) VK-SVD. The residual between the (E) SGK-reconstructed data and the original data, (F) K-SVD-reconstructed data and the original data, (G) VSGK-reconstructed data and the original data, and (H) VK-SVD-reconstructed data and the original data. The noise that is removed by (I) SGK, (J) K-SVD, (K) VSGK, and (L) VK-SVD.
Abbreviations: K-SVD: K-singular value decomposition; SGK: Sequential generalization of K-means; V: Variational sparse representation.

data structures (Figure 10A and B), and the recovery of the missing trace was not ideal, compromising the continuity of the events. Figure 10C and G shows the results of reconstruction and denoising using VSGK and the removed noise profile. The experimental results clearly indicate that the method successfully retrieved the missing seismic channels, although there is still some leakage of useful signals. Specifically, the comparative results in Figure 10E-H intuitively demonstrate that the reconstruction performance of the method proposed in this study is significantly superior to that of other comparative methods. After processing with VK-SVD, the seismic events continuity remained effectively maintained, with negligible useful signals detectable in the removed noise profile.

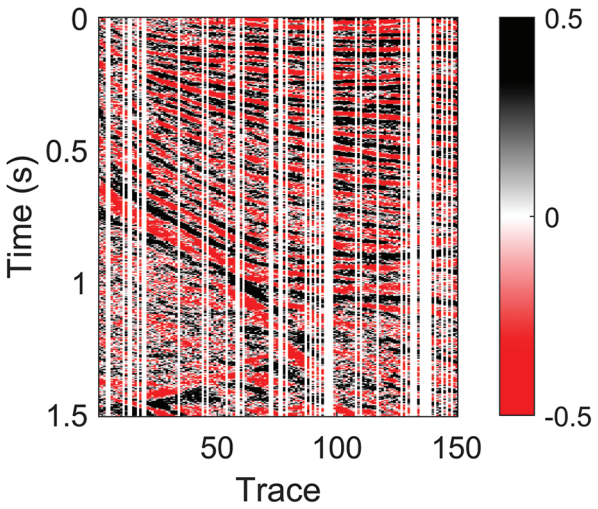


**Figure 9.** The second field data.

Next, we adopted the data shown in Figure 11 for numerical experiments. Figure 11 displays a post-stack seismic section with layered structures. Extracted from the post-stack seismic dataset of a real working area, this section was used as a test model to further validate the stability and generalization capability of the proposed method in layered geological settings. The results of reconstruction and denoising are presented in Figure 12. It is observed that SGK and K-SVD did not effectively

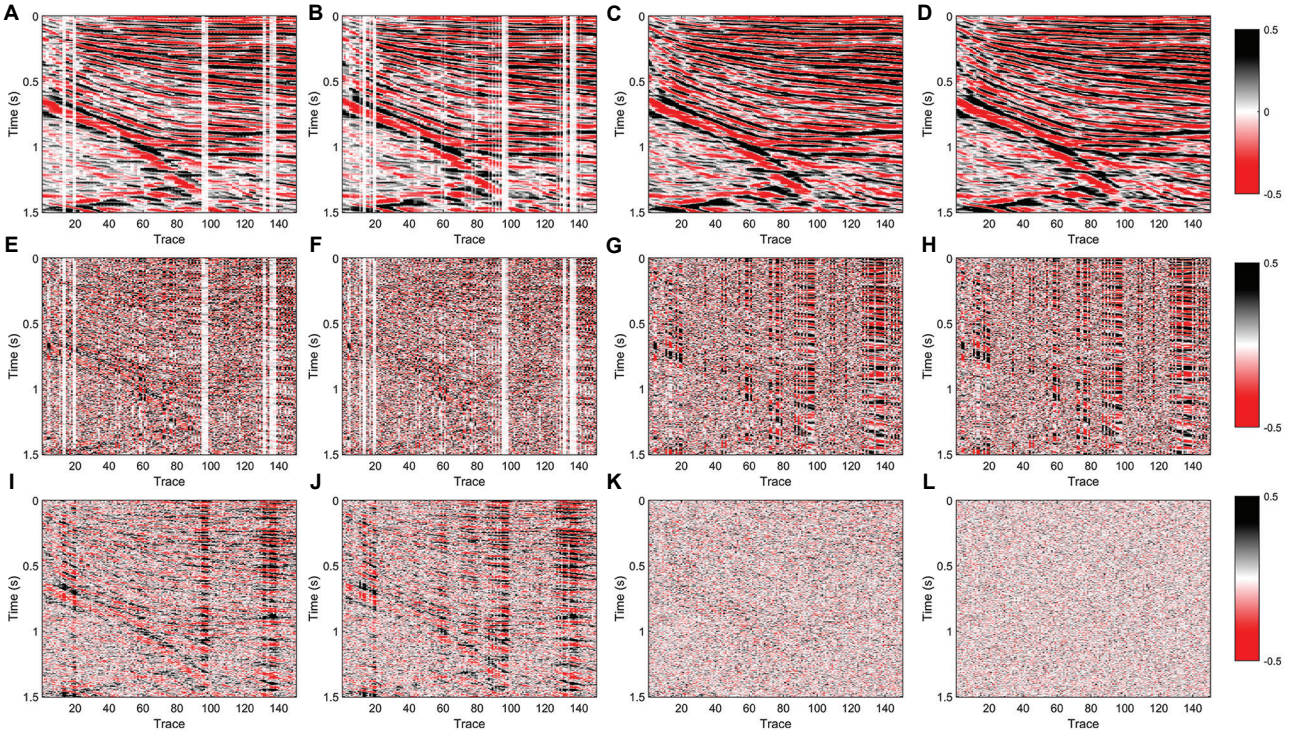


**Figure 10.** Comparison of the second field data results processed using various approaches. The result processed by (A) SGK, (B) K-SVD, (C) VSGK, and (D) VK-SVD. The residual between the (E) SGK-reconstructed data and the original data, (F) K-SVD-reconstructed data and the original data, (G) VSGK-reconstructed data and the original data, and (H) VK-SVD-reconstructed data and the original data. The noise that is removed by (I) SGK, (J) K-SVD, (K) VSGK, and (L) VK-SVD.
Abbreviations: K-SVD: K-singular value decomposition; SGK: Sequential generalization of K-means; V: Variational sparse representation.

recover the partially missing seismic data after processing (Figure 12A and B), and caused damage to a significant amount of useful signals while suppressing noise. In contrast, the results processed by VSGK and VK-SVD (Figure 12C and D) showed clearer events and retained more details of the seismic data structure compared to the first two methods. Further analysis revealed that the proposed method exhibited excellent data reconstruction performance, whereas the SGK and K-SVD methods showed distinctly unsatisfactory reconstruction results (Figure 12E-H).

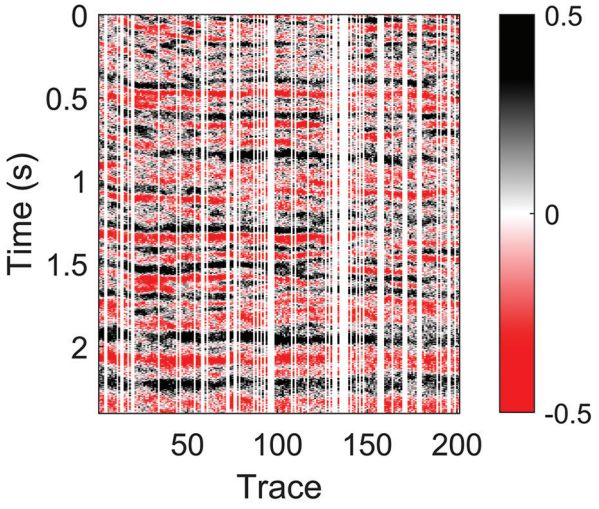


**Figure 11.** The third field data.

### 4.3. Robustness analysis in seismic denoising and reconstruction

To verify the applicability of the method proposed in this study in complex data scenarios, the original data were subjected to a 0.5 random missing treatment (Figure 13). From the denoising and reconstruction results (Figure 14), it can be seen that both VSGK and VK-SVD repaired the missing regions in the data and effectively suppressed random noise, fully demonstrating the advantages of the two methods in denoising and reconstruction.

To further investigate the robustness of the methods, the noise intensity was additionally increased based on 0.5 random missing values of the original

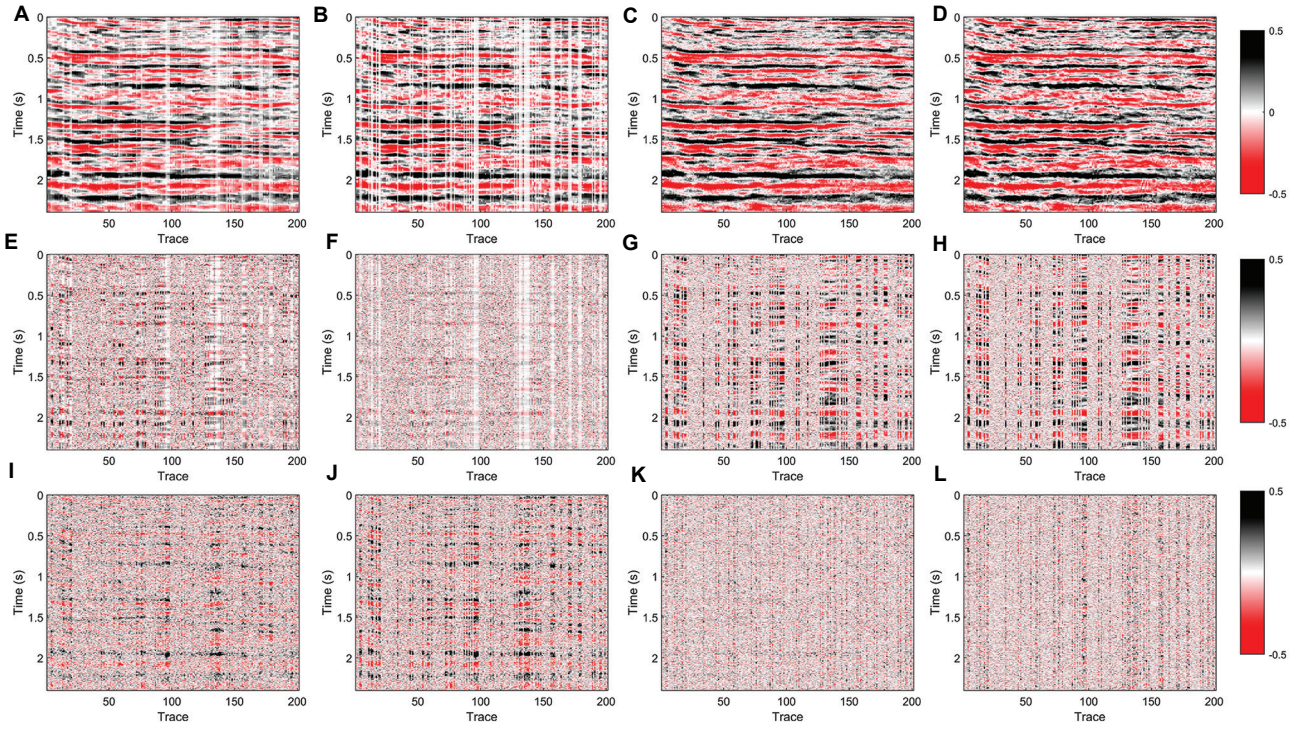


**Figure 12.** Comparison of the third field data results processed using various approaches. The result processed by (A) SGK, (B) K-SVD, (C) VSGK, and (D) VK-SVD. The residual between the (E) SGK-reconstructed data and the original data, (F) K-SVD-reconstructed data and the original data, (G) VSGK-reconstructed data and the original data, and (H) VK-SVD-reconstructed data and the original data. The noise that is removed by (I) SGK, (J) K-SVD, (K) VSGK, and (L) VK-SVD.
Abbreviations: K-SVD: K-singular value decomposition; SGK: Sequential generalization of K-means; V: Variational sparse representation.

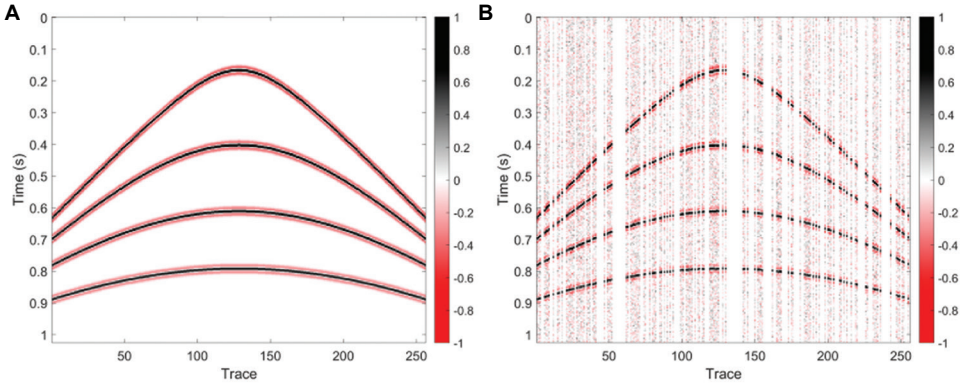


**Figure 13.** Original data and noisy data with random missing 0.5 data. (A) Original data, (B) noisy data with random missing 0.5 data.

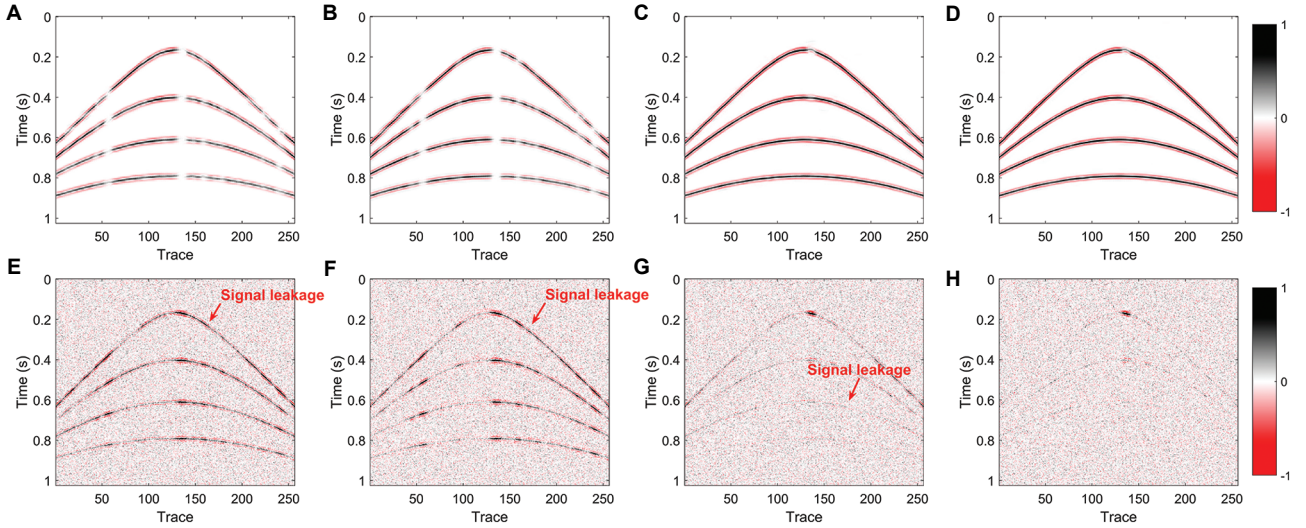


**Figure 14.** Comparison of the results of data with 0.5 missing treatment processed using various approaches. The result processed by (A) SGK, (B) K-SVD, (C) VSGK, and (D) VK-SVD. The noise that is removed by (E) SGK, (F) K-SVD, (G) VSGK, and (H) VK-SVD.
Abbreviations: K-SVD: K-singular value decomposition; SGK: Sequential generalization of K-means; V: Variational sparse representation.

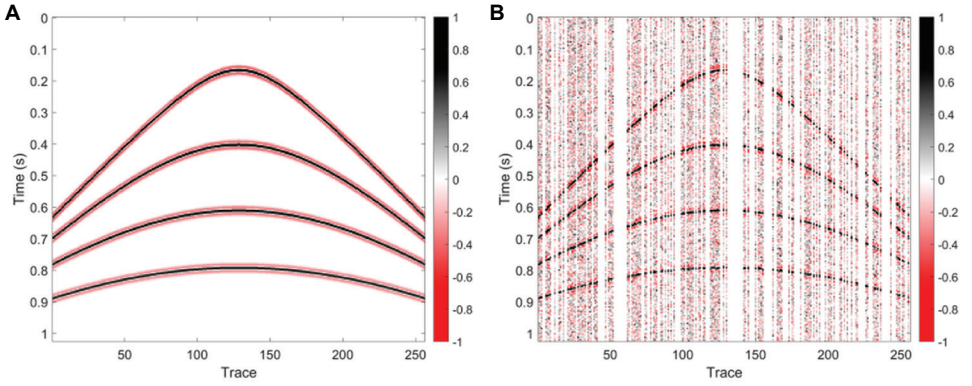


**Figure 15.** Original data and noisy data with random missing 0.5 data (with enhanced noise intensity). (A) Original data, (B) noisy data with random missing 0.5 data.

data (Figure 15). The comparative experimental results (Figure 16) indicate that the denoising and reconstruction effects of VSGK and VK-SVD were significantly superior to those of the traditional SGK

and K-SVD methods, with obvious advantages in terms of data integrity and SNR improvement. However, due to the dual interference of high missing rate and strong noise, there is still a small amount of noise residue in the reconstruction results of the two methods, which have not yet reached the ideal state of complete noise-free. This also provides a direction for the subsequent optimization of the methods.

To verify the comprehensive performance of the method proposed in this study, two groups of comparative experiments were designed on synthetic seismic data. The first group was subjected to a block-missing combined with noise test experiment. Based on the original data in Figure 17, a noisy dataset with a 0.2 block missing rate was constructed. The denoised and reconstructed results obtained by the proposed method are shown in Figure 18, which indicates that the method still maintains excellent performance under the interference of complex missing and noise. The second group was subjected to a horizontal comparison experiment of algorithms. Taking the original data in Figure 2 as the benchmark, the dataset was processed using three methods, namely VSGK, VK-SVD, and damped rank-reduction (DRR). The experimental results are presented in Figure 19. VSGK and VK-SVD can accurately reconstruct the missing seismic events while denoising, and their performance was significantly superior to that of DRR, whereas DRR exhibited an advantage in computational efficiency.

Seismic data denoising and reconstruction are key steps for subsequent geological structure interpretation. In practical production applications, it is necessary to balance the dual requirements of processing accuracy and computational efficiency.

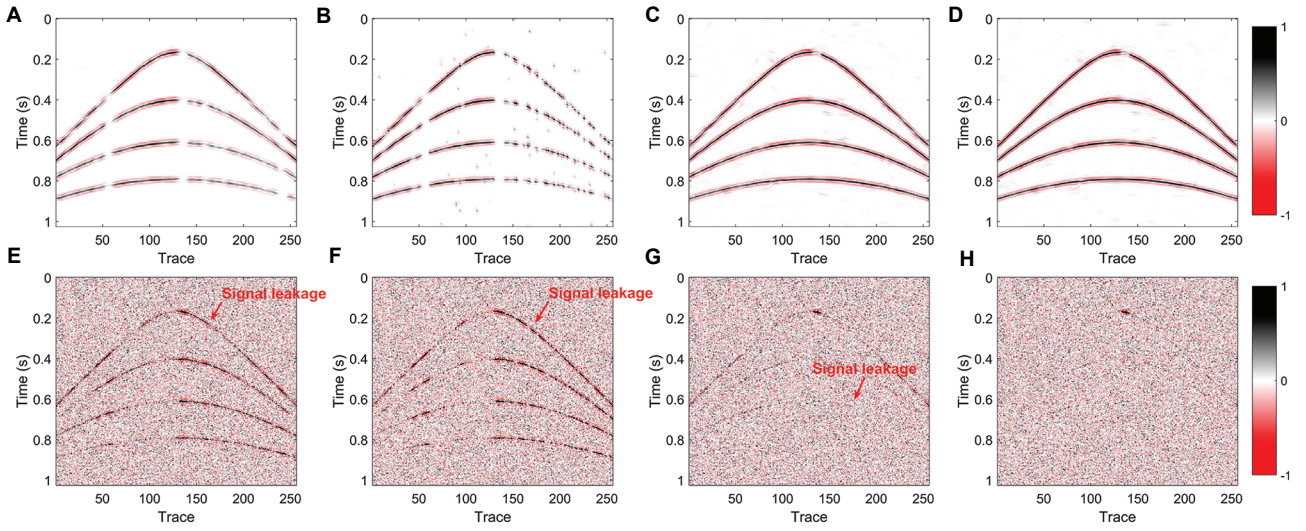


**Figure 16.** Comparison of the results of data with random missing 0.5 data (with enhanced noise intensity) processed using various approaches. The result processed by (A) SGK, (B) K-SVD, (C) VSGK, and (D) VK-SVD. The noise that is removed by (E) SGK, (F) K-SVD, (G) VSGK, and (H) VK-SVD. Abbreviations: K-SVD: K-singular value decomposition; SGK: Sequential generalization of K-means; V: Variational sparse representation.

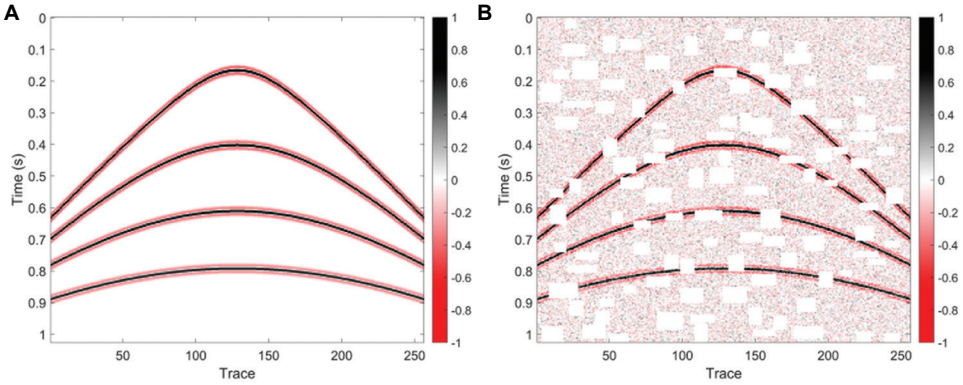


**Figure 17.** Original data and noisy data with a block missing 0.2 data. (A) Original data, (B) noisy data with block missing 0.2 data.

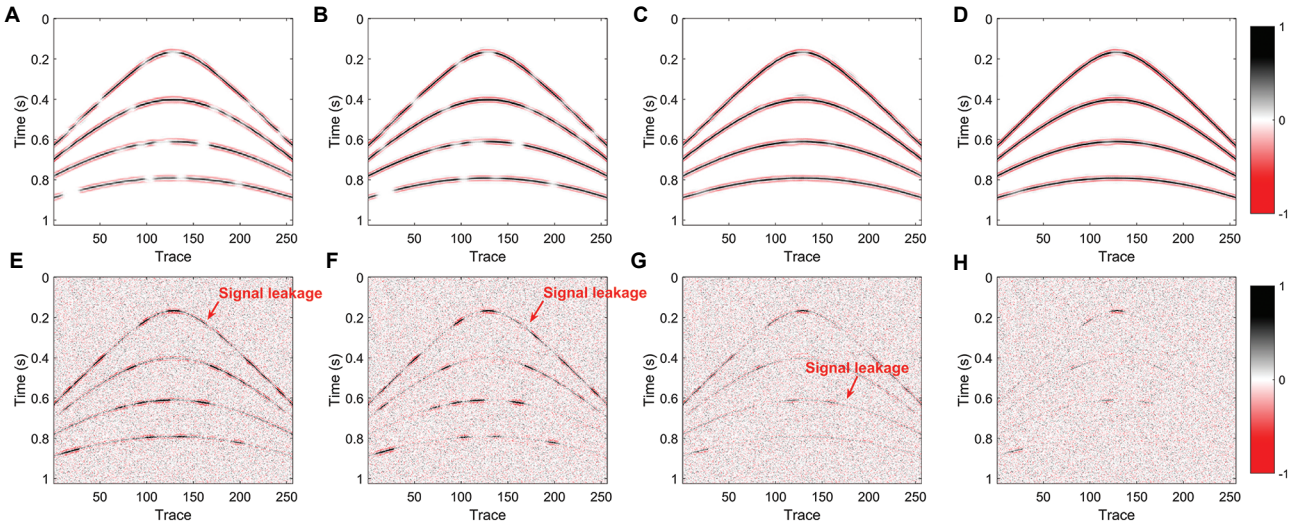


**Figure 18.** Comparison of the results of the block missing 0.2 data processed using various approaches. The result processed by (A) SGK, (B) K-SVD, (C) VSGK, and (D) VK-SVD. The noise that is removed by (E) SGK, (F) K-SVD, (G) VSGK, and (H) VK-SVD.
Abbreviations: K-SVD: K-singular value decomposition; SGK: Sequential generalization of K-means; V: Variational sparse representation.

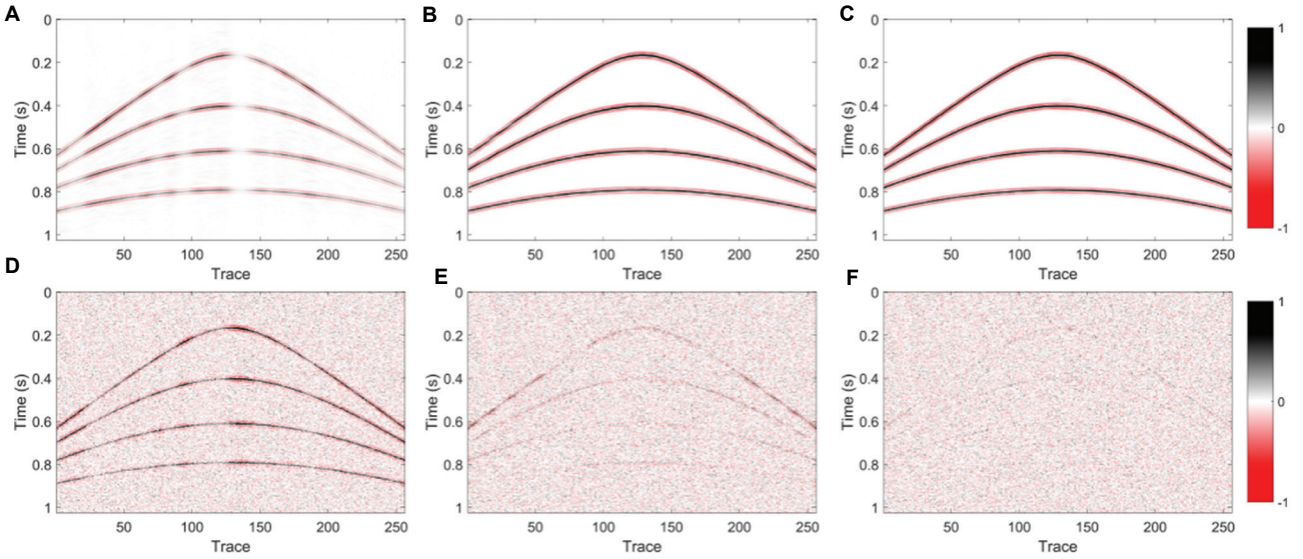


**Figure 19.** Comparison of the results of the block missing 0.2 data processed using various approaches. The result processed by (A) DRR, (B) VSGK, and (C) VK-SVD. The noise that is removed by (D) DRR, (E) VSGK, and (F) VK-SVD.
Abbreviations: DRR: Damped rank-reduction; K-SVD: K-singular value decomposition; SGK: Sequential generalization of K-means; V: Variational sparse representation.

**Table 1. Comparison of different algorithms**

| Algorithm | Time (s) | SNR (dB) | Peak SNR (dB) | SSIM |
|---|---|---|---|---|
| SGK | 102.82 | 6.95 | 23.51 | 0.894 |
| K-SVD | 1,538.46 | 10.09 | 26.65 | 0.930 |
| VSGK | 36.41 | 11.64 | 27.77 | 0.953 |
| VK-SVD | 66.11 | 15.43 | 32.00 | 0.964 |

Abbreviations: DRR: Damped rank-reduction; K-SVD: K-singular value decomposition; SGK: Sequential generalization of K-means; SNR: Signal-to-noise ratio; SSIM: Structural similarity index measure; V: Variational sparse representation.

Table 1 presents the comparison of the four methods when processing 256 × 256-sized data. The running time of VSGK was significantly shorter than that of SGK, and the running time of VK-SVD was lower than that of KSVD. Both improved methods greatly enhanced the efficiency of data processing, with further comparison showing that VSGK and VK-SVD improved the accuracy of reconstruction and denoising. Therefore, the proposed methods of variational sparse representation for pre-trained dictionary learning (VK-SVD and VSGK) not

only improved the accuracy of reconstruction and denoising but also greatly reduced computing time. These improvements could be attributed to the closer resemblance of the variational sparse representation-based pre-trained atoms to the characteristics of seismic data; hence, they converge faster during the iterative process, thus achieving high accuracy and saving computing time.

### 4.4. Impact of POCS initialization on reconstruction

To quantitatively assess the actual contribution of POCS as an initialization step in the dictionary-driven reconstruction process, this study compared the reconstruction performance of the VSGK and VK-SVD methods with and without POCS initialization on the same test dataset, and systematically contrasted the results with those of conventional SGK, K-SVD, and standalone POCS.

**Algorithm 1.** Adaptive-threshold projections onto convex sets for seismic data reconstruction

**Input:** Noisy and incomplete data $\mathbf{d}_0$,
mask $\mathbf{M}$, Maximum iterations N,
threshold decay ε,
Curvelet parameters: $n_{scales}$, $n_{angles}$
**Output:** Reconstructed data $\mathbf{D}_{rec}$
**Initialization:** $\mathbf{X}^{(0)} \leftarrow \boldsymbol{d}_0$, $\mathbf{1} \leftarrow ones\ (n_1, n_2)$;
**for** $i$=1 **to** $N$ $\mathbf{d}_0$

Forward Curvelet transform: $\mathbf{C} \leftarrow$ CURVELET $(\mathbf{X}^{(i-1)}, n_{scales}, n_{angles})$;
Compute maximum coefficient: $c_{max}=\max_{j,k}|\mathbf{C}[j, k]|$;
Adaptive exponential threshold: $\tau_i = c_{max} \cdot \exp\left(\frac{(i-1)\cdot(\ln \varepsilon - \ln c_{max})}{N-1}\right)$;
Hard thresholding: $\mathbf{C}[j, k] \leftarrow \mathbf{C}[j, k] \cdot \mathbf{1}_{|\mathbf{C}[j,k]|>\tau_i}$, $\forall j, k$;
Inverse Curvelet transform: $\mathbf{X}_{temp} \leftarrow$ INVERSE CURVELET $(\mathbf{C})$;
Data consistency (POCS): $\mathbf{X}^{(i)} \leftarrow (\mathbf{1} - \mathbf{M}) \odot \mathbf{X}_{temp} + \mathbf{d}_0$;

Final reconstruction:
$\mathbf{C}_{final} \leftarrow$ CURVELET $(\mathbf{X}^{(N)}, n_{scales}, n_{angles})$
$\mathbf{D}_{rec} \leftarrow$ Re (INVERSE CURVELET $(\mathbf{C}_{final})$)
**return** $\mathbf{D}_{rec}$

The POCS algorithm employed in this paper is presented in Algorithm 1.

Figure 20 compares the reconstruction results of different algorithms on noisy seismic data. Figure 20A-E shows the reconstructed profiles. POCS exhibited significant residual noise, while VSGK and VK-SVD recovered the seismic events and suppressed random noise reasonably well, though their performance decreased in highly curved regions. Combining POCS with VSGK or VK-SVD (VSGK+POCS and VK-SVD+POCS) significantly improved the reconstruction, enhancing the continuity of seismic events. Figure 20F-J displays the removed noise for each method. POCS removed limited energy, appearing as narrow-band streaks; VSGK and VK-SVD removed more random noise but partially attenuated the useful signals. When combined with POCS, noise was effectively suppressed while preserving the signals. Figure 20K-O presents the residuals between the reconstructed results and the original data, showing that the seismic event energies for VSGK+POCS and VK-SVD+POCS were significantly higher than those of other methods, further demonstrating their superiority in reconstruction accuracy and structural preservation.

Table 2 compares the performance of seven reconstruction algorithms on noisy seismic data in terms of run time, SNR, PSNR, SSIM, SNR gain, and SNR gain rate. Among the methods, VK-SVD + POCS achieved the highest reconstruction quality, with an SNR of 15.43 dB, PSNR of 32.00 dB, and SSIM of 0.964, indicating excellent noise suppression and structural preservation. Although K-SVD and SGK can also reconstruct the data, they require higher computational costs and deliver inferior results compared to methods combined with POCS. POCS alone has limited denoising capability, but when combined with VSGK or VK-SVD, it enhances SNR gain and seismic event continuity, yielding better reconstruction. Overall, POCS-

**Table 2. Performance comparison of reconstruction algorithms with and without POCS initialization**

| Algorithm | Time (s) | SNR (dB) | Peak SNR (dB) | SSIM | SNR gain (dB) | SNR rate (dB/s) |
|---|---|---|---|---|---|---|
| POCS | 28.42 | 3.51 | 20.07 | 0.201 | 1.44 | 0.0507 |
| VSGK | 9.87 | 9.41 | 25.97 | 0.953 | 7.34 | 0.7437 |
| VK-SVD | 39.78 | 11.13 | 27.70 | 0.947 | 9.06 | 0.2277 |
| VSGK+POCS | 36.41 | 11.64 | 27.77 | 0.953 | 9.57 | 0.2628 |
| VK-SVD+POCS | 66.11 | 15.43 | 32.00 | 0.964 | 13.36 | 0.2021 |
| SGK | 102.82 | 6.95 | 23.51 | 0.894 | 4.88 | 0.0475 |
| K-SVD | 1,538.46 | 10.09 | 26.65 | 0.930 | 8.02 | 0.0052 |

Abbreviations: K-SVD: K-singular value decomposition; POCS: Projections onto convex sets; SGK: Sequential generalization of K-means; SNR: Signal-to-noise ratio; SSIM: Structural similarity index measure; V: Variational sparse representation.

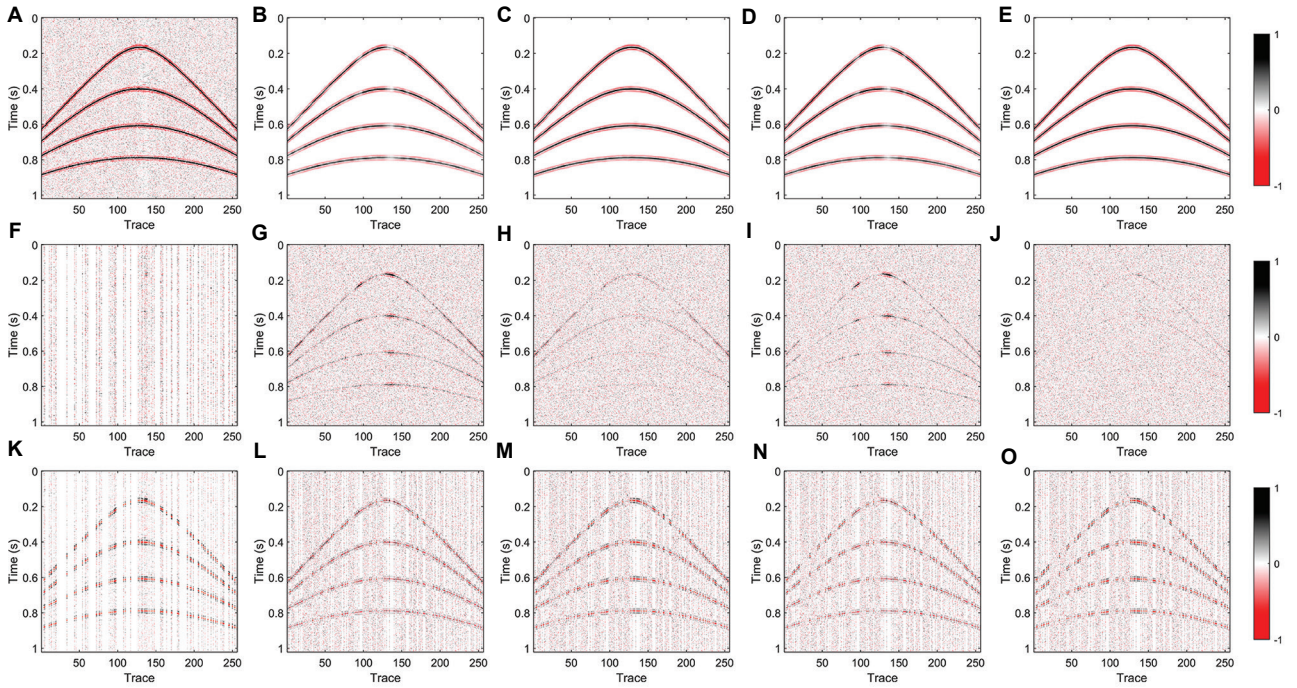


**Figure 20.** Comparison of the results of noisy seismic data processed using various approaches. The result processed by (A) POCS, (B) VSGK, (C) VSGK + POCS, (D) VK-SVD, and (E) VK-SVD + POCS. The noise that is removed by (F) POCS, (G) VSGK, (H) VSGK + POCS, (I) VK-SVD, and (J) VK-SVD + POCS. The residual between the (K) POCS-reconstructed and the original data, (L) VSGK-reconstructed and the original data, (M) VSGK + POCS-reconstructed and the original data, (N) VK-SVD-reconstructed and the original data, and (O) VK-SVD + POCS-reconstructed and the original data
Abbreviations: K-SVD: K-singular value decomposition; POCS: Projections onto convex sets; SGK: Sequential generalization of K-means; V: Variational sparse representation.

based initialization improves reconstruction performance, with VSGK + POCS and VK-SVD+POCS achieving the best results.

## 5. Conclusion

We developed a new dictionary learning method based on a variational sparse representation model. This method performed a pre-training through the variational sparse representation model to conduct feature extraction from seismic signals, generating an initial dictionary. The dictionary was then updated by applying the SGK and K-SVD algorithms to further extract deep features from the data. In addition, multiple iterations of the POCS algorithm were employed to supplement some missing data features. The numerical experiments showed that VSGK and VK-SVD can effectively achieve interpolation and denoising. Compared to traditional SGK and K-SVD methods, the proposed methods learnt deeper features from the data, resulting in significant improvements in the performance of denoising and reconstruction, particularly in maintaining lower signal leakage.

## Acknowledgments

None.

## Funding

This research was supported by the Open Fund of the National Engineering Research Center for Computer Software for Oil & Gas Exploration (grant no. DFWT-ZYRJ-2024-JS-83).

## Conflict of interest

The authors declare no conflicts of interest.

## Author contributions

*Conceptualization:* Jianlei Zhang, Min Bai, Xilin Qin, Baobin Wang, Zhen Zou
*Formal analysis:* Min Bai, Xilin Qin
*Investigation:* Jianlei Zhang, Bo Yang
*Methodology:* Jianlei Zhang, Bo Yang
*Writing–original draft:* Bo Yang
*Writing–review & editing:* Bo Yang, Boyuan Lv

## Availability of data

The data generated or analyzed during this study are available from the corresponding author upon reasonable request.

## References


1. Canning A, Gardner GHF. Regularizing 3-D data sets with DMO. *Geophysics*. 1996;61:1103-1114.

   doi: 10.1190/1.1444031

2. Chemingui N, Biondi B. Handling the irregular geometry in wide-azimuth surveys. *SEG Int Expo Annu Meet*. 1996;10: 32-35.

   doi: 10.1190/1.1826634

3. Spitz S. Seismic trace interpolation in the F-X domain. *Geophysics*. 1991;56:785-794.

   doi: 10.1190/1.1443096

4. Li C, Liu G, Hao Z, Zu S, Mi F, Chen X. Multidimensional seismic data reconstruction using frequency-domain adaptive prediction-error filter. *IEEE Trans Geosci Remote Sens*. 2018;56:2328-2336.

   doi: 10.1109/tgrs.2017.2778196

5. Gao J, Sacchi MD, Chen X. A fast reduced-rank interpolation method for prestack seismic volumes that depend on four spatial dimensions. *Geophysics*. 2012;78:V21-V30.

   doi: 10.1190/geo2012-0038.1

6. Zhang D, Zhou Y, Chen H, Chen W, Zu S, Chen Y. Hybrid rank-sparsity constraint model for simultaneous reconstruction and denoising of 3D seismic data. *Geophysics*. 2017;82:V351-V367.

   doi: 10.1190/geo2016-0557.1

7. Gao J, Stanton A, Naghizadeh M, Sacchi MD, Chen X. Convergence improvement and noise attenuation considerations for beyond alias projection onto convex sets reconstruction. *Geophys Prospect*. 2013;61:138-151.

   doi: 10.1111/j.1365-2478.2012.01103.x

8. Trad DO, Ulrych TJ, Sacchi MD. Accurate interpolation with high-resolution time-variant radon transforms. *Geophysics*. 2002;67:644-656.

   doi: 10.1190/1.1468626

9. Hennenfent G, Fenelon L, Herrmann FJ. Nonequispaced curvelet transform for seismic data reconstruction: A sparsity-promoting approach. *Geophysics*. 2010;75:WB203-WB210.

   doi: 10.1190/1.3494032

10. Fomel S, Liu Y. Seislet transform and seislet frame. *Geophysics*. 2010;75:V25-V38.

    doi: 10.1190/1.3380591

11. Gan S, Wang S, Chen Y, Zhang Y, Jin Z. Dealiased seismic data interpolation using seislet transform with low-frequency constraint. *IEEE Geosci Remote Sens Lett*. 2015;12: 2150-2154.

    doi: 10.1109/lgrs.2015.2453119

12. Li H, Han L, Zhang L, Jia S. Seismic data reconstruction using dictionary learning and the alternating direction method of multipliers. *Geophys Prospect Pet*. 2019;58(3):419-426.

    doi: 10.3969/j.issn.1000-1441.2019.03.011

13. Wang B, Lu W, Chen X, Wang Z. Efficient seismic data interpolation using three-dimensional curvelet transform in the frequency domain. *Geophys Prospect Pet*. 2018;57(1):65-71.

    doi: 10.3969/j.issn.1000-1441.2018.01.009

14. Zhu L, Liu E, McClellan JH. Joint seismic data denoising and interpolation with double-sparsity dictionary learning. *J Geophys Eng*. 2017;14(4):802-810.

    doi: 10.1088/1742-2140/aa6491

15. Gelis LE, Gómez JL, Velis DR. Structured Noise Removal with Dictionary Learning in Seismic Data: The Effect of Atom Filtering. In: *Proceedings of the IEEE International Workshop on Remote Sensing with Intelligent Processing (RPIC)*. Salvador, Brazil: IEEE; 2019. p. 204-208.

    doi: 10.1109/rpic.2019.8882163

16. Wang W, Yang J, Huang J, Li Z, Sun M. Outlier denoising using a novel statistics-based mask strategy for compressive sensing. *Remote Sens*. 2023;15(2):447.

    doi: 10.3390/rs15020447

17. Cai J, Ji H, Shen Z, Ye G. Data-driven tight frame construction and image denoising. *Appl Comput Harmon Anal*. 2014;37:89-105.

    doi: 10.1016/j.acha.2013.10.001

18. Zhou Z, Bai M, Wu J, Cui Y. Coherent noise attenuation by kurtosis-guided adaptive dictionary learning based on variational sparse representation. *IEEE Trans Geosci Remote Sens*. 2023;61:1-10.

    doi: 10.1109/tgrs.2023.3286791

19. Wang W, Yang J, Li Z, Huang J, Zhao C. Seismic data denoising using a new framework of FABEMD-based dictionary learning. *IEEE Trans Geosci Remote Sens*. 2024;62:1-9.

    doi: 10.1109/tgrs.2024.3396459

20. Oropeza V, Sacchi M. Simultaneous seismic data denoising and reconstruction via multichannel singular spectrum analysis (MSSA). *Geophysics*. 2011;76:V25-V32.

    doi: 10.1190/1.3552706

21. Naghizadeh M. Seismic data interpolation and denoising in the frequency-wavenumber domain. *Geophysics*. 2012;77:71-80.

    doi: 10.1190/geo2011-0172.1

22. Siahsar MA, Gholtashi S, Abolghasemi V, Chen Y. Simultaneous denoising and interpolation of 2D seismic data using data-driven non-negative dictionary learning. *Signal Process*. 2017;141:309-321.

doi: 10.1016/j.sigpro.2017.06.017

23. Yu S, Ma J, Zhang X, Sacchi MD. Interpolation and denoising of high-dimensional seismic data by learning a tight frame. *Geophysics*. 2015;80:V119-V132.

doi: 10.1190/geo2014-0396.1

24. Turquais P, Asgedom EG, Söllner W, Gelius L. Parabolic dictionary learning for seismic wavefield reconstruction across the streamers. *Geophysics*. 2018;83:V263-V282.

doi: 10.1190/geo2017-0694.1

25. Beckouche S, Ma J. Simultaneous dictionary learning and denoising for seismic data. *Geophysics*. 2014;79(3):A27-A31.

doi: 10.1190/geo2013-0382.1

26. Turquais P, Asgedom EG, Söllner W. A method of combining coherence-constrained sparse coding and dictionary learning for denoising. *Geophysics*. 2017;82(3):V137-V148.

doi: 10.1190/geo2016-0164.1

27. Siahsar MA, Gholtashi S, Torshizi EO, Chen W, Chen Y. Simultaneous denoising and interpolation of 3-D seismic data via damped data-driven optimal singular value shrinkage. *IEEE Geosci Remote Sens Lett*. 2017;14: 1086-1090.

doi: 10.1109/lgrs.2017.2697942

28. Chen W, Saad OM, Oboué YASI, Yang L, Chen Y. Retrieving the leaked signals from noise using a fast dictionary-learning method. *Geophysics*. 2021;87(1):V39-V49.

doi: 10.1190/geo2021-0243.1

29. Aharon M, Elad M, Bruckstein A. K-SVD: An algorithm for designing overcomplete dictionaries for sparse representation. *IEEE Trans Signal Process*. 2006;54(11):4311-4322.

doi: 10.1109/tsp.2006.881199

30. Rubinstein R, Zibulevsky M, Elad M. Double sparsity: Learning sparse dictionaries for sparse signal approximation. *IEEE Trans Signal Process*. 2009;58(3):1553-1564.

doi: 10.1109/tsp.2009.2036477

31. Wang B, Wu R, Chen X, Li J. Simultaneous seismic data interpolation and denoising with a new adaptive method based on dreamlet transform. *Geophys J Int*. 2015;201(2):1182-1194.

doi: 10.1093/gji/ggv072

32. Almadani M, Waheed UB, Masood M, Chen Y. Dictionary learning with convolutional structure for seismic data denoising and interpolation. *Geophysics*. 2021;86(5):V361-V374.

doi: 10.1190/geo2019-0689.1

33. Li C, Wen X, Liu X, Zu S. Simultaneous seismic data interpolation and denoising based on nonsubsampled contourlet transform integrating with two-step iterative log thresholding algorithm. *IEEE Trans Geosci Remote Sens*. 2022;60:1-10.

doi: 10.1109/tgrs.2022.3192531

34. Kaplan ST, Sacchi MD, Ulrych TJ. Sparse coding for data-driven coherent and incoherent noise attenuation. In: *SEG Technical Program Expanded Abstracts*; 2009. p. 3327-3331.

doi: 10.1190/1.3255551

35. Wang H, Chen W, Zhang Q, Liu X, Zu S, Chen Y. Fast dictionary learning for high-dimensional seismic reconstruction. *IEEE Trans Geosci Remote Sens*. 2021;59(8):7098-7108.

doi: 10.1109/tgrs.2020.3030740

# Our Journals

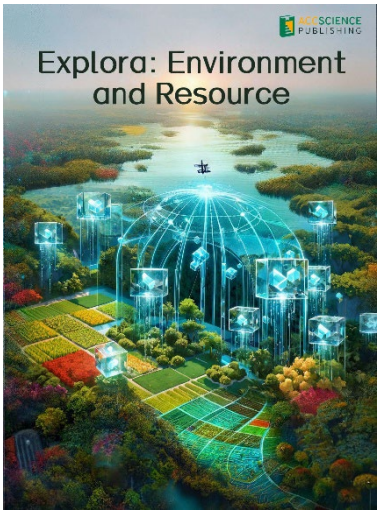


*Explora: Environment and Resource (EER)* is an international and multidisciplinary journal covering all aspects of the environmental impacts of socio-economic development. It is concerned with the complex interactions among society, development, and the environment, aiming to explore ways and means of achieving sustainability in all human activities related to development.

*EER* covers subject areas, including but not limited to the following:

- Water reclamation, wastewater treatment and waste management for eco-environment sustainability
- Innovative nanotechnology, catalysis, photocatalysis and nano materials for decontamination practices and renewable energy resources.
- Climate change-related sustainable resource and environment quality analysis
- Microorganisms and plants-oriented low-carbon processes and strategies for clean energy, water and resource management

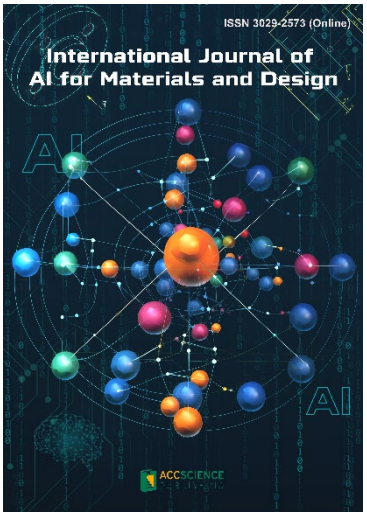


*International Journal of AI for Materials and Design* is an international, peer-reviewed open-access journal that aims to bridge the cutting-edge research between AI and materials, AI and design. In recent years, the tremendous progress in AI is leading a radical shift of AI research from a mainly academic endeavor to a much broader field with increasing industrial and governmental investments. The maturation of AI technology brings about a step change in the scientific research of various domains, especially in the world of materials and design. Machine learning (ML) algorithms enable researchers to analyze extensive datasets on material properties and accurately predict their behavior in different conditions. This subsequently impact the industry to leverage on big data and advanced analytics to build scientific strategies, scale operational performance of processes and drive innovation. In addition, AI and ML are uniquely positioned to enable advanced manufacturing technologies across the value chain of different industries. Integration of multiple and complementary AI techniques, such as ML, search, reasoning, planning, and knowledge representation, will further accelerate advances in scientific discoveries, engineering excellence and the future of cyber-physical systems manufacturing.

*International Journal of AI for Materials and Design* covers the following topics: AI or machine learning for material discovery, AI for process optimization, AI and data-driven approaches for product or systems design, application of AI in advanced manufacturing processes such as additive manufacturing, IoT, sensors, robotics, cloud-based manufacturing, intelligent manufacturing for various applications, autonomous experiments, material intelligence, energy intelligence, and AI-linked decarbonization technologies.

## Start a new journal

Write to us via email if you are interested to start a new journal with AccScience Publishing. Please attach your CV, professional profile page and a brief pitch proposal in your email. We shall inform you of our decision whether we are interested to collaborate in starting a new journal.

**Contact:** info@accscience.com

https://accscience.com/journal/JSE

Access Science Without Barriers

**Contact**

www.accscience.com
9 Raffles Place, Republic Plaza 1 #06-00 Singapore 048619
E-mail: editorial@accscience.com
Phone: +65 8182 1586